Université catholique de Louvain
Faculté des sciences
Institute of Condensed Matter and Nanosciences (IMCN)
MOST - Inorganic Chemistry

Place L. Pasteur 1, bte L4.01.03, 1348 Louvain-la-Neuve, Belgium
Tél. : + 32 (0) 10 47 28 31 – fax : +32 (0) 10 47 23 30
http://www.uclouvain.be/262038.html

Spin crossover (SCO) molecular switches have emerged as remarkable functional materials. Novel FeII SCO 1D chains with 4-amino-1,2,4-triazole (NH2trz) and diverse fluorinated inorganic anions varying in geometry/size/charge were investigated and a data bank based on the transition temperature and anions volume was delineated. Further insights on the role of anionic sublattice were gained thanks to 119Sn Mössbauer spectroscopy. The origin of the large hysteresis loop, accompanying the SCO in 1D chains as revealed and attributed to an extensive intra and inter molecular H-bonding network involving the counter anion. The precursor NH2trz was modified into 4-hydroxy-1,2,4-triazole and new Fe(II) chains were prepared.
For the first time 1,2,4-triazole derivatives of α- and ß-aminoesters were designed and introduced to produce new SCO 1D coordination polymers. A strong sensitivity of the SCO behavior was observed on increasing carbon spacer on going to ßAlatrz. An atypical two-step SCO behavior was thoroughly probed by spectroscopic studies. Further, an acid analogue, 4H-1,2,4-triazol-4-yl acetic acid, has been engineered and introduced as a superlative supramolecular synthon which has interesting topology wherein the two extremities are occupied by two potentially coordinating groups. Diverse topologies ranging from a 1D coordination polymer, 2D chiral helicate and a 3D MOF with a unique array of porous nanoballs architecture were obtained and their gas adsorption properties were studied.

Marinela M. Dîrtu, born in 1979 in Podu-Iloaiei, holds a Bachelor degree in Physical-Chemistry and a Master degree in Solid State Chemistry at University "Al I. Cuza"-Iasi and a DEA in Chemistry at UCL. During her PhD studies (2003-2010) she worked as a teaching assistant at UCL.

Engineering and functionality of molecular materials based on 1,2,4-triazole Marinela M. Dîrtu 281 | 2012

UCL

Engineering and functionality of new molecular materials based on 1, 2, 4-triazole building blocks: from molecular sensors to metal-organic/amino-acid frameworks

Marinela M. Dîrtu

Septembre 2012

Thèse présentée en vue de l'obtention
du grade de docteur en sciences

Faculté des sciences

Université catholique de Louvain

Engineering and functionality of new molecular materials based on 1, 2, 4-triazole building blocks: from molecular sensors to metal-organic/amino-acid frameworks

Thèse présentée en vue de l'obtention du grade
de docteur en sciences par

Marinela M. Dîrtu

Université Catholique de Louvain
Institut de la Matière Condensée et des Nanosciences,
Pôle Molécules, Solides et RéacTivité

This platform is an opportunity for me to acknowledge the personalities, who were directly or indirectly associated with this stretched, though but pleasant journey of one of the best period of my life. I would like to express my deepest gratefulness to all the people who made these years a “pleasant cruise”, molded my career and let wonderful everlasting memories in me.

It has been my distinct privilege to have the meaning of research and education exemplified to me by my research advisor Prof. Dr. Yann Garcia, IMCN, Université Catholique de Louvain. He is a superb and creative mentor. All of his ideas and innovations have inevitably found their way into this thesis. I am grateful for his doctrine to my learning and research and thankful to his everlasting support and counsels during all these years of my research. I thank him for all the opportunities he provided to me, to have collaborations with top international researchers including Mössbauer community and his generous sponsorship to present my research results in number of national and international conferences (GFSM, GDR, ICAME, in France, Austria, Italy, India), to widen my knowledge and to provide international exposure.

I also consider myself very fortunate to have been associated with some excellent collaborators, Professors Francois Varret, Jorge Linares, Brigit Weber, Kamel Boukheddaden, Cristian Enachescu and Grace Morgan. I would like to acknowledge my indebtness to them for giving so freely their time and helping me in many ways.

I owe special thanks to Dr. Juliusz Wolny, for fruitful discussions and in carrying out IR and Raman at variable temperature, Prof. Bernard Tinant and Dr. Christine Neuhausen for determination of crystal structures of my compounds and Dr. Aurelian Rotaru for SQUID measurements and diffuse reflectivity measurements under hydrostatic pressure. I am also

grateful to Prof. J. Ladrière and Prof. J. Linares who allowed me to use the Mössbauer spectrometers of their laboratories and for their precious help.

I express my gratitude to the members of the Chemistry Departement, Prof. M. Devillers, Prof. J. Marchand, Prof. O. Riant, Dr. K. Snoussi and the late Prof. J-L. Habib Jiwan for the interest they aroused in both inorganic and organic chemistry.

I wish to thank Dr. Anil D. Naik from the bottom of my heart for sharing his research experience. His knowledge of synthetic chemistry, his scientific rigor and his ability to give advice regardless of the matter of debate were very useful for me. I thank him for his constant support and encouragements.

I would like to thank Damien and France for the wonderful job they did during their research stay with us, and the way they responded to my research enthusiasm. I also thank and value the help of my colleagues, Antoine, Pierre-Loïc, Dr. Damir A. Safin, Dr. N. N. Adarsh and to J–F. Statsyns for the technical support.

I thank the "Université Caholique de Louvain", for the financial support and the opportunity to work as Teaching Assistant during my PhD work. Also special acknowledgement to all the members of CMAT/MOST department, who provided a vibrant and inspiring environment.

There are many friends who helped throughout my research. They know who they are and I hope they will accept my sincere thanks for all that they did. In particular I acknowledge the help of: Victor Ţilea, Anamaria Dumitrean, Elena Hrecinic, Ioana Obreja, Alina Georgescu. I am fortunate to have all these most patient and understanding friends.

My family has contributed much to the thesis, tangible and intangible, visible and invisible. My parents (Maria and Vasile Dîrţu and Marieana and Aurel Budaciu), my brother and sister (Liviu and Carmen Dîrtu), my husband (Andrei) and my children (Rafaïl and Ilie) who have tolerated and provided much over the years including love and support. They

“have been there” when I needed their unique help. To all of them go my deepest gratitude and thanks. I dedicate the present work to them.

Finally, I express my gratitude to all jury members for agreeing to reading and correcting this manuscript.

Jury Members:

Prof. Y. Garcia	Supervisor Université Catholique de Louvain
Prof. M. Devillers	Chair Université Catholique de Louvain
Prof. C-A. Fustin	Secretary Université Catholique de Louvain
Prof. J. Marchand-Brynaert	Université Catholique de Louvain
Prof. E. Goovaerts	Departementsraad Fysica Universiteit Antwerpen
Prof. J. Linares	UFR de Sciences - GEMaAC Versailles, France
Dr. V. Ksenofontov	Johannes Gutenberg Universität Mainz, Germany

Table of contents

Introduction.....**1**
Spin transition molecular materials **2**
Background of SCO phenomenon.....2
Application of ST compounds.....7
Influence on spin crossover behavior ……..….12
Spin transition in Fe(II) 1D chains based on 4-R-1,2,4-triazole..**15**

Aim and strategy.....**27**
Methodology **31**

Part I: Spin transition in M(II)- 4- amino-1,2,4-triazole Chain complexes: revealing the role of intermolecular interactions in NH_2trz, OH-trz and phtp-trz systems **37**

Chapter I: Prediction of the Spin Transition Temperature in Fe^{II} 1D NH_2trz Coordination Polymers: an anion based data base…….…… ……...**31**

Introducing remarks ……**37**
Synthesis ….…….……...**38**
X-ray crystal structure of $[Cu(NH_2trz)_3]ZrF_6 \cdot H_2O$…….....**41**
Thermal spin-crossover properties
SQUID magnetometry……..…….…….... 46
^{57}Fe Mössbauer spectroscopy ……...48
Differential scanning calorimetry (DSC) ……58
Diffuse reflectivity measurements under hydrostatic pressure….61
Discussion ……..**63**
Notes and references …….……**70**

Chapter II: Use of an Anionic Nuclear Probe to Sense the Spin Transition of 1D Coordination Polymers……...**75**

Introducing remarks ……**75**
Synthesis and general characterization ……..……...**75**
Study of the spin transition in $[Fe(NH_2trz)_3]SnF_6 \cdot nH_2O$…….....**80**
SQUID magnetometry ……81
^{57}Fe Mössbauer spectroscopy ……...83
X-ray powder diffraction ……..89
Calorimetric measurements ……..90
^{119}Sn Mössbauer spectroscopy ……...91
Discussion .……..**95**
Notes and references ……..**99**

Chapter III: Insights into the Origin of Cooperative Effects in the Spin Transition of $[Fe(NH_2trz)_3](NO_3)_2$ ……..……..…101

Introducing remarks ……...**101**

Synthesis and general characterization ……..……..**102**
X-ray crystal structure of $[Cu(NH_2trz)_3](NO_3)_2 \cdot H_2O$ (18).....**104**
Thermally Induced Spin Transition in $[Fe(NH_2trz)_3](NO_3)_2$ (17)
UV-Vis Diffuse reflectance spectroscopy……...112
^{57}Fe Mössbauer spectroscopy ……...…..113
X-ray powder thermo-diffractometry……..115
Differential scanning calorimetry……...….118
Magnetic susceptibility measurements……..…….....**119**
SQUID investigation ……..119
FORC diagram investigation ……..120
Discussion ……**125**
Notes and references ……..……..**130**

Chapter IV: Supramolecular Interactions and spin crossover properties of M(II) – 4 hydroxyl-1,2,4-triazole coordination compounds ……..**133**

Introducing remarks ……..….**133**

Synthesis and general characterization ……..……...**134**
X-ray crystal structure determination ……..…….....**138**
$[Cu(OH\text{-}trz)(ReO_4)OH] \cdot 2H_2O$ (**19**) 138
$[Zn(OHtrz)_2Cl](NO_3)$ (**20**) 142
Thermal spin-crossover properties
UV-Vis Diffuse reflectance spectroscopy ……..148
^{57}Fe Mössbauer spectroscopy 150
Discussion…….…….……**154**
Notes and references ……..……..…**158**

Chapter V: Thermo-switchable spin crossover iron(II)-phtalimido–propyl based coordination polymers……...…..**161**

V.1 Weak cooperativity in selected iron(II) 1D coordination polymers, based on phtalimido–propyl-1,2,4-triazole core ……**162**

Introducing remarks ……..…..**162**

Synthesis and general characterization ……..…….....**163**
Thermal spin-crossover properties
SQUID magnetometry……..…….…….167
^{57}Fe Mössbauer spectroscopy ……169

Discussion ……....**170**

V.2 Cooperativity variation in iron(II) 1D coordination polymers, based on monovalent counteranions…….…....**173**

Introducing remarks …… ……..…**173**

Synthesis and general characterization ……..…….....**173**

Thermal spin-crossover properties

SQUID magnetometry……..…….…….178

^{57}Fe Mössbauer spectroscopy ……180

Discussion ……..……...**184**

Chapter V.3: Steering molecular architecture and magnetism with remote and bulky *N*4-substitution on 1,2,4-triazole; A case study of 4-(3'-N-phtalimido-propyl)-1,2,4-triazole ……..……..**189**

Introducing remarks ……...**189**

Synthesis and structural characterization ……**190**

Crystal structures study:

4-(3'-N-phtalimido-propyl)-1,2,4-triazole (**phtptrz**) ……..191

$[Cu_3(phtptrz)_{10}(H_2O)_2](SiF_6)_3 \cdot 44H_2O$ (**28**) ….....193

$[Cu_3(phtptrz)_8(H_2O)_4](ZrF_6)_3 \cdot 19H_2O$ (**29**) 202

Magnetic study of $[Cu_3(phtptrz)_{10}(H_2O)_2](SiF_6)_3 \cdot 44H_2O$ (28) and $[Cu_3(phtptrz)_8(H_2O)_4](ZrF_6)_3 \cdot 19H_2O$ (29) 206

Discussion ……....210

Notes and references ……...…….216

PART II: Molecular sensors based on α – and β – amino-acid..**221**

Chapter VI: Superlative scaffold of 1,2,4-triazole α–amino-acid steering molecular architecture, increasing dimensionality from 1D to 3D……...……**222**

Introducing remarks ……..……..**222**

Synthesis and general characterization ..……...……**224**

Crystal structure study of ethyl-4H-1,2,4-triazol-4-yl acetic acid (**HGlytrz**) ……230

Crystal structure study of ethyl-4H-1,2,4-triazol-4-yl-acetate (**GlytrzE**)……..……..232

Crystal structure study of [Cd(HGlytrz) (Glytrz)Cl]· $2H_2O$ (**30**)……....237

Crystal structure study of $[Cd_2(Glytrz)_2Cl_2]$ (**31**)……....241

Crystal structure study of $[Cu_3(\mu_3\text{-}O)(HGlytrz)_3 \cdot (H_2O)_3]BF_4$ H_2O (**32**)……..246

Sorption Studies of $[Cd_2(Glytrz)_2Cl_2]$ (31) ……**252**
CdO preparation by controlled pyrolysis of $[Cd_2(Glytrz)_2Cl_2$…..**255**
Thermal analyses of $[Cu_3(\mu_3\text{-}O)(HGlytrz)_3\cdot(H_2O)_3]BF_4\cdot H_2O$...**256**
Sorption studies of $[Cu_3(\mu_3\text{-}O)(HGlytrz)_3\cdot(H_2O)_3]\ BF_4\cdot H_2O$....**258**
Concluding Remarks ……..……..**265**
Notes and references ……**269**

Chapter VII: Hysteretic spin transition materials, inspired and derived from an α–amino-acid derivative ……...…**275**

Chapter VII.1: Neutral and anionic duality of 1,2,4-triazole α–amino acid scaffold in 1D coordination polymers ……...…..**276**

Introducing remarks ……..**276**
Synthesis and characterization ……..….**277**
Thermal spin-crossover properties
^{57}Fe Mössbauer spectroscopy ……281
Discussion ……..……..**284**

Chapter VII.2: Hysteretic spin transition materials inspired and derived from an α-amino-acid derivative ……..…**287**

Introducing remarks ……...**287**
Synthesis and general characterization ……....**287**
Thermal spin-crossover properties
^{57}Fe Mössbauer spectroscopy ……294
SQUID magnetometry……..…….……..303
Dynamics of solvent molecules and influence on morphology after thermal treatment at 390 K ..……**307**
Differential Scanning Calorimetry……..**326**
Discussion ……...…..**331**
Notes and references ……..……..**343**

Chapter VIII: One step versus two steps spin crossover molecular sensors, based on β - amino-esters …...……..……**347**

Chapter VIII.1: Impact of counter-anion in selected 1D iron(II) spin crossover coordination polymers……..…..……**347**

Introducing remarks ……..……..**347**
Synthesis and general characterization ……..……**347**
Vibrational studies:

a) FT-IR and Raman analyses at room temperature …..……..350
b) FT-IR and RAMAN analyses at variable temperature for $47 \cdot H_2O$ ……351
Thermal spin-crossover properties - One step Iron(II) 1D Chain Compounds
SQUID magnetometry ……359
^{57}Fe Mössbauer spectroscopy ……361
Differential Scanning Calorimetry ……365
Discussion ……..……....**367**

Chapter VIII. 2: Thermal spin-crossover properties - two step iron (II) 1D Chain Compounds……..……....**370**
SQUID magnetometry ……370
^{57}Fe Mössbauer spectroscopy ……372
Differential Scanning Calorimetry ……377
FORC diagram investigation ……381
Discussion ……..…**384**
Notes and references ……..……..**397**

General discussion and concluding remarks ……...**401**

Perspectives ……**411**

List of publications and communications ……**415**

Written communications ……417
Oral communications ……423
Poster communications ……..424

Appendix ………....**a**
Crystal structure data ……**a**
Mösbauer Data ……**t**
Thermodynamic data ……**uu**
Materials ……...……..**ww**
Experimental section
Organic molecules ……...……ccc
Inorganic molecules ……..……..ggg

Abstract

Molecular electronics attained a rapid pace with the arrival of some of the ultimate switchable materials and foresees harvesting them as prospective components in fabricating accessories for information processing, data storage, sensors, etc. Spin crossover (SCO) molecular switches have emerged as remarkable switchable materials. Developing conventions that allow the tailoring of such functional materials with predictable architecture and properties is an important objective and in this respect, exhaustive physico-chemical, spectroscopic, magnetic, microscopic and structural investigation of SCO systems are expected.

Fe(II) coordination polymers (CP) based on 4-amino-1,2,4-triazole (NH_2trz) are known to yield excellent SCO materials. Novel Fe(II) SCO 1D CP materials with NH_2trz ligand with diverse fluorinated inorganic anions varying in geometry (TiF_6^{2-}, ZrF_6^{2-}, SnF_6^{2-}, GeF_6^{2-}, SbF_6^{2-}, TaF_7^{2-}) were investigated and a database on their transition temperature according to their volume is delineated based on magnetic data and ^{57}Fe Mossbauer spectroscopy. The internal electrostatic pressure of these anions located in the neighboring cationic chains, as well as chain lengths of these coordination polymers, was also estimated. Further insights on the role of non coordinating species (SnF_6^{2-}) were gained by ^{119}Sn Mössbauer spectroscopy which allowed tracking, for the first time, the SCO process. The origin of the large hysteresis loop, accompanying the SCO in 1D CP, $[Fe(NH_2trz)_3](NO_3)_2$, was revealed and was attributed to an extensive intra and inter molecular H-bonding involving the NO_3^- counter anion which was demonstrated with a model system. The precursor NH_2trz was slightly modified into 4-hydroxy-1,2,4-triazole (OHtrz) and a new Fe(II) chains were prepared and the crystal structures of 1D CPs, $[Cu(OH\text{-}trz)(ReO_4)OH]\cdot 2H_2O$ and $[Zn(OHtrz)_4Cl_2]$ were presented.

With predictable design strategy of transamination, for the first time 1,2,4-triazole derivatives of α- and β-aminoesters were designed and introduced to produce new SCO 1D CP. The impact of the variation of anions/solvents/pH of medium during the synthesis on the SCO behavior was demonstrated experimentally and supported by a theoretical approach on the series of $[Fe(L)_3]A_2$, L = αGlytrz (ethyl-4H-1,2,4-triazol-4-yl-acetate), βAlatrz (4H-1,2-4-triazol-4-yl-propionate), A = ClO_4^-, NO_3^-, BF_4^-, $CF_3SO_3^-$. An unprecedented large hysteresis width of 60 K was discovered for $[Fe(\alpha Glytrz)_3](NO_3)_2$ which operates around RT which would have huge technological significance. A strong sensitivity of the SCO behaviour was observed on increasing carbon spacer on going from αGlytrz to βAlatrz. In particular, $[Fe(\beta Alatrz)_3](BF_4)_2 \cdot H_2O$, undergo an atypical two-step spin transition which has been thoroughly probed by vibration studies. Further with crystal engineering approach, an acid analogue of αGlytrz, HGlytrz (4H-1,2,4-triazol-4-yl acetic acid) has been introduced as a superlative supramolecular synthon which has interesting topology wherein the two extremities are occupied by two potentially coordinating groups. Diverse topologies ranging from 1D CP, $[Cd(HGlytrz)(Glytrz)Cl] \cdot 2H_2O$, 2D chiral helicate - $[Cd_2(Glytrz)_2Cl_2]$ and a stunning self assembly into 3D MOF with an unique array of porous nanoballs architecture - $[Cu_3(\mu_3\text{-}O)(HGlytrz)_6 \cdot (H_2O)_3]BF_4 \cdot H_2O$ were obtained and their gas adsorption properties are reported.

Further re-designing the precursor for SCO, a new module for 1D CP, 4-(3'-N-phtalimido-propyl)-1,2,4-triazole (phtptrz) was then introduced. Its aromatic group, although bulky, is a potential promoter of supramolecular interactions due to π–π stacking and H-bonding interactions involving carbonyl groups, as evidenced in the crystal structures of $[Cu_3(phtptrz)_{10}(H_2O)_2](SiF_6)_3 \cdot 44H_2O$ and $[Cu_3(phtptrz)_8(H_2O)_4](ZrF_6)_3 \cdot 19H_2O$. Further, influence of modifying anions geometry (spherical I-,

trigonal NO_3^-, tetrahedral ReO_4^-, ClO_4^-, BF_4^-, monocapped trigonal prism TaF_7^{2-}) and charge was evidenced in the series $[Fe(phtptrz)_3](A)_{1\ or\ 2}\cdot$Solvent (Solvent = H_2O or CH_3OH) whose spin switching properties revealed a gradual SCO behavior which was explained.

List of abbreviations, symbols and molecules

Abbreviations and symbols

ST: Spin Transition
SCO: Spin crossover
$T_{1/2}$: Temperature where half of SCO ions have changed their spin state
ΔT^{80}: Temperature range where 80 % of sites undergo a SCO[1] (from γ_{HS} = 10 % to 90%)
FTIR: Fourier Transformed Infrared Spectroscopy
TGA: Thermogravimetric analysis
UV: Ultraviolet
F(R): Kubelka-Munk (KM) Function, defined as $F(R)= (1-R^2)/2R$ where R = absolute reflectance
vib.: Vibrational
XRPD: X-ray powder diffraction
DSC: Differential Scanning Calorimetry
C_p: Specific Heat at constant pressure
ΔH: Enthalpy difference ($kJ.mol^{-1}$)
ΔS: Entropy difference ($J.mol^{-1}.K^{-1}$)
SQUID: Superconducting Quantum Interference Device
ZFS: Zero Field Splitting
ZF-μSR: Zero Field Muon Spin Relaxation
AF: Antiferromagnetism
F: Ferromagnetism
ΔE_Q: Quadriplolar splitting ($mm.s^{-1}$)
Ref.: Reference
DTA: Differential Thermal Analysis
Dist.: Distance (Å)
Σ: Distortion parameter for octahedral coordination sphere
EXAFS: Extended X-ray Absorption Fine Structure
$\Gamma/2$: Half width at half maximum ($mm.s^{-1}$)
HS: High-spin
LS: Low-spin
δ: Isomer shift (Mössbauer, $mm.s^{-1}$) and chemical shift (NMR, ppm)
J: Magnetic coupling constant (cm^{-1})
MS: Mass spectrometry
MLCT: Metal-to-Ligand Charge Transfer
γ_{HS}: Molar fraction of HS iron(II) ions
χ: Molar magnetic susceptibility

Organic molecules

NH_2trz: 4-amino-1,2,4-triazole

OH-trz: 4-hydrohy-1,2,4-triazole

Phtp-trz: 4-(3'-N-phtalimido-propyl)-1,2,4-triazole

HGlytrz: 4H-1,2,4-triazol-4-yl acetic acid

GlytrzE: ethyl 4H-1,2,4-triazol-4-yl-acetate

βAlatrz: 4H-1,2-4-triazol-4-yl-propionate

I: *N*,*N*-Dimethylformamide Azine Dihydrochloride

II: *N*,*N*-Dimethylformamide azine

Inorganic complexes and hybrid materials

1: [Fe(**NH_2trz**)$_3$]TiF_6·0.5H_2O

2: [Fe(**NH_2trz**)$_3$]TiF_6·H_2O

3: [Fe(**NH_2trz**)$_3$]ZrF_6·0.5H_2O

4: [Fe(**NH_2trz**)$_3$]ZrF_6

5: [Fe(**NH_2trz**)$_3$]SnF_6·0.5H_2O

6: [Fe(**NH_2trz**)$_3$]SnF_6·H_2O

7: [Fe(**NH_2trz**)$_3$]TaF_7·3H_2O

8: [Fe(**NH_2trz**)$_3$]TaF_7·2.5H_2O

9: [Fe(**NH_2trz**)$_3$]GeF_6·H_2O

10: [Fe(**NH_2trz**)$_3$]GeF_6·0.5H_2O

11: [Cu(**NH_2trz**)$_3$]ZrF_6·H_2O

12: [Fe_3(**NH_2trz**)$_{10}$(H_2O)$_2$](SbF_6)$_6$·1.5CH_3OH

13: [Fe_3(**NH_2trz**)$_{10}$(H_2O)$_2$](SbF_6)$_6$·0.5C_2H_5OH

14: [Fe(**NH_2trz**)$_3$]SnF_6· H_2O

15: [Fe(**NH_2trz**)$_3$]SnF_6· 0.5H_2O

16: [Fe(**NH_2trz**)$_3$]SnF_6· 1.5H_2O

17: [Fe(**NH_2trz**)$_3$](NO_3)$_2$

18: [Cu(**NH_2trz**)$_3$](NO_3)$_2$· H_2O

19: [Cu(**OH-trz**)(ReO_4)OH]· 2H_2O

20: [Zn(**OH-trz**)$_2$Cl](NO_3)

LOH-NO_3: [Fe(**OH-trz**)$_3$](NO_3)$_2$·H_2O

LOH-BF_4: [Fe(**OH-trz**)$_3$](BF_4)$_2$·H_2O

LOH-ClO_4: [Fe(**OH-trz**)$_3$](ClO_4)$_2$·H_2O

LOH-TRF: [Fe(**OH-trz**)$_3$](CF_3SO_3)$_2$·H_2O

21-phtptrz-I: [Fe(**phtptrz**)$_3$]I_2

22- phtptrz-ReO_4: [Fe(**phtptrz**)$_3$](ReO_4)$_2$·CH_3OH

23- phtptrz-TaF_7: [Fe(**phtptrz**)$_3$](TaF_7)$_2$·$6H_2O$

24-Pht-ptrz-NO_3: [Fe(**Phtptrz**)$_3$](NO_3)$_2$·H_2O

25-Pht-ptrz-BF_4: [Fe(**Phtptrz**)$_3$](BF_4)$_2$·H_2O

26-Pht-ptrz-ClO_4: [Fe(**Phtptrz**)$_3$](ClO_4)$_2$·H_2O

27-Pht-ptrz-TRF: [Fe(**Phtptrz**)$_3$](CF_3SO_3)$_2$·H_2O

28: [Cu_3(**phtptrz**)$_{10}$(H_2O)$_2$](SiF_6)$_3$·$44H_2O$

29: [Cu_3(**phtptrz**)$_8$(H_2O)$_4$](ZrF_6)$_3$·$19H_2O$

30: [Cd(**HGlytrz**)(**Glytrz**)Cl]·$2H_2O$

31: [Cd_2(**Glytrz**)$_2$$Cl_2$]

32: [Cu_3(μ_3-O)(**HGlytrz**)$_6$·(H_2O)$_3$]BF_4·H_2O

33-HGlytrz-ClO_4: [Fe_2(**HGlytrz**)(**Glytrz**)$_2$](ClO_4)$_2$·$2CH_3OH$

34-HGlytrz-NO_3: [Fe(**HGlytrz**)$_3$](NO_3)$_2$·CH_3OH

35-HGlytrz-BF_4: [Fe_2(**HGlytrz**)(**Glytrz**)$_2$](BF_4)$_2$·CH_3OH

36-HGlytrz-TRF: [Fe_2(**HGlytrz**)(**Glytrz**)$_2$](CF_3SO_3)$_2$·CH_3OH

37- GlytrzE-ClO_4: [Fe(**GlytrzE**)$_3$](ClO_4)$_2$

38- GlytrzE-ClO_4: [Fe(**GlytrzE**)$_3$](ClO_4)$_2$·CH_3OH

39-GlytrzE-NO_3: [Fe(**GlytrzE**)$_3$](NO_3)$_2$·H_2O

40-GlytrzE-NO_3: [Fe(**GlytrzE**)$_3$](NO_3)$_2$

41-GlytrzE-BF_4: [Fe(**GlytrzE**)$_3$](BF_4)$_2$$0.5H_2O$

42-GlytrzE-BF_4: [Fe(**GlytrzE**)$_3$](BF_4)$_2$

43-Glytrz-TRF: [Fe(**GlytrzE**)$_3$](CF_3SO_3)$_2$·$2H_2O$

44·0.5H_2O: [Fe(**βAlatrz**)$_3$](CF_3SO_3)$_2$·$0.5H_2O$

45: [Fe(**βAlatrz**)$_3$](CF_3SO_3)$_2$

46·H_2O: [Fe(**βAlatrz**)$_3$](ClO_4)$_2$·H_2O

47·H_2O: [Fe(**βAlatrz**)$_3$](BF_4)$_2$· 2H_2O

48: [Fe(**βAlatrz**)$_3$](BF_4)$_2$

Introduction

The era of inorganic switchable materials virtually began with the serendipitous discovery of curious switchable complexes - tris(N,N-dialkyldithiocarbamatoiron(III) by Cambi et al. that dated back to 1931[1]. Such metal centered switchable materials were later designated as *spin-crossover* (SCO) materials. Subsequently large numbers of organic and inorganic switchable materials were investigated, whose performance is based on a kinetically and thermodynamically steady equilibrium involving electrons, protons, isomerism, bond conjugation, etc. The topic had morphed tremendously over the last decades due to the vast investment of academic and industrial research which gave birth to contemporary *molecular electronics*.[2-10]

Molecular electronics explores small organic or inorganic switchable ensembles or even individual molecules as functional building blocks in electronic circuits as they possess the potential for creating high-density devices with low power consumption in combination with high speed.[11] Some of the applications that are envisioned with such molecules are display and data storage, memory devices in information processing, smart sensors, bio-markers, biological imaging etc. Besides switchable materials, *molecular electronics* also encompasses 'Single molecule magnets',[12] quantum dots,[13] thermo-photo-electro-chromic materials that could compete to silicon based technologies. The flagship of switchable materials is represented by iron(II) SCO compounds that have incredible potential in future molecular based electronic industries.[3]

The principle that governs such materials is the molecular bistability wherein two stable readable states that can be switched reversibly with an external trigger. Although SCO phenomenon have been investigated with $3d^4$-$3d^7$ transition metal ions, Fe(II) has received extensive consideration. In the case of Fe(II), (with a $3d^6$ electronic configuration), the entropy driven intra-ionic

electron transfer from a diamagnetic low-spin (LS) state to a thermally populated paramagnetic high-spin (HS) state can be reversibly induced by external stimuli like temperature, pressure and light irradiation. This ultra-sensitive electron spin equilibrium which holds great potential has aroused immense interest in technological sectors. Each of the terminologies like, abruptness, gradual, reversible, irreversible, wide temperature regime, hysteresis holds its own merit[14]. SCO domain had seen intensive theoretical, experimental and computational investigation over the years. Not lagging behind, contemporary probing technique like optical imaging,[15] AFM,[16] TEM,[17] STM,[18] ellipsometry,[19] etc. inventively provided wealth of information that supported other routine spectroscopic techniques in probing and understanding the process and dynamics of SCO solids, nanoparticles, liquids, liquid crystals and thin-films.[11]

The ***principle goal*** of this thesis revolves around iron(II) SCO phenomenon that include design and synthesis of new 1D coordination polymers, characterizations, supporting theories, models and prospects of these materials. Following section gives a brief introduction to the principles underlying this phenomenon, factors affecting this process, criteria for SCO and design-function relationships. This will be followed by a discussion on chronology of 1D coordination polymers (CPs) based on 4-R-1,2,4-triazole.

Spin transition molecular materials

Background of SCO phenomenon

For transition metal ions with d^4–d^7 electron configuration in octahedral symmetry, the inequality $10D_q(LS) > \Delta > 10D_q(HS)$ determines the ground state, where $10D_q$ is the energy gap between t_{2g} and e_g orbitals, i.e. the ligand field and Δ is the spin-pairing energy. It expresses the condition for having a transition metal complex, in the HS state (with a weak ligand field $\Delta >$

$10D_q$(HS)) or LS state (with a strong ligand field $\Delta < 10D_q$(LS)). Thus iron(II) complexes can be classified in one of these families, or in an intermediate spin state (IS).

In the case of iron(II) complexes, 'weak ligands' like H_2O, favor the HS $^5T_2$ ground state whereas increasing the ligand field strength, the $^1A_1$ LS state is quickly lowered in energy; consequently, from a critical ligand field where Δ and 10Dq are of similar magnitude, it becomes the ground state of the complex. This is the case for instance for an iron(II) complex with six CN^- ligands.

Transition metal compounds which have ligand field strengths in close vicinity of the mean spin pairing energy can exhibit thermally induced SCO. The phenomenon can be considered as an intra-ionic electron transfer, where the electrons move between the e_g and t_{2g} orbitals. For iron(II) complexes with six 3*d* electrons in the valence shell of the metal center, thermal SCO is denoted, in the "strong field approach" of ligand field theory, as $(t_{2g})^6$, LS $\leftrightarrow$ $(t_{2g})^4(e_g)^2$, HS (Figure *i*, top).

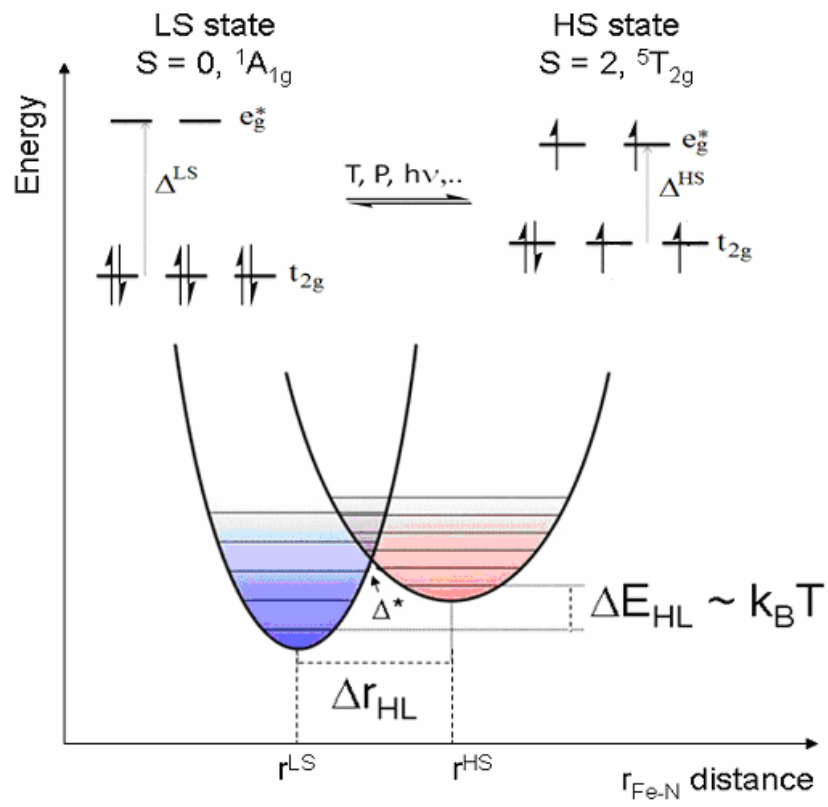

Figure i Distribution of electrons over 3*d* orbitals in HS and LS states of iron(II) ion (top) and potential wells of the LS and HS species an in iron(II) complex meeting SCO conditions $\Delta E_{HL} \sim k_B T$ (k_B = Boltzmann constant); Δ* is the critical ligand field value.

Within the "weak field approach" of ligand field theory, LS ↔ HS transition in iron(II) complexes is denoted as $^1A_{1g}$ (*Oh*), $S = 0 \leftrightarrow {}^5T_{2g}$ (*Oh*), $S = 2$, where $^1A_{1g}$ and $^5T_{2g}$ refer to the Mulliken ligand field terms under octahedral (O_h) symmetry, and S to the total spin quantum number. In the HS state, the population of the e_g orbitals with an antibonding character leads to an elongation of the metal-ligand bond distances. On the other hand, a depopulation of the t_{2g} orbitals affects the electron donation between the metal ion and the vacant π* orbitals of the ligands. The typical metal-ligand

bond length change Δr_{HL} is around 0.2 Å for iron(II) during the spin-state conversion[6].

For ligands presenting an intermediate ligand field, the ligand field is approximated with $10Dq \sim \mu/d_{Fe-N}$, where μ is the dipole moment of the ligand and d_{Fe-N} is the averaged metal–ligand distance. Averaged values for LS and HS complexes of iron(II) can be evaluated from the Cambridge Structural Data Base being *ca*. 1.97 and 2.17 Å, respectively.[6]

When the system switches from the LS to the HS state, an increase of this bond length is followed by an increase of the vibrational entropy.[5] This increase of vibrational entropy is the driving force of the SCO phenomenon. Under external perturbations like temperature, pressure or irradiation a SCO system responds to the imposed perturbation. Thus for a simple complete change in spin state, the SCO temperature, $T_{1/2}$, is defined as the temperature at which the two states for active sites are present in a ratio 1:1 ($\gamma_{HS} = \gamma_{LS} = 0.5$). Spin-change or spin-state change is the result of change of the adopted spin state due to the external or internal factors, like ligand, loss of the crystal solvent[20, 21] or an independent phase transition [22].

Perhaps the most impressive property of SCO materials is the ability to display a bistability of macroscopic properties that might be used in memory devices[23], for “intelligent” contrast agents for biomedical imaging[24], temperature threshold indicators[23], or optical elements in display devices[23]. Concerning the reading process, for theoretical purposes the most convenient way to detect a SCO is the magnetic method; however, for practical purposes other methods detecting the optical or thermodynamic response are often used.

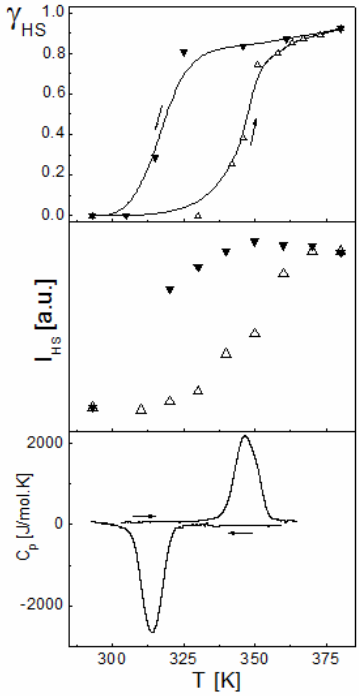

Figure ii Thermal hysteresis loop detected by [3]magnetic, X-ray powder diffraction and thermodynamic properties in the same SCO complex $[Fe(NH_2trz)_3](NO_3)$, adopted from [25] (γ_{HS} = HS molar fraction, I_{HS} = the intensity of the peak corresponding to the HS state, C_p = molar heat capacity).

As an example of bistability, three types of response of the same compound (thermodynamic, optical or XRPD and magnetic) are shown in Figure ii (compound = $[Fe(NH_2trz)_3](NO_3)$, where NH_2trz is 4-amino-1,2,4-triazole)[25]. The changes in all three physical channels occur as first-order phase transitions with 33 K wide hysteresis loops centered around 330.5 K. The memory effect operates around 330.5 K by the storage of a high or low state.

Application of ST compounds

In the last forty years the bit length (physical length of one binary digit in passive information storage devices) has decreased from 250 μm (the first hard disk from IBM in 1950) to 1 μm in audio compact disks and even 0.6 μm (through the use of frequency doubling techniques).[23] The recent appearance, in popular language, of "buzzwords" such as nanotechnology and micro-machines, gives an indication of the increasing scientific and public interest in miniaturisation. Molecular electronics is another term that stems from the miniaturisation trend and refers to molecular-based compounds exhibiting a property, or set of properties, which can be used in devices.[26] ST compounds have been cited as a potential group of materials for use in molecular electronics. Technological fields where ST may find application include information storage, signal processing, optical switching, optical display, as well as temperature and pressure sensors.

To further increase the achievable capacity, there is a crucial need for new nanomaterials. ST coordination polymers offer many interesting capabilities in nanosize reduction, particularly the rich family of 4R-1,2,4-triazole polymers[11, 27-32]. At the molecular level, ST corresponds to an electron transfer accompanied by the spin flip of the transferred electrons. This means that the electrons are transferred from the t_{2g} to the e_g orbitals but remain in the immediate environment of the metal ion, which gives to ST systems no fatigability in electronic processing[33].

This gives ST compounds a clear advantage over competing materials. Application of a molecular species in information storage or signal processing requires it to have the ability to change electronic ground state as a function of external perturbation. In addition, information storage requires the transition between the two states to present a hysteresis, to be abrupt, to

have $T_{1/2}$ near room temperature, to be associated with a colour change and to be chemically stable.[26, 33] The chemical stability of ST compounds is generally acceptable and technical preparative methods, such as hermetic encapsulation of granules in resins, lead to even better stability.[23, 26]

The requirement of colour change which is associated with the transition is virtually guaranteed for Fe(II) ST compounds since the d-d transitions are not obscured by intra-ligand or charge-transfer bands. It then remains to define, as accurately as possible, the factors that control the abruptness, hysteresis and critical temperatures of ST compounds. This has been the object of most recent research on ST. But that abruptness and hysteresis are dependent on the cooperative character in the material, which is effective in 1D Fe(II) triazole polymers.

Kröber et al[34] used the technique of molecular alloying to design a polymeric ST compound with room temperature in the hysteresis loop. The basic compound is $[Fe(Htrz)_3](ClO_4)_2$, (where Htrz = 1H-1,2,4-triazole) with an 1D chain structure. The hysteresis loop of $[Fe(Htrz)_3](ClO_4)_2$ is just above room temperature. $T_{1/2}$ is shifted to lower temperatures by replacing Htrz with a mixture of Htrz and NH_2trz (where NH_2trz = 4-amino-1,2,4-triazole). Information is stored on magnetic storage media in binary format, i.e. 1 and 0. A ST material with its hysteresis loop around r.t. ($T_{1/2}\downarrow < RT < T_{1/2}\uparrow$) can be used in a similar way, with the LS state symbolising 0 and the HS state symbolising *1*. If the material is heated to above $T_{1/2}\uparrow$, the compound changes to the HS state and a 1 is stored. When the compound is cooled to below $T_{1/2}\downarrow$ the compound changes to the LS state and a 0 is stored (Figure IIi).

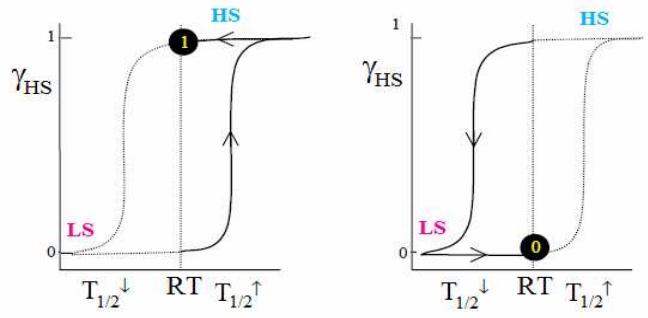

Figure IIi Schematic representation of information storage with ST compounds.

If the hysteresis is large, (the spin state observed optically or magnetically) gives an indication of the last operation performed on the material and thus a memory effect is obtained.

Incorporation of a ST compound into a display device makes it necessary to implement it in a homogeneous layer. This has been performed with screen printing technology. Resistive heating and Peltier element cooling is used for switching the display elements (pixels) between the two states (Figure IIIi).[26]

Kahn & Martinez[23] have proposed possible application of ST compounds as in situ temperature indicators in magnetic resonance imaging (MRI).

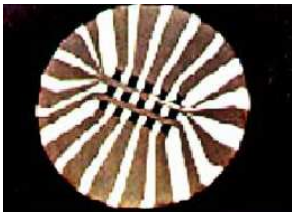

(a)

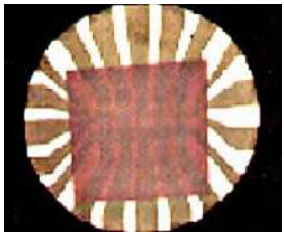

(b)

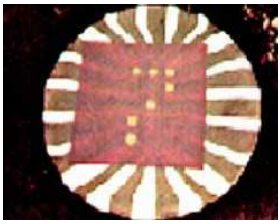

(c)

Figure IIIi (a) Addressing matrix for an ST active layer; (b) ST screen printed layer before writing; (c) ST screen printed layer after writing[26].

Garcia et al.[20] proposed the application of a specific ST compound, $[Fe(hyetrz)_3]A_2 \cdot xH_2O$ (hyetrz = 4-(2'-hydroxy-ethyl)-1,2,4- triazole) which exhibits a non-classical ST behaviour, in the simple, accurate detection of a specific temperature, which is important in temperature control devices (Figure IVi).

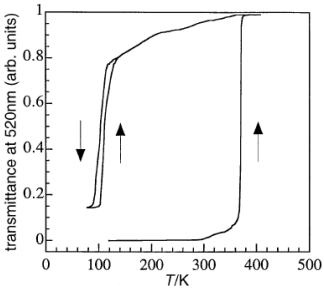

(a)

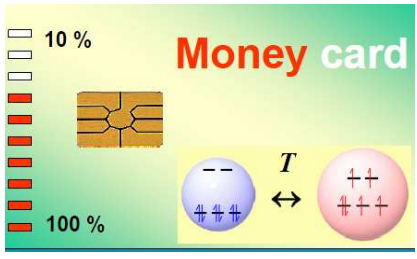

(b)

Figure IVi (a) Optical detection of the ST for the couple $[Fe(hyetrz)_3](3\text{-nitrophenyl sulfonate})_2 \cdot 3H_2O$ – $[Fe(hyetrz)_3](3\text{-nitro-phenylsulfonate})_2$; (b) Application for displays (e.g. a money card).

Zarembowitch & Kahn[33] investigated the possibilities of ST compounds in signal processing, but a lot of work still needs to be done.

In the mean time the ST polymers can be used as pressure sensors.[2, 35] In the figure described below, we see how the ST compounds can be used in critical pressure applications. In Figure Vi (a) the pressure in the vacuum chamber is below the critical pressure, P_c, causing the ST compound to turn white. The white surface reflects the laser light to the light detector, which can be connected to a computer or an alarm. On Figure Vi (b) the pressure in the vacuum chamber is above the critical pressure, P_c, causing the ST compound to turn purple. The purple surface will absorb the light or reflect it to a lesser degree, depending on the wavelength of the light used. The change in pressure can thus be observed at a critical point.

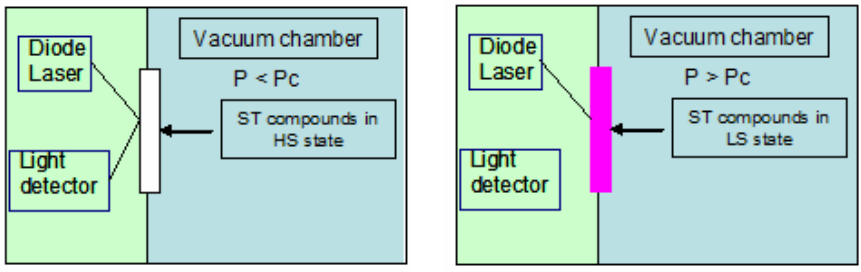

(a) (b)

Figure Vi ST polymers can be used as pressure sensors: (a) the ST compound reflects the light to detector, indicating that the pressure is below the transition point; (b) the ST compound does not reflect the light to detector, indicating that the pressure is above the transition point.[2, 35]

Influence on spin crossover behavior

The SCO behavior can be influenced by various factors, most important among these are:

1. Nature of ligand.

A substitution of one ligand by another can favors or alters the SCO characteristics. For example, the system $[Fe(py)_4(NCS)_2]$ (py = pyridine) is HS at room temperature (r.t.) and does not undergo any magnetic change on cooling[36]. The substitution of two of the pyridine (py) molecules by 1,10-phenanthroline (phen) molecule, which present a strong field, gives access to a new system, $[Fe(phen)(py)_2(NCS)_2]$ which now undergoes a thermal SCO[37, 38], as does the species in which the remaining two pyridines are substituted $[Fe(phen)_2(NCS)_2]$[39, 40] $T_{1/2}$ for the previous complex (106 K) is lower than that for the latter (176 K). The substitution of the two thiocyanato groups by phenanthroline (phen) produces the completely LS complex $[Fe(phen)_3]^{2+}$. The replacement by the strong field cyanide ion or the weak field chloride ion produces LS $[Fe(phen)_2(CN)_2]$ or HS $[Fe(phen)_2Cl_2]$, respectively[40].

2. Intra-ligand substitution.

The variation of the substituent within a ligand may induce an important change in the spin state of a system. This is illustrated by the effects of substitution within LS $[Fe(phen)_3]^{2+}$. This effect is explained by the influence of the decreasing ligand field strengths (and thus increasing tendency towards paramagnetic state) of the $[Fe(2\text{-}R\text{-}phen)_3]^{2+}$ (R = H > CH_3O- > - CH_3 > - Cl[41]. In the substituted complexes, the N-methyl donor

to the metal atom has an important effect to de-stabilize the LS state of the complex.

3. Nature of counter-anion.

In $[Fe(2\text{-pic})_3](X)_2$ (2-pic = 2-picolylamine) the degree of the steepness exhibits the followed trend, function of the increase of the electro-negativity of the halogen: iodine < bromide < chloride[6]. In other case as for the compounds $[Fe(tba)_3](CF_3SO_3)_2 \cdot 2H_2O$ and $[Fe(tba)_3](BF_4)_2 \cdot 2H_2O$ (tba = 5-bis(alkoxy)-*N*-(4*H*-1,2,4-triazol-4-yl)benzamide)[42], the properties exhibited can be explained by the fact that both types of the anions can be involved in the hydrogen bonding with the triazole units and the higher transition temperatures of the reported triflate-based compounds probably originate from a larger electrostatic pressure created by this type of anion. [42, 43]

The effect of the anion is not always consistent from one system to another and is not readily predictable, as in the case of $[Fe(C6\text{-trenH})](A)_2H_2O$ (with $A = ClO_4^-$, F^-, Cl^-, Br^- and C6-trenH = tris[3-aza-4-((5-hexadecyloxy)(6-H)(2-pyridyl))but-3-enyl]amine)[44]. Replacement of the anion is expected to modify the lattice phonon distribution resulting from different crystal packing geometry or strength of the intermolecular forces.[44] Thus, changing the chemical composition of the lattice could modify the degrees of "chemical pressure" on the SCO centers and thereby influence the transition temperature. Therefore the degree to which a counter-anion molecule can be connected by hydrogen bond with the SCO centre will probable influence the nature of the transition.

4. Nature of non-coordinated solvent molecules.

In the model system $[Fe(2\text{-pic})_3]Cl_2 \cdot Solv$ the SCO properties changes by the increasing of the stabilization of the LS state in the order given, from

ethanol, to methanol and water solvates[45]. There are also other numerous examples in which loss of crystal water dramatically modified the SCO properties[34, 46-51].

Non-coordinated solvent molecules can play an important role to promote intermolecular interactions between SCO centers.[25, 52] In other cases, if the ligand presents a benzene ring, the solvent molecules can strengthen π–π interactions and thus influence the SCO behavior.[53, 54] The crystal packing analysis of $[Fe(dpp)_2(NCS)_2]\cdot py$ (dpp = 2,9-diphenyl-1,10-phenantroline) shows an important number of C···C contacts.[55] This situation is especially accentuated in the dppz (dppz = dipyrido[3,2-*a*:2′3′-*c*]phenazine) derivative leading to abrupt transition with huge hysteresis width (~ 40 K). Therefore, for these materials the magnetic response is correlated with the extent of their intermolecular interactions in the crystalline state.

In the 1D triazole system, non-coordinated water molecules were found to influence substantially the abruptness of the SCO curve, whereas the loss of it resulted into a gradual transition[23, 34]. The influence of the nature and the amount of solvent on the SCO behaviour is however still difficult predict, because solvent and counter-anion molecules often interact.

5. Lattice defects.

Thermal and mechanical treatment of samples or different synthetic procedures has been shown to influence strongly the SCO behavior[39, 56-60]. The origin of these effects stems from crystal quality considerations, in particular crystal defects introduced during sample preparation either by milling (sheared deformations) or rapid precipitation, the size of the particles playing a major role.

Spin transition in Fe(II) 1D chains based on 4-R-1,2,4-triazole

Although synthetic organic and inorganic chemistry plays crucial role in the design of appropriate ligands and SCO materials, crystal engineering and supramolecular chemistry concepts too govern some part of the SCO behavior these materials. Such SCO materials could be prepared by several ways which depends normally on ligand design. The pragmatic approach in the synthesis of SCO materials is to design ligands that can form mononuclear complexes or that are capable of forming 1D chain compounds to 3D metal-organic frameworks.

A growing interest in the coordination chemistry of 4-substituted-1,2,4-triazole derivatives has been withered while searching for crystal structure-magnetic properties relationships for 3d transition metal complexes with these ligands.[61-63] Indeed, such bidentate molecules are able to propagate elastic[64] and magnetic interactions[43, 65] between transition metal ions in polynuclear complexes, which are of fundamental importance in molecular magnetism. In particular, several 1D SCO chains of formula [Fe(4-R-1,2,4-triazole)$_3$](anion)$_2$ have been prepared and thoroughly investigated.[66] These CP generally display in the solid state a SCO accompanied by a hysteresis width of variable extent, sometimes centered near room temperature.[34, 64, 66-69]. Their associated thermochromism make them potentially useful for various applications such as display and memory devices units,[26] sensors,[70, 71] cold channel control units in food and medicals storage[72], to name a few.

The origin of the hysteresis loop of these materials and its thermal extent are not yet been however fully understood.[73] It is recognized that strengthening of intramolecular interactions by triple 1,2,4-triazole bridges connecting spin changing molecules can promote cooperative effects, resulting in the observation of hysteresis width ranging between 2-20 K.[66] Indeed, 1D

chains where the Fe^{II} ions are linked by loose bridges all display gradual SCO behavior without any hysteresis effect. This is the case when triple bis-tetrazoles bridges with flexible spacers are employed[73] or when single bridges are used (e.g. 1,2-bis(4-pyridyl)etha(e)ne,[74] 4,4'-bipyridine,[75, 76] dicyanamide[77]). Intermolecular interactions are believed to also contribute to the SCO cooperative mechanism, thus resulting in larger hysteresis loops. There indeed exist three examples of 1D chains where intermolecular interactions in combination with the above mentioned intramolecular interactions may contribute to the effective propagation of elastic interactions between spin changing molecules. This is the case for $[Fe(Htrz)_2trz]BF_4$ (Htrz = 4-H-1,2,4-triazole, trz = triazolato) that displays a SCO above room temperature with a hysteresis width of ~ 40 K,[56] and for $[Fe(hyptrz)_3](4\text{-chloro-3-nitrophenylsulfonate})_2 \cdot H_2O$ (hyptrz = 4-(3'-hydroxypropyl)-1,2,4-triazole) that display a SCO with an hysteresis width of ~ 50 K below room temperature[78]. For the first case, the BF_4^- anion directly bridges neighboring chains through hydrogen bonding as deduced from WAXS experiments.[79] For the second case, π–π stacking interactions of the anions as well as direct hydrogen bonding between the 4-R substituent of neighboring chains were observed in the analogous Cu^{II} crystal structure of the 1D chain[79].

The reversible thermochromic SCO of 1D chain compounds of formula $[Fe(NH_2trz)_3](anion)_2 \cdot nH_2O$ (NH_2trz = 4-amino-1,2,4-triazole), that can occur around room temperature, has been thoroughly investigated.[21, 80-92]. Because these materials hardly crystallize, their structure was deduced by EXAFS at the Fe-K edge[65, 67, 78, 88, 93-99] and confirmed by single crystal X-ray analyses of a few Cu^{II} analogues[43, 65, 78, 100] It shows linear chains where Fe^{II} ions are bridged by three N_1,N_2-1,2,4-triazoles in the LS state as well as in the HS state.[21, 80-91] Most of these Fe^{II} complexes exhibit an abrupt SCO with hysteresis that is accompanied by a pronounced thermochromic effect,

characteristics which can suit potential applications cited above.[101] The effective propagation of short-range elastic cooperative effects through the rigid NH_2trz bridges between neighboring spin changing Fe^{II} ions located at ~ 3.5 Å each are partly responsible of the cooperative nature of their SCO behaviour.[21, 80-91] Indeed, the use of a more flexible bridging ligand connecting the active centers, such as 1,2-bis(tetrazol-1-yl)propane, afforded a linear chain with triply bridged bis monodentate ligands linking the Fe^{II} ions at ~ 7 Å. As a result, this compound displays a gradual SCO behavior on cooling.[73] The intriguing magnetic behavior of the non diluted sample, $[Fe(NH_2trz)_3](NO_3)_2$, that displays a hysteresis loop of 33-35 K wide [80, 86] was recently accounted by an extended hydrogen bonding network involving the nitrate anion as part of a 3D supramolecular lattice of high connectivity involving the 1D chain[102]. Thus the large hysteresis could originate from intermolecular interactions involving the nitrate as concluded from muon spin relaxation (μSR) experiments.[102] It is however known that the SCO regime of $[Fe(NH_2trz)_3](anion)_2$ chain compounds can be tuned over a wide thermal domain by modifying the nature of the non coordinated anion in the crystal lattice.[66] This hypothesis was probed by preparing novel Fe^{II}-NH_2trz chain compounds including anions having planar aromatic rings (benzene sulfonate,[86, 87, 89] naphthalene sulfonate derivatives[21]) which can eventually promote π–π interactions. However, the hysteresis width of such SCO materials did not exceed 20 K.[66] Thus, it can be concluded that the use of planar aromatic anions is not a sufficient condition to observe a wide hysteresis loop. In the absence of crystal structure of a 1D Fe^{II}-NH_2trz SCO chain containing the nitrate anion, without solvent molecules, we can only use the data of the LS complex $[Fe(NH_2trz)_3](NO_3)_2 \cdot 2H_2O$[91]. As expected from μSR, counter-anion and water molecules weave a dense interaction network linking all chains[91]. This example points out at the role of interchain spacing that was not systematically considered in earlier studies.[21, 86-88, 90, 103] In particular, it is interesting to note that the SCO of

Fe^{II} 1D chain compounds bearing bulky substituents on the 4-position of the 1,2,4-triazole[104-108] is much less cooperative pointing out at the importance of chain packing in the crystal lattice. It was also noted that the modification of the nature and the geometry of non coordinated anions can affect the transition temperature, $T_{1/2}$, of these materials without dramatically modifying the hysteresis loop. This feature has been observed for monovalent inorganic anions (Cl^-, Br^-, I^-, BF_4^-, ClO_4^-)[80-82] and organic sulfonate anions (alkyl[88, 90, 103], phenyl derivatives[86, 87, 89], 2-naphthalene derivatives[21] and spiropyrane sulfonate[89]) for the series $[Fe(NH_2trz)_3](anion)_2 \cdot nH_2O$. Indeed, the insertion of spherical counteranions, such as halogen anions, leads to higher $T_{1/2}$ as compared with bulkier anions such as BF_4^- and ClO_4^-. A relationship was proposed between the anion radii and the transition temperatures for $[Fe(hyetrz)_3]A_2 \cdot nH_2O$ (hyetrz = 4-(2'-hydroxyethyl)-1,2,4-triazole ; A = Cl^-, NO_3^-, Br^-, I^-, BF_4^-, ClO_4^-, PF_6^-)[68], but little is known however on the role of divalent anions in promoting/decreasing interchain interactions in such 1D switchable systems.

This extensive investigation on N-heterocycles building blocks overshadowed an interesting class of bio-molecules that could be used for MOFs construction: aminoacids. Comparatively, less work has been reported so far on MOFs or coordination networks constructed from these units,[109-115] particularly in SCO area largely due to the lack of proper functionalization of aminoacids.

The recent endeavor of introducing new family of 1,2,4-triazole derivatives based on biomolecule amino acid, fruitfully yielded interesting SCO materials[69, 116-120]. With these molecules several factors like electronic polarity in the ligand framework, supramolecular interaction factors, controlling inter and intra molecular spacing, shock absorbing flexibility around iron centers and its periphery, constrained occupancy for solvent and

anions could be regulated thus justified their inclusion in synthon/tecton library. It is also shown that with these bio-based precursors chain spacing in 1D SCO chains can be controlled due to possibility of varying the carbon spacer (C1-C3 carbon spacers in α, β and γ – aminoacids respectively)[121].

Notes and references

[1] L. Cambi, L. Szego. *Ber. dtsch. Chem. Ges. A/B* **1931**, *64*(10), 2591-2598.

[2] J. Linares, E. Codjovi, Y. Garcia. *Sensor* **2012**, *12*(4), 4479-4492.

[3] Y. Garcia, F. Robert, A. D. Naik, G. Zhou, B. Tinant, K. Robeyns, S. Michotte, L. Piraux. *J. Am. Chem. Soc.* **2011**, *133*(40), 15850-15853.

[4] P. Gütlich, Y. Garcia, H. Spiering. Spin Transition Phenomena et New Trends in Spin Crossover Research, In: (Eds.: J. S. Miller and M. Drillon), *Magnetism : Molecules to Materials IV - Nanosized Magnetic Materials*, Wiley-VCH Verlag GmbH & Co, **2002**, pp. 2-46-69-90.

[5] P. Gütlich, Y. Garcia, H. Spiering. *Magnetism: From Molecules to Materials*, Wiley-VCH, Verlag GmbH, **2003**, p. 271.

[6] P. Gütlich, H. A. Goodwin. Spin Crossover in Transition Metal Compounds III, In: *Top. Curr. Chem.*, Springer, Berlin-Heidelberg, **2004**, pp. 233-235.

[7] P. Gütlich, J. Jung, H. A. Goodwin. In: (Eds.: E. Coronado, P. Delhaès, D. Gatteschi, and J. S. Miller), *Molecular Magnetism: From Molecular Assemblies to the Devices*, **1996**, p. 327.

[8] P. Gütlich, P. J. van Koningsbruggen, F. Renz. Recent Advances of Spin Crossover Research, In: *Optical Spectra and Chemical Bonding in Transition Metal Complexes*, Springer Berlin / Heidelberg, **2004**, pp. 27-75.

[9] O. Kahn, E. Codjovi, Y. Garcia, P. J. van Koningsbruggen, R. Lapouyade, Sommier L. In: (Eds.: M. M. Turnbull, T. Sugimoto, and L. K. Thompson), *Molecule-Based Magnetic Materials*, **1996**, p. 298.

[10] O. Kahn. *Molecular magnetism*, VCH, **1993**.

[11] A. D. Naik, L. Stappers, J. Snauwaert, J. Fransaer, Y. Garcia. *Small* **2010**, *6*(24), 2842-2846.

[12] S. Brooker, J. A. Kitchen. *Dalton Trans.* **2009**, (36), 7331-7340.

[13] G. D. Lilly, A. C. Whalley, S. Grunder, C. Valente, M. T. Frederick, J. F. Stoddart, E. A. Weiss. *J. Mater. Chem.* **2011**, *in press.*

[14] J. Linares, E. Codjovi, Y. Garcia. *Sensors* **2012**, *12*(4), 4479-4492.

[15] C. chong, H. Mishra, K. Boukheddaden, S. Denise, G. Bouchez, E. Collet, J. C. ameline, A. D. Naik, Y. Garcia, F. Varret. *J. Phys. Chem. B* **2010**, *114*(5), 1975-1984.

[16] C. Chong, B. Berini, K. Boukheddaden, E. Codjovi, J. Linares, Y. Garcia, A. D. Naik, F. Varret. *Physica Status Solidi A-Applied Research* **2010**, *207*, 1227-1231.
[17] E. Coronado, J. R. Galan-Mascaros, Monrabal-capilla M., Garcia-Martinez J., Pardo-Ibànez P. *Adv. Mater.* **2007**, *19*, 1359-1361.
[18] M. S. Alam, M. Stocker, K. Gieb, P. Müller, M. Haryono, K. Student, A. Grohmann. *Angew. Chem. Int. Ed. Engl.* **2010**, *49*(6), 1159-1163.
[19] K. Boukheddaden, E. D. Loutete-Dangui, M. Koubaa, C. Eypert. *Phys. Status Solidi (c)* **2008**, *5*(5), 1003-1006.
[20] Y. Garcia, P. J. vanKoningsbruggen, E. Codjovi, R. Lapouyade, O. Kahn, L. Rabardel. *J. Mater. Chem.* **1997**, *7*(6), 857-858.
[21] P. J. van Koningsbruggen, Y. Garcia, E. Codjovi, R. Lapouyade, O. Kahn, L. Fournes, L. Rabardel. *J. Mater. Chem.* **1997**, *7*(10), 2069-2075.
[22] S. Hayami, Y. Shigeyoshi, M. Akita, K. Inoue, K. Kato, K. Osaka, M. Takata, R. Kawajiri, T. Mitani, Y. Maeda. *Angew. Chem. Int. Ed. Engl.* **2005**, *44*(31), 4899-4903.
[23] O. Kahn, C. Jay-Martinez. *Science* **1998**, *279*(5347), 44-48.
[24] R. N. Muller, L. Vander Elst, S. Laurent. *J. Am. Chem. Soc.* **2003**, *125*(27), 8405-8407.
[25] M. M. Dîrtu, C. Neuhausen, A. D. Naik, A. Rotaru, L. Spinu, Y. Garcia. *Inorg. Chem.* **2010**, *49*(12), 5723-5736.
[26] O. Kahn, J. Krober, C. Jay. *Adv. Mater.* **1992**, *4*(11), 718-728.
[27] J. Larionova, L. Salmon, Y. Guari, A. Tokarev, K. Molvinger, G. Molnaür, A. Bousseksou. *Angew. Chem. Int. Ed. Engl.* **2008**, *47*(43), 8236-8240.
[28] F. Volatron, L. Catala, E. Rivière, A. Gloter, O. Stéphan, T. Mallah. *Inorg. Chem.* **2008**, *47*(15), 6584-6586.
[29] M. Cavallini, I. Bergenti, S. Milita, G. Ruani, I. Salitros, Z. R. Qu, R. Chandrasekar, M. Ruben. *Angew. Chem. Int. Ed. Engl.* **2008**, *47*(45), 8596-8600.
[30] C. Thibault, G. Molnaür, L. Salmon, A. Bousseksou, C. Vieu. *Langmuir* **2009**, *26*(3), 1557-1560.
[31] G. Molnar, S. Cobo, J. A. Real, F. Carcenac, E. Daran, C. Vieu, A. Bousseksou. *Adv. Mater.* **2007**, *19*(16), 2163-2167.
[32] M. Cavallini, I. Bergenti, S. Milita, J. C. Kengne, D. Gentili, G. Ruani, I. Salitros, V. Meded, M. Ruben. *Langmuir* **2011**, *27*(7), 4076-4081.
[33] J. Zarembowitch, O. Kahn. *New J. Chem.* **1991**, *15*, 181.
[34] J. Krober, E. Codjovi, O. Kahn, F. Groliere, C. Jay. *J. Am. Chem. Soc.* **1993**, *115*(21), 9810-9811.

[35] V. Ksenofontov, G. Levchenko, H. Spiering, P. Gütlich, J. F. Létard, Y. Bouhedja, O. Kahn. *Chem. Phys. Lett.* **1998**, *294*(6), 545-553.
[36] W. Huang, T. Ogawa. *J. Mol. Struct.* **2006**, *785*(1ΓÇô3), 21-26.
[37] R. Claude, J. A. Real, J. Zarembowitch, O. Kahn, L. Ouahab, D. Grandjean, K. Boukheddaden, F. Varret, A. Dworkin. *Inorg. Chem.* **1990**, *29*(22), 4442-4448.
[38] P. Spacu, M. Teodorescu, G. Filotti, P. Telnic. *Z. anorg. allg. Chem.* **1972**, *392*(1), 88-92.
[39] E. W. Müller, H. Spiering, P. Gütlich. *Chem. Phys. Lett.* **1982**, *93*(6), 567-571.
[40] J. A. Real, B. Gallois, T. Granier, F. Suez-Panama, J. Zarembowitch. *Inorg. Chem.* **1992**, *31*(24), 4972-4979.
[41] P. Gütlich. Metal Complexes - Spin crossover in iron(II)-complexes, In: Springer Berlin / Heidelberg, **1981**, pp. 83-195.
[42] M. Seredyuk, A. B. Gaspar, V. Ksenofontov, Y. Galyametdinov, M. Verdaguer, F. Villain, P. Gutlich. *Inorg. Chem.* **2008**, *47*(22), 10232-10245.
[43] Y. Garcia, P. J. van Koningsbruggen, G. Bravic, D. Chasseau, O. Kahn. *Eur. J. Inorg. Chem.* **2003**, (2), 356-362.
[44] M. Seredyuk, A. B. Gaspar, V. Ksenofontov, Y. Galyametdinov, J. Kusz, P. Gutlich. *J. Am. Chem. Soc.* **2008**, *130*(4), 1431-1439.
[45] M. Sorai, J. Ensling, K. M. Hasselbach, P. Gütlich. *Chem. Phys.* **1977**, *20*(2), 197-208.
[46] S. Bonhommeau, G. Molnar, A. Galet, A. Zwick, J. A. Real, J. J. McGarvey, A. Bousseksou. *Angew. Chem. Int. Ed.* **2005**, *44*(26), 4069-4073.
[47] G. Ritter, E. Koenig, W. Irler, H. A. Goodwin. *Inorg. Chem.* **1978**, *17*(2), 224-228.
[48] S. Hayami, R. Moriyama, Y. Shigeyoshi, R. Kawajiri, T. Mitani, M. Akita, K. Inoue, Y. Maeda. *Inorg. Chem.* **2005**, *44*(21), 7295-7297.
[49] J. A. Real, M. C. Munoz, E. Andres, T. Granier, B. Gallois. *Inorg. Chem.* **1994**, *33*(16), 3587-3594.
[50] R. Hernandez-Molina, A. Mederos, S. Dominguez, P. Gili, C. Ruiz-Perez, A. Castineiras, X. Solans, F. Lloret, J. A. Real. *Inorg. Chem.* **1998**, *37*(20), 5102-5108.
[51] W. Vreugdenhil, J. H. Vandiemen, R. A. G. Degraaff, J. G. Haasnoot, J. Reedijk, A. M. vanderKraan, O. Kahn, J. Zarembowitch. *Polyhedron* **1990**, *9*(24), 2971-2979.
[52] M. M. Dîrtu, A. Rotaru, D. Gillard, J. Linares, E. Codjovi, B. Tinant, Y. Garcia. *Inorg. Chem.* **2009**, *48*(16), 7838-7852.
[53] P. Gütlich, H. Köppen, H. G. Steinhäuser. *Chem. Phys. Lett.* **1980**, *74*(3), 475-480.

[54] B. Gallois, J. A. Real, C. Hauw, J. Zarembowitch. *Inorg. Chem.* **1990**, *29*(6), 1152-1158.
[55] Z. Jin Zhong, J. Q. Tao, Z. Yu, C. Y. Dun, Y. J. Liu, X. Z. You. *J. Chem. Soc. , Dalton Trans.* **1998**, (3), 327-328.
[56] J. Krober, J. P. Audiere, R. Claude, E. Codjovi, O. Kahn, J. G. Haasnoot, F. Groliere, C. Jay, A. Bousseksou, J. Linares, F. Varret, A. Gonthiervassal. *Chem. Mater.* **1994**, *6*(8), 1404-1412.
[57] P. Ganguli, P. Gütlich, E. W. Müller, W. Irler. *J. Chem. Soc. , Dalton Trans.* **1981**, -, 441-446.
[58] E. W. Müller, H. Spiering, P. Gütlich. *Inorg. Chem.* **1984**, *23*(1), 119-120.
[59] M. S. Haddad, M. W. Lynch, W. D. Federer, Hendrickson, D.N. *Inorg. Chem.* **1981**, *20*(1), 123-131.
[60] M. S. Haddad, W. D. Federer, M. W. Lynch, D. N. Hendrickson. *Inorg. Chem.* **1981**, *20*(1), 131-139.
[61] J. G. Haasnoot. *Coord. Chem. Rev.* **2000**, *200*, 131-185.
[62] U. Beckmann, S. Brooker. *Coord. Chem. Rev.* **2003**, *245*(1ΓÇô2), 17-29.
[63] J. A. Kitchen, S. Brooker. *Coord. Chem. Rev.* **2008**, *252*(18–20), 2072-2092.
[64] O. Kahn, E. Codjovi, Y. Garcia, P. J. van Koningsbruggen, R. Lapouyade, L. Sommier. *Molecule-Based Magnetic Materials* **1996**, *644*, 298-310.
[65] Y. Garcia, P. J. van Koningsbruggen, G. Bravic, P. Guionneau, D. Chasseau, G. L. Cascarano, J. Moscovici, K. Lambert, A. Michalowicz, O. Kahn. *Inorg. Chem.* **1997**, *36*(27), 6357-6365.
[66] Y. Garcia, V. Niel, M. C. Munoz, J. A. Real. *Top. Curr. Chem.* **2004**, *233*, 229-257.
[67] T. Yokoyama, Y. Murakami, M. Kiguchi, T. Komatsu, N. Kojima. *Phys. Rev. B.* **1998**, *58*, 14238.
[68] Y. Garcia, P. J. van Koningsbruggen, R. Lapouyade, L. Rabardel, O. Kahn, M. Wieczorek, R. Bronisz, Z. Ciunik, M. F. Rudolf. *C. R. Acad. Sci. Paris, IIc* **1998**, *1*(8), 523-532.
[69] M. M. Dîrtu, A. D. Naik, J. Marchand-Brynaert, Y. Garcia. *J. Phys. : Conf. Ser.* **2010**, *217*(1), 012085.
[70] Y. Garcia, V. Ksenofontov, P. Gutlich. *Hyp. Int.* **2002**, *139*(1-4), 543-551.
[71] Y. Garcia, V. Ksenofontov, S. Mentior, M. M. Dîrtu, C. Gieck, A. Bhatthacharjee, P. Gutlich. *Chem. Eur. J.* **2008**, *14*(12), 3745-3758.
[72] K. S. Murray, C. P. Kepert. *Top. Curr. Chem.* **2004**, *233*, 195-228.
[73] P. J. van Koningsbruggen, Y. Garcia, O. Kahn, L. Fournes, H. Kooijman, A. L. Spek, J. G. Haasnoot, J. Moscovici, K. Provost,

A. Michalowicz, F. Renz, P. Gutlich. *Inorg. Chem.* **2000**, *39*(9), 1891-1900.
[74] G. S. Matouzenko, M. Perrin, B. Le Guennic, C. Genre, G. Molnar, A. Bousseksou, S. A. Borshch. *Dalton Trans.* **2007**, (9), 934-942.
[75] G. S. Matouzenko, G. Molnar, N. Brefuel, M. Perrin, A. Bousseksou, S. A. Borshch. *Chem. Mater.* **2002**, *15*(2), 550-556.
[76] C. Genre, G. S. Matouzenko, E. Jeanneau, D. Luneau. *New J. Chem.* **2006**, *30*(11), 1669-1674.
[77] C. Genre, E. Jeanneau, A. Bousseksou, D. Luneau, S. A. Borshch, G. S. Matouzenko. *Chem. Eur. J.* **2008**, *14*(2), 697-705.
[78] Y. Garcia, J. Moscovici, A. Michalowicz, V. Ksenofontov, G. Levchenko, G. Bravic, D. Chasseau, P. Gutlich. *Chem. Eur. J.* **2002**, *8*(21), 4992-5000.
[79] M. Verelst, L. Sommier, P. Lecante, A. Mosset, O. Kahn. *Chem. Mater* **1998**, *10*, 980.
[80] L.G.Lavrenova, V. N. Ikorskii, V. A. Varnek, I. M. Oglezneva, S. V. Larionova. *Koord. Khim.* **1986**, *12*, 207.
[81] L. G. Lavrenova, V. N. Ikorskii, V. A. Varnek, I. M. Oglezneva, Larionov S.V. *Koord. Khim.* **1990**, *16*, 654.
[82] L. G. Lavrenova, N. G. Yudina, V. N. Ikorskii, V. A. Varnek, I. M. Oglezneva, S. V. Larionov. *Polyhedron* **1995**, *14*(10), 1333-1337.
[83] L. G. Lavrenova, O. G. Shakirova, Y. G. Shvedenkov, V. N. Ikorskii, V. A. Varnek, L. A. Sheludyakova, S. V. Larionov. *Koord. Khim.* **1999**, *25*(3), 192-197.
[84] L. G. Lavrenova, O. G. Shakirova, V. N. Ikorskii, V. A. Varnek, L. A. Sheludyakova, S. V. Larionov. *Koord. Khim.* **2003**, *29*(1), 22-27.
[85] Drabent, K., Bronisz, R., and Rudolf, M. F. ICAME 95 51, 7. 1996. 1995.
Ref Type: Conference Proceeding
[86] E. Codjovi, L. Sommier, O. Kahn. *New J. Chem.* **1996**, *20*, 503.
[87] S. Toyazaki, Y. Murakami, T. Komatsu, N. Kojima, Yokoyama T. *Mol. Cryst. Liq. Cryst.* **2000**, *343*, 175-180.
[88] N. Kojima, Y. Murakami, T. Komatsu, T. Yokoyama. *Synthetic Met.* **1999**, *103*, 2154.
[89] S. Toyazaki, M. Nakanishi, T. Komatsu, N. Kojima, D. Matsumura, T. Yokoyama. *Synthetic Met.* **2001**, *121*(1-3), 1794-1795.
[90] N. Kojima, S. Toyazaki, M. Itoi, Y. Ono, W. Aoki, Y. Kobayashi, M. Seto, T. Yokoyama. *Mol. Cryst. Liq. Cryst.* **2002**, *376*(1), 567-574.
[91] A. Grosjean, N. Daro, B. Kauffmann, A. Kaiba, J. F. Letard, P. Guionneau. *Chem. Commun.* **2011**, *47*(45), 12382-12384.

[92] E. D. Loutete-Dangui, F. Varret, E. Codjovi, P. R. Dahoo, H. Tokoro, S. Ohkoshi, C. Eypert, J. F. Letard, J. M. Coanga, K. Boukheddaden. *Phys. Rev. B* **2007**, *75*(18), 184425-1-184425 - 7.
[93] N. Bausk, S. B. Erenburg, L. Mazalov, L. Lavrenova, V. Ikorskii. *J. Struct. Chem.* **1994**, *35*(4), 509-516.
[94] S. B. Erenburg, N. V. Bausk, L. G. Lavrenova, L. N. Mazalov. *Journal of Synchrotron Radiation* **1999**, *6*, 576-578.
[95] S. B. Erenburg, N. V. Bausk, L. G. Lavrenova, L. N. Mazalov. *Journal of Magnetism and Magnetic Materials* **2001**, *226*, 1967-1969.
[96] A. Michalowicz, J. Moscovici, B. Ducourant, D. Cracco, O. Kahn. *Chem. Mater.* **1995**, *7*(10), 1833-1842.
[97] A. Michalowicz, K. O. Moscovici. *J. Phys. IV* **1997**, *7*(C2), 633-635.
[98] A. Michalowicz, J. Moscovici, Y. Garcia, O. Kahn. *Journal of Synchrotron Radiation* **1999**, *6*, 231-232.
[99] A. Michalowicz, J. Moscovici, J. Charton, F. Sandid, F. Benamrane, Y. Garcia. *Journal of Synchrotron Radiation* **2001**, *8*, 701-703.
[100] K. Drabent, Z. Ciunik. *Chem. Commun.* **2001**, (14), 1254-1255.
[101] Y. Garcia, V. Niel, M. C. Munoz, J. A. Real. *Top. Curr. Chem.* **2004**, *233*, 229-257.
[102] Y. Garcia, S. J. Campbell, J. S. Lord, Y. Boland, V. Ksenofontov, P. Gutlich. *J. Phys. Chem. B* **2007**, *111*(38), 11111-11119.
[103] Drabent, K., Polomka, P., and Rudolf, M. F. ICAME 95 50, 11. 1996.
Ref Type: Conference Proceeding
[104] G. Schwarzenbacher, M. S. Gangl, M. Goriup, M. Winter, M. Grunert, F. Renz, W. Linert, R. Saf. *Monatsh. Chem.* **2001**, *132*(4), 519-529.
[105] T. Fujigaya, D. L. Jiang, T. Aida. *J. Am. Chem. Soc.* **2005**, *127*(15), 5484-5489.
[106] M. Seredyuk, A. B. Gaspar, V. Ksenofontov, S. Reiman, Y. Galyametdinov, W. Haase, E. Rentschler, P. Gütlich. *Chem. Mater.* **2006**, *18*(10), 2513-2519.
[107] M. Seredyuk, A. Gaspar, V. Ksenofontov, S. Reiman, Y. Galyametdinov, W. Haase, E. Rentschler, P. Gütlich. *Hyp. Int.* **2005**, *166*(1), 385-390.
[108] P. Sonar, C. M. Grunert, Y. L. Wei, J. Kusz, P. Gütlich, A. D. Schlüter. *Eur. J. Inorg. Chem.* **2008**, *2008*(10), 1613-1622.
[109] A. Mantion, L. Massuger, P. Rabu, C. Palivan, L. B. McCusker, A. Taubert. *J. Am. Chem. Soc.* **2008**, *130*(8), 2517-2526.
[110] L. F. Ma, X. K. Huo, L. Y. Wang, J. G. Wang, Y. T. Fan. *J. Solid State Chem.* **2007**, *180*(5), 1648-1657.

[111] L. F. Ma, L. Y. Wang, J. G. Wang, Y. F. Wang, X. Feng. *Z. anorg. allg. Chem.* **2006**, *632*(3), 487-490.
[112] B. Wisser, A. C. Chamayou, R. Miller, W. Scherer, C. Janiak. *Cryst. Eng. Comm.* **2008**, *10*(5), 461-464.
[113] B. Wisser, Y. Lu, C. Janiak. *Z. anorg. allg. Chem.* **2007**, *633*(8), 1189-1192.
[114] J. N. Rebilly, J. Bacsa, M. J. Rosseinsky. *Chem. Asian J.* **2009**, *4*(6), 892-903.
[115] M. J. Ingleson, J. Bacsa, M. J. Rosseinsky. *Chem. Commun.* **2007**, (29), 3036-3038.
[116] M. M. Dîrtu, F. Schmit, A. D. Naik, A. Rotaru, J. Marchand-Brynaert, Y. Garcia. *Int. J. Mol. Sci.* **2011**, *12*(8), 5339-5351.
[117] A. Naik, M. M. Dîrtu, Y. Garcia. *Hyp. Int.* **2011**, 1-5.
[118] A. Naik, M. Dîrtu, A. Railliet, J. Marchand-Brynaert, Y. Garcia. *Polymers* **2011**, *3*(4), 1750-1775.
[119] A. D. Naik, J. Beck, M. M. Dîrtu, C. Bebrone, B. Tinant, K. Robeyns, J. Marchand-Brynaert, Y. Garcia. *Inorg. Chim. Acta* **2011**, *368*(1), 21-28.
[120] A. D. Naik, M. M. Dîrtu, A. Leonard, B. Tinant, J. Marchand-Brynaert, B. L. Su, Y. Garcia. *Crystal Growth & Design* **2010**, *10*(4), 1798-1807.
[121] M. M. Dîrtu, F. Schmit, A. Naik, A. Rotaru, J. Marchand-Brynaert, Y. Garcia. *Hyp. Int.* **2012**, 1-5.

Aim and strategy

The aim of this work was to develop new SCO inorganic complexes and to identify and understand physical and structural parameters influencing their SCO properties. One of the attractive aspects of these materials is the molecular bistability wherein two stable readable states are switched reversibly with an external stimulus.[1-4] So far the SCO materials have been investigated with $3d^4$-$3d^7$ transition metal ions, but Fe(II) has been the most studied. In the case of Fe(II), ($3d^6$), the entropy driven intra-ionic electron transfer from a diamagnetic LS state to a thermally populated paramagnetic HS state can be reversibly induced by external stimuli like temperature, pressure and light irradiation. What is technologically important are cascade of events (thermochromism, abruptness, hysteresis), with variable operating transition temperature regime, that happens during the spin transition.

The observation of abrupt transitions and memory effects in SCO materials, which arise due to elastic coupling between the SCO sites and long range elastic interactions within the lattice or through meticulously designed rigid networks, has led to suggestions that these materials may be candidates for applications in information storage and retrieval, visual displays and sensors.

For this purpose, we had to select a suitable system in order to synthesize new solid-state thermo sensitive molecules with coordinating atoms compatible with a SCO metal ion environment.

The 4-R-1,2,4-triazole was chosen because of its very promising magnetic properties in the solid state and the possibility to design coordinating moieties bound on these molecules (Figure VIi).

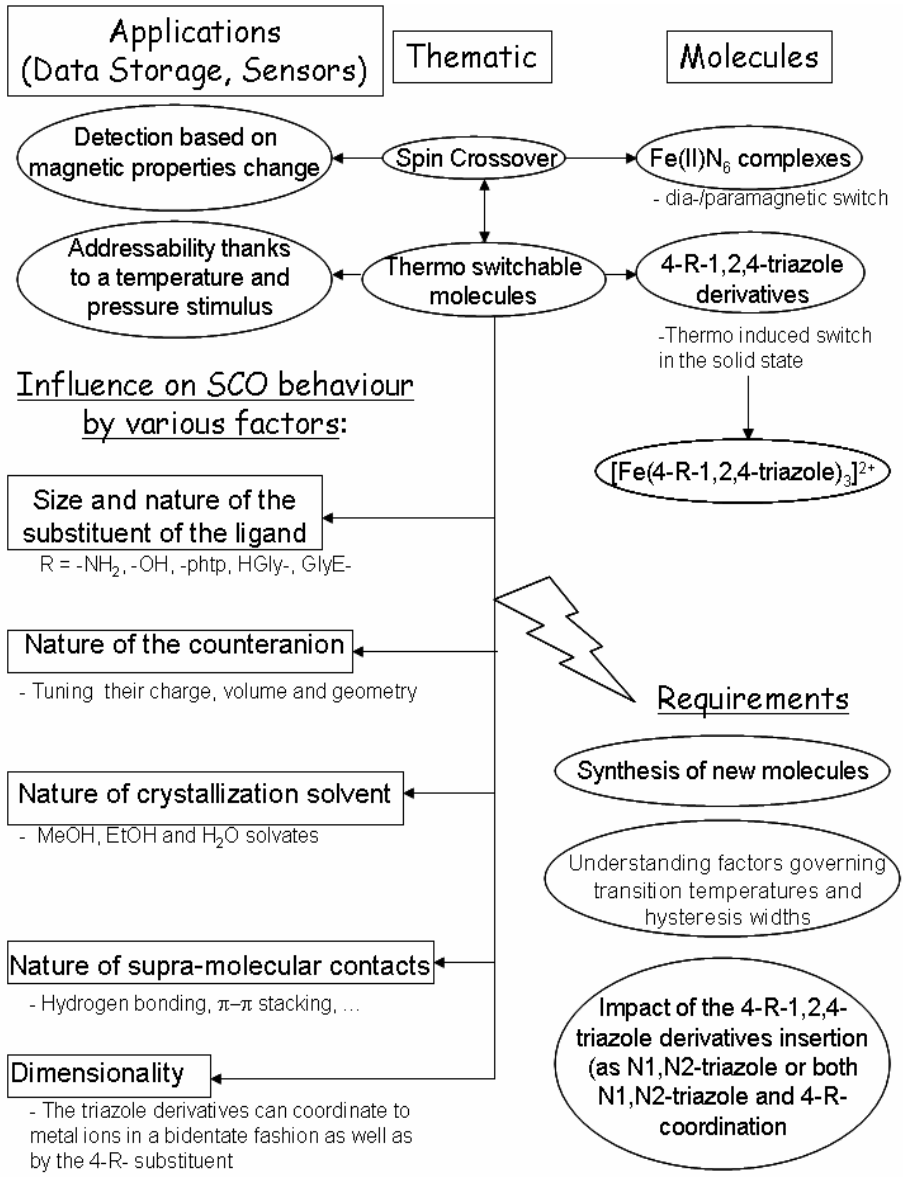

Figure VIi Synoptic view of the thematic of this thesis and associated requirements

This manuscript will be divided in two main sections devoted on one hand to the synthesis and the prediction of the spin transition (ST) temperature in Fe^{II}-4-R-1,2,4-triazole 1D coordination polymers (CP), followed by the use of an anionic nuclear probe to sense the ST and also to the study of the

influence of chemical parameters (size of the substituent on the 4th position of the ligand as well the counteranion size) on the SCO properties.

The second part is devoted to the synthesis of new suitable 1,2,4-triazole precursors, based on α- and β-amino-acids and their esters. Flexibility of the ligand (as 'shock absorber' during SCO) and supra-molecular interactions will play a crucial role in the transition temperature which will be taken care during ligand design in addition to factors like variation of ligands/anions/solvents during the synthesis.

The properties of this class of materials could become important and thus more suitable than the widely studied Fe(II)-amino-triazole switches, including diverse fluorinated inorganic anions varying in geometry (TiF_6^{2-}, ZrF_6^{2-}, SnF_6^{2-}, GeF_6^{2-}, SbF_6^{2-}, TaF_7^{2-})[5]. However, the search of a thermo-magnetic phenomenon with such materials is a very challenging task in view of the fact that no information about the influence of the internal pressure of these anions located in the neighboring cationic chains, as well as chain lengths of these coordination polymers, was available. Thus, Chapter I, II and III is devoted to this queries which will clarify this question.

Moreover, the perspective to modify the magnetic behaviour of SCO complexes by using novel type of substituent on the 4-R-1,2,4-triazole, will also be investigated: 4-hydroxy-1,2,4-triazole (Chapter IV) and 4-(3'-N-phtalimido-propyl)-1,2,4-triazole (Chapter V) which were never reported earlier. Their coordination perspectives will be described.

With predictable design strategy of transamination, for the first time 1,2,4-triazole derivatives of α- and β-amino-acids and -esters were designed and introduced to produce new SCO 1D coordination polymers. Thus, in the second part of the work, the goal was to understand the impact of the influence of the functional groups on the SCO properties, for a new class of SCO materials. The advantage of these molecules is their natural

miscellaneous framework with rich functional groups which is amenable to copious derivatization, and also their structural diversity.

Different Cu, Cd, Zn materials are obtained with the new 4-R-1,2,4-triazole ligands. These metals ions are selected for their tendency to form single crystals which are important to gain access to structural information such as coordination mode of the ligand or crystal packing. In addition, it may happen that Cu(II), Cd(II), Zn(II) and Fe(II) complexes are isomorphous. In that case, the structural information obtained from Cu(II), Cd(II) or Zn(II) complexes may replace the structural data for Fe(II) materials which are often not available for 1D coordination polymers.

Further with crystal engineering approach, an α–amino acid HGlytrz (4H-1,2,4-triazol-4-yl acetic acid) has been introduced as a superlative supramolecular synthon which has interesting topology wherein the two extremities are occupied by two potentially coordinating groups. Diverse topologies ranging from 1D coordination polymers, $[Cd(HGlytrz)(Glytrz)Cl]\cdot 2H_2O$, 2D chiral helicate - $[Cd_2(Glytrz)_2Cl_2]$ and a stunning self assembly into 3D MOF with an unique array of porous nanoballs architecture - $[Cu_3(\mu_3\text{-}O)(HGlytrz)_6\cdot(H_2O)_3]BF_4\cdot H_2O$ were obtained and their gas adsorption properties are reported (Chapter VI).

The goal was to rationalize the observations and to make links between chemical and physical characteristics (coordination type, molecular rigidity and packing) of molecules. Thus it leads to an overview of parameters which enable establishing structure-functional relationship.

Finally, the synthesis of new derivatives of $[Fe(\alpha Glytrz)_3]A_2$, αGlytrz = ethyl-4H-1,2,4-triazol-4-yl-acetate, $[Fe(\beta Alatrz)_3]A_2$, βAlatrz = 4H-1,2-4-triazol-4-yl-propionate, comprising non-coordinating ClO_4^-, NO_3^-, BF_4^-, $CF_3SO_3^-$ anions will be also investigated (Chapter VII). The impact of the

variation of anions/solvents medium during the synthesis on the SCO behavior will be analyzed.

A strong sensitivity of the SCO behaviour was observed on increasing carbon spacer on going from αGlytrz to βAlatrz. In particular, $[Fe(\beta Alatrz)_3](BF_4)_2 \cdot H_2O$, undergoes an atypical two-step spin transition which has been thoroughly probed by vibrational studies (IR, Raman).

Methodology

SCO phenomenon can be studied by a large variety of analytical techniques (SQUID magnetometry, ^{57}Fe Mössbauer spectroscopy, Differential Scanning Calorimetry, Infrared, Raman and UV/Vis, spectroscopies, etc).[6] We briefly present the key techniques that have been used throughout the thesis and that afforded useful information on the studied SCO processes.
Thus only a global consideration of a combination of key techniques discussed above leads to an understanding of the complexity of the SCO process and helps us to determine the structure-SCO properties relationships in the light of both new data and data from literature.

Magnetic susceptibility measurements (SQUID magnetometry)

The temperature dependent magnetic behavior of any SCO system in solid state may be characterized by measuring its molar magnetic susceptibility χ_M by SQUID magnetometry (Superconducting Quantum Interference Device). Two contributions must be considered arising from diamagnetism and paramagnetism.

Diamagnetism is a property of all atoms and molecules, caused by the field-induced electron circulation of paired electrons. Thus to obtain the paramagnetic susceptibility, the diamagnetic susceptibility must by

subtracted from the net susceptibility. This is routinely done using Pascal's constants[7].

Thus it is possible to delineate the HS molar fraction (γ_{HS}) when the magnetic susceptibility of both spin state (χ_{HS} and χ_{LS}) is known, according to: $\chi(T) = \gamma_{HS}(T) \cdot \chi_{HS} + (1 - \gamma_{HS}(T)) \cdot \chi_{LS}$ [8]. For Fe(II) compounds, taking in account the spin only approximation (the effective magnetic moment $\mu_{eff} = 2.83\sqrt{\chi_M T}$) the $\chi_M T$ (HS) and $\chi_M T$ (LS) products are respectively equal to 3 and 0 $cm^3 \cdot mol^{-1} \cdot K$. However due to spin orbit coupling and zero-field-splitting (ZFS), the $\chi_M T$ product can be slightly different from the expected value.

The χ_M values obtained by this method can be normalized thanks to Mössbauer spectroscopy information (if the SCO process is complete or not) and thus to get γ_{HS}. The magnetic data can be converted to the HS molar fraction $\gamma_{HS}(T)$ by means of eq. (a):

$$\gamma_{HS} = \frac{\chi_M \cdot T - \chi_M^{LS} \cdot T}{\chi_M^{HS} \cdot T_{max} - \chi_M^{LS} \cdot T} \qquad \text{(a)}$$

$\chi_M^{LS}(T)$ = $184 \cdot 10^{-6}$ cm^3 mol^{-1},[29] $\gamma(T_{max}, \chi_{max}) = 1$ and $\chi_M^{HS}(T)$ is the paramagnetic susceptibility determined by fitting the susceptibility data in the HS region with the Curie law.

^{57}Fe Mössbauer spectroscopy

^{57}Fe Mössbauer spectroscopy is an elegant and powerful method in probing the different valence state (oxidation and spin state) of iron compounds.[9] Indeed this is the unique method that provides explicitly the spin state and the ratio of the HS and LS ions. Mössbauer spectroscopy is based on the recoilless absorption of γ rays by nuclei without excitation of the vibration of the lattice, and is thus appropriate for the analysis of solid samples.[8] Since

the nuclear level energies are influenced by the environment of the nucleus, this analysis provides physical-chemical information. The isomer shift δ (usually given relative to α-iron) and the quadrupole splitting ΔE_Q, are two of the most important parameters derived from a Mössbauer spectrum, and differ for Fe(II) HS and LS states.

The *isomer shift* δ is function of the s-electron density at the nucleus.[8] In the case of iron the higher this density, the more negative is δ. Because t_{2g} orbitals have the required symmetry for π-back donation, the 3d electron density is lower in the LS state than in the HS state configuration. Thus the shielding of d-electrons decreases and the s-electron density at the nucleus increases.[8] Consequently, δ_{LS} is shifted towards negative values and is smaller than δ_{HS}. In addition the distinction between Fe(II) and Fe(III) is easy, as in the case of Fe(III) the 3d electrons provide a decrease in the s-electron shielding and a δ smaller is obtained. Thus a partial oxidation of Fe(II) compounds may therefore be evidenced by Mössbauer spectroscopy, thanks to the isomer shift value.

The *quadrupole splitting* ΔE_Q, which is correlated to the electric field gradient, may arise from a non-spherical distribution of the metal electrons (valence shell contribution of from a non cubic symmetry of iron or dipole surrounding the nucleus (lattice contribution). In the LS configuration the six electros are equally shared between the t_{2g} orbitals. Thus no valence shell contribution is expected. The possible presence of a ΔE_Q could be attributed to a lattice contribution. In the HS state ΔE_Q is correlated to a non-spherical electronic distribution which leads to large quadrupole splitting. Indeed, in the HS state presence of a Jahn-Teller distortion can translate a non-uniform distribution of the electrons.[10, 11] Thus for Fe(II) HS almost always a ΔE_Q is present due to a valence shell contribution. Presence of a lattice contribution can be identified when there are structural changes. Anyway the lattice

contribution is much smaller than the valence shell contribution, due to the $1/r^2$ (r = distance between the electric charges) dependence of the electric interaction.

In conclusion the HS and the LS states differ in both in isomer shift and in quadrupole splitting ($\delta^{HS}>\delta^{LS}$, $\Delta E_Q{}^{HS} >> \Delta E_Q{}^{LS}$). Consequently, their signatures are different and their signals can be easily distinguishes by Mössbauer spectroscopy.

Calorimetry

The spin transition can be related to a phase transition associated with a change of the Gibbs free energy $\Delta G = \Delta H - T\cdot\Delta S$. The enthalpy change $\Delta H = H_{HS}-H_{LS}$ is typically 10 to 20 kJ/mol and the entropy change $\Delta S = S_{HS}-S_{LS}$ is of the order of 50-80 J/mol·K.[8, 12] These quantities are temperature dependent, where ΔG, ΔH and ΔS are obtained from Differential Scanning Calorimetry (DSC) measurements and plotted as a function of temperature.

The DSC is a powerful method to determine the transition temperature and thermodynamic parameters associated to the SCO process. In addition it enables to get information on other lattice changes such as for instance an order disorder transition of counter-anion. However it is difficult to follow gradual transition by DSC because they are associated with small entropy variation.

Notes and references

[1] O. Kahn, C. Jay-Martinez. *Science* **1998**, *279*(5347), 44-48.
[2] O. Kahn, J. Kröber, C. Jay. *Adv. Mater.* **1992**, *4*(11), 718-728.
[3] P. Gütlich, Y. Garcia, H. A. Goodwin. *Chem. Soc. Rev.* **2000**, *29*(6), 419-427.
[4] Y. Garcia, V. Niel, M. C. Muñoz, J. A. Real. *Top. Curr. Chem.* **2004**, *233*, 229-257.
[5] M. M. Dîrtu, A. Rotaru, D. Gillard, J. Linares, E. Codjovi, B. Tinant, Y. Garcia. *Inorg. Chem.* **2009**, *48*(16), 7838-7852.
[6] P. Gütlich, Y. Garcia, H. Spiering. Spin Transition Phenomena et New Trends in Spin Crossover Research, In: (Eds.: J. S. Miller and M. Drillon), *Magnetism : Molecules to Materials IV - Nanosized Magnetic Materials*, Wiley-VCH Verlag GmbH & Co, **2002**, pp. 2-46-69-90.
[7] G. A. Bain, J. F. Berry. *J. Chem. Educ.* **2008**, *85*(4), 532.
[8] P. Gütlich, J. Jung, H. A. Goodwin. In: (Eds.: E. Coronado, P. Delhaès, D. Gatteschi, and J. S. Miller), *Molecular Magnetism: From Molecular Assemblies to the Devices*, **1996**, p. 327.
[9] P. Gütlich, B. Eckhard, A. X. Trautwein. *Mössbauer Spectroscopy and Transition Metal Chemistry*, In: Springer Berlin Heidelberg, **2011**, pp. 1-5.
[10] N. N. Greenwood, T. C. Gibb. *Mössbauer spectroscopy*, (Ed.: T. C. Gibb), London, Chapman and Hall, **1971**.
[11] J. E. Huheey, E. A. Keiter, R. L. Keiter. *Inorganic Chemistry: Principles of Structure and Reactivity*, Harper Collins College Publisher, **1997**.
[12] P. Gütlich, A. Hauser, H. Spiering. *Angew. Chem. Int. Ed.* **1994**, *33*(20), 2024-2054.

Part I: Spin transition in M(II)- 4- amino-1,2,4-triazole Chain complexes: revealing the role of intermolecular interactions in NH_2trz, OH-trz and phtp-trz systems

Chapter I: Prediction of the Spin Transition Temperature in Fe^{II} 1D NH_2trz Coordination Polymers: an anion based data base*

Introducing remarks

The reversible thermochromic ST of 1D chain compounds of formula $[Fe(NH_2trz)_3](anion)_2 \cdot nH_2O$ (NH_2trz = 4-amino-1,2,4-triazole), that can occur around room temperature, has been thoroughly investigated,[1-11] with prospective potential applications (e.g. thermal displays, memory devices and sensors)[12-15]. In the literature it is noted that the modification of the nature and the geometry of non coordinated anions can affect the transition temperature, $T_{1/2}$, of these materials without dramatically modifying the hysteresis loop. This feature has been observed for monovalent inorganic anions (Cl^-, Br^-, I^-, BF_4^-, ClO_4^-)[1-3] and organic sulfonate anions (alkyl[9, 11, 16], phenyl derivatives[6, 8, 10], 2-naphthalene derivatives[7] and spiropyrane sulfonate[10]) for the series $[Fe(NH_2trz)_3](anion)_2 \cdot nH_2O$. Indeed, the insertion of spherical counteranions, such as halogen anions, leads to higher $T_{1/2}$ as compared with bulkier anions such as BF_4^- and ClO_4^-. A relationship was proposed between

* Adapted from M.M. Dîrtu, Y. Garcia, M. Nica, A. Rotaru, J. Linares, F. Varret, *Polyhedron* **2007**, 26, 2259; M. M. Dîrtu, A. Rotaru, D. Gillard, J. Linares, E. Codjovi, B. Tinant, Y. Garcia, *Inorg. Chem*. **2009**, *48*, 7838.

the anion radii and the transition temperatures for $[Fe(hyetrz)_3]A_2 \cdot nH_2O$ (hyetrz = 4-(2'-hydroxyethyl)-1,2,4-triazole ; A = Cl^-, NO_3^-, Br^-, I^-, BF_4^-, ClO_4^-, PF_6^-)[17], but little is known however on the role of divalent anions in promoting/decreasing interchain interactions in such 1D switchable systems.

Thus in this work, novel fluorinated inorganic anions (TiF_6^{2-}, ZrF_6^{2-}, SnF_6^{2-}, GeF_6^{2-}, TaF_7^{2-}) that are expected to favor the engineering of H-bonding networks thanks to their fluorine atoms[18] were selected to build 1D coordination polymers of formula $[Fe(NH_2trz)_3]Anion \cdot nH_2O$. Their ST was investigated with care by a set of relevant physical techniques. We also describe the crystal structure of $[Cu(NH_2trz)_3]ZrF_6 \cdot H_2O$ which represents a rare example of crystallized 1D chain complex with triple *N1*,*N2*-1,2,4-triazole bridges, which serves as a model for the related Fe(II) coordination polymers.

Synthesis

The 1D coordination polymers were obtained as white powders by self assembly of the corresponding Fe^{II} inorganic precursors $[Fe(H_2O)_6]Anion$, prepared *in situ* and in air, with an alcoholic solution of NH_2trz (methanol or ethanol). These compounds were successfully characterized by CHN and TGA analyses, atomic absorption, X-ray powder diffraction (293 K), IR, UV-Vis, and ^{57}Fe Mössbauer spectroscopy. Thermogravimetric and elemental analyses did not reveal alcohol guest molecules but non-coordinated water molecules instead affording the following general formula $[Fe(NH_2trz)_3]Anion \cdot nH_2O$: {anion = TiF_6^{2-}, n = 0.5 (**1**) and n = 1 (**2**); anion = ZrF_6^{2-}, n = 0.5 (**3**) and n = 0 (**4**); anion = SnF_6^{2-}, n = 0.5 (**5**) and n = 1 (**6**); anion = TaF_7^{2-}, n = 3 (**7**) and n = 2.5 (**8**); anion = GeF_6^{2-}, n = 1 (**9**) and n = 0.5 (**10**)}. Hemihydrate or monohydrate compounds were thus obtained, except for Zr and Ta. Inclusion of solvent used for synthesis was only observed for $[Fe_3(NH_2trz)_{10}(H_2O)_2](SbF_6)_6 \cdot S$ {S = 1.5 CH_3OH (**12**), 0.5

C_2H_5OH (**13**)} whose trinuclear nature was confirmed by both elemental analysis and Mössbauer spectroscopy (*vide infra*).

(a)

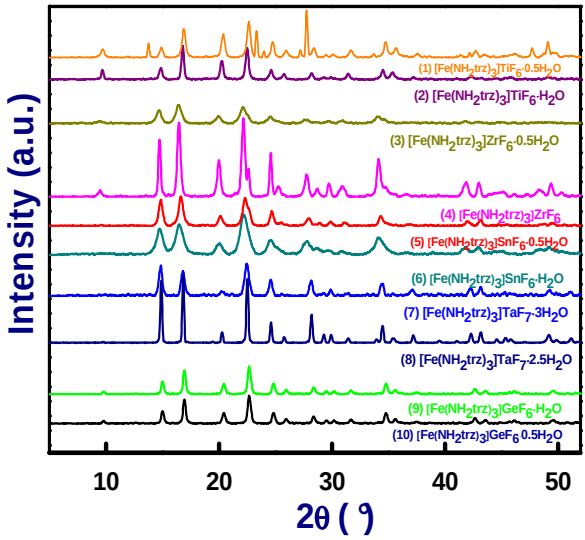

(b)

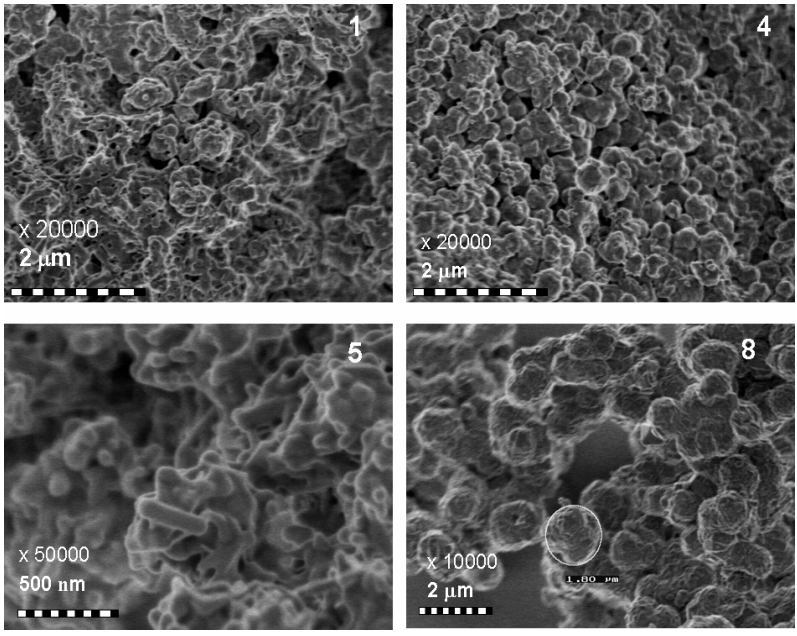

Figure 1 (a) X-ray powder diffraction patterns at 293 K for **1-10**. (b) SEM imaging at 293 K for **1**, **4**, **5** and **8**.

Isostructurality of the chain complexes was concluded from X-ray powder diffraction patterns that revealed principal peaks in all diffractograms (Fig. 1a). Compounds **4** and **8** show the better resolved diffractograms of the series. Spherical particles of 484 nm (**4**) and 1.80 μm (**8**) diameter are distinguished in the aggregates, as well as elongated rods of dimensions (457 x 108 nm) for (**5**) by SEM imaging. Compound **1** is however much less crystalline (Fig. 1b). This series of materials have also essentially identical IR spectra. The band assigned to ring torsion of NH_2trz at $\nu = 619$ cm^{-1} and the N-N stretching band at $\nu = 1197$ cm^{-1} are shifted[19] upon complexation to 624 cm^{-1} and 1210 cm^{-1}, respectively; e.g. for $[Fe(NH_2trz)_3]ZrF_6$ (**4**)**.** These values confirm a coordination of the iron to the 1,2,4-triazole ring.[20] Presence of non coordinated divalent counteranions originating from the inorganic precursors is also confirmed by IR as listed in the synthesis section. ^{57}Fe Mössbauer spectroscopy confirms the presence of only one $Fe^{II}N_6$ site, undergoing SCO behavior on cooling and the absence of oxidation product of iron (See Fig. 5). Mössbauer parameters of these compounds (See Mössbauer section) are typical for 1D polymeric chains with NH_2trz as ligand.[21]

All materials were prepared as white powders, present a reversible thermochromism to pink on cooling. These colors depend on the spin state of the Fe^{II} centers. The white color is due to the location of the spin-allowed lowest energy d-d transition, $^5T_{2g} \rightarrow {}^5E_g$, for the HS sites in the near infrared region (~ 11800 cm^{-1})[1]. The pink color is due to the $^1A_{1g} \rightarrow {}^1T_{1g}$ d-d transition of LS Fe^{II} sites observed at ~ 19250 cm^{-1}.

X-ray crystal structure of $[Cu(NH_2trz)_3]ZrF_6 \cdot H_2O$[†]

(a)

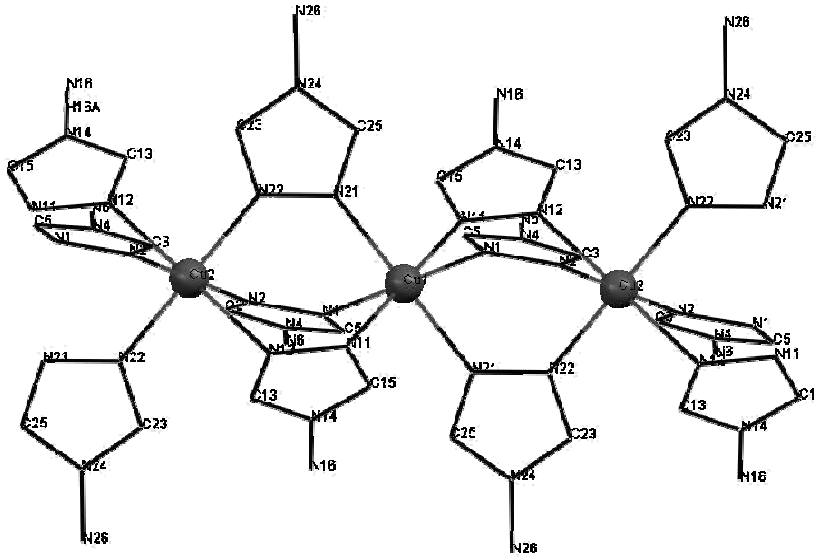

(b)

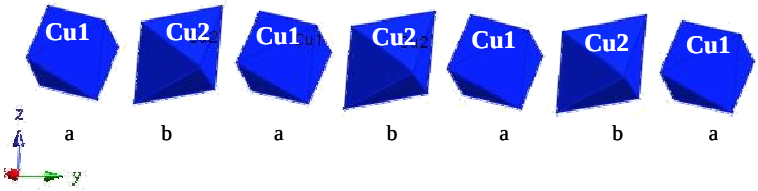

Figure 2 (a) Drawing and atomic labeling system showing the 1D chain of $[Cu(NH_2trz)_3]ZrF_6 \cdot H_2O$ along the *a*-axis. Non-coordinated counter anions and water molecules have been omitted for clarity. (b) Orientation of CuN_6 octahedra in a $[Cu(NH_2trz)_3]ZrF_6\ H_2O$ chain.

Blue needles single crystals of the model material $[Cu(NH_2trz)_3]ZrF_6 \cdot H_2O$ (**11**) were successfully obtained by slow evaporation of an aqueous solution

[†] Crystal structure was solved by Prof. B. Tinant (UCL).

of $[Cu(H_2O)_6]ZrF_6$ and NH_2trz at room temperature. Attempts to crystallize other Fe^{II} and Cu^{II} complexes of the series failed. Crystallographic data at 100(1) K and structure refinement of **11** that crystallizes in the monoclinic $P2_1/n$ space group are given in Table 1 (Appendix-Crystal structure data). Fig. 2a shows a view of the 1D polymeric chain built of cationic $[Cu(NH_2trz)_3]^{2+}$ units. The asymmetric unit consists of two Cu^{II} atoms, Cu1 and Cu2, located on inversion centers. These copper ions are linked by three bidentate bridging NH_2trz ligands through *N1*, *N2* atoms. Both copper ions are arranged in a CuN_6 core of octahedral geometry within the chain. The basis of the octahedron is formed by four ligands with bond lengths ranging between 2.014(3) – 2.080(3) Å (Table 2). Two NH_2trz ligands are axially coordinated to copper (Cu1-N1 = 2.080(3), Cu2-N12 = 2.385(3) Å) with difference in bond length indicating a distortion. The ligand bridges Cu1 and Cu2 ions almost at the same distance with Cu1-N21 = 2.029(3) Å and Cu2-N22 = 2.029(3) Å. The Cu1-N11 distance is 2.014(3) Å which corresponds to an angle of 122.6(2)º for Cu1-N11-N12. As the distance Cu2-N12 = 2.385(3) Å increases, the (Cu2-N12-N11) angle widens to 125.5(2)°. In this case, only a torsion angle (Cu1-N11-N12-Cu2) = -12.8(3)º maintains this geometry. The coordination mode of *N*1, *N*2 of NH_2trz presents quite a high degree of asymmetry compared to the Cu-N-N bridge angles, which are 127.2(3)º for Cu1-N1-N2 and 122.1(3)º for Cu2-N2-N1. The Cu1-N1-N2-Cu2 torsion angle is +18.5(3)º. In fact, the connexion of Cu^{II} ions, whose octahedra are distorted, should involve a deviation from the *b* axis which is clearly seen on Fig. 3a.

The Cu octahedra are oriented in an *ababa* fashion (Fig. 2b) as observed for $[Cu(NH_2trz)_3](BF_4)_2 \cdot H_2O$[22] and two other 1D Cu^{II} chain complexes[23, 24]. Other arrangements were found for $[Cu(NH_2trz)_3]SiF_6 \cdot 8/3H_2O$ (*abcabc)*[25] and $[Cu(hyetrz)_3](ClO_4)_2 \cdot 3H_2O$ (*abcbab*)[26].

The Cu•••Cu intrachain distance of 3.8850(3) Å is shorter than the Cu•••Cu distance found for $[Cu(NH_2trz)_3]A_x{\cdot}nH_2O$, (A = BF_4^-, (x = 2, n = 1); SiF_6^{2-} (*x = 1*, n = 8/3)),[22] with 3.922 Å and 3.904 Å, respectively (Table 3). In $[Cu(hyetrz)_3](CF_3SO_3)_2{\cdot}2H_2O$,[24] there exist three types of Cu^{II} ions, with Cu1•••Cu2 = 3.8842(4) Å and Cu2•••Cu3 = 3.9354(4) Å, which reflects a difference between the coordination geometry of two pairs of triple *N1-N2*-1,2,4-triazole bridges. A similar situation is found for $[Cu(hyetrz)_3](ClO_4)_2{\cdot}3H_2O$ with two types of distances at 3.853(2) Å for Cu1••• Cu2 and 3.829(2) Å for Cu2•••Cu3. These distances are a little shorter than the ones observed in **11**, which gives a very slight zigzag arrangement of the chain. This can also be seen by the value of the angle between the vectors of Cu^{II} pairs ions, (Cu1, Cu2) and (Cu2, Cu3) which is 175º. For $[Cu(hyptrz)_3]$(4-chloro-3-nitrophenylsulfonate)$_2{\cdot}2H_2O$ (hyptrz = 4-(3'-hydroxypropyl)-1,2,4-triazole)[23], the Cu1•••Cu2 distance increases up to 3.962 Å.

Non coordinated species are also found in the crystal packing (Fig. 3a). A hexafluorozirconate anion is connected to the amino group of the triazole through hydrogen bonding. In addition, the fluorine atoms allow interchain interactions though the connection to nitrogen atoms belonging to two different chains. The involvement of the counteranion in the H-bonding network is probed by its distortion parameter Σ = 22.05(5)° that was determined following ref. [27].

Table 3 Gathering of crystallographic data for the $[Cu(NH_2trz)_3]$Anion 1D chain complexes.

Anion	**V_{anion} (nm^3)[34]**	**Intrachain Cu •••Cu (Å)**	**Interchain Cu •••Cu (Å)**	**Octahedra Arrangement**	**Crystal system**	**Space group**	**Ref.**
BF_4^-	0.073	3.922	10.4, 10.6	ab ab ab	Triclinic	P-1	[22]
ClO_4^-	0.082	-	-	-	Triclinic	P-1	[28]
$BF_4^-/(SiF_6^{-2})_{0.5}$	0.073/0.112	3.877, 3.886	10.3, 11.3, 13.3	ab ab ab	Triclinic	P-1	[22]
SiF_6^{-2}	0.112	3.855, 3.886, 3.904	10.5, 11.4, 12.3	abc abc	Monoclinic	P-1	[22]
ZrF_6^{-2}	0.121	3.885	10.99, 11.04, 11.70	ab ab ab	Triclinic	$P2_{1/n}$	[a]

[a]this work

(a)

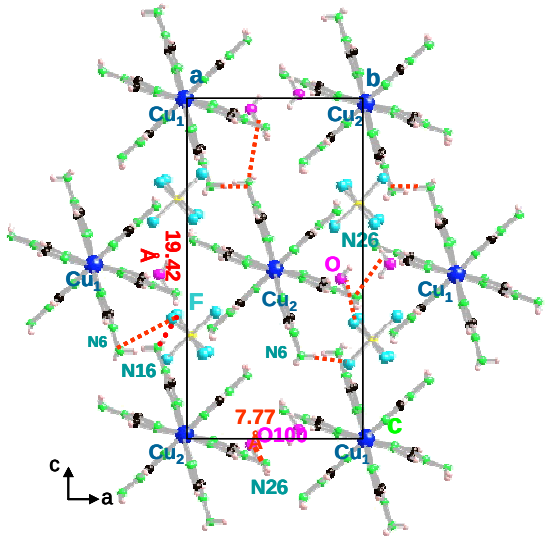

(b)

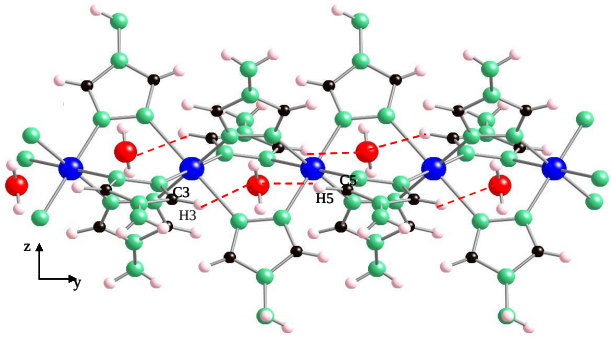

Figure 3 (a) Projection of the crystal structure of $[Cu(NH_2trz)_3]ZrF_6 \cdot H_2O$ on the (*ac*) plane showing hydrogen-bonded chains; (b) View of the cationic chain of $[Cu(NH_2trz)_3]ZrF_6 \cdot H_2O$ along the *b* axis showing intramolecular CH•••O interactions involving the water molecules and the triazole ring. On the (*bc*) plane, the H atoms belonging to the amino groups are actually masked by the N atoms.

Indeed, there are two intermolecular interactions between fluoride and the non-coordinated water molecule, (O1-H-F2 and F4), but both fluorine F2 and F4 are linked to N6 and N16, respectively. There is one hydrogen bond between the water molecule and the amino group of the triazole at 2.836 Å, O1•••N6 (Table 2b). Water molecules also connect two metallic sites by C-H•••O interactions through the triazole rings (Fig. 3b). It is found at 2.12 Å (C5-H5•••O1) and at 2.20 Å (C3-H3•••O1). Thus, these interactions set up a dense hydrogen bonding network.

Thermal spin-crossover properties

SQUID magnetometry

Magnetic susceptibility data for (**1**, **2**, **9**, **10**) were recorded by Dr. A. Rotaru (Versailles) over the temperature range 70-300 K range, and over 4-300 K for **3** – **8**, in order to track a possible spin state transition.

On cooling and warming, compounds **1** - **10** reveal unambiguously an abrupt hysteretic spin transition. At room temperature, **1** - **4** are fully HS. γ_{HS} first decreases slightly to ~ 235 K, and more abruptly down to ~ 100 K reaching ~ 0.17 for **1** and 0.22 for **2**, indicating an incomplete spin transition. The transition temperatures on slow cooling and warming are $T_{1/2}^{\downarrow}$ = 194 K and $T_{1/2}^{\uparrow}$ = 200 K for **1**, and $T_{1/2}^{\downarrow}$ = 189 K and $T_{1/2}^{\uparrow}$ = 196 K for **2**, respectively. The ST of **3** and **4** is more complete at the lowest temperature investigated and shifted upwards with $T_{1/2}^{\downarrow}$ = 208 K and $T_{1/2}^{\uparrow}$ = 226 K for **3**, and $T_{1/2}^{\downarrow}$ = 214 K and $T_{1/2}^{\uparrow}$ = 238 K for **4**, respectively.

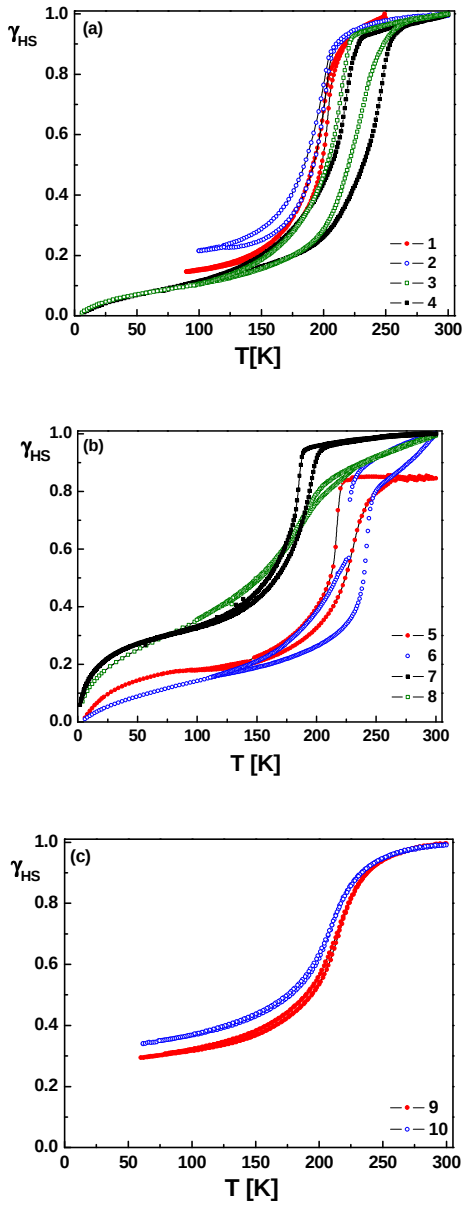

Figure 4 γ_{HS} *vs. T* curves on cooling and warming modes for $[Fe(NH_2trz)_3]Anion \cdot nH_2O$ complexes (a) **1**-**4**; (b) **5**-**8**; (c) **9**, **10**, as deduced from magnetic susceptibility measurements.

Contrary to all other compounds, only 85% HS Fe^{II} ions are found over a plateau region 300-230 K for **5**, after which γ_{HS} decreases abruptly at $T_{1/2}^{\downarrow}$ = 211 K and then smoothly down to 18% at 100 K indicating an incomplete spin transition. On warming the hysteresis is found at $T_{1/2}^{\uparrow}$ = 225 K. The ST curve of **6** is shifted upwards by 12 K, compared to **5** with $T_{1/2}^{\downarrow}$ = 226 K and $T_{1/2}^{\uparrow}$ = 242 K. The ST of **7** and **8** occurs around 180 K. **8** displays the most gradual SCO of the series with $T_{1/2}^{\downarrow}$ = 172 K and $T_{1/2}^{\uparrow}$ = 174 K, with ~ 30 % Fe^{II} HS active sites at 100 K. **7** presents a more abrupt ST but still incomplete with $T_{1/2}^{\downarrow}$ = 176 K and $T_{1/2}^{\uparrow}$ = 184 K. **9** and **10** presents similar incomplete SCO behavior with a small hysteresis width (**9**: $T_{1/2}^{\uparrow}$ = 211 K, $T_{1/2}^{\downarrow}$ = 209 K; **10**: $T_{1/2}^{\uparrow}$ = 205 K, $T_{1/2}^{\downarrow}$ = 204 K). The lowering in γ_{HS}, recorded below 25 K for **3-8** is due to zero-field splitting but antiferromagnetic interactions between HS Fe^{II} ions cannot be fully excluded[30]. A careful analysis of the low temperature tail of the magnetic curves of compounds **3-6** and **8** evidences no freezing-in effect, as shown on $[FeL_3](PF_6)_2$ with L = 2-[3-(2´-pyridyl)pyrazole-1-ylmethyl]pyridine][31].

^{57}Fe Mössbauer spectroscopy

Mössbauer spectra of Fe^{II} compounds (**1-10**) were recorded on cooling and warming over the temperature range 78-300 K. These results were confirmed by Prof. J. Linares (Versailles). Fig. 5 shows representative spectra for compound **4**. Mössbauer parameters are listed in Table 4 and in the supplementary section for all other compounds (Tables 4-13).

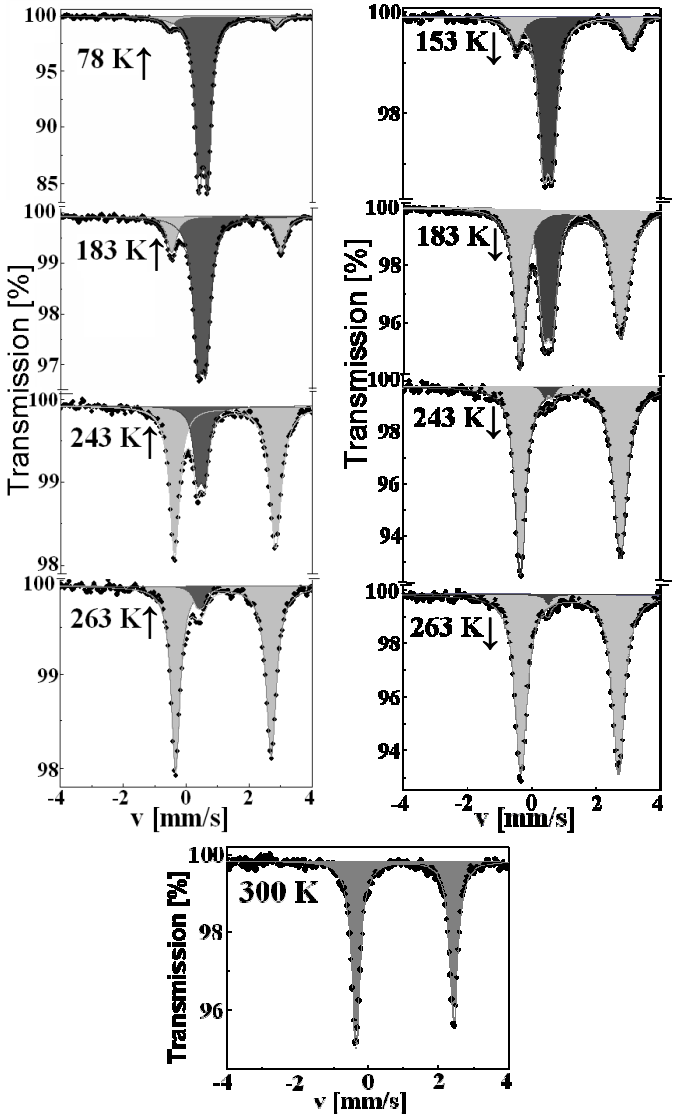

Figure 5 Selected ^{57}Fe Mössbauer spectra of **4** on warming (left) and cooling modes (right). Grey and dark grey correspond to the HS and LS doublets, respectively.

The spectrum at 78 K shows two quadrupole doublets attributed to HS Fe^{II} ions (δ^{HS} = 1.15(1) mm·s^{-1} and $\Delta E_Q{}^{HS}$= 3.41(2) mm·s^{-1}) and LS Fe^{II} ions (δ^{LS}

= 0.53(1) mm·s^{-1} and ΔE_Q^{LS}= 0.29(1) mm·s^{-1}) in population 7/93, indicating an incomplete ST in good agreement with magnetic susceptibility measurements (Fig. 4a). This latter value that represents the lattice contribution to the electric field gradient reveals the presence of local distortions as expected within a constrained chain where some Fe^{II} ions have not been switched.[32] Upon warming, the relative intensity of the HS doublet slowly increases until 183(1) K to reach ~15 %, and then more abruptly. At 300 K, the spectrum consist of only one HS doublet (δ^{HS} = 1.05(1) mm·s^{-1} and ΔE_Q^{HS}= 2.77(1) mm·s^{-1}). On cooling from room temperature to 78 K, the reverse situation is observed. The spectra shown on cooling and warming modes at 243 K and 183 K clearly evidence a hysteresis effect. Indeed, the ST curve deduced by plotting the variation of the temperature dependence of A_{HS}/A_{tot} shows an hysteresis loop, with $T_{1/2}^{\downarrow}$ = 179 K and $T_{1/2}^{\uparrow}$ = 206 K (Fig. 6). Other compounds also reveal incomplete and hysteretic SCO behavior over the temperature range 300-50 K as shown in Fig. 6. These curves were transformed in γ_{HS} by assuming equal Lamb Mössbauer factors for the LS and HS states. Surprisingly, unusually broad hysteresis loops were derived, sometimes temperature shifted as compared to the $\gamma_{HS}(T)$ curves deduced from SQUID measurements (Fig. 4). These features prompted us to revise our hypothesis and to accurately determine *f* factors for both spin states employing the Debye model.[33] The logarithm of the surface of the Mössbauer peaks shows two temperature domains, as expected for the HS and LS states. The slope is proportional to the Debye temperature, θ_D, which is determined in the two spin states for **1**-**6** (Table 14). Taking into account the respective *f* factor, we could correct the ST curves (Fig. 6) and derive the real ST temperatures (Table 14). No major differences are

found except for **2**, **3** and **5**. The Debye temperatures allow determining the rigidity of these chains in the two spin states. The LS lattice is always more rigid than the HS one since the vibrational frequencies increase during the HS to LS transition, as a result of the decrease in the Fe-N bond lengths. For comparison, θ_D^{HS} for **2** and **6** is similar as for $[Fe(NH_2trz)_3](ClO_4)_2$ with θ_D^{HS} = 188(12) K[34]. Overall, the variation of the lattice rigidity, $\Delta\theta_D = \theta_D^{LS} - \theta_D^{HS}$, accompanying the ST of **1**-**6** is of the same order of magnitude (~ 21 K).

Fig. 7 shows the evolution of the isomer shift at 78 K in the LS state, δ_{LS}^{78K} *vs.* $T_{1/2}^{\uparrow}$ for $[Fe(NH_2trz)_3]^{2+}$ 1D complexes including monovalent and divalent anions, prepared in aqueous methanol or ethanol. In both cases, a linear decrease of δ_{LS}^{78K} when increasing $T_{1/2}^{\uparrow}$ is observed. This behavior corresponds to an increase of the Fe-N bond covalency when anions of smaller volumes are inserted between the chains, resulting in higher transition temperatures (See Fig. 8). This increase in covalency may originate from the chains bringing closer together as a consequence of the insertion of small guest anions.

Table 14 Selection of Mössbauer parameters and transition temperatures for $[Fe(NH_2trz)_3]Anion \cdot nH_2O$ (**1-10**).

Chain	Anion	n	Synthesis Solvent	ΔE_Q^{HS} (295(5)K) [mm s^{-1}]	ΔE_Q^{LS} (78 K) [mm s^{-}]	γ_{HS} (78K)	$\theta_D^{(HS)}$ [K]	$\theta_D^{(LS)}$ [K]	$\Delta\theta_D$ [K]	$T_{1/2}\uparrow$ [K]	$T_{1/2}\downarrow$ [K]	ΔT [K]
1	TiF_6^{2-}	0.5	MeOH	2.760(1)	0.296(1)	0.16	218(5)	244(5)	26(10)	212	195	17
2	TiF_6^{2-}	1	EtOH	2.763(4)	0.306(2)	0.27	188(5)	209(5)	21(10)	202	192	10
3	ZrF_6^{2-}	0.5	MeOH	2.770(3)	0.293(1)	0.10	122 (5)	148(5)	26(10)	218	190	28
4	ZrF_6^{2-}	0	EtOH	2.794(6)	0.293(1)	0.085	151(5)	171(5)	20(10)	216	179	37
5	SnF_6^{2-}	0.5	MeOH	2.777(2)	0.318(6)	0.23	132(5)	149(5)	17(10)	218	200	18
6	SnF_6^{2-}	1	EtOH	2.784(2)	0.317(2)	0.20	167(5)	184(5)	17(10)	225	189	36
7	TaF_7^{2-}	3	MeOH	2.804(5)	0.292(4)	0.38				199		
8	TaF_7^{2-}	2.5	EtOH	2.785(1)	0.299(2)	0.28				217	217	
9	GeF_6^{2-}	1	MeOH	2.889(5)	0.282(3)	0.32				230		
10	GeF_6^{2-}	0.5	EtOH	2.890(1)	0.280(2)	0.39				223		

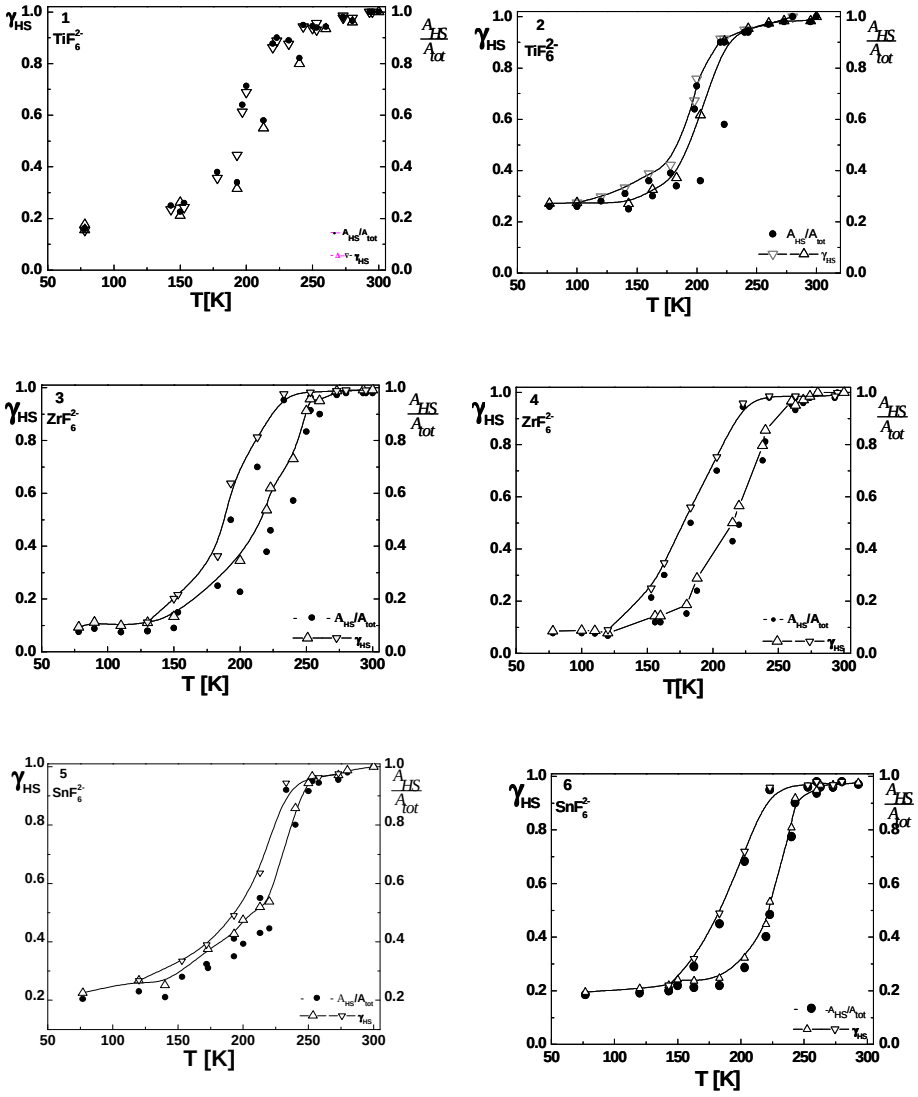

Figure 6 Overview of selected γ_{HS} *vs*. *T* curves as deduced from Mössbauer spectroscopy, before (•) and after (▲,▼) Debye-Waller corrections for **1-6**. The line is a guide to the eyes after corrections.

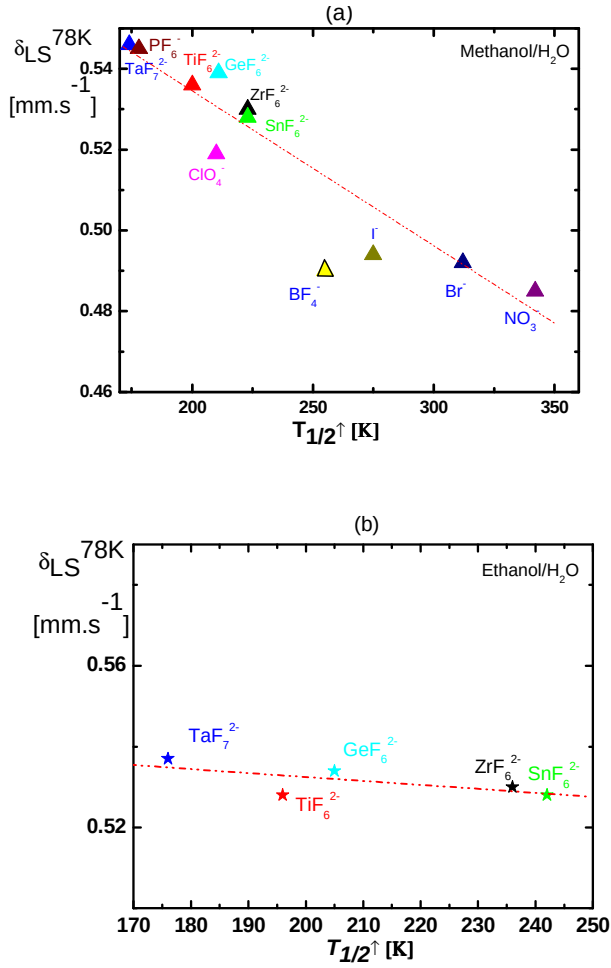

Figure 7 δ_{LS} $^{(78\ K)}$ *vs.* $T_{1/2}{}^{\uparrow}$ for $[Fe(NH_2trz)_3](Anion)_{x\ (x\ =\ 1,\ 2)}$ prepared in aqueous (a) CH_3OH or (b) C_2H_5OH. The data for monovalent anions are from [35].

As a result, the local distortion of the FeN_6 octahedron increases as seen on Fig. 8b for ΔE_Q ^{HS} (295 K). It is worth noting that in the LS state, ΔE_Q ^{LS} remains constant at 0.30(1) mm/s (Fig. 9a). Because there is no valence contribution to consider, the lattice contribution to the quadrupole splitting indicates that the Fe^{II} sites are distorted, as expected for such metal centers

connected within a chain by three *N*1,*N*2-1,2,4-triazole bridges. A ^{57}Fe Mössbauer spectrum was also recorded on $[Fe_3(NH_2trz)_{10}(H_2O)_2](SbF_6)_6 \cdot 1.5CH_3OH$ (**12**) at 143 K (Fig. 10). This spectrum was fitted best taking into account three quadrupole doublets. The central signal corresponds to LS Fe^{II} ions (δ^{LS} = 0.53(1) mm·s^{-1} and $\Delta E_Q{}^{LS}$= 0.27(1) mm·s^{-1}) after switching whereas the two other signals correspond to HS Fe^{II} ions (δ^{HS1} = 1.43(1) mm·s^{-1} and $\Delta E_Q{}^{HS1}$= 3.76(2) mm·s^{-1}, δ^{HS2} = 1.19(1) mm·s^{-1} and $\Delta E_Q{}^{HS2}$= 3.57(1) mm·s^{-1}). The relative area fraction of these signals of 70/15/15 does not correspond to the LS/HS1/HS2 spin population due to the Debye Waller factor differences of the spin states in this system. An incomplete ST was systematically observed at low temperature for the chain compounds **1**-**10**. This character could originate from crystal defects nearby ends of chains resulting from an imperfect packing of the polymeric chains, HS inactive FeN_6 sites or water molecules in the coordination sphere of ends of chains. A closer look at the Mössbauer spectra of **1**-**10** at 78 K reveals only one Fe^{II} site being in the LS and HS states (Fig. 5 for **4** and Fig. 13 for **2**, **9**, **10**). Thus, there is no indication of an FeN_3O_3 environment which would be characteristic of three terminal coordinated water molecules[36] provided these are present in sufficient concentration. Nevertheless, ends of polymeric chains with less coordinated water molecules may not be detected by Mössbauer spectroscopy[37] and thus cannot be *a priori* excluded. However, none of these species are distinguished in our Mössbauer spectra contrary to what is found for the trinuclear complex **12** that clearly reveals two lattice sites: a SCO one and a HS one corresponding to a FeN_5O core with one coordinated water molecule at the extremity of the oligomer (Fig. 10).

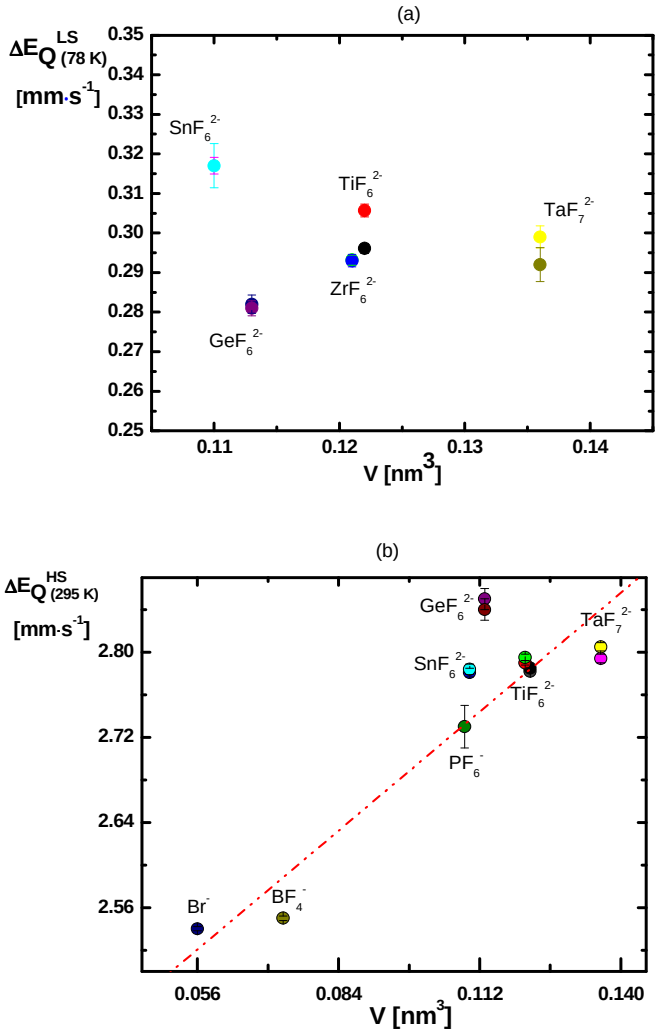

Figure 8 $\Delta E_Q^{LS}{}_{(78\ K)}$ *vs.* $V\ [nm^3]$ (a) and $\Delta E_Q^{HS}{}_{(295\ K)}$ *vs.* $V\ [nm^3]$ (b) for $[Fe(NH_2trz)_3](Anion)_{x\ (x\ =\ 1,\ 2)}$ prepared in aqueous CH_3OH. Data from monovalent anions [35] have been added.

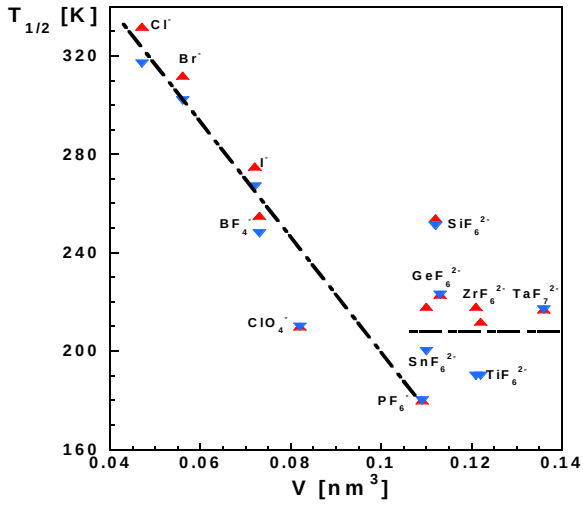

Figure 9 Variation of the transition temperatures, $T_{1/2}$, as deduced from 57Fe Mössbauer spectroscopy, on cooling (▼) and warming modes (▲) *vs.* the anion volume for $[Fe(NH_2trz)_3]\cdot$Anion.

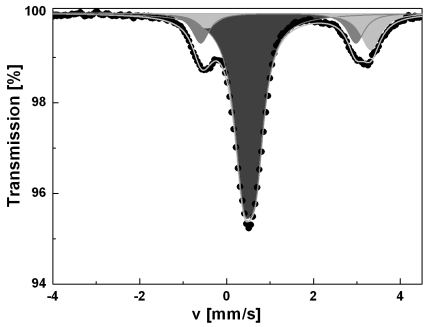

Figure 10 ^{57}Fe Mössbauer spectra at 143 K for $[Fe_3(NH_2trz)_{10}(H_2O)_2(SbF_6)_6]\cdot 1.5\ CH_3OH$ (**13**). Grey and light grey corresponds to two HS sites. Dark grey correspond to a LS doublet.

Differential scanning calorimetry (DSC)

Compounds **1**-**10** were investigated by differential scanning over the temperature range 100 – 295 K at 5 K/min for both cooling and heating rates. Representative heat and cooling capacity profiles are depicted in Fig. 11. An endothermic peak is observed on warming for **1** at $T_{max}^{\uparrow}$ = 210 K and an exothermic peak is recorded at $T_{max}^{\downarrow}$ = 200 K, on cooling, thus revealing a hysteresis loop (10 K). These peaks correspond to the first-order phase transition associated to the SCO behavior of **1**. The hysteresis width matches rather well the one recorded by magnetic susceptibility measurements (6 K). It is however, in comparison, temperature shifted due to the different heating and cooling rates used for the calorimetric experiments. All compounds present the same behavior except **6** for which a broad satellite peak is associated to the main exothermic peak. This technique confirms the gradual character of the SCO behavior (e.g. **7**, **10**) by the observation of broad peaks.

The hysteresis width as well as thermodynamic parameters derived from these measurements (ΔH_{HL}, ΔS_{HL}, ΔS_{vib}) are listed in Table 15. Note that the enthalpy values were evaluated taking into account the active Fe^{II} ions only, as deduced by Mössbauer spectroscopy, in order to strictly refer to SCO sites. The entropy gain is much larger than the characteristic value for the electronic contribution to the entropy ($R \cdot \ln 5$ = 13.4 J/mol.K) which indicates a contribution to the change in the frequencies of the vibrational modes.[1] Such values are however not sufficiently high to suggest another transition type, such as an order-disorder transition of the anion for instance, as earlier noted for $[Fe(NH_2trz)_3]SnF_6 \cdot 0.5H_2O$.[38]

Table 15 Transition temperatures as deduced from DSC measurements, thermodynamic parameters, chain lengths and transition temperatures for **1-10**.

Entry	$T_{max}^{\uparrow}$ (K)	$T_{max}^{\downarrow}$ (K)	ΔT *(K)*	as (%)[a]	ΔH_{HL} (kJ mol^{-1})	ΔS_{HL} (J mol^{-1} K^{-1})	ΔS_{vib} (J mol^{-1} K^{-1})	N^{b}	τ *(nm)*[c]	*p (kbar)*[d]
1	210	200	10	72	7.1	34.5	21.1	7	2.15	2.7
2	206	201	5	75	7.3	36	22.6	8	2.50	3.4
3	233	209	24	85	7.4	33.6	20.2	13	4.30	3.6
4	256	220	36	85	6.7	30.5	17.1	13	4.30	1.8
5	224	203	21	75	6.3	31.2	17.8	8	2.50	0.9
6	244	224	20	80	8	34.3	20.9	10	3.58	5.0
7	206	197	9	72	5.9	30	17	7	2.15	p_0
8	-	200		60	5.8	29	16	5	1.43	p_0
9	213	211	2	62	6.4	30	17	5	1.43	1.1
10	213	207	6	58	6.9	32	19	5	1.43	2.5

[a] as = active sites; [b] number of atoms in a chain; [c] τ = chain length; [d] = internal pressure.

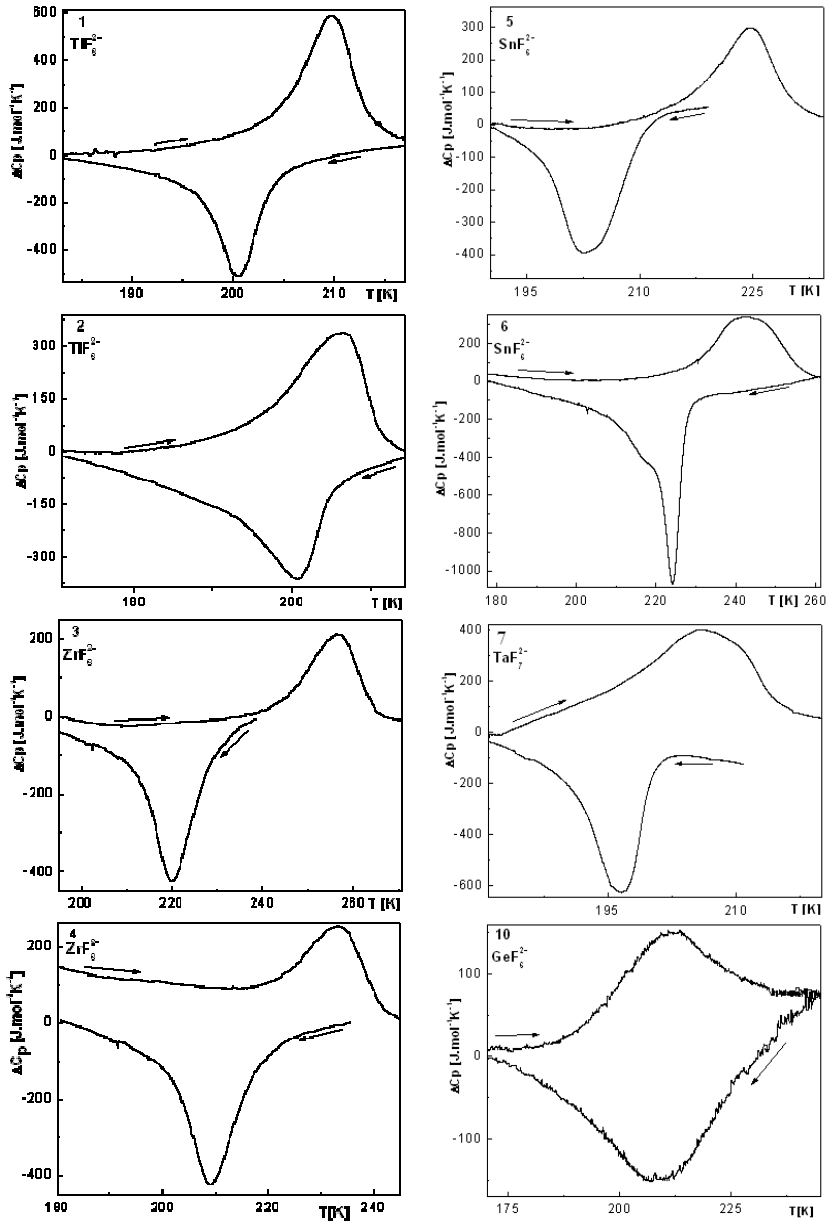

Figure 11 Selected DSC profiles for $[Fe(NH_2trz)_3]$Anion (**1**-**6**, **8**, **10**) in the 100-295 K temperature range in the cooling and warming modes.

Diffuse reflectivity measurements under hydrostatic pressure

The temperature dependence of the normalized reflectivity at the excitation wavelength of 550 nm was investigated over the pressure range (1 bar - 1.7 kbar) for compounds **3** and **4** by Dr. A. Rotaru and Dr. E. Codjovi (Versailles) (Fig. 12a). At 1 bar, the hysteresis loops are delineated at ($T_{1/2}{}^{\uparrow}$ = 225(1) K, $T_{1/2}{}^{\downarrow}$ = 212(1) K and ($T_{1/2}{}^{\uparrow}$ = 224(1) K, $T_{1/2}{}^{\downarrow}$ = 212(1) K) for **3** and **4**, respectively. The transition temperatures recorded by optical reflectivity differ from the ones obtained by magnetic and calorimetric measurements because of the difference of recording mode (only the surface is probed) and the acquisition rate is much slower 0.3 K/min. As the pressure is increased, a shift of the hysteresis loops to higher temperatures is observed while their shape is essentially unchanged. This temperature shift is attributed to the increase of the energy difference between the first vibronic levels corresponding to the HS and LS states under pressure because the volume of the LS Fe^{II} ions is smaller.[39-45] A decrease of the hysteresis width was also observed under pressure as noted on the phase diagram ($T_{1/2}$ *vs.* P) for compounds **3** and **4** (Fig. 12b). Extrapolating the $T_{1/2}$ vs. P curves, we estimate that the hysteresis should disappear at a critical pressure of ~7.8 and ~8.5 kbar for **3** and **4**, respectively, provided there are no other effects to consider, such as for instance a structural phase transition. Thus, although the transition temperatures under 1 bar are similar, the critical pressure is different.

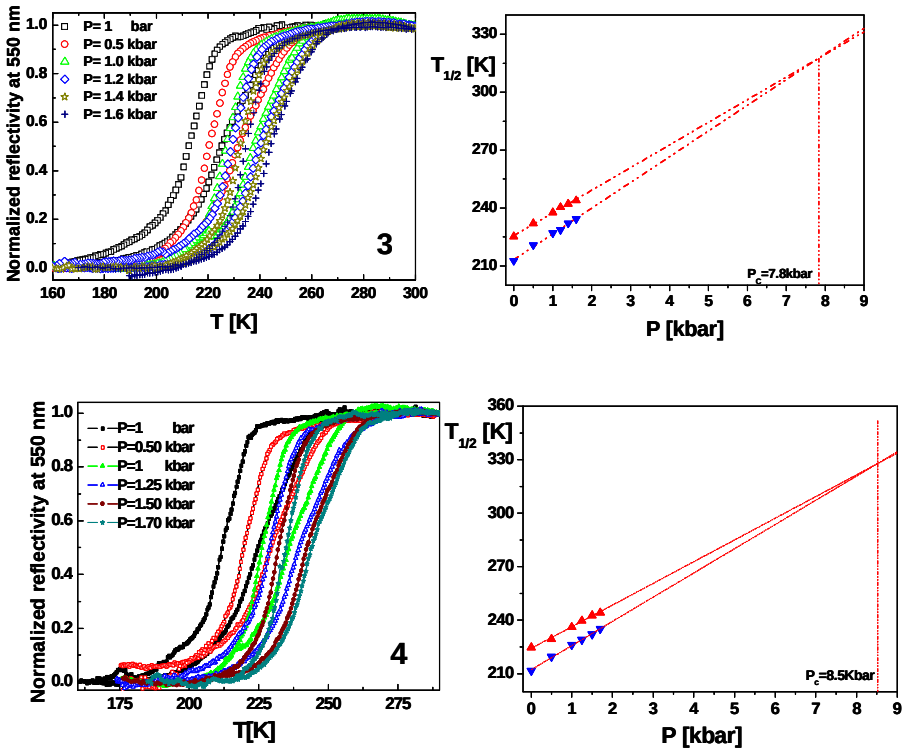

Figure 12 (a) Normalized reflectivity at 550 nm *vs*. T over the temperature range 100-300 K on cooling and warming at several pressures (1 bar up to 1.7 kbar). (b) Variation of transitions temperatures on warming (▲) and cooling (▼) *vs*. *P* for $[Fe(NH_2trz)_3]ZrF_6 \cdot 0.5H_2O$ (**3**) (top) and $[Fe(NH_2trz)_3]ZrF_6$ (**4**) (bottom). The dotted line indicates the pressure at which the hysteresis loop should disappear.

In order to estimate the magnitude of the internal pressure *p*, introduced by the anions within the chains, the results obtained from reflectance measurements have been coupled to the calorimetric ones. Thus, the enthalpy variation associated to the ST can be written as:

$$\Delta H = \Delta H_o + p\Delta V_{HL} \qquad \text{(b)}$$

with ΔH_o = 5.8(1) kJ mol^{-1}, our reference enthalpy corresponding to compounds **7** and **8**, that do not display any hysteresis loops and present the lower enthalpies of the series.

The volume change associated to the ST, ΔV_{HL}, can be evaluated as 7.25 $Å^3$ from the ($T_{1/2}$-P) phase diagram displayed in Fig. 12, where P refers to the external pressure applied to the system, and from the entropy associated to the spin transition ΔS_{HL}, (Table 15) using the Clausius - Clapeyron relationship (eq. c)[46]:

$$\Delta V_{HL} = \Delta S_{HL} \frac{dT_{1/2}}{dP} \quad \textbf{(c)}$$

Thus, using eq. d, we derive the internal pressure that range between ~ 1 and 5 kbar (Table 15).

$$p = \frac{\Delta H - \Delta H_0}{\Delta V_{HL}} \quad \textbf{(d)}$$

Discussion

The rational design of highly efficient and specific functional SCO materials is a very active area of investigation. Several 1D chain compounds of formula $[Fe(NH_2trz)_3]Anion \cdot nH_2O$ including monovalent or a few divalent counteranions had been synthesized but no rationalization of their ST properties has been proposed up to now. These compounds display thermally induced ST behavior whose working temperature range actually depends on the nature of the counter-anion (geometry, H-bonding ability …) and particularly their size. Indeed, relatively small anions, such as NO_3^- [1] or Br^- [2] , allow observation of spin transitions around room temperature, e.g.

whereas bulkier anions (e.g. BF_4^-[2]) afford SCO at much lower temperatures. A somehow linear trend between the transition temperature $T_{1/2}$ and the anion radii for $[Fe(NH_2trz)_3](Anion)_2 \cdot nH_2O$ was preliminarily suggested by Lavrenova et al.[1-5] but later invalidated by the same authors[5]. In the present work, we have carefully investigated the ST of a series of Fe^{II} 1D NH_2trz coordination polymers including new divalent inorganic anions of different size (TiF_6^{2-}, ZrF_6^{2-}, TaF_7^{2-}, SnF_6^{2-}, GeF_6^{2-}) allowing to evidence two linear size regimes to be considered to account for the ST range observation (Fig. 8). Here, we consider the variation of $T_{1/2}$ (on cooling and warming) *vs*. the volume of the inserted anion[47] instead of considering the radius only determined from Kapustinskii's equation[48]. This choice allowed us to take into account the dimensional size of the anions. Two linear regimes are effective: (i) between $0.04 \leq V\ (nm^3) \leq 0.09$, where a decrease of the $T_{1/2}$ is observed with increasing the volume. In this volume range, less energy is needed to switch the spin state of the metallic ions as much as we increase in volume and space out the chains; (ii) above $V \geq 0.11\ nm^3$, with a saturation of $T_{1/2} \sim 200$ K. This behavior corresponds to a chain spacing limit in such a way that when the LS-HS transition occurs, FeN_6 sites have enough freedom to increase their bond length and expand along the chain axis, the counter anion being affected very little by the ST itself due to the large distance between a pair of chains where these anions are located. Thus, insertion of a bigger counteranion between the chains decreases the relative vertical displacement of the potential wells, in favor of the HS state, thereby inducing a negative pressure effect. What would be the SCO situation when the anion volume increases further? We extrapolate that the chains would become isolated to each other and that the $T_{1/2}$ would either stay in the same temperature range (~ 200 K) or decrease thus favoring a fully HS state. This

second hypothesis has actually been recently confirmed for the HS 1D chain $[Fe(NH_2trz)_3]B_{10}H_{10}\cdot H_2O$[49] that includes a counteranion of V ~ 0.23 nm^3,[50] that is much higher than the one of TaF_7^{2-}, which is the biggest anion investigated in the present study. This compound stays paramagnetic on cooling over the temperature range 300-2 K.

As deduced by comparison of the X-Ray powder diffraction patterns recorded at 293 K for compounds **1-10** (Fig. 1), the insertion of this series of divalent anions does not affect much the structural organization of the chains, allow to validate complementary spectroscopic comparisons. Indeed, Mössbauer spectroscopy confirms that whatever the inserted divalent anion, the local symmetry of the Fe octahedra is not modified as deduced by the constant value of the quadrupole splitting in the HS state. For lower size anion, a decrease of ΔE_Q^{HS}(295K) is however noted (Fig. 8b) thus indicating an increase of the local distortion around the metallic ion. Indeed, it is worth noting that the electric field gradient contribution of the lattice is usually of opposite sign as compared to that of the valence electrons.[51] This increase of local distortion indicates that chains are much closer in the case of lower size anions than for larger size anions. This geometric feature is also seen on the evolution of the isomer shift for the LS state, δ^{LS}, vs. $T_{1/2}$ (Fig. 8). Indeed, when $T_{1/2}$ increases, that is when the anion volume decreases (See Fig. 7), δ_{LS}^{78K} decreases. Because the isomer shift is of opposite sign to the electronic density seen by the iron atoms, the covalency degree of the Fe-N bond increases, which is consistent with the chains that are moved closer. Such structural features are deduced by X-ray diffraction when comparing the crystal structures of $[Cu(NH_2trz)_3]A_{2\ or\ 1}\cdot nH_2O$ ($A = BF_4^-$, SiF_6^{2-}) that crystallizes in the *P-1* space group[22]. Indeed, when the anion volume

increases ($V(BF_4^-)$ = 0.073 nm^3 < $V(SiF_6^{2-})$ = 0.112 nm^3 Å), the chain spacing increases (Table 3).

In the absence of suitable single crystals for these Fe^{II} compounds, and to better understand the impact of the supramolecular organization of these materials, the crystal structure of a model compound including a divalent anion of the present series was solved: $[Cu(NH_2trz)_3]ZrF_6 \cdot H_2O$ (**11**). The structure is stabilized by a dense hydrogen bonding network, involving the counter-anion, ZrF_6^{2-}, located in the third coordination sphere, the amino group of the 1,2,4-triazole ligand and a non-coordinated water molecule (Fig. 3a). More precisely, the anion is linked to both amino group and water molecules and to two 1D chains through the anion setting up interchain interactions. Intrachain interaction is also found because a non-coordinated water molecule establishes a bridge between metallic sites within a chain (Fig. 3b), as noted for $[Cu(tba)_3](CF_3SO_3)_2 \cdot 3H_2O$ (tba = N-(4H-1,2,4-triazole-4-yl)benzamide.[52, 53] Such supramolecular interactions may well play an effective role in the propagation of elastic cooperative interactions within **3** resulting in the observation of a wide hysteresis loop of 28 K (Fig. 4a). Such an extended 3D hydrogen bonding network was also suggested to account for the 35 K hysteresis width of $[Fe(NH_2trz)_3](NO_3)_2$.[54] These results thus point out the high potential of H-bonds for transmitting cooperative interactions during a ST as recently highlighted for a structurally characterized Fe^{II} mononuclear SCO compound that displays a 70 K wide thermal hysteresis loop.[55] We thus cannot separate the influence of H-bonding[5] from the size effect of the anions on the SCO behavior of the Fe derivatives because the selected fluoride anions could favor extended H-bonding networks as found in the crystal structure of **11**.

Hydrostatic pressure measurements were carried out on selected SCO compounds, **3** and **4**. Under pressure the chains are expected to get closer to each other, which should increase the connections in the crystal lattice and render the transition more abrupt. The steepness of the transition curves is however preserved whatever the applied pressure which indicates that the chain character is maintained.[56] The slopes of the $T_{1/2}$ *vs*. P line, $dT_{1/2}/dP$ = 11.7(5) K $kbar^{-1}$ and 13.6(5) K $kbar^{-1}$ for **3** and **4**, respectively, are similar to the one observed for the mononuclear compound $[Fe(2\text{-pic})_3]Cl_2 \cdot EtOH$ (2-pic = 2-picolylamine)[57] but lower than the one found for the 1D chain $[Fe(hyetrz)_3]$(3-nitro-phenylsulfonate)$_2$ (24 K $kbar^{-1}$)[56] and the 2D ST compound $[Fe(btr)_2(NCS)_2]\cdot H_2O$ (btr = 4,4'-bis-1,2,4-triazole)[58] (19.0(5) K $kbar^{-1}$) that was also studied by diffuse reflectivity[59, 60]. Interestingly, a decrease of the hysteresis width is observed, which may indicate a weakening of supramolecular interactions for this system, in particular intra-chain interactions that were identified for $[Cu(NH_2trz)_3]ZrF_6\cdot H_2O$ (Fig 3b). Hysteresis decrease has been predicted by mean field theory[46] but only once observed for a 1D chain compound, $[Fe(hyptrz)_3]$(4-chlorophenylsulfonate)$_2\cdot H_2O$ (hyptrz = 4-(3'-hydroxy-propyl)-1,2,4-triazole), with an additional reentrance phenomenon[61].

It is here important to distinguish between the *external pressure* P that corresponds to a given energy provided to the system (as one can consider the temperature ($T_{1/2}$) necessary to be provided to switch the system from the LS to the HS state) from the *internal pressure* set up by anion-cation interactions, p, that we have here estimated numerically, for the first time. This pressure can also be regarded, by comparison, as a 'chemical pressure'[62-64] because it corresponds to a variation of the composition of the

material depending on the nature of the inserted non coordinated species. This internal pressure is however different from the local elastic pressure set up during thermal relaxation after LIESST irradiation and that is induced by the neighboring spin changing molecules as described by Hauser[65-68].

It is of interest to note that a large internal pressure range is found for the investigated compounds (Table 15). This is not surprising because a tiny change in the nature or number of non coordinated species can dramatically modify the transition temperature.[56, 69] The number of atoms in a chain, *N*, also reported in Table 15, has been evaluated following eq. (e)[70, 71]:

$$N = 2\left(\frac{100}{100 - as}\right) \quad \text{(eq. } \mathbf{e}\text{)}$$

where *as* is the number of active sites undergoing the SCO behavior that has been accurately determined by ^{57}Fe Mössbauer spectroscopy in the higher and lower thermal branches of the ST curves for **1**-**10**. The chains (**3**, **4**) comprising the larger number of atoms {13} display the wider hysteresis loop as expected for longer chains with enhanced cooperative effects. Unfortunately, it was not possible to compare these results with dynamic light scattering data because of the low solubility of the present coordination polymers. Because, the Fe···Fe distance of the cationic chain $[Fe(NH_2trz)_3]^{2+}$ was determined by EXAFS spectroscopy (3.58 Å)[72], it was possible to estimate for the first time, the chain length distribution τ which range between 1 and 4 nm (Table 15).

Conclusion

In this chapter, we have focussed on 1D coordination polymers with 4-amino-1,2,4-triazole and more precisely on complexes with formula $[Fe(NH_2trz)_3]A\cdot nH_2O$, {A = TiF_6^{2-}, n = 0.5 (**1**) and n = 1 (**2**); A = ZrF_6^{2-}, n = 0.5 (**3**) and n = 0 (**4**); A = SnF_6^{2-}, n = 0.5 (**5**) and n = 1 (**6**); A = TaF_7^{2-}, n = 3 (**7**) and n = 2.5 (**8**); A = GeF_6^{2-}, n = 1 (**9**) and n = 0.5 (**10**), NH_2trz = 4-amino-1,2,4-triazole}. We have shown that the nature, geometry and the volume of the counteranions as well as the chain length govern the ST behavior of these materials. Because these magnetic are thermochromic, such characteristics could be useful for selecting appropriate candidates for a given application (displays, sensors, …) in a certain temperature or pressure working range. These materials constitute the first SCO complexes with TiF_6^{2-}, ZrF_6^{2-}, SnF_6^{2-}, TaF_7^{2-} and GeF_6^{2-}, thus affording a new generation of inorganic precursors that could be used in the future syntheses of SCO systems, and extending the panel of anions usually employed in SCO research such as BF_4^-, ClO_4^- and PF_6^-, to name a few.

The internal electrostatic pressure established by these anions located in the neighboring of cationic chains, as well as chain lengths (1-4 nm) of these coordination polymers, was also estimated.

These materials provide a unique platform for the study of intermolecular interactions in such 1D system with the inclusion of Mössbauer active atoms such as ^{119}Sn, ^{73}Ge and ^{181}Ta. This will be the focus of the next chapter (for Sn).

Notes and references

[1] L.G.Lavrenova, V. N. Ikorskii, V. A. Varnek, I. M. Oglezneva, S. V. Larionova. *Koord. Khim.* **1986**, *12*, 207.

[2] L. G. Lavrenova, V. N. Ikorskii, V. A. Varnek, I. M. Oglezneva, Larionov S.V. *Koord. Khim.* **1990**, *16*, 654.

[3] L. G. Lavrenova, N. G. Yudina, V. N. Ikorskii, V. A. Varnek, I. M. Oglezneva, S. V. Larionov. *Polyhedron* **1995**, *14*(10), 1333-1337.

[4] L. G. Lavrenova, O. G. Shakirova, Y. G. Shvedenkov, V. N. Ikorskii, V. A. Varnek, L. A. Sheludyakova, S. V. Larionov. *Koord. Khim.* **1999**, *25*(3), 192-197.

[5] L. G. Lavrenova, O. G. Shakirova, V. N. Ikorskii, V. A. Varnek, L. A. Sheludyakova, S. V. Larionov. *Koord. Khim.* **2003**, *29*(1), 22-27.

[6] E. Codjovi, L. Sommier, O. Kahn. *New J. Chem.* **1996**, *20*, 503.

[7] P. J. van Koningsbruggen, Y. Garcia, E. Codjovi, R. Lapouyade, O. Kahn, L. Fournes, L. Rabardel. *J. Mater. Chem.* **1997**, *7*(10), 2069-2075.

[8] S. Toyazaki, Y. Murakami, T. Komatsu, N. Kojima, Yokoyama T. *Mol. Cryst. Liq. Cryst.* **2000**, *343*, 175-180.

[9] N. Kojima, Y. Murakami, T. Komatsu, T. Yokoyama. *Synthetic Met.* **1999**, *103*, 2154.

[10] S. Toyazaki, M. Nakanishi, T. Komatsu, N. Kojima, D. Matsumura, T. Yokoyama. *Synthetic Met.* **2001**, *121*(1-3), 1794-1795.

[11] N. Kojima, S. Toyazaki, M. Itoi, Y. Ono, W. Aoki, Y. Kobayashi, M. Seto, T. Yokoyama. *Mol. Cryst. Liq. Cryst.* **2002**, *376*(1), 567-574.

[12] O. Kahn, J. Krober, C. Jay. *Adv. Mater.* **1992**, *4*(11), 718-728.

[13] O. Kahn, E. Codjovi, Y. Garcia, P. J. van Koningsbruggen, R. Lapouyade, Sommier L. In: (Eds.: M. M. Turnbull, T. Sugimoto, and L. K. Thompson), *Molecule-Based Magnetic Materials*, **1996**, p. 298.

[14] O. Kahn, C. Jay-Martinez. *Science* **1998**, *279*(5347), 44-48.

[15] Y. Garcia, V. Ksenofontov, P. Gutlich. *Hyp. Int.* **2002**, *139*(1-4), 543-551.

[16] Drabent, K., Bronisz, R., and Rudolf, M. F. ICAME 95 51, 7. 1996. 1995.
Ref Type: Conference Proceeding

[17] Y. Garcia, P. J. van Koningsbruggen, R. Lapouyade, L. Rabardel, O. Kahn, M. Wieczorek, R. Bronisz, Z. Ciunik, M. F. Rudolf. *Comptes Rendus de l Academie des Sciences Serie Ii Fascicule C-Chimie* **1998**, *1*(8), 523-532.

[18] P. Metrangolo, F. Meyer, T. Pilati, G. Resnati, G. Terraneo. *Angew. Chem. Int. Ed.* **2008**, *47*(33), 6114-6127.

[19] J. G. Haasnoot, G. Vos, W. L. Groeneveld. *Zeitschrift fur Naturforschung Section B-A Journal of Chemical Sciences* **1977**, *32*, 421.

[20] V. P. Sinditskii, V. I. Sokol, A. E. Fogelzang, M. D. Dutov, V. V. Serushkin, M. A. Poraikoshits, B. S. Svetlov. *Russ. J. Inorg. Chem.* **1987**, *32*(8), 1950-1955.

[21] P. J. vanKoningsbruggen, Y. Garcia, E. Codjovi, R. Lapouyade, O. Kahn, L. Fournes, L. Rabardel. *J. Mater. Chem.* **1997**, *7*(10), 2069-2075.

[22] K. Drabent, Z. Ciunik. *Chem. Commun.* **2001**, (14), 1254-1255.

[23] Y. Garcia, J. Moscovici, A. Michalowicz, V. Ksenofontov, G. Levchenko, G. Bravic, D. Chasseau, P. Gutlich. *Chem. Eur. J.* **2002**, *8*(21), 4992-5000.

[24] Y. Garcia, P. J. van Koningsbruggen, G. Bravic, D. Chasseau, O. Kahn. *Eur. J. Inorg. Chem.* **2003**, (2), 356-362.

[25] J. G. Haasnoot, G. Vos, W. L. Groeneveld. *Zeitschrift fur Naturforschung Section B-A Journal of Chemical Sciences* **1977**, *32*, 421.

[26] Y. Garcia, P. J. van Koningsbruggen, G. Bravic, P. Guionneau, D. Chasseau, G. L. Cascarano, J. Moscovici, K. Lambert, A. Michalowicz, O. Kahn. *Inorg. Chem.* **1997**, *36*(27), 6357-6365.

[27] M. Marchivie, P. Guionneau, J. F. Letard, D. Chasseau. *Acta Crystallogr. B* **2005**, *61*, 25-28.

[28] V. P. Sinditskii, A. E. Fogelzang, M. D. Dutov, V. I. Sokol, V. V. Serushkin, B. S. Svetlov, M. A. Poraikoshits. *Russ. J. Inorg. Chem.* **1987**, *32*(8), 1944-1949.

[29] K. D. Carlin, A. J. van Duynevedt. *Magnetic properties of transition metal compounds*, Springer-Verlag (New York), **1977**.

[30] C. Timm, V. Schollwöck. *Phys. Rev. B* **2005**, *71*(22), 224414-224422.

[31] V. Mishra, R. Mukherjee, J. Linares, J. Codjovi, F. Varret, M. Lawson-Daku. *Hyp. Int.* **2009**, *188*(1-3), 71-78.
[32] M. M. Dirtu, Y. Garcia, M. Nica, A. Rotarii, J. Linares, F. Varret. *Polyhedron* **2007**, *26*(9-11), 2259-2263.
[33] K. Boukheddaden, F. Varret. *Hyp. Int.* **1992**, *72*(4), 349-356.
[34] V. A. Varnek, L. G. Lavrenova. *J. Struct. Chem.* **1995**, *36*(1), 104-111.
[35] L. G. Lavrenova, V. N. Ikorskii, V. A. Varnek, I. M. Oglezneva, S. V. Larionov. *Journal of Structural Chemistry* **1993**, *34*(6), 960-965.
[36] Y. Garcia, P. Guionneau, G. Bravic, D. Chasseau, J. A. K. Howard, O. Kahn, V. Ksenofontov, S. Reiman, P. Gutlich. *Eur. J. Inorg. Chem.* **2000**, (7), 1531-1538.
[37] M. Thomman, O. Kahn, J. Guilhem, F. Varret. *Inorg. Chem.* **1994**, *33*(26), 6029-6037.
[38] Y. Garcia, V. Ksenofontov, S. Mentior, M. M. Dîrtu, C. Gieck, A. Bhatthacharjee, P. Gutlich. *Chem. Eur. J.* **2008**, *14*(12), 3745-3758.
[39] P. Gütlich, A. Hauser, H. Spiering. *Angew. Chem.* **1994**, *106*, 2109.
[40] P. Gütlich, A. Hauser, H. Spiering. *Angew. Chem. Int. Ed.* **1994**, *33*(20), 2024-2054.
[41] P. Gütlich, Y. Garcia, H. A. Goodwin. *Chem. Soc. Rev.* **2000**, *29*(6), 419-427.
[42] B. P. Lever, Solomon E.I. *Inorganic Electronic Structure and Spectroscopy*, **1999**, p. 575.
[43] P. Gütlich, Y. Garcia, T. Woike. *Coord. Chem. Rev.* **2001**, *219*, 839-879.
[44] P. Gütlich, Y. Garcia, H. Spiering. *Magnetism: Molecules to Materials*, Wiley-VCH, Verlag GmbH, **2003**, p. 271.
[45] P. Gütlich, H. A. Goodwin. Spin Crossover in Transition Metal Compounds III, In: *Top. Curr. Chem.*, Springer, Berlin-Heidelberg, **2004**, pp. 233-235.
[46] V. Ksenofontov, H. Spiering, A. Schreiner, G. Levchenko, H. A. Goodwin, P. Gütlich. *J. Phys. Chem. Solids* **1999**, *60*, 393.
[47] H. Donald, B. Jenkins, H. K. Roobottom. *Inorg. Chem.* **1999**, *38*, 3609.
[48] K. B. Yatsimirskii. *Thermochemistry of Complex Compounds, Moscow* **1951**.

[49] M. N. Bushuev, L. G. Lavrenova, Y. G. Shvedenkov, V. A. Varnek, L. A. Sheludyakova, V. V. Volkov, S. V. Larionov. *Koord. Khim.* **2008**, *34*, 195.
[50] A. Kaczmarczyk, R. D. Dobrott, W. N. Lipscomb. *Proc. Natl. Acad. Sci. U. S. A* **1962**, *48*(5), 729-733.
[51] R. Ingalls. *Phys. Rev.* **1964**, *133A*, 787.
[52] M. Seredyuk, A. B. Gaspar, M. C. Muñoz, M. Verdaguer, F. Villain, P. Gütlich. *Eur. J. Inorg. Chem.* **2007**, (28), 4481-4491.
[53] M. Seredyuk, A. B. Gaspar, V. Ksenofontov, Y. Galyametdinov, M. Verdaguer, F. Villain, P. Gutlich. *Inorg. Chem.* **2008**, *47*(22), 10232-10245.
[54] Y. Garcia, S. J. Campbell, J. S. Lord, Y. Boland, V. Ksenofontov, P. Gutlich. *J. Phys. Chem. B* **2007**, *111*(38), 11111-11119.
[55] B. Weber, W. Bauer, J. Obel. *Angew. Chem. Int. Ed.* **2008**, *47*, 10098-10101.
[56] Y. Garcia, P. J. van Koningsbruggen, R. Lapouyade, L. Fournes, L. Rabardel, O. Kahn, V. Ksenofontov, G. Levchenko, P. Gutlich. *Chem. Mater.* **1998**, *10*(9), 2426-2433.
[57] H. Köppen, E. W. Müller, C. P. Köhler, H. Spiering, G. P. E.Meissner. *Chem. Phys. Lett.* **1982**, *91*, 348.
[58] Y. Garcia, V. Ksenofontov, G. Levchenko, G. Schmitt, P. Gutlich. *J. Phys. Chem. B* **2000**, *104*(21), 5045-5048.
[59] J. Jeftíc, N. Menendez, A. Wack, E. Codjovi, J. Linares, A. Goujon, G. Hamel, S. Klotz, Syfosse G., F. Varret. *Meas. Sci. Techno.* **1999**, *10*, 1059.
[60] R. Tanasa, A. Stancu, J. F. Letard, E. Codjovi, J. Linares, F. Varret. *Chem. Phys. Lett.* **2007**, *443*, 435.
[61] Y. Garcia, V. Ksenofontov, G. Levchenko, P. Gutlich. *J. Mater. Chem.* **2000**, *10*(10), 2274-2276.
[62] S. Schenker, A. Hauser, W. Wang, I. Y. Chan. *Chem. Phys. Lett.* **1998**, *297*, 281.
[63] A. Hauser, N. Amstutz, S. Delahaye, A. Sadeli, S. Schenker, R. Sieber, M. Zerara. *Chimia* **2002**, *56*, 685.
[64] J. Jeftíc, C. Ecolivet, A. Hauser. *High Press. Res.* **2003**, *23*, 359.
[65] A. Hauser. *Chem. Phys. Lett.* **1992**, *192*, 65.
[66] J. Jeftíc, A. Hauser. *Chem. Phys. Lett.* **1996**, *248*, 458.
[67] J. Jeftíc, A. Hauser. *J. Phys. Chem. B* **1997**, *101*, 10262.
[68] A. Hauser, J. Jeftíc, H. Romstedt, R. Hinek, H. Spiering. *Coord. Chem. Rev.* **1999**, *190-192*, 471.

[69] Y. Garcia, P. J. van Koningsbruggen, R. Lapouyade, L. Rabardel, O. Kahn, M. Wieczorek, R. Bronisz, Z. Ciunik, M. F. Rudolf. *Comptes Rendus de l Academie des Sciences Serie Ii Fascicule C-Chimie* **1998**, *1*(8), 523-532.

[70] O. Roubeau, J. M. A. Gomez, E. Balskus, J. J. A. Kolnaar, J. G. Haasnoot, J. Reedijk. *New J. Chem.* **2001**, *25*(1), 144-150.

[71] M. Quesada, F. Prins, E. Bill, H. Kooijman, P. Gamez, O. Roubeau, A. L. Spek, J. G. Haasnoot, J. Reedijk. *Chem. Eur. J.* **2008**, *14*(28), 8486-8499.

[72] T. Yokoyama, Y. Murakami, M. Kiguchi, T. Komatsu, N. Kojima. *Phys. Rev. B.* **1998**, *58*, 14238.

Chapter II: Use of an Anionic Nuclear Probe to Sense the Spin Transition of 1D Coordination Polymers[1]

Introducing remarks

As a continuation of the work presented in Chapter I, an internal anionic nuclear probe was successfully implanted into the crystal lattice of a 1D chain compound for the first time in view of sensing elastic cooperative interactions associated to their propagation in the crystal lattice. These new materials, including SnF_6^{2-} as counter-anions, offer an unique opportunity to probe locally the thermally induced ST by means of two Mössbauer isotopes located within the chain (^{57}Fe) and in the anionic sublattice (^{119}Sn). The partial and the total removal of the non-coordinated solvent molecules are accompanied by a change of the morphology, texture and magnetic properties of the compounds. This change has been examined by a variety of techniques that include TGA, DSC and SQUID measurements, followed by a texture study by SEM.

Syntheses[2] and characterisation

A monohydrate complex was precipitated as a white powder by mixing warm methanolic solutions of $[Fe(H_2O)_6]SnF_6$ and NH_2trz (1:3); the precipitate was washed with methanol and dried in air. Elemental analyses and thermogravimetric measurements confirmed the composition as $[Fe(NH_2trz)_3]SnF_6 \cdot H_2O$ (**14)**, (Figure 14). The synthetic method used in this

[1]Adapted from: Y. Garcia, V. Ksenofontov, S. Mentior, M. M. Dîrtu, C. Gieck, A. Bhatthacharjee, P. Gütlich, *Chem. Eur. J.*, **2008**, *14*, 3745.

[2] The synthesis and the thermal treatement were realized by S. Mentior during her Master thesis (UCL).

case (different from the *in situ* method followed to obtain homologues compounds presented in Chapter I (compounds **5** and **6**). The white colour of the precipitate is characteristic of the HS state of the Fe^{II} centres. Indeed, the absence of charge-transfer transitions in the visible range allows an easy identification of the spin state because the spin-allowed lowest energy d-d transition, $^5T_{2g} \rightarrow {}^5E_g$, for the HS Fe^{II} ions occurs in the near IR region (ν ~11900 cm^{-1}). The precipitate obtained during the synthesis of **14** was pumped under vacuum at 50°C for 30 min. This annealing process afforded $[Fe(NH_2trz)_3]SnF_6 \cdot 0.5H_2O$ (**15**) and its degree of hydration was confirmed by TGA measurements (Figure 14). The reproducibility of this preparation method under the very same conditions was checked twice.

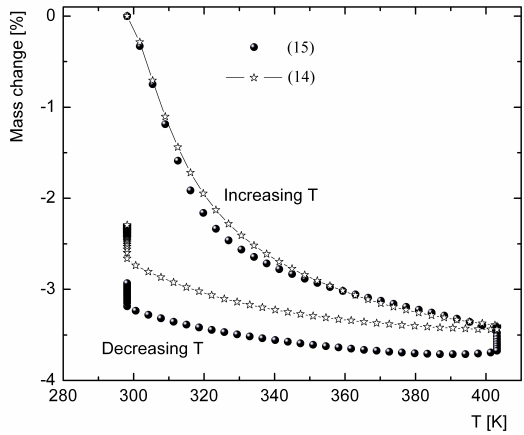

Figure 14 Thermogravimetric analysis (recorded at 1 K min^{-1}) for (**14**) and (**15**) over the temperature range (298-403 K) on warming and cooling. A standby period of 30 min at 403 K was included for (**15**) in its temperature program.

On standing in air for a long period, (**15**) transforms slowly into (**14**) (as confirmed by thermogravimetric measurements), but the degree of hydration of (**15**) can be maintained provided the sample is kept under a nitrogen atmosphere. Attempts to isolate the fully dehydrated material (**15d**) from (**14**) or (**15**) under ambient conditions failed because the dehydrated materials slowly reabsorb water molecules in ambient air, as seen in Figure 14, both on cooling from 403 K and on standing at room temperature.

Compounds (**14**) and (**15**) present reversible thermochromism to deep purple on quenching of the sample in liquid nitrogen. This colour change is a signature of a thermally induced SCO phenomenon. Indeed, this purple colour is due to the $^1A_{1g} \rightarrow {}^1T_{1g}$ d-d transition of LS Fe^{II} ions which occurs at ~ 520 nm.[1, 2] The nature of the SCO behaviour in these samples on cooling and re-warming has been tracked by using several techniques (see below).

In order to test if the synthesis pathway could play a role on the SCO properties of these systems, another complex was prepared, $[Fe(NH_2trz)_3]SnF_6 \cdot 1.5H_2O$ (**16**). For this purpose we carried out the synthesis in a different solvent (DMF) and did not perform any annealing process during the preparation. As a result, the hydration degree was varied and no DMF was inserted as concluded from the absence of any characteristic peak in the IR spectrum of (**16**). The sample was studied by ^{57}Fe Mössbauer spectroscopy similarly to compound (**15**) (*vide infra*).

Infrared spectroscopy

Compounds (**14**) and (**15**) have essentially identical IR spectra at room temperature. The ring stretch found at ν = 1544 cm^{-1}, δ(NH_2) at ~1630 cm^{-1} and the exocyclic N-N bond stretch at 1216 cm^{-1} exactly correspond to the vibrations reported in the spectroscopic study of $[Cu(NH_2trz)_3](ClO_4)_2 \bullet 0.5H_2O$, a Cu^{II} complex containing triple N_1,N_2-triazole bridges whose 1D network was recognized[3]. This indicates that coordination to the Fe(II) ion takes place exclusively through the azole ring.[3] The absence of noticeable splitting for the IR active vibration ν_3 for SnF_6^{2-} observed at 555 cm^{-1} calls for a symmetric octahedron (O_h)[4].

X-ray powder diffraction and SEM studies

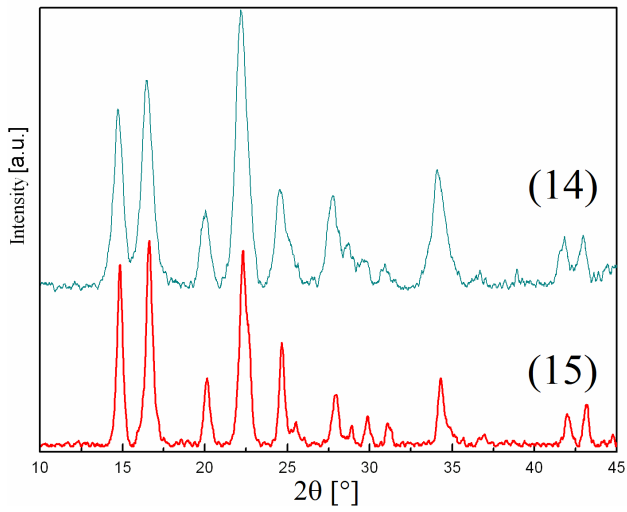

Figure 15 X-ray powder diffraction diagrams at 293 K for (**14**) and (**15**).

The dehydration process of compound **14** was investigated by TGA (Figure 14). The X-ray powder diffraction patterns and the SEM imaging were carried out before and after the annealing process. From the X-ray powder diffraction patterns, **14** and **15** are isomorphous as deduced by comparison of

the X-ray powder diffraction patterns recorded at room temperature (Figure 15). Thus, variance in the water content does not noticeably modify the structural organisation of these materials which support a location of the water molecules far from the iron chains.

From X-ray powder diffraction pattern (Figure 15) we can conclude too that compounds **14** and **15** are rather crystalline, this is not apparent in SEM imaging. Indeed SEM visualisation of the particles in the solid state (Figure 16) of powders samples of **14** and **15** reveal spherical particles. Unlike sample **5** (Chapter I), which has a morphology of elongated rods of dimensions (457 x 108 nm), compound **15** is less crystalline with spherical particles of ~ 84 nm diameter that are distinguished in the aggregates.

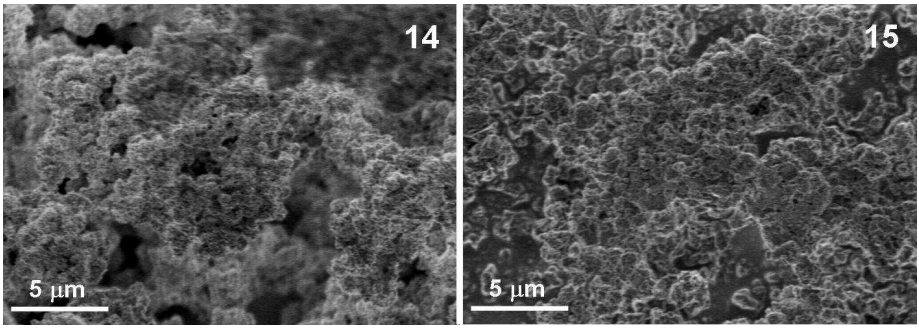

Figure 16 SEM analyses (x 20000) of sample **14** and **15**. The effect of thermal treatment under vacuum on the framework integrity is evidenced.

Compared to their homologues (compounds **5** and **6**, Chapter I) the SEM pictures show less crystallinity for the powdered compounds **14** and **15**, which has an influence on the SCO properties (see below in the magnetic part). In the same time, the loss of 0.5 H_2O molecules from **14** to **15**, by annealing treatment does not influence the crystallinity. However structured aggregates are observed for **14** after the thermal treatment (Figure 16).

Mössbauer spectroscopy

The present Fe^{II} compounds are stable to oxidation because no ferric species were detected in the ^{57}Fe Mössbauer spectra of **15**. The Mössbauer parameters, reported in Table 16, are consistent with other 1D Fe(II) coordination polymers with the NH_2trz ligand[5]. The ^{119}Sn Mössbauer spectrum of (**15**) recorded at 300 K, by Dr. V. Ksenofontof (Mainz) shows a single line with an isomer shift δ ~ -0.3 mm/s (relative to the source $^{119}Sn(CaSnO_3)$), which confirms the Sn(IV) oxidation state for the anion. This low isomer shift fits very well with the value obtained at 300 K for $CuSnF_6$: δ = -0.35(5) mm/s[6] but is less negative than those found for the hydrated salts at 300 K ($[Fe(H_2O)_6]SnF_6$: δ = -0.437 mm/s[7] and $CuSnF_6{\cdot}4H_2O$: δ = -0.46(1) mm/s[6]). This behaviour suggests that the SnF_6^{2-} octahedron in (**15**) is not hydrogen bonded to water molecules. Indeed, in the crystal structure of $[Fe(H_2O)_6]SnF_6$, the SnF_6^{2-} octahedron is hydrogen bonded to the coordinated water molecules[8] which reduces the donation of electron from fluorine and thus decreases the s-electron density at the Sn atom thereby shifting the isomer shift to a more negative value. The absence of quadrupole splitting at 300 K for (**15**) is consistent with the IR observation described above that suggested a regular octahedral coordination sphere.

Study of the spin transition in $[Fe(NH_2trz)_3]SnF_6{\cdot}nH_2O$

In this part, the study of thermally induced ST of $[Fe(NH_2trz)_3]SnF_6{\cdot}nH_2O$ (n = 0 – 1.5) by slow cooling (SC) and warming below room temperature using SQUID magnetometry, Mössbauer spectroscopy (^{57}Fe, ^{119}Sn), X-ray powder diffraction and differential scanning calorimetry (DSC) will be presented.

SQUID magnetometry

The temperature dependence of the molar magnetic susceptibility of (**14**), (**15**) and (**15d**) (fully dehydrated compound, n = 0), recorded by Dr. A. Bhattacharjee (Mainz) on cooling and warming over the temperature range 300-5 K, is displayed in Figure 17 in the form of a $\chi_M T$ versus T plot, χ_M being the molar magnetic susceptibility.

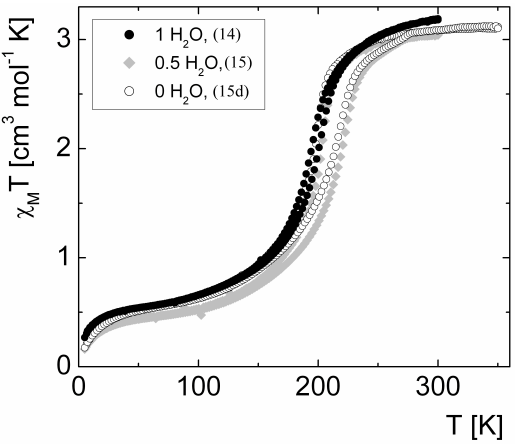

Figure 17 Temperature dependence of $\chi_M T$ on cooling and warming for $[Fe(NH_2trz)_3]SnF_6 \cdot nH_2O$ (n = 1 (**14**) •, n = 0.5 (**15**) ♦, and n = 0 (**15d**) o).

At room temperature $\chi_M T$ is equal to 3.19 cm^3 mol^{-1} K for (**14**) which corresponds to a major fraction of Fe^{II} ions in the HS state, some Fe^{II} ions being also presumably in the LS state. As T is lowered, $\chi_M T$ first decreases very slowly down to 225 K and then rapidly down to 150 K. Below this temperature, $\chi_M T$ decreases very slowly and shows a plateau with a value of 0.56 cm^3 mol^{-1} K at 50 K, indicating an incomplete HS → LS transition. The slow fall of $\chi_M T$ below 25 K is due to the effect of zero-field splitting of the remaining HS Fe^{II} ions, and the preferred Boltzmann population of the lowest levels with decreasing temperatures. As the temperature is increased, $\chi_M T$ follows the same pathway as seen while cooling except in the range of

150-225 K, indicating a hysteresis loop of width ~ 7 K, centred at 190 K. The transition temperatures (the temperatures at which 50% of active LS and HS molecules are present) in the cooling and warming modes, respectively, are $T_{1/2}\downarrow$ = 193 K and $T_{1/2}\uparrow$ = 200 K. This hysteresis is retained over successive cooling and heating thermal cycles, provided the temperature does not exceed 300 K to avoid dehydration of the sample, as shown to occur by thermogravimetric measurements (see Figure 14). The magnetic properties of the hemihydrate (**15**) were also investigated by SQUID measurements. $\chi_M T$ is constant at 3.04 cm^3 mol^{-1} K over the temperature range (300-250 K) which suggests the presence of a fraction of LS Fe^{II} ions, which was detected by Mössbauer spectroscopy (see Figure 18). The shape of the ST curve is similar to that of (**14**), reaching however lower $\chi_M T$ values at 50 K (0.42 cm^3 mol^{-1} K) indicating a more complete ST. The ST is shifted upwards to higher temperatures and a larger width of ~ 16 K ($T_{1/2}\downarrow$ = 201 K and $T_{1/2}\uparrow$ = 217 K) is observed.

A fresh sample of compound (**15**) was loaded in the SQUID cavity at 300 K and the temperature was raised up to 350 K. The magnetisation data was subsequently recorded, on cooling and warming, over the temperature range 350-5 K in steps of 2 K. This *in situ* thermal treatment allows recording the magnetic properties of the fully dehydrated sample of $[Fe(NH_2trz)_3]SnF_6$ (**15d**). Indeed, on warming the sample from 298 K up to 350 K at 1K/min, only 0.2 water molecules remain in the sample as concluded from complementary TGA measurements (Figure 14). Since the material is first warmed from 300 K to 350 K within the SQUID cavity, then slowly cooled down to 293 K and has to stabilise its temperature at each 2 K to allow data recording, we can be confident that full dehydration is reached with this process. The shape of the ST curve is preserved compared to (**15**) but the ST is slightly shifted downwards ($T_{1/2}\downarrow$ = 197 K and $T_{1/2}\uparrow$ = 210 K).

^{57}Fe Mössbauer spectroscopy

Selected Mössbauer spectra of (**15**) recorded in the heating mode after cooling the sample slowly from room temperature, by Dr. V. Ksenofontof (Mainz), are displayed in Figure 18, Table 16. At 82 K, the spectrum consists of two quadrupole doublets of different resonance area fractions. The major quadrupole doublet with isomer shift δ = 0.53(1) mm/s and quadrupole splitting, ΔE_Q = 0.31(2) mm/s correspond to the LS state of Fe^{II}. The presence of the quadrupole splitting in this case stems from a so called lattice contribution to the electric field gradient and thus reveals a distorted character for the LS octahedron as expected within a chain, where constraints may not be negligible. Another doublet, corresponding to HS Fe^{II} ions of weaker population (20.6%), is also observed (δ = 1.16(4) mm/s and ΔE_Q = 3.38(8) mm/s). The presence of this doublet confirms the incomplete nature of the ST at 82 K as also found by SQUID magnetometry (Figure 17). Most likely, the incomplete character of the ST may stem from terminal of chains of the FeN_6 type having a ligand field strength too weak for meeting conditions for a thermally induced SCO to occur.[9] It is unlikely that end of chains of the FeN_3O_3 type with three terminal coordinated water molecules are responsible for the residual HS fraction. In that case the quadrupole splitting would be expected to be much smaller than the actually observed of 3.38 mm/s, since the lattice contribution to the electric field gradient (EFG) arising from the mixed ligand coordination sphere FeN_3O_3 is expected to be larger than that from a FeN_6 entity and due to the known opposite sign to that of the valence electron contribution which reduces the total EFG more than in the case of FeN_6.

This is observed for the terminal Fe^{II} ions of the trinuclear $[Fe_3(4\text{-ethyl-}1,2,4\text{-triazole})_6(H_2O)_6](CF_3SO_3)_6$ with ΔE_Q = 2.51 mm/s at 77 K.[10] In other cases, however, the quadrupole splitting for external iron(II) ions can be larger than for a FeN_6 octahedron as noticed in the ^{57}Fe Mössbauer studies of

structurally characterized trinuclear complexes of formula $[Fe_3(4\text{-isopropyl-}1,2,4\text{-triazole})_6(H_2O)_6](Tos)_6\cdot 2H_2O$[11] and $[Fe_3(4\text{-}2'\text{-hydroxy-ethyl-}1,2,4\text{-triazole})_6(H_2O)_6](CF_3SO_3)_6$[12]. This situation is explained by the negligible lattice contribution to the EFG due to the local FeN_3O_3 *fac*-isomer configuration.[13, 14] In the present case, the observed quadrupole splitting of 3.38 mm/s is close to that expected for Fe^{II} HS compounds with little or no lattice contribution to the EFG. We believe that the terminal entities of the chains only consist of FeN_6 octahedra since a unique site was observed on varying the temperature.

Table 16 Overview of the ^{57}Fe Mössbauer parameters for **15**.

T [K]	*δ* [mm/s]	ΔE_Q [mm/s]	*Γ/2* [mm/s]	Rel. Area [%]	Sites
82	1.16(4)	3.38(8)	0.32(1)	20.6(6)	HS
	0.53(1)	0.31(2)	0.28(1)	79.4(4)	LS
120 ↑	1.15(1)	3.34(1)	0.32(1)	23.3(4)	HS
	0.52(1)	0.30(1)	0.28(1)	76.7(3)	LS
170 ↑	1.12(2)	3.22(2)	0.30(1)	32.7(6)	HS
	0.51(1)	0.28(1)	0.26(1)	67.3(4)	LS
190 ↑	1.11(2)	3.17(2)	0.30(1)	37.8(7)	HS
	0.50(1)	0.28(1)	0.26(1)	62.2(4)	LS
210 ↑	1.10(2)	3.11(1)	0.30(1)	48.6(7)	HS
	0.49(2)	0.27(1)	0.26(1)	51.4(5)	LS
230 ↑	1.10(1)	3.05(1)	0.28(1)	75.6(8)	HS
	0.48(1)	0.25(1)	0.28(1)	24.4(6)	LS
250 ↑	1.08(1)	2.98(1)	0.28(1)	89.8(1)	HS
	0.46(2)	0.22(2)	0.34(1)	10.2(1)	LS
270 ↑	1.06(1)	2.89(1)	0.26(1)	95.2(8)	HS
	0.39(4)	0	0.6(2)	4.8(1)	LS
300	1.05(2)	2.78(1)	0.26(1)	97.1(2)	HS
	0.19(1)	0.4(1)	0.2(1)	2.9(1)	LS
270 ↓	1.06(1)	2.87(2)	0.28(1)	96.3(1)	HS
	0.45*	0.3*	0.6(3)	3.7(2)	LS
250 ↓	1.08(1)	2.95(2)	0.28(1)	93.9(1)	HS
	0.42(5)	0	0.6(1)	6.1(2)	LS
230 ↓	1.08(1)	3.03(2)	0.28(1)	91.3(9)	HS
	0.46(2)	0.22(5)	0.36(4)	8.7(9)	LS
210 ↓	1.10(1)	3.10(2)	0.28(1)	80.5(8)	HS
	0.49(1)	0.25(1)	0.30(1)	19.5(6)	LS
190 ↓	1.11(2)	3.16(2)	0.28(1)	42.9(1)	HS
	0.50(1)	0.28(1)	0.26(1)	57.1(4)	LS
170 ↓	1.12(2)	3.21(2)	0.30(1)	35.0(1)	HS
	0.51(1)	0.287(2)	0.26(1)	65.0(4)	LS
120 ↓	1.15(3)	3.33(1)	0.30(1)	23.0(7)	HS
	0.52(1)	0.30(2)	0.28(1)	77.0(1)	LS

↑ indicates warming and ↓ indicates cooling; δ = isomer shift relative to α-iron, ΔE_Q = quadrupole splitting, Γ/2 = half width at half maximum.

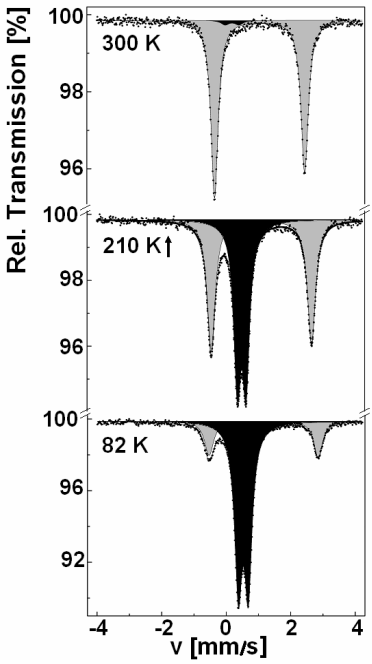

Figure 18 ^{57}Fe Mössbauer spectra for (**15**) at selected temperatures on warming after slow cooling the sample to 82 K. The light grey and black signals refer to HS and LS Fe^{II} ions, respectively.

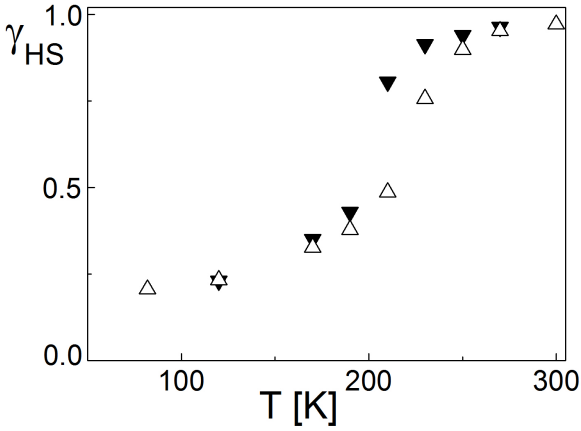

Figure 19 Temperature dependence of the molar fraction of HS molecules, γ_{HS}, for (**15**) as deduced from ^{57}Fe Mössbauer spectroscopy, by slow warming (Δ) and cooling (▼) over the temperature range 80-300 K.

The presence of two terminal coordinated water molecules that may not be detected by Mössbauer spectroscopy[15] should however also be considered. On warming to 210 K, the intensity of the HS doublet increases at the

expense of that of the LS doublet, confirming a thermally induced LS → HS conversion for a single Fe^{II} site. At 300 K, the spectrum clearly shows a major signal corresponding to HS Fe^{II} ions, with a remaining weaker fraction of LS ions (3.0%), which had to be taken into account for the reliability of the fitting procedure. This confirms the incomplete character of the ST at room temperature as suggested in the SQUID investigation. The asymmetry of the quadrupole doublet corresponding to HS Fe^{II} ions is attributed to a texture effect. The ST curve deduced from ^{57}Fe Mössbauer spectroscopy considering equal Lamb-Mössbauer factors for the LS and HS Fe^{II} ions closely resembles the one deduced from magnetic measurements with $T_{1/2}\uparrow$ = 216 K, and $T_{1/2}\downarrow$ = 196 K (Figure 19).

An overview of Mössbauer parameters of (**16**), in the heating and cooling mode between, 84 K and room temperature are given in Table 17 and the HS molar fraction derived from these experiments is shown in Figure 20. At 84 K the compound is mostly in the LS state, ~ 20% of Fe(II) ions staying in the HS state as found for (**15**).

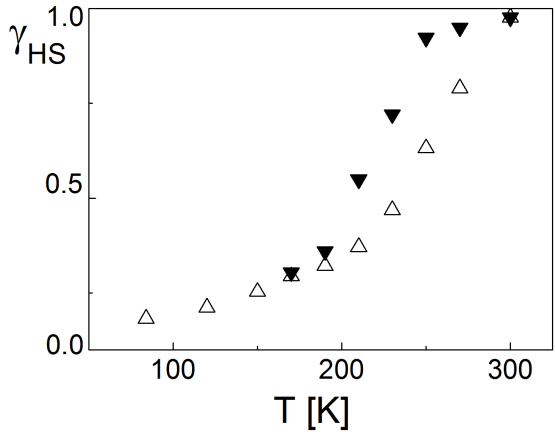

Figure 20 Temperature dependence of γ_{HS} for (**16**) as deduced from ^{57}Fe Mössbauer spectroscopy. The sample was studied on slow warming (Δ) and cooling (▼) over the temperature range (84-300 K).

Upon warming, a LS $\rightarrow$ HS transition is observed at $T_{1/2}\uparrow$ = 248 K. On slow cooling, a SCO curve with $T_{1/2}\downarrow$ = 218 K is delineated.

A brief comparison between the SCO properties of this family of compounds, based on $[Fe(NH_2trz)_3]SnF_6 \cdot nH_2O$ (**5** and **6** - Chapter I with **14, 15, 15d** and **16**) which are temperature shifted, allows to conclude that the "signature" of the solvent, used in the synthetic method of the framework is evidenced.

Table 17 (a) Overview of the ^{57}Fe Mössbauer parameters for **16**; (b) Selection of transition temperatures variation function of synthetic method, for $[Fe(NH_2trz)_3]Anion \cdot nH_2O$ (**5-6, 15-16**) .

(a)

T [K]	*δ* [mm/s]	*ΔE*$_Q$ [mm/s]	*Γ/2* [mm/s]	Rel. Area [%]	Sites
84	1.16(2)	3.37(1)	0.30(1)	18.2(8)	HS
	0.52(1)	0.29(2)	0.26(1)	81.8(5)	LS
120 ↑	1.15(3)	3.33(1)	0.30(1)	21.2(6)	HS
	0.52(1)	0.28(1)	0.26(1)	78.8(4)	LS
150 ↑	1.14(1)	1.14(1)	0.28(1)	25.3(1)	HS
	0.51(1)	0.51(1)	0.26(1)	74.7(6)	LS
170 ↑	1.12(2)	3.21(1)	0.28(1)	29.4(6)	HS
	0.50(1)	0.27(2)	0.26(1)	70.6(4)	LS
190 ↑	1.11(1)	3.16(3)	0.28(1)	32.2(4)	HS
	0.50(1)	0.26(1)	0.26(1)	67.7(2)	LS
210 ↑	1.10(2)	3.10(1)	0.28(1)	37.1(5)	HS
	0.48(1)	0.26(2)	0.26(1)	62.9(4)	LS
230 ↑	1.10(1)	3.04(1)	0.28(1)	46.9(1)	HS
	0.47(3)	0.24(1)	0.26(1)	53.1(8)	LS
250 ↑	1.08(1)	2.96(1)	0.28(1)	63.2(8)	HS
	0.46(2)	0.23(2)	0.24(1)	36.8(6)	LS
270 ↑	1.07(1)	2.87(2)	0.26(1)	79(1)	HS
	0.45(1)	0.22(1)	0.24(1)	21(1)	LS
300	1.05(1)	2.76(2)	0.26(1)	97.7(1)	HS
	0.3(1)	0.1(2)	0.28(4)	2.3(2)	LS
270 ↓	1.07(1)	2.88(2)	0.26(1)	95(1)	HS
	0.38(4)	0.1(7)	0.58(1)	5(1)	LS
250 ↓	1.08(2)	2.97(4)	0.26(1)	92.3(2)	HS
	0.47(2)	0.21(4)	0.22(1)	7.7(1)	LS
230 ↓	1.09(1)	3.04(2)	0.28(1)	72.1(8)	HS
	0.47(3)	0.24(5)	0.26(1)	27.9(6)	LS
210 ↓	1.10(2)	3.11(4)	0.28(1)	54.9(1)	HS
	0.48(3)	0.25(4)	0.26(1)	45.1(7)	LS
190 ↓	1.11(2)	3.16(4)	0.28(1)	36(1)	HS
	0.49(1)	0.26(2)	0.26(1)	64(1)	LS
170 ↓	1.13(4)	3.22(1)	0.26(1)	30.4(1)	HS
	0.50(2)	0.27(3)	0.26(1)	69.6(7)	LS

δ = isomer shift relative to α-iron, ΔE_Q = quadrupole splitting, Γ = width at half maximum.

(b)

Compound code	**n**	**Synthesis Solvent**	**$T_{1/2}\uparrow$ [K]**	**$T_{1/2}\downarrow$ [K]**	**ΔT [K]**
5	0.5	MeOH	218	200	18
6	1	EtOH	225	189	36
14	1	MeOH	200	193	7
15	0.5	Annealing process of (**14**), 50°C under vacuum (30')	217	201	16
15d	0	Annealing process of (**14**), 50°C under vacuum (90')	210	197	13
16	1.5	DMF	248	218	30

X-ray powder diffraction

X-ray diffraction patterns of (**15**) have been recorded on cooling and warming over the temperature range (270 K – 100 K), by Dr. C. Gieck (EPFL). Figure 21 shows three typical diffraction patterns. The diffraction patterns are essentially similar suggesting the absence of a crystallographic phase transition. However, a decrease in the intensity of some peaks is observed while other peaks grow in intensity comparing the patterns at 270 K and 100 K. This behaviour is correlated to the spin state crossover occurring around 200 K as tracked by SQUID and ^{57}Fe Mössbauer spectroscopy. It is evident that at the intermediate temperature of 180 K, the spectrum shows a superposition of the patterns for the HS and LS phases with a temperature dependent intensity. On this basis, we selected the intensity of a peak at 2θ ~2.5° as a marker to track the ST and the hysteresis loop whose dependence is shown in the inset to Figure 21. The transition temperatures of $T_{1/2}\downarrow$ ~ 197 K and $T_{1/2}\uparrow$ ~ 224 K were derived. These values are in good agreement with the ones obtained by Mössbauer spectroscopy.

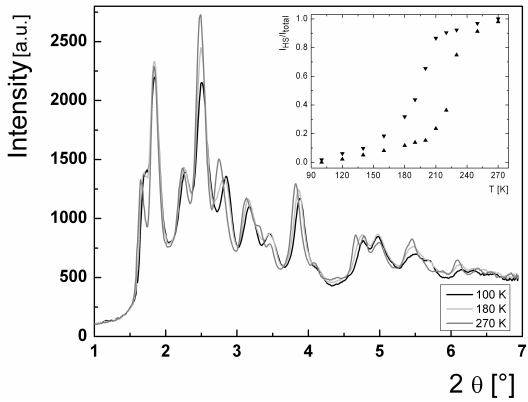

Figure 21 X-ray diffraction patterns of (**15**) at selected temperatures on slowly cooling from 270 K to 100 K. The inset shows the temperature dependence of the relative intensity of the HS phase I_{HS}/I_{Total} peak at 2θ ~2.5°. The data were recorded on cooling and warming.

Calorimetric measurements

Compounds (**14**) and (**15**) were investigated over the temperature range (98-298 K) on cooling and warming at 5 K/min. Transition temperatures, enthalpy and entropy values are gathered in Table 18. The DSC response for (**15**) is given as an example in Figure 22. Exothermic and endothermic peaks are observed at T_{max} ~ 203 K and 225 K, respectively, thus clearly confirming the presence of a hysteresis loop. These peaks are obviously related to the ST detected by Mössbauer, magnetic and XRPD studies, and probably may call for the presence of a first order phase transition.

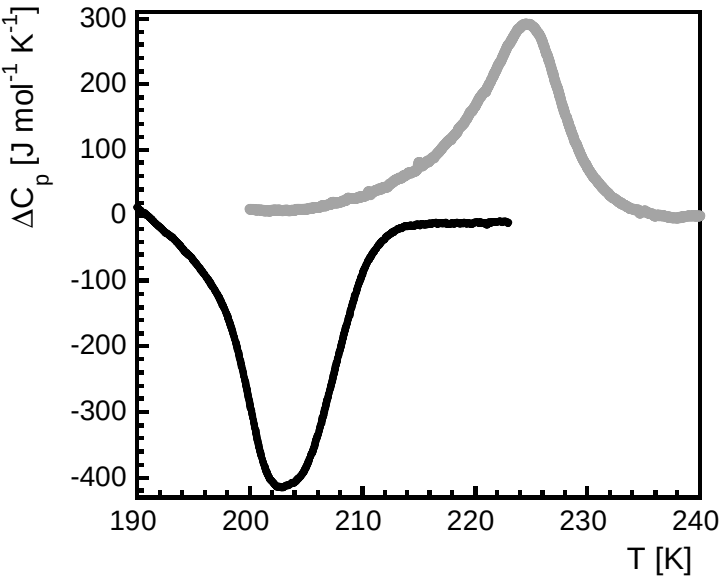

Figure 22 DSC measurements for (**15**) in the 190-240 K temperature range. The cooling and warming modes are in black and grey, respectively.

The enthalpy and entropy variations have been evaluated as ΔH = 6.9 kJ mol^{-1} and ΔS = 34 J mol^{-1} K^{-1}, respectively, considering the transition of the active Fe^{II} ions (76.5%) and the fraction of iron spins undergoing the SCO on this temperature range (40%) as deduced from Mössbauer measurements.

The experimentally measured entropy variation can be accounted for by an electronic contribution, R*ln5 = 13.4 J mol^{-1} K^{-1}, and a vibrational contribution (20.6 J mol^{-1} K^{-1}).[16-19] The presence of a structural phase transition accompanying the ST should dramatically increase the ΔS value which is not observed here (Table 18). [16-19]

Table 18 Thermodynamic parameters and transition temperatures for **14** and **15**.

	$T_{max}\downarrow$ [K]	$T_{max}\uparrow$ [K]	ΔH [kJ mol^{-1}]	ΔS [J mol^{-1} K^{-1}]	ΔS_{vib} [J mol^{-1} K^{-1}]
14	207	-	7	34	20.6
15	203	225	6.9	34	20.6

^{119}Sn Mössbauer spectroscopy

^{119}Sn Mössbauer spectra on (**15**) were recorded by slow cooling and warming, over the temperature range (300-80 K) followed by another cooling mode down to 4.2 K in order to track any possible hysteresis loop, by Dr. V. Ksenofontov (Mainz). The ^{119}Sn Mössbauer parameters are given in Table 19. Figure 23 shows a representative ^{119}Sn Mössbauer spectrum recorded at 80 K on cooling from 300 K. The temperature variation of δ shown in Figure 24 reveals a linear increase on cooling which is attributed to the second order Doppler shift. The normalized resonance area shown in Figure 25 clearly evidences two linear temperature domains of different slopes.

Interestingly, a jump is found on cooling around 190 K, a feature that is a clear signature of a phase transition. Indeed, such a jump is observed by ^{57}Fe Mössbauer spectroscopy while crossing the ST range.

Table 19 Overview of the ^{119}Sn Mössbauer parameters for **15**.

T [K]	*δ* [mm/s]	*ΔE$_Q$* [mm/s]	*Γ/2* [mm/s]	Rel. Area [%]
300	-0.37(6)	0	0.4(1)	100
230 ↓	-0.29(2)	0	0.55(3)	100
190 ↓	-0.29(3)	0	0.52(1)	100
130 ↓	-0.28(1)	0.28(2)	0.57(1)	100
80 ↓	-0.27(2)	0.34(2)	0.54(1)	100
130 ↑	-0.282(2)	0.29(2)	0.52(1)	100
190 ↑	-0.29(1)	0	0.52(1)	100
230 ↑	-0.30(1)	0	0.53(2)	100
260 ↑	-0.30(2)	0	0.49(4)	100
300	-0.29(6)	0	0.4(1)	100
210 ↓	-0.30(1)	0	0.50(1)	100
160 ↓	-0.29(1)	0.24(3)	0.49(1)	100
110 ↓	-0.28(2)	0.28(2)	0.53(1)	100
90 ↓	-0.28(2)	0.31(2)	0.54(1)	100
5 ↓	-0.26(1)	0.40(5)	0.61(2)	100
40 ↑	-0.27(1)	0.36(3)	0.59(1)	100
4.2 ↓	-0.26(1)	0.39(5)	0.62(2)	100

δ = isomer shift relative to the source $^{119}Sn(CaSnO_3)$, ΔE_Q = quadrupole splitting, $\Gamma/2$ = half width at half maximum.

But contrary to Fe^{II} and Fe^{III} SCO compounds,[20, 21] there is no change of effective mass expected with Sn leading to an accurate determination of the Debye temperature, which characterizes the rigidity of the Sn-F bonds.

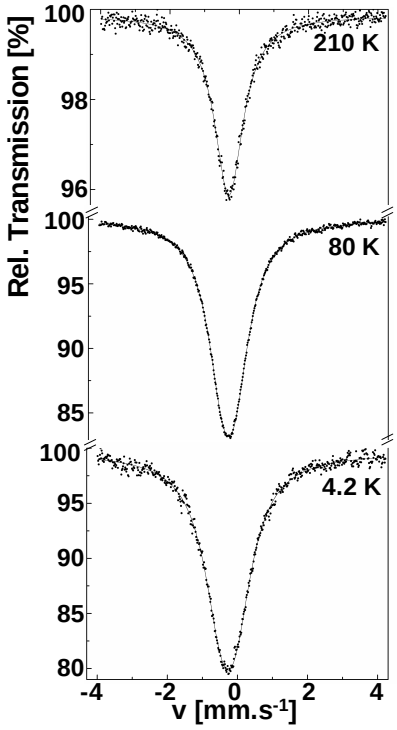

Figure 23 ^{119}Sn Mössbauer spectra for (**15**) at selected temperatures recorded on cooling from 300 K.

This characteristic temperature is nevertheless not expected to be dramatically modified by the SCO in the present case, since the SnF_6^{2-} anions occupy lattice positions which are not in the close neighbourhood of the spin changing iron ions.

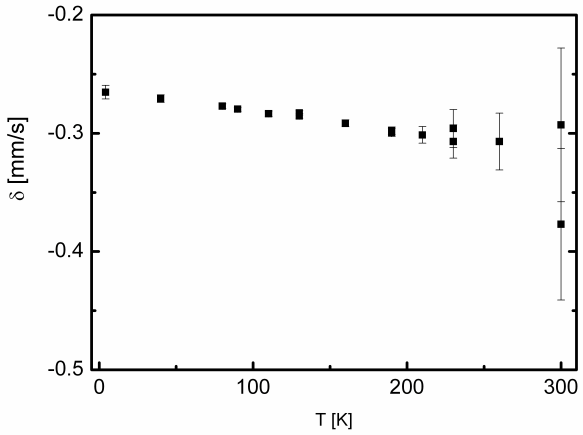

Figure 24 Temperature dependence of the isomer shift δ (relative to the source $^{119}Sn(CaSnO_3)$ for (**15**) over the temperature range (300-4.2 K) on cooling and warming, as deduced from ^{119}Sn Mössbauer spectroscopy.

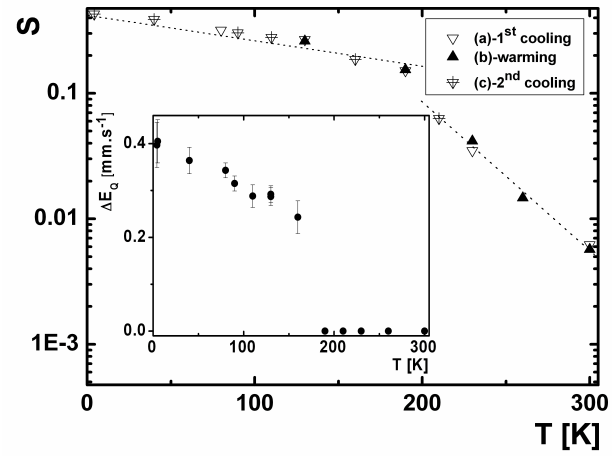

Figure 25 Temperature dependence of the normalized resonance area, S, with a logarithmic scale for (**15**) over the temperature range (300-4.2 K) on cooling and warming, as deduced from ^{119}Sn Mössbauer spectroscopy. The insert shows the temperature dependence of the quadrupole splitting ΔE_Q over the same temperature range.

Interestingly, the appearance of ΔE_Q below 190 K was observed for (**15**) (see inset to Figure 25) which means that the anionic SnF_6^{2-} octahedron becomes distorted below this temperature and is regular above.

This observation satisfactorily matches the IR spectrum at 300 K (presence of bands around 573-622 cm^{-1}) that suggested a regular octahedron[4]. This overall behaviour reflects a phase transition around 190 K resulting from the spin state change in individual chains that was detected in the same temperature range by other physical methods.

Discussion and conclusions

The origin of the hysteretic magnetic behaviour of 1D 1,2,4-triazole Fe^{II} chain compounds is still debated.[22] In addition to short range interactions promoted by the triazoles linking the Fe^{II} ions, H-bonding and anion-cation interactions are believed to play a decisive role in the cooperative effects associated with the spin transition. Such long range interactions could be mediated by lattice solvent molecules, non coordinated counter-anions or hydrogen bonding through the substituent of the triazole ligand.[22] Direct hydrogen bonding between chains through the non-coordinated tetrafluoroborato anion (B-F$\cdots$H) were deduced from WAXS (wide-angle X-ray scattering) experiments for the ST material $[Fe(Htrz)_2trz](BF_4)$ which displays a broad hysteresis effect.[23] Hydrogen bonding involving the anion was also suggested from recent muon spin relaxation experiments performed on the ST chain compound $[Fe(NH_2trz)_3](NO_3)_2$ which also displays a broad hysteresis loop,[21] and that will be structured in the next chapter. Hydrogen bonding between linear chains through the hydroxyl group of the triazole substituent were observed in the crystal structure of $[Cu(hyptrz)_3](4\text{-chloro-}3\text{-nitrophenylsulfonate})_2\cdot H_2O$ (hyptrz = 4-(3'-hydroxypropyl)-1,2,4-triazole), a configuration that was thought to be also present in the related Fe^{II} analogue which displays a cooperative ST with a hysteresis loop of ~ 50 K.[24]

In this work, we have successfully incorporated an internal probe into the crystal lattice of $[Fe(NH_2trz)_3]^{2+}$ without modifying the chemical nature of the chains, to study the role of lattice dynamics and supramolecular interactions in 1D chain compounds.

We directed our choice to a non-coordinated counter-anion and turned our interest to hexafluorostannate metal salt, which is expected to be weakly coordinating. Indeed, this salt is not only a precursor for the synthesis of new molecular compounds but it also offers the possibility of using the SnF_6^{2-} anion as a ^{119}Sn Mössbauer probe to study the local surroundings in the crystal lattice of 1D chains. It would thus provide relevant information on local distortions that could be modified by a phase transition and could also probe H-bonding interactions involving the fluorine atoms.

We successfully prepared new 1D NH_2trz ST compounds with different degrees of hydration incorporating this novel anion as a non-coordinated counter-anion as suggested from IR spectroscopy recorded at room temperature. Monohydrate (**14**) shows a reversible abrupt ST around 190 K, which is not complete but accompanied by a hysteresis loop that is ~ 7 K wide. The ST of hemihydrate (**15**) has a similar character and is shifted upwards to higher temperatures with a hysteresis loop that is ~ 16 K wide. The ST of dehydrated (**15d**), which retains its shape, is shifted downwards and has a hysteresis that is ~ 13 K wide. The effect of solvent molecules on the mechanism and the spin state is hard to predict;[25] however several trends were deduced for 1D 1,2,4-triazole chain materials. It is generally accepted that stabilisation of the LS state occurs upon increasing the number of water molecules[3], and this observation has been found in many other types of SCO compounds. However, stabilisation of the HS state was also encountered.[26] In another case, removing non-coordinated water molecules can even prevent SCO occurring.[24] Here, varying the water content has an effect on the crystal field because the ST is shifted either upwards or

downwards, but no affect is seen on the shape of the ST, which is fully preserved. Such non-coordinated water molecules are expected to be located in the third coordination sphere[27] and bound to the amino group of the triazole of the chains by hydrogen bonding.[28] Hydrogen bonding to the triazole seems reasonable because the ligand field is only modified by water removal. Also, ^{119}Sn Mössbauer has suggested that the anion is not hydrogen bonded to water molecules. We can thus conclude that non-coordinated water molecules play no role in the cooperative nature of the ST of these compounds and that varying the strength of the supramolecular network involving such species does not affect the cooperative nature of the spin transition.

We have also found that the non-coordinated anion, which is found between the chains, is able to feel the ST of individual chains. This behaviour was suggested primarily on the basis of the evolution of its local distortion registered by ^{119}Sn Mössbauer spectroscopy. Indeed, the SnF_6^{2-} octahedron is found to be regular in the HS state and distorted in the LS state, which presumes that the lattice change associated with the spin state change of Fe^{II} ions along the chains influences the local distortion of the anion. Also, Mössbauer resonance dramatically varies on crossing the ST range which is a clear signature of a phase transition (Figure 24). This behaviour may reflect the sensing of long-range elastic interactions between chains associated with ST through the phonons. This result constitutes the second example of ST sensing through the non-coordinated anion and the very first example obtained from Mössbauer spectroscopy. Indeed, a similar conclusion was drawn by following the B-F vibration of the tetrafluoroborato anion in the course of the ST of $[Fe(ptz)_6](BF_4)_2$ (ptz = 1-propyl-tetrazole) by IR spectroscopy.[29] It would also be interesting to complete the Mössbauer results by recording IR spectra for (**15**) on cooling. The current investigation is also the first combined ^{119}Sn and ^{57}Fe study in an Fe^{II} ST molecular

compound. Indeed, to the best of our knowledge, there is only one series of materials on which a combined Mössbauer study could be feasible namely the thiospinels $M_2FeSn_3S_8$ (M^+ = Cu, Ag) that were reported to exhibit a HS $\leftrightarrow$ LS spin equilibrium around $T_{1/2}$ ~ 200 K as deduced from magnetic susceptibility and ^{57}Fe Mössbauer spectroscopy measurements.[30] The rigid lattice of this solid state compound should allow a variable temperature ^{119}Sn Mössbauer study and provide insights into the spin conversion of these solid-state materials.

A few examples of Fe^{II} SCO materials are known to present order-disorder transitions of the counter-anion.[31-35] Such transitions which were detected by DSC or μSR are generally decoupled from the electronic transition. The control of such transitions was recently proposed as a useful tool for the elaboration of a new range of molecular switches for memory or sensing applications.[36] In this case, such an order-disorder of the SnF_6^{2-} anion may be present, but if so, it would be strongly coupled to the SCO because DSC provided the signature of a single-phase transition occurring in the temperature range of the spin transition (Figure 22). Indeed, there is no link between the local distortion of an octahedron and its disorder state because an anion may be distorted/regular and ordered/disordered.

In the next chapter, we shall focus on $[Fe(NH_2trz)_3](NO_3)_2$ whose ST properties are also governed by the nature of the included anion.

Notes and references

[1] O. Kahn, J. Kröber, C. Jay. *Adv. Mater.* **1992**, *4*(11), 718-728.
[2] O. Kahn, C. Jay-Martinez. *Science* **1998**, *279*(5347), 44-48.
[3] V. P. Sinditskii, V. I. Sokol, A. E. Fogelzang, M. D. Dutov, V. V. Serushkin, M. A. Poraikoshits, B. S. Svetlov. *Russ. J. Inorg. Chem.* **1987**, *32*(8), 1950-1955.
[4] P. J. Moehs, H. M. Haendler. *Inorg. Chem.* **1968**, *7*, 2115.
[5] P. J. van Koningsbruggen, Y. Garcia, E. Codjovi, R. Lapouyade, O. Kahn, L. Fournes, L. Rabardel. *J. Mater. Chem.* **1997**, *7*(10), 2069-2075.
[6] F. W. D. Woodhams, R. A. Howie, Knop O. *Can. J. Chem.* **1974**, *52*, 1904.
[7] Y. Calage, R. Tortevois, F. Varret. *J. Phys. Chem. Solids* **1990**, *51*, 911.
[8] A. Benghalem, M. Leblanc, Y. Calage. *Acta Crystallogr. , Sect. C* **1990**, *46*, 2453.
[9] M. M. Dirtu, Y. Garcia, M. Nica, A. Rotarii, J. Linares, F. Varret. *Polyhedron* **2007**, *26*(9-11), 2259-2263.
[10] G. Vos, R. A. G. Degraafe, J. G. Haasnoot, A. M. vanderKraan, P. Devaal, J. Reedijk. *Inorg. Chem.* **1984**, *23*(18), 2905-2910.
[11] J. J. A. Kolnaar, G. vanDijk, H. Kooijman, A. L. Spek, V. G. Ksenofontov, P. Gutlich, J. G. Haasnoot, J. Reedijk. *Inorg. Chem.* **1997**, *36*(11), 2433-2440.
[12] Y. Garcia, P. Guionneau, G. Bravic, D. Chasseau, J. A. K. Howard, O. Kahn, V. Ksenofontov, S. Reiman, P. Gutlich. *Eur. J. Inorg. Chem.* **2000**, (7), 1531-1538.
[13] R. R. Berret, B. W. Fitzsimmons. *Chem. Comm.* **1966**, *91*.
[14] R. R. Berret, B. W. Fitzsimmons. *J. Chem. Soc. A* **1967**, *525*.
[15] M. Thomman, O. Kahn, J. Guilhem, F. Varret. *Inorg. Chem.* **1994**, *33*(26), 6029-6037.
[16] Y. Garcia, V. Ksenofontov, S. Mentior, M. M. Dîrtu, C. Gieck, A. Bhatthacharjee, P. Gutlich. *Chem. Eur. J.* **2008**, *14*(12), 3745-3758.
[17] P. Gütlich, A. Hauser, H. Spiering. *Angew. Chem. Int. Ed.* **1994**, *33*(20), 2024-2054.
[18] P. Gütlich, Y. Garcia, H. A. Goodwin. *Chem. Soc. Rev.* **2000**, *29*(6), 419-427.
[19] P. Gütlich, Y. Garcia, H. Spiering. *Magnetism: From Molecules to Materials*, Wiley-VCH, Verlag GmbH, **2003**, p. 271.
[20] K. Boukheddaden, F. Varret. *Hyp. Int.* **1992**, *72*(4), 349-356.
[21] S. Floquet, M.-L. Boillot, E. Rivière, F. Varret, K. Boukhedddaden, D. Morineau, P. Négrier. *New J. Chem.* **2003**, *27*, 341.

[22] Y. Garcia, V. Niel, M. C. Muñoz, J. A. Real. *Top. Curr. Chem.* **2004**, *233*, 229-257.
[23] M. Verelst, L. Sommier, P. Lecante, A. Mosset, O. Kahn. *Chem. Mater* **1998**, *10*, 980.
[24] Y. Garcia, J. Moscovici, A. Michalowicz, V. Ksenofontov, G. Levchenko, G. Bravic, D. Chasseau, P. Gutlich. *Chem. Eur. J.* **2002**, *8*(21), 4992-5000.
[25] W. Zhang, F. Zhao, L. Tao, M. Yuan, Z.-M. Wang, S. Gao. *Inorg. Chem.* **2007**, *46*, 2541.
[26] Y. Garcia, P. J. van Koningsbruggen, R. Lapouyade, L. Fournes, L. Rabardel, O. Kahn, V. Ksenofontov, G. Levchenko, P. Gutlich. *Chem. Mater.* **1998**, *10*(9), 2426-2433.
[27] Y. Garcia, P. J. van Koningsbruggen, G. Bravic, P. Guionneau, D. Chasseau, G. L. Cascarano, J. Moscovici, K. Lambert, A. Michalowicz, O. Kahn. *Inorg. Chem.* **1997**, *36*(27), 6357-6365.
[28] K. Drabent, Z. Ciunik. *Chem. Commun.* **2001**, (14), 1254-1255.
[29] E. W. Müller, J. Ensling, H. Spiering, P. Gütlich. *Inorg. Chem.* **1983**, *22*, 2074.
[30] M. Womes, J.-C. Jumas, J. Olivier-Fourcade, F. Aubertin, U. Gonser. *Chem. Phys. Lett.* **1993**, *201*, 555.
[31] J. Fleisch, P. Gütlich, K. M. Hasselbach, W. Müller. *Inorg. Chem.* **1976**, *15*, 958.
[32] E. König, G. Ritter, S. K. Kulshrehtha, S. M. Nelson. *Inorg. Chem.* **1982**, *21*, 3022.
[33] J. M. Holland, J. A. McAllister, Z. Lu, C. A. Kilner, M. Thornton-Pett, M. A. Halcrow. *Chem. Comm.* **2001**, (6), 577.
[34] S. J. Campbell, V. Ksenofontov, Y. Garcia, J. S. Lord, Y. Boland, P. Gutlich. *J. Phys. Chem. B* **2003**, *107*(51), 14289-14295.
[35] N. Ortega-Villar, A. L. Thompson, M. C. Munoz, V. M. Ugalde-Saldivar, A. E. Goeta, R. Moreno-Esparza, J. A. Real. *Chemistry* **2005**, *11*(19), 5721-5734.
[36] O. Jeannin, R. Clerac, M. Fourmigue. *J. Am. Chem. Soc.* **2006**, *128*(45), 14649-14656.

Chapter III: Insights into the Origin of Cooperative Effects in the Spin Transition of $[Fe(NH_2trz)_3](NO_3)_2$[1]

Introducing remarks

The origin of the wide hysteresis loop (~ 35 K,[1-3]) occurring above room temperature for $[Fe(NH_2trz)_3](NO_3)_2$ (**17**) will be discussed in the present chapter, in light of a careful examination of the magnetic properties along with DSC, Mössbauer and structural studies. This study is focused on the intra-molecular interactions realized by triply 1,2,4-triazole bridges connecting spin changing molecules as well as intermolecular interactions which may mediated by a tripodal planar anion promoting strong cooperative effects,[4] resulting in the observation of large hysteresis width, free of any structural phase transition.

But the use of planar aromatic anions is not a sufficient condition to observe a wide hysteresis loop. In the absence of crystal structure of a 1D Fe^{II}-NH_2trz chain containing the nitrate anion, it was difficult to draw further conclusions. These materials indeed hardly crystallize and only a few Cu^{II} analogues were obtained by slow evaporation of the reaction medium or by recrystallization of the powders of the target compounds.[5-10] In this context, recrystallization of powders of $[Cu(NH_2trz)_3](NO_3)_2 \cdot H_2O$ (**18**) after hydrothermal treatment afforded single crystals that were analyzed in this work by single crystal X-ray diffraction. The crystal structure reveals 1D triple bridged *N1*,*N2* –1, 2, 4–triazole Cu^{II} chains and allows to study the supramolecular organization of the anion respective to other components of

[1] Adapted from M. M. Dîrtu, C. Neuhausen, A. D. Naik, A. Rotaru, L. Spinu, Y. Garcia *Inorg. Chem*. 49, **2010**, *5723*.

the system. In order to get deeper insights to the origin of cooperative effects of the ST of **17**, First-Order Reversal Curves (FORCs) were recorded along with SQUID measurements. This study was completed by DSC and variable temperature X-ray powder diffraction and ^{57}Fe Mössbauer spectroscopy carried out above 293 K where the ST proceeds.

Results

Synthesis and general characterization

17 was precipitated as a pink powder containing nanorods (length ~ 300-800 nm and thickness ~ 66 nm) that were identified by scanning electronic microscopy (SEM) (Figure 26a, b). Attempts to obtain single crystals of **17** by slow evaporation, slow diffusion, recrystallization and hydrothermal methods, all failed. The X-ray powder diffraction pattern (Figure 27) indicates a rather crystalline material which is similar to the one displayed by **18**. Repeated attempts to grow single crystals of **18** by slow evaporation, from an aqueous solution of the reaction medium at room temperature afforded needle shape type crystals that were analyzed by Dr. C. Neuhausen (EPFL). Recrystallization of a powder of **17** afforded a microcrystalline powder that provided a well resolved X-ray diffractogram (Figure 27), but no single crystals suitable for an X-ray analysis.

The high crystalline morphology of this sample was confirmed by SEM with elongated rods of 120 - 330 nm length (Figure 26c, d). These features prompted us to invest more efforts in the recrystallization process. The powder of **18** was then dissolved in distilled water and treated hydrothermally in an acid digestion bond at 155 °C for 36 h.

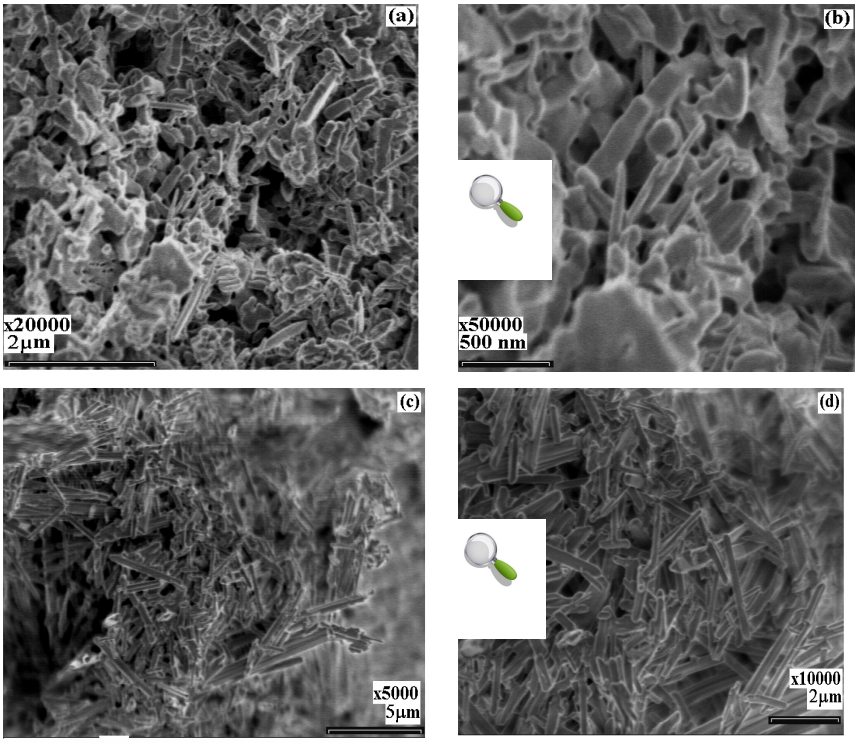

Figure 26 SEM images of powders at different resolutions of $[Fe(NH_2trz)_3](NO_3)_2$, **17**: (a), (b) and of $[Cu(NH_2trz)_3](NO_3)_2 \cdot H_2O$, **18**: (c), (d).

After cooling to room temperature, slow evaporation of the solution afforded after one week thin needles that are isostructural to the powder of **18**, as deduced from X-ray powder diffraction (Figure 27) and suitable for a single crystal X-ray diffraction analysis. A thermogravimetric measurement was carried out for **18** over the temperature range 25-900 °C. The residue obtained after ~ 900 °C was identified as CuO by comparison of its X-ray powder diffractogram with the JPCDS-JCDD database. This allowed us to derive the Cu % from the TGA analysis which is in agreement with the expected one for **18**. The crystals and powder of **18** have identical IR spectra. The bands assigned to ring torsion of triazole (619 cm^{-1}) and the N-N stretching bands (1197 cm^{-1}) are shifted to 621 cm^{-1} and 1218 cm^{-1}, respectively, thus confirming the coordination of Cu^{II} to the triazole ring.[8] The strong band ν_3 ~ 1384 cm^{-1} and the weak band ν_2 ~ 827 cm^{-1} are

characteristic of the asymmetric stretch and out-of-plane bend of nitrate anion,[11] thus confirming the presence of a non-coordinated counteranion. Diffuse reflectance spectra of **18** as powder or crystals show a broad asymmetric band in the range 440 - 870 nm which is due to a d-d transition, with a maximum at 15385 cm^{-1}, which is in agreement with the presence of a CuN_6 chromophore and a tetragonal distortion of Cu^{II} octahedra.[12]

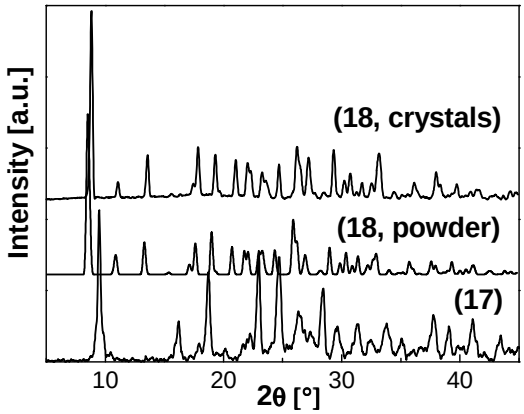

Figure 27 X-ray powder diffraction patterns at 293 K for **17** and **18**.

X-ray Crystal Structure of $[Cu(NH_2trz)_3](NO_3)_2 \cdot H_2O$ (18)

$[Cu(NH_2trz)_3](NO_3)_2 \cdot H_2O$ (**18**) crystallizes in the monoclinic system (C2/c). The crystallographic data are presented in Table 1 (Appendix-Crystal Structure data) and selected bond lengths and angles are given in Table 20a. Each Cu^{II} ion is coordinated to six N atoms belonging to six NH_2trz ligands setting up an octahedral symmetry, as indicated by the bond lengths and angles involving Cu^{II} (Table 20a). The basal plane of the octahedra is formed by four nitrogen donor atoms at 1.991(4) Å and 2.081(4) Å and two NH_2trz ligands that coordinate axially at 2.372(4) Å. The axial bond lengths are larger than the equatorial ones due to the Jahn-Teller effect. These Cu-N bond lengths are shorter than for other Cu^{II} 1D chain with NH_2trz including other anions (Table 21). The bidentate NH_2trz ligand bridges the copper ions

through the N1- and N2- nitrogen atoms to form a 1D infinite polymer (Figure 28). Compared to other crystallized Cu^{II} 1D chain compounds, only one repeating Cu^{II} type has been found within the chain, the octahedron thus appears to be less distorted (distortion parameter[13] $\Sigma = 13.0(5)^o$) (Table 21). The Cu^{II} octahedra are oriented in an ababa arrangement within a chain (Figure 28). The intra-chain distance Cu•••Cu = 3.903(1) Å, is in the expected range for 1D Cu^{II} coordination polymers with 1,2,4-triazole ligands. This value varies depending on the counteranion and the number of Cu^{II} types within a chain (Table 21). This distance is however more higher than for the Fe^{II} derivatives, with a Fe•••Fe ~ 3.5 Å as deduced by EXAFS (Extended x-ray absorption fine structure) measurements.[14, 15] For **18**, the inter-chain distance Cu•••Cu distance is 13.223(4) Å.

All 1,2,4-triazole rings are planar; the deviation from the least-square plane through the ring atoms is smaller than 0.18 Å.

Table 21 Collection of crystallographic data for the $[Cu(NH_2trz)_3]Anion \cdot nH_2O$ 1D chain complexes.

Anion	n	Bond distances (Å)	Octahedra sequence	Crystal system / Space group	Octahedral distortion (Σ)	
BF_4^-	1	Cu •••Cu = 3.922 Cu1-N11 = 2.379 Cu2-N12 = 1.977 Cu1-N21 = 2.003 Cu2-N22 = 2.423 Cu1-N31 = 2.067 Cu2-N32 = 2.059	ab ab ab	Triclinic/ P-1	$\Sigma_{(Cu1)} = 12.68(5)°$ $\Sigma_{(Cu2)} = 22.20(5)°$	[9]
ClO_4^-	1/3	- Cu-N = 2.01-2.11 (eq. plane) Cu-N = 2..26-2.38 (axial plane)	-	Triclinic/ P-1	-	[16]
BF_4^- /$(SiF_6^{-2})_{0.5}$	2	Cu •••Cu = 3.877, 3.886 Cu1-N11 = 2.426 Cu2-N12 = 2.017 Cu1-N21 = 2.018 Cu2-N22 = 2.327 Cu1-N31 = 2.040 Cu2-N32 = 2.042 Cu3-N41 = 2.315 Cu2-N42 = 2.018 Cu3-N51 = 2.013 Cu2-N52 = 2.369 Cu3-N61 = 2.096 Cu2-N62 = 2.037	ab ab ab	Triclinic / P-1	$\Sigma_{(Cu1)} = 21.92(5)°$ $\Sigma_{(Cu2)} = 14.55(5)°$ $\Sigma_{(Cu3)} = 12.56(5)°$	[9]

SiF_6^{-2}	8/3	Cu •••Cu = 3.855, 3.886, 3.904 Cu1-N11 = 2.065 Cu2-N12 = 2.069 Cu1-N21 = 2.329 Cu2-N22 = 1.985 Cu1-N31 = 2.006 Cu2-N41 = 1.992 Cu2-N51 = 2.317 Cu3-N42 = 2.353 Cu3-N52 = 2.048 Cu4-N72 =2.314 Cu3-N62 = 2.039 Cu4-N82 =2.082 Cu3-N71 = 2.030 Cu4-N92 =2.019 Cu3-N82 = 2.031 Cu3-N91 = 2.039	abc abc	Triclinic/ P-1	$\Sigma_{(Cu1)} = 10.96(5)°$ $\Sigma_{(Cu2)} = 15.87(5)°$ $\Sigma_{(Cu3)} = 25.47(5)°$ $\Sigma_{(Cu4)} = 13.44(5)°$	[9]
ZrF_6^{-2}	1	Cu •••Cu = 3.8850(3) Cu1-N1 = 2.299(3) Cu2-N12 = 2.385(3) Cu1-N21 = 2.080(3) Cu2-N2 = 2.023(3) Cu1-N11 = 2.014(3) Cu2-N22 = 2.029(3)	ab ab ab	Monoclinic / $P2_1/n$	$\Sigma_{(Cu1)} = 12.76(5)°$ $\Sigma_{(Cu2)} = 19.44(5)°$	[17]
NO_3^-	1	Cu •••Cu = 3.903(1)	ab ab ab	Monoclinic / C2/c	$\Sigma_{(Cu1)} = 13.00(5)°$	[18]

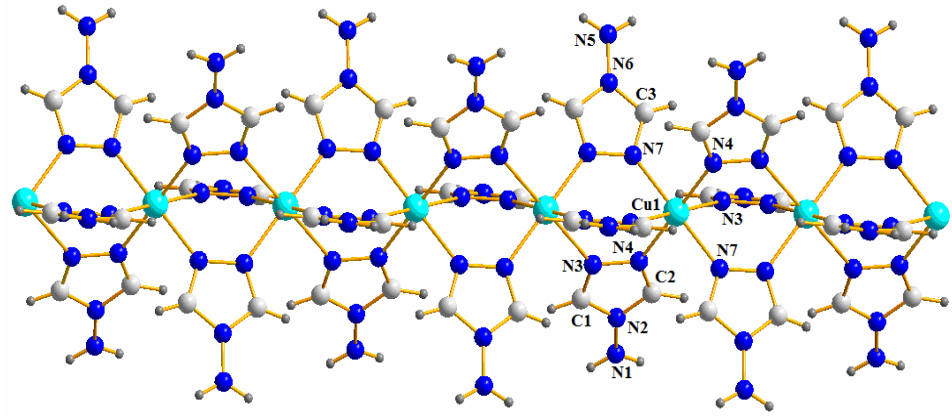

Figure 28 1D chain of $[Cu(NH_2trz)_3](NO_3)_2 \cdot H_2O$ running along the *c* axis illustrating the atomic labelling scheme (counteranions have been omitted for clarity).

The crystal packing is formed by an infinite octahedral array of $[Cu(NH_2trz)_3]^{2+}$ linear chains running along the *c* axis, with two NO_3^- counteranions and a non coordinated water molecules in the vacancies (Figure 29a). Many intra- and inter-chain H-bonding interactions involving the nitrate with the non-coordinated water molecule and with the amino group of the triazole ring are found (Figure 29).

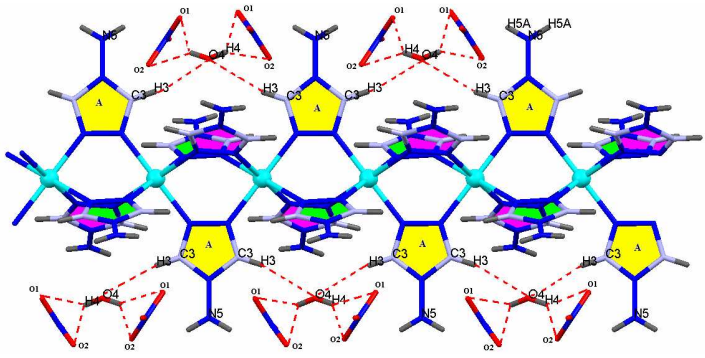

(a)

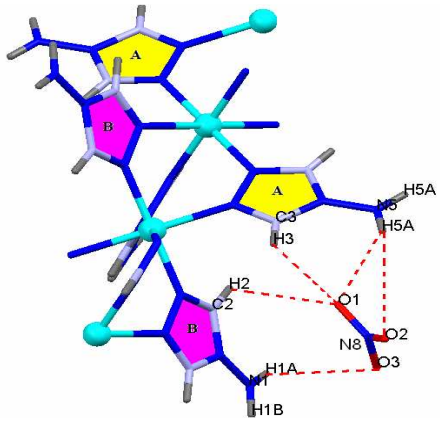

(b)

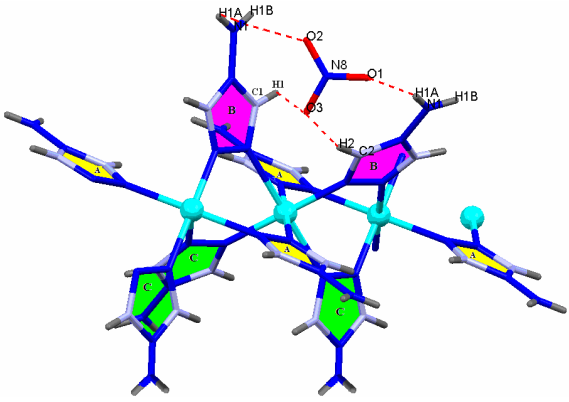

(c)

Figure 29 Intra-chain H-bonds interactions involving H_2O or nitrate for **18**: (a) the water molecule is connected to neighboring triazole (in yellow) by C-H···O interactions. (b) A nitrate is found to link the –C-H and the amino group of two triazole ring belonging to different planes (A in yellow and B pink). (c) a nitrate is connected to two amino groups and C-H of two triazole rings located in the B plane.

Intra-chain interactions are clearly identified between triazoles belonging to the same chain and the nitrate anion. Indeed, two amino groups of a triazole, of the A and B planes are connected through H-bonding to two different oxygen atoms of the same nitrate group: N5-H5A···O1 at 3.126 Å and N1-

H1A···O3 at 3.224 Å (Figure 29b). An additional H-bond is found between the amino group of the A plane and the O2 atom of the nitrate at 3.229 Å (N5-H5A···O2). A bifurcated H-bonding type is also found between O1 atom of nitrate and the –C-H of triazole rings in two different planes, C2-H2···O1 and C3-H3···O1 at 3.087 Å and 3.048 Å, respectively (Figure 29b).

In the B plane, the second NO_3^- group makes short intra-molecular interactions between: a) the -NH_2 groups of two adjacent triazole rings: N1-H1A···O1 at 3.151 Å and N1-H1A···O2 at 3.159 Å; b) the -C-H of two different triazole rings at 3.125 Å (C1-H1···O3) and at 3.129 Å C2-H2···O3 (Figure 29c).

The water molecule also connects two octahedra within a chain by C-H···O interactions through the triazole rings of the A plane at 3.215 Å (C3-H3···O4). The same water molecule is connected through H-bonding to oxygen atoms of nitrate groups at 3.339 Å (O4-H4···O1) and at 2.931 Å (O4-H4···O2) (Figure 29a). This water molecule is located between the chains and forms two bifurcated H-bonds with two nitrates which are related to different chains thanks to electrostatic interactions thus establishing indirect inter-chain interactions (Figure 30a). In addition, the nitrate anions strengthen inter-chain interactions: a trifurcated hydrogen interaction is found for O1: with amino groups belonging to two different chains: N5-H5A···O1 = 3.126 Å, N1-H1A···O1 = 3.151 Å, and with a -CH group of a chain (C2-H2···O1 = 3.087 Å). O2 is also connected to a amino group (N5-H5A···O2 = 3.229 Å) (Figure 30b) and the third oxygen of the nitrate (O3) is connected to a triazole ring (C2-H2···O3 = 3.129 Å).

Nitrate groups are thus implied in different intermolecular interactions (bi- and trifurcated) and set up a dense hydrogen bonding network.

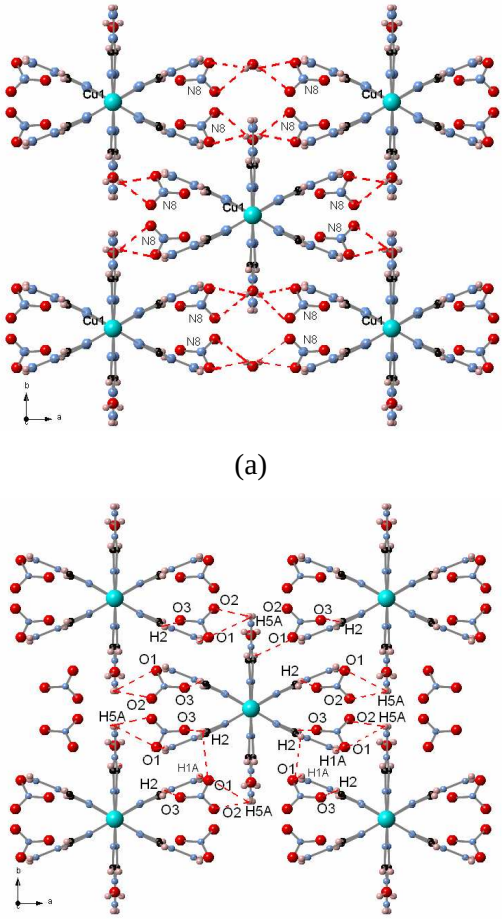

Figure 30 Projection of the crystal structure of **18** on the *(ab)* plane showing inter-molecular hydrogen-bonded chains involving: (a) both nitrate and water molecule. (b) nitrate and triazole rings.

Intramolecular interactions involving a non coordinated molecule were also identified for related Cu^{II} 4R-1,2,4-triazole chains.[10, 19] In the case of $[Cu(hyetrz)_3](ClO_4)_2 \cdot 3H_2O$ (hyetrz = 4-(2'-hydroxyethyl)-1,2,4-triazole),[5] a hydrogen bond between hydroxyl groups from the ligands, originating from neighboring triple μ-triazole links is identified as a intra-chain H-bonding lock. In $[Cu(hyetrz)_3](CF_3SO_3)_2 \cdot H_2O$,[20] and in $[Cu(NH_2trz)_3](BF_4)_2 \cdot H_2O$,[9] a weak double hydrogen bonding –C-H···X···H-C- (X = $CF_3SO_3^-$ or BF_4^-) that connect the anions to the chains is found.[10] In $[Cu(NH_2trz)_3]ZrF_6 \cdot H_2O$

no hydrogen bonds between the fluorine atom of ZrF_6^{2-} and the –C-H of triazole ring is identified,[21] but a pseudo 3D hydrogen bonding network is formed by H-bonding between fluorine atom and the -NH_2 group of the triazole and with the oxygen atom of water molecule. In **18**, the situation is unique because all types of interactions could be identified. The 'tripod' character of nitrate groups allows linking the NH_2trz rings by their –C-H and amino groups, which does rigidify the H-bonding network. The H-bonding network is reinforced by four different hydrogen bonds between water molecule and two different nitrate groups that belong to two different chains, –N-O···H(H_2O)···O-N- by double hydrogen bonding –C-H···X···H-C-. However, the hydrogen bonding network can be overall considered of moderate strength because hydrogen bonds range from 2.931 to 3.339 Å with bond angles varying from 84° to 165°, which deviates from linearity.

Thermally Induced Spin Transition in $[Fe(NH_2trz)_3](NO_3)_2$ (17)

UV-Vis Diffuse reflectance spectroscopy

Compound **17** presents a reversible thermochromism from pink to white on warming above room temperature (Figure 31). These colors depend on the spin state of the Fe^{II} centers. The pink color, at 293 K, is due to the $^1A_{1g} \rightarrow {}^1T_{1g}$ d-d transition of LS Fe^{II} sites observed at ~ 18700 cm^{-1}. A second band identified around 26700 cm^{-1} is attributed to $^1A_{1g} \rightarrow {}^1T_{2g}$ d-d transition. The white color, at 400 K, results from the location of the d-d transition, $^5T_{2g} \rightarrow {}^5E_g$, for the HS sites in the near infrared region (~ 12300 cm^{-1}). The ligand field strength for the HS and LS states have been evaluated thanks to eq. (f) and (g).[22-24]

$$10Dq^{HS} = E(^5E) - E(^5T_2), \qquad \text{(eq. } \mathbf{f}\text{)}$$

$$10Dq^{LS} = E(^1T) - E(^1A_1) + \frac{E(^1T_2) - E\left(^1T_1\right)}{4}, \text{(eq. } \mathbf{g})$$

The following values were obtained: $10D_q^{HS} \sim 12300$ cm^{-1} and $10D_q^{LS}$ 25375 cm^{-1}. These are typical of Fe^{II} complexes presenting a thermally induced SCO behavior.[22-24]

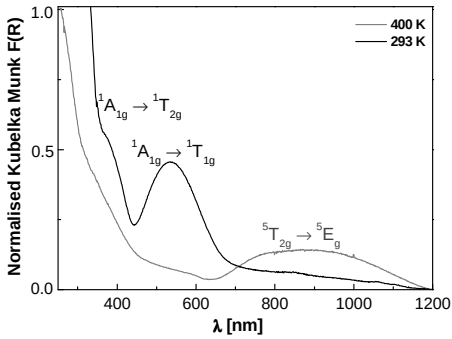

Figure 31 Kubelka-Munk function F(R) of **17** showing the d–d transitions at 293 K and at 400 K.

^{57}Fe Mössbauer spectroscopy

An inspection of the SCO properties for **17** using ^{57}Fe Mössbauer spectroscopy was undertaken over the temperature range 293 K - 380 K (Figure 32a, b). Mössbauer parameters are listed in Table 22 (see Appendix-Mössbauer data) and representative spectra are shown in Figure 32b. The spectrum at 293 K shows one quadrupole doublet attributed to LS Fe^{II} ions (δ^{LS} = 0.44 (1) mm·s^{-1} and $\Delta E_Q{}^{LS}$= 0.19(1) mm·s^{-1}) in good agreement with literature data that were only reported at room temperature.[2, 3] The detection of a quadrupole splitting stems from a lattice contribution to the electric field gradient which points out to a distortion of the LS octahedra within the chain.[25, 26] The compound remains in the LS state on warming up to 330 K, after which a second quadrupole doublet attributed to HS Fe^{II} ions grows in intensity (e.g. at 342 K, δ^{HS} = 0.98(3) mm·s^{-1} and $\Delta E_Q{}^{HS}$= 2.59(1) mm·s^{-1}).

This larger quadrupole splitting is due to the rising of the valence contribution of HS Fe^{II} ions.

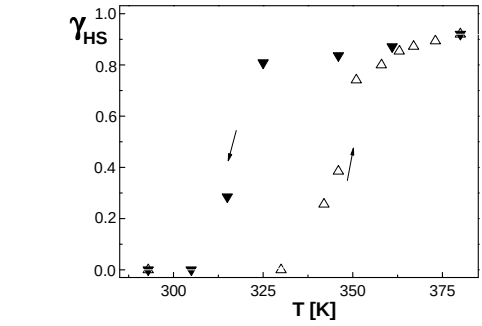

(a)

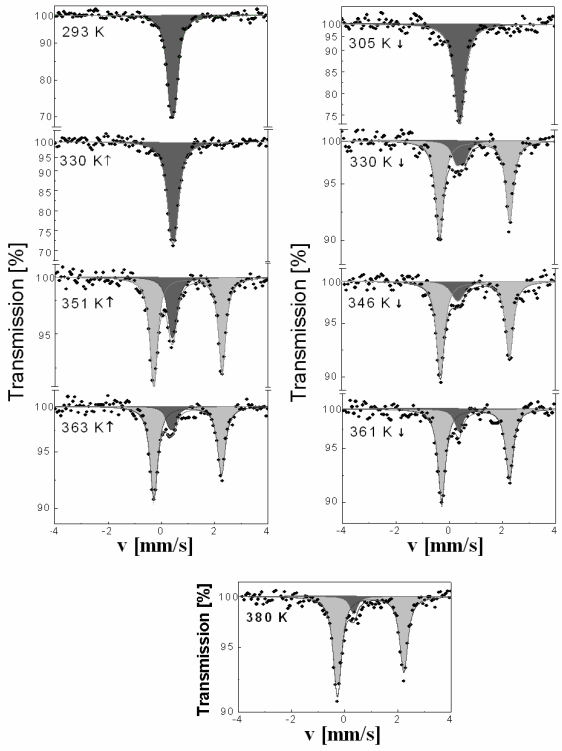

(b)

Figure 32 (a) γ_{HS} *vs. T* curves on cooling (▼) and on warming (Δ) modes for **17**. (b) Selected ^{57}Fe Mössbauer spectra of **17** on warming and on cooling mode. Grey and dark grey correspond to the HS and LS doublets, respectively.

The relative area fraction of the HS doublet slowly increases to ~ 38.5 % at 346 K and then more abruptly at 351 K where the spectrum consists of a dominant HS doublet, 74 % (δ^{HS} = 0.99 (1) mm·s^{-1} and $\Delta E_Q{}^{HS}$= 2.57(2) mm·s^{-1}). The slight asymmetry of the lines observed in the HS state is attributed to a texture effect. After this temperature the relative area of HS Fe^{II} ions increases again slowly to reach 92 % at 380 K, with δ^{HS} = 0.97(1) mm·s^{-1} and $\Delta E_Q{}^{HS}$= 2.49(1) mm·s^{-1}, indicating an incomplete ST at this temperature. Upon cooling to room temperature, the reverse situation is observed. The spectra shown on cooling and warming modes at 330 K clearly evidence a hysteretic effect (Figure 32b). Indeed, the ST curve deduced by plotting the variation of the temperature dependence of the HS molar fraction, γ_{HS}, shows a hysteresis loop, with $T_c{}^{\uparrow}$ = 347(1) K and $T_c{}^{\downarrow}$ = 317(1) K (Figure 32a). These values are in good agreement with the ones obtained by magnetic susceptibility measurements $T_c{}^{\uparrow}$ = 348 K and $T_c{}^{\downarrow}$ = 313 K,[2] μSR spectroscopy $T_c{}^{\uparrow}$ = 346 K and $T_c{}^{\downarrow}$ = 312 K,[3] DSC and XRPD at variable temperature (*vide infra*).

X-Ray powder thermo-diffractometry

The rather resolved X-ray powder diffraction pattern of **17** at 293 K (Figure 27) prompted us to investigate its thermo-diffractometry on warming in order to track the ST and an eventual crystallographic phase transition that could be at the origin of the observed hysteresis loop. X-ray diffraction patterns of **17** were thus recorded on cooling and warming over the same temperature range investigated by Mössbauer spectroscopy (298 - 380 K), where the ST reversibly proceeds, by Dr. C. Neuhausen (EPFL). The heating/cooling rate was fixed at 10 K/min between each temperature steps. Figure 33a shows typical diffraction patterns which are found to be similar on cooling and on warming mode and suggest that there is no crystallographic phase transition over the temperature variation. The

intensity of a peak at $2\theta = 24.6°$, corresponding to the HS state, was selected as a marker to follow the ST and the hysteresis loop of **17**, which is included in Figure 33b. On warming, the intensity of the peak at 24.3°, corresponding to the LS state, decreases in favor of the HS peak (Figure 33b). The peaks recorded for intermediate temperatures consist of the sum of these two contributions. The transition temperatures derived from the evolution of $I^{HS}(T)$ are $T_c^{\uparrow}$ = 347 K and $T_c^{\downarrow}$ = 314 K. These values agree very well with those obtained e.g. by Mössbauer spectroscopy and by μSR.[3] Indexation of the 10 most intense peaks of the diffractogram of **17** (Figure 33), at 293 K (LS) and 380 K (HS), provided preliminary unit cell parameters: at 293 K, a = 11.801 Å, b = 9.702 Å, c = 6.363 Å, V = 728.585 $Å^3$ and at 380 K, a = 14.346 Å, b = 9.650 Å, c = 6.801 Å, V = 941.501 $Å^3$. An elongation of the a axis along with a large volume change of 212.92 $Å^3$ and a preservation of an orthorhombic primitive lattice, are observed for **17**. A full Rietveld analysis was not possible due to the presence of broad peaks and a low signal/noise ratio. Assuming 2 molecules in the asymmetric unit, as in the analogous compound **18**, the volume change per unit chain would be 106 $Å^3$. This value is four fold increased compared to ΔV_{HL} which is the volume difference between HS and LS states for mononuclear complexes (~ 25 $Å^3$).[14, 15] For **17**, one should consider the combined effect of thermal dilatation, spin state change of the FeN_6 core, along with variation of interactions between the counteranions and the ligands of the 1D dimensional chains.

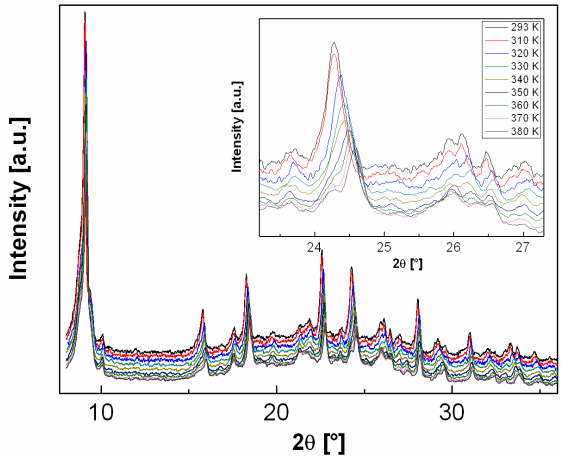

(a)

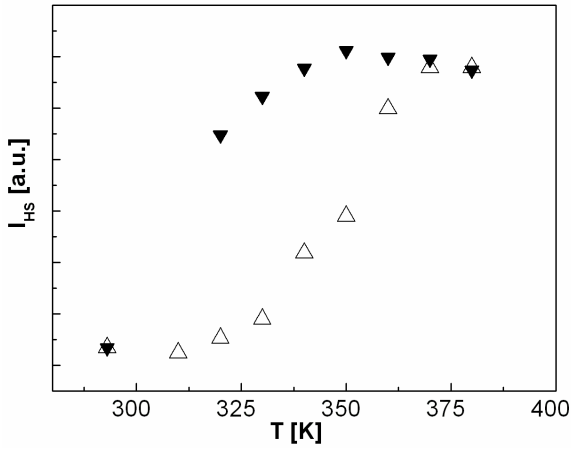

(b)

Figure 33 (a) X-Ray powder diffraction of **17**, recorded on warming, between 293 K and 380 K. The insert shows a zoom of the X-Ray powder diffraction recorded on warming. (b) The temperature dependence of the relative intensity of the HS phase I^{HS} peak at 2θ = 24.6°, the data were recorded on cooling (▼) and warming (□) modes.

Differential scanning calorimetry (DSC)

Differential scanning measurements of **17** were carried out at a scan rate of 10 K/min over the temperature range 293 - 400 K on warming and cooling modes. An endothermic peak is observed on warming at $T_{max}^{\uparrow}$ = 347 K and an exothermic peak is recorded at $T_{max}^{\downarrow}$ = 314 K, on cooling, thus revealing a hysteresis loop of width 33 K (Figure 34). This behavior is characteristic of a first-order phase transition and can be related to the ST detected by magnetic measurements,[2] XRPD and Mössbauer spectroscopy studies. The enthalpy and entropy variation have been evaluated as ΔH = 23(1) kJ.mol^{-1} and ΔS = 69.6(1) J mol^{-1}K^{-1}. The enthalpy variation agrees well with the one obtained by isobaric heat capacity measurements ΔH = 22.8(4) kJ.mol^{-1}.[27] The vibrational contribution to the entropy variation is evaluated as ΔS_{vib} = 56.2 J mol^{-1}K^{-1}, the electronic contribution being equal to R·ln5 = 13.4 J mol^{-1}K^{-1} for Fe^{II} SCO compounds.[22-24] These entropy values are somewhat larger than usually observed for Fe^{II} mononuclear SCO compounds,[28] but conforms well with the strong cooperative nature of the ST for this 1D coordination polymer.[29, 30]

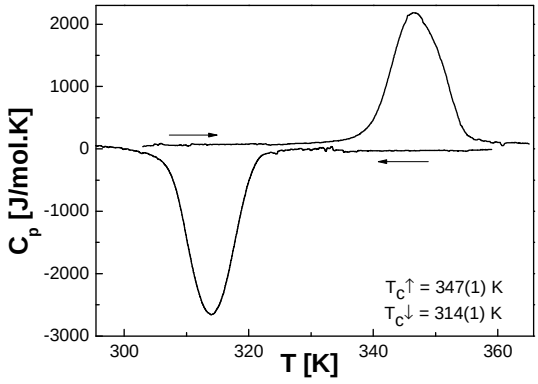

Figure 34 DSC profile of **17** in the 293 – 400 K temperature range in the cooling (←) and warming (→) modes.

Magnetic susceptibility measurements

SQUID investigation

The magnetic data were collected over the temperature range 274-380 K on warming and cooling modes under an applied field of 1000 Oe, by Dr. A. Rotaru at University of New Orleans, USA. The temperature dependence of the molar magnetic susceptibility is displayed in Figure 35 in the form of a $\chi_M T$ vs. T plot, χ_M being the molar magnetic susceptibility per Fe^{II} ion corrected for diamagnetic contributions. At 274 K, $\chi_M T$ is equal to 0.34 $cm^3mol^{-1}K$, which indicates Fe^{II} ions in the LS state with few paramagnetic ions that were also identified at room temperature in a previous ^{57}Fe Mössbauer spectrum.[3] Such HS ions were not detected in our Mössbauer investigation (Figure 32b) presumably due to the less resolution of our spectrum (compared with the one from the reference study [3]). As T is increased, $\chi_M T$ progressively increases reaching ca. 0.8 $cm^3mol^{-1}K$ around 338 K, after which $\chi_M T$ increases sharply at 352 K. Above this temperature, $\chi_M T$ increases very slowly and shows a plateau of 3.47 $cm^3mol^{-1}K$ at 380 K, which indicates HS Fe^{II} ions. In the cooling mode, as the temperature is decreased, $\chi_M T$ follows the same pathway as that observed when warming except in the range 350 – 319 K, which indicates a hysteresis loop ~ 37 K wide centred at 328 K. The transition temperatures at which 50 % of active LS and HS molecules are present in the warming and cooling modes are $T_c^{\uparrow}$ = 347(1) K and $T_c^{\downarrow}$ = 310(1) K. The hysteresis loop is retained over successive cooling and heating thermal cycles, which confirm the ST reversibility of **17**.

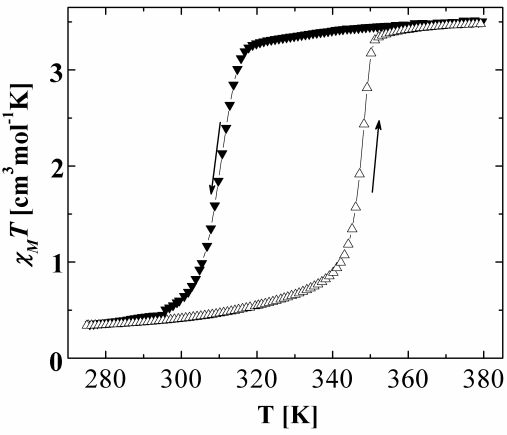

Figure 35 $\chi_M T$ vs.T plot for **17** over the temperature range 274-380 K.

FORC diagram investigation

The recording of magnetic measurements in DC mode reported above only provides a primary analysis of the hysteresis loop of **17**. We have extended this study by recording First-Order Reversal Curves (FORCs) to determine the distribution of switching temperatures and interactions fields for all of the 'particles' that contribute to the hysteresis loop.[31] FORCs actually represents a specific class of minor hysteresis loops, for which the sweeping process of the input parameter, here temperature, is reversed only once.[32] The measurement of a FORC begins with the saturation of the sample in the HS (or LS) state, where $\gamma_{HS} = 1$ (or $\gamma_{HS} = 0$). The temperature is then ramped down (or up) to a reversal temperature called T_a (or T_a*). The FORC consists of a measurement of γ_{HS} as the temperature is then increased from T_a (or T_a*) back up (or down) to saturation. The HS fraction at T_b (or T_b*) on the FORC with reversal point T_a is denoted by $\gamma_{HS}(T_a,T_b)$ (see Figure 36). Two sets of FORCs data can thus be recorded but here we have restricted ourselves to one mode (*vide infra*).

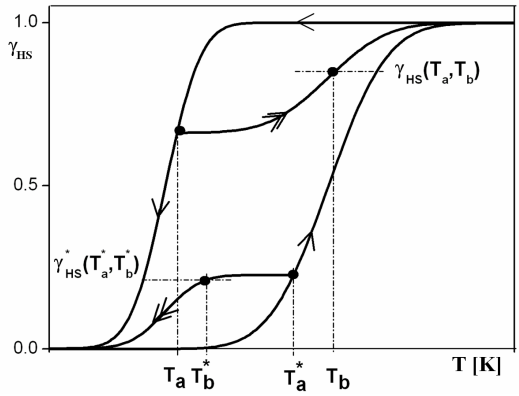

Figure 36 Thermal FORC in warming/cooling modes.[32]

The temperature step is chosen with T_a and T_b being regularly spaced, which means that $\gamma_{HS}(T_a,T_b)$ can be plotted on a regular grid. We also define the equilibrium temperature in the frame of an Ising like model as:

$$T_{1/2} = \frac{\Delta}{k_B} \ln \frac{g_{HS}}{g_{LS}}, \qquad \text{(eq. } \mathbf{h}\text{)}$$

where g_{HS}/g_{LS} is the ratio of the degeneracy of states, which results from the change in entropy for a total spin conversion ($\Delta S = R \ln g$, R is the gaz constant).[33]

The FORC distribution $\rho(T_a,T_b)$ is defined as the mixed second derivative:

$$\rho(T_a,T_b) = -\frac{\partial^2 \gamma_{HS}(T_a,T_b)}{\partial T_a \partial T_b}, \quad \text{(eq. } \mathbf{i}\text{)}$$

and plotted with rotated axes from switching temperatures (T_a,T_b) to a 'bias' (b) –'coercivity' (c) diagram following eq. (**j**) and (**k**), respectively.

The b and c parameters are defined as follows:

$$b = \frac{T_a + T_b}{2}, \quad \text{(eq. } \mathbf{j}\text{)}$$

$$c = \frac{T_a - T_b}{2}, \quad \text{(eq. } \mathbf{k}\text{)}$$

The 'bias' parameter, which is related to the equilibrium temperature $T_{1/2}$, roughly corresponds to the energy gap Δ between HS and LS states. The 'coercivity', which is related to the width of the thermal hysteresis loop, reflects the strength of intra-domain interactions, which is characterized by the J parameter.[33, 34] J is an interaction parameter derived from a two-level Ising like description of interacting SCO units.

Figure 37 shows the experimental FORCs for **17** obtained on a SQUID magnetometer. The sample was slowly warmed up to a reversal temperature located on the upper branch of the hysteresis loop and the sample was subsequently cooled. The temperature step was fixed at 0.5 K for both T_a and T_b, with a sweeping rate of 0.8 K/min. It was essential to use such a small temperature step to obtain the best accurate data.[33] Kinetic effects were also avoided by working in cooling mode only. Indeed, preliminary measurements attempted in the warming mode revealed that it was not possible to fix the reversal temperature on the lower branch of the hysteresis loop due to the thermal inertia of the SQUID magnetometer.

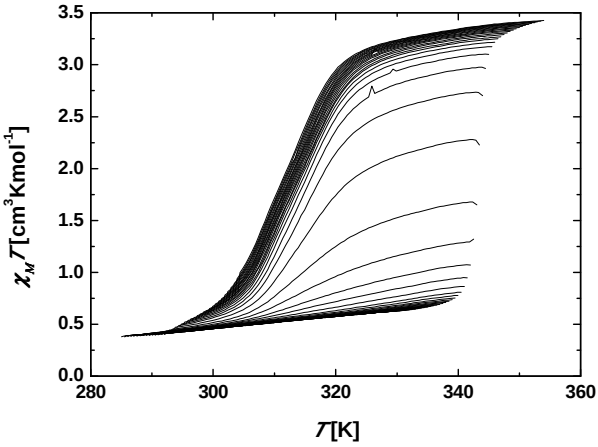

Figure 37 FORCs of the thermal hysteresis loop of **17** recorded in the cooling mode, with T_a, T_b increments of 0.5 K.

As it has been shown in ref. 35 by using the Jacobian transformation, a correspondence can be performed between FORC distributions in *c-b* and *J-Δ* coordinates. The FORC diagram is actually a 3D image represented by the

2D contour plot of the FORC distribution. Colors provide information about the probability that a single domain could be characterized by a given value *c-b* or $J-\Delta$ (Figure 14, 15). The probability is very low in the blue region and becomes very high in the red region. In the present case, an interaction parameter J = 496 K and an energy gap Δ = 2813 K were obtained (Table 23). It is much higher than the one found for the 2D ST compound $[Fe(btr)_2(NCS)_2]\cdot H_2O$ (J = 235 K)[34] which presents an hysteresis width of 25 K,[36] free of any structural phase transition,[4, 35] compared to 33 K for **17**.

We have also performed a statistical analysis after the procedure described in ref. [34] that allowed us to derive the average values of bias ($\overline{b}$), coercivity ($\overline{c}$), the standard deviations, σ(b) and σ(c), and the dimensionless correlation parameter $r_{c,b}$ (Table 23).

Table 23 Statistical analysis of the FORC distributions from Figure 38.

$\overline{b}$ [a] [K]	σ(b) [K]	$\overline{c}$ [a] [K]	σ(c) [K]	$r_{c,b}$	$\overline{\Delta}$ [a] [K]	σ(Δ) [K]	$\overline{J}$ [a] [K]	σ(J) [K]	$r_{J,\Delta}$
329.4	3.7	14.7	4.4	-0.67	2813	20	496.4	17.8	-0.75

[a] $\overline{b}$, $\overline{c}$, $\overline{\Delta}$, $\overline{J}$ represent the mean values of the parameters *b*, *c*, Δ and *J*, respectively.

It represents the degree of correlation between the joint distributions following eq. (***I***).

$$r_{c,b} = cov(b,c)/\sigma(b)\sigma(c) \qquad \text{(eq. } \boldsymbol{I}\text{)}$$

A negative correlation is found with $r_{c,b}$ = -0.67 and $r_{\Delta,J}$ = -0.75, which is traduced on the FORC diagram by a rotation of the distribution counter-clockwise. A similar effect has been observed in diluted $[Fe_xM_{1-x}(btr)_2(NCS)_2]\cdot H_2O$ 2D SCO materials (M^{II} = Zn, Co, Ni), where the correlation parameter increases with increasing the dilution.[33, 36]

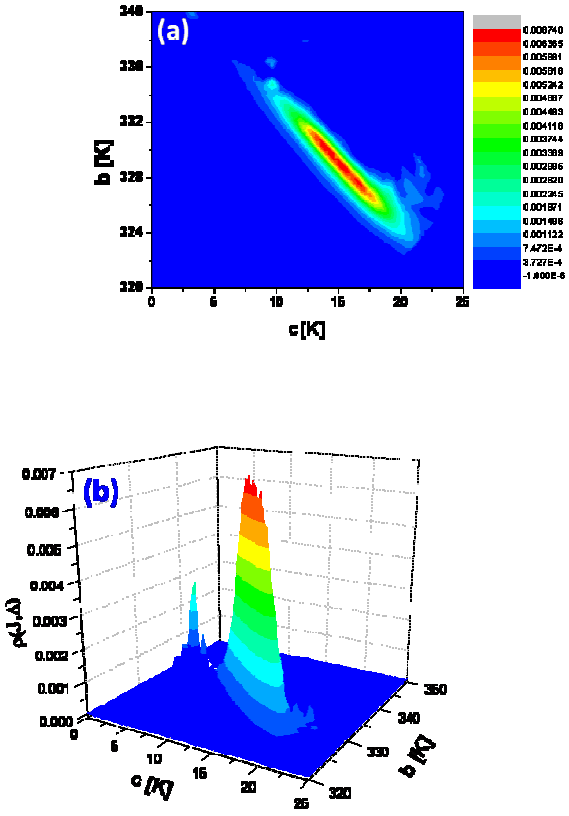

Figure 38 Experimental FORC diagram derived from Figure 13, in coercivity-bias coordinates: (a) 2D contour plot representation and (b) 3D representation.

Such correlation may be ascribable to the counteranion effect on the chains which is acting as a negative pressure on these later.[37, 38] A detailed study of this effect could be part of a future work where the size of the counter-anion will be modified in order to track a correlation between the counter-anion size and the cooperativity of the system.

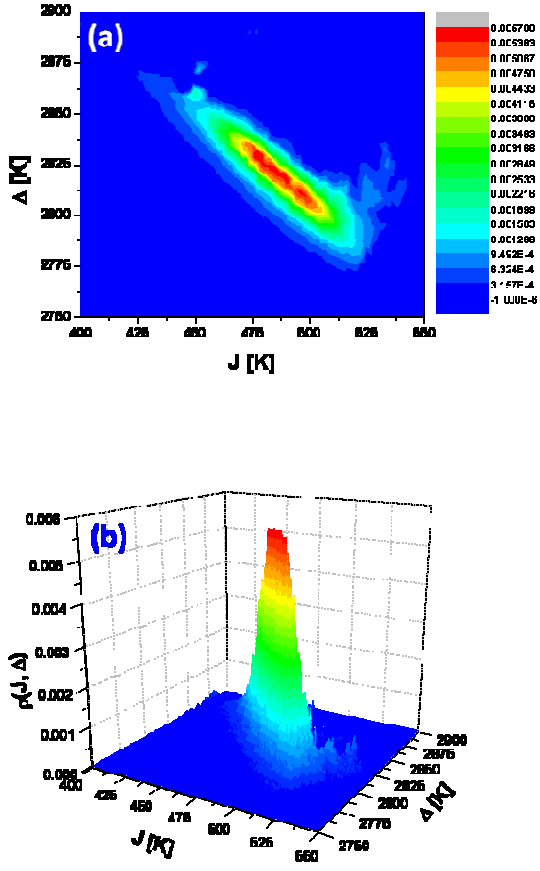

Figure 39 Experimental joint FORC diagram in *J-Δ* coordinates: (a) 2D contour plot representation and (b) 3D representation.

Discussion

The exclusive ST properties of $[Fe(NH_2trz)_3](NO_3)_2$ (**17**) being associated to an unusually large hysteresis loop feeds the debate about the origin of cooperative effects for 1D 1,2,4–triazole Fe^{II} chain compounds.[4, 39] A crystallographic phase transition that would occur concomitantly with the ST[40] could explain the increase of hysteresis width for **17** compared to other NH_2trz chains that also present an hysteretic ST but of lower width (Figure 40.

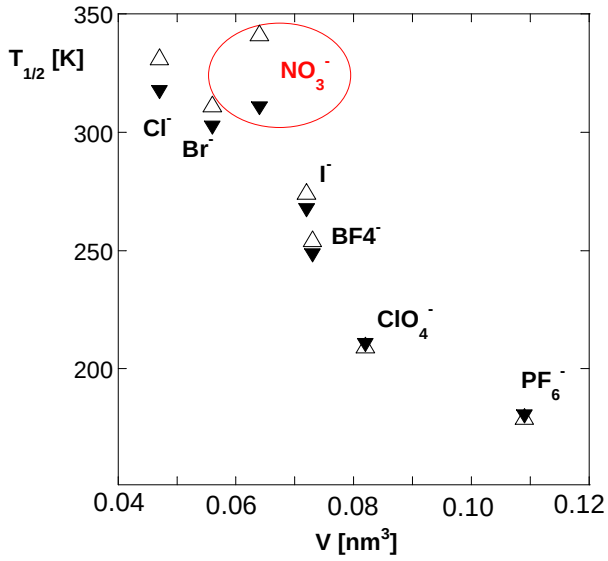

Figure 40 Variation of transition temperature, $T_{1/2}$, as deduced from Mössbauer spectroscopy, on cooling (▼) and warming modes (Δ) versus the anion volume for $[Fe(NH_2trz)_3](anion)_2$.[17] The circle highlights the wider hysteresis width of the nitrate derivative.

This situation has already been encountered for instance for Fe^{II} mononuclear complexes $[Fe(1\text{-}n\text{-propyl-tetrazole})_6](BF_4)_2$,[41] and $[Fe(PM\text{-}AzA)_2(NCS)_2]$ (PM = *N*-2'-pyridylmethylene, AzA = 4-(phenylazo)aniline),[42] that both display a ST on cooling below room temperature. XRPD patterns recorded on warming at variable temperatures for **17** have however revealed the absence of a crystallographic phase transition (Figure 33), a result which was confirmed by DSC that did not reveal an unusually large entropy value.[28] The hysteresis width developed by **17** can thus fully be ascribed to solid state cooperative effects that have been investigated in this work.

Compared to **17** the presence of a water molecule in the 1D chain, $[Fe(NH_2trz)_3](NO_3)_2 \cdot H_2O$[43, 44] has a negative effect in term of cooperativity but not in the term of temperature domain ($T_{1/2}^{\uparrow}$ = 347 K; $T_{1/2}^{\downarrow}$ = 327 K); the hysteresis loop being larger for the non-hydrated compound (compound **17**)

than for the hydrated one (ΔT = 15 K). The presence of water molecules increase the network of hydrogen bonds connections and at the same time the distance between the chains increases (a = 7.311(2), b = 10.562(3), c = 11.339(3) in the LS state[44]) and the cooperativity is weaker.

The transition temperatures and the hysteresis width are usually employed to characterize hysteretic SCO curves and to establish comparisons between SCO systems.[22-24] However, due to the various combinations of ligands, anions, grain size, internal stress and elastic interactions among active SCO sites, different systems can be characterized by the same transition temperatures and even by the same external thermal envelope of the hysteresis loop, whereas a completely different behavior occur within their hysteresis loop, particularly regarding domains distribution.[45, 46] In an attempt to remove some of the ambiguities inherent to conventional hysteresis measurements, Pike *et al* developed a novel characterization tool based on First-Order Reversal Curve (FORC) measurements.[31] It was also successfully used for the characterization of other systems presenting hysteretic behavior such as ferroelectric materials,[47, 48] nanowires,[49, 50], multilayers,[51, 52] spin glasses,[53, 54] and ST materials presenting pressure, thermal and light induced thermal hysteresis[55, 56]. Based on the thermodynamic characterization of **17** derived by DSC, the extent of cooperative effects effective in **17** was probed, for the first time in a 1D SCO system, through a FORC investigation. The mean value of the interaction parameter derived from this FORC analysis was evaluated as J = 496 K. This value is relatively high and suggests that intra-chain interactions between the spin active molecules play an important role on the cooperativity of this system (see magnetic section). Furthermore, the FORC diagram reveals a strong correlation between distributions in *c*-*b* and *J*-*Δ* coordinates which has been attributed to internal pressure effect induced by the nitrate anion on the chain.

Since Fe^{II}–1,2,4-triazole systems hardly crystallize, due to insolubility of the coordination polymers and potential Fe(II) oxidation, it was necessary to obtain single crystals of an analogous material containing a nitrate anion so as to gain further insights to the ST phenomenon of **17**. Hydrothermal pre-treatement as a method of recrystallization of 1D chains was proposed and provided single crystals of **18** suitable for a X-ray analysis. The first crystal structure of a 1D chain triazole derivative with a nitrate anion was thus obtained. It also represents one of the rare example of crystallized 1D chain complexes with triple *N*1,*N*2-1,2,4-triazole bridges.[5, 6, 8-10, 20, 57] The crystal structure of **18** is stabilized by a sophisticated and dense hydrogen bonding network, involving the nitrate, the amino group of the triazole ligand and a non-coordinated water molecule (Figure 30b). The anion is bonded to both amino groups of adjacent triazole molecules belonging to two 1D chains setting up inter-chain interactions. Thus, each chain is hydrogen bonded to four others, only by implication of the nitrate group with the ligand (-NH_2, -C-H) of different neighboring chains. Intra-chains interactions are identified between the nitrate groups and the amino groups of two adjacent (in the same or in different planes) triazole rings. Intra-chain interactions are also found between a non coordinated water molecule and -C-H of two triazole rings within the chain. The water molecule (Figure 29a) plays a double role because it participates in intermolecular interactions and increase supramolecular contacts between the chains. We thus conclude on the relevance of water molecules in the stabilization of the structure, which relates two different NO_3^- groups, involved also in intra- and inter-chains interactions in different chains. Indeed this stabilization is supported by the systematic single crystals degradation of **18** into a powder observed by taking out the samples from the mother solution at room temperature and ambient pressure.

Intra- and intermolecular interactions are thus assumed to strengthen elastic interactions between switching centers in **17**, thus resulting in a wide

hysteresis loop. Such interactions may not only be facilitated by the planar geometry of the nitrate anion but also by its 'tripod' character. In particular the role of the nitrate anion that acts as a fourth supramolecular bridge in addition to the triple 1,2,4-triazole bridge between metallic centers is pointed out (Figure 29b). This extra-bridge is believed to strengthen elastic interactions within the chain of **17** compared to classic chains that show hysteresis of lower width (Figure 40). These findings are consistent with the literature. Indeed, it was observed for **17** by μSR spectroscopy[2] that the amino group of the 1,2,4-triazole cannot freely rotate as a consequence of its likely hydrogen bonding to a nitrate anion, that would support intra-and inter-chain interactions claimed for **17**. Worthwhile to note that the role of hydrogen bonds to promote wide hysteresis loop has also recently been recognized in SCO research for an iron(II) mononuclear material presenting a 70 K wide hysteresis loop below room temperature.[58]

In the next chapter, we shall investigate SCO materials with a related ligand, 4-hydroxy-1,2,4-triazole (OH-trz), whose synthesis and coordination chemistry is reported here for the first time.

Notes and references

[1] O. Kahn, E. Codjovi, Y. Garcia, P. J. van Koningsbruggen, R. Lapouyade, Sommier L. In: (Eds.: M. M. Turnbull, T. Sugimoto, and L. K. Thompson), *Molecule-Based Magnetic Materials*, **1996**, p. 298.

[2] L.G.Lavrenova, V. N. Ikorskii, V. A. Varnek, I. M. Oglezneva, S. V. Larionova. *Koord. Khim.* **1986**, *12*, 207.

[3] Y. Garcia, S. J. Campbell, J. S. Lord, Y. Boland, V. Ksenofontov, P. Gutlich. *J. Phys. Chem. B* **2007**, *111*(38), 11111-11119.

[4] Y. Garcia, V. Niel, M. C. Munoz, J. A. Real. *Top. Curr. Chem.* **2004**, *233*, 229-257.

[5] Y. Garcia, P. J. van Koningsbruggen, G. Bravic, P. Guionneau, D. Chasseau, G. L. Cascarano, J. Moscovici, K. Lambert, A. Michalowicz, O. Kahn. *Inorg. Chem.* **1997**, *36*(27), 6357-6365.

[6] Y. Garcia, J. Moscovici, A. Michalowicz, V. Ksenofontov, G. Levchenko, G. Bravic, D. Chasseau, P. Gutlich. *Chem. Eur. J.* **2002**, *8*(21), 4992-5000.

[7] S. Toyazaki, Y. Murakami, T. Komatsu, N. Kojima, Yokoyama T. *Mol. Cryst. Liq. Cryst.* **2000**, *343*, 175-180.

[8] V. P. Sinditskii, V. I. Sokol, A. E. Fogelzang, M. D. Dutov, V. V. Serushkin, M. A. Poraikoshits, B. S. Svetlov. *Russ. J. Inorg. Chem.* **1987**, *32*(8), 1950-1955.

[9] K. Drabent, Z. Ciunik. *Chem. Commun.* **2001**, (14), 1254-1255.

[10] M. Seredyuk, A. B. Gaspar, M. C. Muñoz, M. Verdaguer, F. Villain, P. Gütlich. *Eur. J. Inorg. Chem.* **2007**, (28), 4481-4491.

[11] K. Nakamoto. *Infrared and Raman Spectra of Inorganic and Coordination Compounds : Applications in Coordination, Organometallic, and Bioinorganic Chemistry*, **1997**.

[12] B. J. Hathaway, D. E. Billing. *Coord. Chem. Rev.* **1970**, *5*, 143.

[13] M. Marchivie, P. Guionneau, J. F. Letard, D. Chasseau. *Acta Crystallogr. B* **2005**, *61*, 25-28.

[14] A. Michalowicz, J. Moscovici, B. Ducourant, D. Cracco, O. Kahn. *Chem. Mater.* **1995**, *7*(10), 1833-1842.

[15] A. Michalowicz, K. O. Moscovici. *J. Phys. IV* **1997**, *7*(C2), 633-635.

[16] V. P. Sinditskii, A. E. Fogelzang, M. D. Dutov, V. I. Sokol, V. V. Serushkin, B. S. Svetlov, M. A. Poraikoshits. *Russ. J. Inorg. Chem.* **1987**, *32*(8), 1944-1949.

[17] M. M. Dîrtu, A. Rotaru, D. Gillard, J. Linares, E. Codjovi, B. Tinant, Y. Garcia. *Inorg. Chem.* **2009**, *48*(16), 7838-7852.

[18] M. M. Dîrtu, C. Neuhausen, A. D. Naik, A. Rotaru, L. Spinu, Y. Garcia. *Inorg. Chem.* **2010**, *49*(12), 5723-5736.
[19] M. M. Dirtu, A. Rotaru, D. Gillard, J. Linares, E. Codjovi, B. Tinant, Y. Garcia. *Inorg. Chem.* **2009**, *48*(16), 7838-7852.
[20] Y. Garcia, P. J. van Koningsbruggen, G. Bravic, D. Chasseau, O. Kahn. *Eur. J. Inorg. Chem.* **2003**, (2), 356-362.
[21] M. M. Dirtu, A. Rotaru, D. Gillard, J. Linares, E. Codjovi, B. Tinant, Y. Garcia. *Inorg. Chem.* **2009**, *48*(16), 7838-7852.
[22] P. Gütlich, J. Jung, H. A. Goodwin. In: (Eds.: E. Coronado, P. Delhaès, D. Gatteschi, and J. S. Miller), *Molecular Magnetism: From Molecular Assemblies to the Devices*, **1996**, p. 327.
[23] P. Gütlich, A. Hauser, H. Spiering. *Angew. Chem. Int. Ed.* **1994**, *33*(20), 2024-2054.
[24] P. Gütlich, Y. Garcia, H. Spiering. *Magnetism: From Molecules to Materials*, Wiley-VCH, Verlag GmbH, **2003**, p. 271.
[25] M. M. Dirtu, Y. Garcia, M. Nica, A. Rotarii, J. Linares, F. Varret. *Polyhedron* **2007**, *26*(9-11), 2259-2263.
[26] M. M. Dirtu, A. Rotaru, D. Gillard, J. Linares, E. Codjovi, B. Tinant, Y. Garcia. *Inorg. Chem.* **2009**, *48*(16), 7838-7852.
[27] V. G. Bessergenev, G. A. Berezovskii, L. G. Lavrenova, S. V. Larionov. *Zhurnal Fizicheskoi Khimii* **1997**, *71*(5), 809-813.
[28] E. König. Complex Chemistry, In: *Structure & Bonding*, Springer Berlin, **1991**, pp. 51-152.
[29] Y. Garcia, V. Ksenofontov, S. Mentior, M. M. Dîrtu, C. Gieck, A. Bhatthacharjee, P. Gutlich. *Chem. Eur. J.* **2008**, *14*(12), 3745-3758.
[30] J. Krober, J. P. Audiere, R. Claude, E. Codjovi, O. Kahn, J. G. Haasnoot, F. Groliere, C. Jay, A. Bousseksou, J. Linares, F. Varret, A. Gonthiervassal. *Chem. Mater.* **1994**, *6*(8), 1404-1412.
[31] C. R. Pike, A. P. Roberts, K. L. Verosub. *J. Appl. Phys.* **1999**, *85*, 6660.
[32] Tanasa R., C. Enachescu, A. Stancu, F. Varret, J. Linares, E. Codjovi. *Polyhedron* **2007**, *26*(9-11), 1820-1824.
[33] C. Enachescu, R. Tanasa, A. Stancu, E. Codjovi, J. Linares, Varret F. *Physica B* **2004**, *343*, 15.
[34] R. Tanasa, C. Enachescu, A. Stancu, E. Codjovi, J. Linares, F. Varret, J. G. Haasnoot. *Phys. Rev. B* **2005**, *71*, 014431.
[35] Garcia, Y., Gieck, C., Stauf, S., Tremel, W., and Gütlich P. *4th TMR TOSS-Meeting*. 2001. Bordeaux, France. Ref Type: Conference Proceeding
[36] A. Rotaru, M. M. Dîrtu, C. Enachescu, R. Tanasa, J. Linares, A. Stancu, Garcia Y. *Polyhedron* **2009**, *28*, 2531.
[37] M. M. Dirtu, Y. Garcia, M. Nica, A. Rotarii, J. Linares, F. Varret. *Polyhedron* **2007**, *26*(9-11), 2259-2263.

[38] M. M. Dirtu, A. Rotaru, D. Gillard, J. Linares, E. Codjovi, B. Tinant, Y. Garcia. *Inorg. Chem.* **2009**, *48*(16), 7838-7852.
[39] K. S. Murray, C. P. Kepert. *Top. Curr. Chem.* **2004**, *233*, 195-228.
[40] J. Kusz, P. Gütlich, Spiering H. *Top. Curr. Chem.* **2004**, *234*, 129-153.
[41] J. Jeftic. *High Press. Res. Inter. J.* **2009**, *2*, 369.
[42] J.-F. Létard, P. Guionneau, E. Codjovi, O. Lavastre, G. Bravic, D. Chasseau, O. Kahn. *Journal of American Chemical Society* **1997**, *119*(44), 10861-10862.
[43] G. Galle, D. Deldicque, J. Degert, T. Forestier, J. F. Letard, E. Freysz. *Appl. Phys. Lett.* **2010**, *96*(4), 041907.
[44] A. Grosjean, N. Daro, B. Kauffmann, A. Kaiba, J. F. Letard, P. Guionneau. *Chem. Commun.* **2011**, *47*(45), 12382-12384.
[45] M. Sorai, S. Seki. *J. Phys. Soc. Japan* **1972**, *33*, 575.
[46] C. Chong, B. Berini, K. Boukheddaden, E. Codjovi, J. Linares, Y. Garcia, A. D. Naik, F. Varret. *Physica Status Solidi A-Applied Research* **2010**, *207*, 1227-1231.
[47] A. Stancu, D. Ricinschi, L. Mitoseriu, P. Postolache, M. Okuyama. *J. Appl. Phys.* **2003**, *83*, 3767-3770.
[48] A. Stancu, L. Mitoseriu, L. Stoleriu, D. Piazza, C. Galassi, D. Ricinschi, M. Okuyama. *Physica B* **2006**, *372*(1-2), 226-229.
[49] F. Beron, L. Clime, M. Ciureanu, D. C. R. W. Menard, A. Yelon. *J. Appl. Phys.* **2007**, *101*(9), 91107.
[50] R. Lavin, J. C. Denardin, J. Escrig, D. Altbir, A. Cortes, H. Gomez. *IEEE Trans. Magn.* **2008**, *44*(11), 2808-2811.
[51] J. E. Davies, O. Hellwig, E. E. Fullerton, G. Denbeaux, J. B. Kortright, K. Liu. *Phys. Rev. B* **2004**, *70*, 224434-224442.
[52] J. Yin, H. Zhang, F. Hu, B. Shen, L. Q. Pan. *Phys. Rev. B* **2009**, *106*(10), 103901-103906.
[53] H. G. Katzgraber, F. Pazmand, C. R. Pike, K. Liu, R. T. Scalettar, K. L. Verosub, G. T. Zimanyi. *Phys. Rev. Lett.* **2002**, *89*, 257202.
[54] H. G. Katzgraber, D. Herisson, M. Osth, P. Nordblad, A. Ito, H. A. Katori. *Phys. Rev. B* **2007**, *76*, 092408-092412.
[55] C. Enachescu, R. Tanasa, A. Stancu, F. Varret, J. Linares, E. Codjovi. *Phys. Rev. B.* **2005**, *72*, 054413-054420.
[56] C. Enachescu, R. Tanasa, A. Stancu, F. Varret, J. Linares, E. Codjovi. *Physica B* **2006**, *372*, 211.
[57] M. M. Dirtu, A. Rotaru, D. Gillard, J. Linares, E. Codjovi, B. Tinant, Y. Garcia. *Inorg. Chem.* **2009**, *48*(16), 7838-7852.
[58] B. Weber, W. Bauer, J. Obel. *Angew. Chem. Int. Ed.* **2008**, *47*, 10098-10101.

Chapter IV: Supramolecular Interactions and spin crossover properties of M(II) – 4 hydroxyl-1,2,4-triazole coordination compounds

Introducing remarks

Cooperativity factors which determine the credibility in iron(II) spin crossover (SCO) materials performances have long been the subject matter of intensive efforts, tuning with proposed applications in sensor and memory devices[1, 2]. Therefore the conditions which can explore strength of cooperative interactions in SCO complexes, which are the abrupt, complete and large hysteresis of magnetic profiles, may be influenced by ligand design, anion geometry and charge, crystal defects, solvent occupancy, etc.[3].

In this chapter, we report and discuss the spin transition characteristics of polynuclear iron(II) compounds of formula $[Fe(OH\text{-}trz)_3](Anion)_2 \cdot nH_2O$ where OH-trz is the ligand 4-hydroxy-1,2,4-triazole (see Figure 41). This ligand was selected in order to increase the dimensionality of an 1D materials through hydrogen bonding interactions, using a less voluminous substituent on the 4th position of the 1,2,4-triazole system. This also offers a splendid comparison with the analogous NH_2trz 1D system that has been thoroughly investigated in the literature and in Chapters I-III.

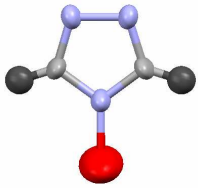

Figure 41 Molecular structure of 4-hydroxy-l,2,4-triazole (**OH-trz**).

The synthesis and the detailed structural characterization of two linear copper(II) and zinc(II) chain containing single and double *N*1,*N2*-1,2,4-triazole bridges of the ligand OH-trz is reported, namely [Cu(OH-trz)(ReO_4)OH]·$2H_2O$ (**19**) and [Zn(OHtrz)$_2$Cl](NO_3) (**20**). Exploration of supramolecular contacts in this structure is interesting in view of their potential input in the spin state structure of SCO materials.

We also would like to emphasize that this study is of particular interest in view of the peculiar Fe(II) SCO behavior of [Fe(OH-trz)$_3$](Anion)$_2$·nH_2O, (Anion = NO_3^-, BF_4^-, ClO_4^-, $CF_3SO_3^-$ and *n* stands for the number of noncoordinated water molecules) which shows of a thermally induced spin change below and above room temperature.

Results

Synthesis and general characterization

A new protocol for the preparation of 4-hydroxy-1,2,4-triazole (OH-trz), not accessible by the Bayer method[4], is reported. Direct transamination of Hydroxylamine hydrochloride (**II**) with *N*,*N*-dimethylformamide azine dihydrochloride (I) in refluxing toluene readily yields the target molecule in short duration of time (3-4 hours) with appreciable yield (65%). This modified method deviates from the reported transamination reaction[5] with respect to selection of solvent and purification procedure. Benzene was effectively replaced by toluene and Soxhlet method was employed to eliminate insoluble impurities. Because the product is obtained as hydrochloride salt, it was treated with sodium ethoxide to liberate the free molecule.

Complexes were prepared as pink or white powders by reacting OH-trz to $[Fe(H_2O)_6]^{2+}$ including a suitable counteranion (NO_3^-, BF_4^-, ClO_4^-, $CF_3SO_3^-$) in a 3:1 ratio in MeOH/H_2O following ref. [3]. These complexes were successfully characterized by elemental analysis, TGA-DTA analyses,

atomic absorption (AAS), X-Ray powder diffraction, IR, SEM and ^{57}Fe Mössbauer spectroscopy. The thermogravimetric and elemental analyses reveal the presence of guest water molecules, affording the following general formula $[Fe(OH\text{-}trz)_3](NO_3)_2 \cdot H_2O$ (**LOH-NO$_3$**) $[Fe(OH\text{-}trz)_3](BF_4)_2 \cdot H_2O$, (**LOH-BF$_4$**), $[Fe(OH\text{-}trz)_3](ClO_4)_2 \cdot H_2O$ (**LOH-ClO$_4$**), $[Fe(OH\text{-}trz)_3](CF_3SO_3)_2 \cdot H_2O$ (**LOH-TRF**).

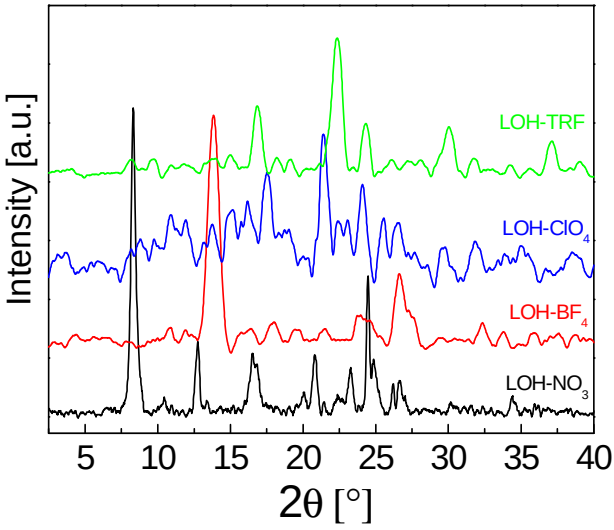

Figure 42 X-Ray powder diffraction patterns at 293 K for **LOH-NO$_3$**, **LOH-BF$_4$**, **LOH-ClO$_4$**, **LOH-TRF**.

These compounds present a slightly crystalline character as revealed from X-ray powder diffraction (XRPD) patterns (Figure 42). X-ray powder diffraction patterns revealed that principal peaks are different in all diffractograms (Fig. 42), which exclude the isostructurality of the chain complexes. Compared to **LOH-BF$_4$**, **LOH-ClO$_4$**, **LOH-TRF** which are amorphous, compound **LOH-NO$_3$** show the better resolved diffractogram of the series.

Morphology of these compounds is illustrated by the SEM analysis with aggregation of sponge covered with amorphous powder for **LOH-NO$_3$** and amorphous surface for **LOH-BF$_4$**, **LOH-ClO$_4$**. Different block of plates are distinguished in the aggregates for **LOH-TRF** (Figure 43). Attempt

to grow single crystals of Fe(II) complexes failed due to their rapid oxidation in aqueous solution at room temperature.

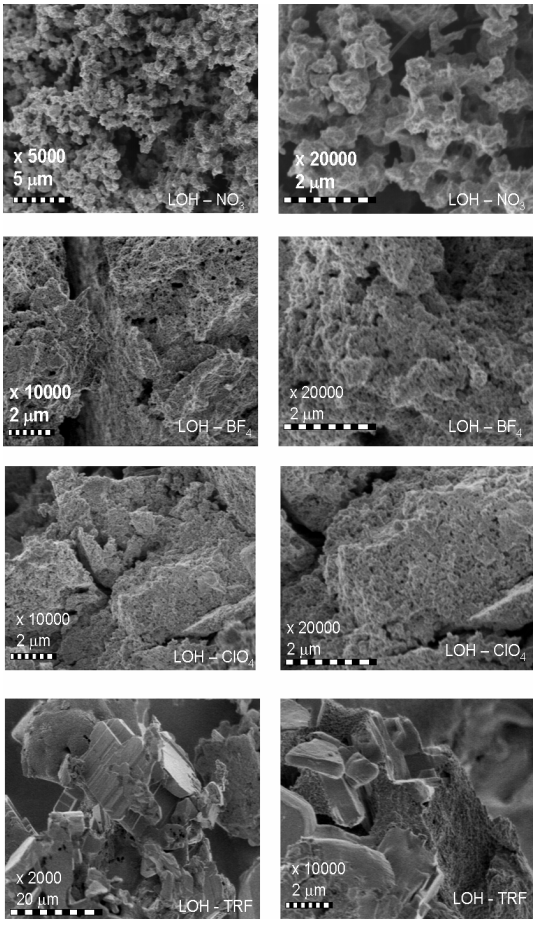

Figure 43 SEM images of microcrystalline particles of **LOH-NO_3**, **LOH-BF_4**, **LOH-ClO_4**, **LOH-TRF**.

FT-IR analyses were performed to ascertain the coordination mode of iron to the ligand and the presence of the counter-anions in the crystal lattice (Figure 44).

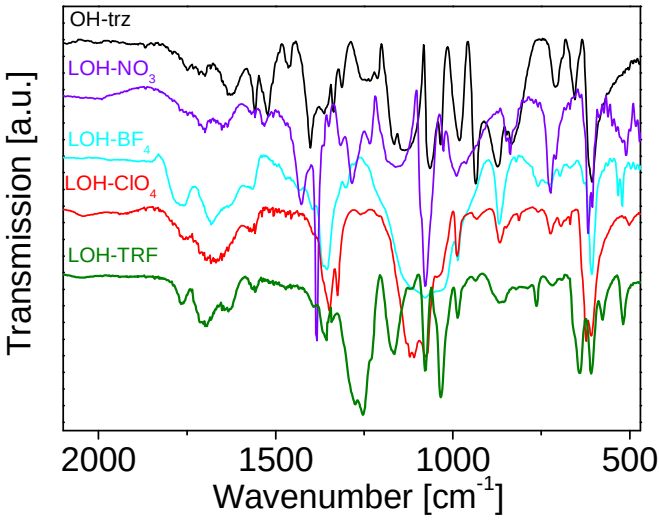

Figure 44 IR spectra of the ligand **OH-trz** and of complexes **LOH-NO_3**, **LOH-BF_4**, **LOH-ClO_4**, **LOH-TRF**. over the range 400-2300 cm^{-1}.

For **OH-trz**, the band assigned to ring torsion of triazole at ν = 606 (m) cm^{-1}, the $\nu_{C=N}$ stretching vibration at 1562 (m) cm^{-1} and the N-N stretching band at ν = 1031 (s) cm^{-1}, are all shifted upon complexation, for example in **LOH-BF_4** to 610 cm^{-1}, $\nu_{C=N}$ = 1566 cm^{-1}, and ν_{N-N} = 1077 cm^{-1}, respectively. These values confirm the coordination of the iron to the 1,2,4-triazole ring.[6, 7] Indeed, the characteristic bands of the ligand are not only present in the spectra of the complexes but also are shifted towards larger wave numbers, from 3 to 10 cm^{-1} respectively[8, 9].

In the case of **LOH-NO_3**, **LOH-ClO_4** and **LOH-TRF**, a splitting of the band assigned to ring torsion of triazole is identified, at 606 cm^{-1} and 620 cm^{-1}, 609 cm^{-1} and 636 cm^{-1} and at 607 cm^{-1} and 642 cm^{-1}, respectively. Accordingly, some vibration modes of monodentate triazole are active in IR spectroscopy while forbidden or strongly suppressed for bidentate triazoles. Two rings torsion vibrations are allowed in the 600-700 cm^{-1} range for monodentate 1,2,4-triazole (γ_1 and γ_2), γ_1 being observable at higher frequencies than γ_2, that is strongly suppressed when triazoles assume a μ_1-*N1,N2*-triazole coordination mode[10]. As for μ_1-*N1,N2* triazoles

uncoordinated 4-R-1,2,4-triazole the γ_1 remains very weak. Since the IR spectrum of **LOH-ClO$_4$** exhibits a strong peak at 623 cm^{-1}due to the δ_{Cl-O} of perchlorate counteranion, another strong peak at 609 cm^{-1} (γ_2) and a weak peak at 636 cm^{-1} (γ_1). The weak intensity of γ_1 indicated a *μ_1-N1,N2* coordination mode. But the 27 cm^{-1} separation between the γ_1 and γ_2 frequencies could not exclude the presence of unidentate triazole ($\Delta\nu$ = 30 cm^{-1})[10]. It is the same situation for compounds **LOH-NO$_3$** and **LOH-TRF** which present a separation between the γ_1 and γ_2 less then 30 cm^{-1}. Because the splitting is very small a nearly identical environment for the triazole rings of the OH-trz molecule in these complexes is assumed. But a possible presence of a deprotonated form of the ligand (as triazolate, trzO$^-$) or a different environment for the triazole rings of the OH-trz molecule cannot be excluded[10]. However the presence of two different Fe(II) sites were not identified by ^{57}Fe Mössbauer spectroscopy (see ^{57}Fe Mössbauer part).

Presence of the monovalent counter-anion is also confirmed by IR (cm^{-1}) $\upsilon_{(N-O)}$ ~ 1384(vs), (**LOH-NO$_3$**); $\upsilon_{(B-F)}$ ~ 1070 (shoulder, s), (**LOH-BF$_4$**); $\upsilon_{(Cl-O)}$ ~ 1111 (s), (**LOH-ClO$_4$**); $\upsilon_{(S-O)}$ ~ 1251 (s), (**LOH-TRF**).[11]

^{57}Fe Mössbauer spectroscopy confirms, for **LOH-NO$_3$**, **LOH-BF$_4$**, **LOH-ClO$_4$** and **LOH-TRF** the presence of one $Fe^{II}N_6$ site, and excludes any oxidation product of iron. These spectroscopic data supports a linear chain structure with Fe^{II} ions linked by triple *N1,N2*-1,2,4-triazole bridges[3, 12].

X-ray crystal structure determination

[Cu(OH-trz)(ReO4)OH]·2H$_2$O (19)

Complex **19** crystallizes in the orthorhombic space group *Pnma*. Crystallographic data, obtained by Dr. C. Neuhausen (EPFL), are summarized in Table 24, 25, 26. Figure 45 shows a single Cu(OH-

$trz)_2(ReO_4)_2(OH)_2$ unit. The octahedral coordination sphere around the Cu ion is formed by two oxygen atoms from coordinated ReO_4^{2-} at 2.535(3) Å in axial position. In the equatorial plane, two bridging 1,2,4-triazole binds monodentately by their nitrogen to copper with 1.996(8) Å. The coordination sphere is completed by two Cu – O bonds belonging to the hydroxyl group with 1.929(4) Å thus forming a CuN_2O_4 octahedra.

It has to be noted that the bond length of Cu…O (ReO) in axial position is considerably longer (0.54-0.60 Å) than other bonds in the equatorial position due to a Jahn-Teller effect. Here tetrahedral ReO_4 anion also act as bidentate ligand, linking adjacent $Cu(OH\text{-}trz)_2(OH)_2$ centers. The Cu•••Cu distance in the resulting 1D chains is 3.380 Å (Figure 46) which has favorable three-way electron exchange pathways due to these different types of bridging.

Perrhenate anion has been reported to show diverse bridging and binding modes besides acting as anion. Due to increased attention to perrhenate in radio-labeling in bioinorganic and medical imaging, binding and bridging mode of this moiety has received increased attention[13-16]

Lippard et al[17] reported a rare mode of bridging of perrhenate molecule. In their reported 2D structure this molecule acts as tridentate bridging entity forming a $Cu_3(\mu_3\text{-}ReO_4)$ cluster.

Simultaneous bridging by three different ligands is rather uncommon which impart slight distortion around copper which is around $\Sigma(Cu) = 8.72°$. Three zigzag chains are arranged around copper ions. One plane containing 1,2,4-triazole bridging is nearly perpendicular to the plane containing the bridging ReO_2 zigzag chain. The third chain containing hydroxyl group is interestingly accommodated in the same plane as that of triazole bridging but faces opposite due to steric clashes. Bond lengths among Re-O are different, those which bind to copper ions are (Re-O = 1.735 Å) slightly longer than non-bound Re-O (1.715 and 1.729 Å). These 1D chains are further inter- and

intra connected via hydrogen bonding to form a supramolecular 3D structure. The unbound oxygen atoms of perrhenate molecules form two types of H-bonding that leads to interchain connectivity. O2 of ReO_4 forms H-bonding with lattice water molecules, Re-O2…O(H2) = 2.9 Å which in turn connects to hydroxyl bridging by (H2)O2…O(H) = 2.79 Å. Further O3 forms bifurcated H-bonding with two neighboring triazole protons Re-O3…H1(C1) = 2.369 Å strengthening interconnectivity. Intra chain connectivity is laid by O2 of ReO4 which also forms bifurcated H-bonds within the chain with triazole protons (Re-O2…H1(C1) = 2.713 Å. Hydroxy group of hydroxyl triazole terminal also forms H-bonding with lattice water molecule trz(O5H)…O6(H2) = 2.258 Å.

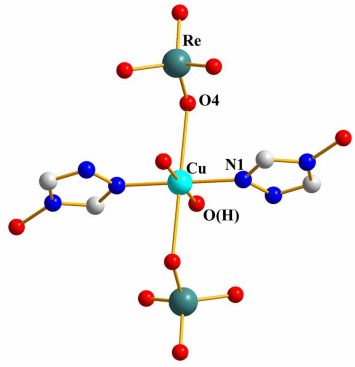

Figure 45 Structure of a single $Cu(OH\text{-}trz)_2(ReO_4)_2(OH)_2$ unit.

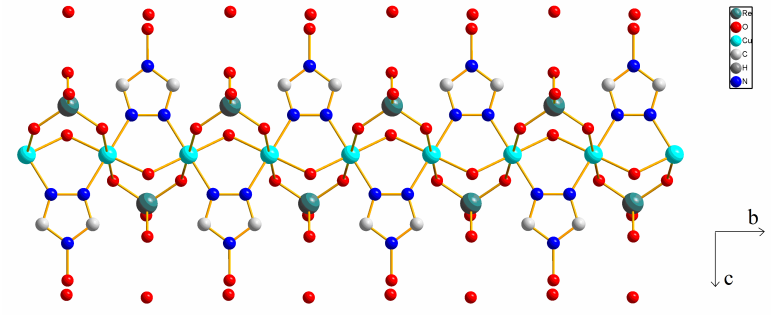

Figure 46 Projection of the crystal structure of a 1D $[Cu(OH\text{-}trz)(ReO_4)OH]$ chain, along the *bc* plane.

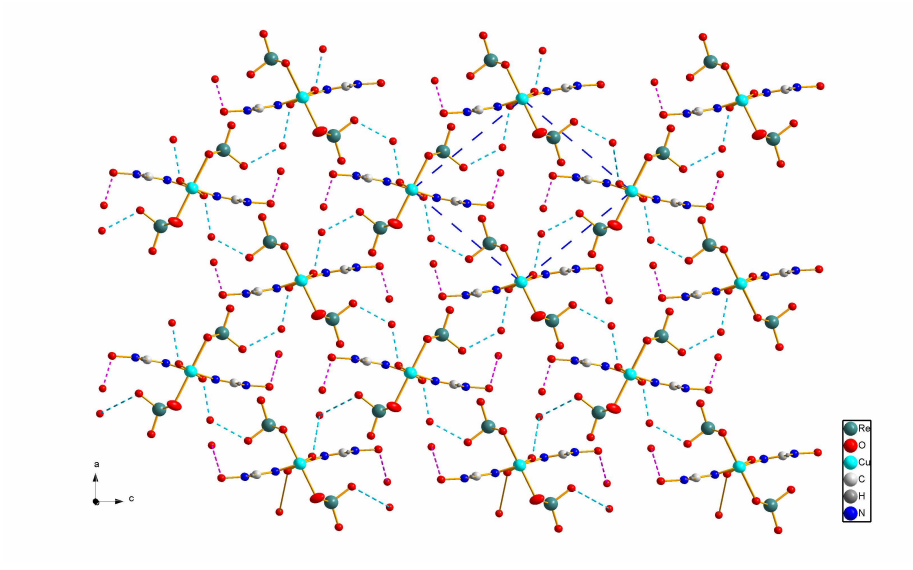

Figure 47 View of supramolecular interactions between adjacent chains. Projection on the (ac) plane.

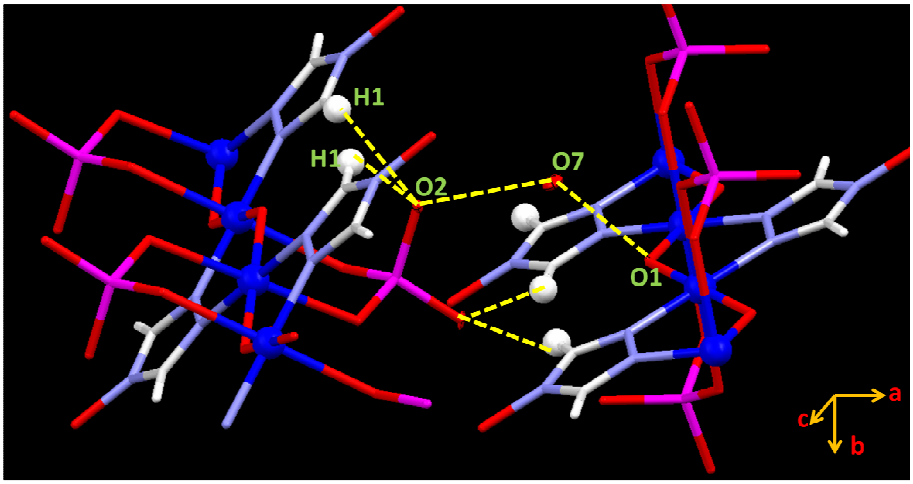

Figure 48 View showing selected hydrogen bonding network in **19.**

$[Zn(OHtrz)_2Cl](NO_3)$ (20)

Colorless crystals of **20** crystallizes in monoclinic (P2(1)/m) space group. Crystallographic data, obtained by Dr. C. Neuhausen (EPFL), are summarized in Table 24 and 27. Each zinc ion is surrounded by four nitrogen atoms originating from four ligands and two chloride atoms to form a ZnN_4Cl_2 coordination sphere. This octahedral repeats it self to form a 1D coordination polymer (Figure 49).

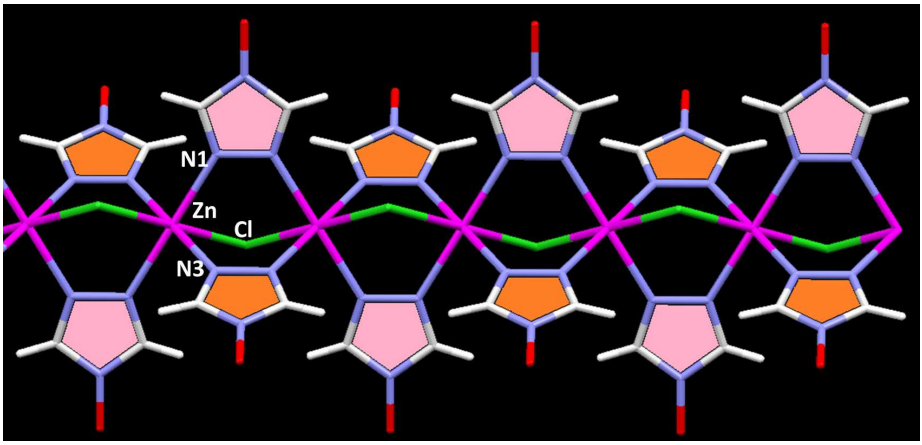

Figure 49 View of Zn(II) 1D coordination polymer formed by triple bridges.

Zn-N distances are different for Zn-N1 = 2.128 Å whereas Zn-N3 = 2.149 Å. These distance are higher than those observed for Cu-N = 1.996(8) Å found in **19** but lower than those observed for Cd-N= 2.343 Å (in $[Cd(HGlytrz)(Glytrz)Cl]\cdot 2H_2O$[18], with HGlytrz = ethyl-4H-1,2,4-triazol-4-yl acetic acid and Glytrz its deprotonated form, chapter VI). The Zn-Cl = 2.477 Å is higher than the one found for Zn(trz)Cl (trz = 1,2,4-1H-triazole)[19] which is equal to 2.214(2) Å, and is lower than Cd-Cl = 2.616 Å found in 1D coordination polymer[18]. In the same time Zn-N distance in Zn(trz)Cl complex (2.006 Å)[19] is much lower then the one identified for

19. Thus the increase in M-N distance from Cu-N (in **19**) to Cd-N results in larger separation of M-M distance compared to Cu···Cu = 3.380 Å < Zn···Zn = 3.575 Å < Cd···Cd = 3.845 Å. Interestingly this trend is disrupted if we compare with the 1D CP of copper built from aminotriazole with Cu···N = 1.991 to 2.371 Å resulting in Cu···Cu = 3.902 Å which is larger than[18] the above series (see Chapter III). The doubly bridging triazole rings and bridging chlorides around zinc ions forms mutually perpendicular zig-zag planes. The neighbouring 1D chains are closely packed with Zn···Zn = 7.336 Å which is much smaller than the one found for Cu···Cu = 12.17 Å in **19**. It is useful to compare some of these parameters with topologically relevant analogue aminotriazole 1D system. In fact in Cu-4-amino-1,2,4-triazole[3, 12] chains, the mutually perpendicular triply bridged chains are intervened by neighbouring chains keeping an inter-chain Cu···Cu separation (along *c*-axis) of 13.223 Å. This is still larger in inter-chain distance of Cu···Cu = 16.63 Å in *a*-axis where interpenetration of chains is significant.

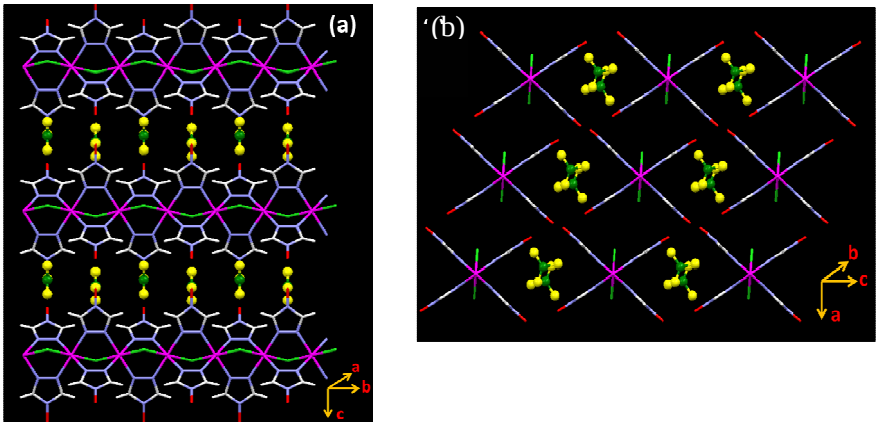

Figure 50 (a and b) Views along different axis to show positioning of planar anion, of **20**.

Many intra- and inter-chain H-bonding interactions involving the nitrate with

the hydroxy and –C-H groups of the triazole ring are found (Figure 50). Planar nitrate anion is aligned perpendicular to the bridging triazole plane and connects them establishing *intra-chain connectors* C1-H1···O4(N5) ···H1-C1 = 2.492 Å and C2-H2···O5(N5)···H2-C2 = 2.888 Å (Figure 50c1).

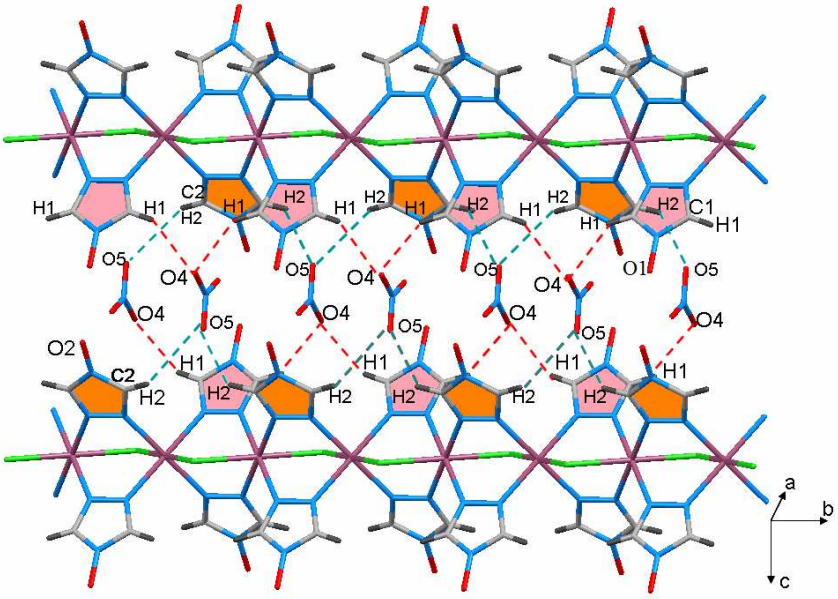

Figure 50c1 Intra-chain H-bonds interactions involving nitrate counteranion for **20**: a nitrate counteranion is found to link the –C-H groups of two triazole rings belonging to the same planes (depicted in pink and in orange).

Nitrate counteranion is found to link the –C-H of two triazole rings belonging to same planes (depicted in orange) at 2.888 Å, and the –C-H of two triazole rings belonging to pink planes at 2.492 Å. Indeed, two –C-H of a triazole, of the pink and orange planes are connected through H-bonding to two different oxygen atoms of the same nitrate group (Figure 50c1).

Neighboring 1D chains are connected directly by the intermediate of -OH group, with short contact of N2-O1···O2-N4 = 2.786 Å providing *inter-chain connectivity* (Figure 50c2).

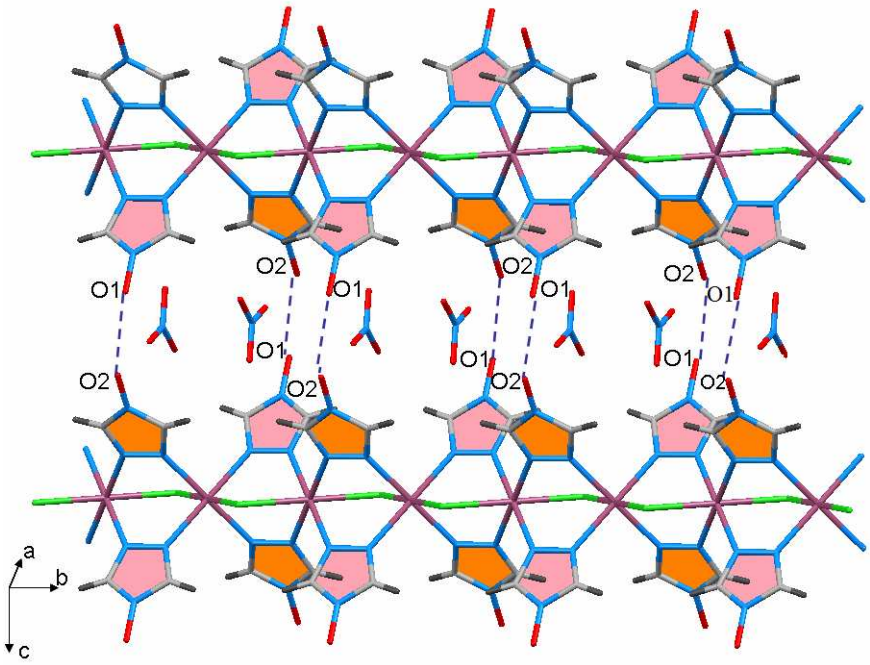

Figure 50c2 Direct inter-chain H-bonds interactions involving the hydroxy- groups, of two triazole rings belonging to different planes (depicted in orange and pink) of two different neighbor 1D chains.

These short interactions are strengthened by a set of interaction realized between neighboring 1D chains, connected *via nitrate anion* with short contact of N2-O1···O3-N5 = 2.652 Å (Figure 50c3). This is in contrary to the aminotriazole 1D CP, where nitrate anions are trapped in the groove created by the bridging triazole planes[12]. In the region around the nitrate anion, 'oxygen triangle' formed by O3, O1, O2, wherein O3 is from nitrate, O1 and O2 are from OH-triazole terminals of neighboring chains converge to form short contacts triangle with O2···O3 = 2.932 Å, O2···O1 = 2.786 Å, and O1···O3 = 2.652 Å (Figure 50c3).

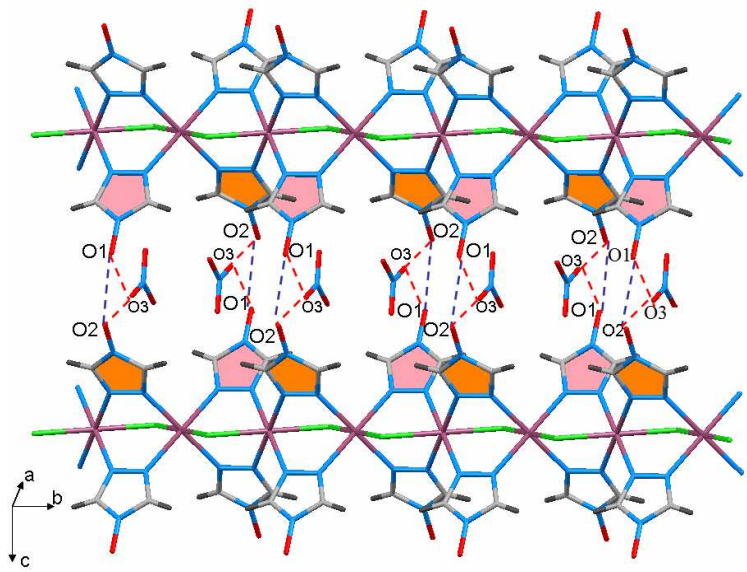

Figure 50c3 Projection of the crystal structure of **20** showing inter-molecular hydrogen-bonding chains involving nitrate counteranion and hydroxy- groups, of two triazole rings belonging to different planes.

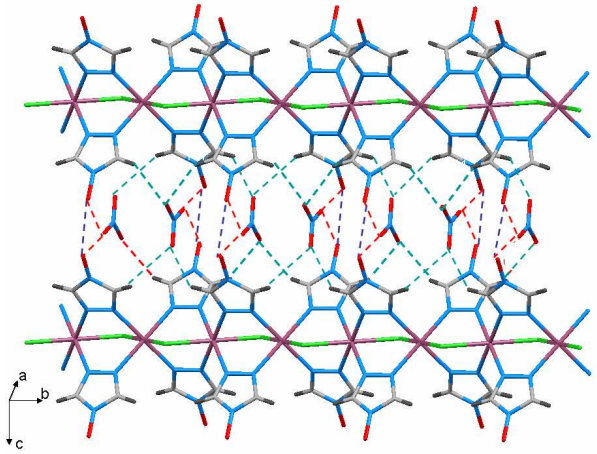

Figure 50c4 Projection of the crystal structure of **20** on the *(abc)* plane showing intra- and inter-molecular hydrogen-bonding chains involving nitrate counteranion and triazole rings.

Compared to **18** (Chapter III) the situation for **20** is exceptional because not all types of interactions could be identified. In **20** the nitrate counteranion didn't allows tripodal H-bonding starting from a unique oxygen atom. The

nitrate groups allow linking the OHtrz rings by their –C-H and hydroxy groups, which does rigidify the H-bonding network. The H-bonding network is reinforced by different hydrogen bonds between two different hydroxy-groups that belong to two different chains, -N2-O1···O2-N4- and by double hydrogen bonding –C-H···O···H-C-. However, the hydrogen bonding network can be overall considered of moderate strength because hydrogen bonds range from 2.492 Å to 2.932 Å with bond angles varying from 75° to 170°, which deviates from linearity.

It was difficult to locate the hydrogen atoms in structure refinement on the hydroxyl terminal of the ligand. The N2-O1 distance is 1.381 Å which lower than the corresponding distance in **19**. Interestingly, this N-O distance is slightly different in ligand belonging to different planes (N4-O2 = 1.370 Å). The distance between zinc ions along the c-axis is Zn…Zn = 11.312 Å which is equal to the crystallographic *c*-axis. This large distance is created due to the anion plane sandwiched between 1D chains. On the other hand distance between Zn…Zn = 7.336 Å which is considerable lower in *a*-axis which is again equal to the crystallographic *a*-axis and the distance between Zn…Zn = 3.575 which is half the value of the crystallographic *b*-axis.

Thermal spin-crossover properties

UV-Vis Diffuse reflectance spectroscopy

Preliminary indications of SCO occurrence were obtained by a clear thermochromic response on quench cooling of the materials to $N_{2(l)}$. Indeed, white powders of **LOH-ClO$_4$** and **LOH-TRF** show reversible colors change to pink, except for **LOH-BF$_4$** which did not change its pale rose color by cooling in the liquid N_2. The white color of these complexes, is due to the presence of the spin-allowed lowest energy d-d transition, $^5T_{2g} \rightarrow {}^5E_g$, for the HS sites in the near infrared region (~ 12000 cm^{-1})[12, 20, 21]. Two supplementary bands, of less absorption intensity, corresponding to the $^1A_{1g} \rightarrow {}^1T_{1g}$ and $^1A_{1g} \rightarrow {}^1T_{2g}$ d-d transitions of LS Fe^{II} sites are observed at ~ 18300 cm^{-1} and ~ 28300 cm^{-1}, respectively suggesting that some proportion of Fe^{II} may be in the LS state at room temperature (Figure 51). The pink powder of **LOH-NO$_3$** show reversible colors change to white, on warming. The pink color of **LOH-NO$_3$**, is due to the presence to the $^1A_{1g} \rightarrow {}^1T_{1g}$ and $^1A_{1g} \rightarrow {}^1T_{2g}$ d-d transitions of LS Fe^{II} sites, observed at ~ 18300 cm^{-1} and ~ 27300 cm^{-1}, respectively suggesting that the Fe^{II} is in the LS state at room temperature.

The ligand field strengths for the HS and the LS state, given by equations $10D_q^{HS} = E(^5E) - E(^5T_2)$ and $10D_q^{LS} = E(^1T) - E(^1A_1) + (E(^1T_2) – E(^1T_1))/4$,[20, 21] allowed us to estimate $10D_q^{HS}$ and $10D_q^{LS}$ to be approximately 12000 cm^{-1} (for **LOH-BF$_4$**, **LOH-ClO$_4$** and **LOH-TRF**) and 25375 cm^{-1}, for **LOH-NO$_3$** complex. These values are characteristic for SCO complexes[20, 21]. Presence of LS state at room temperature has been confirmed by ^{57}Fe Mössbauer spectroscopy, for all materials except **LOH-TRF**.

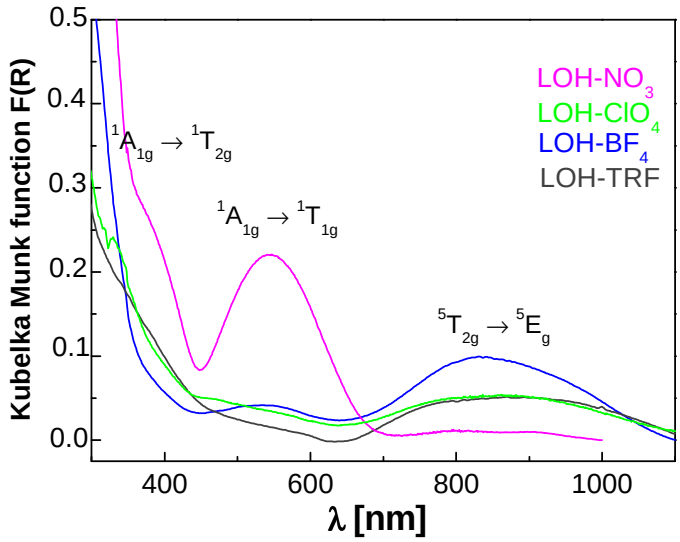

Figure 51 Kubelka-Munk function, F(R) of **LOH-NO_3**, **LOH-BF_4**, **LOH-ClO_4** and **LOH-TRF** showing the d–d transitions at room temperature.

^{57}Fe Mössbauer spectroscopy

^{57}Fe Mössbauer spectroscopy further reveals variation of temperature dependent population of spin states in **LOH-NO$_3$**, **LOH-BF$_4$**, **LOH-ClO$_4$** and **LOH-TRF**, over the T range (77-300 K). Mössbauer spectra are shown in Figure 52 and hyperfine parameters are summarized in Table 28.

In **LOH-NO$_3$**, two quadrupole doublets of different resonance area fractions are identified at 77 K. The major quadrupole doublet (90 %) with isomer shift δ = 0.49(1) mm/s and quadrupole splitting, ΔE_Q = 0.19(1) mm/s corresponds to the LS state of Fe^{II}. The presence of a LS quadrupole splitting stems from a lattice contribution to the electric field gradient and therefore reveals a distorted character for the LS octahedron as expected for a constrained 1D chain with a rigid linkage[22]. Another doublet, corresponding to HS Fe^{II} ions (10 %), with δ = 1.21(2) mm/s and ΔE_Q = 3.37(1) mm/s is identified at 77 K. The compound remains in the LS state on warming up to room temperature, e.g. at 300 K δ^{HS} = 1.06(1) mm·s^{-1} and $\Delta E_Q{}^{HS}$= 2.76(1) mm·s^{-1} (10 %), LS and δ^{LS} = 0.41(1) mm·s^{-1} and $\Delta E_Q{}^{LS}$= 0.19(2) mm·s^{-1} (90 %). The temperature variation of δ^{HS}, of **LOH-NO$_3$**, reveals a slight decrease on warming which is attributed to the second order Doppler shift. δ and ΔE_Q of both LS and HS species are typical of an $Fe^{II}N_6$ chain compound in which iron centers are bonded by triple *N*1,*N*2-triazole bridges[3]. Since the **LOH-NO$_3$** complex remains predominantly LS at room temperature, this sample may present a ST above r.t.. However because of expected dehydration and a possible oxidation of the sample, ^{57}Fe Mössbauer data were not recorded above room temperature.

Contrary to **LOH-NO$_3$,** compound **LOH-BF$_4$** present only 20 % of LS ions at 77 K (Table 28). The major quadrupole doublet (80 %) with isomer shift δ = 1.19(1) mm/s and quadrupole splitting, ΔE_Q = 3.34(1) mm/s corresponds to

the HS state of Fe^{II}. The compound remains preponderantly in the HS state on warming up to room temperature, e.g. at 300 K, δ^{HS} = 1.06(1) mm·s^{-1} and ΔE_Q^{HS}= 2.80(1) mm·s^{-1} (80 %) and δ^{LS} = 0.41(1) mm·s^{-1} and ΔE_Q^{LS}= 0.38(1) mm·s^{-1} (20%). The temperature variation of δ^{HS}, of **LOH-BF$_4$**, reveals a slight decrease on warming which is attributed to the second order Doppler shift.

In the case of **LOH-ClO$_4$** the situation is different. At 77 K, the spectrum consists of two quadrupole doublets of different resonance area fractions. The major quadrupole doublet with isomer shift δ^{HS} = 1.20(1) mm/s and quadrupole splitting, ΔE_Q^{LS} = 3.36(1) mm/s correspond to the HS state of Fe^{II}. Another doublet, corresponding to LS Fe^{II} ions of weaker population (28 %), with parameters (δ^{LS} = 0.55(1) mm/s and ΔE_Q^{HS} = 0.26(1) mm/s) confirms a mixed spin state at 77 K. Upon warming, the intensity of the HS doublet slowly increases to 88 % at 273 K, after which it increases considerably to 92 % at 300 K, confirming an incomplete thermally induced LS → HS conversion for a single Fe^{II} site. The presence of LS ions at room temperature could be related to crystal defects or end of chains.

For **LOH-TRF**, only 19 % of LS ions switch to the HS state on warming, from 77 K to r.t., confirming an incomplete thermally induced LS → HS conversion (Table 28). δ and ΔE_Q of both LS and HS species are typical of an $Fe^{II}N_6$ chain compound in which iron centers are bonded by triple *N*1,*N*2-triazole bridges[3, 23]

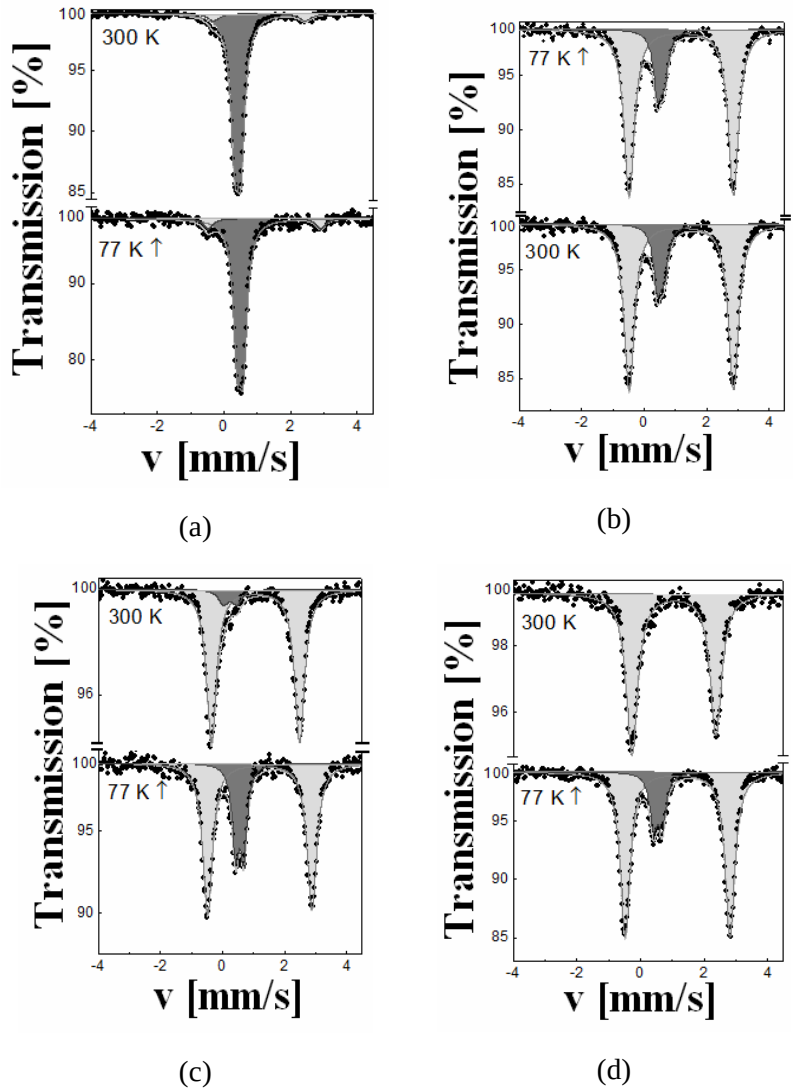

Figure 52 ^{57}Fe Mössbauer spectra for (a) **LOH-NO_3**, (b) **LOH-BF_4**, (c) **LOH-ClO_4** and (d) **LOH-TRF**.

Table 28 Comparison of ^{57}Fe Mössbauer parameters for **LOH-NO_3**, **LOH-BF_4**, **LOH-ClO_4** and **LOH-TRF**.

LOH-NO_3

T [K]	*δ* [mm/s]	*ΔE$_Q$* [mm/s]	*Γ/2* [mm/s]	Relative Area [%]	Sites
77(1)	1.21(2)	3.37(1)	0.17(1)	10	HS
	0.49(1)	0.19(1)	0.14(1)	90	LS
300(1)	1.06(1)	2.76(1)	0.22(1)	10	HS
	0.41(1)	0.19(2)	0.14(1)	90	LS
LOH-BF_4					
77(1)	1.19(1)	3.34(1)	0.20(1)	80	HS
	0.53(1)	0.22(2)	0.15(1)	20	LS
300(1)	1.06(1)	2.80(1)	0.24(1)	80	HS
	0.41(1)	0.38(1)	0.24(1)	20	LS
LOH-ClO_4					
77(1)	1.20(1)	3.36(1)	0.19(1)	72	HS
	0.55(1)	0.26(1)	0.13(1)	28	LS
110(1) ↑	1.18(1)	3.34(2)	0.19(1)	76	HS
	0.54(1)	0.26(1)	0.14(1)	24	LS
273(1) ↑	1.08(1)	3.00(1)	0.18(1)	88	HS
	0.25(1)	0.36(1)	0.22(1)	12	LS
300(1)	1.06(1)	2.84(1)	0.19(1)	92	HS
	0.24(1)	0.42(1)	0.20 (1)	8	LS
93(1) ↓	1.18(1)	3.34(2)	0.18(1)	76	HS
	0.54(1)	0.27(1)	0.14(1)	24	LS

LOH-TRF					
77(1)	1.17(1) 0.55(1)	3.30(1) 0.27(1)	0.18(1) 0.14(1)	81 19	HS LS
300(1)	1.06(1)	2.95(1)	0.22(1)	100	HS

δ: isomer shift (with respect to α-Fe at 300 K); ΔE_Q: quadrupole splitting; Γ/2: half width at half maximum; A_{HS}: Area of HS doublet; A_{tot}: total area. *Fixed parameter. The arrows indicate the warming (↑) and cooling (↓) modes.

Discussion

In this work, we aimed to test the influence of the replacement of a NH_2- by hydroxyl group in the 1D $[Fe(OH\text{-}trz)_3](Anion)_2 \cdot H_2O$ system, where (Anion = NO_3^-, BF_4^-, ClO_4^-, $CF_3SO_3^-$ and *n* stands for the number of non-coordinated water molecules) which have been investigated herein.

Relatively small anions, such as NO_3^- or BF_4^- , allow observation of spin transitions above room temperature, e.g. whereas bulkier anions (e.g. ClO_4^-, $CF_3SO_3^-$) afford SCO at much lower temperatures. A somehow trend between the transition temperature $T_{1/2}$ and the anion volume for $[Fe(OH\text{-}trz)_3]Anion \cdot nH_2O$ is difficult to be estimated at this stage, because of the incomplete magnetic data due to the sensitivity of the system to Fe(II) oxidation. Nevertheless the % of the HS fraction of HS Fe(II) ions decreases when the anion volume decreases. Since the molecular system is identical, to the 4-amino-1,2,4-triazole one, a decrease of the switching temperatures with the increasing of anion volume is expected.

As deduced by comparison of the X-Ray powder diffraction patterns recorded at 300 K for all compounds (Figure 42), the insertion of monovalent anions, in this series, affect the structural organization of the chains. This observation validates complementary spectroscopic

comparisons. Indeed, Mössbauer spectroscopy confirms that the inserted monovalent anion, the local symmetry of the Fe octahedra is modified as deduced by the large value of the quadrupole splitting in the HS state.

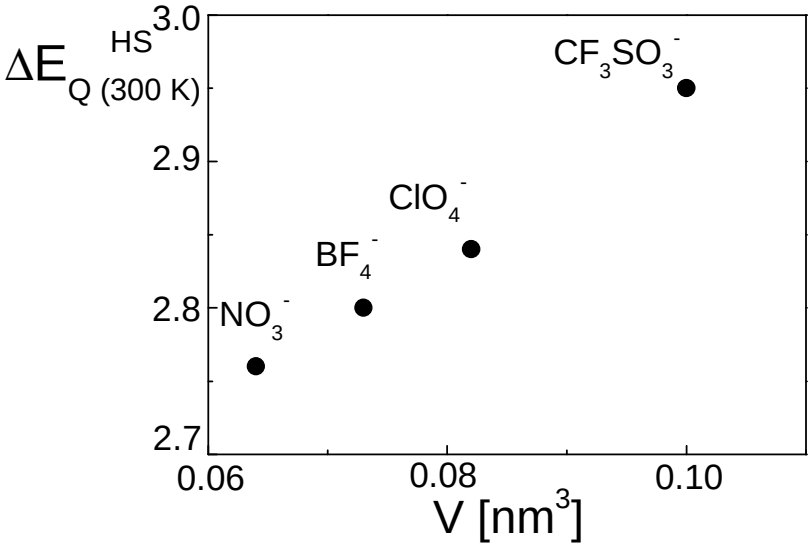

Figure 53 Variation of the quadrupole splitting at 300 K *vs.* the anion volume for $[Fe(OH\text{-}trz)_3]^{2+}$ systems. The volume of the $CF_3SO_3^-$ was fixed as 0.1 nm^3.

For lower size anion, a decrease of ΔE_Q^{HS}(300 K) is however noted (Figure 53) thus indicating an increase of the local distortion around the metallic ion. Indeed, it is worth noting that the electric field gradient contribution of the lattice is usually of opposite sign as compared to that of the valence electrons.[24] This increase of local distortion indicates that chains are much closer in the case of lower size anions than for larger size anions, as observed for NH_2trz systems also[3]. This geometric feature is also seen on the evolution of the isomer shift for the LS state, δ^{LS}, function of the volume of counteranion (Table 28). Indeed, when the anion volume decreases, δ_{LS}^{78K} decreases. Because the isomer shift is of opposite sign to the electronic density seen by the iron atoms, the covalency degree of the Fe-N bond increases, which is consistent with the chains that are moved closer. As seen

in Chapter I, we assume that when the anion volume increases the chain spacing increases[3].

In the absence of suitable single crystals for these Fe^{II} compounds, and to better understand the impact of the supramolecular organization of these materials, the crystal structure of two model compounds including a monovalent anion of the present series were solved: $[Cu(OH\text{-}trz)(ReO_4)OH]\cdot 2H_2O$ (**19**) and $[Zn(OHtrz)_2Cl](NO_3)$ (**20**).

The structures are stabilized by a dense hydrogen bonding network, involving the counter-anion, ReO_4^- and Cl^-, located in the third coordination sphere and the hydroxyl group of the 1,2,4-triazole ligand (Figures 47, 48). The 1D chains, of **19** (eg. in *b*-direction both above and below the plane) is intervened by neighboring 1D chains thus increasing the distance between copper centers to 12.17 Å. This is much larger than the one found in 8.58 Å in 1D Cd-CP[18]. This observation demonstrates a lesser compactness of packing despite having smaller substituent on N4 position, the diagonal distance between copper centers of intervened chain being 9.49 Å. This dilation in compactness is due to larger anion which subside the doubly or triply bridging possibility of OH-triazole with copper ions. These results might bring insight to the cooperativity modulation in substituted triazole iron(II) spin crossover systems analogues.

In the case of $[Zn(OHtrz)_2Cl](NO_3)$, the NO_3^- anion is linked to both hydroxyl group to two 1D chains through the anion setting up interchain interactions. Neighbouring 1D chains are connected via nitrate anion with short contact of (2.652 Å) forming inter-chain connectivity. Such supramolecular interactions may well play an effective role in the propagation of elastic cooperative interactions within Fe(II) systems, switching above room temperature, resulting in the observation of a LS Fe(II) ions at 300 K (for **LOH-NO_3**). However, we cannot differentiate the influence of H-bonding from the size effect of the anions on the SCO

behavior of the Fe derivatives because the selected nitrate anion could favor extended H-bonding networks as found in the crystal structure of **20**.

Supramolecular interactions are thus assumed to strengthen elastic interactions between switching centers in **20**. Such interactions may not only be facilitated by the planar geometry of the nitrate anion but also by its 'tripod' character. In particular the role of the nitrate anion that acts as a fourth supramolecular bridge in addition to the triple 1,2,4-triazole bridge between metallic centers was pointed out. Worthwhile to note that the role of hydrogen bonds to promote cooperative SCO systems has also recently been recognized in SCO research for an iron(II) mononuclear material presenting a wide hysteresis loop below room temperature.[25]

Notes and references

[1] O. Kahn, J. Krober, C. Jay. *Adv. Mater*. **1992**, *4*(11), 718-728.

[2] Y. Garcia, V. Ksenofontov, P. Gutlich. *Hyp. Int.* **2002**, *139*(1-4), 543-551.

[3] M. M. Dîrtu, A. Rotaru, D. Gillard, J. Linares, E. Codjovi, B. Tinant, Y. Garcia. *Inorg. Chem.* **2009**, *48*(16), 7838-7852.

[4] Bayer, H. O., Cook, R. S., and Von Meyer, W. C. Fungicidal use of a 1.2,4-triazole nickel salt complex. [3,821,376], 1-12. 1974. US. Ref Type: Patent

[5] A. D. Naik, J. Marchand-Brynaert, Y. Garcia. *Synthesis* **2008**, *1*, 149-154.

[6] J. G. Haasnoot, G. Vos, W. L. Groeneveld. *Zeitschrift fur Naturforschung Section B-A Journal of Chemical Sciences* **1977**, *32*, 421.

[7] V. P. Sinditskii, V. I. Sokol, A. E. Fogelzang, M. D. Dutov, V. V. Serushkin, M. A. Poraikoshits, B. S. Svetlov. *Russ. J. Inorg. Chem.* **1987**, *32*(8), 1950-1955.

[8] J. G. Haasnoot, G. Vos, W. L. Groeneveld. *Zeitschrift fur Naturforschung Section B-A Journal of Chemical Sciences* **1977**, *32*, 421.

[9] V. P. Sinditskii, A. E. Fogelzang, M. D. Dutov, V. I. Sokol, V. V. Serushkin, B. S. Svetlov, M. A. Poraikoshits. *Russ. J. Inorg. Chem.* **1987**, *32*(8), 1944-1949.

[10] J. G. Haasnoot, G. Vos, W. L. Groeneveld. *Zeitschrift fur Naturforschung Section B-A Journal of Chemical Sciences* **1977**, *32*(12), 1421-1430.

[11] K. Nakamoto. *Infrared and Raman Spectra of Inorganic and Coordination Compounds : Applications in Coordination, Organometallic, and Bioinorganic Chemistry*, **1997**.

[12] M. M. Dîrtu, C. Neuhausen, A. D. Naik, A. Rotaru, L. Spinu, Y. Garcia. *Inorg. Chem.* **2010**, *49*(12), 5723-5736.

[13] M. B. Varfolomeev, A. N. Zemenkova, V. N. Chrustalev, J. Struìkov, H. J. Lunk, B. Ziemer. *Journal of Alloys and Compounds* **1994**, *215*(1ГÇô2), 339-343.

[14] S. Khranenko, E. Shusharina, S. Gromilov, A. Smolentsev. *Journal of Structural Chemistry* **2009**, *50*(6), 1201-1203.

[15] E. Shusharina, S. Khranenko, S. Gromilov. *Journal of Structural Chemistry* **2011**, *52*(1), 203-205.

[16] B. P. Aryal, P. Brugarolas, C. He. *J Biol Inorg Chem* **2012**, *17*(1), 97-106.

[17] R. Cao, B. D. McCarthy, S. J. Lippard. *Inorg. Chem.* **2011**, *50*(19), 9499-9507.
[18] M. M. Dîrtu, C. Neuhausen, A. D. Naik, A. Leonard, F. Robert, J. Marchand-Brynaert, B. L. Su, Y. Garcia. *Crystal Growth & Design* **2011**, *11*(4), 1375-1384.
[19] J. Kröber, I. Bkouche-Waksman, C. Pascard, M. Thomann, O. Kahn. *Inorg. Chim. Acta* **1995**, *230*(1-2), 159-163.
[20] P. Gütlich, A. Hauser, H. Spiering. *Angew. Chem. Int. Ed.* **1994**, *33*(20), 2024-2054.
[21] P. Gütlich, J. Jung, H. A. Goodwin. In: (Eds.: E. Coronado, P. Delhaès, D. Gatteschi, and J. S. Miller), *Molecular Magnetism: From Molecular Assemblies to the Devices*, **1996**, p. 327.
[22] M. M. Dîrtu, Y. Garcia, M. Nica, A. Rotarii, J. Linares, F. Varret. *Polyhedron* **2007**, *26*(9-11), 2259-2263.
[23] M. M. Dîrtu, C. Neuhausen, A. D. Naik, A. Rotaru, L. Spinu, Y. Garcia. *Inorg. Chem.* **2010**, *49*(12), 5723-5736.
[24] R. Ingalls. *Phys. Rev.* **1964**, *133A*, 787.
[25] B. Weber, W. Bauer, J. Obel. *Angew. Chem. Int. Ed.* **2008**, *47*, 10098-10101.

Chapter V: Thermo-switchable spin crossover iron(II)- phtalimido–propyl based coordination polymers

In the previous chapters, we have shown that nature and geometry of the ligand substituent and the counteranion may be considered to properly predict magnetic properties.

In this chapter, we thus propose a designing of a new precursor for SCO, a new module for 1D CP, 4-(3'-N-phtalimido-propyl)-1,2,4-triazole (phtptrz), where a bulky substituent is attached to *N4* of 1,2,4-triazole via a multiple carbon spacer. This aromatic group, although bulkier, is a potential promoter of supramolecular interactions due to π–π stacking and H-bonding interactions involving carbonyl groups. Although bulky substituent on the triazole ring with multiple carbon spacer of the ligand scaffold is not favorable for cooperative SCO, as trinuclear species formation can be expected[1]. Influence of modifying anions geometry (spherical I^-, trigonal NO_3^-, tetrahedral ReO_4^-, ClO_4^-, BF_4^-, monocapped trigonal prism TaF_7^{2-}) and charge will be evidenced in the series $[Fe(phtptrz)_3](A)_{1\ or\ 2}\cdot$Solvent (Solvent = H_2O or CH_3OH) whose spin switching properties will be analyzed (Chapter V.1 and Chapter V.2). Supramolecular organization is always better visualized in the crystal structure of any system. As with iron systems it is difficult to grow single crystals, this complementary information about structural organization is evidenced in the crystal structure of copper complexes. Thus potential promoter of supramolecular interactions due to π–π stacking and H-bonding interactions involving carbonyl groups, **phtptrz** was used to design two new molecular building, $[Cu_3(phtptrz)_{10}(H_2O)_2](SiF_6)_3\cdot 44H_2O$ and $[Cu_3(phtptrz)_8(H_2O)_4]$

$(ZrF_6)_3 \cdot 19H_2O$, for which the crystal structures packing are described in sections V.3.

V.1 Weak cooperativity in selected iron(II) 1D coordination polymers, based on phtalimido–propyl-1,2,4-triazole core*

Introduction remarks

Abruptness, completeness and hysteresis width/shape of transition curves are key elements to probe strength of cooperative interactions in SCO complexes which can be influenced by ligand design, anion geometry and charge, crystal defects, solvent occupancy etc.[2]. Self-assembled coordination polymers (CPs) represent a family of compounds where precisely organised molecular building blocks generate a long range cooperative phenomenon that has effective means of propagation through rigid covalent bonding and flexible supramolecular interactions[3]. Although this situation is usually set for small ligand modules, larger molecular fragments such as dendrimers[4] or extended alkyl chains[5] often show promising SCO profiles without cooperativity loss thus reviewing the selection criteria of ligand topology. We introduce in this context a new module for CPs: **phtptrz** (Figure 54). Thus in the first part of the chapter we analyse the influence of modifying anions geometry (tetrahedral ReO_4^- and monocapped trigonal prism TaF_7^{2-}) and charge (monovalent and bivalent), evidenced in the series of $[Fe(phtptrz)_3](ReO_4)_2 \cdot CH_3OH$ (**21- phtptrz-ReO_4**)

*Adapted from : M. M. Dîrtu, D. Gillard, A. Naik, A. Rotaru, Y. Garcia *Hyperfine Interact.* **2012**, 1-5.

and $[Fe(phtptrz)_3]TaF_7 \cdot 6H_2O$ (**22-phtptrz-TaF$_7$**) whose spin switching properties are discussed herein.

Results

Synthesis and general characterization

The **phtptrz** molecule was prepared according to ref. [6], Figure 54.

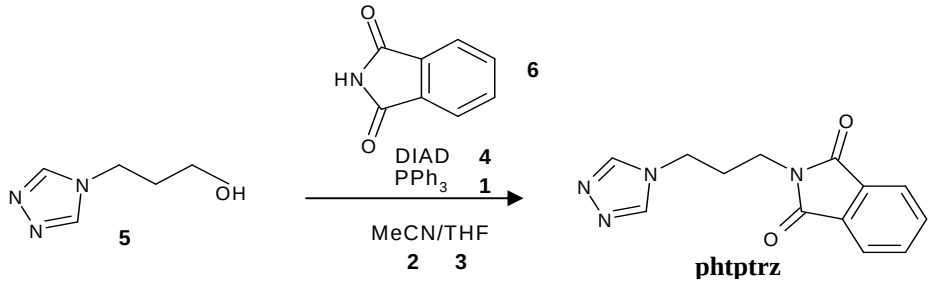

Figure 54 Synthetic protocol used for 4-(3'-N-phtalimido-propyl)-1,2,4-triazole (**phtptrz**) (**1** – Triphenylphosphine; **2** – Acetonitrile; **3** – Tetrahydrofuran; **4** - Diisopropyl azodicarboxylate; **5** - 4-(3'-hydroxy-propyl)-1,2,4-triazole[6]; **6** – Phthalimide)

Phtptrz was obtained in good yield (64 %) as off white crystalline blocks. Complexes were prepared as off white powders by reacting **phtptrz** to $[Fe(H_2O)_6]^{2+}$ including a suitable anion (ReO_4^-, TaF_7^{-2}, Figure 55) in a 3:1 ratio in $MeOH/H_2O$ following ref. [7]. These complexes were successfully characterized by elemental analysis, TGA-DTA analyses, atomic absorption (AAS), X-Ray powder diffraction, IR, SEM, DSC, SQUID magnetometry and ^{57}Fe Mössbauer spectroscopy. The thermogravimetric and elemental analyses reveal the presence of guest water molecules, affording the following general formula $[Fe(phtptrz)_3]$ $(ReO_4)_2 \cdot CH_3OH$ (**21-phtptrz-ReO$_4$**) and $[Fe(phtptrz)_3]TaF_7 \cdot 6H_2O$ (**22-phtptrz-TaF$_7$**).

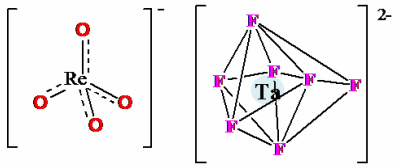

Figure 55 Variation of anion geometry and charge, used to building $[Fe(phtptrz)_3]^{2+}$ systems.

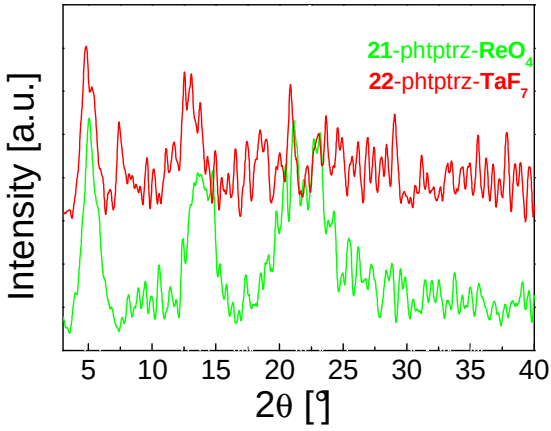

Figure 56 X-Ray powder diffraction patterns at 293 K for **21-phtptrz-ReO_4** and **22-phtptrz-TaF_7**.

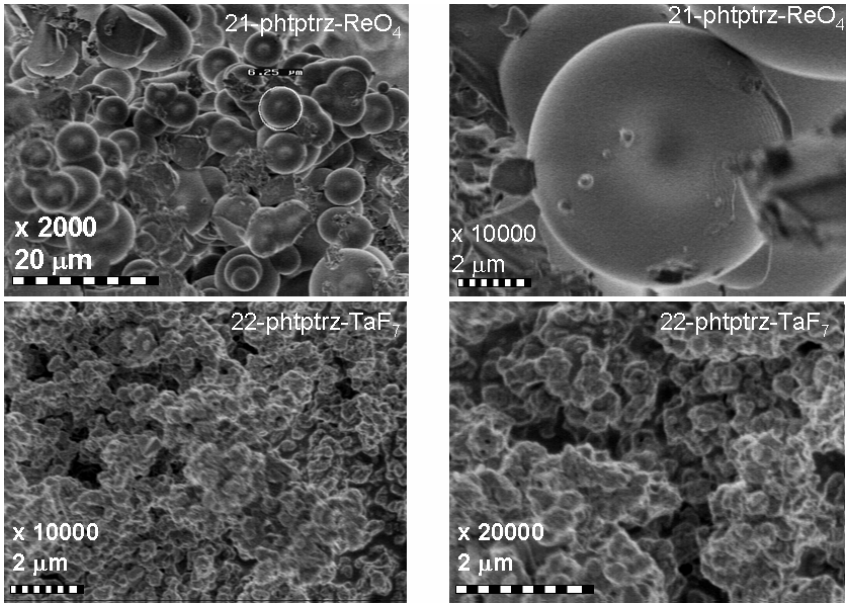

Figure 57 SEM images of microcrystalline particles of **21-phtptrz-ReO_4** and **22-phtptrz-TaF_7** at 293 K.

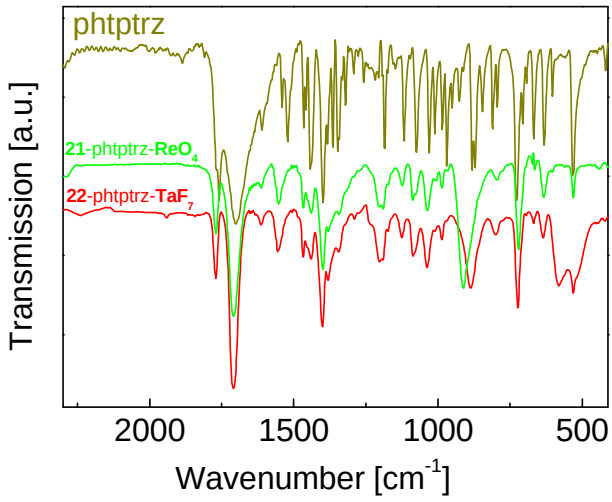

Figure 58 IR spectra of the ligand **phtptrz** and of complexes **21-phtptrz-ReO$_4$** and **22-phtptrz-TaF$_7$**, over the range 400-2100 cm^{-1}.

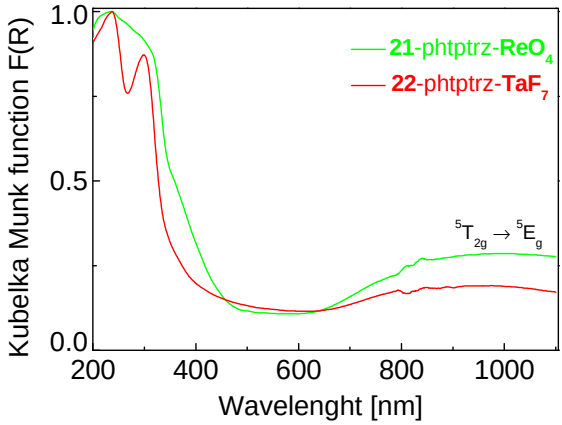

Figure 59 UV-Vis diffuse reflectance spectra of **21-phtptrz-ReO$_4$** and **22-phtptrz-TaF$_7$** showing d–d transitions at r.t..

21-phtptrz-ReO$_4$ and **22-phtptrz-TaF$_7$** present a slightly crystalline character as revealed from X-ray powder diffraction (XRPD) patterns (Figure 56). This result is also illustrated by the SEM analysis with nearly spherical aggregates granules for **22-phtptrz-TaF$_7$**. Contrary to this compound, **21-phtptrz-ReO$_4$** presents astonishing spherical granules with a smooth surface (Figure 57).

FT-IR analyses were performed to ascertain the coordination mode of iron to the ligand and the presence of the counter-anions in the crystal lattice (Figure 58). Two sharp IR bands at 3109 (m) and 2536 (m) cm^{-1} of **phtptrz**, are assigned to the νCH_2 modes.[8] The -C=O group of phtalimido shows two stretching vibrations at 1700 (s) and 1770(m) which are shifted to 1711 and 1771 cm^{-1} in **21-phtptrz-ReO_4** confirming the involvement of –C=O group in hydrogen bond interactions[9]. For **phtptrz** the band assigned to ring torsion of triazole at ν = 633(m) cm^{-1}, the $\nu_{C=N}$ stretching vibration at 1521, ν_{N-N} = 970(m) cm^{-1}, are all shifted upon complexation in **21-phtptrz-ReO_4** to 633 cm^{-1}, $\nu_{C=N}$ = 1553 cm^{-1}, and ν_{N-N} = 983 cm^{-1}(w), respectively. These values confirm the coordination of the iron to the 1,2,4-triazole ring[10, 11]. Indeed, the characteristic bands of the ligand are not only present in the spectra of the complexes but also are shifted towards larger wave numbers, from 3 to 15 cm^{-1} respectively[12, 13].Presence of the mono- and bivalent counter-anion is also confirmed by *IR* (cm^{-1}) $\upsilon_{(Re-O)}$ ~ 1398; 910 (s), (**21-phtptrz-ReO_4**); $\upsilon_{(Ta-F)}$ ~ 1400; 530 (s), (**22-phtptrz-TaF_7**).[9]

^{57}Fe Mössbauer spectroscopy confirms for **21-phtptrz-ReO_4** and **22-phtptrz-TaF_7**, the presence of one $Fe^{II}N_6$ site, and excludes any oxidation product of iron. These spectroscopic data supports a linear chain structure with Fe^{II} ions linked by triple *N*1,*N*2-1,2,4-triazole bridges[7, 14].

Preliminary indications of SCO occurrence were obtained by a clear thermochromic response on quench cooling of the materials to $N_{2(l)}$. Indeed, off white powder of **21-phtptrz-ReO_4** show reversible colors change to pink, contrary to **22-phtptrz-TaF_7**.

The off white color of all complexes, is due to the presence of the spin-allowed lowest energy d-d transition, $^5T_{2g} \rightarrow {}^5E_g$, for the HS sites in the near infrared region (~ 10500 cm^{-1})[15, 16]. The ligand field strengths for the HS, given by equations $10D_q^{HS} = E(^5E) - E(^5T_2)$ allowed us to estimate $10D_q^{HS}$ to be approximately 10500 cm^{-1}. These values are characteristic for SCO

complexes[15, 16]. No other bands, characteristic of d-d transition, are identified on the UV-VIS spectra (Figure 59). The absence of LS state at room temperature has been confirmed by ^{57}Fe Mössbauer spectroscopy (*vide infra*).

Thermal spin-crossover properties

SQUID magnetometry

Variable temperature magnetic susceptibility measurements for **21-phtptrz-ReO$_4$** and **22-phtptrz-TaF$_7$** were recorded over the temperature range 300 – 4 K (Figure 60), by Dr. A. Rotaru (USV, Romania).

These SQUID measurements reveal a very smooth incomplete spin conversion for **21-phtptrz-ReO$_4$** with transition temperatures $T_{1/2}$ ~ 163 K and 137 K, respectively.

For **21-phtptrz-ReO$_4$** the r. t. $\chi_M T$ value of 3.42 cm^3 mol^{-1} K corresponds to high-spin (HS) Fe^{II} species. When cooled, this value gradually decreases to 2.06 cm^3 mol^{-1} K around 72 K after which the inflection becomes more gradual until 30 K, revealing an incomplete spin conversion. The subsequent drop of $\chi_M T$ at lower temperatures is attributed to zero-field splitting (ZFS) of remaining HS Fe^{II} species. This type of spin conversion is commonly observed for Fe^{II} complexes having a voluminous substituent on the *N4* position of the triazole ring[17].

In contrast, the magnetic curve of **22-phtptrz-TaF$_7$** does not apparently reflect any SCO process. As the temperature is lowered, the $\chi_M T$ value smoothly decreases until 50 K and drops rapidly below this temperature reaching a minimum at 4 K. Such a magnetic curve indicates very weak antiferromagnetic (AF) interactions between HS Fe^{II} ions.

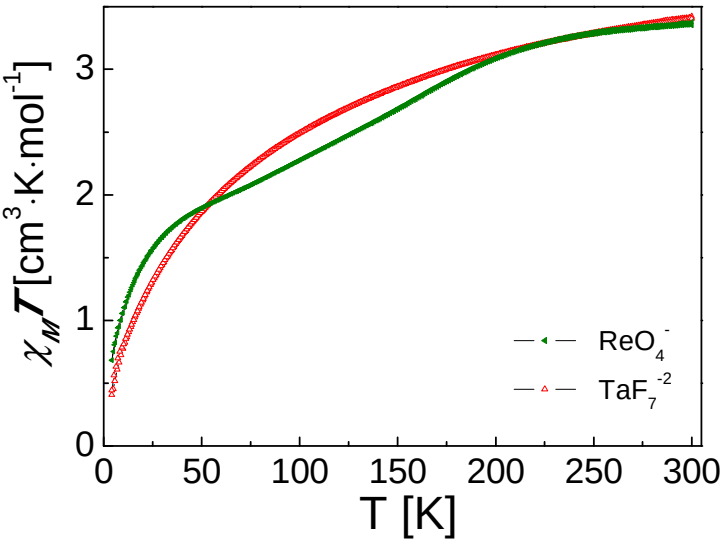

Figure 60 Variable temperatures magnetic susceptibility measurements for **21-phtptrz-ReO$_4$** and **22-phtptrz-TaF$_7$,** recorded over the temperature range 300 – 4 K.

Since the inverse susceptibility plot is linear as a function of temperature (Figure 61 and 62), the Curie-Weiss law was used to fit the magnetic data[18]:

$$\chi = \frac{Ng^2\mu_B^2 S(S+1)}{3k_B(T-\theta)} \text{ and } \theta = \frac{zJS(S+1)}{3k_B}$$

The used parameters are Boltzmann constant, $k_B = 1.38 \cdot 10^{-16}$ erg K^{-1}, Bohr magneton, $\mu_B = 9.27 \cdot 10^{-21}$ erg Oe^{-1}, Avogadro constant, $N = 6.023 \cdot 10^{23}$ mol^{-1}, S = 2.

The best fit of the magnetic data with a Curie-Weiss law afforded a Weiss temperature θ = -55 K, g = 2.30(5) and by considering the number of nearest neighbors atoms (z = 2)[19], J/k_B = -13(1) K was derived. The absence of maximum in the χ_M *vs. T.* plot confirms the weak AF coupling nature in **22-phtptrz-TaF$_7$**. The slight discrepancy, between recorded data and magnetic fitting suggest the presence of a magnetic anomaly which will be confirmed by ^{57}Fe Mössbauer spectroscopy (see next section).

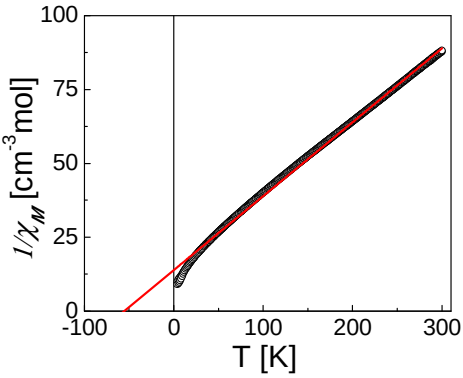

Figure 61 Inverse magnetic susceptibility of **22 - phtptrz-TaF$_7$** plotted as a function of temperature. The line through the points is the best fit of the data.

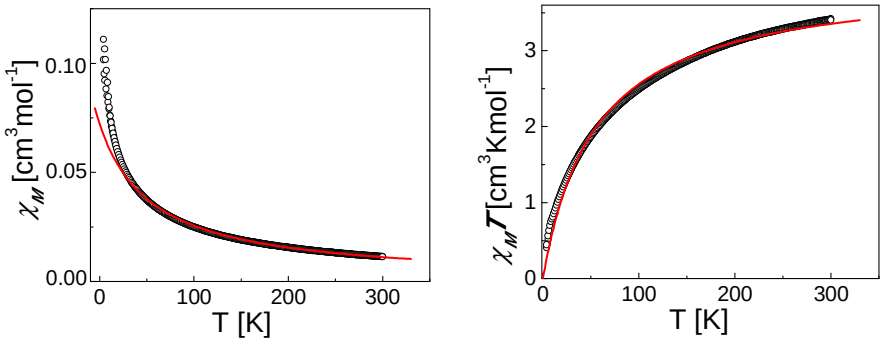

(a) (b)

Figure 62 (a) Thermal dependency of magnetic susceptibility and (b) $\chi_M T$ *vs.* T curve of **22-phtptrz-TaF$_7$**. The line through the points is the best fit of the data as described in text.

^{57}Fe Mössbauer spectroscopy

^{57}Fe Mössbauer spectroscopy further reveals variation of temperature dependent population of spin states in **21-phtptrz-ReO$_4$** and **22-phtptrz-TaF$_7$**. Selected Mössbauer parameters are summarized in Table 29.

In **21-phtptrz-ReO$_4$**, a quadrupole doublet (100 % population) with isomer shift δ = 1.09(1) mm·s^{-1} and quadrupole splitting ΔE_Q = 2.84(1) mm·s^{-1} is identified at 300 K which is clearly indicative of HS Fe^{II} species. A slight asymmetry of the lines is observed which is attributed to a texture effect. On

cooling, a spin conversion to the low-spin (LS) state is identified with appearance of a new signal depicted in blue at 77. Indeed, at 77 K, another quadrupole doublet with δ^{LS} = 0.51(1) mm·s^{-1} and ΔE_Q^{LS} = 0.10(1) mm·s^{-1} is found, thus confirming the incomplete nature of the SCO process.

For **21-phtptrz-ReO$_4$**, only 25% of HS ions have switched to the LS state at 77 K in full agreement with SQUID data. Interestingly, δ^{HS}(77 K) for **21-phtptrz-ReO$_4$** and **22-phtptrz-TaF$_7$** is identical (Table 29) indicating absence of any appreciable change in the electronic distribution around each individual iron atoms. The absence of SCO is not confirmed for **22-phtptrz-TaF$_7$** as HS ions are detected at 300 K, wheareas a mixture of LS/HS ions is probed at 77 K. Most interestingly, ΔE_Q^{LS}(77 K) is higher for **22-phtptrz-TaF$_7$** compared to **21-phtptrz-ReO$_4$** which indicate an important strained situation at the iron centers.

Table 29 Comparison of ^{57}Fe Mössbauer parameters for 21-phtptrz-ReO$_4$ and 21-phtptrz-TaF$_7$.

Compound	T [K]	δ [mm/s]	ΔE_Q [mm/s]	$\Gamma/2$ [mm/s]	$A_{HS}/A_{tot.}$	Spin state
21-phtptrz-ReO$_4$	300	1.09(1)	2.84(1)	0.22(1)	100	HS
	77	1.18(1)	3.21(1)	0.18(1)	75	HS
		0.51(1)	0.10(1)	0.19(1)	25	LS
22-phtptrz-TaF$_7$	300	1.09(1)	2.84(2)	0.18(1)	100	HS
	77	1.18(1)	3.36(1)	0.17(1)	75	HS
		0.31(1)	0.65(1)	0.23(1)	25	LS

δ: isomer shift (with respect to α-Fe at 300 K); ΔE_Q: quadrupole splitting; $\Gamma/2$: half width at half maximum; A_{HS}: Area of HS doublet; A_{tot}: total area.

Discussion

The trend in loss of SCO properties from **21-phtptrz-ReO$_4$** and **22-phtptrz-TaF$_7$** can be explained based on certain structural aspects. Although bulky

substituent on the triazole ring with multiple carbon spacer of the ligand scaffold is not expected to give a favorable situation for cooperative SCO, as trinuclear species formation could have been expected[1], the affinity of π-π stacking of aromatic groups and supramolecular interaction through carbonyl groups on the framework overcomes this barrier thus promoting the observed weak SCO in **21-phtptrz-ReO_4**. This behaviour indicates a cooperativity weakening which can be attributed too to a decrease of intermolecular contacts between chains. A clear influence of anion size in **21-phtptrz-ReO_4** is consistent with a chain spacing[7]. The doubly charged voluminous anion in **22-phtptrz-TaF_7** considerably weakens cooperativity of the SCO system compared to singly charged anions[7], thereby leading to a HS material, as shown in chapter I. Further incompleteness of SCO at lower temperature can also be attributed to steric growth of LS population. The progressively network shrinking during HS to LS conversion, on cooling, is thus halted due to network instability to further shrink that encounter steric clashes in the molecular packing with bulkier substitution, compared to 1D chains of the [Fe(4-amino-1,2,4-triazole)$_3$](anion)$_2$ series[7, 20].

V.2 Cooperativity variation in iron(II) 1D coordination polymers, based on monovalent counteranions

Introducing remarks

A clear influence of increasing anion size is consistent with a chain spacing[7]. The doubly charged voluminous anion in **21-phtptrz-ReO_4** (presented in Chapter V.1) considerably weakens cooperativity of the SCO system compared to singly charged anions[7], thereby leading to a HS material. In this context we introduce monovalent anions, (I^-, NO_3^- BF_4^-, ClO_4^-, and $CF_3SO_3^-$) with different sizes, to effect the cooperativity of the SCO system based on **phtptrz** ligand framework, $[Fe(phtptrz)_3](A)_2 \cdot$ Solvent. Thus the spin switching properties of five new 1D coordination polymers: $[Fe(phtptrz)_3]I_2$ (**23-phtptrz-I**), $[Fe(Phtptrz)_3](NO_3)_2 \cdot H_2O$ (**24-Pht-ptrz-NO_3**) $[Fe(Phtptrz)_3](BF_4)_2 \cdot H_2O$, (**25-Pht-ptrz-$BF_4$**), $[Fe(Phtptrz)_3](ClO_4)_2 \cdot H_2O$ (**26-Pht-ptrz-ClO_4**), $[Fe(Phtptrz)_3]$ $(CF_3SO_3)_2 \cdot H_2O$ (**27-Pht-ptrz-TRF**) are discussed below.

Results

Synthesis and general characterization

Complexes were prepared as off white powders by reacting **phtptrz** with $[Fe(H_2O)_6]^{2+}$ including a suitable anion (I^-, NO_3^-, BF_4^-, ClO_4^-, $CF_3SO_3^-$) in a 3:1 ratio in MeOH/H_2O following ref. [7]. The thermogravimetric and elemental analyses reveal the presence of guest water molecules, affording the following general formula $[Fe(phtptrz)_3]I_2$ (**23-phtptrz-I**),

$[Fe(Phtptrz)_3](NO_3)_2 \cdot H_2O$ (**24-Pht-ptrz-NO_3**) $[Fe(Phtptrz)_3](BF_4)_2 \cdot H_2O$, (**25-Pht-ptrz-$BF_4$**), $[Fe(Phtptrz)_3](ClO_4)_2 \cdot H_2O$ (**26-Pht-ptrz-ClO_4**), $[Fe(Phtptrz)_3]\ (CF_3SO_3)_2 \cdot H_2O$ (**27-Pht-ptrz-TRF**).

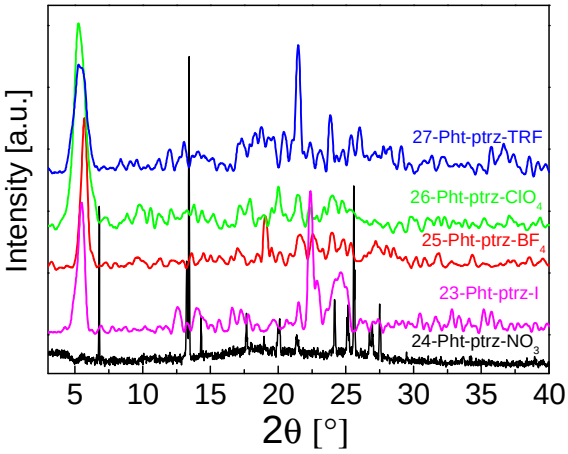

Figure 64 X-Ray powder diffraction patterns at 293 K for **23-phtptrz-I, 24-Pht-ptrz-NO_3, 25-Pht-ptrz-BF_4, 26-Pht-ptrz-ClO_4, 27-Pht-ptrz-TRF**.

Except for **24-Pht-ptrz-NO_3**, all compounds present a slightly crystalline character as revealed from X-ray powder diffraction (XRPD) patterns (Figure 64). Morphology of these compounds is illustrated by the SEM analysis with uniform spherical aggregates, of ~ 400 µm diameter for **23-phtptrz-I,** with uniform spherical granules, with rough surface for **24-Pht-ptrz-NO_3** and spherical granules, with smooth surface for **25-Pht-ptrz-BF_4** and **26-Pht-ptrz-ClO_4**. Contrary to these compounds, **27-Pht-ptrz-TRF** presents highly amorphous surface (Figure 65).

FT-IR analyses were performed to ascertain the coordination mode of iron to the ligand and the presence of the counter-anions in the crystal lattice (Figure 66).

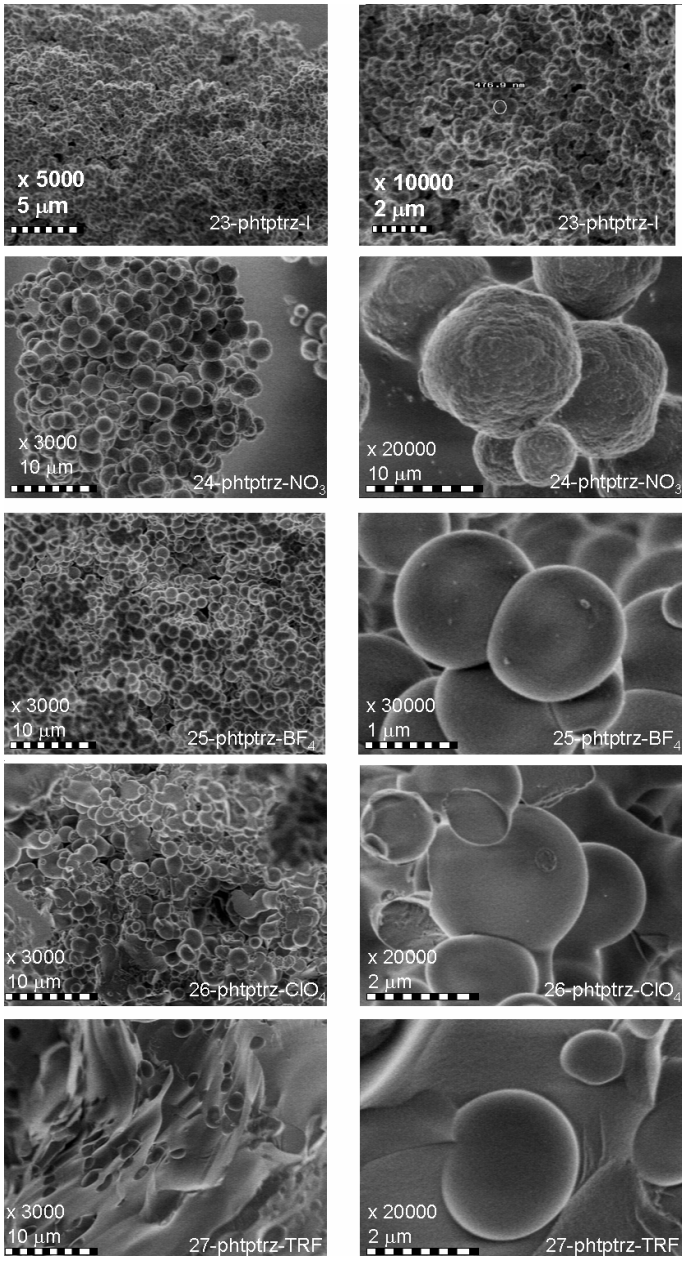

Figure 65 SEM images of microcrystalline particles of **23-phtptrz-I**, **24-Pht-ptrz-NO_3**, **25-Pht-ptrz-BF_4**, **26-Pht-ptrz-ClO_4**, **27-Pht-ptrz-TRF**, at 293 K.

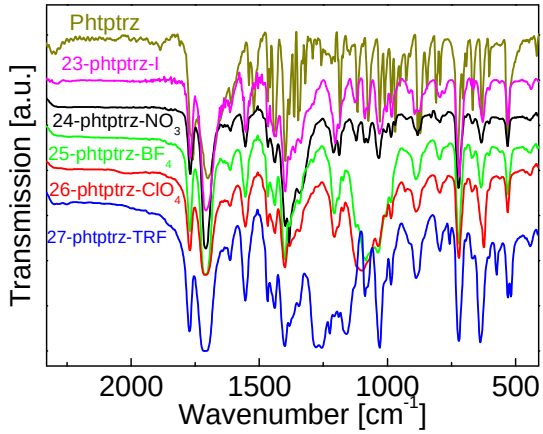

Figure 66 IR spectra of the ligand **phtptrz** and of complexes **23-phtptrz-I, 24-Pht-ptrz-NO_3, 25-Pht-ptrz-BF_4, 26-Pht-ptrz-ClO_4, 27-Pht-ptrz-TRF**, over the range 400-2300 cm^{-1}.

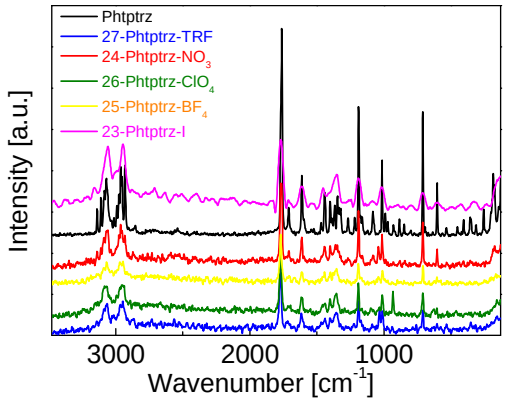

Figure 67 Raman spectra of the ligand **phtptrz** and of complexes **23-phtptrz-I**, **24-Pht-ptrz-NO_3**, **25-Pht-ptrz-BF_4**, **26-Pht-ptrz-ClO_4**, **27-Pht-ptrz-TRF**, over the range 400-2300 cm^{-1}.

Two sharp IR bands at 3109 (m) and 2536 (m) cm^{-1} of **phtptrz**, are assigned to the νCH_2 modes.[8] The -C=O group of phtalimido shows two stretching vibrations at 1700 (s) and 1770(m) which are shifted to 1710 and 1773 cm^{-1} in all complexes, thus confirming reshuffling of hydrogen bonding interactions involving –C=O groups. For **phtptrz** the band assigned to ring torsion of triazole at ν = 633(m) cm^{-1}, the $\nu_{C=N}$ stretching vibration at 1521, ν_{N-N} = 970(m) cm^{-1}, are all shifted upon complexation, in **27-Pht-ptrz-TRF** to 641 cm^{-1}, $\nu_{C=N}$ = 1551 cm^{-1}, and ν_{N-N} = 989 cm^{-1}(w), respectively. These values confirm the coordination of the iron to the 1,2,4-triazole ring[11, 21]. Indeed, the characteristic bands of the ligand are not only present in the spectra of the complexes but also are shifted towards larger wave numbers, from 3 to 10 cm^{-1} respectively[13, 22]. For a better understanding of the

molecular structure of these systems, additionally Raman spectra were studied (Figure 67). The band present around 1765-1770 cm^{-1} for **phtptrz** is assigned to a C=O vibration. In complexes this band is retained and appears around 1769 cm^{-1}. Presence of the monovalent counter-anion is also confirmed by IR and Raman: *IR* (cm^{-1}) $\upsilon_{(N-O)}$ ~ 1383(s), (**24-Pht-ptrz-NO_3**); $\upsilon_{(B-F)}$ ~ 1087 (s), (**25-Pht-ptrz-BF_4**); $\upsilon_{(Cl-O)}$ ~ 1104 (s), (**26-Pht-ptrz-ClO_4**); $\upsilon_{(S-O)}$ ~ 1256 (s), (**27-Pht-ptrz-TRF**); *Raman* (cm^{-1}) $\upsilon_{(N-O)}$ ~ 1044(w), (**24-Pht-ptrz-NO_3**); $\upsilon_{(B-F)}$ ~ 890 (vw) (**25-Pht-ptrz-BF_4**); $\upsilon_{(Cl-O)}$ ~ 984 (s), 450 (m-w), (**26-Pht-ptrz-ClO_4**); $\upsilon_{(S-O)}$ ~ 1038 (m), 762 (w) (**27-Pht-ptrz-TRF**).[9]

^{57}Fe Mössbauer spectroscopy confirms, for **23-phtptrz-I**, **24-Pht-ptrz-NO_3**, **25-Pht-ptrz-BF_4**, **26-Pht-ptrz-ClO_4** and **27-Pht-ptrz-TRF**, the presence of one $Fe^{II}N_6$ site, and excludes any oxidation product of iron. These spectroscopic data supports a linear chain structure with Fe^{II} ions linked by triple *N1*,*N2*-1,2,4-triazole bridges[7, 23].

Preliminary indications of SCO occurrence were obtained by a clear thermochromic response on quench cooling of the materials to liquid N_2. Indeed, off white powders of **23-phtptrz-I**, **24-Pht-ptrz-NO_3**, **25-Pht-ptrz-BF_4**, **26-Pht-ptrz-ClO_4** and **27-Pht-ptrz-TRF** show reversible colors change to pink. The off white color of all complexes, is due to the presence of the spin-allowed lowest energy d-d transition, $^5T_{2g} \rightarrow {}^5E_g$, for the HS sites in the near infrared region (~11345 cm^{-1})[15, 16, 23]. Two supplementary bands, corresponding to the $^1A_{1g} \rightarrow {}^1T_{1g}$ and $^1A_{1g} \rightarrow {}^1T_{2g}$ d-d transitions of LS Fe^{II} sites are observed at ~ 18073 cm^{-1} and ~ 28170 cm^{-1}, respectively suggesting that some proportion of Fe^{II} may be in the LS state at room temperature. The ligand field strengths for the HS and the LS state, given by equations $10D_q^{HS} = E(^5E) - E(^5T_2)$ and $10D_q^{LS} = E(^1T) - E(^1A_1) + (E(^1T_2) – E(^1T_1))/4$,[15, 16] allowed us to estimate $10D_q^{HS}$ and $10D_q^{LS}$ to be approximately 11345 cm^{-1} and 25116 cm^{-1}, respectively. These values are characteristic for SCO complexes[15, 16]. Presence of LS state at room

temperature has been confirmed by ^{57}Fe Mössbauer spectroscopy (*vide infra*).

Thermal spin-crossover properties

SQUID magnetometry

Variable temperature magnetic susceptibility measurements for all compounds were recorded over the temperature range 305 – 4 K, except for 23-**phtptrz-I** which was analyzed over the temperature range 305 K - 70 K (Figure 68), by Dr. A. Rotaru (USV, Romania).

For **23-phtptrz-I** the r. t. $\chi_M T$ value of 3.18 $cm^3 mol^{-1} K$ corresponds to high-spin (HS) Fe^{II} species. When cooled, this value gradually decreases to 1.1 $cm^3 mol^{-1} K$ around 72 K after which the inflection becomes more gradual until 27 K, revealing an incomplete spin conversion. The subsequent drop of $\chi_M T$ at lower temperatures is attributed to zero-field splitting (ZFS) of remaining HS Fe^{II} species. This type of spin conversion is commonly observed for Fe^{II} complexes having a voluminous substituent on the *N4* position of the triazole ring[17].

The ST behavior was also confirmed by the magnetic measurements of **24-Pht-ptrz-NO_3**. At 305 K, the product of molar magnetic susceptibility and temperature, is 3.06 $cm^3 mol^{-1} K$, which is close to the expected value for a HS state iron(II) ion, with a less diamagnetic contribution. Upon cooling, $\chi_M T$ gradually decreases to a value of 1.81 $cm^3 mol^{-1} K$ at 200 K and reaches a minimum value of ca. 0.84 $cm^3 mol^{-1} K$ at 77 K. The latter value can be attributed to the iron(II) LS state. This weak paramagnetism at low temperature may be related to a small residual HS fraction (confirmed by ^{57}Fe Mössbauer measurements, ~ 35 % HS Fe(II) ions, at 77 K), which can appear due to the defects in the material, linked to different lengths of the polymeric chains. The same magnetic behavior was observed in the warming

mode. No thermal hysteresis ($T_{1/2}$ = 192 K) was found for this relatively gradual spin transition between HS and LS electronic states.

The magnetic properties of the complex **25-Pht-ptrz-BF_4** are represented in Figure 68 in the form of a $\chi_M T$ versus T plot. At 300 K, $\chi_M T$ is equal to 3.2 cm^3 K mol^{-1} and corresponds to a quintet spin state (Fe(II) HS state). Just below room temperature, this value decreases gradually upon cooling to 220 K and then descends more steeper to 140 K. The spin conversion temperature $T_{1/2}^{\downarrow}$ is found at 163 K. Upon further cooling of the sample to 77 K, the value of $\chi_M T$ attains 1.28 cm^3 K mol^{-1}. The similar magnetic behavior was observed in the warming mode. Measurements performed in both heating ($T_{1/2}^{\uparrow}$ = 171 K) and cooling ($T_{1/2}^{\downarrow}$ = 163 K) cycles have revealed the occurrence of ca. 8 K wide thermal hysteresis loop. The presence of a thermal hysteresis loop for compound **25-Pht-ptrz-BF_4** clearly demonstrates the existence of a significant level of cooperativity in the solid state, in comparison with **24-Pht-ptrz-NO_3,** and is unprecedented for this series.

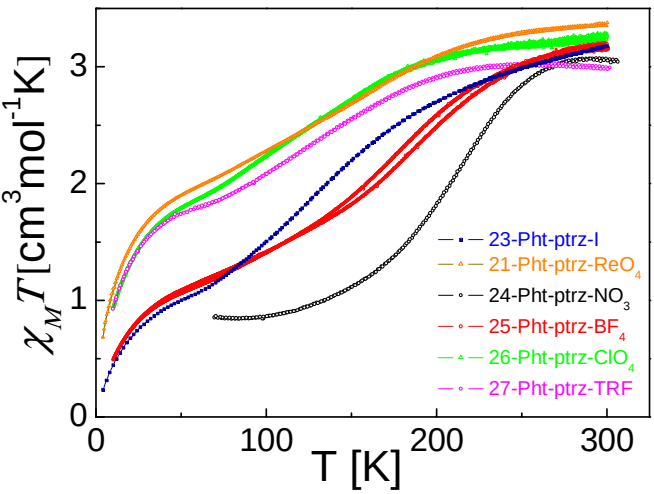

Figure 68 Variable temperatures magnetic susceptibility measurements for 23-phtptrz-I, 24-Pht-ptrz-NO_3, 25-Pht-ptrz-BF_4, 26-Pht-ptrz-ClO_4 and 27-Pht-ptrz-TRF recorded over the temperature range 300 – 4 K, in comparison with the magnetic behaviors of 21-phtptrz-ReO_4.

These SQUID measurements reveal a very smooth incomplete spin conversion for **26-Pht-ptrz-ClO$_4$** and **27-Pht-ptrz-TRF** with transition temperatures $T_{1/2}$ ~ 142 K and $T_{1/2}$ ~ 135 K, respectively. These complexes have a similar magnetic profile with **21-phtptrz-ReO$_4$**; however, the decrease in $\chi_M T$ begins at a higher value, 3.27 cm^3 mol^{-1} K (for **26-Pht-ptrz-ClO$_4$**) and 3 cm^3 mol^{-1} K (for **27-Pht-ptrz-TRF**) at 300 K, which is consistent with the HS state, with a less diamagnetic contribution. It is followed by a gradual decrease to 1.7 cm^3 mol^{-1} K at 40 K, for both, after which ZFS causes a decrease in $\chi_M T$ product.

^{57}Fe Mössbauer spectroscopy

^{57}Fe Mössbauer spectroscopy further reveals variation of temperature dependent population of spin states in **23-phtptrz-I**, **24-Pht-ptrz-NO$_3$**, **25-Pht-ptrz-BF$_4$**, **26-Pht-ptrz-ClO$_4$** and **27-Pht-ptrz-TRF**. Mössbauer spectra are shown in Figure 69 and 70 and hyperfine parameters are summarized in Table 30.

In **23-phtptrz-I**, (Fig. 69) a quadrupole doublet (100 % population) with isomer shift δ = 1.13(1) mm·s^{-1} and quadrupole splitting ΔE_Q = 2.78(1) mm·s^{-1} is identified at 300 K which is clearly indicative of HS Fe^{II} species. A slight asymmetry of the lines is observed which is attributed to a texture effect. On cooling, a spin conversion to the low-spin (LS) state is identified with appearance of a new signal depicted in blue at 203 K and 143 K. Indeed, at 77 K, another quadrupole doublet with δ^{LS} = 0.55(1) mm·s^{-1} and $\Delta E_Q{}^{LS}$ = 0.29(1) mm·s^{-1} is found, thus confirming the incomplete nature of the SCO process.

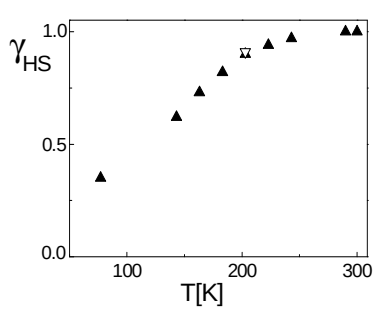

(a)

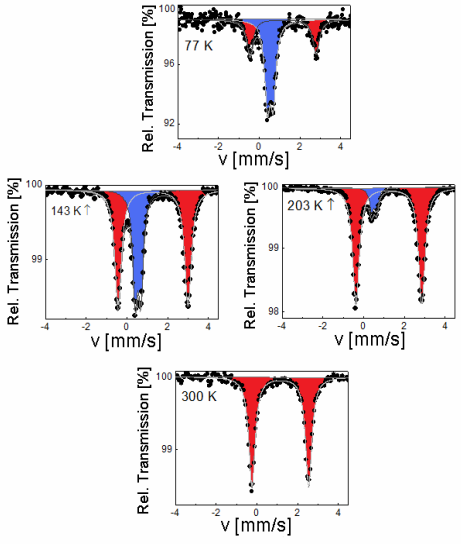

(b)

Figure 69 (a) γ_{HS} *vs. T* curve on cooling and warming modes for **23-phtptrz-I**; (b) Selected ^{57}Fe Mössbauer spectra for **23-phtptrz-I**.

In **24-Pht-ptrz-NO$_3$**, two quadrupole doublets of different resonance area fractions are identified at 77 K. The major quadrupole doublet (65 %) with isomer shift δ = 0.54(1) mm/s and quadrupole splitting, ΔE_Q = 0.31(1) mm/s corresponds to the LS state of Fe^{II}. The presence of a LS quadrupole splitting stems from a lattice contribution to the electric field gradient and therefore reveals a distorted character for the LS octahedron as expected for a constrained 1D chain with a rigid linkage, as previously pointed out in Chapter I. Another doublet, corresponding to HS Fe^{II} ions (35 %), with δ = 1.17(2) mm/s and ΔE_Q = 3.34(1) mm/s confirms the incomplete nature of the ST at 77 K. Upon warming to 300 K, the area fraction of the HS doublet increases until it reaches 88 %, confirming a thermally induced LS → HS conversion. Indeed, at 300 K, a second quadrupole doublet with δ^{LS} = 0.41(1) mm.s^{-1} and $\Delta E_Q{}^{LS}$ = 0.12(2) mm.s^{-1} is found, thus confirming the incomplete nature of the SCO process.

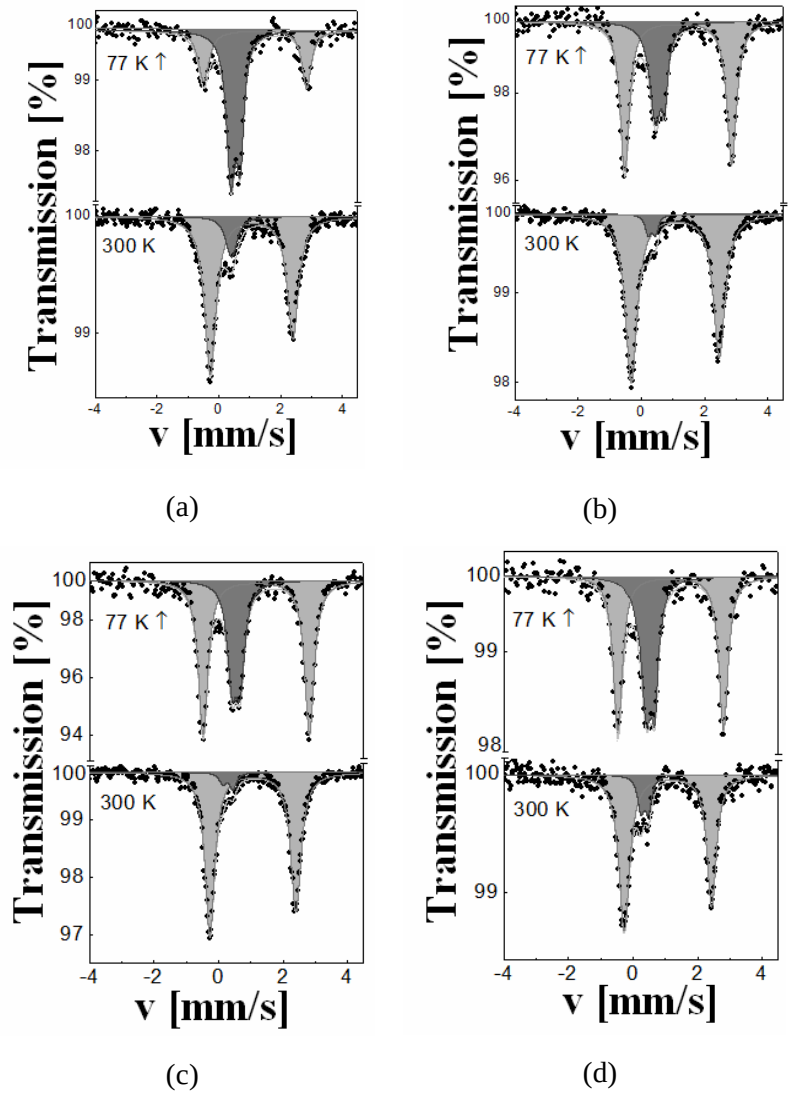

Figure 70 ^{57}Fe Mössbauer spectra for (a) **24-Pht-ptrz-NO$_3$**, (b) **25-Pht-ptrz-BF$_4$**, (c) **26-Pht-ptrz-ClO$_4$** and (d) **27-Pht-ptrz-TRF**.

The temperature variation of δ^{HS}, of **24-Pht-ptrz-NO$_3$**, reveals a slight decrease on warming which is attributed to the second order Doppler shift. δ and ΔE_Q of both LS and HS species are typical of an $Fe^{II}N_6$ chain compound in which iron centers are bonded by triple *N*1,*N*2-triazole bridges[7].

Table 30 Comparison of ^{57}Fe Mössbauer parameters for $[Fe(phtptrz)_3](A)_2 \cdot Solvent$ (δ: isomer shift (with respect to α-Fe at 300 K); ΔE_Q: quadrupole splitting; Γ/2: half width at half maximum).

23-Pht-ptrz-I

T [K]	*δ* [mm/s]	*ΔE_Q* [mm/s]	*Γ/2* [mm/s]	Rel. Area [%]	Sites
77(1)	1.13(1)	2.78(1)	0.18(1)	100	HS
	1.17(1)	3.25(1)	0.19(1)	35	HS
	0.55(1)	0.29(1)	0.16(1)	65	LS
300(1)	1.13(1)	2.78(1)	0.18(1)	100	HS
	1.17(1)	3.25(1)	0.19(1)	35	HS
	0.55(1)	0.29(1)	0.16(1)	65	LS

24-Pht-ptrz-NO_3

77(1)	1.17(2)	3.34(1)	0.18(1)	35	HS
	0.54(1)	0.31(1)	0.13(1)	65	LS
300(1)	1.06(1)	2.67(1)	0.22(1)	88	HS
	0.41(1)	0.12(2)	0.19(1)	12	LS

25-Pht-ptrz-BF_4

77(1)	1.17(1)	3.39(1)	0.19(1)	34	HS
	0.60(1)	0.29(2)	0.10(1)	66	LS
300(1)	1.07(1)	2.78(1)	0.23(1)	94	HS
	0.33(1)	0.23(1)	0.11(1)	6	LS

26-Pht-ptrz-ClO_4

77(1)	1.17(1)	3.30(1)	0.18(1)	64	HS
	0.54(1)	0.26(1)	0.17(1)	36	LS
300(1)	1.06(1)	2.66(1)	0.19(1)	94	HS
	0.29(1)	0.31(1)	0.13(1)	6	LS

27-Pht-ptrz-TRF

77(1)	1.16(1)	3.27(1)	0.17(1)	57	HS
	0.54(1)	0.26(1)	0.12(1)	43	LS
300(1)	1.08(1)	2.71(1)	0.18(1)	87	HS
	0.36(1)	0.23(1)	0.12(1)	13	LS

For **26-Pht-ptrz-ClO_4** and **27-Pht-ptrz-TRF** only 28 % and 30 %, respectively, of LS ions has switched to the HS state on warming, from 77 K to r.t. (Table 30). Interestingly, δ^{HS}(77 K) for **25-Pht-ptrz-BF_4** and **26-Pht-ptrz-ClO_4** and **27-Pht-ptrz-TRF** is identical (Table 30) indicating absence of any appreciable change in the electronic distribution around each individual iron atoms, i.e. the monovalent anions could be located at similar distances to the chains.

Discussion

SCO compounds based on the cation $[Fe(phtptrz)_3]^{2+}$ and I^-, NO_3^-, BF_4^-, ClO_4^- and $CF_3SO_3^-$ anions display a modest cooperativity, as shown by magnetic and ^{57}Fe Mössbauer spectroscopy. Obviously the factors that could influence the magnetic properties of these systems could be the type of the anion (NO_3^-, BF_4^-, ClO_4^- and $CF_3SO_3^-$), the water content of the compound and the size of the substituent on the triazole core.

The first and most important effect on the SCO phenomenon is the effect of counter-anion. Nitrate is a favourable anion which promotes the H-bond interactions, due to the planar geometry and also by it 'tripod' character, to give access to a cooperative ST trend, as found in $[Fe(NH_2trz)_3](NO_3)_2$ system[23], discussed in Chapter III. Unexpectedly in the case of $[Fe(phtptrz)_3]^{2+}$ system, the presence of NO_3^- anion between and inside the chains is not enough to obtain a cooperative system. **23-Pht-ptrz-I** and **24-Pht-ptrz-NO_3** present a SCO phenomenon around 171 K and 192 K, respectively, without thermal hysteresis. This effect is due probably to the presence of a bulky substituent on the triazole ring with multiple carbon spacer of the ligand scaffold, which is not a favourable to obtain cooperative SCO systems. In the same time their affinity of π-π stacking of aromatic groups and supramolecular interaction through carbonyl groups on the

framework overcomes this barrier thus promoting weak SCO phenomenon. This behaviour is translated also by the Mössbauer signals (only 53 % of the Fe(II) active site, which present a switch from LS to HS state) (Figure 69 and 70), which indicates a cooperativity weakening which can be attributed to a decrease of intermolecular contacts between chains. At this point, the origin of hysteresis in **25-Pht-ptrz-BF_4** is not clear; it is probably mediated by the hydrogen bonds, promoted by the tetrahedral geometry of the tetrafluoroborate anion. Noticeably, $T_{1/2}$ of complex **24-Pht-ptrz-NO_3** is 21 K higher than that of the complex **25-Pht-ptrz-BF_4**.

The last two compounds **26-Pht-ptrz-ClO_4** and **27-Pht-ptrz-TRF**, have similar SCO behaviours (Figure 68). They display relatively smooth and reversible incomplete HS-to-LS transitions in the range of 300 - 4 K for further cooling-heating cycles, corresponding to more than 50% of active Fe(II) ions, presenting a spin conversion.

Coordination polymers **26-Pht-ptrz-ClO_4** and **21-phtptrz-ReO_4** with **ClO_4^-** and **ReO_4^-** as anions, in fact have almost identical transition temperatures, which can be related to the comparable size of these anions. The direct correlation between T and the volume of the tetrahedral anion in this type of materials is therefore confirmed here also. However, for the systems including a voluminous counter-anion, the ST temperature decreases. For example, **24-Pht-ptrz-NO_3** polymer give higher transition temperature compared with the sulfonate type anion, **27-Pht-ptrz-TRF**.

Since volume is not the main parameter in this case, interaction between anionic species and cationic chains has to be considered. It has been shown previously, for spherical anions that the Fe-N distance in the LS state decreases when the diameter of the spherical anion decreases.[7, 24, 25] Anion - cation interactions can give rise to an electrostatic pressure that grows with the interaction and gives higher ligand fields and therefore higher ST temperature.[7, 24-27] This effect is related also to the application of an external

pressure, which may display the transitions to higher temperatures.[7, 28] In the same time, for the same reason the amount of lattice water is important and for direct comparison has to be identical, as in the case of $[Fe(phtptrz)_3]^{2+}$ systems. Thus the different anions fixed in between the Fe(II) - phtptrz chains can affect the transition temperature, by increasing the internal electrostatic pressure.[7] In the series $[Fe(phtptrz)_3]^{2+}$, discussed below, the direct effect of the size of the counter-anion was observed (Figure 70).

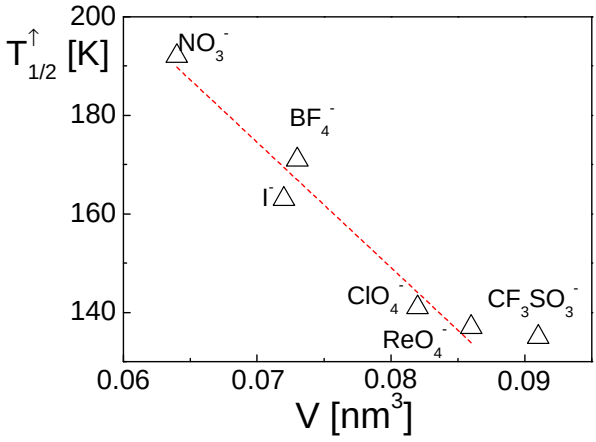

Figure 70 Variation of the transition temperatures, $T_{1/2}$, as deduced from SQUID, on warming mode (△) *vs.* the anion volume for $[Fe(phtptrz)_3]^{2+}$ systems.

In the present work, we have carefully investigated the ST of a series of Fe^{II} 1D phtptrz coordination polymers including monovalent inorganic anions of different size, allowing to evidence one linear size regime taking in account the ST range observation (Fig. 70). Here, we consider the variation of $T_{1/2}$ (on warming) *vs*. the volume of the inserted anion[29] instead of considering the radius only determined from Kapustinskii's equation[30]. This choice allowed us to take into account the dimensional size of the anions. One linear regime is identified between $0.04 \leq V\ (nm^3) \leq 0.09$, where a decrease of the $T_{1/2}$ is observed with increasing the volume. In this volume range, less energy is needed to switch the spin state of the metallic ions as much as we

increase in volume and space out the chains. Above $V \geq 0.1$ nm^3, we can identify that the $CF_3SO_3^-$ anion is out from the linear regime identified until this volume. This behavior may corresponds to a chain spacing in such a way that when the LS-HS transition occurs, FeN_6 sites have enough freedom to increase their bond length and expand along the chain axis, the counter anion being affected very little by the ST itself due to the large distance between a pair of chains where these anions are located. Thus, insertion of a bigger counteranion between the chains decreases the relative vertical displacement of the potential wells, in favor of the HS state, thereby inducing a negative pressure effect, even though the aromatic ring of the counter-anion can favourites a stacking with the phtptrz. Since that the tail on the triazole is rather big (lengthy and bulky), the anions NO_3^- and BF_4^- favour an abrupt and cooperative transition more than the ClO_4^- and the triflate anion. Probably hydrogen bonding between the chains has to be considered, since it can still be an efficient pathway for interchain interaction.

Considering the gradual SCO which characterizes these transition curves, this can be evaluated by the temperature range ΔT_{80} in which 80 % of the transiting Fe(II) ions undergo their spin transition. The rather large values of ΔT_{80} (more then 100 K) do not indicate the absence of intra-chain cooperativity, only an overall lower cooperativity that may be due to a lower long range interaction.

The expected lowering of cooperativity with increasing size of the substituent on the triazole of chain-like ST compounds $[Fe(phtptrz)_3](Anion)\cdot H_2O$, has been observed. The correlation found between the ST temperature and the volume of the counter-anion, has attributed to the lowering of anion-cation electrostatic interaction by increasing the distance between the ionic species. Nevertheless the lowering ST temperature is promoted also by the effect of increasing the size of the

substituent on triazole ring. However, when using ClO_4^- and ReO_4^- and $CF_3SO_3^-$ as anions the effect observed is an increase of the paramagnetic percentage at low temperature. Thus incompleteness of SCO at lower temperature can also be attributed to steric factors that delay further growth of LS population. The progressive network shrinking during HS to LS conversion, on cooling, is thus halted due to network instability to further shrink that encounter steric clashes in the molecular packing with bulkier substitution, compared to 1D chains of the [Fe(4-amino-1,2,4-triazole)$_3$](anion)$_2$ series[7, 20]. The electrostatic anion-cationic chain interactions may be also at the origin of the differences between the anions used, mediated through the electrostatic pressure it creates on the ST chains.

In summary, we have presented novel SCO molecules exhibiting spin-state transition below the room-temperature region. The compounds display changes of color from violet (LS) to off-white (HS). By the virtue of their less crystalline nature, it is not possible to prepare the compounds as single crystals. The compounds investigated represent new examples of systems of type where the counter anion directly influences the spin state change of the Fe(II) ions but it is not the driving force of the SCO phenomenon.

A complete control of the parameters that affect the SCO behaviour is a quite difficult task to achieve, since it depends essentially on the nature of the ligands, the non-coordinating anions, the solvent molecules, the crystal packing, the material defects, etc. … . In polymeric compounds, the communication between the SCO centers is achieved through intermolecular interactions, such as H-bonding or π–π interactions between aromatic ligands, anions and/or solvent molecules. Thus, a total substitution of these intermolecular interactions by covalent linkage of the metal centers may lead to a more predictable control of the ST behaviour going to the 2D and 3D thermo-switchable SCO systems.

Chapter V.3: Steering molecular architecture and magnetism with remote and bulky *N4*-substitution on 1,2,4-triazole; A case study of 4-(3'-N-phtalimido-propyl)-1,2,4-triazole

Introducing remarks

Aromatic groups are not very often[31, 32, 32-51] substituted on *N*4 position of triazole. This could impose a different type of supramolecular interactions and subsequent molecular packing resulting in diverse architecture and magnetic interactions among metal centers. The advantages of such systems are the following: they are easier to crystallize, can present strong multiple secondary interactions, but at the same time compromising cooperative interactions in SCO systems.

Potential promoter of supramolecular interactions due to π–π stacking and H-bonding interactions involving carbonyl groups, **phtptrz** was used to design two new molecular building, $[Cu_3(phtptrz)_{10}(H_2O)_2](SiF_6)_3 \cdot 44H_2O$ (**28**) and $[Cu_3(phtptrz)_8(H_2O)_4](ZrF_6)_3 \cdot 19H_2O$ (**29**) which are described in the following sections. These crystal structures have been obtained[52] and precisely analyzed in the light of our knowledge about the bulky substituent in order to transpose the information to the SCO phenomenon of this class of materials.

Results and discussions

Synthesis and structural characterization[†]

Inorganic syntheses were carried out with **phtptrz** (for which the synthesis is presented in Chapter V.1, Figure 54) and copper (II) salts with TaF_7^{2-} and ZrF_6^{2-} counter-anions. It leads to strong competition for the complexation between all coordination molecules present in the synthetic medium, oxygen functions of phtptrz, the nitrogen atoms from 1, 2, 4-triazole, but also the anion (e.g. TaF_7^{2-}, CH_3COO^- etc.) and the solvent, such as water. On the basis of our analyses, **phtptrz** give two different type of inorganic complexes. Thus in this section, we will then focus on compounds with formula $[Cu_3(phtptrz)_{10}(H_2O)_2]$ $SiF_6)_3 \cdot 44H_2O$ (**28**) and $[Cu_3(phtptrz)_8(H_2O)_4](ZrF_6)_3 \cdot 19H_2O$ (**29**). Single crystals of copper(II) complexes were grown in water by slow evaporation. **28** has been obtained by slow evaporation of a mother solution as follows: an equivalent of an aqueous solution of $Cu(CH_3COO)_2 \cdot H_2O$ and $(NH_4)_2TaF_7$ has been added to three equivalents of a methanolic solution of **phtptrz**. The blue colored precipitate is filtered and the filtrate is left to crystallize by slow evaporation at r.t.. After one night, blue crystals of square shape have been obtained. These crystals were found to contain SiF_6^{2-}. This ion comes probably from the reaction between the silicium oxides of the glassware by the solution containing TaF_7^{2-}. This is common type of reaction when fluorinated ions are involved.[53] Single crystals of **29** have been obtained through the slow diffusion of an aqueous solution containing an equivalent of salt $CuZrF_6.6H_2O$ and three equivalents of phtptrz. Blue square crystals were obtained in 2 weeks by slow evaporation.

[†] The synthesis was realized by D. Gillard during his Master thesis (UCL).

Crystal structures study[‡]

4-(3'-N-phtalimido-propyl)-1,2,4-triazole (**phtptrz**)

(a) (b)

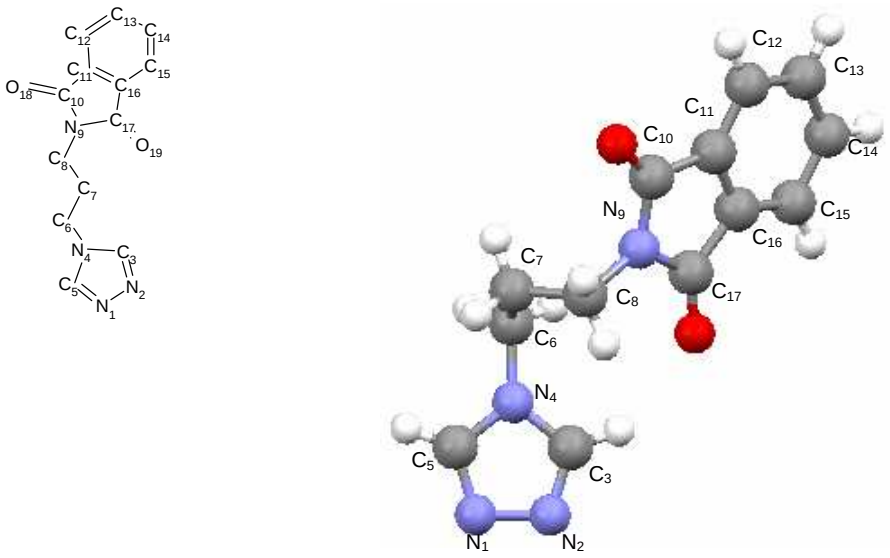

Figure 71 (a) Schematic view of phtptrz and (b) crystal structure of phtptrz.

The crystal structure of **phtptrz** was solved at 293(2) K. It crystallizes in monoclinic space group $P2_1/a$ (Table 31, Appendix Crystal Data). The molecular structure of **phtptrz** is depicted in Figure 71b. The propyl group is out of the triazole plane (N_4-C_6-C_7 angle is of 112.8°) and the propyl branch of the phtalimido group is not aligned in the same plane as the triazole. The triazole and the phtalimido are arranged on both sides of the propyl branch C_6-C_7-C_8 plane (Figure 72a). In the same time they are both situated on the same side of the plane which is perpendicular to the C_6-C_7-C_8 plane passing

[‡] Structures were solved by Prof. B. Tinant (UCL).

through C_6 and C_8. This fact is clearly indicated by the 113.23° value of the C_6-C_7-C_8 angle (due to the repulsion of the two groups) (Figure 72b).

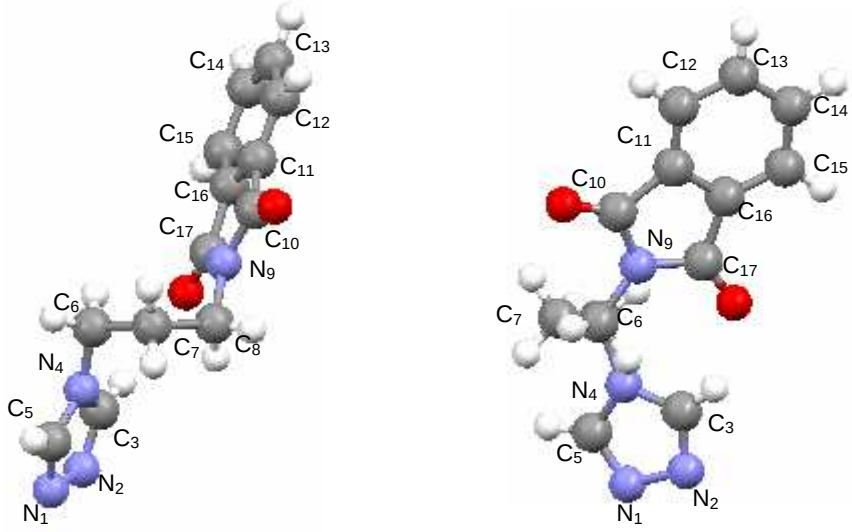

(a) (b)

Figure 72 View of the asymmetric part of the unit cell of **phtptrz**, showing the plane C_6-C_7-C_8 (a) and the plane C_6-C_7-C_8 following C_6-C_8 axis (b).

There are neither hydrogen bonding nor π-stacking interactions (long distances between the planes explain this later lack of interaction). It is only possible to have a very weak stacking between the triazole and the N9-C10-C11-C16-C17 cycle of a neighboring phtptrz. The angle between the planes is of 3.87° and the distance between them is 3.6331 Å. This relatively long distance indicates that this interaction is relatively weak.

The inter-atomic distances between the triazole atoms and the C6 and C7 atoms are indicated in Table 32.

Thus the distances between the triazole atoms are the same as those described for 4-(2'-hydroxy-ethyl)-1,2,4-triazole (hyetrz)[54].

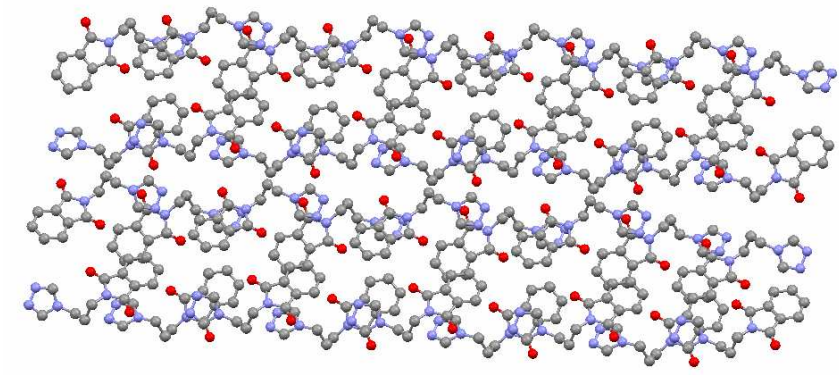

Figure 73 Projection of the crystal packing of **phtptrz** along the *b* axis.

Table 32 Inter-atomic distances present in **phtptrz.**

Atoms	Inter-atomic distances (Å)
N1-N2	1.3906
N2-C3	1.3073
C3-N4	1.3574
N4-C5	1.3569
C5-N1	1.3057
N4-C6	1.4688
C6-C7	1.5265

In order to better understand the organization of the inorganic anions in these materials, the crystal structures of the following model compounds have been solved, $[Cu_3(phtptrz)_{10}(H_2O)_2](SiF_6)_3 \cdot 44H_2O$ et $[Cu_3(phtptrz)_8(H_2O)_4](ZrF_6)_3 \cdot 19H_2O$.

$[Cu_3(phtptrz)_{10}(H_2O)_2](SiF_6)_3 \cdot 44H_2O$ (**28**)

The X-Ray of $[Cu_3(phtptrz)_{10}(H_2O)_2](SiF_6)_3 \cdot 44H_2O$ (**28**) were recorded at 120 K. The compound crystallizes in a triclinic system with the $P\bar{1}$ space

group and the following crystal unit parameters: a = 14.164(4) Å, b = 17.830(5) Å and c = 19.554(7) Å (Table 31).

The asymmetric unit includes 1.5 Cu(II) atoms, 5 phtptrz ligands, 5 SiF_6^{2-} and 23 water molecules (one of them coordinated to Cu). The crystal shows a trinuclear complex (Figure 74).

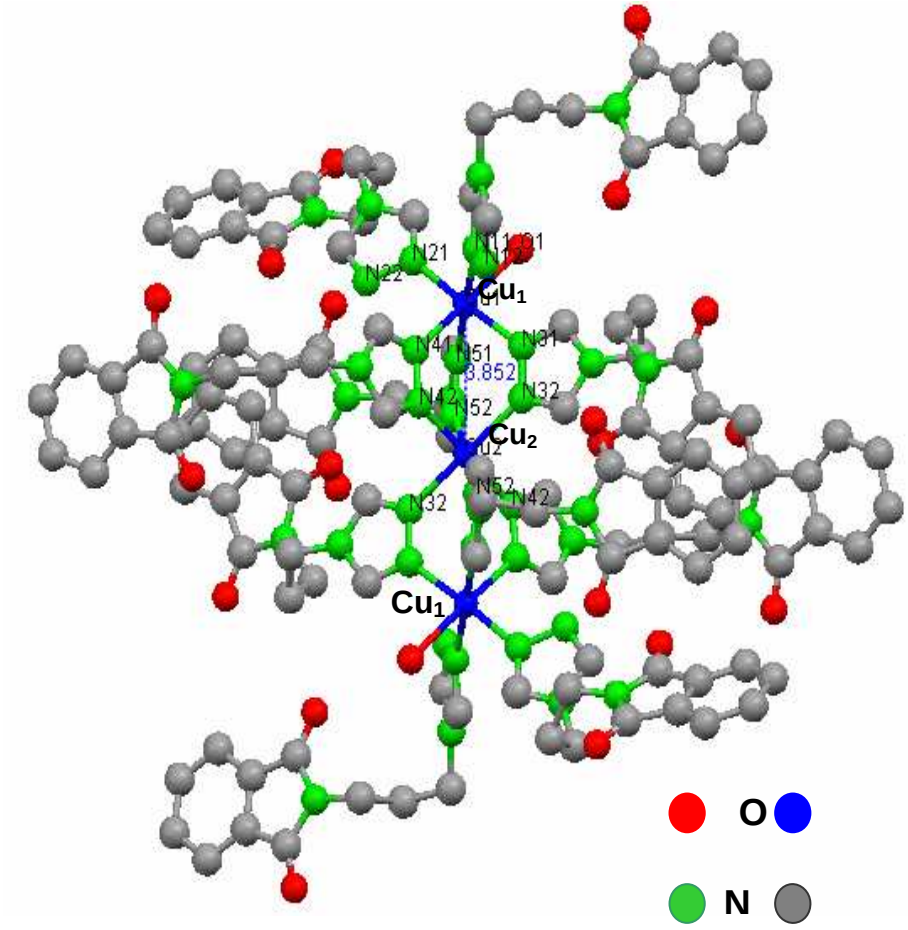

Figure 74 Trinuclear unit of $[Cu_3(phtptrz)_{10}(H_2O)_2](SiF_6)_3 \cdot 44H_2O$ (**28**). For a better visibility, the anions, the non-coordinated water molecules and the hydrogen atoms have not been represented.

The copper atoms present an octahedral configuration. The central Cu_2 is coordinated to six **phtptrz** ligands by the nitrogen atoms N_{32}, N'_{32}, N_{42}, N'_{42}, N_{52}, N'_{52} of the triazole. N' represents the nitrogen atoms across the copper

centers. The Cu_1 atoms are coordinated by 5 phtptrz ligands and one water molecule. Three phtptrz are coordinated in a bridging way between Cu_1 and Cu_2 and two are coordinated in a monodentate manner to Cu_1 through the nitrogen N_1 and N_2 atoms. The structure of this copper complex shows that the **phptrz** ligand coordinates itself through nitrogen atoms, in the N_1 and N_2 positions of the triazole and not through the oxygen atoms of the ketonic function, O_{18}, O_{19}. This kind of bond is also due to the fact that the N_9 of the ligand is seriously congested; it is not therefore accessible for the coordination.

The O_{18} and O_{19} position are accessible but this behavior is explained by the HSAB rule: the nitrogen has more affinity for Fe and Cu than oxygen because the nitrogen is softer than oxygen.

As copper is a d^9 transition metal, it presents a Jahn-Teller effect, and a Z-out deformation is important. The Cu_1 ions are in an octahedral environment with four nitrogen atoms in a plane (N_{11}, N_{21}, N_{31}, N_{51}) at 2.019 Å to 2.028 Å distances. The oxygen of the water (O_1) and the fifth nitrogen (N_{41}) are in *trans* position compared to the copper plane at longer distances of 2.468 Å and respectively 2.266 Å. The distances Cu_1-ligand and the angles around Cu_1 are presented in the Table 32.

The central copper atom (Cu_2), which is also the center of symmetry of the molecule, presents also a Z-out distortion of the octahedron, but this time in an identical manned in the two directions –z, +z. Table 32 show the Cu_2-ligand distance (a) and the angles around the Cu_2 (b). The (N_{32}, N_{42}, N'_{32}, N'_{42}) plane is not perpendicular to the N_{52}, N'_{52} axis. As one can see in the Figure 75, the N_{52}-Cu_1-N_{32} angle is of 94.5°.

The copper atoms are separated by a 3.852 Å distance. This distance is close to the one found for other trinuclear compounds based on copper atoms[36, 55, 56].

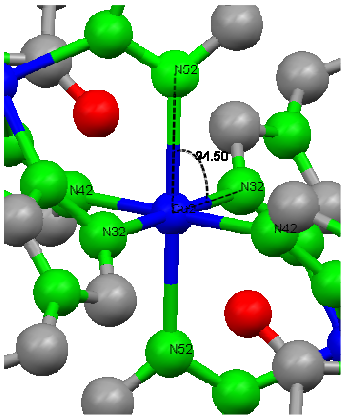

Figure 75 Octahedral geometry around Cu2.

This distance is also close to the one of the chain complex based on 4R-1,2,4-triazole having a smaller volume than the phtalimide group. For example hyetrz, in the $[Cu(hyetrz)_3](ClO_4)_2 \cdot 3H_2O$ compound, the Cu-Cu distances are of 3.8530 Å et 3.8292 Å[57]. One can therefore observe that the phtalimido-propyl group does not influence the inter-metallic distance inside the polymer. This is logic because the bond is made in similar mode, exclusively through the triazole.

Let us observe the influence of the phtalimido-propyl branch on the inter-metallic distance between the trinuclear groups. The distance between metallic atoms of neighboring trinuclear units is equal to 14.164 and 17.830 Å, (Figure 76). These distances are greater than in the triazole trinuclears with less voluminous clusters.[36, 55, 56] As we can see in Table 31, they are greater by 1 to 4 Å. The larger space between metallic centers can have an influence on the cooperativity if it is also larger in the iron chains. It can also decrease the cooperativity and make the SCO phenomenon more progressive.

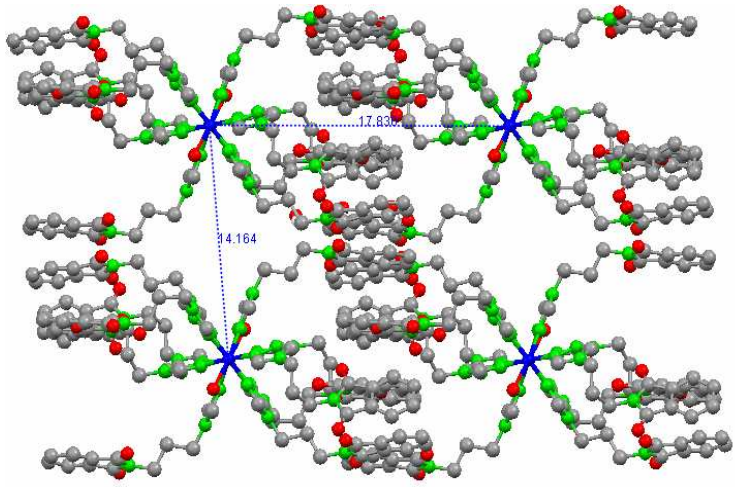

Figure 76 View of the crystalline structure of the $[Cu_3(phtptrz)_{10}(H_2O)_2](SiF_6)_3 \cdot 44H_2O$ (**28**) following the perpendicular plane to the alignment axis Cu-Cu-Cu. For a better visibility, the anions, the non-coordinated water molecules and the hydrogen have not been represented. The spheres represent: blue - Cu, green - N, grey- C, red – O.

A few types of interactions can be observed in **28**. As the synthesis has been realized in a mostly aqueous medium, many water molecules are inserted in the structure in order to stabilize it. Forty four water molecules are present in each trinuclear unit cell, which is particularly high compared to the structures already obtained for other Cu^{II} trinuclears based on a triazole core[36, 55, 56]. These water molecules form a hydrogen bonds network between trinuclears. The main identified H-bonding are situated between the hydrogen of the water molecule coordinated to the Cu_1 and the fluorine atoms F_3 and F_5 of the SiF_6^{2-}. Other hydrogen bonds are also present: between the noncoordinated water molecules and the nitrogen atom N_{12} of the phtptrz triazole mono-coordinated to the Cu_1, between the oxygen atoms (O_{419} and O_{519}) of the phtalimide and the fluor atoms of another SiF_6^{2-} molecule (Figure 77). The list of hydrogen bonds can be found in the Table 33.

A more complex network between the numerous non coordinated water molecules can be observed. The list of these interactions can be found in Table 33. This intense network of interaction, realized by the help of the higher number of water molecules could suggest that the metal ions bonded to **phtptrz** ligands, present an important cooperativity effect between the units.

Stacking type interactions between aromatic cycles have been observed also. The complex arrangement of the structure made difficult the identification of all these interactions. We can however observe some of these interactions in Figure 78. This Figure allows visualizing the stacking between two benzene cycles and one triazole cycle of the phtalimide group.

The three phtalimido groups of a trinuclear unit interact through the stacking of the aromatic cycles, in black (6 atoms cycle of a phtalimido), in violet (6 atoms cycle of another phtalimido) and turquoise (5 atoms cycle of the third phtalimido).

The π-π interactions are however not clearly defined. They are considered as a stacking of aromatic groups with molecular plans approximately parallel separated by an inter planar distance between 3.3 Å and 3.8 Å.[58] Let us analyze the interaction between the violet and turquoise cycles in Figure 78. The distance from center to center between the two cycles (violet and turquoise) is of 3.968 Å. This distance seems important but the shortest distance between two carbon atoms is of 3.421 Å as one can observe in Figure 79. This is explained by the shift between the cycles (as one of the cycles would slip on the other). The dihedral angle between the cycles is of 13.58°. Therefore, π-π interactions are possible.

One can observe in Figure 80 the compact arrangement of the phtalimido-propyl branches between the trinuclears. In this central zone the stacking interactions are efficient.

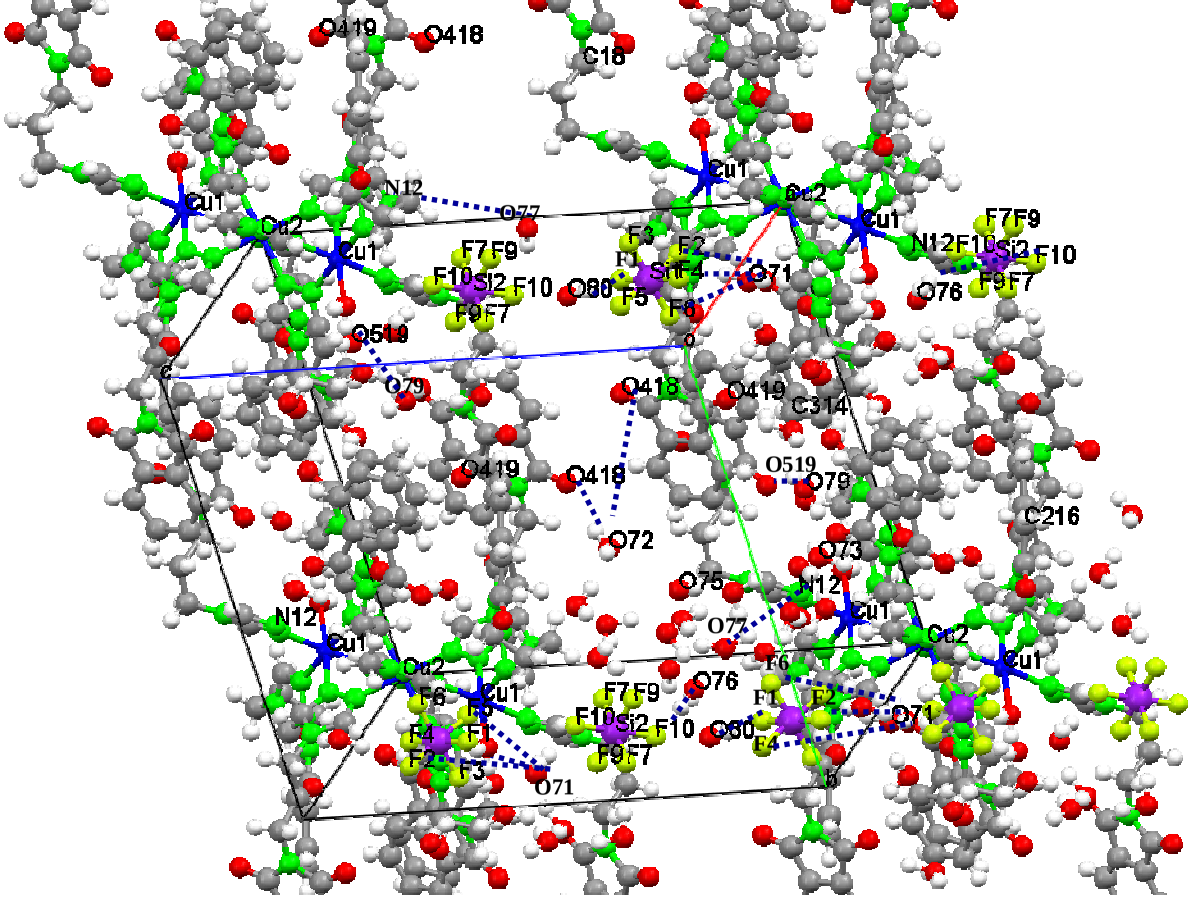

Figure 77 Projection of the crystal structure of **28** showing hydrogen-bonded trinuclear units.

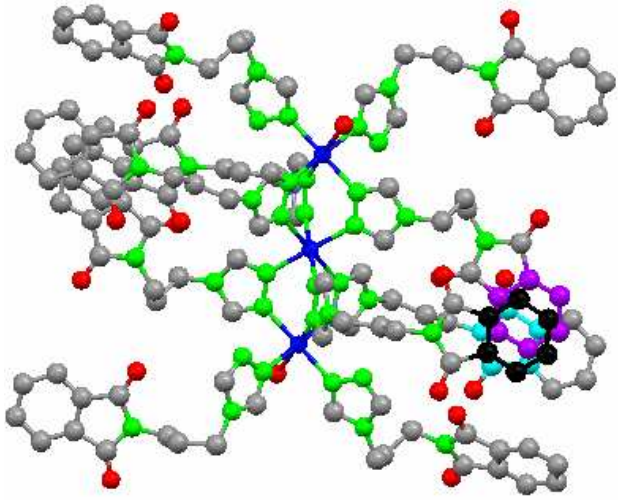

Figure 78 View of the stacking type interactions, in the compound $[Cu_3(phtptrz)_{10}(H_2O)_2](SiF_6)_3 \bullet 44H_2O$, in black (6 atoms cycle of a phtalimido), in violet (6 atoms cycle of another phtalimido) and turquoise (5 atoms cycle of the third phtalimido).

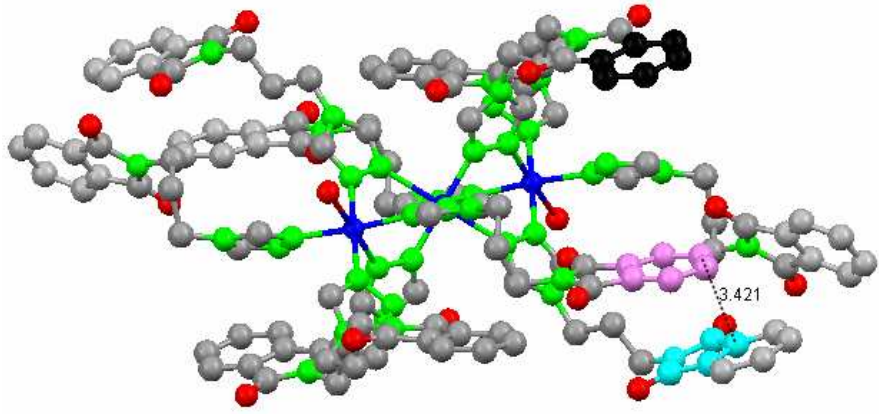

Figure 79 View of the π-π interactions in **28**.

Thus the system is stabilized by supra-molecular interactions of hydrogen bridge type or stacking, forming a tridimensional network of trinuclear units, as shown in Figure 80.

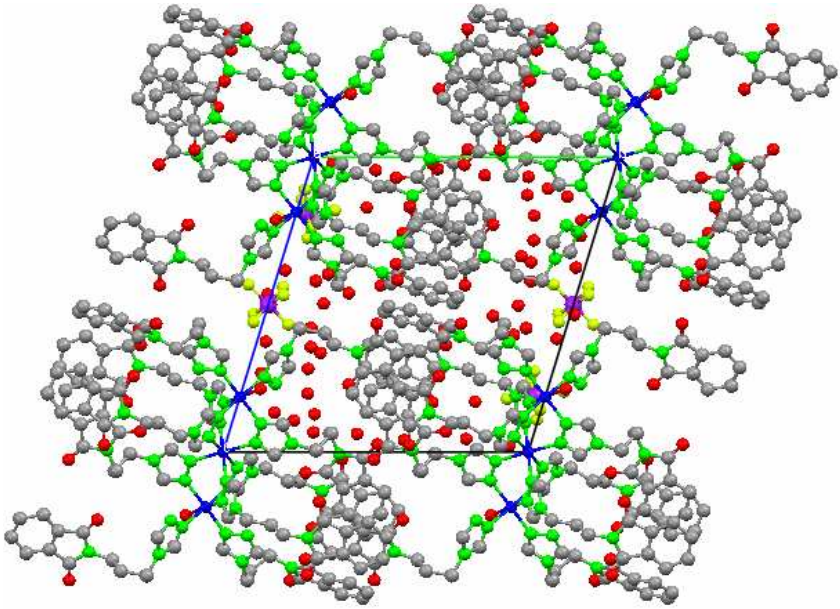

Figure 80 View of the crystalline structure of **28** on the (bc) plane. For clarity, hydrogen atoms have not been represented.

In conclusion the XRD analysis on single crystals allowed us to verify that the **phtptrz** ligand is coordinated in bi-dentate mode through the N_1 and N_2 positions of the triazole for the central copper atom and in a mono-dentate manner for the external copper atoms. The copper atoms are in an octahedral environment presenting a Jahn -Teller, Z-out effect. The distance between two coppers is similar to copper trinuclears with other ligands of the 4R-1,2,4-triazole type. On the other hand the distance between the trinuclears units is high because of the presence of voluminous phtalimido-propyl

group. An important number of non-coordinated water molecules have also been observed.

$[Cu_3(phtptrz)_8(H_2O)_4](ZrF_6)_3 \bullet 19H_2O$ (**29**)

$[Cu_3(phtptrz)_8(H_2O)_4](ZrF_6)_3.19H_2O$ (**29**) is the second crystal structure characterized through XRD in which the **phtptrz** ligand realizes the bridging mode of N_1,N_2-1,2,4-triazole between copper(II) ions. The structure has been determined at 293 K. The compound crystallizes in a triclinic system, with a space group $P\bar{1}$. The lattice parameters are: a = 14.164(4) Å, b = 17.830(5) Å and c = 19.554(7) Å. The asymmetric unit contains 1.5 copper(II) ions, 4 phtptrz ligands, 1.5 ZrF_6^{2-} and 11.5 water molecules. Two water molecules are coordinated to the copper ions, from the extremities. The crystallographic data are presented in the Table 31. As shown in Figure 81 shows, the central copper(II) ion (Cu_2), is located on a symmetry center sits in an octahedral environment CuN_6 formed by six **phtptrz** ligands. The external copper(II) ions (Cu_1) present a CuN_4O_2 environment with four phtptrz ligands and two water molecules. The phtptrz ligands form a bridge between copper atoms Cu_1 and Cu_2 by bidentate coordination through the N_1 and N_2 atoms of the 1,2,4-triazole.

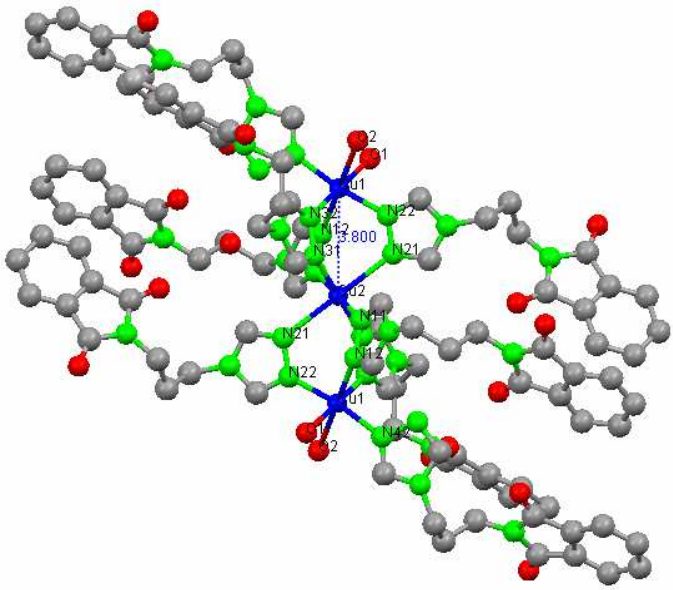

Figure 81 View of trinuclear unit of $[Cu_3(phtptrz)_8(H_2O)_4](ZrF_6)_3 \cdot 19H_2O$ (**29**). For a better visibility the non-coordinated water anions and molecules and the hydrogen have not been represented. The spheres represent: blue - Cu, green - N, grey - C, red - O.

The two coppers, Cu1 and Cu2, present a Z-out Jahn-Teller deformation (for Cu_1: 2.258 Å and 2.558 Å; for Cu_2: 2.429 Å and 2.429 Å). Cu_2 is located on the center of symmetry of the trinuclear and presents an identical elongation of the bonds Cu_2-N_{32} and Cu_2-N'_{32}. The coppers ions from the extremities present an elongation of Cu_1-N_{12} and Cu_1-O_2 bonds. The elongation of the bond realized with oxygen of the water is the most important (Table 34).

The distance between two coppers ions in the trinuclear is ~ 3.8 Å and those between the copper of the neighbor trinuclears (Figure 82) are equal to 12.596 Å and 18.010 Å. The distance between two neighboring copper ions

inside the trinuclear is similar to the one of the trinuclears copper already reported.[36, 55, 56] This greater distance is probably explained by the voluminous size of the phtalimido-propyl group.

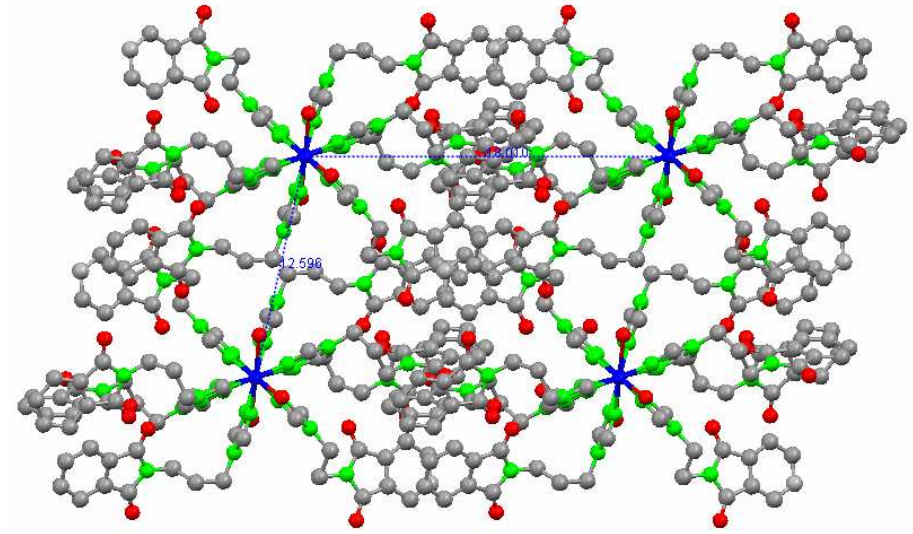

Figure 82 View of the crystalline structure of **29** following the perpendicular plane to the axis of the Cu-Cu-Cu alignment. For a better visibility, the anions and the non-coordinated water molecules are not represented. The spheres represent: blue - Cu, green - N, grey - C, red – O.

By analogy with $[Cu_3(phtptrz)_{10}(H_2O)_2](SiF_6)_3 \cdot 44H_2O$ **(28)**, we can assume that the supra-molecular arrangement of the trinuclear presents hydrogen bond interactions through the water molecules and the non-coordinated anions. But these interactions have not been clearly identified as the positions of the Hydrogen ions could not be defined. For this structure numerous water molecules, 19 per trinuclear unit allows a stabilization of the structure. The structure presents also stabilization through interactions between aromatic cycles. It does not present intra-molecular interactions but

several types of intermolecular interactions have been identified. One of these interactions, of π-π type, is represented in the Figure 83.

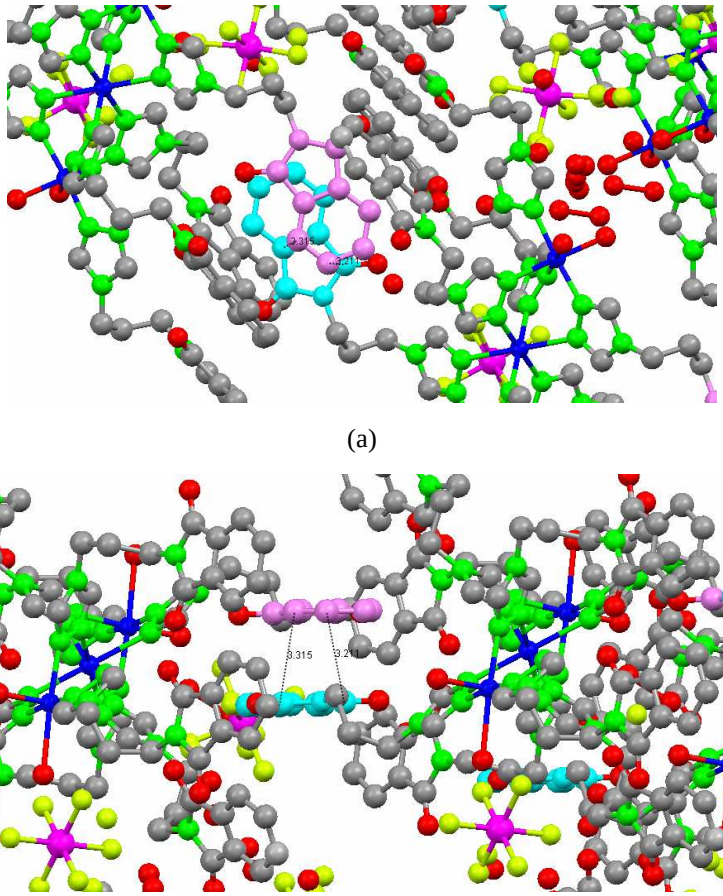

(a)

(b)

Figure 83 View of the π-π type interactions, in compound $[Cu_3(phtptrz)_8(H_2O)_4](ZrF_6)_3.19H_2O$ following the perpendicular plane to the aromatic cycle (a) and parallel to the cycle (b).

The interaction between the aromatic cycles is an interaction between the phtalimides groups of two different trinuclear units. The distance between the center of the cycles of 5 atoms and the center of the cycle of 6 atoms of

the other phtalimide is equal to 3.627 Å and the dihedral angle is of 3.42°. The distance between some of these atoms is shorter. As the cycles are displaced, the shortest distance is equal to 3.211 Å. Figure 84 also allows visualizing the ZrF_6^{2-} anion that may links trinuclear units, at ~ 2.79 Å.

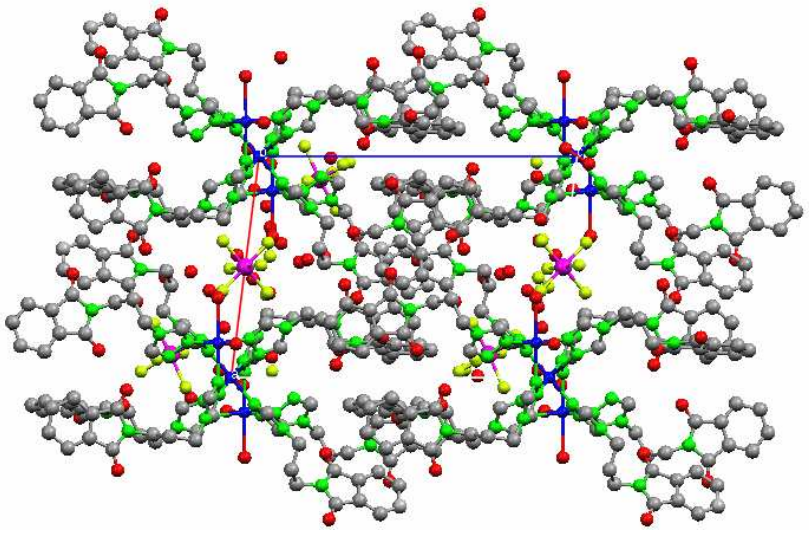

Figure 84 View of the crystalline structure of $[Cu_3(phtptrz)_8(H_2O)_4](ZrF_6)_3 \cdot 19H_2O$ following the (ac) plane. For a better visibility, the hydrogen atoms have not been represented. The spheres represent: blue - Cu, green - N, grey - C, red - O, violet - Zr, yellow - F.

Magnetic study of $[Cu_3(phtptrz)_{10}(H_2O)_2](SiF_6)_3 \cdot 44H_2O$ (28) and $[Cu_3(phtptrz)_8(H_2O)_4](ZrF_6)_3 \cdot 19H_2O$ (29)

The temperature dependence of the susceptibility (χ_M) and the product $\chi_M T$ of **28** are shown in Figure 85 (range 5 K – 300 K, applied field 1000 G).

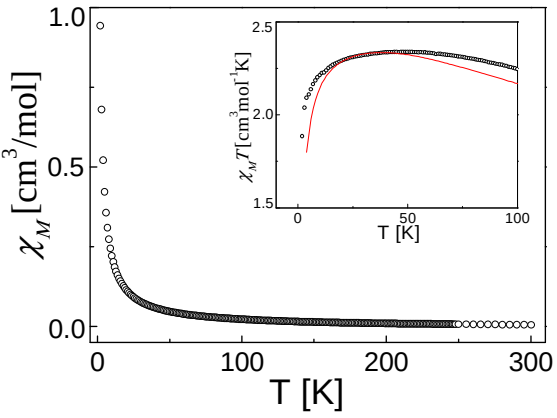

(a)

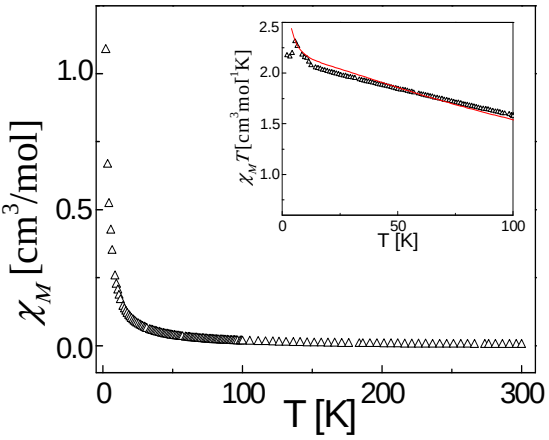

(b)

Figure 85 Temperature dependence of χ_M and $\chi_M T$ (*a* and *b*) for **28** (○) and **29** (Δ). The solid red line is the best-fit curve.

In the case of **28**, the 2 K value for $\chi_M T$ (1.88 cm^3 mol^{-1} K) increase rapidly upon further warming and reach 2.34 cm^3 mol^{-1} K at 50 K. The $\chi_M T$ curve decrease when the compound is warmed until room temperature to 1.58 cm^3

mol^{-1} K, which corresponds to a ½ spin value (considering g = 2) expected for a Cu(II) ions. This dependence is indicative of ferromagnetic coupling between the Cu(II) centers thought the budging 1,2,4-triazole ligand. Below 50 K, the further decrease of $\chi_M T$ sets in, can only be attributed to intermolecular interactions between S = ½ trimeric units.

Therefore this behaviour was modeled using the spin Hamiltonian given in the following equation[59]:

$$H = g\beta S_z H - J_1(S_1 \cdot S_2 + S_{1a} \cdot S_3) - J_2(S_1 \cdot S_{1a}) - zJ'\langle S_z \rangle S_z \quad \textbf{(eq. m)}$$

The first term of this Hamiltonian corresponds to the Zeeman term, for which a single isotropic 'g' tensor has been considered for two different Cu(II) ions in **28**. The second and third term include isotropic nearest neighbor and next-nearest neighbor the exchange parameter between neighboring Cu(II) ions and J_2 the exchange parameter between terminal Cu(II) ions. The fourth term takes into account intermolecular interactions in the mean-field approximation[18], with with J' being the intermolecular exchange interaction and *z* the number of trimeric neighbours, in this case four. In our case, where the trinuclear array is perfectly linear, J_2 can be neglected, and was thus set to zero. The resulting expression of the molar magnetic susceptibility in the $\beta H/k_b T << 1$ approximation, with an additional term to take into account a temperature-independent paramagnetism (TIP), is given in the following equation:

$$\chi_M(T) = \frac{Ng^2\beta^2 F(T)}{4k_B(T - zJ'F(T))} + TIP \quad \textbf{(eq. n)}$$

$$F(T) = \frac{1 + \exp(J_1 / k_B T) + 10\exp(3J_1 / 2k_B T)}{1 + \exp(J_1 / k_B T) + 2\exp(3J_1 / 2k_B T)}$$ (**eq. *o***),

with, k_B=1.38·10^{-16} erg K^{-1}, μ_B=9.27·10^{-21} erg Oe^{-1}, N=6.022·10^{23} mol^{-1}. The best sets of parameters obtained (full red line in Figure 85) for **28** were J1 = 229(1) cm^{-1}, g = 2.30(5) and zJ' = -0.83(2) cm^{-1}, with TIP value of -10^{-3} cm^3/mol.

The result (positive exchange integrals, J = 229(1) cm^{-1}) suggests operation of a ferromagnetic spin-exchange interaction between these adjacent Cu(II) ions govern the magnetochemistry of **28**.

The trinuclear complex **29** was studied also by magnetic susceptibility measurements in the 2–300 K regions. The magnetic behaviour of 29 is shown in Figure 85 in the form of a $\chi_M T$ and χ_M versus T plot. The $\chi_M T$ value at room temperature is 0.83 cm^3 mol^{-1} K for three isolated Cu(II) (S = 1/2). Upon cooling, the $\chi_M T$ value increases continuously to reach a value of 2.17 cm^3 mol^{-1} K at 2 K, indicating a dominant ferromagnetic interaction between adjacent Cu(II) ions. Below 5 K, the additional decrease of $\chi_M T$ sets in, may be attributed to intermolecular interactions between S = ½ trimeric units.

The experimental magnetic susceptibility data were analyzed as in previous case, for **28**. The best fitting for the experimental data gives J1 = 139(3) cm^{-1}, g = 2.10(5) and zJ' = 0.34(3) cm^{-1}, with TIP value of -2.5·10^{-3} cm^3/mol.

Discussion

We can remark that the two compounds $Cu_3(phtptrz)_{10}(H_2O)_2](SiF_6)_3 \cdot 44H_2O$ and $[Cu_3(phtptrz)_8(H_2O)_4](ZrF_6)_3 \cdot 19H_2O$, crystallize in the same crystallographic system (triclinic) with the same space group $P\bar{1}$. This situation indicates an important similarity in the supra-molecular organization of their networks. These compounds present however an important difference with respect to the number of water molecules coordinated to the two extremities of the trinuclear. There are two for $[Cu_3(phtptrz)_{10}(H_2O)_2](SiF_6)_3 \cdot 44H_2O$ and four for $[Cu_3(phtptrz)_8(H_2O)_4](ZrF_6)_3 \cdot 19H_2O$.

This structural study by XRD allowed us to highlight two coordination ways of the 4-(3'-N-phtalimido-propyl)-1,2,4-triazole: the mono-dentate and bi-dentate ways through the N_1 and N_2 positions of the triazole. It also highlighted the trend of the **phtptrz** ligand to realize inter- and intra-molecular stacking type interactions. It has also been observed that the metal, here Cu^{II}, finds itself in an octahedral environment CuN_6, CuN_4O_2 or CuN_5O.

These two structures of copper trinuclear complexes based on triazole are also remarkable through the presence of high number of non-coordinated water molecules, 44 for the SiF_6^{2-} trinuclear and 19 for the ZrF_6^{2-} trinuclear complexes.

A detailed bibliographic survey showed us that such an important number of non-coordinated water molecules has never been found in a trinuclear copper complex with a 4R-1,2,4-triazole ligand type. The very few examples of linear trinuclears for which the crystalline structure has been determined are

presented in Table 35. All of them crystallize with the space group $P\bar{1}$. As we can observe, the size of the R substituent of the ligand does not allow drawing any conclusions concerning the presence of non-coordinated water molecules. For $[Cu_3(pytrz)_8(H_2O)_4](NO_3)_6$ (pytrz = 4-(2-pyridyl)-1,2,4-triazole)[55], the R substituent is a pyridyl and the trinuclear does not present any solvation water molecule despite the presence of the aromatic cycle on the triazole. This lack of water is probably due to the comparatively greater hydrophobic environment created the pyridyl group compared to the phtalimido moiety.

Table 35 Copper trinuclear with 4R-1,2,4-triazole ligands

Compound	Space group	Cu···Cu (Å)	J (cm^{-1})	Cell parameters (Å)			Ref.
				a	b	c	
$[Cu_3(pytrz)_8(H_2O)_4](NO_3)_6$	$P\bar{1}$	-	-23.6	11.971	13.079	14.439	[55]
$[Cu_3(patrz)_{10}(H_2O)_2](ClO_4)_6 \cdot 2CH_3OH$	$P\bar{1}$	3.853	+ 1.99	12.02	14.089	14.449	[56]
$[Cu_3(pytrz)_{10}(H_2O)_2](ClO_4)_6 \cdot 7H_2O$	$P\bar{1}$	3.854	-5.41	13.627	14.054	15.452	[36]
$[Cu_3(phtptrz)_{10}(H_2O)_2](SiF_6)_3 \cdot 44H_2O$	$P\bar{1}$	3.852	+ 228.95(1)	14.164	17.836	19.554	*
$[Cu_3(phtptrz)_8(H_2O)_4](ZrF_6)_3 \cdot 19H_2O$	$P\bar{1}$	3.800	+ 138.76(3)	12.596	14.637	18.01	*

* this work

Through its significant volume and phtalimide functions, the phtalimide group of the ligand creates inter-molecular spaces capable to incorporate solvent molecules. This combination of factors, size and hydrophilicity confer a particular property to the trinuclear that could be used to trap other molecules than water in order to modulate the properties of the complexes (for example molecules like the methanol or ethanol by the variation of the crystallization solvent).

Let us also note that the ligand/Cu ratio is of 3/10 for $[Cu_3(phtptrz)_{10}(H_2O)_2](SiF_6)_3 \cdot 44H_2O$ and of 3/8 for $[Cu_3(phtptrz)_8(H_2O)_4](ZrF_6)_3 \cdot 19H_2O$. This confirms the importance of the ligand for the presence of non-coordinated water molecules. The synthesis of compounds presenting a high ratio ligand/Cu, as a trinuclear complex with three phtptrz ligands coordinated in a monodentate manner to the extremities, is expected to increase even more the number of non-coordinated water molecules.

The synthesis of iron trinuclear chains, presenting an important number of water molecules, as well as the study of their ST would also be very interesting for a better understanding of the supramolecular interactions in **phtptrz** complexes.

These stable linear trinuclear copper complex $[Cu_3(phtptrz)_{10}(H_2O)_2](SiF_6)_3 \cdot 44H_2O$ and $Cu_3(phtptrz)_8(H_2O)_4](ZrF_6)_3 \cdot 19H_2O$ present a strong ferromagnetic coupling between adjacent copper ions. *J* value is comparable with that observed in the complex $[Cu_3(Ettrz)_9(H_2O)_3](CF_3SO_3)_6$, ($J = +6.8$ cm^{-1}, $g = 2.11$), where Ettrz = 4-ethyl-1,2,4-triazole[60], which appeared to be weakly ferromagnetic, but is

different from that found in the complexes $[Cu_3(H_2ahmt)_6Cl_4]Cl_2$ (J = - 16.9 cm^{-1}, g = 2.00), where H_2ahmt = 4-amino-3,5-bis(hydroxy-methyl)-1,2,4-triazole[61], and the 1D chain $[Cu(hyetrz)_3](ClO_4)_2 \cdot H_2O$ (J = - 0.59 cm^{-1}, g = 2.03) where hyetrz = 4-(2'-hydroxy-ethyl) -1,2,4-triazole [57], which present a global antiferromagnetic behaviour.

The ferromagnetism found for these compounds could be related to a non-planarity of the bridging network, which significantly reduces especially the antiferromagnetic part of the interaction to the extent, enabling the ferromagnetic part to be predominant ($J = J_{AF} + J_F$). The Cu…Cu separation is large (> 3Å, Table 35), indicating that no direct exchange mechanism is likely to contribute to the magnetic coupling. Therefore, the strong ferromagnetic coupling in **28** and **29** is ascribed solely to interactions within the central-terminal Cu(II) pairs. The moderately weak intermolecular interactions observed in **29**, compared to **28**, can be explained by the intense hydrogen bonding network (see Figure 77) in which the coordinated SiF_6^{2-} is involved.

A possible explication is that the unpaired electron for the d^9 ion resides in the $d(x^2 - y^2)$ orbital, with any spin density in the direction of the axially coordinating 1,2,4-triazole ligands. The magnitude of the ferromagnetic interaction between Cu(II) ions can, therefore, be explained by the exchange pathway involving the σ orbitals of the *N*1,*N*2-phtptrz bridging triazole network.[57] Even if the $d(x^2 - y^2)$ orbitals located on the Cu(II) ions are favorably oriented to give a significant overlap on the 1,2,4-triazole ligand linking the metal(II) ions, the Cu-N distances and between Cu1 and Cu2 are quite longer. Consequently, the main pathway for the ferromagnetic interactions may proceeds through the triazole ligand. Nevertheless, the

bridging geometry of the phtptrz ligand involves a Cu1-N11-N12 angle normal, equal to about 120° (for **28**) and 125° (for **29**). These features lead to a rather efficient propagation of the ferromagnetic interactions.

The crystalline structure of two trinuclear copper compounds with the phtptrz, $[Cu_3(phtptrz)_{10}(H_2O)_2](SiF_6)_3 \bullet 44H_2O$ and $[Cu_3(phtptrz)_8(H_2O)_4](ZrF_6)_3 \bullet 19H_2O$, highlighted the presence of a very important number of non-coordinated water molecules. The synthesis of linear trinuclear complexes, having extremities containing only mono-dentate **phtptrz**, $[Cu_3(phtptrz)_{12}]A_3.nH_2O$, would certainly allow to increase even more the volume available for the solvent and therefore the number of non-coordinated molecules inserted in the lattice of the system $[Cu_3L_{12-x}(H_2O)_x]^{3+}$.

The crystalline structures of these compounds also show the presence of supra-molecular interactions: aromatics and hydrogen bonds. If we extrapolate these systems to the iron(II) one, the presence of supra-molecular interactions in these trinuclears suggests that polymeric complexes in iron chains with this ligand would present an important cooperativity. However the gradual pace of the ST for these compounds could therefore be explained by the presence of the propyl spacer, capable to play a role of shock absorber blocking the elastic propagation from one iron(II) ion to another.

The use of anions with an important volume and ligands with a voluminous group such as phtalimido opens a new way in the synthesis of molecular materials with diverse ST properties. The presence of a voluminous anion produces an isolation of the chains through distancing allowing thus a better understanding of the internal cooperative behavior of a chain.

Notes and references

[1] Y. Garcia, P. Guionneau, G. Bravic, D. Chasseau, J. A. K. Howard, O. Kahn, V. Ksenofontov, S. Reiman, P. Gutlich. *Eur. J. Inorg. Chem.* **2000**, *1*(7), 1531-1538.

[2] A. D. Naik, B. Tinant, K. Muffler, J. A. Wolny, V. Schunemann, Y. Garcia. *J. Solid State Chem.* **2009**, *182*, 1365-1376.

[3] Y. Garcia, V. Niel, M. C. Munoz, J. A. Real. *Top. Curr. Chem.* **2004**, *233*, 229-257.

[4] T. Fujigaya, D. L. Jiang, T. Aida. *J. Am. Chem. Soc.* **2005**, *127*(15), 5484-5489.

[5] S. Schlamp, B. Weber, A. D. Naik, Y. Garcia. *Chem. Comm.* **2011**, *47*(25), 7152-7154.

[6] Y. Boland, A. Attout, J. Marchand-Brynaert, Y. Garcia. *Journal of Chromatography A* **2007**, *1141*(1), 145-149.

[7] M. M. Dîrtu, A. Rotaru, D. Gillard, J. Linares, E. Codjovi, B. Tinant, Y. Garcia. *Inorg. Chem.* **2009**, *48*(16), 7838-7852.

[8] D. Chwaleba, M. M. Ilczyszyn, M. Ilczyszyn, Z. Ciunik. *J. Mol. Struct.* **2007**, *831*(1-3), 119-134.

[9] K. Nakamoto. *Infrared and Raman Spectra of Inorganic and Coordination Compounds : Applications in Coordination, Organometallic, and Bioinorganic Chemistry*, **1997**.

[10] J. G. Haasnoot, G. Vos, W. L. Groeneveld. *Zeitschrift fur Naturforschung Section B-A Journal of Chemical Sciences* **1977**, *32*, 421.

[11] J. H. Adriaanse, S. H. C. Askes, Y. van Bree, S. van Oudheusden, E. D. van den Bos, E. Gunay, I. Mutikainen, U. Turpeinen, G. A. van Albada, J. G. Haasnoot, J. Reedijk. *Polyhedron* **2009**, *28*(14), 3143-3149.

[12] J. G. Haasnoot, G. Vos, W. L. Groeneveld. *Zeitschrift fur Naturforschung Section B-A Journal of Chemical Sciences* **1977**, *32*, 421.

[13] V. P. Sinditskii, A. E. Fogelzang, M. D. Dutov, V. I. Sokol, V. V. Serushkin, B. S. Svetlov, M. A. Poraikoshits. *Russ. J. Inorg. Chem.* **1987**, *32*(8), 1944-1949.

[14] M. M. Dîrtu, C. Neuhausen, A. D. Naik, A. Rotaru, L. Spinu, Y. Garcia. *Inorg. Chem.* **2010**, *49*(12), 5723-5736.

[15] P. Gütlich, A. Hauser, H. Spiering. *Angew. Chem. Int. Ed.* **1994**, *33*(20), 2024-2054.

[16] P. Gütlich, J. Jung, H. A. Goodwin. In: (Eds.: E. Coronado, P. Delhaès, D. Gatteschi, and J. S. Miller), *Molecular Magnetism: From Molecular Assemblies to the Devices*, **1996**, p. 327.
[17] Y. L. Wei, P. Sonar, M. Grunert, J. Kusz, A. D. Schlüter, P. Gütlich. *Eur. J. Inorg. Chem.* **2010**, *2010*(25), 3930-3941.
[18] O. Kahn. *Molecular magnetism*, VCH, **1993**.
[19] Y. Garcia, P. Guionneau, G. Bravic, D. Chasseau, J. A. K. Howard, O. Kahn, V. Ksenofontov, S. Reiman, P. Gutlich. *Eur. J. Inorg. Chem.* **2000**, (7), 1531-1538.
[20] Y. Garcia, V. Niel, M. C. Munoz, J. A. Real. *Top. Curr. Chem.* **2004**, *233*, 229-257.
[21] J. G. Haasnoot, G. Vos, W. L. Groeneveld. *Zeitschrift fur Naturforschung Section B-A Journal of Chemical Sciences* **1977**, *32*, 421.
[22] J. G. Haasnoot, G. Vos, W. L. Groeneveld. *Zeitschrift fur Naturforschung Section B-A Journal of Chemical Sciences* **1977**, *32*, 421.
[23] M. M. Dîrtu, C. Neuhausen, A. D. Naik, A. Rotaru, L. Spinu, Y. Garcia. *Inorg. Chem.* **2010**, *49*(12), 5723-5736.
[24] N. V. Bausk, S. B. Erenburg, L. G. Lavrenova, L. N. Mazalov. *Journal of Structural Chemistry* **1995**, *36*(6), 925-931.
[25] S. B. Erenburg, N. V. Bausk, L. G. Lavrenova, V. A. Varnek, L. N. Mazalov. *Solid State Ionics* **1997**, *101*, 571-577.
[26] N. Bausk, S. B. Erenburg, L. Mazalov, L. Lavrenova, V. Ikorskii. *J. Struct. Chem.* **1994**, *35*(4), 509-516.
[27] S. B. Erenburg, N. V. Bausk, V. A. Varnek, L. G. Lavrenova. *Journal of Magnetism and Magnetic Materials* **1996**, *158*, 595-596.
[28] Y. Garcia, P. J. van Koningsbruggen, R. Lapouyade, L. Fournes, L. Rabardel, O. Kahn, V. Ksenofontov, G. Levchenko, P. Gutlich. *Chem. Mater.* **1998**, *10*(9), 2426-2433.
[29] H. Donald, B. Jenkins, H. K. Roobottom. *Inorg. Chem.* **1999**, *38*, 3609.
[30] K. B. Yatsimirskii. *Thermochemistry of Complex Compounds, Moscow* **1951**.
[31] J. A. Kitchen, N. G. White, M. Boyd, B. Moubaraki, K. S. Murray, P. D. W. Boyd, S. Brooker. *Inorg. Chem.* **2009**, *48*(14), 6670-6679.
[32] X. C. Zhang, Y. H. Chen, B. Liu. *Bull. Korean Chem. Soc.* **2008**, *29*(2), 511.

[33] F. Weldon, L. Hammarstrom, E. Mukhtar, R. Hage, E. Gunneweg, J. G. Haasnoot, J. Reedijk, W. R. Browne, A. L. Guckian, J. G. Vos. *Inorg. Chem.* **2004**, *43*(14), 4471-4481.
[34] E. J. Browne. *Aust. J. Chem.* **1975**, *28*(11), 2543-2546.
[35] Z. Song, H. Gao, G. Li, Y. Yu, Z. Shi, S. Feng. *Cryst. Eng. Comm.* **2009**, *11*(8), 1579-1584.
[36] J. Liu, Y. Song, Z. Yu, J. Zhuang, X. Huang, X. You. *Polyhedron* **1999**, *18*(10), 1491-1494.
[37] F. Barigelletti, L. Decola, V. Balzani, R. Hage, J. G. Haasnoot, J. Reedijk, J. G. Vos. *Inorg. Chem.* **1991**, *30*(4), 641-645.
[38] L. Decola, F. Barigelletti, V. Balzani, R. Hage, J. G. Haasnoot, J. Reedijk, J. G. Vos. *Chem. Phys. Lett.* **1991**, *178*(5-6), 491-496.
[39] E. A. Medlycott, K. A. Udachin, G. S. Hanan. *Dalton Transactions* **2007**, *0*(4), 430-438.
[40] H. A. Nieuwenhuis, J. G. Haasnoot, R. Hage, J. Reedijk, T. L. Snoeck, D. J. Stufkens, J. G. Vos. *Inorg. Chem.* **1991**, *30*(1), 48-54.
[41] R. Prins, R. A. G. Degraaff, J. G. Haasnoot, C. Vader, J. Reedijk. *J. Chem. Soc. , Chem. Comm.* **1986**, (18), 1430-1431.
[42] S. B. Sanni, H. Behm, P. T. Beurskens, J. P. Cornelissen, J. G. Haasnoot, A. T. H. Lenstra. *Journal of Crystallographic and Spectroscopic Research* **1987**, *17*(1), 81-89.
[43] S. B. Sanni, J. M. M. Smits, P. T. Beurskens, J. G. Haasnoot, J. Schild, A. T. H. Lenstra. *Journal of Crystallographic and Spectroscopic Research* **1986**, *16*(6), 823-832.
[44] M. Shakir, S. Parveen, N. Begum, P. Chingsubam. *Trans. Met. Chem.* **2004**, *29*(2), 196-199.
[45] O. G. Shakirova, L. G. Lavrenova, Y. Shvedenkov, G. A. Berezovskii, D. Y. Naumov, L. A. Sheludyakova, G. V. Dolgushin, S. V. Larionov. *Russian Journal of Coordination Chemistry* **2004**, *30*(7), 473-479.
[46] P. M. Slangen, P. J. vanKoningsbruggen, J. G. Haasnoot, J. Jansen, S. Gorter, J. Reedijk, H. Kooijman, W. J. J. Smeets, A. L. Spek. *Inorg. Chim. Acta* **1993**, *212*(1-2), 289-301.
[47] P. Stupik, W. M. Reiff, R. Hage, J. Jacobs, J. G. Haasnoot, J. Reedijk. *Hyp. Int.* **1988**, *40*(1-4), 343-345.
[48] E. Szlyk, A. Wojtczak, M. Jaskolski, M. Gilski, J. G. Haasnoot, J. Reedijk. *Inorg. Chim. Acta* **1997**, *260*(2), 145-150.
[49] P. J. van Koningsbruggen, K. Goubitz, J. G. Haasnoot, J. Reedijk. *Inorg. Chim. Acta* **1998**, *268*(1), 37-42.

[50] W. C. Velthuizen, J. G. Haasnoot, A. J. Kinneging, F. J. Rietmeijer, J. Reedijk. *J. Chem. Soc. , Chem. Comm.* **1983**, (22), 1366-1368.
[51] X. C. Zhang, Y. H. Chen, B. Liu. *Inorg. Chem. Comm.* **2008**, *11*(8), 876-878.
[52] D. Gillard,*Master Thesis UCL* . **2006**.
[53] K. Drabent, Z. Ciunik. *Chem. Commun.* **2001**, (14), 1254-1255.
[54] Schmidt, M. U., Hu, C., Bats, J. W., and Kühne, J. 4-(2-Hydroxyethyl)-4*H*-1,2,4-triazole, an intermediate in the synthesis of iron-triazole spin-crossover compounds. Acta Crystallographica Section E 61, 4343-4344. 2005. Ref Type: Abstract
[55] O. G. Shakirova, A. V. Virovets, D. Y. Naumov, Y. G. Shvedenkov, V. N. Elokhina, L. G. Lavrenova. *Inorg. Chem. Comm.* **2002**, *5*(9), 690-693.
[56] J. K. Tang, H. M. Wang, P. Cheng, X. Liu, Z. Dai, Z. H. Jiang, S. P. Yan. *Polyhedron* **2001**, *20*(7ΓÇô8), 675-680.
[57] Y. Garcia, P. J. van Koningsbruggen, G. Bravic, P. Guionneau, D. Chasseau, G. L. Cascarano, J. Moscovici, K. Lambert, A. Michalowicz, O. Kahn. *Inorg. Chem.* **1997**, *36*(27), 6357-6365.
[58] C. Janiak. *J. Chem. Soc. , Dalton Trans.* **2000**, *21*(21), 3885-3896.
[59] Y. Song, P. Gamez, O. Roubeau, I. Mutikainen, U. Turpeinen, J. Reedijk. *Inorg. Chim. Acta* **2005**, *358*(1), 109-115.
[60] W. Vreugdenhil, J. G. Haasnoot, M. F. J. Schoondergang, J. Reedijk. *Inorg. Chim. Acta* **1987**, *130*(2), 235-242.
[61] P. J. van Koningsbruggen, J. W. Vanhal, R. A. G. Degraaff, J. G. Haasnoot, J. Reedijk. *Dalton Trans.* **1993**, (14), 2163-2167.

PART II: Molecular sensors based on α – and β – amino-acid

Amino acids are the building blocks of proteins and the central trunk from which many diverse applied fields have branched out.[1] Not only amino-acids but also their derivatives have surfaced into biochemistry, pharmacology, peptide station, bio-mimics, enantioselective catalysis and separation, non-linear optics and materials science[1-3]

With predictable design strategy of transamination, for the first time 1,2,4-triazole derivatives of α- and β-amino-acids and -esters were designed and introduced to produce new SCO 1D coordination polymers.

Thus, in this second part of the work, the aim is to understand the impact of the influence of the functional groups on the thermochromic properties, for a new class of SCO materials. The advantage of these molecules is their natural miscellaneous framework with rich functional groups which is amenable to copious derivatization, and also their structural diversity.

Chapter VI: Superlative scaffold of 1,2,4-triazole α-amino-acid steering molecular architecture, increasing dimensionality from 1D to 3D*

Introducing remarks

Thus this chapter has been directed to make novel high dimensional networks containing Cd(II) and Cu(II) with 4H-1,2,4-triazol-4-yl acetic acid, **HGlytrz** (Figure 88). This versatile synthon is also polydentate by having *N*1,*N*2-coordination sites at one end with carboxylate pincer at the other end, an ideal configuration for self assembly. **HGlytrz** belongs to a family of flexible molecules having symmetric or asymmetric multi-donor moieties, as found for instance for 1,2-bis(1,2,4-triazol-4-yl)ethane, 4,4´-bis(1,2,4-triazole), tetrazole-1-acetic acid, which are capable of bridging metal ions in infinite connectivity and were thus sought in crystal engineering as they favor self assembly MOFs construction.[4-16] Crystal structure determination of two Cd(II) CPs, **[Cd(HGlytrz)(Glytrz)Cl]·2H_2O (30)** and **[Cd_2(Glytrz)$_2Cl_2$] (31)** was herein undertaken to navigate the self-assembly process and $N_{2(g)}$ and $H_{2(g)}$ gas adsorption studies were performed. Possibility of using these complexes as 'soft' sacrificial precursors to produce CdO with shape and phase selectivity is also described.

HGlytrz it is recognized also for its ability of spontaneous crystallization in a chiral, non-centrosymmetric space group despite its achiral origin.[17] This combination give thus for the first time this potentially multidentate

*Adapted from : M. M. Dîrtu, C. Neuhausen, A. D. Naik, A. Léonard, F. Robert, J. Marchand-Brynaert, Bao-Lian Su, Y. Garcia, *Cryst. Growth & Design* **2011**, *11*, 1375*;* A. D. Naik, M. M. Dîrtu, A. Léonard, B. Tinant, J. Marchand-Brynaert, B. L. Su, Y. Garcia, *Cryst. Growth & Design* **2010**, *10*, 1798.

molecule for engineering a porous MOF of nanoball type, **[$Cu_3(\mu_3$-O)(HGlytrz)$_3\cdot(H_2O)_3$]$BF_4\cdot H_2O$** (**32**) which encompasses a voluminous void and laid a foundation for a new family of porous MOFs.

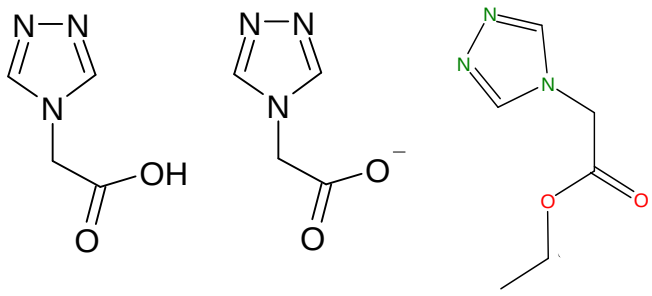

(a) (b) (c)

Figure 88 Molecular structures of (a) **HGlytrz**, (b) **Glytrz** and **GlytrzE**

Advantage of such systems would be the diverse set of coordinating groups on the same ligand backbone: a carboxylic group and an *N*-heterocycle. To do so, we have recently reported a simplified transamination procedure for converting the amine functional group of glycine into 1,2,4-triazole.[18] Moderate yield and delicacy in synthesis lead us to revisit the synthesis and to employ here an even more attractive precursor, an ester of glycine, affording a novel molecule (**GlytrzE**) which can be easily hydrolyzed to 4H-1,2,4-triazol-4-yl acetic acid (**HGlytrz**). The molecular framework of **HGlytrz** is built from a 1,2,4-triazole head and a carboxylic tail, both of which are known for their diverse coordinating ability, separated from conformably flexible methylene group, which can form mixed coordination environment around metals (Figure 89).

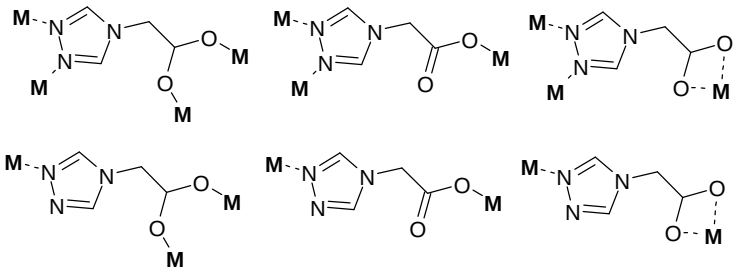

Figure 89 Possible coordination preferences of 1,2,4-triazole and carboxylic groups.

Results and discussions

Synthesis and general characterization

Transamination is a good synthetic strategy to build 1,2,4-triazoles from primary amines. Ever since its first report by Bartlett and Humphrey,[19] there were hardly any efforts to exploit this versatile method in synthetic chemistry. During our investigation on 4,4'-bis-1,2,4-triazole synthesis, a celebrated precursor for iron(II) spin crossover,[20] we simplified the existing method.[18] Thus we revise the synthetic route wherein we started with glycine ethyl ester (Figure 90). This reaction not only gave a new molecule, ethyl 4H-1,2,4-triazol-4-yl-acetate (**GlytrzE**) which can be easily purified by flash column chromatography but also the hydrolysis of **GlytrzE** gave almost quantitative yield of **HGlytrz**. This molecule is an appealing "synthon" bearing triazole and carboxylic group on the same backbone.

Reaction of **HGlytrz** with $CdCl_2$ in water afforded a white powder. Recrystallization with and without solvothermal treatment provided either large rectangular blocks formulated as [Cd(**HGlytrz**)(**Glytrz**)Cl]$\cdot 2H_2O$ (**30**) or hexagonal crystals formulated as $[Cd_2(\mathbf{Glytrz})_2Cl_2]$ (**31**).

Reaction of **HGlytrz** with aq. $Cu(BF_4)_2$ in water afforded an immediate blue insoluble solid that precipitated from a dark green solution.

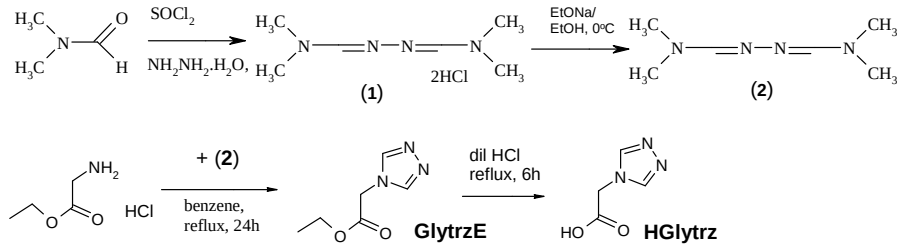

Figure 90 Synthetic protocol used for ethyl 4H-1,2,4-triazol-4-yl-acetate (**GlytrzE**) and 4H-1,2,4-triazol-4-yl acetic acid (**HGlytrz**).

After separation of this solid, slow evaporation of the green filtrate for a period of 2 weeks afforded single crystals of **32** in low yield. A higher yield (35 %) was obtained when **GlytrzE** was reacted with aq. $Cu(BF_4)_2$ to afford dark blue cubic crystals of **32** by slow evaporation of the mother solution. The idea was not only to have control over crystal growth to form the thermodynamically favored product by slowly hydrolyzing the ester moiety but also to encode the intrinsic tendency of –COOH over ester group to form supramolecular aggregation through its unique coordination mode (Figure 89). Prolonged stirring of the above reaction mixture leads to isolation of microcrystalline powder of **32**. Both **GlytrzE** and **HGlytrz** are easily soluble in water, alcoholic and halogenated solvents, whereas **32** is soluble in only in DMF.

SEM analysis qualitatively confirmed the morphology of microcrystal in bulk samples with that of millimeter size crystals.

Thin blocks of **30** of around 20 μm length and hexagonal plates of 5-10 μm length in **31**, were observed (Figure 91). FTIR spectra of **30** and **31** provide useful information about the coordination mode of 1,2,4-triazole and carboxylic group to the metal (Figure 92). The carboxylic group of **HGlytrz** shows two strong stretching vibrations corresponding to (-C=O) and (C-O) at 1731 cm^{-1} and 1197 cm^{-1}, respectively.[17]

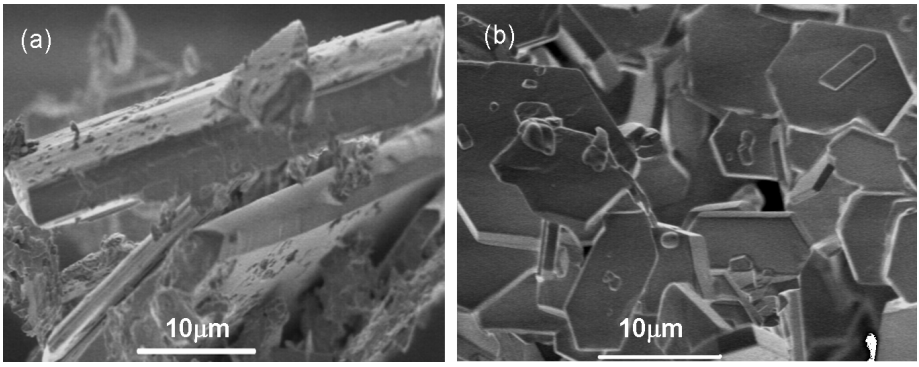

Figure 91 SEM images of **30** (a) and **31** (b), prepared respectively from solvothermal and classical synthesis.

These vibrations are almost unchanged in the FTIR spectrum of **30** (1739 cm^{-1} and 1234 cm^{-1}) thus confirming the non-involvement of the -C=O group in coordination whereas the (-C=O) stretch vanishes in **31** together with the apparition of new broad bands around 1698 cm^{-1}, thus confirming involvement of carboxylate in coordination along with triazole ring. For **HGlytrz**, the band assigned to ring torsion of triazole at ν = 629 cm^{-1}, the $\nu_{C=N}$ stretching vibration at 1568 cm^{-1}, and the N-N stretching band at ν = 1024 cm^{-1}, are all slightly shifted upon complexation in **31** to ν = 630 cm^{-1}, $\nu_{C=N}$ = 1573 cm^{-1} and ν_{N-N} = 1042 cm^{-1}, respectively. In **31**, bands are assigned to ring torsion of 1,2,4-triazole at ν = 628 cm^{-1}, $\nu_{C=N}$ = 1592 cm^{-1} and ν_{N-N} = 1033 cm^{-1} also confirms coordination to Cd(II). Electronic and luminescence spectra of **HGlytrz** and **31** were recorded on solid samples at 293 K. Diffuse reflectance spectra of **HGlytrz** show strong bands at 258 nm, with a shoulder at 294 nm and are assigned to intra-ligand transitions (Figure 93).[21, 22] They appear in **31** around the same region (252 nm, 290 nm) but with slightly reduced intensity which could be due to alteration of electron density in the ligand due to coordination. **HGlytrz** is weakly fluorescent. Emission spectra of **31** show a broad intense band around 465 nm with a shoulder at 492 nm when excited with 290 nm (Figure 93), which was

assigned to ligand to metal charge transfer transition.[21, 22] The thermal stability of **31** determined by TGA is relatively high. After an initial loss of moisture around 40°C, the compound is stable until 170°C and thereafter decomposes in four ill-defined steps (Figure 109e). Only some prominent peaks in experimental XRPD of **31** matches to that of simulated one from CIF file, which could be due to slight uptake of moisture by **31** resulting in minor network reshuffle (Figure 94).

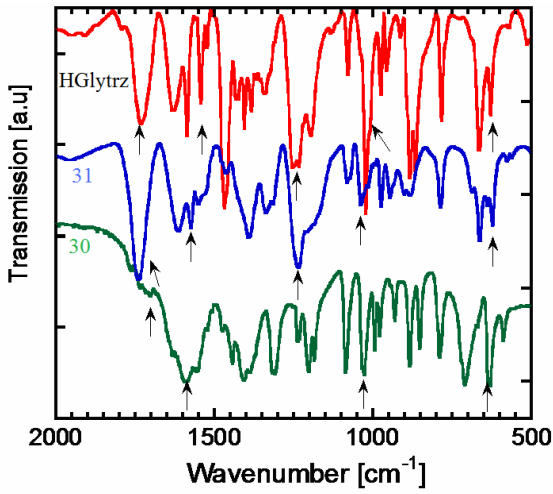

Figure 92 FTIR of **HGlytrz**, **30** and **31**. An expanded region is shown between 500 to 2000 cm^{-1}. Arrows are used to mark relevant vibrations (see text).

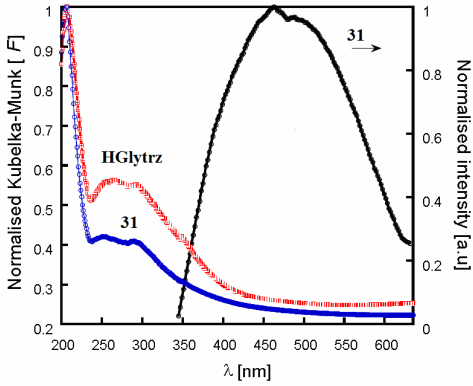

Figure 93 Solid state diffuse reflectance and emission spectra (black line) of **31** and **HGlytz** (red line) at 293 K with λ^{ex}= 290 nm.

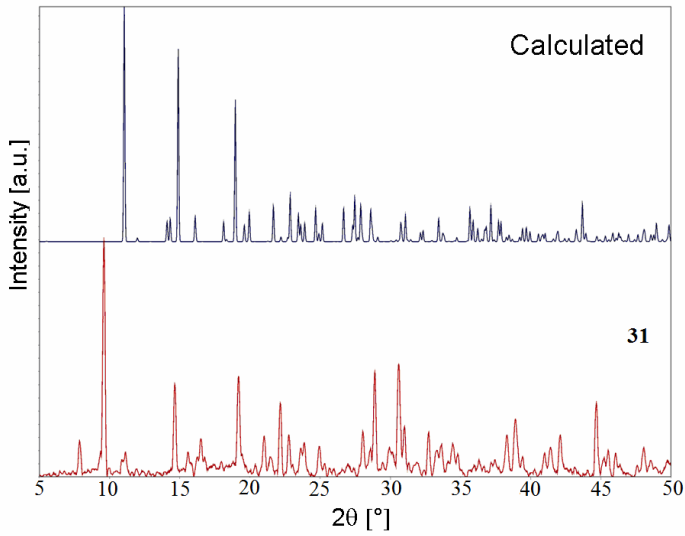

Figure 94 Comparison of experimental XRPD of **31** and from CIF file.

Compound **32,** $[Cu_3(\mu_3\text{-}O)(\mathbf{HGlytrz})_3\cdot(H_2O)_3]BF_4\cdot H_2O$, was characterized by elemental analysis, IR, Raman, Uv-vis, thermogravimetric analysis, SEM-EDX (Figure 117), X-ray powder diffraction, and by a X-ray crystal structure analysis. Two sharp Raman bands at 2980 and 2944 cm^{-1} are assigned to the ν_a (CH_2) and ν_s (CH_2) modes, respectively. The strong, broad band around 1731 cm^{-1} identified for -COOH group by IR spectroscopy for **HGlytrz** is shifted to 1650 cm^{-1} in **32** due to its coordination to copper. The asymmetric and symmetric stretching bands for coordinated carboxylate anions with corresponding $\Delta[\nu_{asym}(\text{-COO-})\text{-}\nu_{sym}(\text{-COO-})] \sim 266$ cm^{-1}, agrees well with the presence of carboxylate functional group coordinated in an unidentate fashion,[23] a feature also confirmed by the X-ray crystal structure (*vide infra*). Very intense splitted bands around 1091 cm^{-1} are assigned to the BF_4^- anion.[23] The Raman shifts identified at 1732(w) and 1412(s) cm^{-1} in **HGlytrz** are assigned to the asymmetric and symmetric vibrations of carboxylic group that almost vanish in **32**, a weak signal being only observed at 1381 cm^{-1}. The diffuse reflectance spectrum of **32** displays a broad absorption band in the range 460-900 nm attributed to the *d-d* transition, in

which three maxima at 620 and 670 nm and a shoulder at ~ 580 nm are observed (Figure 95).[5]

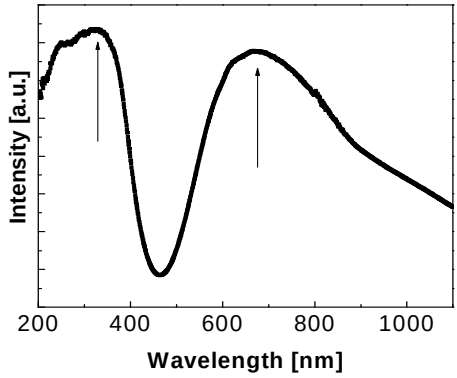

Figure 95 Diffuse reflectance spectrum of **32** at 293 K. The arrows indicate maximum absorption bands within the *d-d* region.

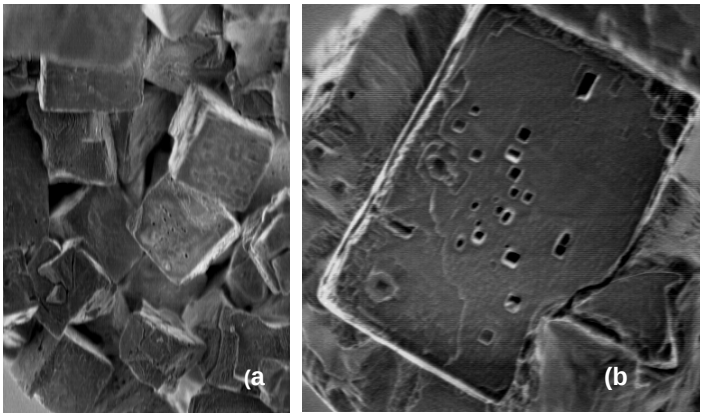

Figure 96 (a) SEM micrograph of polycrystalline sample of **32** revealing cubic crystals. (b) An enlarge view shows approximately square shaped openings (500 x 500 nm) on the crystal surface.

A close look on the morphology of the crystals of **32** by Scanning electronic microscopy (SEM) reveals cubic shaped crystals with nearly square shaped openings, likely originating from solvent loss or crystals defects, which are approximately, 500 x 500 nm in dimension (Figure 96). Indeed, because SEM experiments are run in vacuum, evacuation of lattice solvent molecules

is expected. Noteworthy is that these crystals are not degraded under such treatment.

Crystal structure study of ethyl-4H-1,2,4-triazol-4-yl acetic acid (HGlytrz)[†]

The recrystallization of ethyl-4H-1,2,4-triazol-4-yl acetic acid (**HGlytrz**) from methanol results in colorless single crystals. **HGlytrz** crystallizes in the Fdd2 polar space group with 16 molecules in the asymmetric unit. A perspective view of the molecule is shown in Figure 97.

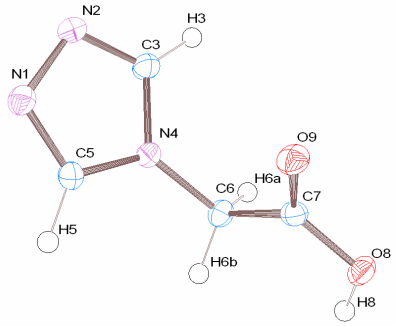

Figure 97 Thermal ellipsoidal plot of the unit cell of **HGlytrz** with atom labeling.

Crystallographic data are given in Table 36 and bond distances and bond angles are given in Table 37. The molecule is made of two planes, made by the triazole ring and by the -CH_2-COOH group, which are mostly perpendicular to each other. Indeed, the dihedral angle between the mean planes through N1-C5 and N4-O9 is 83.7(1)°. The molecular units are not isolated; they are linked to each other by intermolecular hydrogen bonding interactions (Table 38) forming a pseudo-2D arrangement along the *b* axis (Figure 98).

[†] This structure was solved by Prof. B. Tinant (UCL).

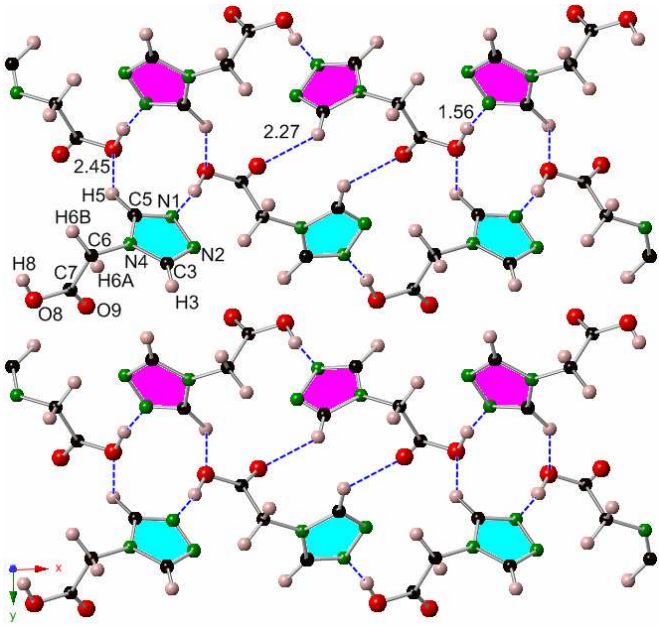

Figure 98 View of the antiparallel chains of O-H···N and other subsidiary hydrogen bonding network as seen in the crystal packing of **HGlytrz**. Opposite 1D chains are marked with pink and cyan colors. The d (H···A) distances are given in Å.

The hydrogen bonding located between the nitrogen atoms of triazole ring and the hydroxy group from the carboxylic part (O-H8···N1, 2.570(3) Å) in *b* direction is strong, as evidenced by the angle of 171(2)° which tends to linearity (Table 38). The other source of H-bonding are weak C-H···O interactions between the two C-H of the triazole and the O8 and O9 of the carboxylic acid groups with angles of 129(2)° and 130(2)° indicating moderate strength (Table 38). The origin of the non-centrosymmetry of the crystal structure may be found in the electronic asymmetry [24] of **HGlytrz** and in the packing of the molecular units.[25-28]It is to be noted that the direction of 1D chains of H-bonding (O-H8···N1) are antiparallel (Figure 98) netted by the inter-chain C-H···O bonding paralyzing further the symmetry.[29, 30] Such a non centrosymmetric structure with electric polarization may exhibits non linear optical (NLO) effects such as a second

harmonic generation (SHG).[31] It has to be noted that crystal packing supported by multiple secondary interactions has skipped the less favorable dimmer configuration through H-bonding between carboxylic groups. The 1,2,4-triazole head and carbonyl of carboxylic acid group occupy *cis* position with respect to each other as in most of the glycine derivatives.[32]

Present ligand **HGlytrz** is the premier member of triazole-carboxylate family whose crystal structure has been determined. Glycine and its derivatives have long been the focus of biochemists since they are constituents of proteins and enzymes and major inhibitory neurotransmitters in spinal cord and brain stem of vertebrate nervous system.[32] Determination of the dihedral angles between the plane containing methylene spacer with 1,2,4-triazole ring and also with carboxylate plane was necessary to understand the spatial arrangement of this molecule not only for the present fabrication of MOF but also possibly in drug chemistry.[33] Its ability to create supramolecular interactions in un-complexed form and possibly in MOF could be decisive for the better understanding of the self assembly process in MOF. A similar multifunctional ligand tetrazole-1-acetic acid with carboxylate and tetrazolyl ring on the same framework was also recently reported.[15]

Crystal structure study of ethyl-4H-1,2,4-triazol-4-yl-acetate (GlytrzE)‡

The recrystallization of **GlytrzE** from methanol upon slow evaporation, afforded needle shaped colorless single crystals.

‡ This structure was solved by Prof. B. Tinant (UCL).

GlytrzE crystallizes in a non-centrosymmetric tetragonal space group (P 41 polar) with four molecules in the asymmetric unit. A perspective view of the molecule is shown in Figure 99a. Crystallographic data are given in Table 36 and bond distances and angles are given in Table 37.

The crystal structure shows two nearly perpendicular planes containing 1,2,4-triazole ring and $–CH_2COOCH_2$- moiety (ø, C5-N4-C6-C7=81°). The later bearing terminal CH_3 group deviates from perpendicularity by 35°. The two extremities of **GlytrzE**, the triazole and the ethyl group forms hydrophilic and hydrophobic part respectively with a bent spacer that could establish secondary interactions due to the presence of carboxylate group (Figure 99a). The molecular units are not isolated and their conformations are influenced by several intra- and intermolecular contacts. Triazole and carboxylate groups could form an acceptor type H-bond whereas CH_2 (C6-H6B) of the spacer and CH of the triazole ring (C3-H3) could form donor type H-bonds. Mutual orientations of these potential groups and are crucial for the self- assembly process. The H-acceptor group (-C7=O8) on the spacer is situated *trans* to the H-donor (C6-H6B) which is ideal for supramolecular chain propagation. With these encoded supramolecular logistics the molecule translate itself during the spontaneous self-assembly process leading to an astonishing supramolecular helicity. The helicals are exclusively constructed from the complimentary and slightly parallel (N2-N1-H6B = 93° and N1-N2-H3 = 103°) infinite H-bonding between triazole moiety (acceptor-head) and spacer (donor-side) belonging to neighboring molecules in 'head-side connectivity' fashion along '*c*' direction(N1-H6B(C6)=2.438Å, and N2-H3(C3)=2.383Å with C6-H6B-N1=162.19°, and C3-H3-N2=155.77°). Each helical turn comprises nearly eighth molecules and thus the helicate is significantly elongated with approximately 20 Å pitch height that means to a length of two crystallographic unit cell in 'c' direction (*c* =10.2Å). This leaves behind a nearly square shaped cavity with a distance of 6.391 Å

between opposite spacer (C3H3···H3C3). Each helicate connects neighboring helicates further by H-bonding, this time involving C7O8···H5C5 = 3.326 Å (Table 38). This helical arrangement explicitly results in chirality producing single handed helicity around principal axes and the close packing of such single stranded homochiral helicates in two directions constitute 2D-helical network. The helical twist of the strand results from the directional H-bonding supplemented by significant torsion in the spacer. Thus the inherent electronic and structural asymmetry of **GlytrzE** and the H-bonding constituting helicity in the crystal packing explain the origin of the non-centrosymmetry of the crystal structure[24-28] Such conformational statistics on spatial arrangements of functional groups of a designed molecule are vital for constructing desired 1D SCO coordination polymers. **GlytrzE** is the first member of the triazole functionalized amino acid ester whose crystal structure has been determined, after ethyl-4H-1,2,4-triazol-4-yl acetic acid, its acid counterpart[17] was reported earlier to understand the supramolecular self assembly and crystal engineering of MOF.

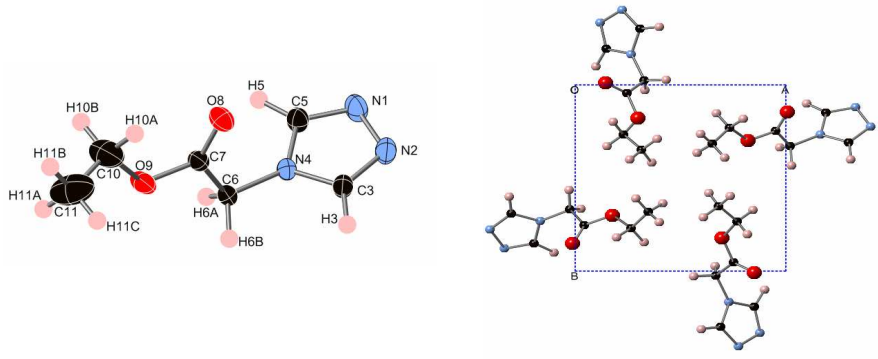

(a) (b)

Figure 99 (a) Perspective view of thermal ellipsoid plot of a molecular unit in **GlytrzE**, with atom labelling; (b) view of **GlytrzE** in the unit cell.

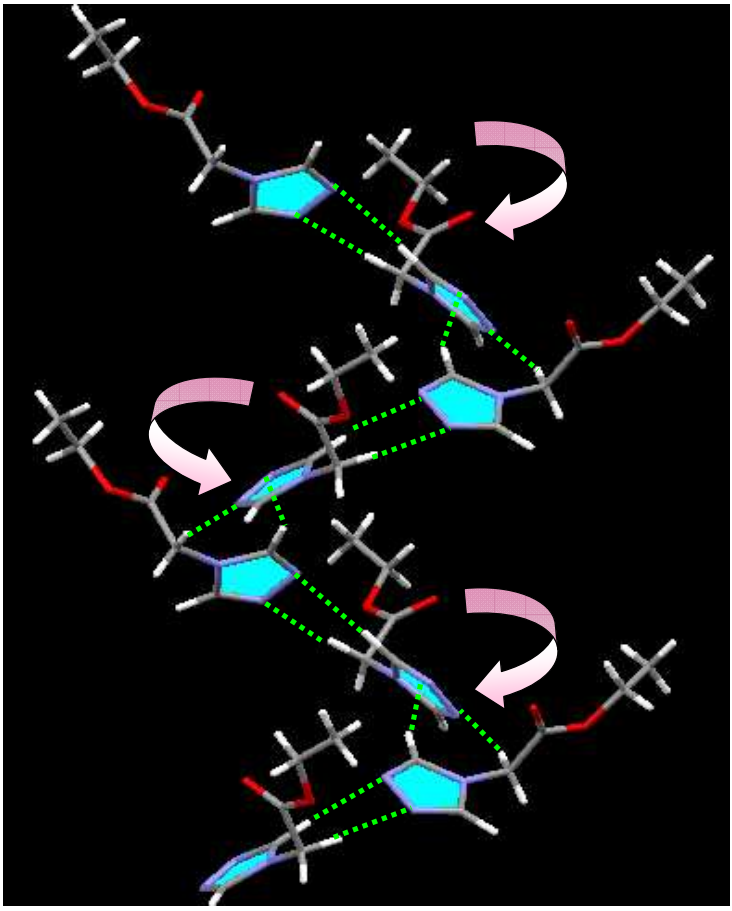

(c)

Figure 99 (c) View showing homochiral helicate in **GlytrzE**.

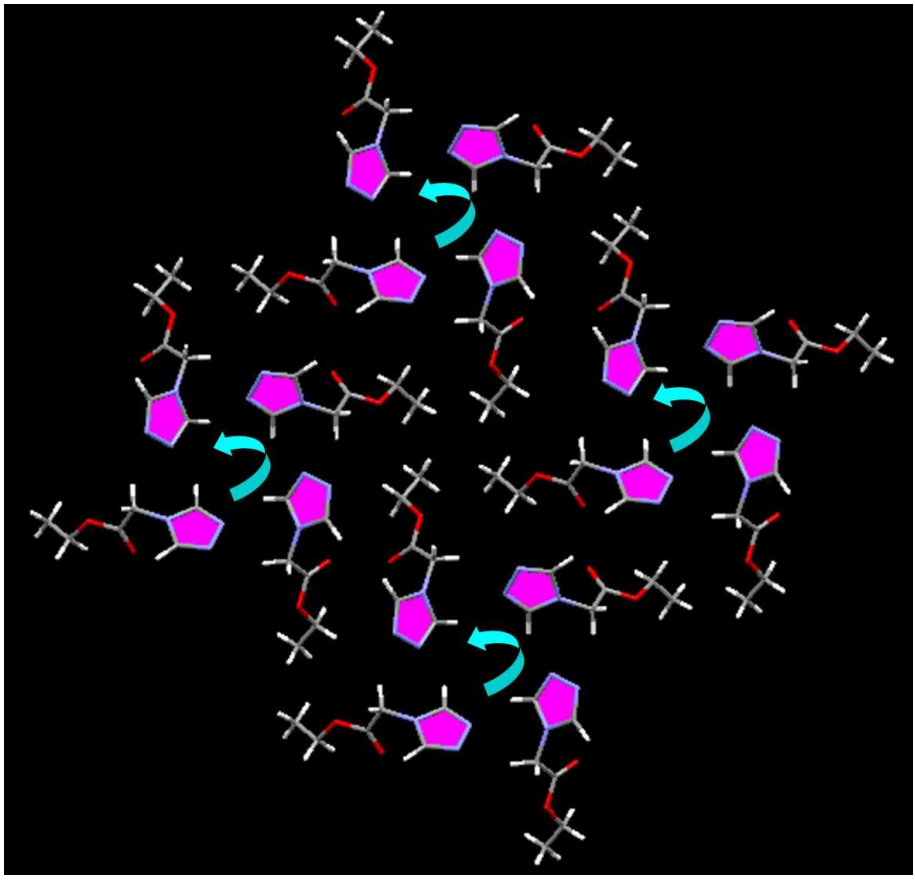

(d)

Figure 99 (d) Perspective view of 2D helicates in **GlytrzE**.

Crystal structure study of [Cd(HGlytrz)(Glytrz)Cl]·2H$_2$O (30)[§]

[Cd(HGlytrz)(Glytrz)Cl]·2H$_2$O (**30**) crystallizes in the monoclinic space group $P2_1/c$, with Z = 4. Crystallographic data are provided in Table 39 and a selection of bond lengths and angles are given in Table 40. The asymmetric unit of **30** is shown in Figure 100a. Each Cd atom is coordinated by two chloride atoms (Cd-Cl, 2.656(1), 2.616(6) Å), in axial position and four nitrogen atoms (Cd-N1, 2.343(3) Å, Cd-N2, 2.312(3) Å, Cd-N4, 2.374(3) Å and Cd-N5, 2.339(3) Å) belonging to four different ligands forming the equatorial plane, thus completing an octahedral geometry. The elongation in the axial direction is evident from the bond lengths. The triple bridge that is made up of one *μ*-chloride and two *μ-N1,N2*-1,2,4-triazole of different **HGlytrz/Glytrz** (Figure 100b) connect neighboring cadmium centers leading to a 1D coordination polymer with Cd···Cd distance of 3.845 Å. The 1,2,4-triazole rings of **Glytrz** are fairly planar; the deviation from the least squares plane through the ring atoms is smaller than 0.02(1) Å. There are number of interesting similar Cd MOFs of 1,2,4-triazole derivatives.[34] Lu et al. reported a series of Cd coordination compounds ranging from 0 to 3D thanks to substitution of the 1,2,4-triazole or variation of the anion.[21, 22]

In a coligand modulated Cd-1,2,4-triazolate framework, tri and pentacadmium clusters were reported with a slightly longer Cd···Cd distance (4.049 Å) than for **30**.[21, 22] Interesting cases of μ-OH$_2$ bridged 3,5-disubstituted 1,2,4-triazole systems and polymer chains containing μ_3-Cl were also reported[35] It is worth mentioning too the series of 3D Cd-triazolate complexes involving anions like F^-, Cl^-, Br^-, I^-, NO_3^-, SO_4^{2-} which

[§] This structure was solved by Dr. C. Neuhausen (EPFL)

show diversity in coordination.[36, 37] What makes **30** unique is related to the dual contribution of its ligand system. Indeed, **HGlytrz**/**Glytrz** not only acts as a bridging ligand, but also as anion due the presence of a deprotonated carboxylate group in **30**. Interestingly, the carboxylic group is kept away from the coordination sphere, a crucial point for the design of 1D coordination polymer involving switchable iron(II) spin crossover centers with a MN_6 core.[20, 38]

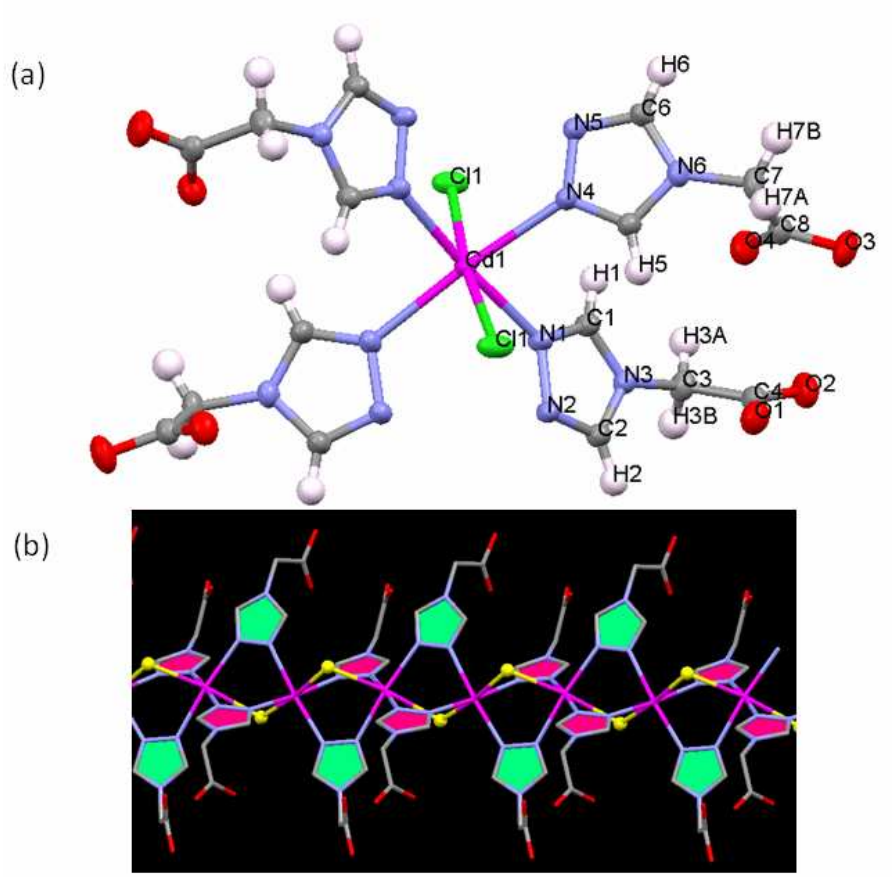

Figure 100 (a) Asymmetric unit in **30**; (b) Crystal packing depicting 1D chain in **30** deprotonated ligands forms separate plane (colored in pink).

The ligands in the 1D chain are arranged in zig-zag fashion along the *a* direction (Figure 100). The three planes containing ligands are mutually perpendicular around cadmium ions and are threaded by μ-Cl anions as intersecting points. It was difficult to locate the hydrogen atoms in structure refinement on the carboxylic group of the ligand, but a comparison of bond length of -C-O and -C=O between ligands contributing to the two planes with that of free **HGlytrz** gave evidence of deprotonation. In the free ligand,[17] the -C=O distance is 1.215(3) Å and the –C-O$^-$ bond length is 1.307(2) Å. It is interesting to note that the ligand exhibiting dual nature forms an exclusively separate plane (Figure 100b, plane colored in pink) with shortened C(4)-O(1) = 1.255(5) Å and C(4)-O(2) = 1.251(4) Å distances, which indicate resonance double bond nature as a result of deprotonation. The ligand molecule in the other plane shows bond lengths of C8-O3 = 1.306(4) and C8-O4 = 1.206(4) Å similar to free ligand. The consequence of the dual nature of the ligand, which exists in both protonated and deprotonated in the crystal structure of **30** can also be seen in the different bond angles, bond lengths and dihedral angles (Table 40). Although the environment around both Cd atoms is the same, there is a change in bond angles and distances. Chloride forms two unequal bonds with cadmium and all the Cd-N bond lengths are different as indicated above. Thus the CdN_4Cl_2 octahedron is distorted with a distortion parameter of $\Sigma = 20.44°$[39]. The opposite μ-*N1*,*N2*-triazole rings bridging two Cd atoms are different with respect to bond angles and distances within them and with cadmium. The tail ends bearing carboxylic groups of the ligands of one plane forming this 1D network face in the same direction. Similarly this region is also shared by a plane from neighboring chain creating a super hydrophilic region (Figure 101). The formation of triple μ-*N*1,*N*2-triazole bridging, as found for instance for $[Cu(hyetrz)_3](CF_3SO_3)_2 \cdot H_2O$,[16] or double chloro- bridges plus a single μ-*N*1, *N*2-triazole bridging,[34] was not favored in this network, due to the possibility for the ligand to act as monoanionic. A significant deviation

of planes containing the carboxylic group with respect to the triazole planes in **Glytrz** of **31**, was noted. In **HGlytrz**, these planes are orthogonal but in **30** they deviate by nearly 21° (torsion angle (ø), C2-N3-C3-C4, 69.13°) and 25° (ø, C5-N6-C7-C8, 65.40°). This deviation is not only due to sterical reasons but also to secondary interactions in the super hydrophilic region. The hydrophilic region is rich in hydrogen bonds, the lattice water molecules being the epicentres of the H-bonding network. Carboxylic groups also greatly contribute to favor a dense H-bonding network. The lattice water molecule which is absent in **31** (described in following section), forms two H-bonds with the carboxylic groups of different 1,2,4-triazoles from different planes (C4-O2···O6, 2.751 Å with an angle C4-O2-O6 of 105.08° and C8-O3···O6, 2.568 Å and an angle of C8-O3-O6 of 119.25°). The deprotonated ligand forms additional H-bonds; one with 2.764 Å (O1···H(O5)) with lattice water which in turn forms an H-bond with the chloride bridge (Cl···H(O5), 3.228Å). As a consequence, the bond angle of 122.64° for -COO^- in the free ligand is stretched out to 127.02° in the complex. The CH_2 spacer is also involved in H-bonding with lattice water molecules with 2.628 Å (C3(H3A)···O1). The proton on the triazole ring C6(H6)···O5 forms a strong H-bond with 2.242 Å. Interestingly, the bridging mode of two ligands and one chloride around two Cd atoms create a bicyclo 7-membered metallomacrocycle ring.[40] This 1D coordination network is totally different from the 2D helical structure in **31** despite sharing the same components, thus indicating the role of reaction conditions in the self-assembly process.

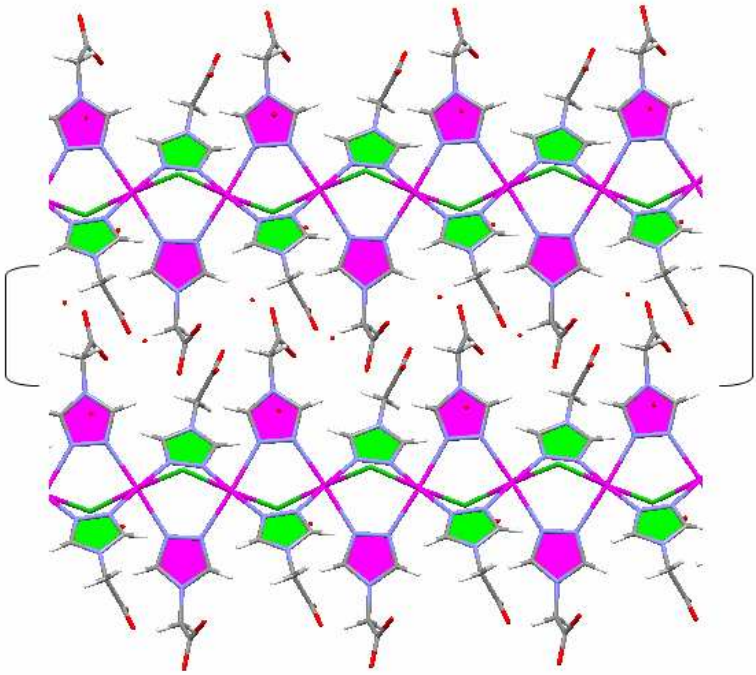

Figure 101 View of crystal packing of **30** showing hydrophilic interior (in *ab* plane).

*Crystal structure study of [Cd2(Glytrz)2Cl2] (31)***

$[Cd_2(Glytrz)_2Cl_2]$, **31** crystallizes in the non-centrosymmetric orthorhombic space group $P2_12_12_1$, with Z = 8. Crystallographic data are provided in Table 39 and a selection of bond lengths and angles is given in Table 41. Asymmetric unit is shown in Figure 102a. The self-assembling motif consists of two cadmium ions, five ligands and three chloride ions. Although both cadmium ions share the same central core of $CdN_2O_2Cl_2$, they differ in their bond distances and angles. Each Cd1 atom is coordinated by

** This structure was solved by Dr. C. Neuhausen (EPFL).

two bridging Cl atoms (Cd1-Cl11, 2.543(2) Å; Cd1-Cl5, 2.598(2) Å), two **Glytrz** molecules via the nitrogen atoms of the ring (Cd1-N6, 2.368(6) Å, Cd1-N2, 2.273(5) Å) and one **Glytrz** molecule via both O atoms of the carboxylate group (Cd1-O4, 2.274(4) Å; Cd1-O3, 2.516(4) Å) in a bidentate fashion (Figure 102a).

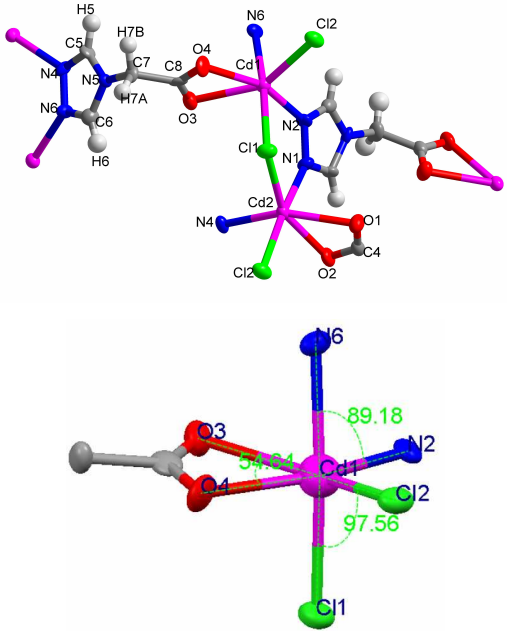

Figure 102 (a) Asymmetric unit in **31**; (b) Homo *cis* angles around cadmium.

The Cd2 has a similar environment with slight variation in the Cd2-N, Cd2-O and Cd2-Cl bond distances (Table 41). The single μ–*N*1,*N*2–triazole and μ-Cl bridging hold the neighboring cadmium atoms at a distance of Cd···Cd = 4.101 Å whereas across the full length of ligand the Cd···Cd distance is 8.907 Å. The homo *cis* angles CdN_2, CdO_2 and $CdCl_2$ around each central Cd atoms adopt mutually perpendicular conformations (Figure 102b). This pattern of dissimilar environment around each Cd1(*a*) and Cd2(*b*) propagates in *abbaab* order along the chain in *c* direction. This simultaneous use of 1,2,4-triazole and carboxylic groups in coordination with cadmium ions in a

self-assembly process leads to a 2D network. The dihedral angle between 1,2,4-triazole plane and $–CH_2COO^-$ planes connected to Cd1 (C40-N5-C24-C1) is 80.72° whereas across Cd2 (C34-C38-N3-C7) it is 114.0°, which is significantly larger than the value found for the free ligand **HGlytrz**.[17] An overview of the crystallographic parameters of related compounds is given in Table 42. Navigation along the different planes of this structure reveals that this 2D network has a spiral connectivity leading to helicates.[28, 41-44] The propagating chains running along the *a* axis (Figure 103) are made up of head to tail coordinated **Glytrz** molecules connecting Cd1 atoms to form a helical chain. The resulting intrinsically spontaneous helicity reveals a skeletal structure with a single stranded helix consisting of ligand and cadmium in each turn. Only two cadmium and two ligands span one helical turn so that the helix is considerably compressed. The pitch height of the helix is equal to the length of the crystallographic *a* axis (7.579 Å). Helical arrangement implicitly results in chirality producing right (Δ = P) or left-handed (Λ = M) helicity around principal axes.[28, 41-44] The cylindrical helices are arranged in an alternating right-handed and left-handed fashion in the intrachain '*a*' direction with a distance of 10.3 Å (Figure 103) which are domains of opposite helicity. Thus the complex is racemic because the right and left handed chains are alternatively arranged but in *b* direction, it shows single handedness.

The helical twist of the strand results from the torsion between the 1,2,4-triazole plane and the spacer connecting the chelating carboxylic group. The orientation of the $–CH_2$[45] (winged, (*w*) or pinched, (*p*)) is crucial to direct the spirality. Both the $–CH_2$ of each turn adopt a favorable *winged* orientation. This spiral 'staircase' leaves behind a roughly polygonal cavity of 4.89 Å (O3-O3) x 6.224 Å (C24-C24).

Table 42 Comparison of crystallographic parameters among related compounds.

Compound	Space Group	Torsion angle (°)	-C=O, -C-O distance (Å) /Mode of coordination	M···M Distance (Å)	Network (Coordination sphere)	Ref.
HGlytrz	non-centrosymmetric orthorhombic (*Fdd2*)	C5-N4-C6-C7=80.6	-C=O = 1.215(3) -C-O = 1.307(2)	-	Supramolecular 2D network	[17]
GlytrzE	non-centrosymmetric tetragonal (P 41)	C5-N4-C6-C7=81	-C=O = 1.202(4) -C-O = 1.312(4)	-	Supramolecular 2D network	
30	centrosymmetric monoclinic ($P2_1/c$)	C5-N6-C7-C8=66.4 C1-N3-C3-C4=109.96	C4-O2=1.251(4) C4-O1=1.255(5) C8-O4=1.206(4) C8-O3=1.306(4)/not involved	3.845	1D coordination polymer, CdN_4Cl_2	[46]
31	non-centrosymmetric orthorhombic ($P2_12_12_1$)	C40-N5-C24-C1=80.72 C7-N3-C38-C34=114	C34-O1 = 1.257(8) C34-O2 = 1.229(8) C1-O4 =1.261(8) C1-O3 = 1.235(8)/bidentate	4.101	Supramolecular 2D network (helical); $CdCl_2N_2O_2$	[46]
32	non-entrosymmetric, cubic ($I\bar{4}3m$)	N3-N4-C6-C7=87.37	C7-O8=1.19(2) C7-O9=1.29(2)/monodentate	3.368	3D chains of nanoballs, CuN_2O_3	[17]

Helicity has been earlier noticed on a few 1,2,4-triazole CPs. Indeed, in a related system constructed from of 3-amino-1,2,4-triazolate, where additionally cadmium ions are bridged by bromide ions, two kinds of helical channels with opposite chirality were observed.[47] With 3-amino-1,2,4-triazole, a Cd(II) coordination framework with 2D helical channel was also recently reported.[40]

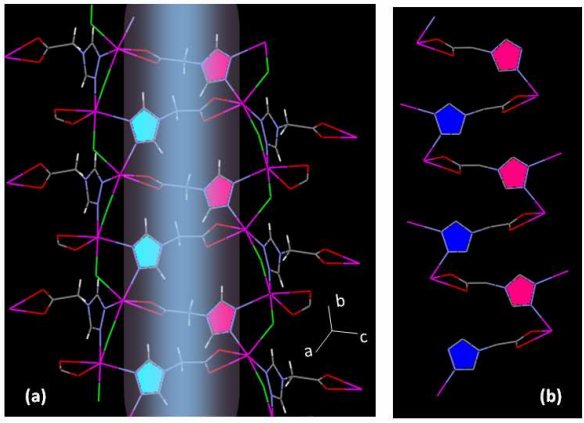

Figure 103 (a) Single stranded helical polymer showing the helical repeat distance along the *b* axis in **31;** (b) View of 'spiral staircase'.

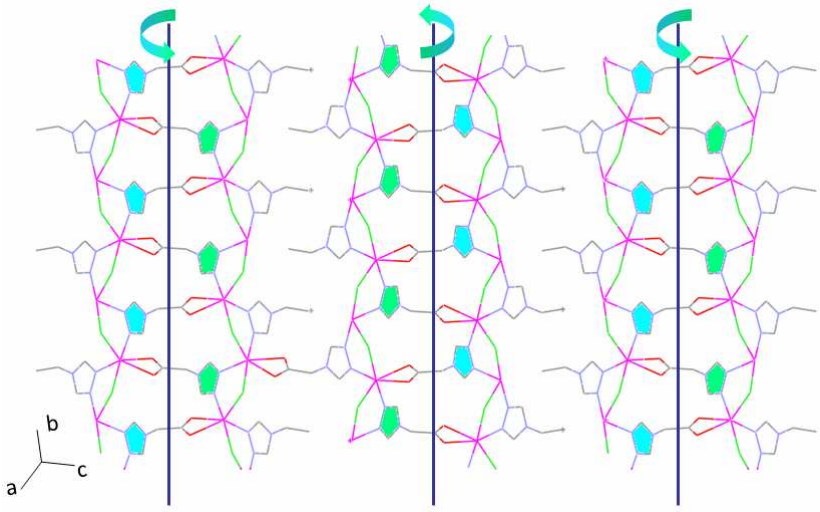

Figure 103c View along the *bc* plane showing alternate placement of left and right handed helices in **31**.

Crystal structure study of $[Cu_3(\mu_3\text{-}O)(HGlytrz)_3 \cdot (H_2O)_3]\ BF_4 \cdot H_2O$ (32)[††]

$[Cu_3(\mu_3\text{-}O)(HGlytrz)_3 \cdot (H_2O)_3]BF_4 \cdot H_2O$, **32** crystallizes in a cubic space group ($I\bar{4}3m$) at 120 K (Table 39). Mixed coordination environments of N and O are seen around copper. Three copper atoms are lodged at the vertices of an equilateral triangle around μ_3-O keeping Cu···Cu distance of 3.368 Å (Figure 104). This value compares well with a similar triangular tricopper MOF built from unsubstituted 1,2,4-triazole (Cu···Cu = 3.439 Å).[15]

[††] The synthesis was realised by Dr. A. D. Naik. This structure was solved by Prof. B. Tinant (UCL).

The copper centre is in '4+1' square pyramidal geometry and each copper binds 3 ligands: two ligands coordinate through nitrogen of 1,2,4-triazole in a N_1, N_2 bridging mode (Cu-N2 = 1.950(9) Å) while one ligand coordinates through a carboxylate group in an unidentate fashion (Cu-O9 = 1.943(1) Å). The Addison structural index parameter τ, which is relevant for five-coordinate structures as an index of the degree of trigonality,[48] was evaluated as 0.014 thus confirming a square pyramidal geometry. This triangular, tricopper(II) unit (Figure 104) supported by -μ_3-O bridging and six ligands, forms the secondary building unit (SBU). The μ_3-O atom is in nearly planar triangular coordination sphere with an average Cu···μ_3-O distance of 1.946(2) Å. The Cu-O-Cu angle is of nearly 120° (119.8(1)°) which is indicative of a sp^2 configuration of oxygen atom.[15] This SBB has a three-fold axis of symmetry passing through μ_3-O.

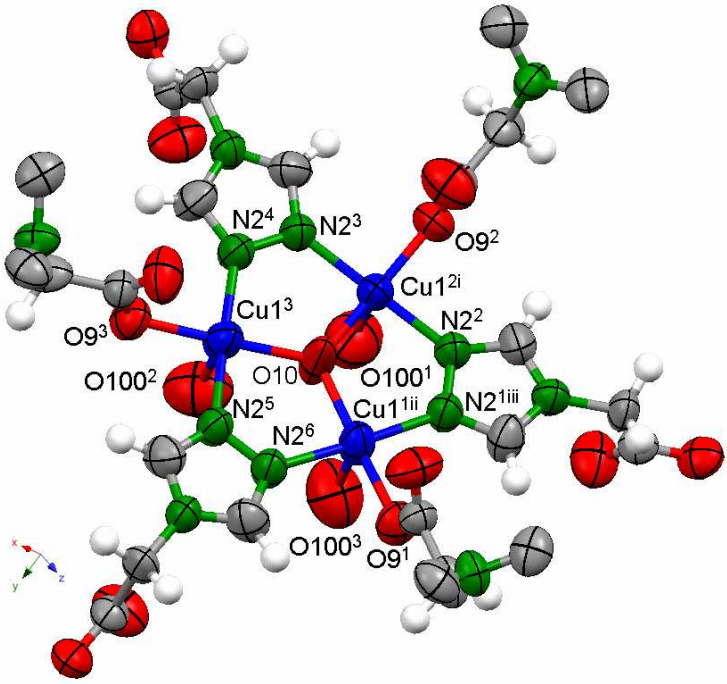

Figure 104 View of the triangular tricopper μ_3-oxo bridged SBU with atom labelling. Symmetry code: (I) x, y, z; (II) –z+3, y, -x+3; (III) x, -z+3, -y+3

Thus coordination around copper is formed by a CuN_2O_3 chromophore. Indeed, there is a squared basal plane of CuN_2O_2 which has a water molecule loosely coordinated to copper (2.32(2) Å). The basal plane is not perfectly planar; the N-Cu-N and O-Cu-O angles being 175.8(6)° and 176.7(1)°, respectively. Crystallographic data are summarized in Table 39 and Table 43.

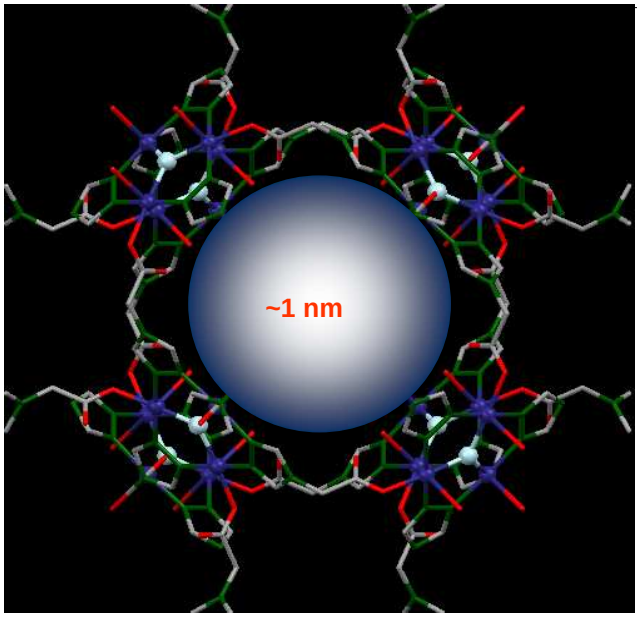

Figure 105 View of the self assembly of the SBUs to a TBU, architecturing a nanoball type cavity.

The self assembly of this rigid SBU in 3D generates a cage like structure. The interlinking arrangement of 8 such SBUs generates a molecular cage/porous ball which can be considered as tertiary building unit (TBU) or 'supercluster' (Figure 105).[49, 50]

The axially bound 24 water molecules on each of 24 copper atoms of TBU cage, decorate a hydrophilic interior pointing towards the void. The total solvent accessible volume is 4477.5 $Å^3$ which accounts for 48 % of the cell volume. The distance between opposite oxo-centres is 18.219 Å. Considering van der Waals radii, the void may admit a sphere of 1 nm of diameter (Figure 105). Each nanoball is the artifact of 96 molecules (24 Cu^{2+} ions, 24 water molecules, and 48 ligands) self-assembling in 3-dimensions. Each nanoball is tunneled into six neighboring nanoballs

through a roughly square window/aperture. These mutually perpendicular 3D channels represent a kind of undulating passages (Figure 106).

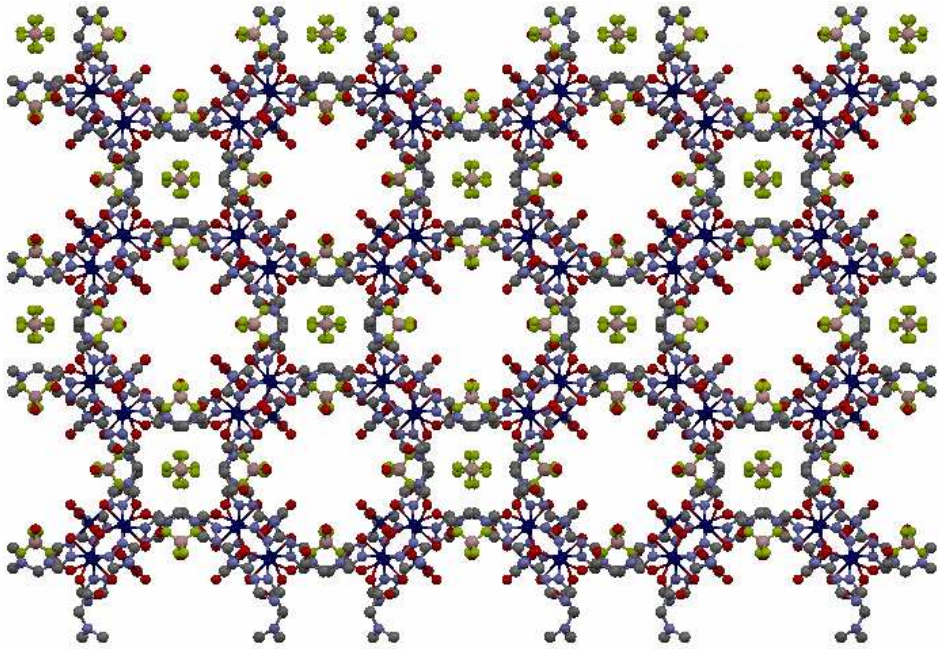

Figure 106 View of hydrophilic channels (larger voids) and hydrophobic channels (with smaller voids, where BF_4^- anion are stranded) formed by the 3D expansion of TBU (Projection along the *a* axis).

Since each TBU is roughly spherical, their specific spatial arrangement in 3D obviously generates smaller voids/interstices as can be seen in the body centered cubic arrangement of spheres (Figure 106). The larger channels open into smaller hydrophobic ones which are roughly square shaped (6.328 x 6.328 Å) and where the non coordinated BF_4^- anions are stranded. Indeed, anions are distributed in both periphery of hydrophilic and centre of hydrophobic channels. Water molecules of crystallization are lying within the cavity anchored by H-bonding. The -C=O of carboxylic group with a

length of 1.215(3) Å in free ligand is lowered to 1.187(2) Å in the complex due to H-bonding with the water molecules, whereas the C-O length in the ligand is lowered by approximately 0.06 Å to 1.294(1) Å, upon coordination to copper. The non-classical H-bonding between -C(H) of triazole and fluoride of BF_4^- is 3.182(12) Å. **32** can also be viewed as chains of nanoballs (Figure 107).

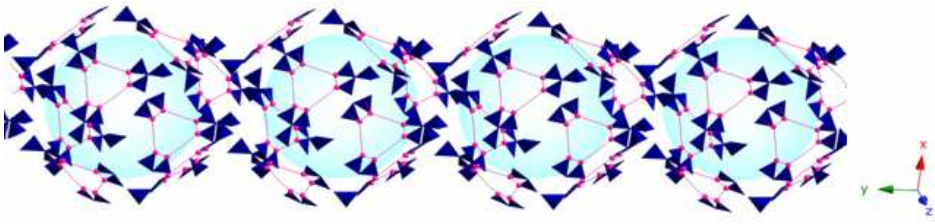

Figure 107 View of the nanoballs along the *c* axis.

The semi-rigid nature of the ligand framework was realized after closely studying the bond length and torsion angle changes upon complexation. The crooked ligand with an obtuse angle of 110.6(2)° between N4-C6-C7 has flexed out to 112.0(1)°, while that of C6-C7-O8 with 115.5(2)° bent to 122.2(1)° in **32**. The dihedral angle between two planes involving N4-C6-C7-O9 in **32** is exactly 180° which means that the two planes are stiffened to lie parallel as opposed to an angle of 176(1)° in the ligand. The flexibility is also evident from the change in dihedral angle between triazole plane and plane containing $–CH_2$-O group from 81°(1) in **HGlytrz** to 87° in **32**. These parameters may assist in redesigning the framework for specific applications like gas storage where a spacer length and bent angle, pore volume could be tuned.

The space group of **32** is non-centrosymmetric. The uses of an asymmetrical **HGlytrz** ligand as well as the directional nature of the metal ions favor a supramolecular chirality. The bent CH_2 spacer group may also offer prospect for lower symmetry networks compared to those based upon 'straight' spacers. The conformational flexibility of **HGlytrz** may also be at the origin of the chiral network developed by **32**.[24-27, 30, 31, 51] Such characteristic may also be appealing for NLO effects such as a SHG.

Sorption Studies of $[Cd_2(Glytrz)_2Cl_2]$ (31)

Channels found in the crystal structure of **31** prompted us to investigate gas adsorption capacities and to measure porosity partitioning. A gas sorption study for **31** was carried out using $N_{2(g)}$ and $H_{2(g)}$ (Figure 108). Before measurements, the crystalline sample was vacuumed at room temperature (r.t.) in order to remove surface moisture which was observed by TGA analysis (Figure 109e). Within the relative pressure range investigated, $N_{2(g)}$ adsorption measurements did not show any significant uptake but a low irreversible $H_{2(g)}$ uptake of 4 cm^3/g could be detected. This difference in adsorption properties could be due to size difference of adsorbing gases or simply to a low surface adsorption.

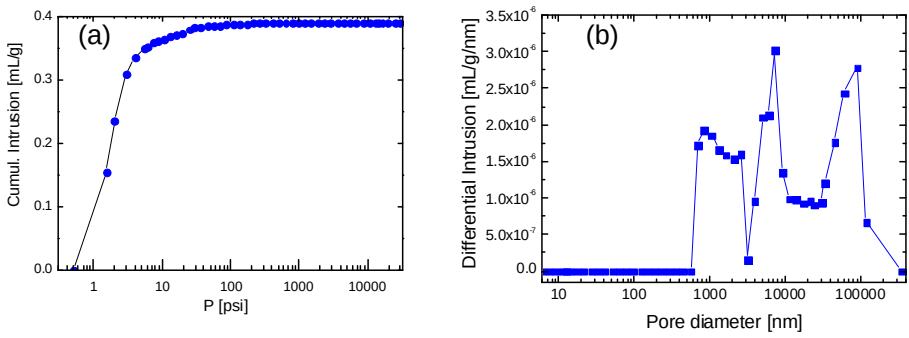

Figure 108 Intrusion curve (a) and corresponding pore size distribution (b) for **31** as observed by Hg porosimetry.

'Porosity partitioning' in **31** was also investigated by Hg intrusion porosimetry (MIP).[52, 53] Both techniques of gas adsorption and MIP rely upon balances between surface tension forces, capillary forces and pressure but their outcome may not be comparable due to distinctly different physical interactions involved in the two methods.[53] Intrusion curve and the corresponding pore size distribution are displayed in Figure 108, which shows the volume of intruded Hg as a function of applied pressure. We recall that pressure is inversely proportional to the pore size according to Washburn equation (high pressures being necessary to fill small pores by inverted capillary effect[52]. Mercury fills largest pores first, entering the smallest pores last under high pressure unlike gas adsorption. Analysis of Figure 108 allows identification of three steps. Indeed, as the pressure is gradually increased and as soon as it corresponds to a pore size, Hg enters the pores and a new step is recorded. When considering the pore size distribution (by applying the Washburn equation assuming constant contact angle and surface tension[52], the recorded steps can be understood as

follows: the step between 1 and 5 psi corresponds to pores centered at ~80 µm, between 10 and 50 psi to pores of ~7000 nm, and a hardly visible step between 60 and 200 psi to pores of ~1000 nm. All of these pores would originate from inter-particular porosity, which is also in accordance with the SEM observations that reveal non-porous crystals (Figure 91b). After that, the curve reaches a plateau indicating that there are no smaller pores present. Earlier in the nanoporous Cu(II) network based on the same ligand, we could observed pores of diameter 50 µm, 6000 nm, 2000 nm which were assigned to inter-particular porosity whereas pores of 350 nm diameter were traced by SEM. These results illustrate the usefulness of Hg porosimetry for a complete porosity characterization of such coordination polymers.

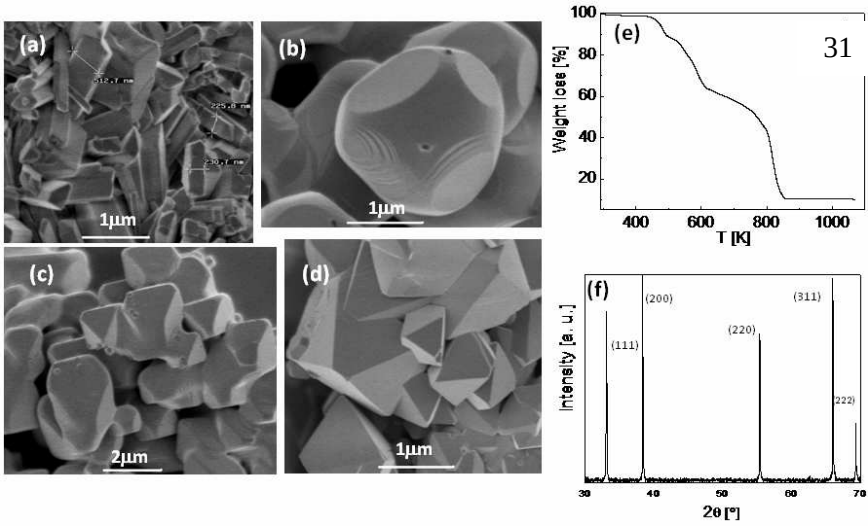

Figure 109 Morphology of CdO crystals obtained at different conditions of pyrolysis: (a) rectangle blocks (*white residue of CdO*). (b) truncated octahedra. (c) hexagonal blocks. (d) octahedra. (e) TGA pattern of **31**. (f) XRPD of red form of CdO (β-form).

CdO preparation by controlled pyrolysis of $[Cd_2(Glytrz)_2Cl_2]$, 31

In material sciences, metal threaded 'soft' non-aromatic networks like **31** give tangible perception for facile generation of oxide material upon controlled breakdown of their network. Such methods where surface energy and growth kinetics can be fine tuned offer tailoring architecture of nano and microcrystals oxide.[54-60] Various synthetic methods were explored to prepare cadmium oxides owing to their shape and size dependent technological applications such as photovoltaic cells, gas sensors, transparent conductive oxides, phototransistors, photodiodes, transparent electrodes, in the form of rods and wires[61], whiskers[60], disk[58], cubes, belts[55, 57], most of which are based on physical and chemical technique such as sol-gel, spray pyrolysis, sputtering method, Langmuir-Blodgett deposition, solvothermal synthesis and controlled decomposition of MOF.[54, 55]TGA of **31** (Figure 109e) provides an overview of thermal stability and decomposition pattern. After the initial weight loss around 45 °C which is due to surface moisture, the compound was stable until 170 °C and then decomposes into three ill-defined broad steps from 200 to 900°C. At 850 °C a complete destruction of the ligand framework is evidenced. In a typical pyrolysis procedure, **31** was heated at a rate of 10 °C/min until 850 °C and allowed to rapidly cool to r.t. which leads to isolation of a white residue. SEM images (Figure 109a) on this residue showed the presence of nearly cubic rods with thickness of 800 nm. The poor quality of the XRPD pattern did not allow to assign it to any known phase. As mild sputtering was frequently observed with this procedure, the isolation of sufficient quantity

of residue was difficult. This led us to use a mild thermal treatment of 1°C/min until 850 °C instead, followed by rapid cooling to r.t. The obtained reddish-brown residue was considered for further investigation for phase identification, purity and morphological characterization. The XRPD pattern shown in Figure 8f, was indexed to the powder pattern of the pure cubic phase of CdO (β-form) (JCPDS file No. 05-0640).[54-60] The diffractogram shows prominent peaks at 2θ (°) = 32.99, 38.29, 55.27, 65.94, 69.26 which are associated to (111), (200), (220), (311) and (222) planes, respectively. It clearly shows that CdO crystallizes in rock-salt cubic structure. The pattern does not reveal any other peaks thereby confirming excellent phase purity. SEM images of this oxide (Figure 109b) shows truncated octahedron shaped crystals of 1-2 μm size. The shaping of these oxides can be further tuned and same results of phase purity (based on XRPD pattern) was observed for the reddish brown residue obtained when pyrolysis was extended up to 850°C or 900°C, and subsequently allowed to be slowly cooled to r.t.. In the former case hexagonal blocks were obtained (Figure 109c) whereas a treatment at 900 °C afforded well-defined octahedral crystals (Figure 109d), both of them in the range of 1-2 μm.

Thermal analyses of $[Cu_3(\mu_3\text{-}O)(HGlytrz)_3\cdot(H_2O)_3]BF_4\cdot H_2O$, 32

A crystalline sample was heated from 25 to 900 °C in air at a heating rate of 10°C /min (Figure 110a). Three weight loss steps were observed. The first weight loss that occurred between 25 to ~150 °C is gradual and corresponds

to the combined loss of coordinated and uncoordinated water molecules, which is an endothermic process, as seen by DTA. The relatively low temperature for the loss of water molecules (below 60 °C) reveals their loose coordination.

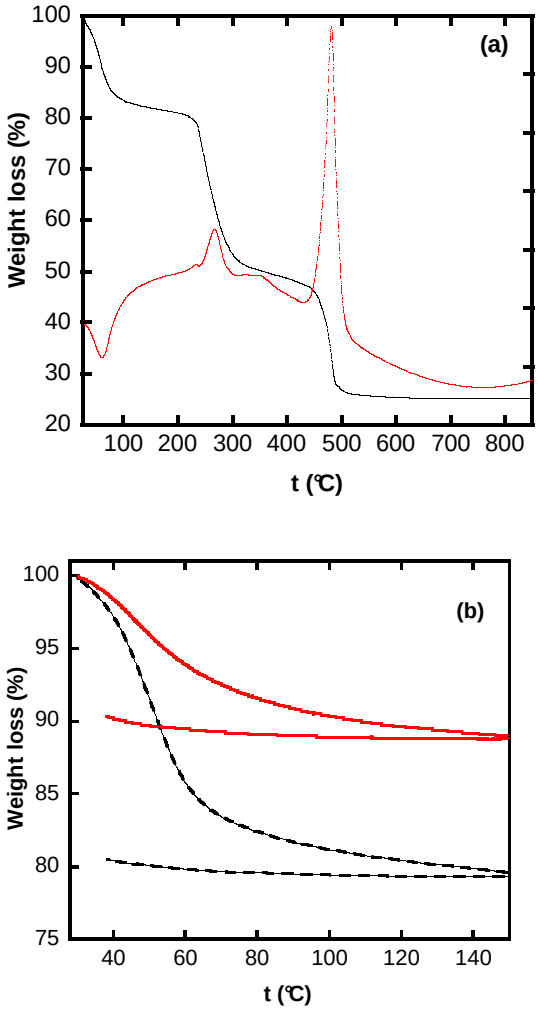

Figure 110 (a) TGA-DTA showing a complete thermal decomposition (10 °C/min) for **32**. (b) TGA of desolvation profile for **32** (heated to 150°C with 1 °C/min, dotted

line). The desolvated sampled was exposed to air for 12 h and remeasured by TGA (thick line).

Although desolvation is complete around 100°C, the compound continues to loose weight until the onset of a next decomposition step. So a well defined plateau was not reached and thereafter decomposes in two distinct steps which are both exothermic as indicated by DTA. This behaviour corresponds to a slow collapse of the network upon guest removal. A crystalline sample was also subjected to a TGA-DTA analysis at 1°C/min following the thermal cycle (25 °C → 150 °C → 25 °C) (Figure 110b). After dehydration, a blue-turquoise compound was obtained and kept at room temperature and ambient air overnight. Surprisingly, although there was no indication of moisture/water gain during the TGA cooling run, this sample regains its original dark blue colour. We rerun a TGA on this moisture absorbed sample to evaluate the amount of water uptake. Approximately 50% of total water lost in the first TGA run (Figure 110b) was taken up by the compound. When the desolvated compound was re-suspended in water it immediately turns back to a dark blue colour and follows the same thermal decomposition pattern as that of the fresh sample, thus indicating a complete resolvatation of (Figure 110a).

Sorption studies of $[Cu_3(\mu_3\text{-}O)(HGlytrz)_3\cdot(H_2O)_3]BF_4\cdot H_2O$, 32

A gas sorption study for **32** was carried out using $N_{2(g)}$ and $H_{2(g)}$. Before measurements, the crystalline sample was vacuumed either with a gradual increase of temperature or rapid heating until 150°C, the temperature

corresponding to the end of dehydration according to TGA analysis (Figure 110b). Within the relative pressure range investigated, the $N_{2(g)}$ adsorption measurements did not show any uptake of nitrogen, thus making impossible the determination of the specific surface area by routine BET calculation. An adsorption was however observed for $H_{2(g)}$ suggesting no preference for $N_{2(g)}$. This adsorption difference between these two molecules could be related to their size, their kinetic diameter being 2.8 Å ($H_{2(g)}$) and 3.6 Å ($N_{2(g)}$).[62]

The $H_{2(g)}$ adsorption of 1.8 cm^3/g and 2.7 cm^3/g for the fast and slow out-gassing, respectively, is irreversible and several consecutive runs always lead to the same result. These low values could account for little surface adsorption as observed for a related SBU system, for which a small $N_{2(g)}$ sorption was recorded.[21, 22]

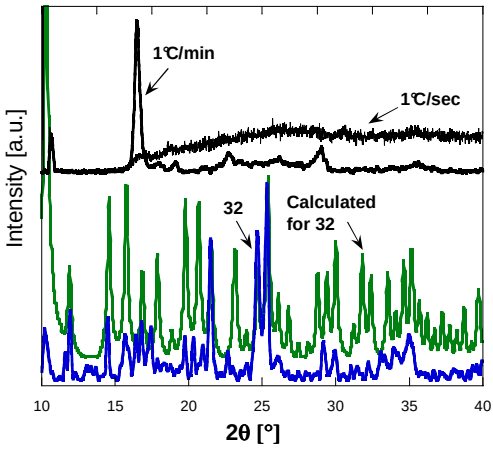

Figure 111 Top: X-ray powder diffraction patterns of microcrystals of **32** thermally treated compounds at 1°C/min and 1°C/sec, respectively. Bottom: diffractogram of **32** as well as the calculated one from its CIF file. Pronounced effect of thermal treatment on framework integrity is evidenced.

These poor adsorption properties could also result from the breakdown of the network after thermal treatment. Indeed, as seen from TGA, no stable plateau was observed after solvent loss at 150 °C (Figure 110a) and complete degassing was difficult to achieve. In order to ascertain the framework rupture, we have studied the X-ray powder diffraction pattern of the desolvated compound from TGA (which was heated slowly to 150 °C at 1° C/min) and of a sample which was rapidly heated to 150 °C at 1°C/sec. It is compared with the diffractogram of air dried fresh crystals. Interestingly, fast heating results in an amorphization of the sample compared to slow heating and only very weak signals are observed (Figure 111).

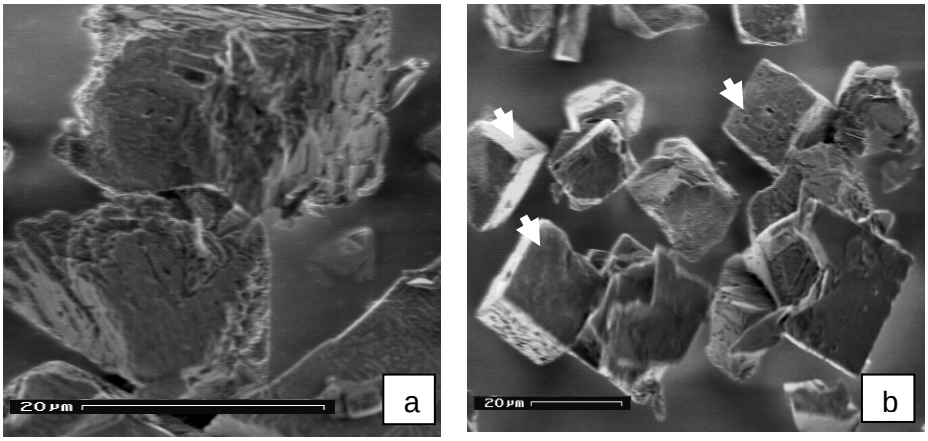

Figure 112 SEM analysis of a TGA sample of **32** warmed at 1°C/min. (a) View of damaged crystals. (b) Some unaffected **32** crystals (shown with arrow mark) are also seen.

We then studied the morphology of these thermally heated samples by SEM (Figure 112 and 113). Deterioration of crystals is seen in slowly heated sample while some crystals are unaffected showing the effect of thermal gradient in the sample container (Figure 112).

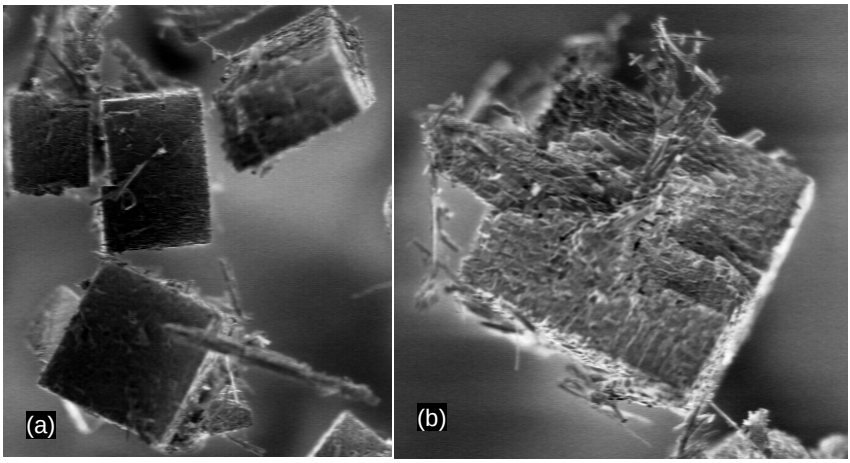

Figure 113 SEM analysis of a sample of **32** warmed up to 150 °C at 1°C/sec (a) general view. (b) Enlarged view. Deterioration is clearly visible.

More deterioration is observed for the rapidly heated sample by SEM analysis (Figure 113). These results support the fact that crystallinity is affected with thermal pre-treatment destabilizing the framework, although hardly any difference is seen in the IR of these treated and fresh crystals (Figure 114). This prompted us to revisit the gas adsorption measurement with mild pre-treatment at ambient condition. The fresh crystals were evacuated overnight under vacuum without any warming treatment. Figure 115 shows improved adsorption behaviour of **32**. $H_{2(g)}$ adsorption gradually raises to 21 cm^3/g with increase of pressure. It not only bettered the earlier value but also shows narrow hysteretic reversibility. But again no preference for $N_{2(g)}$, which strengthens the hypothesis of size discrepancy discussed above. Consequent runs do not follow the same trend. It reduces to ~6-7 cm^3/g in second and third runs.

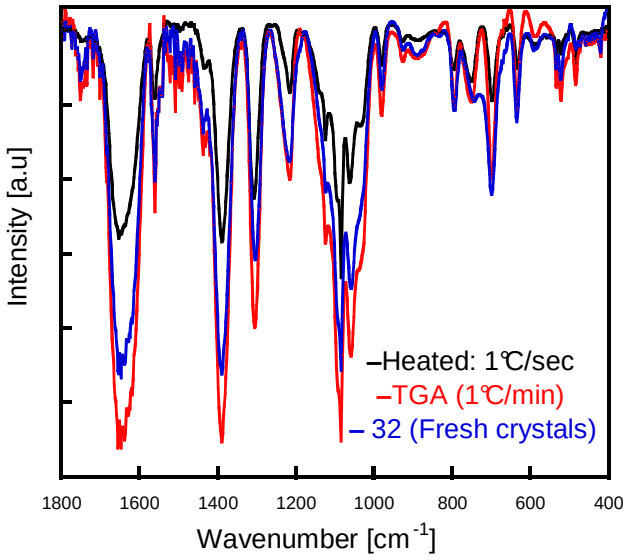

Figure 114 FT-IR (only fingerprint range is expanded for clarity) spectra of microcrystals of **32** and thermally treated compounds. Deterioration is hardly detected by IR.

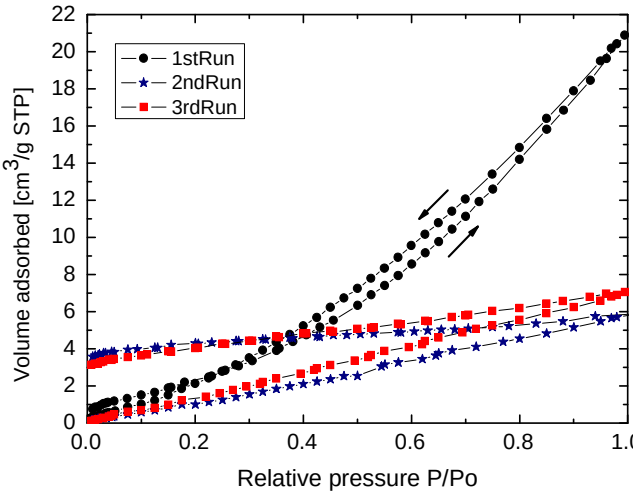

Figure 115 Adsorption and desorption isotherms at 77K of $H_{2(g)}$ on **32**, degassed at room temperature.

Thus adsorption efficiency is not only reduced but also becomes irreversible. It is possible that, after the initial $H_{2(g)}$ sorption where the increasing pressure flexes-out the network to open the 'gate' to accommodate the guest, it keeps the network under stress and the subsequent desorption probably partially collapses the network while shrinking back. The retention of almost half of the adsorbed gas (3 cm^3/g) in second or third run after depressurization at low temperature although less, is interesting and such retentions are significant in systems which show high sorption-desorption property.[63]

Square shaped openings discovered on the cubic crystal surface of stimulated us to investigate the 'porosity partitioning' by Hg porosimetry. [64, 65]. Intrusion curve and the corresponding pore size distribution are displayed in Figure 116. Figure 116a shows the volume of intruded Hg as a function of applied pressure. We recall that pressure is inversely proportional to the pore size according to Washburn equation (high pressures being necessary to fill small pores by inverted capillary effect).[52] A fine analysis of Figure 13a allows identification of several steps. Indeed, as the pressure is gradually increased and as soon as it corresponds to a pore size, mercury enters the pores and a new step is recorded. When considering the pore size distribution (Figure 116b) (by applying the Washburn equation assuming constant contact angle and surface tension),[52] the recorded steps can be understood as follows: the step between 1 and 5 psi corresponds to pores cantered at ~50 µm, between 10 and 25 psi to pores of about 6000 nm, between 30 and 80 psi to pores of about 2000 nm and the remaining uptake between 100 and 500 psi reveals pores with sizes smaller than 350 nm.

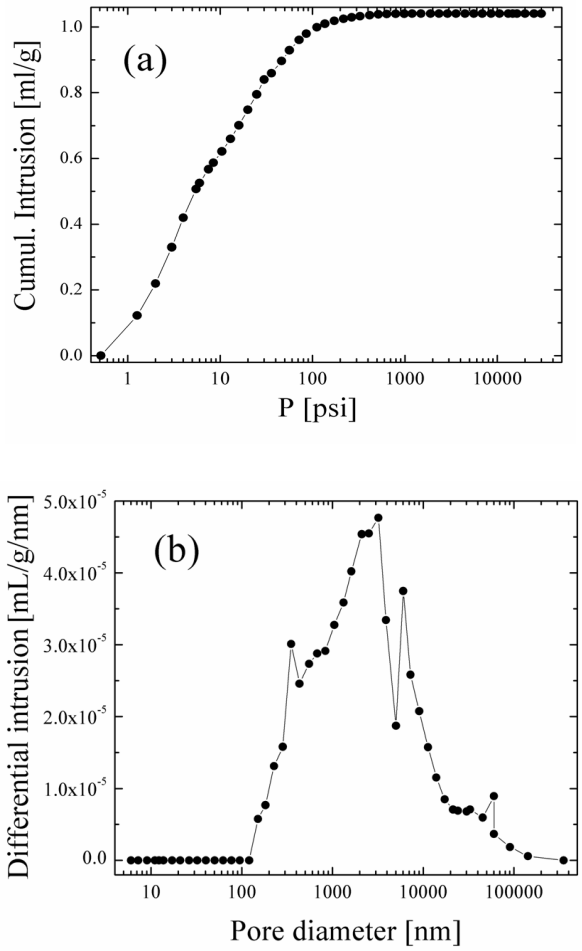

Figure 116 Intrusion curve (a) and corresponding pore size distribution (b) with a logarithmic scale for **32** as observed by Hg porosimetry.

After that, the curve reaches a plateau indicating that there are no smaller pores present. The major contributions at 50 µm, 6000 nm and 2000 nm would rather originate from inter-particular porosity, whereas the pores of 350 nm could correspond to the voids identified by SEM (Figure 96). These

results illustrate the usefulness of Hg porosimetry for a complete porosity characterization of **32**.

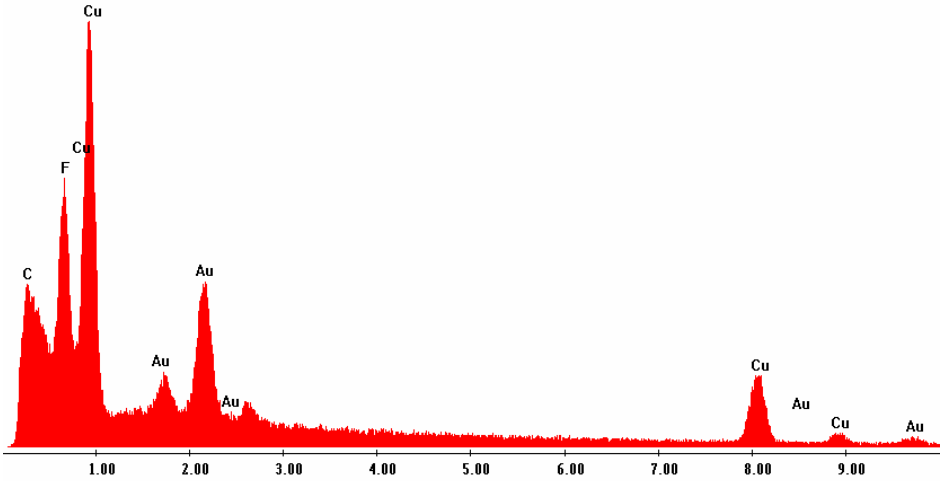

Figure 117 EDX showing constituents in microcrystals (identical for 50 μm^3 and 15 μm^3 crystals) of **32**.

Concluding Remarks

Amine derivatization in amino acids provides natural and ideal topology having synchronized conformational orientations of two reverent potential coordinating functional groups, namely carboxylic and triazole moieties on the same framework. Present work justifies that 1,2,4-triazole functionalized amino acids/esters would find their niche in the design of functional 1D, 2D and 3D MOFs.

Glycine ethyl ester was recruited in an amine exchange process based on a transamination to afford ethyl 4H-1,2,4-triazol-4-yl-acetate (**GlytrzE**). The

acid hydrolysis of this molecule leads to quantitative isolation of 4H-1,2,4-triazol-4-yl acetic acid (**HGlytrz**).

The crystal structure of 4H-1,2,4-triazol-4-yl acetic acid, **HGlytrz** reveals that the whole molecular packing is supported and directed by H-bonding interactions. The amazing nanoporous network constructed from this supramolecular synthon proved **HGlytrz** to be an ideal scaffold for designing a MOF. **GlytrzE** crystallizes in a non-centrosymmetric tetragonal space group (P 41) with Z = 4. This is the first crystal structure in 1,2,4-triazole-aminoester family.

A prominent feature of this work is the spontaneous self-assembly of $[Cd(HGlytrz)(Glytrz)Cl]\cdot 2H_2O$, **30**, which forms a linear 1D chain have origin in centrosymmetric space group would provide logistics for the design of 1D spin crossover polymers.

On the other hand a helicity observed in $[Cd_2(Glytrz)_2Cl_2]$ (**31**), despite sharing same synthetic recipe with **30** due to the hierarchical self-assembly of tiny synthon **HGlytrz** originating in non-centrosymmetric space group. Although the use of chiral molecules is the most common strategy[29, 66] for obtaining products with a non-centrosymmetric arrangement in the crystal lattice, it is not a rule. It is found that only 10-15% of achiral organic molecules crystallize in non-centrosymmetric space groups.[29, 66] In contrast to the chiral amino acids, non-chiral glycine (as a structural unit) cannot enforce non-centrosymmetry[67] of a crystal structure. But its electronic and structural asymmetry together with consolidated effort of non-covalent interactions with suitable metal ions as connectors may lead to crystallization in a non-centrosymmetric space group. By using bridging

ligands with a significant kink in the topology instead of linear rigid molecules, the formation of networks with a lower symmetry and helicity is possible.[25, 44] The simple torsion angle count around the spacer in such molecules forms the basis of the assessment of molecular flexibility in them. Such conformationally flexible backbone and electronic asymmetry (push-pull effect) have high chances of ending up in non-centrosymmetric space group and such compounds have an enormous significance because of technological properties like single harmonic generator (SHG), piezo-pyro-ferro electricity, triboluminescence.[25] Reaction of **GlytrzE** or **HGlytrz** with aq. $Cu(BF_4)_2$ in aq. DMF gives dark blue crystals which crystallize in a non-centrosymmetric, cubic space group ($I\bar{4}3m$) and which were formulated as $[Cu_3(\mu_3\text{-}O)(HGlytrz)_6\cdot(H_2O)_3]BF_4\cdot H_2O$ (**32**). This opens up a new juvenile impending way of heterocyclic derivatization in aminoacid chemistry. This is particularly intriguing because aminoacid derivatives can offer a virtually unlimited structural diversity. This tailored synthon undergoes stunning self assembly to form a 3D array of nanoball architecture. The nanoporous void obtained in the present system is the artifact of angular framework of the ligand, thus hinting that fine tune of the void shape and size should be possible with variation of methylene ankle in the ligand and even impose network interpenetration. Since axially bound water molecules can be easily removed, not necessarily thermally, it could possibly allow access to the Lewis acid sites for catalytic applications as nano-reactors for catalysis or anion/cation recognization. Another appealing perspective in the context of molecular magnetism would be to design a switchable magnetic MOF since preliminary experiments have shown that **GlytrzE** was appropriate to set a suitable ligand field strength for Fe^{II} spin crossover behaviour.[38] Along this

line, the investigation of the magnetic properties of **32** would be a valuable addition potentially in the frame of spin frustration[68-71].

Although it was understood from TGA that the thermal stability of **32** is not very high, SEM analysis was very informative to clarify the texture alteration of the crystals and to understand the poor adsorption properties. The 'soft' skeleton of the ligand is not robust enough to withstand high temperature treatment unlike their unsubstituted counterparts.[4]

Finally, we have also shown that, these CPs could be suitable host to carve desired metal oxides with shape and phase selectivity.

Notes and references

[1] E. V. Boldyreva. Models, Mysteries, and Magic of Molecules, In: (Eds.: J. C. A. Boeyens and J. F. Ogilvie), *Crystalline amino acids - A link between chemistry, materials sciences and biology*, Springer-Verlag, New York, **2007**, p. 167.

[2] S. Pizzarello, A. L. Weber. *Science* **2004**, *303*(5661), 1151.

[3] S. J. Zuend, M. P. Coughlin, M. P. Lalonde, E. N. Jacobsen. *Nature* **2009**, *461*(7266), 968-970.

[4] J. P. Zhang, X. M. Chen. *J. Am. Chem. Soc.* **2008**, *130*(18), 6010-6017.

[5] C. Di Nicola, Y. Y. Karabach, A. M. Kirillov, M. Monari, L. Pandolfo, C. Pettinari, A. J. L. Pombeiro. *Inorg. Chem.* **2006**, *46*(1), 221-230.

[6] M. Casarin, C. Corvaja, C. Di Nicola, D. Falcomer, L. Franco, M. Monari, L. Pandolfo, C. Pettinari, F. Piccinelli. *Inorg. Chem.* **2005**, *44*(18), 6265-6276.

[7] Y. Garcia, P. J. van Koningsbruggen, H. Kooijman, A. L. Spek, J. G. Haasnoot, O. Kahn. *Eur. J. Inorg. Chem.* **2000**, *2000*(2), 307-314.

[8] Y. Garcia, G. Bravic, C. Gieck, D. Chasseau, W. Tremel, P. Gutlich. *Inorg. Chem.* **2005**, *44*(26), 9723-9730.

[9] H. A. Habib, J. Sanchiz, C. Janiak. *Dalton Transactions* **2008**, (13), 1734-1744.

[10] H. A. Habib, A. Hoffmann, H. A. Hoppe, G. Steinfeld, C. Janiak. *Inorg. Chem.* **2009**, *48*(5), 2166-2180.

[11] S. K. Henninger, H. A. Habib, C. Janiak. *J. Am. Chem. Soc.* **2009**, *131*(8), 2776-2777.

[12] H. A. Habib, J. Sanchiz, C. Janiak. *Inorg. Chim. Acta* **2009**, *362*(7), 2452-2460.

[13] C. Janiak. *Dalton Transactions* **2003**, (14), 2781-2804.

[14] A. B. Lysenko, E. V. Govor, H. Krautscheid, K. V. Domasevitch. *Dalton Transactions* **2006**, (31), 3772-3776.

[15] Y. Qing, Xiuqing Z., Hedong B., Hong L., Bin Z., Shiping Y., Daizheng L. *Crystal Growth & Design* **2008**, *8*(4), 1140-1146.

[16] Y. Garcia, P. J. van Koningsbruggen, G. Bravic, D. Chasseau, O. Kahn. *Eur. J. Inorg. Chem.* **2003**, (2), 356-362.

[17] A. D. Naik, M. M. Dîrtu, A. Leonard, B. Tinant, J. Marchand-Brynaert, B. L. Su, Y. Garcia. *Crystal Growth & Design* **2010**, *10*(4), 1798-1807.

[18] A. D. Naik, J. Marchand-Brynaert, Y. Garcia. *Synthesis* **2008**, *1*, 149-154.

[19] R. K. Bartlett, I. R. Humphrey. *J. Chem. Soc. C* **1967**, 1664-1666.

[20] Y. Garcia, O. Kahn, L. Rabardel, B. Chansou, L. Salmon, J. P. Tuchagues. *Inorg. Chem.* **1999**, *38*(21), 4663-4670.

[21] Q. G. Zhai, C. Z. Lu, S. M. Chen, X. J. Xu, W. B. Yang. *Crystal Growth & Design* **2006**, *6*(6), 1393-1398.

[22] Q. G. Zhai, C. Z. Lu, X. Y. Wu, S. R. Batten. *Crystal Growth & Design* **2007**, *7*(11), 2332-2342.

[23] K. Nakamoto. *Infrared and Raman Spectra of Inorganic and Coordination Compounds : Applications in Coordination, Organometallic, and Bioinorganic Chemistry*, **1997**.

[24] O. R. Evans, W. Lin. *Acc. Chem. Res.* **2002**, *35*(7), 511-522.

[25] K. T. Holman, A. M. Pivovar, M. D. Ward. *Science* **2001**, *294*(5548), 1907-1911.

[26] R. Ahlers, U. Ruschewitz. *Solid State Sciences* **2009**, *11*(6), 1058-1064.

[27] E. Craven, E. Mutlu, D. Lundberg, S. Temizdemir, S. Dechert, H. Brombacher, C. Janiak. *Polyhedron* **2002**, *21*(5-6), 553-562.

[28] G. Seeber, B. Tiedemann, K. Raymond. Supramolecular Chirality in Coordination Chemistry, In: (Eds.: M. Crego-Calama and D. Reinhoudt), *Supramolecular Chirality*, Springer Berlin / Heidelberg, **2006**, pp. 147-183.

[29] B. K. Saha, A. Nangia, J. F. Nicoud. *Crystal Growth & Design* **2006**, *6*(6), 1278-1281.

[30] G. R. Desiraju. *Crystal Engineering: The design of organic solids*, Elsevier Science & Technology, Amsterdam, **1989**.

[31] H. Toshiya, T. Nuida, K. Hashimoto, S. Ohkoshi. *Crystal Growth & Design* **2006**, *6*(8), 1736-1737.

[32] D. Chwaleba, M. M. Ilczyszyn, M. Ilczyszyn, Z. Ciunik. *J. Mol. Struct.* **2007**, *831*(1-3), 119-134.

[33] G. Desiraju, T. Steiner. The weak hydrogen bond in structural chemistry and biology, In: *IUCr Monographs on Crystallography*, Oxford University Press/International Union of Crystallography, **1999**.

[34] J. G. Haasnoot. *Coord. Chem. Rev.* **2000**, *200*, 131-185.

[35] L. Yi, B. Ding, P. Cheng, D.-Z. Liao, S.-P. Yan, Z.-H. Jiang. *Inorg. Chem.* **2003**, *43*(1), 33-43.

[36] W. Ouellette, B. S. Hudson, J. Zubieta. *Inorg. Chem.* **2007**, *46*(12), 4887-4904.

[37] W. Ouellette, H. Liu, C. J. O'Connor, J. Zubieta. *Inorg. Chem.* **2009**, *48*(11), 4655-4657.

[38] M. M. Dirtu, A. D. Naik, J. Marchand-Brynaert, Y. Garcia. *Journal of physics: conference series* **2010**, *217*(1), 012085.

[39] M. Marchivie, P. Guionneau, J. F. Letard, D. Chasseau. *Acta Crystallogr. B* **2005**, *61*, 25-28.

[40] K. A. Siddiqui, M. Bolte, G. K. Mehrotra. *Inorg. Chim. Acta* **2010**, *363*(2), 457-463.

[41] K. Maeda, E. Yashima. *Top. Curr. Chem.* **2006**, *265*, 44-88.

[42] A. Scarso, J. Jr. Rebek. *Top. Curr. Chem.* **2006**, *265*, 1-46.

[43] U. Knof, A. V. Zelewsky. *Angewandte Chemie International Edition* **1999**, *38*(3), 302-322.

[44] P. A. Maggard, C. L. Stern, K. R. Poeppelmeier. *J. Am. Chem. Soc.* **2001**, *123*(31), 7742-7743.

[45] J. P. W. Eggert, J. Harrowfield, U. Lüning, B. W. Skelton, A. H. White, F. Löffler , S. Konrad. *Eur. J. Org. Chem.* **2005**, *2005*(7), 1348-1353.

[46] M. M. Dîrtu, C. Neuhausen, A. D. Naik, A. Leonard, F. Robert, J. Marchand-Brynaert, B. L. Su, Y. Garcia. *Crystal Growth & Design* **2011**, *11*(4), 1375-1384.

[47] Z. Chen, X. Li, F. Liang. *J. Solid State Chem.* **2008**, *181*(8), 2078-2086.

[48] A. W. Addison, T. N. Rao, J. Reedijk, J. Van Rijn, G. C. Verschoor. *J. Chem. Soc. , Dalton Trans.* **1984**, *null*(null), 1349.

[49] J. J. Perry IV, J. A. Perman, M. Zaworotko. *Chemical Society Reviews* **2009**, *38*(5), 1400-1417.

[50] A. J. Fletcher, M. K. Thomas, J. M. Rosseinsky. *J. Solid State Chem.* **2005**, *178*(8), 2491-2510.

[51] G. Seeber, B. E. F. Tiedemann, K. N. Raymond. *Top. Curr. Chem.* **2006**, *265*, 147-183.

[52] E. W. Washburn. *Phys. Rev.* **1921**, *17*, 273-283.

[53] P. A. Webb, C. Orr, R. W. Camp, Olivier J.P. *Analytical methods in fine particle technology*, Micromeritics Instrument Corp, **1997**.

[54] J. H. Kim, Y. C. Hong, H. S. Uhm. *Jpn. J. Appl. Phys* **2007**, *46*, 4351-4354.

[55] Z. W. Pan, Z. R. Dai, Z. L. Wang. *Science* **2001**, *291*(5510), 1947-1949.

[56] H. Yu, D. Wang, M.-Y. J. Han. *J. Am. Chem. Soc.* **2007**, *129*(8), 2333-2337.

[57] Z. Jia, Y. Tang, L. Luo, B. Li. *Cryst. Growth Des.* **2008**, *8*(7), 2116-2120.

[58] W. Shi, C. Wang, H. Wang, H. Zhang. *Cryst. Growth Des.* **2006**, *6*(4), 915-918.

[59] M. Ghosh, C. N. R. Rao. *Chem. Phys. Lett.* **2004**, *393*(4-6), 493-497.

[60] N. Koparanova, Z. Zlatev, D. Genchev, G. J. Popovich. *J. Mater. Sci.* **1994**, *29*(1), 103-109.

[61] T. B. S. Ghoshal, P. M. G. Nambissan, G. Majumdar, S. K. De. *Cryst. Growth Des.* **2009**, *9*(3), 1287-1292.

[62] H. J. Lee, W. Cho, S. Jung, M. Oh. *Adv. Mater.* **2009**, *21*(6), 674-677.

[63] X. Zhao, B. Xiao, A. J. Fletcher, K. M. Thomas, D. Barshaw, M. J. Rosseinsky, X. Zhao, B. Xiao, A. J. Fletcher, K. M. Thomas, D. Barshaw, M. J. Rosseinsky. *Science* **2004**, *306*(5698), 1012-1015.

[64] H. Giesche. *Part. Part. Syst. Charact.* **2006**, *23*(1), 9-19.

[65] H. Giesche. In: (Eds.: F. Schüth, K. S. W. Sing, and J. Weitkamp), *Handbook of porous solids*, Wiley, VCH, Weinheim, **2002**, p. 103.

[66] E. Pidcock. *Chem. Comm.* **2005**, (27), 3457-3459.

[67] M. Fleck, L. Bohaty. *Acta Crystallogr. , Sect. C* **2004**, (60), 291-295.

[68] S. Ferrer, F. Lloret, I. Bertomeu, G. Alzuet, J. Borras, S. Garcia-Granda, M. Liu-Gonzalez, J. G. Haasnoot. *Inorg. Chem.* **2002**, *41*(22), 5821-5830.

[69] B. Sarkar, M. S. Ray, M. G. B. Drew, A. Figuerola, C. Diaz, A. Ghosh. *Polyhedron* **2006**, *25*(16), 3084-3094.

[70] P. Mukherjee, M. G. B. Drew, M. Estrader, C. Diaz, A. Ghosh. *Inorg. Chim. Acta* **2008**, *361*(1), 161-172.

[71] M. S. Ray, S. Chattopadhyay, M. G. B. Drew, A. Figuerola, J. Ribas, C. Diaz, A. Ghosh. *Eur. J. Inorg. Chem.* **2005**, *2005*(22), 4562-4571.

Chapter VII: Hysteretic spin transition materials, inspired and derived from an α-amino-acid derivative framework

HGlytrz and **GlytrzE** described in Chapter VI are not only the principal core for the design of functional 1D, 2D and 3D MOFs, but also potential ligands for transition metals. Thanks to the presence of two extremities potentially coordinating groups, 1,2,4-triazole and/or carboxylic group can bond a metal ion through the coordination of oxygen and *N1*,*N2*- atoms (Figure 89, Chapter VI). In view of this fact the composition and the properties of materials will strongly depend of the coordination mode. It is very challenging to control such parameters thanks to experimental conditions, as number and nature of ligands, counteranions, presence of other coordination molecules, coordinated solvent, temperature, etc. That can modify polymer chain length, texture … as well as magnetic properties.

Thus in Chapter VII.1 we will focus on the study of SCO complexes, based on **HGlytrz**. These complexes are built by coordination through the two potentially coordinating groups, *N1*, *N2* – 1,2,4-triazole and/or oxygen atoms from the carboxylic group, of the substituent. This part will highlight the impact of the coordination type on the properties of **HGlytrz** molecular switches.

Since two potentially coordinating groups are present in HGlytrz, the research was directed to the employment, for the first time, of 1,2,4-triazole-aminoester of the derivatized amino acid family to build SCO systems (Chapter VII.2). **GlytrzE**, is construct from a 1, 2, 4-triazole head, and an ester tail, separated by a flexible methylene group, which can form a triple bridging around the metals. There are indeed multiple reason for introducing ester substituted on 4 position of 1, 2, 4-triazole core: (a) to enforce

electronic effect thus affecting the donor abilities of 1, 2, 4-triazole; (b) to use an appropriate length of substituent which compromises the distance between 1D chains in complexes; (c) to introduce supramolecular interactions with H-acceptors substituent.

Chapter VII.1: Neutral and anionic duality of 1,2,4-triazole α-amino acid scaffold in 1D coordination polymers*

Introducing remarks

In continuation of our work, we now investigate the iron(II) coordination chemistry of the hydrolyzed derivative of GlytrzE, ethyl-4H-1,2,4-triazol-4-yl acetic acid (**HGlytrz**). As presented in the previous chapter, by X-ray crystallography of a series of metal(II) complexes, we understood that this ligand could act either as anionic or neutral ligand depending upon reaction conditions[1, 2]. In the present Chapter four new iron(II) HGlytrz complexes were prepared with ClO_4^- (**33-HGlytrz-ClO_4)**, NO_3^- **(34-HGlytrz-NO_3)**, BF_4^- (**35-HGlytrz-BF_4)**, $CF_3SO_3^-$ (**36-HGlytrz-TRF)** counteranions. FTIR and ^{57}Fe Mössbauer spectroscopies provide complimentary information about ligand ability to act either as neutral (HGlytrz) or charges as an anionic form (Glytrz). Complexes **33-HGlytrz-ClO_4, 35-HGlytrz-BF_4, 36-HGlytrz-TRF** are 1D coordination polymers (CP) with bridging *N1,N2*-1,2,4-triazole with ligand acting as neutral with concurrent formation of a small amount of 1D CP with dual status of ligand. Interestingly, **34-HGlytrz-NO_3** is exclusively formed of a 1D CP with HGlytrz which opens

*Adapted from : A. D. Naik, M. M. Dîrtu, Y. Garcia, **2012**, *Hyperfine Interact.* **2012**, 205, 57-361.

up a new strategy to induce the formation of linear chains with non-coordinated potentially anchoring carboxylic groups that could be expected to find broad scope in self-assembled monolayers (SAM) in thin film fabrications.

Results

Synthesis and general characterization

Iron(II) complexes were isolated by reaction of the corresponding Fe^{II} salts, $[Fe(H_2O)_6](Anion)_2$ (anion = BF_4^-, ClO_4^-, $CF_3SO_3^-$) and $[Fe(H_2O)_6](NO_3)_2$ (prepared *in situ* [3]) with HGlytrz (1:3 stoichiometry) dissolved in methanol in a $N_{2(g)}$ atmosphere. The off-white powders thus obtained are highly sensitive to air and moisture and therefore stored under N_2 atmosphere/desiccator.

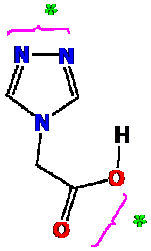

Figure 118 Molecular structure of HGlytrz with * indicating possible bifunctionality.

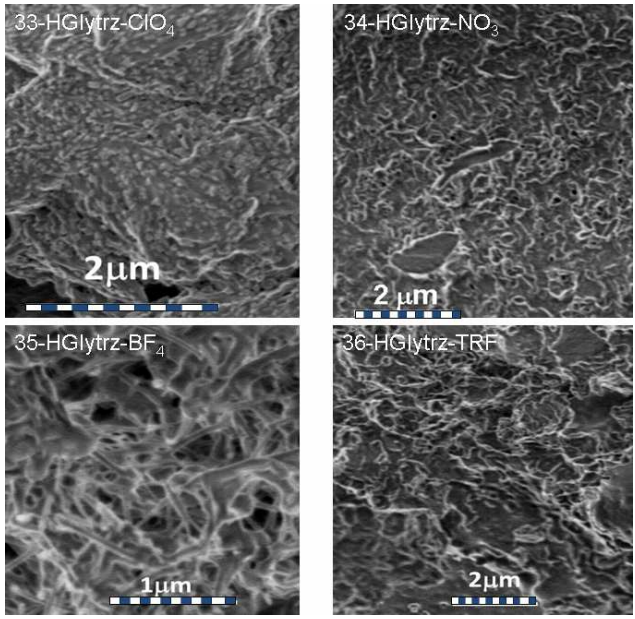

Figure 119 SEM images of microcrystalline particles of **33-HGlytrz-ClO_4, 34-HGlytrz-NO_3, 35-HGlytrz-BF_4, 36-HGlytrz-TRF** at 293 K.

SEM images (Fig. 119) reveals texture of the powders at the microscopic level. The texture is indefinable in **34-HGlytrz-NO_3 and 36-HGlytrz-TRF** which is also evident from poor X-ray powder diffraction pattern (XRPD) (Figure 120).

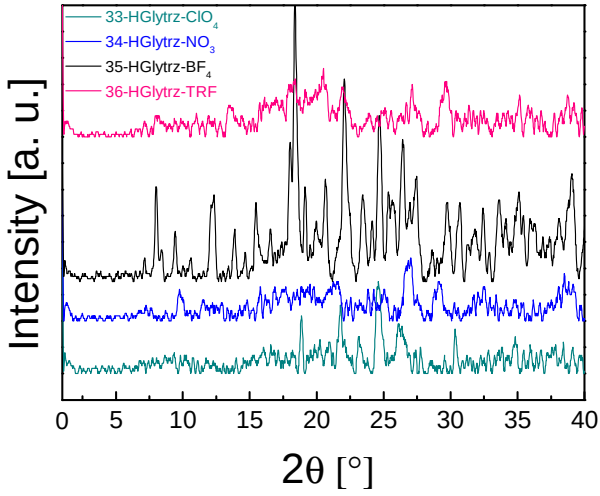

Figure 120 X-Ray powder diffraction patterns at 293 K for **33**-HGlytrz-**ClO_4**, **34**-HGlytrz-**NO_3**, **35**-HGlytrz-**BF_4**, **36**-HGlytrz-**TRF**

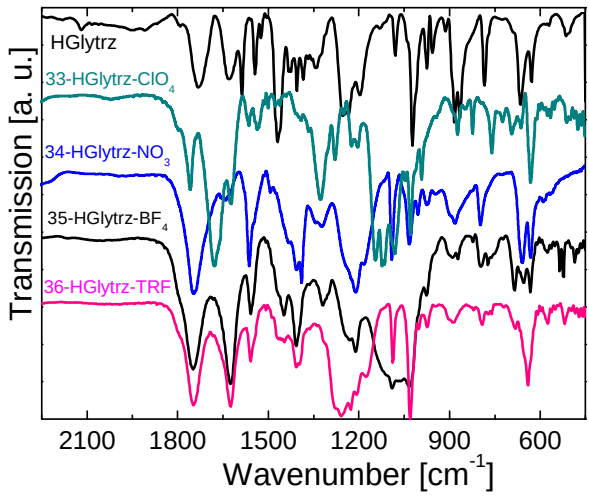

Figure 121 IR spectra of the ligand **HGlytrz** and of **33**-HGlytrz-**ClO_4**, **34**-HGlytrz-**NO_3**, **35**-HGlytrz-**BF_4**, **36**-HGlytrz-**TRF** complexes, over the range 2200-500 cm^{-1}, at r.t..

Comparatively **33-HGlytrz-ClO_4** and **35-HGlytrz-BF_4** have distinct XRPD pattern which is apparent from scanning electron micrograph (SEM) images on the bulk sample. In fact **35-HGlytrz-BF_4** show elongated needles of 60-80 nm thickness. Contrary to its ester analogue[4], **33-HGlytrz-ClO_4, 34-HGlytrz-NO_3, 35-HGlytrz-BF_4, 36-HGlytrz-TRF** were not precipitated instantly during their syntheses thus increasing precipitation probability of more than one species in the bulk sample.

The strong *ν*(C=O) band in FTIR of ligand around 1730 cm^{-1} is still found as a strong band in **33**-HGlytrz-**ClO_4**, **34**-HGlytrz-**NO_3**, **35**-HGlytrz-**BF_4**, **36**-HGlytrz-**TRF** with shift in band position (up to 1744 cm^{-1}) except in **33**-HGlytrz-**ClO_4** where the intensity is reduced comparatively. FTIR also supports the presence of anions with characteristic bands [υ(ClO_4^-) ~1050 cm^{-1} (**33**-HGlytrz-**ClO_4**); υ(NO_3^-) ~ 1382 cm^{-1} (**34**-HGlytrz-**NO_3**); υ(BF_4^-) ~ 1060 cm^{-1} (**35**-HGlytrz-**BF_4**); υ(SO_3^-) ~ 1259 cm^{-1} (**36**-HGlytrz-**TRF**)]. This situation suggests that these complexes form 1D CPs with dangling carboxylic group which is still protonated thus acting as neutral ligand and coordinating iron ions through *N1*,*N2* of 1,2,4-triazole units.

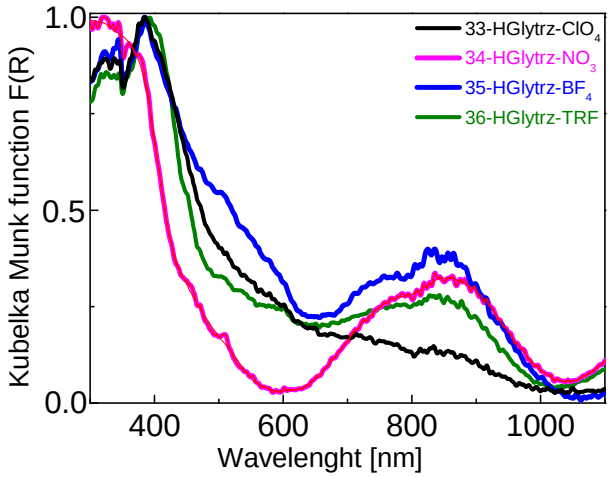

Figure 122 UV-Vis diffuse reflectance spectra of **33**-HGlytrz-**ClO_4**, **34**-HGlytrz-**NO_3**, **35**-HGlytrz-**BF_4**, **36**-HGlytrz-**TRF** showing d–d transitions at r.t..

In addition, except for **34**-HGlytrz-**NO_3**, there is a medium to strong band around 1630 cm^{-1} (1674 cm^{-1} in **33**-HGlytrz-**ClO_4**) which is assigned to asymmetric stretching of $\nu(COO^-)$ and a medium band around 1280 cm^{-1} indicative of symmetric $\nu(COO^-)$ stretching based on our earlier report[2, 5]. This would indicate the presence of 1D chains with deprotonated ligands. Thus this observation leads to the conclusion that bulk samples of **33**-HGlytrz-**ClO_4**, **35**-HGlytrz-**BF_4** and **36**-HGlytrz-**TRF** have co-precipitation of two types of 1D CP with tentative composition: $[Fe(HGlytrz)_3](Anion)_2$ and $[Fe(HGlytrz)_2(Glytrz)](Anion)$. Interesting **34**-HGlytrz-**NO_3** which was prepared in aqueous methanol which does not show $\nu_{asym}(COO^-)$ exclusively forms 1D chain with neutral ligand of the composition $[Fe(HGlytrz)_3](NO_3)_2 \cdot CH_3OH$ (**34**-HGlytrz-**NO_3**). The presence of a non-coordinated solvent molecule was confirmed by thermogravimetric analyses.

Thermal spin-crossover properties

^{57}Fe Mössbauer spectroscopy

Selected ^{57}Fe Mössbauer Spectra are shown in Figure 123 and hyperfine parameters are grouped in Table 44.

Table 44 Selected ^{57}Fe Mössbauer parameters in **33**-HGlytrz-**ClO_4**, **34**-HGlytrz-**NO_3**, **35**-HGlytrz-**BF_4**, **36**-HGlytrz-**TRF**.

Compound	T [K]	δ [mm/s]	ΔE_Q [mm/s]	$\Gamma/2$ [mm/s]	%	Spin state
33-HGlytrz-**ClO_4**	**78**	1.28(1)	3.41(2)	0.16(1)	25.7	HS1
		1.13(1)	3.36(1)	0.18(1)	74.3	HS2
	298	1.13(1)	3.39(2)	0.18(1)	25.4	HS1
		1.04(1)	2.66(1)	0.17(1)	67.3	HS2
		0.34(1)	-	0.2*	7.3	Fe^{III}
34-HGlytrz-**NO_3**	**78**	1.16(1)	3.38(1)	0.17(1)	97	HS
		0.33(1)	0.29(1)	0.10(1)	3	Fe^{III}
	298	1.04(1)	2.74(2)	0.18(1)	92	HS
		0.10(3)	0.49(1)	0.15(1)	8	Fe^{III}
35-HGlytrz-**BF_4**	**78**	1.20(1)	3.54(1)	0.12(1)	23.3	HS1
		1.17(1)	3.19(1)	0.18(1)	76.7	HS2
	298	1.12(1)	3.37(3)	0.14(1)	13.6	HS1
		1.04(1)	2.62(1)	0.20(1)	76.6	HS2
		0.13(3)	0.38(1)	0.16(1)	9.8	Fe^{III}
36-HGlytrz-**TRF**	**78**	1.18(1)	3.20(2)	0.19(1)	38.4	HS1
		1.17(1)	3.51(1)	0.17(1)	54.1	HS2
		0.15(2)	0.43(1)	0.26(1)	7.5	Fe^{III}
	298	1.05(1)	2.91(1)	0.19(1)	33.6	HS1
		1.03(1)	2.69(3)	0.18(1)	54.2	HS2
		0.18(1)	-	0.32(1)	12.2	Fe^{III}

δ: isomer shift (with respect to α-Fe at 300 K); ΔE_Q: quadrupole splitting; $\Gamma/2$: half width at half maximum; *Fixed parameter;

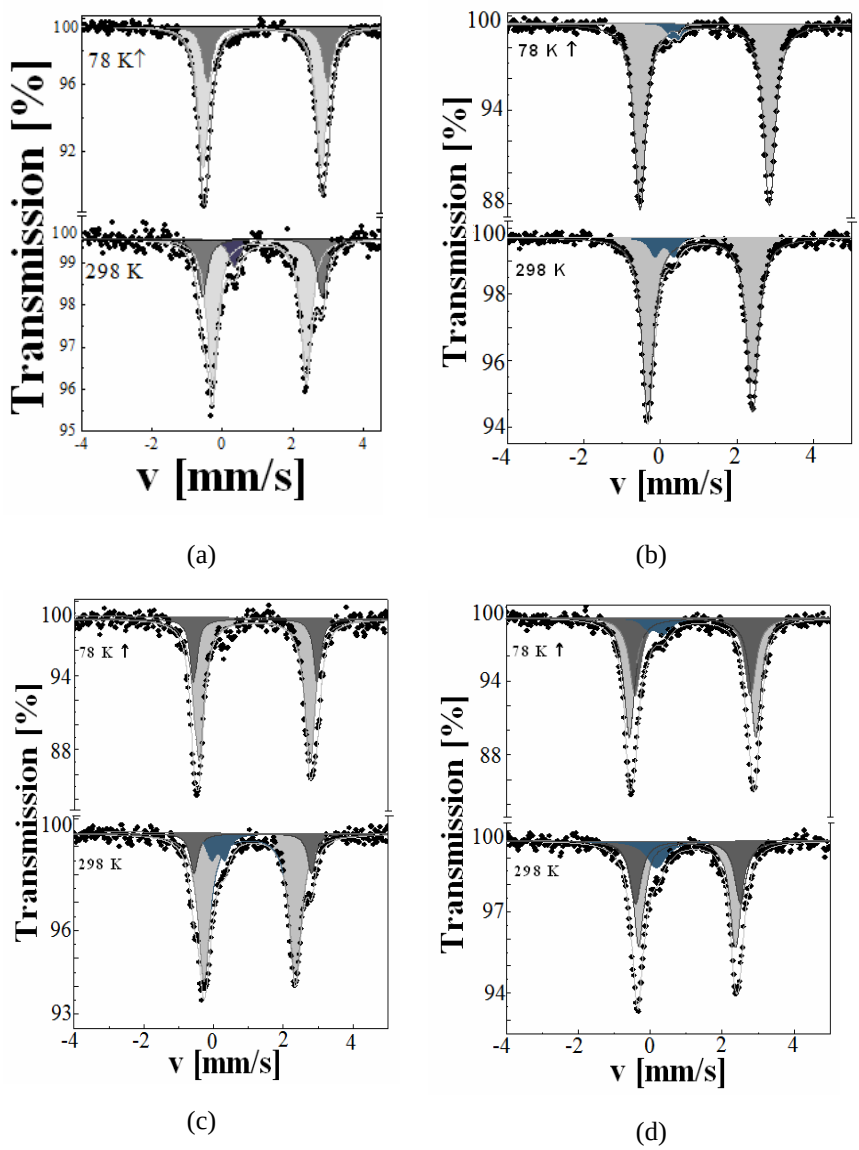

Figure 123 ^{57}Fe Mössbauer spectra of (a) **33**-HGlytrz-**ClO_4**, (b) **34**-HGlytrz-**NO_3**, (c) **35**-HGlytrz-**BF_4**, (d) **36**-HGlytrz-**TRF** at 78 K and 298 K. Grey, dark grey and blue gray correspond to the HS(1), HS(2) and Fe^{III} impurities doublets, respectively.

As a consequence of these formulations, two types of HS sites would be expected for **33**-HGlytrz-**ClO_4**, **35**-HGlytrz-**BF_4**, **36**-HGlytrz-**TRF,** which are indeed observed, hereafter denoted as HS1 and HS2 (Table 44). The

HS1 site, with isomer shift, δ^{HS1} is in the range of 1.05-1.13 mm/s and quadrupole splitting, $\Delta E_Q{}^{HS1}$ is in the range 2.91 to 3.39 mm/s, which is found in 15-30 % in population. The situation is not very different at 77 K in terms of spin state change but the value of ΔE_Q value increases further. The relatively (compared to HS2, Table 44) higher value of ΔE_Q at 298 K indicates significant distortion at the iron centers which could be possible due to the strain created by supramolecular interactions that is established by the deprotonated ligand in **33**-HGlytrz-**ClO_4**, **35**-HGlytrz-**BF_4** and **36**-HGlytrz-**TRF**. The second HS signal (HS2) dominates the spectra (~54-76 %, Table 44). The δ is in the range of 1.03 mm/s and ΔE_Q = 2.62-2.74 mm/s which is in the range of FeN_6 octahedra reported for the analogous complex $[Fe(GlytrzE)_3](ClO_4)_2 \cdot MeOH$[4] (which will be presented in the next chapter). These results are in good agreement with our hypothesis about an admixture of two types of 1D chains in the bulk sample delineated from IR spectra of **33**-HGlytrz-**ClO_4**, **35**-HGlytrz-**BF_4** and **36**-HGlytrz-**TRF**. It has to be noted that in **34**-HGlytrz-**NO_3**, there is exclusively one type of HS species thus strongly supporting the interpretation from FTIR about the composition and coordination mode. The observed decrease in δ (Table 44) on warming from 77 K to 298 K in **33**-HGlytrz-**ClO_4**, **34**-HGlytrz-**NO_3**, **35**-HGlytrz-**BF_4** and **36**-HGlytrz-**TRF** is due to relativistic second order Doppler shift[3]. Due the fact that these complexes are highly susceptible to aerial oxidation, all complexes show 8-12 % of Fe^{III} species.

Further supportive information, on admixture of CP in **33**-HGlytrz-**ClO_4**, **34**-HGlytrz-**NO_3**, **35**-HGlytrz-**BF_4** and **36**-HGlytrz-**TRF**, were obtained from diffuse reflectance spectra (Figure 122). The broad band of $^5T_{2g} \rightarrow {}^5E_g$ around 800 nm clearly indicates the presence of more than one HS species. It has to be noted that even though the spectrum for **34**-HGlytrz-**NO_3** does not show multiple species, the band around 800 nm begin to be splitted

hinting the formation of other species when recorded in air atmosphere. The fact that self-assembly of HGlytz occurs in these CPs is highly desirable in the field of self-assembled monolayers (SAM) where advantage of unbound carboxylic groups could be explored further in binding to a wide variety of substrate while maintaining the functional core intact[6].

Discussion

A tiny supramolecular synthon, ethyl-4H-1,2,4-triazol-4-yl acetic acid (**HGlytrz**) which is bifunctional by design having an electronic asymmetry and conformational flexibility has been introduced to synthesize iron(II) complexes. Having 1,2,4-triazole and carboxylic extremities on the same framework, HGlytrz display dual functionality by acting as a neutral as well as anionic ligand based on the possibility of deprotonation of carboxylic group. Thus the synthesis of four new iron(II) complexes with using **HGlytrz**, **33**-HGlytrz-**ClO_4**, **34**-HGlytrz-**NO_3**, **35**-HGlytrz-**BF_4** and **36**-HGlytrz-**TRF**, have been accomplished. Unlike its ester protected counterpart ethyl-4H-1,2,4-triazol-4-yl-acetate (GlytrzE) which show hysteretic room temperature spin crossover, **33**-HGlytrz-**ClO_4**, **34**-HGlytrz-**NO_3**, **35**-HGlytrz-**BF_4** and **36**-HGlytrz-**TRF**, remain in the HS state as revealed by ^{57}Fe Mössbauer spectroscopy. ^{57}Fe Mössbauer spectroscopy confirm the presence of two different coordination sites Fe(II)N_6 and possible Fe(II)N_4O_2. We note also the absence of SCO behaviour on cooling and the presence of oxidation product of iron at room temperature, due to the sensitivity of these systems. This behaviour, which is also depicted in terms of variation of HS molar fraction derived by integration of Mössbauer signals, indicates a cooperativity weakening which can be attributed too to a decrease of intermolecular contacts between chains, but also to a mixture of the coordination mode type. Based on IR, Raman and ^{57}Fe Mössbauer spectroscopy, for compound **34**-HGlytrz-**NO_3** only one type of coordination

mode was identified at room temperature, which is characteristic of FeN_6 environment, δ = 1.04(1) mm/s, ΔE_Q = 2.74(2) mm/s.

In the next sections, we will discus SCO properties of iron(II) coordination polymers with **GlytrzE**.

Chapter VII.2: Hysteretic spin transition materials inspired and derived from an α-amino-acid derivative †

Introducing remarks

A challenging perspective brought by 4-R-1,2,4-triazole derivatives is the preparation of thermo-sensitive molecular materials that could incorporate ethyl-ester as R substituent on the triazole. In this chapter, we will thus focus on study of 1D coordination polymers, with GlytrzE = ethyl 4H-1,2,4-triazol-4-yl-acetate, of formula $[Fe(GlytrzE)_3](A)_2 \cdot n$Solvent, **37- GlytrzE-$ClO_4$** (A = ClO_4, n = 0); **38- GlytrzE-ClO_4** (A = ClO_4, n = 1, Solvent = CH_3OH); **39-GlytrzE-NO_3** (A = NO_3, n = 1, Solvent = H_2O); **40-GlytrzE-NO_3** (A = NO_3, n = 0); **41-GlytrzE-BF_4** (A = BF_4, n = 0.5, Solvent = H_2O); **42-GlytrzE-BF_4** (A = BF_4, n = 0); **43-Glytrz-TRF** (A = $CF_3SO_3^-$, n = 2, Solvent = H_2O). The results obtained with these molecules leads to an interesting overview of the factors governing the SCO properties of the Fe-GlytrzE system which must be known to target a molecular sensor based on natural amino-acids.

Results

Synthesis and general characterization

GlytrzE was prepared by a transamination reaction[7] as discussed in Chapter VI. Coordination polymers were obtained as pink and off-white powders by reaction of the corresponding Fe(II) inorganic precursor,

† Adapted from : M. M. Dîrtu, A. D. Naik, J. Marchand-Brynaert, Y. Garcia *J. Phys. Conf. Ser*., **2010**, *217*, 012085; *Int. J. Mol. Sci.*, **2011**, *12*, 5339-5351.

$[Fe(H_2O)_6](anion)_2$, in air, with a methanolic solution of **GlytrzE**, except for $[Fe(H_2O)_6](NO_3)_2$ which was prepared *in situ*.[8] The work-up conditions were modified in order to obtain several solvates. In this respect, after filtration in air, they were dried either in air, under a $N_{2(g)}$ flow or under vacuum and stored under a $N_{2(g)}$ atmosphere. All these complexes were successfully characterized by elemental analysis, TGA-DTA analyses, atomic absorption (AAS), Powder X-Ray diffraction (XRPD), IR, Raman, SEM and ^{57}Fe Mössbauer spectroscopy. Thermogravimetric and elemental analyses have revealed in few cases the presence of alcohol or water guest molecules, affording the following formula $[Fe(GlytrzE)_3](A)_2 \cdot n$Solvent, **37-GlytrzE-$ClO_4$** (A = ClO_4, n = 0); **38- GlytrzE-ClO_4** (A = ClO_4, n = 1, Solvent = CH_3OH); **39-GlytrzE-NO_3** (A = NO_3, n = 1, Solvent = H_2O); **40-GlytrzE-NO_3** (A = NO_3, n = 0); **41-GlytrzE-BF_4** (A = BF_4, n = 0.5, Solvent = H_2O); **42-GlytrzE-BF_4** (A = BF_4, n = 0); **43-Glytrz-TRF** (A = CF_3SO_3, n = 2, Solvent = H_2O).

Isostructurality among **37- GlytrzE-ClO_4** to **43-Glytrz-TRF** was concluded from XRPD patterns that revealed the presence of characteristic principal peaks in the diffractograms of this series (Figure 124a). Compound **43-Glytrz-TRF** shows a less resolved diffractogram. Although, a similar molecular organization around iron chains is expected for other members of series, the asymmetric nature of $CF_3SO_3^-$ anion may induce a preferential arrangement which could influence on directional and strength of H-bonds.

The degree of crystallinity, revealed from Figure 124a for **37- GlytrzE-ClO_4** to **42-GlytrzE-BF_4** was not confirmed by SEM analysis (Figure 124b). Indeed, amorphous aggregates were found for **37- GlytrzE-ClO_4** and **41-GlytrzE-BF_4**, with spherical particles of ~ 183 nm diameter distinguished for **41-GlytrzE-BF_4** whereas elongated rods of dimensions (2.5 μm x 180 nm) and small blocks were identified for **40-GlytrzE-NO_3** and **43-Glytrz-TRF**, respectively. Attempt to crystallize these complexes all proved

unsuccessful due to the slow hydrolysis of **GlytrzE** in solution combined to the Fe(II) oxidation.

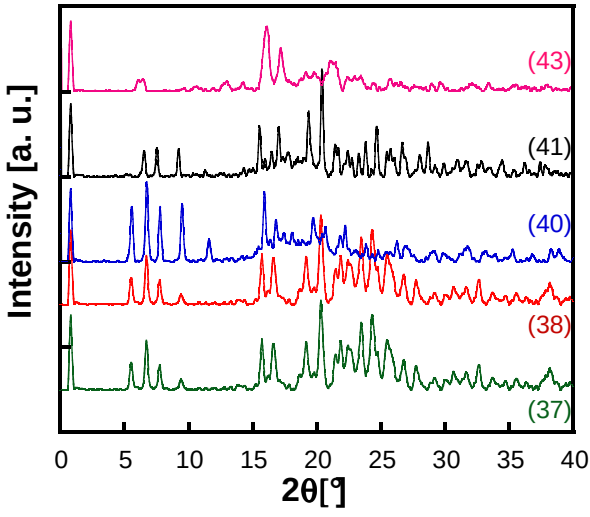

(a)

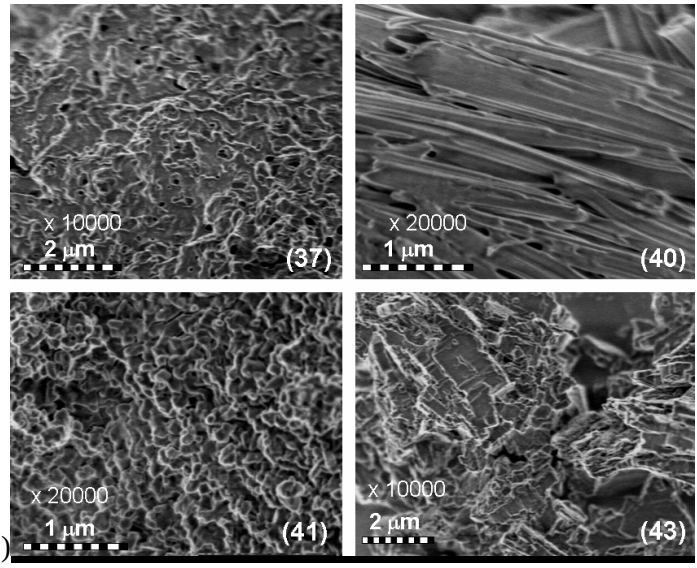

(b)

Figure 124 (a) X-Ray powder diffraction patterns at 293 K for **37- GlytrzE-ClO_4** to **43-Glytrz-TRF**. Diffraction pattern for **39-GlytrzE-NO_3, 42-GlytrzE-BF_4** are identical to **40-GlytrzE-NO_3, 41-GlytrzE-BF_4** and were thus omitted for clarity (b) SEM images of powder particles of **37- GlytrzE-ClO_4**, **40-GlytrzE-NO_3**, **41-GlytrzE-BF_4**, **43-Glytrz-TRF** at 293 K (for clarity only the number of the compound was add in all images).

In view of the difficulty to obtain single crystals for this class of compounds, attention was focused on the vibrational spectroscopic data (FT-IR and Raman) to confirm the identity of the ligand framework upon complexation, as the ester functionality is susceptible to hydrolysis, as well as to ascertain coordination mode of the ligand and presence of non coordinated counter-anions in the complexes (Figure 125).

Three sharp bands at 3112 (s), 3012 (m) and 2933 (m) cm^{-1} are assigned to the νCH_2 modes in the IR spectrum of **GlytrzE** (Figure 125a). The carboxylic group of ester shows two stretching vibrations corresponding to C=O and C-O at 1743 (s) and 1236 (s) cm^{-1}, respectively, which are almost unchanged (1746 and 1240 cm^{-1}) in complexes ruling out the possible ester hydrolysis and also confirming non-involvement of carboxylic ester group in coordination. For **GlytrzE** the band assigned to ring torsion of 1,2,4-triazole at ν = 637 (m) cm^{-1}, the $\nu_{C=N}$ stretching vibration at 1539 (m) cm^{-1} and the N-N stretching band at ν = 1018 (s) cm^{-1}, are all shifted upon complexation, for example in **37** to 625 cm^{-1}, $\nu_{C=N}$ = 1560 cm^{-1}, and ν_{N-N} = 1026 cm^{-1}, respectively. These values confirm the coordination of the iron to the 1,2,4-triazole ring.[9, 10] The ν_{C-N} and ν_{C-C} vibrations are identified to be 1431 (m) cm^{-1} and 1165 (m) cm^{-1}, respectively. The absence of ester hydrolysis for **GlytrzE** was supported by a comparison with the IR bands of 4H-1,2,4-triazol-4-yl acetic acid (**HGlytrz**),[1] which are slightly different. The $-COO^-$ vibrations (asymmetric and symmetric) are found as a strong band at 1583 cm^{-1}, and as a weak band at 1411 cm^{-1}. Carboxylic acids are known to present a strong band due to the stretching vibration of the C-O between 1200 – 1000 cm^{-1} [11]. In **HGlytrz** this band is identified at 1197 cm^{-1}. The other bands, characteristics of the triazole ring, attributed to the ring torsion of triazole, to the $\nu_{C=N}$ stretching vibration, to the N-N stretching band and to the C-N band are observed at ν = 629 (m) cm^{-1}, 1568 (m) cm^{-1}, 1024 (s) cm^{-1}

and 1018 (s) cm^{-1} respectively. A set of bands are also identified at 3123, 2889 and 2837 cm^{-1}, which are assigned to the CH_2 stretching.

For a better understanding of the molecular structure of these complexes, Raman spectra were collected (Figure 125b). The band at 1737 cm^{-1} for **GlytrzE** is assigned to a -C=O vibration. In complexes this band is retained and appears around 1749 cm^{-1}. The C-C stretching is also active in Raman as a medium band at 1104 cm^{-1} for **GlytrzE** and appears in the same wave number range, however being more intense, for the complexes. The Fe-N stretching vibrations could also be identified by Raman spectroscopy in the range 200 – 400 cm^{-1}. The weak band at 349 cm^{-1} (**37- GlytrzE-ClO_4**), 358 cm^{-1} (**39-GlytrzE-NO_3** and **40-GlytrzE-NO_3**), 351 cm^{-1} (**41-GlytrzE-BF_4** and **42-GlytrzE-BF_4**), and 350 cm^{-1} (**43-Glytrz-TRF**) is due to the stretching vibration $\upsilon(Fe_{LS}\text{-}N)$[12]. The spectra of **43-Glytrz-TRF** also contains a low intensity band at 317 cm^{-1}, which is characteristic for $\upsilon(Fe_{HS}\text{-}N)$ stretching vibration. Such minor HS species at room temperature,[12] is also supported by Mössbauer data (*vide infra*).

Presence of non-coordinated monovalent counter-anions originating from the inorganic precursors was also confirmed by IR and Raman as listed in the synthesis section: *IR* (cm^{-1}) $\upsilon_{(Cl\text{-}O)}$ ~ 1105 (s), (**37- GlytrzE-ClO_4**), (**38-GlytrzE-ClO_4**); $\upsilon_{(N\text{-}O)}$ ~ 1384 (s), (**39-GlytrzE-NO_3**); $\upsilon_{(N\text{-}O)}$ ~ 1384 (s), (**40-GlytrzE-NO_3**); $\upsilon_{(B\text{-}F)}$ ~ 522 (w), 1083 (vs) (**41-GlytrzE-BF_4**); $\upsilon_{(B\text{-}F)}$ ~ 522 (w), 1083 (vs) (**42-GlytrzE-BF_4**); $\upsilon_{(S\text{-}O)}$ ~ 1251 (vs), (**43-Glytrz-TRF**); *Raman* (cm^{-1}) $\upsilon_{(Cl\text{-}O)}$ ~ 932 (s), 460 (m) (**37- GlytrzE-ClO_4**), (**38- GlytrzE-ClO_4**); $\upsilon_{(N\text{-}O)}$ ~ 1042 (s), (**39-GlytrzE-NO_3**); $\upsilon_{(N\text{-}O)}$ ~ 1042 (s), (**40-GlytrzE-NO_3**); $\upsilon_{(B\text{-}F)}$ ~ 767 (s) (**41-GlytrzE-BF_4**); $\upsilon_{(B\text{-}F)}$ ~ 767 (s) (**42-GlytrzE-BF_4**); $\upsilon_{(S\text{-}O)}$ ~ 1036 (s), 770 (m) (**43-Glytrz-TRF**).

^{57}Fe Mössbauer spectroscopy confirms the presence of only one $Fe^{II}N_6$ site, for this series of complexes, as well as the absence of oxidation product. Hyperfine parameters are typical for 1D Fe(II) polymeric chain compounds

(Table 45-50)[13]. Based on IR, Raman, and Mössbauer spectroscopy data, a chain character for this class of compounds in which the Fe(II) ions are linked by triple *N1*, *N2*-1,2,4-triazole bridges, can be safely suggested.

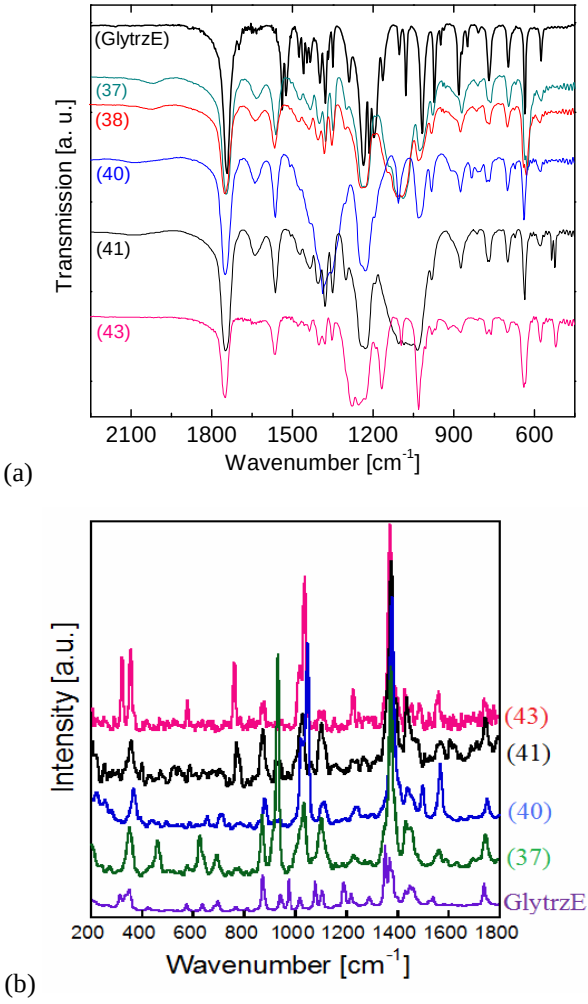

Figure 125 IR spectra of: (a) **GlytrzE** and complexes **37- GlytrzE-ClO_4** to **43-Glytrz-TRF**; (b) Raman spectra of **GlytrzE** and complexes **37- GlytrzE-ClO_4, 40-GlytrzE-NO_3, 41-GlytrzE-BF_4, 43-Glytrz-TRF.** The IR and Raman spectra of **39-GlytrzE-NO_3, 42-GlytrzE-BF_4** are identical to **40-GlytrzE-NO_3, 41-GlytrzE-BF_4** and were thus omitted for clarity; for clarity only the number of the compound was add in all images.

The colour of complexes **37-GlytrzE-ClO_4** to **43-Glytrz-TRF**, being either

pale pink or pink at room temperature, can be reversibly changed to pink and white, on warming and cooling, respectively. For instance, **37-GlytrzE-ClO$_4$** exhibits reversible pronounced thermochromism to pink on quenching of the sample in liquid nitrogen. However, cooling in ice is also sufficient to reveal a strong colour change precluding a spin state change just below room temperature.

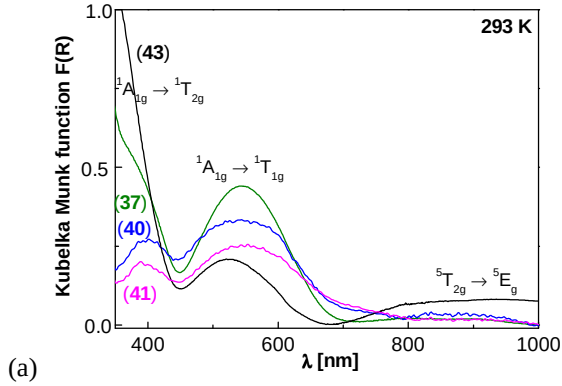

(a)

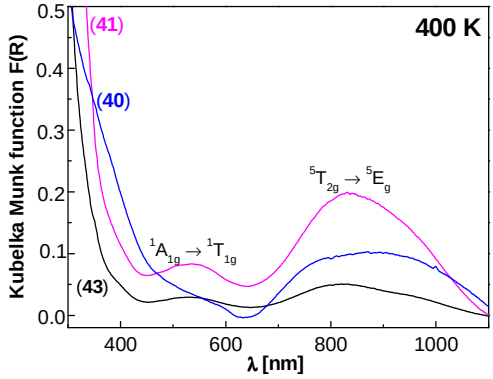

(b)

Figure 126 UV-vis diffuse reflectivity spectra of selected complexes showing the d–d transitions at (a) 293 K and (b) at 400 K; for clarity only the number of the compound was add in all images.

These colors depend on the spin state of the Fe(II) centers, which were analyzed by UV-vis diffuse reflectance spectroscopy (DRS) at 293 K and 400 K (Figure 126a, 126b). The pink color is due to the $^1A_{1g} \rightarrow {}^1T_{1g}$ d-d transition of LS Fe(II) sites observed at 18397 cm^{-1} (for **37- GlytrzE-ClO$_4$**),

at 18225 cm^{-1} (for **40-GlytrzE-NO_3** and **41-GlytrzE-BF_4**) and at 18727 cm^{-1} (for **7**). A second band identified at 26824 cm^{-1} (for **37- GlytrzE-ClO_4**) and 25126 cm^{-1} (for **40-GlytrzE-NO_3** and **41-GlytrzE-BF_4**) is attributed to the $^1A_{1g} \rightarrow {}^1T_2$ d-d transition. For **43-Glytrz-TRF**, another band is found at 11806 cm^{-1} which is attributed to the transition $^5T_{2g} \rightarrow {}^5E_g$ suggesting the presence of a fraction of HS Fe(II) ions at room temperature (Fig. 126a). The white colour is indeed due to the location of the spin-allowed lowest energy d-d transition, $^5T_{2g} \rightarrow {}^5E_g$, for the HS sites in the near infrared region and which is clearly observed at 400 K, e.g. for **41-GlytrzE-BF_4**.[14, 15] A supplementary band is identified at ~ 18700 cm^{-1}, for **41-GlytrzE-BF_4** and **43-Glytrz-TRF** indicating the presence of LS Fe(II) ions (Fig 126b). The ligand field strengths for the HS and LS states, given by equations $10D_q^{HS} = E(^5E) - E(^5T_2)$ and $10D_q^{LS} = E(^1T) - E(^1A_1) + (E(^1T_2) - E(^1T_1))/4$,[14, 15] allowed to estimate $10D_q^{HS}$ and $10D_q^{LS}$ to be approximately 12000 cm^{-1} and 25100 cm^{-1}, respectively. These values are characteristic for SCO complexes.[14, 15]

Thermal spin-crossover properties

^{57}Fe Mössbauer spectroscopy

^{57}Fe Mössbauer Spectroscopy spectra were recorded on cooling and warming modes over the temperature range 78-368 K for compounds **37-GlytrzE-ClO_4** to **43-Glytrz-TRF**. Hyperfine parameters are provided in the appendix (Tables 45-50). At 78 K, the spectrum of $[Fe(GlytrzE)_3](ClO_4)_2$ (**37- GlytrzE-ClO_4**) consists of a single quadrupole doublet corresponding to a LS Fe(II) ion, with an isomer shift δ^{LS} = 0.49(1) $mm.s^{-1}$ and a low quadrupole splitting ΔE_Q^{LS} = 0.19(1) $mm.s^{-1}$ (Figure 128). This quadrupole splitting is characteristic for a lattice contribution to the electric field gradient which implies a distortion of the LS octahedron, as can be expected

for a constrained chain.[16] Upon warming up to 293 K, no change is observed in the spectra but at 298 K, a new quadrupole doublet characteristics of a HS Fe(II) ion is detected, indicating the onset a spin state crossover from LS to HS state, which progresses further at 300 K. Indeed, at this temperature, a minor fraction of LS Fe(II) ions (9%) is detected in agreement with the pale pink colour of the powder. At 308 K, a single HS quadrupole doublet is observed, with $\delta^{HS} = 1.03(1)$ mm/s and $\Delta E_Q{}^{HS}$ = 2.74(4) mm/s, indicating a complete spin state crossover. The asymmetry of the lines is attributed to texture. On cooling, a hysteretic behavior is clearly revealed by comparing Mössbauer spectra recorded at 298 K and 293 K (Figure 128). δ and ΔE_Q of both LS and HS species, listed in Table 45, are typical of a $Fe^{II}N_6$ chain in which metallic centers are bonded by a bridge made of three N1,N2-triazole ligands.[17] The temperature dependence of the HS molar fraction, γ_{HS}, was plotted, assuming equal Debye Waller factors for HS and LS ions (Figure 129a). An abrupt ST is revealed occurring near room temperature with a hysteresis width of 5 K and transition temperatures, on warming and cooling modes, of $T_{1/2}{}^{\uparrow}$ = 296(2) K and $T_{1/2}{}^{\downarrow}$ = 291(2) K, respectively.

The methanol solvate **38-GlytrzE-ClO$_4$** was also studied by Mössbauer spectroscopy over 78-300 K. At 78 K, the compound is fully in the LS state (Figure 130) with same hyperfine parameters (Table 46) as that for **37-GlytrzE-ClO$_4$**. This situation suggests that methanol inclusion is located far from the neighboring environment of chains and has therefore no effect on the local environment of the iron(II) ions. Upon warming further, another quadrupole doublet which is typical of the HS state is detected at 270 K and at 300 K there is no LS doublet, confirming the completeness of the ST in both spin states (Fig. 130). A hysteresis effect is also evidenced by comparing the spectra recorded at the same temperature (270 K or 280 K) either on warming or on cooling modes, which show a different HS/LS population (Fig. 130). The ST profile, drawn on warming and cooling

confirm the hysteretic behavior associated to the ST at $T_{1/2}^{\uparrow}$ = 273 K and $T_{1/2}^{\downarrow}$ = 263 K, that is shifted to lower temperatures compared to **37** (Fig. 129a). Interestingly, the hysteresis loop of 10 K width is dissymmetric which may preclude a structural phase transition.

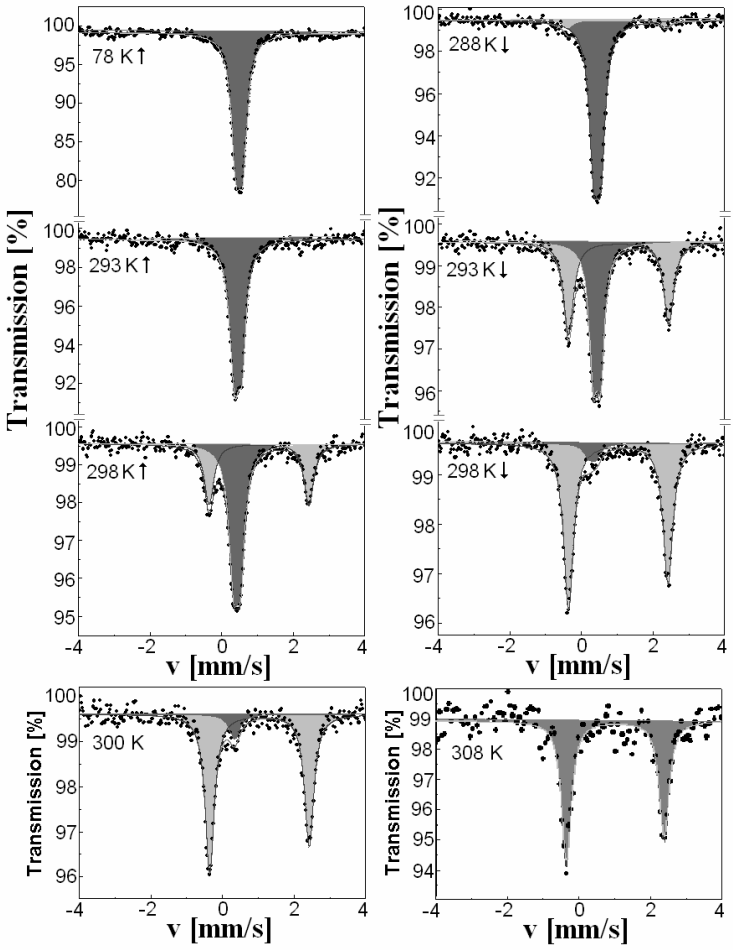

Figure 128 Selected ^{57}Fe Mössbauer spectra of $[Fe(GlytrzE)_3](ClO_4)_2$ (**37- GlytrzE-ClO_4**) on warming (left) and cooling modes (right). Grey and dark grey correspond to the HS and LS doublets, respectively.

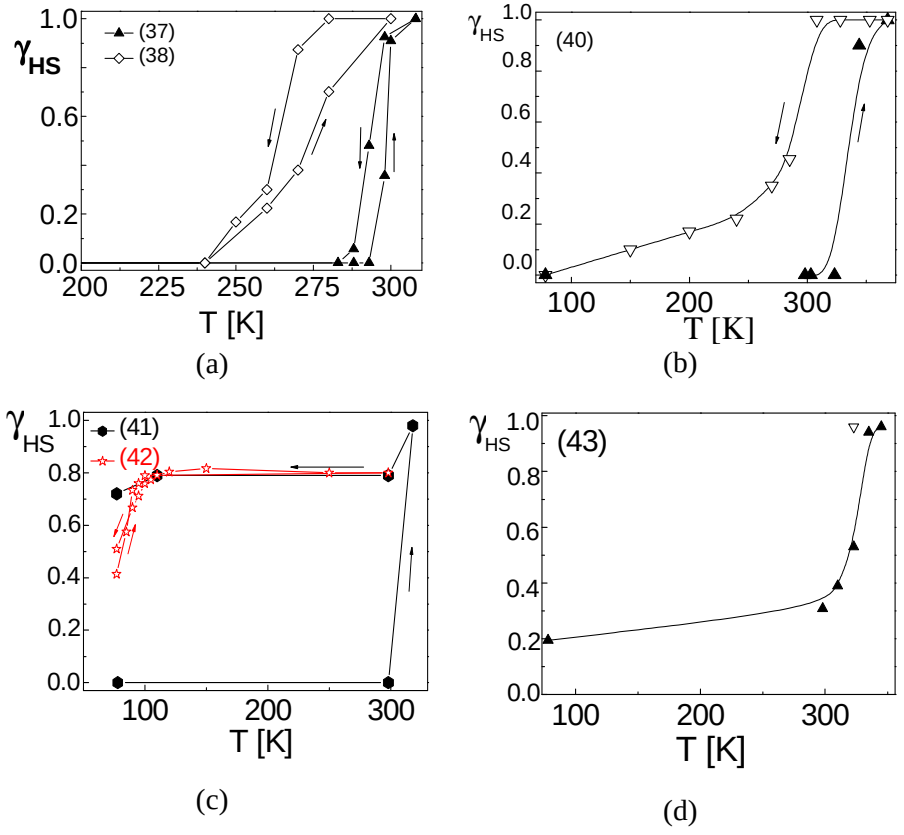

Figure 129 HS molar fraction *vs. T* on cooling and warming modes for: **37-GlytrzE-ClO$_4$** and **38- GlytrzE-ClO$_4$** (a); **40-GlytrzE-NO$_3$** (b); **41-GlytrzE-BF$_4$, 42-GlytrzE-BF$_4$** (c); **43-Glytrz-TRF** (d) as deduced from ^{57}Fe Mössbauer measurements; for clarity only the number of the compound was add in all images.

^{57}Fe Mössbauer measurement on [Fe(GlytrzE)$_3$](NO$_3$)$_2$·H$_2$O (**39-GlytrzE-NO$_3$**) at room temperature reveals a doublet characteristic of Fe(II) LS (δ^{LS} = 0.51(1) mm.s^{-1} and ΔE_Q^{LS} = 0.23(1) mm.s^{-1}). This sample present a ST above r.t. and because of a small resonance effect at high temperature, a dehydration of the sample could not be avoided.

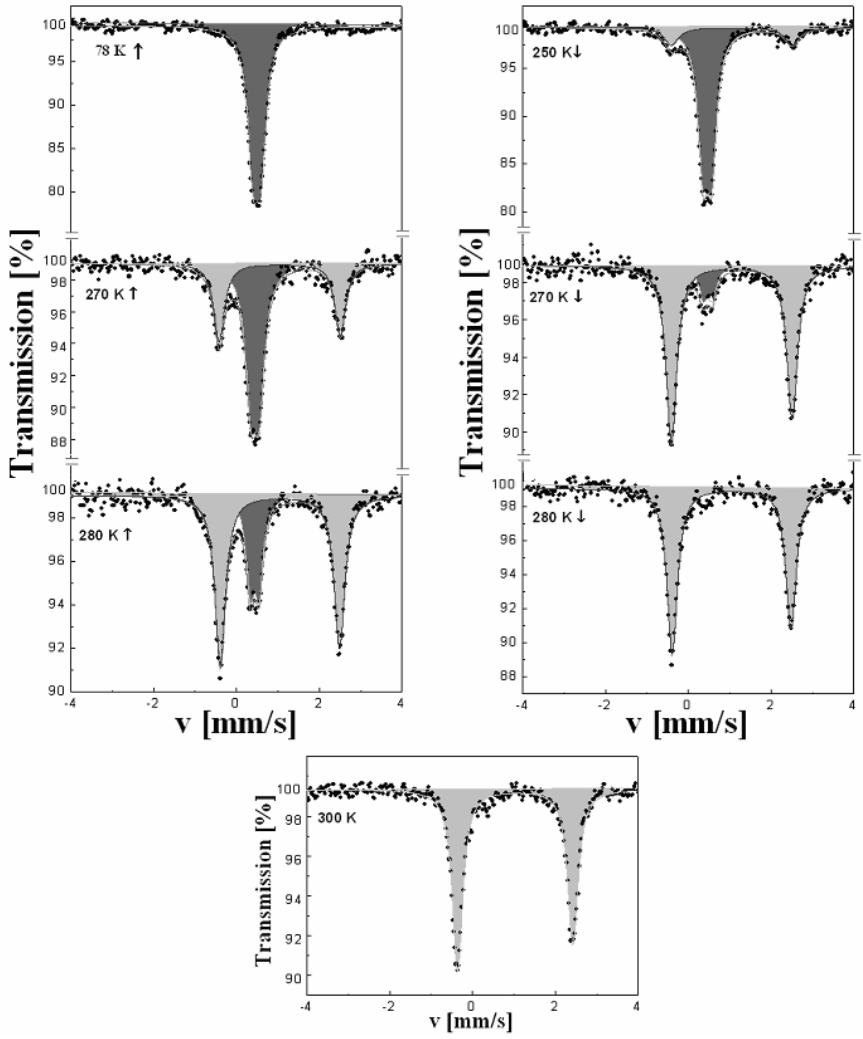

Figure 130 ^{57}Fe Mössbauer spectra of **38-GlytrzE-ClO$_4$** between 78 and 368 K. Grey and dark grey correspond to the HS and LS doublet, respectively.

Selected ^{57}Fe Mössbauer spectra of [Fe(GlytrzE)$_3$](NO$_3$)$_2$ (**40-GlytrzE-NO$_3$**) are shown in Figure 131, Table 47. At 298 K, a single quadrupole doublet with an isomer shift δ^{LS} = 0.39(1) mm.s^{-1} and a quadrupole splitting $\Delta E_Q{}^{LS}$ = 0.19(1) mm.s^{-1} refers to a LS iron(II) ion. ^{57}Fe Mössbauer measurements were recorded on warming up to 368 K in order to track the emergence of a

HS quadrupole doublet that would be the signature of a LS to HS transition. This new signal is detected at 344 K, with δ^{HS} = 1.01(1) mm.s^{-1} and $\Delta E_Q{}^{HS}$ = 2.43(1) mm.s^{-1}, typical of a HS Fe(II) ion. At 368 K the spectrum consists of only one HS doublet δ^{HS} = 0.98(1) mm.s^{-1}, $\Delta E_Q{}^{HS}$ = 2.47(1) mm.s^{-1}, indicating a complete spin transition. On cooling, the reverse HS to LS transition is observed, with a complete character identified at 78 K with one quadrupole doublet corresponding to the LS state (δ^{LS} = 0.46(3) mm.s^{-1}, $\Delta E_Q{}^{LS}$ = 0.19(1) mm.s^{-1}). The spectra shown on cooling and warming modes at 328 and 323 K, respectively, clearly evidence a hysteretic effect of width ($\Delta T \approx$ 60 K), which is better seen on Figure 129b with $T_{1/2}{}^{\downarrow}$ = 280(5) K and $T_{1/2}{}^{\uparrow}$ = 335(5) K.

The Mössbauer spectrum of $[Fe(GlytrzE)_3](BF_4)_2 \cdot 0.5H_2O$ (**41-GlytrzE-BF$_4$**) reveals at 78 K a single quadrupole doublet attributed to LS Fe^{II} ions (δ^{LS} = 0.47(1) mm.s^{-1}, $\Delta E_Q{}^{LS}$ = 0.19(1) mm.s^{-1}) (Fig. 132). The LS state is preserved on warming up to 298 K without any sign of HS ion (Table 48). At 318 K, a HS quadrupole doublet clearly appears with a minor fraction (2%) of LS Fe(II) ions indicating a complete spin state change.

This change is thought to be attributed to dehydration because of the long acquisition time at 318 K of almost two weeks, which should be sufficient to remove the 0.5 non-coordinated water molecules from the sample. Noteworthy is that a modification of the morphology of this sample was noticed after a long heating treatment (see SEM section, Figure 124). Mössbauer spectra recorded in the cooling mode, from 298 K, 110 K to 77 K, (Table 48) indicate that the compound remains in the HS state, in proportion of 79 %, after such treatment. A new desolvated compound (**42-GlytrzE-BF$_4$**) with different magnetic properties is thus obtained, (refer SQUID part).

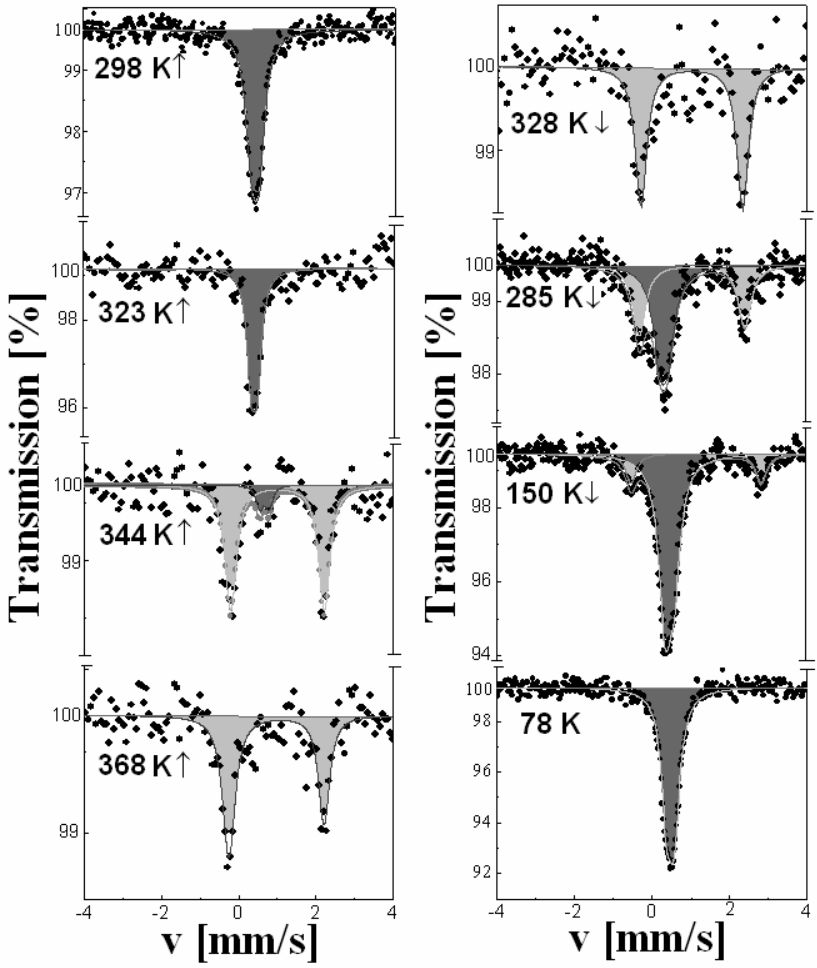

Figure 131 ^{57}Fe Mössbauer spectra of **40-GlytrzE-NO$_3$** between 78 and 368 K. Grey and dark grey correspond to the HS and LS doublet, respectively.

The thermal dependence of the HS molar fraction shown in Figure 129c, clearly evidences a very gradual SCO for compound **42-GlytrzE-BF$_4$**, below room temperature. The spectrum recorded at 78 K (Table 49) is characteristic of the LS and HS of iron(II), respectively, with an isomer shift of δ = 1.16(1) mm.s^{-1} and a quadrupole splitting of ΔE_Q = 3.39(1) mm.s^{-1} and δ = 0.55(3) mm.s^{-1}, ΔE_Q = 0.21(3) mm.s^{-1}, with ~ 51 % of HS species. Upon

heating, the molar fraction of HS increases to 76 % up to 100 K, and followed by a slight increase to 80 % at 298 K. On cooling from room temperature to 77 K, the reverse situation is observed. The SCO behaviour occurs below 100 K in the warming and in the cooling mode respectively. The SCO behaviour could not be studied below 77 K to evidence if the spin conversion was complete or not. In this respect a SQUID measurement at liquid He atmosphere could be required (*vide infra*).

The spectrum recorded at 78 K, for **43-Glytrz-TRF**, (Figure 132b) shows two quadrupole doublets attributed to HS Fe(II) ions (δ = 1.15(1) mm.s^{-1}, ΔE_Q = 3.36(1) mm.s^{-1}) and LS Fe(II) ions (δ = 0.49(1) mm.s^{-1}, ΔE_Q = 0.21(1) mm.s^{-1}) in population 20/80, indicating an incomplete ST at low temperature (Table 50). At room temperature, the relative intensity of the HS doublet slowly increases to reach ~ 31 %. Only 10 % of $Fe^{II}N_6$ site are actives in this temperature range (78-298 K). Upon warming, this value increase very slowly up to 310 K where first LS to HS transition take place at 325 K, identical to the temperature which the release of lattice water molecules has been found by thermogravimetric analysis (323 K), Figure 133. This behavior is typical for the phenomenon that has called a non-classical SCO driven by the release of lattice water molecules[18]. Thermogravimetric measurements performed under air, confirm that after a first heating, of **43-Glytrz-TRF**, to 350 K the compound have been completely dehydrated. Upon cooling, compound **43-Glytrz-TRF** remains in the HS form until room temperature.

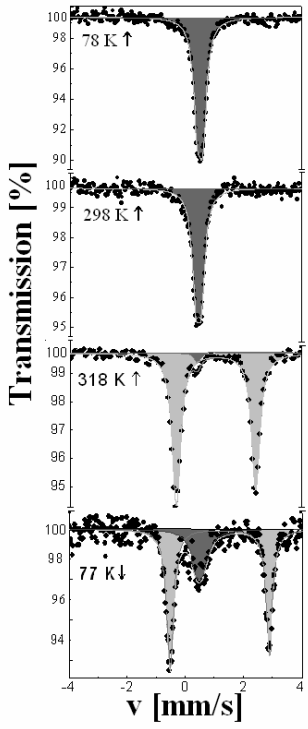

(a)

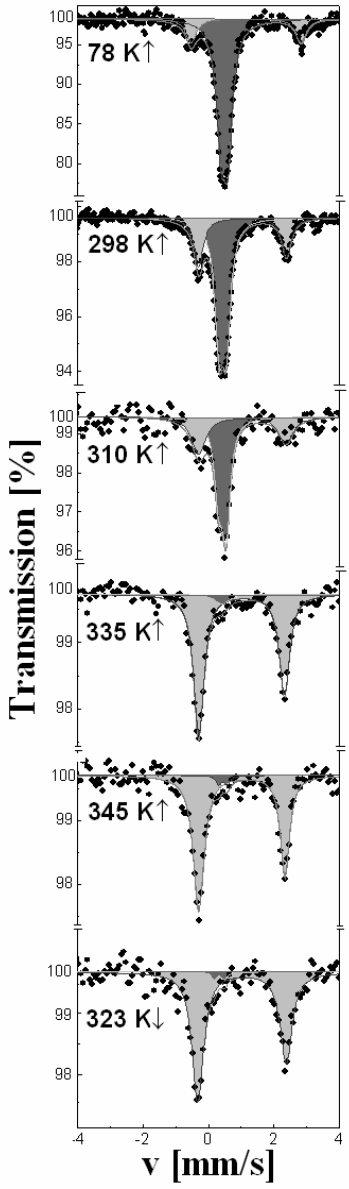

(b)

Figure 132 ^{57}Fe Mössbauer spectra of (a) **41-GlytrzE-BF$_4$** and (b) **43-Glytrz-TRF** between 78 and 368 K. Grey and dark grey correspond to the HS and LS doublet, respectively.

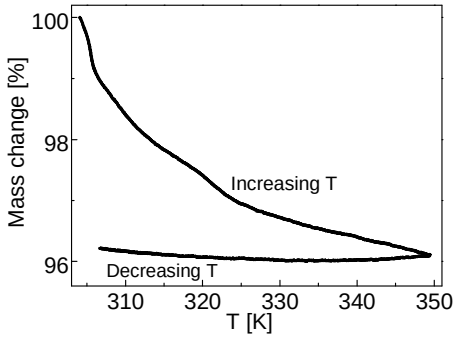

Figure 133 Thermogravimetric analyses recorded at 1K/min, on warming and on cooling mode for compound **43-Glytrz-TRF**.

SQUID magnetometry

After having delineated the ST range by Mössbauer spectroscopy, magnetic susceptibility measurements were undertaken to plot the associated ST profiles over the temperature range 4 - 380 K, by Dr. A. Rotaru (USV, Romania). For **37- GlytrzE-ClO$_4$**, a decrease of the $\chi_M T$ product from 3.42 cm^{3}Kmol^{-1} at 315 K to 3.25 cm^3 K mol^{-1} at 298 K is observed, followed by an abrupt decrease 0.36 cm^3 K mol^{-1} at 260 K, which indicates a diamagnetic iron(II) complex, with a less paramagnetic contribution. Compound **37-GlytrzE-ClO$_4$** undergoes an abrupt ST with $T_{1/2}^{\downarrow}$ = 291 K (Figure 134a). Upon heating, the transition curve differs slightly from the cooling curve and a small hysteresis (5 K) is observed, $T_{1/2}^{\uparrow}$ = 296 K, which is in good agreement with the outcome from ^{57}Fe Mössbauer spectroscopy.

The SQUID measurement of fresh sample of **38- GlytrzE-ClO$_4$** was not possible because of its extreme sensitivity to even trace amount of air and moisture which leads to partial replacement of methanol by water and thus changing the composition and nature of the resulting magnetic properties.

At 4 K, $\chi_M T$ is equal to 0.03 cm^3 K mol^{-1} for **39-GlytrzE-NO_3** (Figure 134b) which corresponds to a major fraction of Fe(II) ions in the LS state. On warming $\chi_M T$ increase slightly until 350 K ($\chi_M T$ = 0.78 cm^3 K mol^{-1}) and the transition is followed by an abrupt change of spin state and reaches 3.35 cm^3 K mol^{-1} at 360 K. On cooling, the $\chi_M T$ remains constant until 350 K and reaches a value of 3.34 cm^3 K mol^{-1} at this temperature. This is followed by an abrupt decrease of the $\chi_M T$ further to 0.48 cm^3 K mol^{-1} at 321 K. At 4 K, the material is fully in the diamagnetic state (χ_MT = 0.03 cm^3 K mol^{-1}). The sharpness of the ST is preserved in the heating and warming modes. The ST is probably induced by a dehydration/hydration process since **39-GlytrzE-NO_3** contains one non-coordinated H_2O molecule, in its crystal lattice. Actually, **39-GlytrzE-NO_3** exhibits an abrupt spin state transition in the warming regime at 353 K accompanied by a loss of one non-coordinated water molecule. This dehydration/hydration process was confirmed by thermogravimetric analysis (Figure 135a). At room temperature the compound is again hydrated and presents a hysteresis loop of ~ 20 K ($T_w^{\downarrow}$ = 333 K, $T_w^{\uparrow}$ = 353 K).

Figure 134b show also the temperature dependence of the magnetic properties of **40-GlytrzE-NO_3** (χT vs. T, depicted in red) analyzed in the temperature range 240 – 350 K, which is a non solvated material. The room temperature value of $\chi_M T$ is equal to 3.21 cm^3 K mol^{-1} (295 K) is characteristic for an iron (II) complex in the HS state. This value remain constant between 350 K and room temperature, in the cooling mode, where an abrupt ST to the LS state is observed, transition centered at $T_{1/2}^{\downarrow}$ = 278 K with a remaining magnetic moment of 0.21 cm^3 K mol^{-1} at 240 K. Upon heating, $\chi_M T$ remains constant up to 320 K (0.27 cm^3 K mol^{-1}), where it increases abruptly to 3.21 cm^3 K mol^{-1} at 338 K. In the heating mode the abrupt character of the ST is more pronounced compared to the cooling mode. A ST, centered on room temperature, with a 60 K hysteresis width

($T_{1/2}^{\downarrow}$ = 278 K, $T_{1/2}^{\uparrow}$ = 338 K) is observed. This loop can be cycled several times (the SQUID measurement was repeated five times and further confirmed even after storing the sample for 4 months in a desiccator). This wide hysteresis is highly significant and would have immense importance for potential applications.

The $\chi_M T$ for **41-GlytrzE-BF$_4$** remains approximately constant at 0.09 cm^3 K mol^{-1} between 77 and 100 K, indicative of LS iron(II) (Figure 134c, depicted in blue). Between 100 and 305 K $\chi_M T$ remains constant (0.23 cm^3 K mol^{-1}) and the values rapidly increases to reach a maximum value of 3.33 cm^3 K mol^{-1} at 350 K, indicating that all the iron(II) sites are in the HS state. The $T_{1/2}^{\uparrow}$ value of this transition is 320 K. In the cooling mode, the abrupt character of the ST is maintained as in the warming mode. A ST with a 15 K wide thermal hysteresis loop is observed at $T_{1/2}^{\downarrow}$ = 305 K. As in the previous case (compound **39-GlytrzE-NO$_3$**) this transition is accompanied by the removal of 0.5 non-coordinated water molecules. Once this compound looses its non-coordinated water molecules, it does not recover its initial form, which prompted us to study morphology of this system. In addition the dehydrated system **42-GlytrzE-BF$_4$** show completely different magnetic properties which were further probed by SQUID measurements.

The magnetic behavior of **42-GlytrzE-BF$_4$** shown in Figure 134c reveal a smooth decrease of $\chi_M T$ from 3.5 cm^{3}K mol^{-1} at 350 K down to 3.3 cm^{3}K mol^{-1} at 270 K, where a blunt decrease is observed, centered to 300 K, which may be due to a fractional amount of **41-GlytrzE-BF$_4$**. Upon cooling, the $\chi_M T$ product slightly decreases, until 118 K where a sharp and incomplete ST in the LS state takes place. On warming back to r.t., a hysteresis loop of 14 K width is delineated with $T_{1/2}^{\downarrow}$ = 91.5 K and $T_{1/2}^{\uparrow}$ = 105.5 K. Below 62 K, a plateau is observed which decrease progressively below 25 K attributed to both zero field splitting of remaining HS Fe(II) ions and/or an overall AF coupling of these ions within a chain.

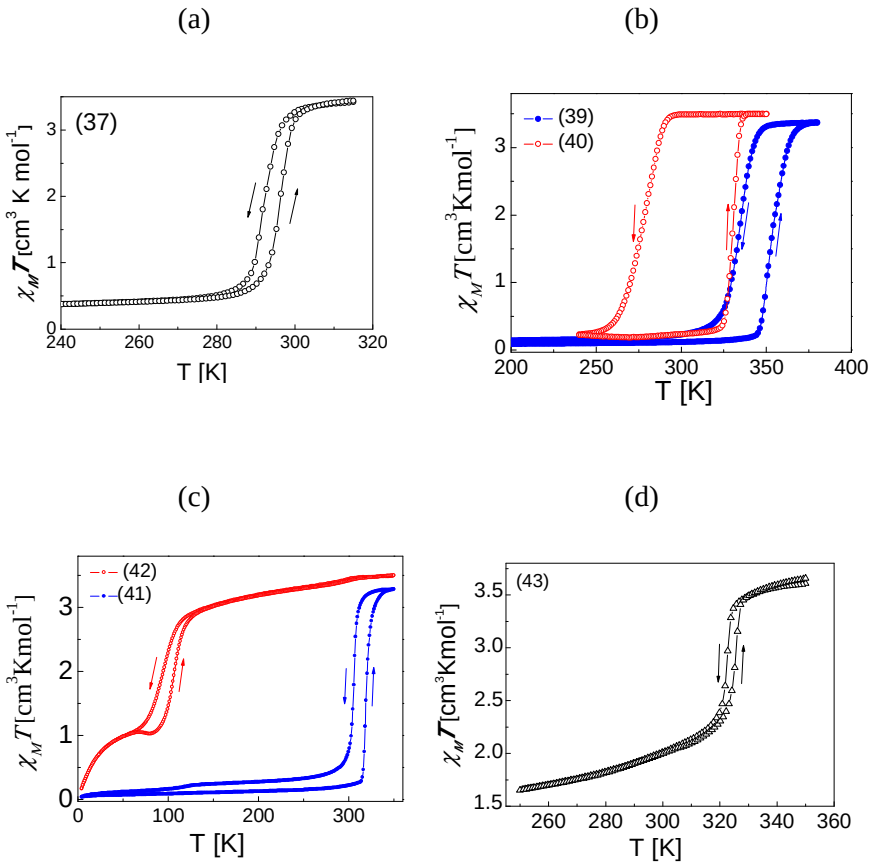

Figure 134 Thermal variation of $\chi_M T$ of compounds: **37- GlytrzE-ClO$_4$** (a); **39-GlytrzE-NO$_3$**, **40-GlytrzE-NO$_3$** (b); **41-GlytrzE-BF$_4$** (A = BF$_4$, n = 0.; **42-GlytrzE-BF$_4$** (c); **43-Glytrz-TRF** (d); for clarity only the number of the compound was add in all images.

Warming sample **43-Glytrz-TRF** revealed a gradual LS → HS transition at $T_w^{\uparrow}$ = 325 K, accompanied by the removal of the two non-coordinated water molecules. This dehydration process was confirmed by thermogravimetric analysis (Figure 133). Cooling this dehydrated compound, **43-Glytrz-TRF,** revealed a HS → LS transition, with the same behavior, as in warming mode, at $T_w^{\downarrow}$ = 322 K, as shown in Figure 134d. In the presence of humidity,

in the sealed container which was used for the SQUID analysis, **43-Glytrz-TRF** transforms back into violet hydrated phase, at room temperature. The synergy between spin state change and dehydration – rehydration process allowed us to obtain a system presenting 3 K of thermal hysteresis loop width.

Dynamics of solvent molecules and influence on morphology after thermal treatment at 390 K

1. Thermal, XRPD and SEM studies

The reversibility of the rehydration and/or dehydration of the framework structure with the change of crystallinity could play an important role in the SCO behaviour of these materials. To check this hypothesis, the dehydration/rehydration process of **39-GlytrzE-NO_3** and **41-GlytrzE-BF_4** were first investigated by TGA, and XRD powder patterns/SEM images that were systematically recorded after each TGA runs. Accordingly, each sample was deposited in a TGA crucible and slowly heated at 1°C/min in air (130 ml/min) to the temperature corresponding to a complete dehydration (110 °C for **39-GlytrzE-NO_3** and only 77 °C for **41-GlytrzE-BF_4**). The samples were subsequently slowly cooled down at 1°C/min to 293 K, and kept at this temperature for 2 h, to study the rehydration process. Sample **39-GlytrzE-NO_3** reabsorbed appreciable amount of water molecules, reaching roughly its original amount of water molecules (Figure 135a) contrary to **41-GlytrzE-BF_4**, which did not reabsorb non-coordinated water molecules; a plateau being identified in the cooling mode in TGA analysis (Figure 135b) in the subsequent rerun.

The three consequent TGA runs on **39-GlytrzE-NO_3** revealed that rehydration capacity after each heating stage are different not reaching its

original composition with a standing period of 25 min. But a rehydration time of 2 h is normally required to regain the original hydrated composition. This observation confirms that the dehydration-rehydration process is reversible.

In order to investigate the framework's thermal robustness of **39-GlytrzE-NO_3** and **41-GlytrzE-BF_4**, we have studied X-ray powder diffraction patterns on the dehydrated/rehydrated compounds from TGA which have been compared with the one of fresh compounds.

The powder XRD patterns of **39-GlytrzE-NO_3** before and after TGA confirm that the integrity of the sample is altered because the intensity of the prominent peaks before and after annealing has decreased but no change is however observed on their position (2θ°) (Figure 136a). It could be due to alteration in the texture (shape and size) of the particles, which was evidenced by SEM images (Figure 137a). Interestingly, for **41-GlytrzE-BF_4**, the heating results in an amorphization compared to the fresh prepared sample and present a slightly altered pattern (Figure 136b). The morphology of these thermally heated samples was studied by SEM (Figure 137).

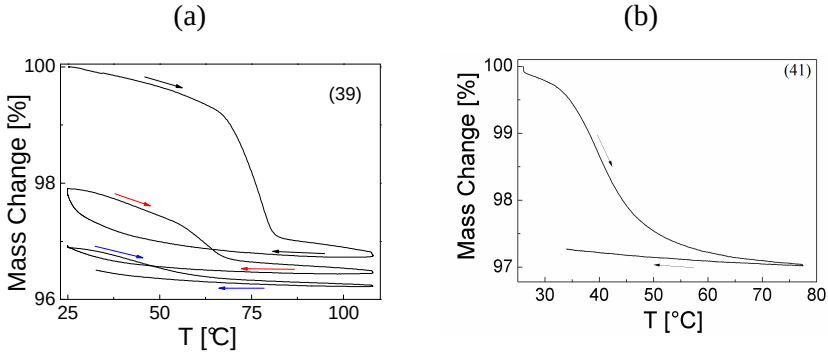

Figure 135 Thermogravimetric analyses (recorded at 1 °C/min) for: (**39-GlytrzE-NO_3**) (a) and (**41-GlytrzE-BF_4**) (b) on warming and cooling. A standby period of 25 min at maximum temperature (110 °C for **39-GlytrzE-NO_3** and 77 °C for **41-GlytrzE-BF_4**) was included in the temperature program of both compounds. Three heating and cooling cycles are shown for **39-GlytrzE-NO_3**; for clarity only the number of the compound was add in all images.

(a)

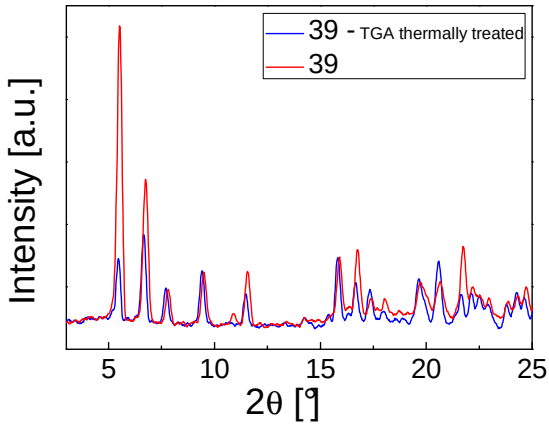

(b)

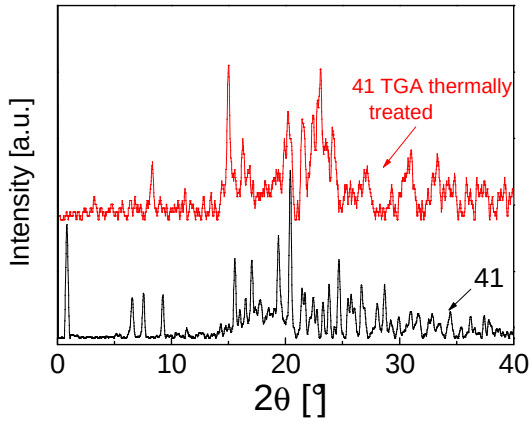

Figure 136 (a) X-ray powder diffraction pattern of **39-GlytrzE-NO_3** thermally treated in TGA and freshly prepared; (b) X-ray powder diffraction patterns of **41-GlytrzE-BF_4** thermally treated in TGA and freshly prepared; for clarity only the number of the compound was add in all images.

Deterioration of **39-GlytrzE-NO_3** and **41-GlytrzE-BF_4** is seen in heated sample showing the effect of thermal treatment in the sample container (Figure 137a, b, c).

(a)

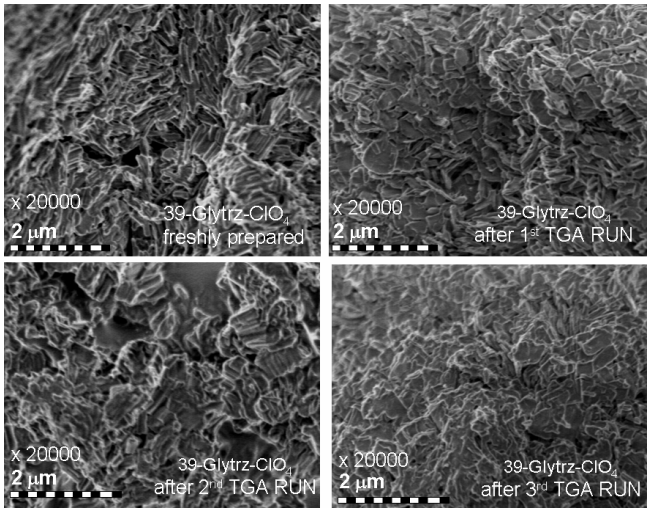

(b)

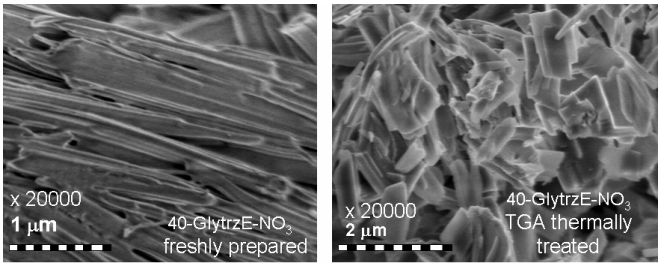

(c)

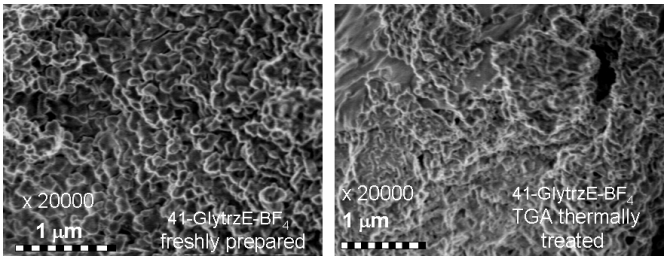

Figure 137 SEM analysis of sample: (a) **39-GlytrzE-NO_3** warmed up to 110 °C; (b) **41-GlytrzE-BF_4** warmed up to 110 °C; (c) **41-GlytrzE-BF_4** warmed up to 77 °C. The effect of thermal treatment on framework integrity is evidenced.

The amorphisation of the sample, related also to the loss of the 0.5 or one non-coordinated H_2O molecules, has an influence on the SCO behavior (see magnetic properties part). For compounds, **39-GlytrzE-NO_3** (Figure 137a) and **41-GlytrzE-BF_4** (Figure 137c), a complete amorphisation of the samples were identified, after TGA thermally treatment. After the annealing treatment, the texture of compound **40-GlytrzE-NO_3** was modified, the elongated rods, observed for **40-GlytrzE-NO_3**, were broken and fused after TGA thermal treatment (Figure 137b).

Figure 138 illustrates the follow-up of SCO by variable temperature XRPD on **41-GlytrzE-BF_4** and **40-GlytrzE-NO_3**, recorded by Dirk Poelman (Lumilab Dept. Solid State Science, Gent).

In the Figure 138a we present an enlarged view of XRD pattern between 15° and 35° for **41-GlytrzE-BF_4**. The most intense peaks (between 15° and 20°, noted as *a*, *b* and *c* in Figure 138c) were selected, from the false color plot (Figure 138c) and a plot of the summed intensity *vs.* temperature (Figure 138b) as well the intensity *vs.* 2θ(°) (Figure 138d) demonstrates spin crossover, for compound **41-GlytrzE-BF_4**.

Figure 138b shows an abrupt change in intensity around 42°C, (315 K) for **41-GlytrzE-BF_4** matching the transition temperature of 320 K recorded by SQUID magnetometry (Figure 134c) thus successfully demonstrating a SCO observation. However, it does not follow the reversibility observed in magnetic measurements, because of a possible departure of a crystal packing water molecules (see green curve in Figure 138b). The irreversibility of the SCO effect is evidenced also for compound **41-GlytrzE-BF_4** in the XRPD pattern of pre-annealing (at 25°C) and post-annealing (measured after heating to 120°C and rapid cooling to 25°C) (Figure 139b) under helium flux shows severe change in intensity and position of signals and possibly hints out at amorphisation or a phase transition supporting the above observation.

(a)

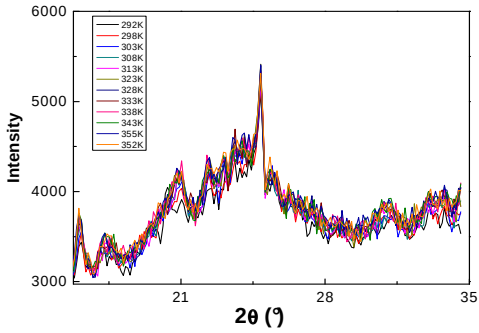
6000
5000
4000
3000
Intensity
21
28
35
2θ (°)
292K
298K
303K
308K
313K
323K
328K
333K
338K
343K
355K
352K

(b)

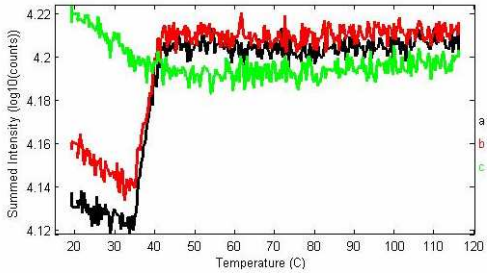
Summed Intensity (log10(counts))
Temperature (C)
a
b
c

(c)

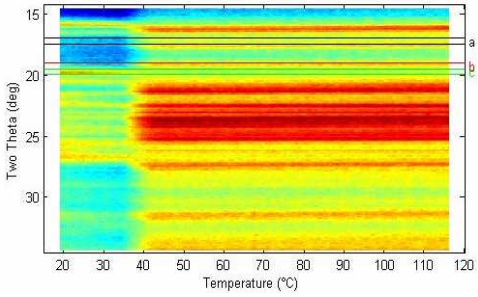
Two Theta (deg)
Temperature (°C)
a
b
c

(d)

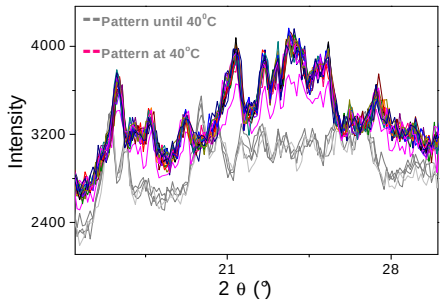

(e)

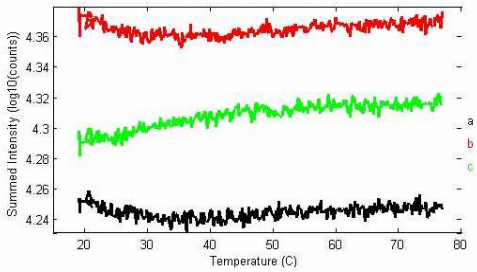

(f)

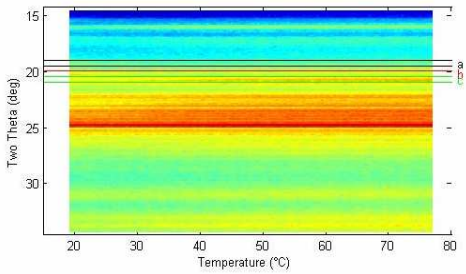

Figure 138 (a) Enlarged view of XRD pattern around selected 2θ (°) for **41-GlytrzE-BF$_4$**; (b) SCO observed by XRPD for (**41-GlytrzE-BF$_4$**); (c) False color plot to select appropriate 2θ (°) for **41-GlytrzE-BF$_4$**; (d) Enlarged view of XRD pattern around selected 2θ (°) for **40-GlytrzE-NO$_3$**; (e) Temperature dependent XRPD for **40-GlytrzE-NO$_3$**; (f) False color plot to select appropriate 2θ (°) for **40-GlytrzE-NO$_3$**.

The situation is similar for **40-GlytrzE-NO$_3$**, compared to **41-GlytrzE-BF$_4$**, the change of diffraction pattern is also severe after annealing process (Figure 139a). But it is difficult to track SCO by T-XRPD for **40-GlytrzE-NO$_3$**. The profile changes around 35-40°C (Figure 138d) and thereafter

follows a particular trend (the intensity of the peaks are different and present a gap, compared to the diffraction pattern recorded until 40°C). It can be concluded that **40-GlytrzE-NO$_3$** which was prepared in methanol/water unlike other complexes which were prepared in MeOH have some surface solvent, which are primarily responsible for secondary interactions in the network, escorted by helium flux and improved in crystallinity during heating but seriously affect the transition temperature of SCO system.

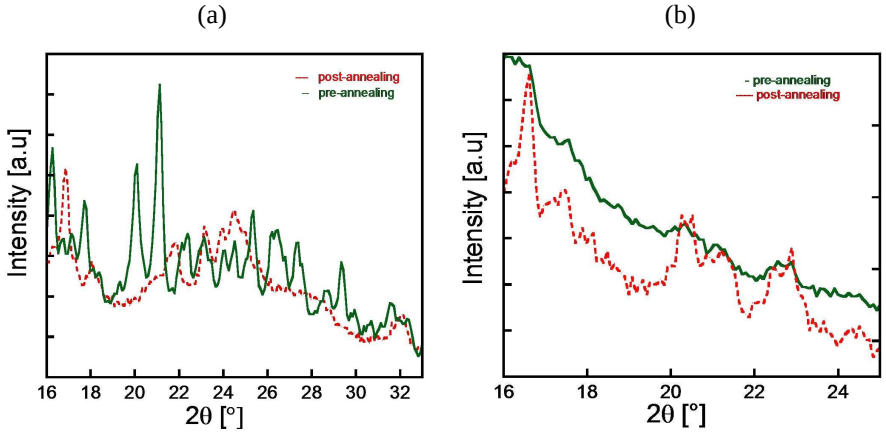

Figure 139 XRPD pattern for the pre- and post-annealing samples of: **40-GlytrzE-NO$_3$** (a) and **41-GlytrzE-BF$_4$** (b).

2. SQUID magnetometry studies on thermally treated 39-GlytrzE-NO$_3$, 40-GlytrzE-NO$_3$ and 41-GlytrzE-BF$_4$ samples

The thermally treated sample of **39-GlytrzE-NO$_3$** at 390 K, for 15 minutes, has an influence on the magnetic properties of the sample, which can be visualized in Figure 140a. After the annealing treatement the SQUID measurements was recorded between 10 K and 360 K. Between 10 and 50 K the $\chi_M T$ product remains constant, to 0.16 cm^{3}Kmol^{-1} which is typical for an iron(II) complex in the low-spin (LS) state. Upon heating, $\chi_M T$ remains constant up to 100 K, then a slight increase of χ_MT product is observed, until

260 K where a partial ST to the HS state takes place, as a "kink". Above this temperature, the $\chi_M T$ value surprisingly decrease abruptly to reach 0.24 cm^3Kmol^{-1} at 289 K, then an abrupt transition to the HS state takes place with a transition temperature (HS molar fraction; $\gamma_{HS} = 0.5$) of $T_{1/2}^{\uparrow} = 343$ K. At 350 K, the $\chi_M T$ product is with 3.37 cm^3Kmol^{-1} in the region typical for an iron(II) complex in the HS state.

Upon cooling the moment remains constant down to 275 K. Below this temperature, a slightly decrease of $\chi_M T$ is followed by three steps SCO (depicted in blue, Figure 140a), around 250 K and 175 K. A small bump, which disappear in the next runs, is identified around 155 K.

In the second run, from 10 to 360 K, the SCO anomaly is following the same behaviour, only the ST temperature is shifted by 10 K, downwards, from 353 K to 343 K (Figure 140a). After the third run the "kink" identified at 260 K vanish and appeared at high values of the $\chi_M T$.

After four cycle of measurements, the transition temperature in the heating mode is shifted to lower temperatures, the transition temperature in the cooling and in the heating mode are $T_{1/2}^{\uparrow} = 245$ K and $T_{1/2}^{\downarrow} = 195$ K. The width of the thermal hysteresis loop increases from 20 K (the transition temperatures characteristic for **39-GlytrzE-NO_3**, without thermal treatement, analyzed by SQUID between 4 K and 380 K, are $T_{1/2}^{\downarrow} = 333$ K, $T_{1/2}^{\uparrow} = 353$ K) to 50 K (orange curve, Figure 140a).

This surprising and unusual influence of the thermal treatement on the SCO properties on **39-GlytrzE-NO_3** may be explained as followed. Since **39-GlytrzE-NO_3** contains one water molecule in the crystal packing, a hydration/dehydration effect is supposed. The reversibility of the water adsorption and the change in the magnetic properties was visualized by the magnetic measurement for $[Fe(PM\text{-}BiA)_2(NCS)_2]$ (PM = N-2-pyridylmethylene, BiA = 4-aminobiphenyl)[19], where the presence of two phases (hydrated and dehydrated one) were presented.

Thus we propose following explanation for this erratic behavior. If we suppose having a SCO material, formed by two different phases, *phase I* (depicted in red in Figure140b) and *phase II (*depicted in black in Figure 140b), which are in non-equilibrium, they ideally presents different SCO temperatures. The sum of this to phases will give ideally in the warming mode a two step SCO which corresponds to the transition temperature of the two phases, hydrated and non-hydrated[19] (Figure 140c).
Based on the TGA measurements (Figure 135a), which shows a dehydration process, step by step, we extrapolate this model, to the anomaly presented in SQUID measurements, of **39-GlytrzE-NO_3**, after thermal treatments.

After partial dehydration process, two phases are obtained: a dehydrated (*phase I*) and a hydrated (*phase II*), respectively. *Phase I* is characterized by switching temperatures $T_{1/2}^{\uparrow}$ = 245 K, $T_{1/2}^{\downarrow}$ = 195 K, respectively (orange curve in Figure 140a). *Phase II* presents a SCO behavior around $T_{1/2}^{\uparrow}$ = 345 K (Figure 140a, curve depicted in blue and in red).

After the thermal treatment at 390 K, by cooling down the sample, it takes partially water. Thus the "kink" which appears around 260 K shows that at this temperature the *phase I* is partially converted into hydrated *phase II*, which means that the evaporated water molecules which are in the gel-cap (used in the SQUID measurements) will be absorbed back by the compound. On the plateau, around 260 K (Figure 140a), one part of molecules are in HS and one part are in the LS states respectively. The HS molecules, formed by the dehydrated phase (*phase I*), in presence of water will be transformed in LS and reach 0.25 cm^3 K mol^{-1} at 298 K.

After the third and fourth measurement the percentage of the dehydration phase increases and reach the maximum of the curve. Upon warming, a small % of the hydrated phase its joins the cooling curve after the dip, at 273 K (Figure 140a).

In the cooling mode we find only an addition of hydration/dehydration phases, in a small percentage. Although this compound loses the water molecules and retrieved back but probably the water molecules do not revert in the same position in the matrix, then altering ST.

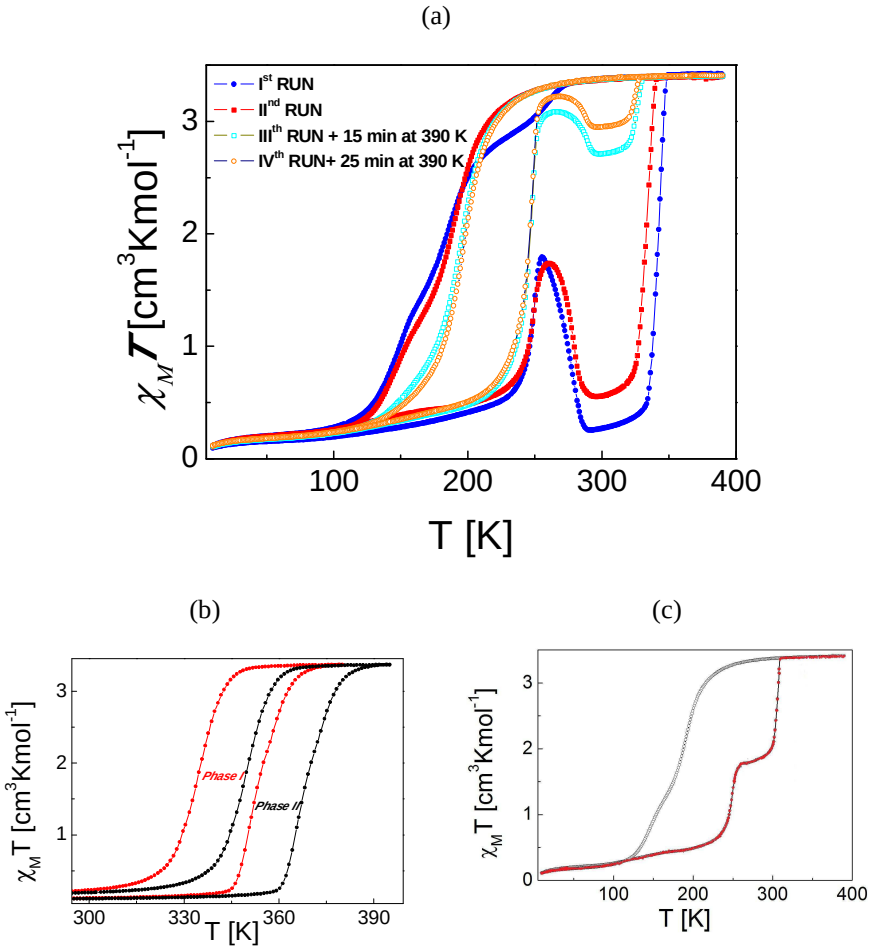

Figure 140 (a) Experimental thermal variation of $\chi_M T$ of compound **39-GlytrzE-NO_3**, between 70 K and 390 K. (b) Model depicting SCO material, formed by two different phases (phase I and phase II); the temperature coordinated is not related to the reality; (c) Model depicting a possible result obtain by magnetic measurement of SCO compound formed by two different phases which are in non-equilibrium;

For compound **40-GlytrzE-NO$_3$**, in the cooling mode a similar behavior was obtaining as for compound **39-GlytrzE-NO$_3$** (Figure 141a). Even if the compound does not contain any solvent molecule in the system (see TGA result, Figure 142), interestingly in the warming mode a "kink" was

(a)

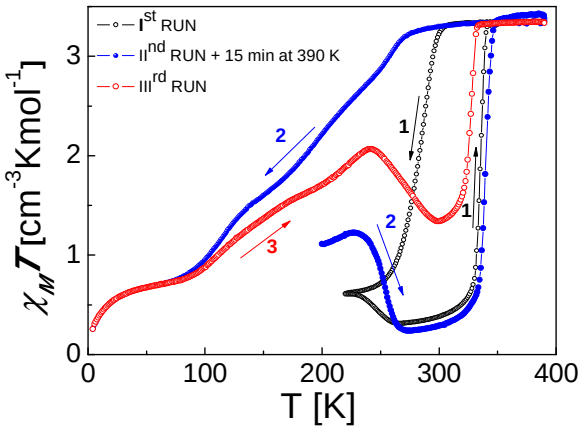

(b)

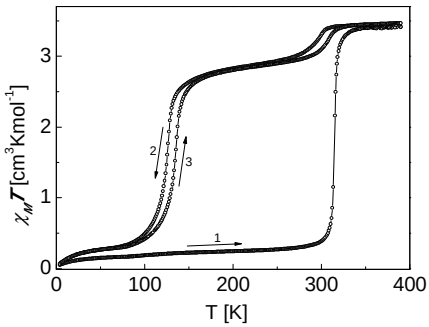

Figure 141 Thermal variation of the $\chi_M T$ product of the complexes **40-GlytrzE-NO$_3$** (a) [between 220 K and 350 K, the first cycle (note with 1), between 200 K and 390 K, the second cycle (after heating the sample to 390 K, note with *2* in the graph) and third curve (heating to 390, note with *3* in the graph)] and **41-GlytrzE-BF$_4$** (b).

identified around 242 K.

Compound **40-GlytrzE-NO$_3$** was cycled in SQUID between 220 K and 350 K, to test if with the times the compound did not absorb water in the surface,

which will affect the SCO properties. This hypothesis was not confirmed by the obtained result, the curve obtained on the sample maintained in desiccator 4 weeks, is identical with the curve obtain for the fresh compound (Figure 141a (cycle 1, depicted in black) and Figure 134b). After that, the sample was hold at 390 K, for 15 minutes. The thermal treatment was followed by SQUID measurements run at 200 K until 390 K (cycle 2, depicted in blue, Figure 141a). In this run, from 200 to 390 K, the compound reach the minimum of the curve after the dip, at 300 K; after that the SCO behaviour is following the same route, only the ST temperature is shifted by 10 K, from 335 K to 340 K (Figure 141a).

Upon cooling the moment remains almost constant down to 273 K. Below this temperature, a slightly decrease of $\chi_M T$ is followed by three steps SCO (curve depicted in blue, Figure 141a), around 250 K, 185 K and 108 K, respectively. In the IIIrd run, from 4 K to 390 K) the "kink" identified at 242 K appears at high values of the $\chi_M T$ (2.08 $cm^3 \cdot K \cdot mol^{-1}$).
Since this sample was hold at 390 K, and no water molecules are present in the crystal packing, this behavior is not attributed to a solvent effect but probably due to alteration of morphology. This idea is supported by SEM imaging (Figure 137b), the morphology change after thermal treatment to 390 K.

Compound **41-GlytrzE-BF_4** was measured between 4 K and 390 K. The $\chi_M T$ remains approximately constant at 0.09 $cm^3 \cdot K \cdot mol^{-1}$ between 77 and 100 K, indicative of LS iron(II) (Figure 141b, noted as *1*). Between 100 and 305 K $\chi_M T$ remains constant (0.23 $cm^3 \cdot K \cdot mol^{-1}$) and the values rapidly increases to reach a maximum value of 3.33 $cm^3 \cdot K \cdot mol^{-1}$ at 390 K, indicating that all the iron(II) sites are in the HS state. The $T_{1/2}{}^{\uparrow}$ value of this transition is 320 K. The sample was maintained after at 390 K for 15 minutes.

Thus in the cooling mode, the compound lose the initial SCO properties, the SCO is realized in two steps (Figure 141b, route *2*), around 294 K and 125 K, respectively.

Warming the sample (route 3, Figure 141b) the compound follows the previous SCO properties, realized in two steps (at 136 K and 307 K), with the presence of two hysteresis loop, of 10 K and 16 K respectively. The first step was attributed to a hydrated phase (~ 1/3) and the second was attributed to the dehydrated form (~ 2/3) (Figure 141b). The SCO temperatures are 307 – 294 K and 136 – 125 K corresponding to hydrated and dehydrated phase respectively, phases which are in equilibrium.

As in the previous case (compound **39-GlytrzE-NO_3**) this transition is accompanied by the removal of 0.5 non-coordinated water molecules. Once this compound looses its non-coordinated water molecules, it does not recover its initial form, which prompted us to study morphology of this system (*wide infra*).

In addition the dehydrated system **42-GlytrzE-BF_4** show completely different magnetic properties which were further probed by SQUID measurements. After the annealing treatment on the sample **42-GlytrzE-BF_4**, at 390 K, no effect on SCO behavior was observed in SQUID measurement. The SCO occurs around $T_{1/2}^{\downarrow}$ = 106 K, $T_{1/2}^{\uparrow}$ = 92 K (Figure 143).

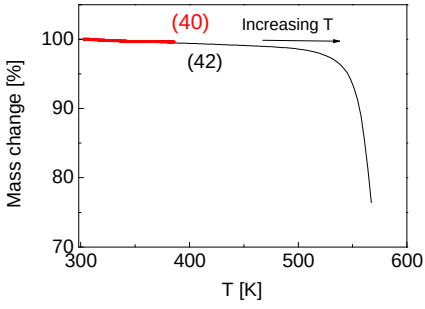

Figure 142 Thermogravimetric analyses (recorded at 1 °C/min) for compounds **40-GlytrzE-NO_3** and **42-GlytrzE-BF_4** on warming mode.

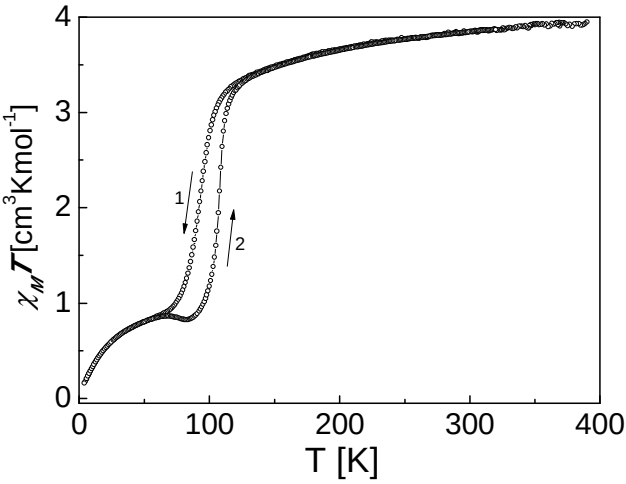

Figure 143 Thermal variation of $\chi_M T$ of compound **42-GlytrzE-BF$_4$**, between 70 K and 390 K.

3. Theoretical approach

To describe the dehydration/hydration process (which gives an unusual kink for **39-GlytrzE-NO$_3$**) by a qualitative theoretical approach, we consider the hypotheses made below. The first dehydration/hydration process takes place when the sample is heated up to 390 K, when a fraction of complexes (or chains) loose their water molecules passing into a dehydrated phase characterized by different magnetic properties in comparison with the initial phase. The kink from the warming branch of the major hysteresis loops appears in the branch of a hydration process when the dehydrated phase (Phase I) is reconverted into the initial hydrated phase (Phase II). The hydration process occurs for temperatures above 280 K (see Figure 144).

If the system is kept at high temperatures for a longer time, all water molecules leave the crystal lattice. Therefore the fraction of molecules which obey the rehydration process is decreased.

All in all, we show that a simple biphasic model based on independent phases provides a good qualitative simulation of experimental data (see Figure 140). We used here the two-level Hamiltonian Ising-like model treated in the mean-field approximation[20, 21]. This model has been widely used and described[19, 22] and provides the kinetic extension in terms of mean-field macroscopic master equation.

The Hamiltonians of the two systems, in the mean field approximation are given by the following equations:

$$H^{I} = \frac{\Delta^{1}_{eff}}{2}\hat{\sigma}_1 - J_1\hat{\sigma}_1 < \hat{\sigma}_1 > \qquad \textbf{(eq. p)}$$

$$H^{II} = \frac{\Delta^{2}_{eff}}{2}\hat{\sigma}_2 - J_2\hat{\sigma}_2 < \hat{\sigma}_2 > \qquad \textbf{(eq. q)}$$

where: $\Delta^{i}_{eff} = \Delta^{i}(P=0) - k_B T \ln r + P\Delta V_i$ (with I = 1, 2), is the electronic energy gap, J_i the effective interaction parameter and ΔV_i the molecular volume increase upon complete spin crossover.

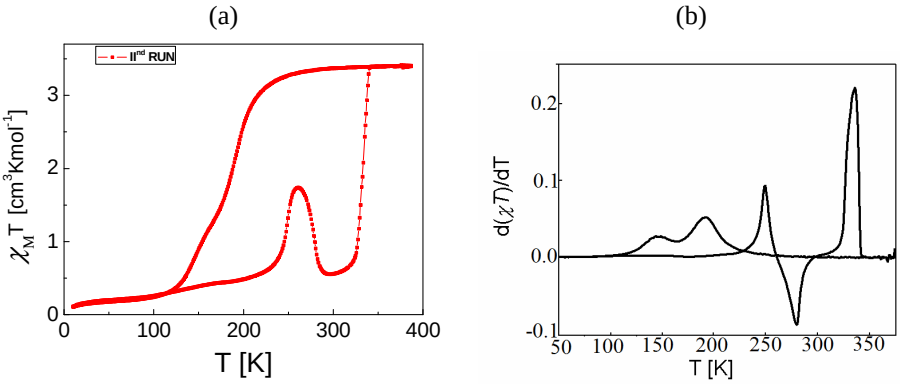

Figure 144 (a) Magnetic data recorded after the **39-GlytrzE-NO$_3$** system has been heated up for a second time to 390 K; (b) Derivative of the magnetic susceptibility dependence on temperature. The negative peak gives the temperature at which the hydration process occurs: about 280 K in this case.

In a first attempt we tried to reproduce the first measurement where beside the kink on the ascending branch, a two step transition on the descending branch is observed. This behavior can be reproduced by considering the two phases characterized by different switching temperatures as shown in Figure 145a. Beside this assumption, we considered that for the temperatures higher than 280 K, the dehydrated phase goes into the hydrated one. The parameter values chosen in order to reproduce the same behavior we observed experimentally are: $J_1 = 650\,\mathrm{K}$, $J_2 = 450\,\mathrm{K}$, $\ln g_1 = 7.25$, $\ln g_2 = 7.68$, $\Delta_1 = 2000\,\mathrm{K}$, $\Delta_2 = 1850\,\mathrm{K}$, $\Delta V_1 = \Delta V_2 = 8.9\ \text{Å}^3$. In this case, we assumed that only a fraction of 30 % of the whole system is dehydrated and this entire fraction goes into the hydrated phase when the system is heated above 280 K. The plateau width is given by the difference between the switching temperature from low to high spin state of the dehydrated phase (Phase I) and the conversion temperature for which Phase II goes into Phase I. The height of the kink is given by the amount of dehydrated phase which obey the hydration process.

After the first two measurements, the descending branch becomes smooth. This behavior indicates that switching temperatures from high to low spin state are almost the same for both hydrated and dehydrated phases. This situation is represented in the Figure 147.

The parameters values chosen in this case are: $J_1 = 650\,\mathrm{K}$, $J_2 = 450\,\mathrm{K}$, $\ln g_1 = 7.25$, $\ln g_2 = 7.68$, $\Delta_1 = 2000\,\mathrm{K}$, $\Delta_2 = 1750\,\mathrm{K}$, $\Delta V_1 = \Delta V_2 = 8.9\ \text{Å}^3$. In Figure 147, the following situations are considered: (a) the magnetic behavior of individual hydrated (Phase II) and dehydrated phase (Phase I) respectively; (b) in this case it has been considered that the system is composed of 70% hydrated phase and a 30% dehydrated fraction which is converted back into the hydrated phase when the system temperature is higher than 280 K; (c) here it was considered 30% of Phase II

and only 20% of the Phase I which is hydrated back; and finally the last case (d) where the system is composed of 5% hydrated phase and only 10% of Phase I which is converted back into Phase II.

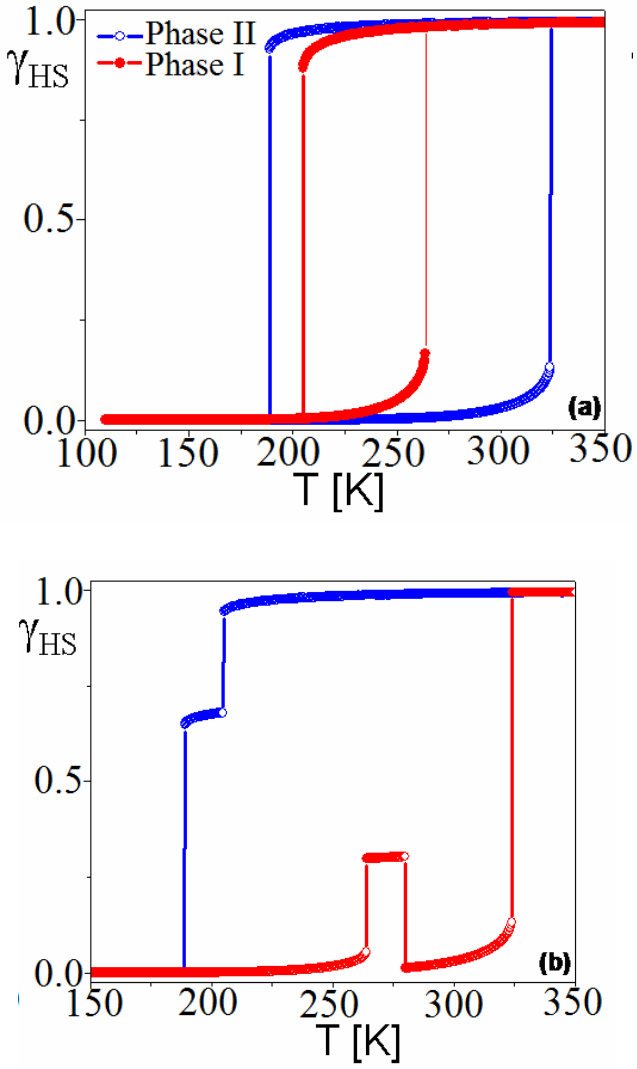

Figure 145 Simulated behavior assuming that the two phases have different switching temperatures: individual behavior (a) and the global behavior (b) respectively.

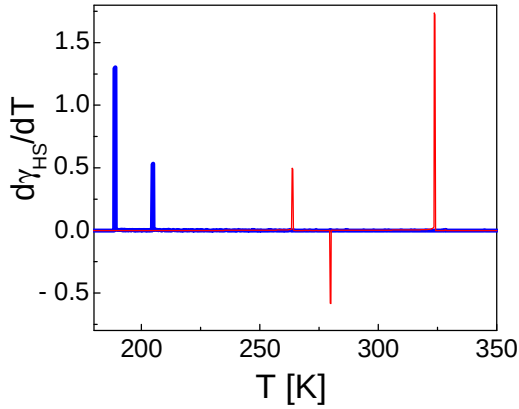

Figure 146 The derivative of γ_{HS} according with the temperature of the thermal dependency of the high spin fraction from Figure 145b. The negative peak indicates the temperature at which the conversion, from dehydrated phase to hydrated one occurs.

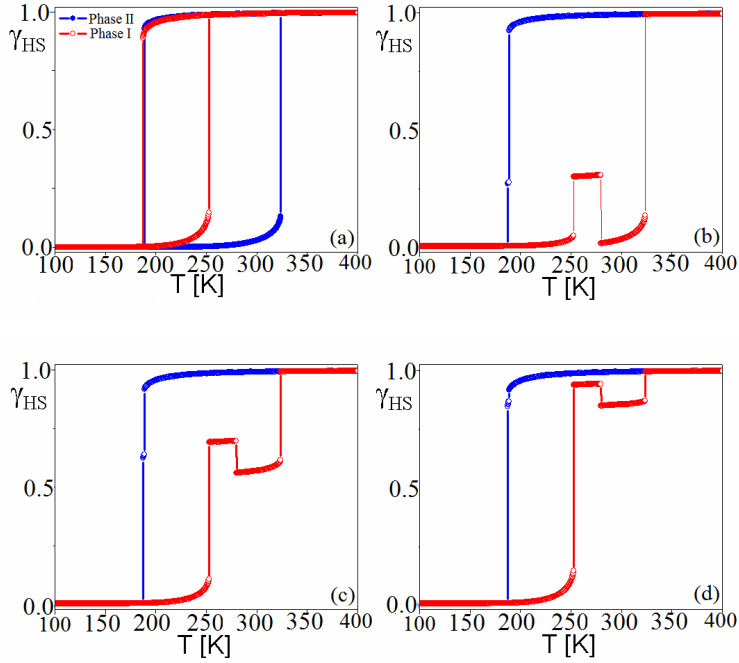

Figure 147 Simulated behavior assuming that the two phases have different switching temperatures: (a) individual behavior; (b) the system is composed of 70% hydrated phase and 30% dehydrated fraction; (c) the system is composed of 30% hydrated phase and only 20% of dehydrated fraction; (d) the system is composed of 5% hydrated phase and only 10% of dehydrated fraction.

Differential Scanning Calorimetry (DSC)

Compounds **37-GlytrzE-ClO$_4$** to **41-GlytrzE-BF$_4$** and **43-Glytrz-TRF** were investigated by differential scanning calorimetry over the temperature range 100 – 310 K, and 293 – 400 K at 10 K min^{-1} for both cooling and heating rates. Heating and cooling capacity profiles are depicted in Figure 148.

An endothermic peak is observed on warming for **37-GlytrzE-ClO$_4$** (Figure 148) at $T_{max}^{\uparrow}$ = 297 K and an exothermic peak is recorded at $T_{max}^{\downarrow}$ = 292 K, on cooling. These peaks correspond to a first-order phase transition associated to the ST behavior of **37-GlytrzE-ClO$_4$**. The hysteresis loop width of 5 K exactly matches the one found by Mössbauer spectroscopy. The slight shift in the hysteresis loop is related to the higher heating and cooling rates used in the calorimetric measurement. The enthalpy and entropy associated to the ST were derived as follows: ΔH_{HL} = 14.4 kJ.mol^{-1} and ΔS_{HL} = 49 J.mol^{-1}K^{-1}. Compound **38-GlytrzE-ClO$_4$**, has a hysteresis loop width of 11 K ($T_{max}^{\uparrow}$ = 272 K, $T_{max}^{\downarrow}$ = 261 K) which matches well with the Mössbauer spectroscopy result; the sample is sensitive, the measurement should be realized on a freshly prepared compound because the non-coordinated methanol molecule is susceptible to a partial desolvation, in air, during the course of time.

The temperature dependence of the DSC response above room temperature in the heating and in the cooling mode for **40-GlytrzE-NO$_3$** is also shown in Figure 148. The DSC curves show an endothermic peak around ($T_{max}^{\uparrow}$) 340 K in the warming mode and an exothermic peak at ($T_{max}^{\downarrow}$) 280 K in the cooling mode. The peaks are separated by a wide temperature domain, which is indicative for the presence of a hysteresis loop of 60 K, as detected in SQUID measurements. All compounds, **37-GlytrzE-ClO$_4$** to **41-GlytrzE-BF$_4$**, present a similar behavior except **43-Glytrz-TRF** for which a broad asymmetric peak is associated to the main endothermic peak.

This effect is presumably due to the progressive loss of the solvent molecules and resulting amorphisation; the difference between compound **43-Glytrz-TRF** and compounds **37-GlytrzE-ClO_4**, **38-GlytrzE-ClO_4**, **40-GlytrzE-NO_3**, **41-GlytrzE-BF_4** is that this compound (**43-Glytrz-TRF**) includes more than, one non-coordinated water molecules. The observation of narrow peaks in DSC measurements allows to confirm the abrupt character of the SCO behavior for **37-GlytrzE-ClO_4**, **39-GlytrzE-NO_3** and **40-GlytrzE-NO_3**.

The hysteresis width as well as thermodynamic parameters derived from these measurements (ΔH_{HL}, ΔS_{HL}, ΔS_{vib}) are listed in Table 51 (see Appendix – Thermodynamic parameters). The entropy gain is much larger than the characteristic value for the electronic contribution to the entropy, $R \cdot \ln 5$ = 13.4 J/mol.K, characteristic for Fe^{II} SCO compounds.[23] Such values are however not sufficiently high to suggest another transition type, such as an order-disorder transition of the anion often observed in SCO systems.[14, 23, 24]

Compound **39-GlytrzE-NO_3** and **40-GlytrzE-NO_3** were analyzed again during several cycles by DSC with the purpose to determine thermodynamic parameters annunciated to the unusual SCO behavior observed by SQUID measurements, over the temperature range 100 – 298 K and 298 – 390 K at 10 K min^{-1}, after the annealing treatement. Heating and cooling capacity profiles are depicted in Figure 149. The samples were encapsulated in aluminum holder capsules with holes, loaded with 20.9 mg of each sample.

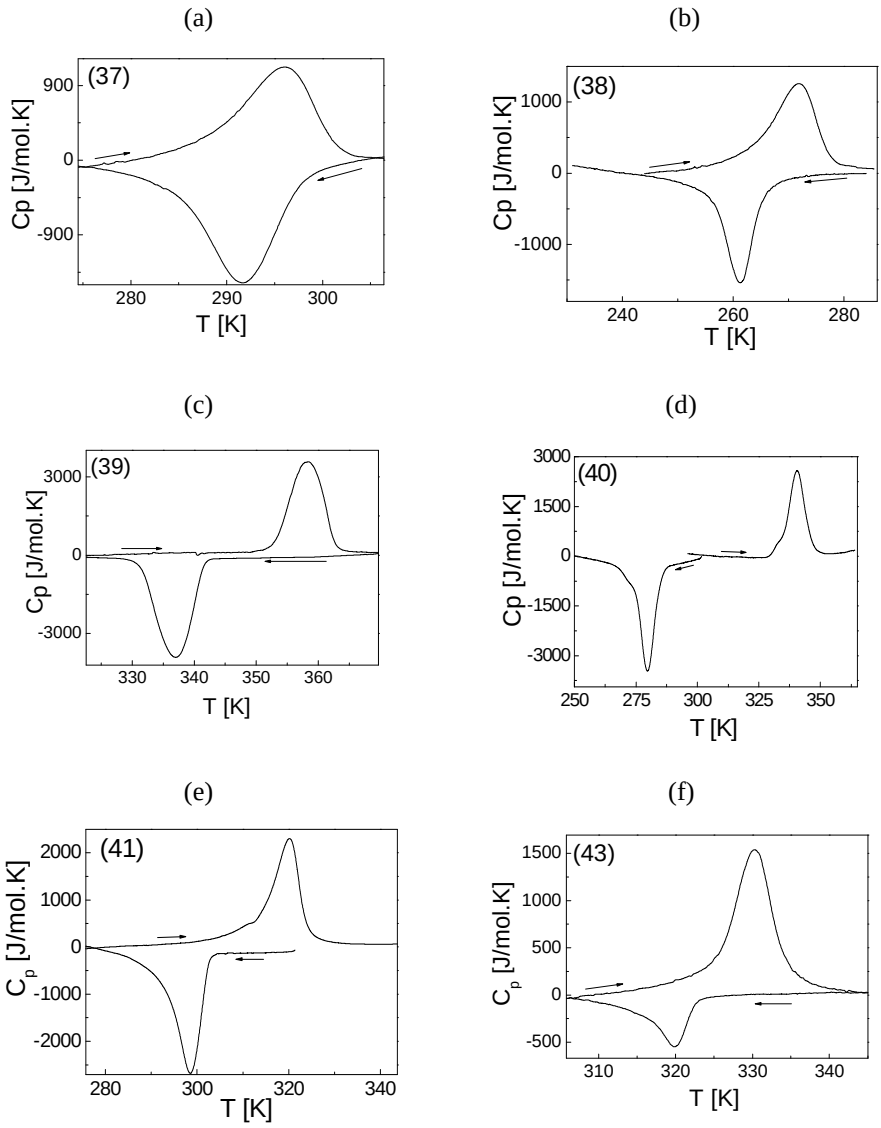

Figure 148 DSC profiles for $[Fe(GlytrzE)_3](Anion)_2 \cdot nSolvent$, in the 230 – 390 K temperature range in the cooling and warming mode for (a) **37- GlytrzE-ClO_4**; (b) **38-GlytrzE-ClO_4**; (c) **39-GlytrzE-NO_3**; (d) **40-GlytrzE-NO_3**; (e) **41-GlytrzE-BF_4**; (f) **43-Glytrz-TRF**; for clarity only the number of the compound was add in all images.

The DSC curves of **39-GlytrzE-NO$_3$** show an endothermic peak around ($T_{max}^{\uparrow}$) 358 K in the warming mode and an exothermic peak at ($T_{max}^{\downarrow}$) 338 K in cooling mode (Figure 148c). The entropy gain is 64.3 J.mol^{-1}.K^{-1}.

The samples, **39-GlytrzE-NO$_3$** and **40-GlytrzE-NO$_3$**, were measured in DSC, in the 100 – 390 K temperature range in the cooling and warming mode, after maintained at 390 K for 15 min for each run, to "simulate" the conditions which were attained in SQUID measurements (*vide infra*).

The classical measurement on **39-GlytrzE-NO$_3$**, is followed by a warming process from room temperature to 390 K, an endothermic peak is identified at the same temperature ($T_{max}^{\uparrow}$ = 358 K) as in Figure 148c). After keeping for 15 minutes at 390 K, and cooling the sample, an exothermic peak is recorded at $T_{max}^{\downarrow}$ = 178 K. The enthalpy and the entropy associated to this transition were derived as follows: ΔH_{HL} = 14 kJ. mol^{-1} and ΔS_{HL} = 78.6 J. mol^{-1} K^{-1}. In the warming mode a signal was identified at $T_{max}^{\uparrow}$ = 253 K (Figure 149a), with an entropy gain of 67.2 J. mol^{-1} K^{-1}. In the second run the transition temperature is shifted to 195 K only in the cooling mode, in the warming mode the transition is maintained in the same area. The third run is identical to the second; the thermodynamic parameters are in the same range of values. No other peaks are identified by DSC analysis, in the 298-390 K range. Compared with the SQUID result (Figure 140c), when the ST occurs with interrupted step, it looks in DSC that the entire Fe(II) atoms switch from the LS to HS and from the HS to LS is complete without any interruption. The partial hydration/dehydration effect is not evidenced by DSC measurement, as in SQUID measurements. The hysteresis loop width of 58 K exactly matches the one found by SQUID magnetometry. These peaks could be attributed to a first-order phase transition, associated to the ST behavior but in the same time the probability of a second order phase transition, such as an order-disorder transition of the anion observed in SCO systems or a phase transition occurring in the hydration-dehydration process, could not be eliminated, seeing the important gain of the entropy (Table 52).

Only a morphology change occurs for **40-GlytrzE-NO_3** after thermal treatment at 390 K in DSC (Figure 137b). In the cooling mode, the thermal profile of **40-GlytrzE-NO_3** is similar to one of **39-GlytrzE-NO_3**. A steep endothermic peak is observed on warming at $T_{max}^{\uparrow}$ = 340 K (Figure 149b). Upon maintaining the sample at 390 K for 15 minutes, and then cooling, from 390 to 100 K, the compound present an exothermic peak identified at 197 K; the transition temperature in the cooling mode is then shifted to lower temperatures by 83 K. In the second cycle, in the warming mode, (from 100 K to 390 K) the transition temperature is also shifted to lower temperatures by 125 K (from 380 K to 255 K). As a consequence, the width of the thermal hysteresis loop is reduced by 2 K (from 60 to 58 K) upon warming to 390 K. This situation was also detected in SQUID measurements (Figure 141a). The transitions temperatures, after the third measurement until 390 K, have been evaluated as $T_{max}^{\uparrow}$ = 255(1) K and $T_{max}^{\downarrow}$ = 197(1) K with $\Delta H_{avg.}$ = 20.6(1) kJ mol^{-1} and ΔS = 90.8(1) J mol^{-1} K^{-1}. The entropy variations for **40-GlytrzE-NO_3** is much larger than the one of **39-GlytrzE-NO_3**, and higher than reported for other 1D 1, 2, 4 – triazole - Fe^{II} coordination polymers[25, 26], but in the same range with the values obtained for 1D and 2D systems $[FeL1(HIm)_2]$ and [FeL2(azpy)]·MeOH, (L1 = (E,E)-[diethyl 2,2'-[1,2-phenylenebis (iminomethylidyne)]bis(3-oxobutanato) (2-)-N,N',O^3,$O^{3'}$}], L2 = [3,3']-[1,2-phenylenebis(iminomethylidyne)bis (4-phenyl-2,4-butanedionato)(2-)-N,N',O^2,$O^{2'}$] , Him = imidazole and azpy = 4,4'-Azopyridine).[27] This high value call for the presence of a structural phase transformation.

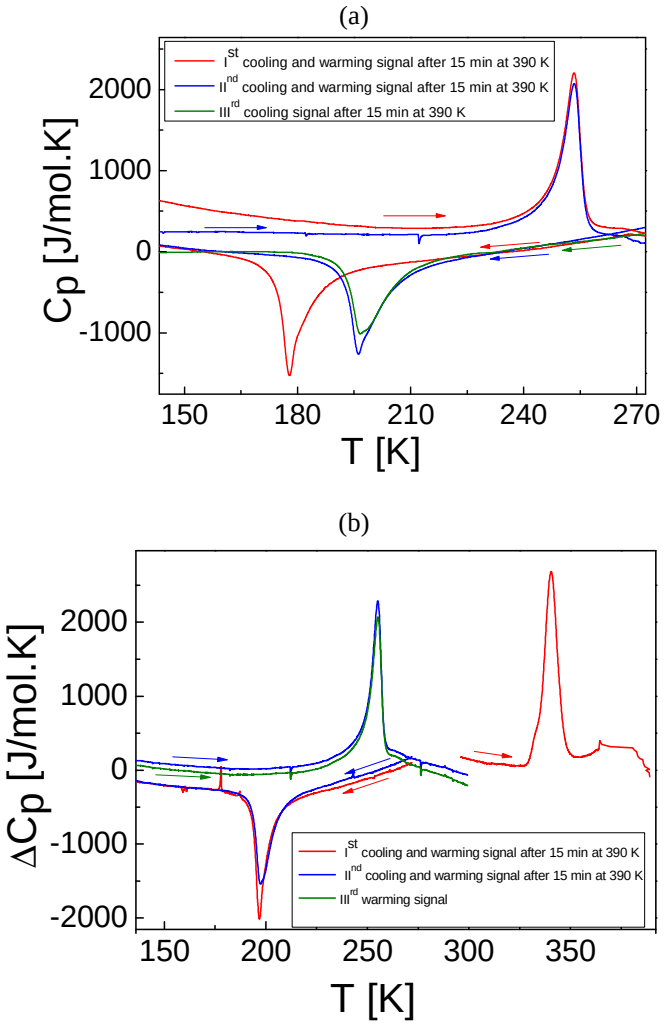

Figure 149 DSC profiles for compounds **39-GlytrzE-NO_3** (a) and **40-GlytrzE-NO_3** (b) in the 100 – 390 K temperature range in the cooling and warming mode; the samples were maintained at 390 K for 15 min for each run to "simulate" the conditions which were attained in SQUID measurements.

Discussion

Meticulously designed novel triazole derivatives are greatly sought in the thriving field of 'bistable molecular systems' which is largely dominated by technologically important SCO materials at the molecular level. Several

factors influence the SCO bistability domain of molecular assemblies. Design of suitable ligand is crucial to exert appropriate ligand strength in these complexes. This will be supplemented by nature of anion and solvent molecules.[28] On our research of amino acid functionalization, we have introduced an ester of glycine[29] into transamination to obtain ethyl-4H-1,2,4-triazol-4-yl-acetate (**GlytrzE**). X-Ray crystal structure of **GlytrzE** gives us an idea about the possible supramolecular organization of **GlytrzE** into the iron(II) systems (see previous chapters). The structure of **GlytrzE** is stabilized by a dense hydrogen intra- and intermolecular interactions, involving the -C=O and the $C\text{-}H_{(triazole)}\cdots N/O$. Such supramolecular interaction of the core of the system may play an effective role in the propagation of the elastic cooperative interactions in the coordination polymers, as demonstrated in a recent study[27]. The advantages of **GlytrzE** and **HGlytrz** are the presence of two independent sets of chelating group, with varied coordinating abilities: a carboxylic group (**HGlytrz**) and a N-heterocycle (**GlytrzE** and **HGlytrz**), are interesting ligands to study the Fe(II) spin crossover compounds behavior[30]. Both of these groups are known for the coordinating ability, separated from conformably flexible methylene group, which can form mixed coordination environment around metals[1, 31].

For the compounds based on **GlytrzE** we expect to obtain a gradual SCO phenomenon because of the bulky substituent of the triazole ring, $\text{-}CH_2\text{-}COO\text{-}C_2H_5$, which can increase the distance between the Fe^{II} active sites and then the cooperativity might decrease[32, 33]. But is not the case, a very abrupt ST at room temperature is identified for **37-GlytrzE-ClO_4**, **39-GlytrzE-NO_3**, **40-GlytrzE-NO_3**, **41-GlytrzE-BF_4**. This could be explained by the preferential coordination by N1, N2-triazole ring and not by oxygen and also by the presence of eventual intra and inter-molecular interactions realized between the substituent on the triazole ring and the counter-anion. These

kinds of interactions are already confirmed in similar systems, by muon study[34] and in a structural characterization of an Fe(II) mononuclear SCO compound[35]. Thus **GlytrzE** is a versatile "building block" to obtain molecular sensors operation near (as **37-GlytrzE-ClO$_4$**, $T_c^{\uparrow}$ = 296 K and $T_c^{\downarrow}$ = 291 K), below (as **42-GlytrzE-BF$_4$**, $T_c^{\uparrow}$ = 105.5 K and $T_c^{\downarrow}$ = 91.5 K) and above room temperature (as **40-GlytrzE-NO$_3$**, $T_c^{\uparrow}$ = 338 K and $T_c^{\downarrow}$ = 278 K, **39-GlytrzE-NO$_3$**, $T_c^{\uparrow}$ = 353 K and $T_c^{\downarrow}$ = 333 K and **43-Glytrz-TRF**, $T_c^{\uparrow}$ = 325 K and $T_c^{\downarrow}$ = 322 K) respectively. Novel iron(II) 1D ST chain compounds presenting a ST in the close vicinity of room temperature, which has been observed only for rare cases.[13, 36-38]

Inclusion of a non coordinated methanol molecule has an important effect on the ST properties. Both compounds (**37-GlytrzE-ClO$_4$** and **38- GlytrzE-ClO$_4$**), with ClO_4^- anion, are fully HS at 308 K (for **37-GlytrzE-ClO$_4$**) and at room temperature (for **38- GlytrzE-ClO$_4$**), and the spin state change abruptly upon cooling below this temperature indicating cooperative spin-state crossover. The thermodynamic parameters, ΔS_{HL} (J mol^{-1} K^{-1}) equal to 41 (for **37-GlytrzE-ClO$_4$**) and 49 (for **38- GlytrzE-ClO$_4$**) suggest the presence of a first order phase transition, associated to the SCO. Comparing the ST behavior of compounds **37-GlytrzE-ClO$_4$** and **38-GlytrzE-ClO$_4$**, it seems that in **38-GlytrzE-ClO$_4$** the cooperativity is higher, the ST temperature decreasing with the inclusion of a methanol molecule in the system, but the hysteresis width and the entropy gain are important. That, the inclusion of solvent molecule, in the framework, will increase the number of the direct short supramolecular interactions between the complex molecules, which will increase the cooperativity of the system. In the same time a negative effect of the introduced methanol molecule is a shift in the transition temperature of **38-GlytrzE-ClO$_4$** to lower temperatures.

Compound **40-GlytrzE-NO$_3$**, which include two NO_3^- counter-anions to balance the valence of the $[Fe(GlytrzE)_3]^{2+}$ core, present an abrupt ST, with a

wide hysteresis loop, of 60 K. This value is beyond the compromise mentioned by O. Kahn[39], and the compound can be a very good candidate as components to be incorporate in devices for displays or recording. The ST is accompanied by an abrupt change of color (Figure 150). The two spin states, LS and HS, are easily distinguishable, by SQUID and Mössbauer spectroscopy and the ST is centered to room temperature (Figure 151).

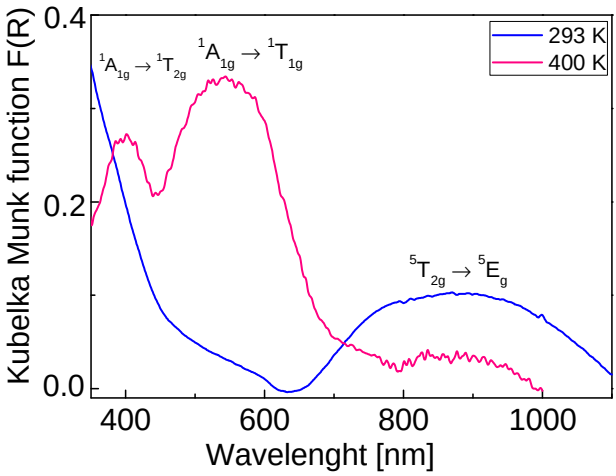

Figure 150 UV-Vis diffuse reflectivity spectra of $[Fe(GlytrzE)_3](NO_3)_2$ (**40-GlytrzE-NO_3**) showing the d–d transitions at (a) 293 K and (b) at 400 K.

This wide hysteresis loop value is large than from the one observed for the classical 1D SCO systems[40], but it is in the same range as $[Fe(NH_2trz)_3](NO_3)_2$ (NH_2trz = 4-amino-1,2,4-triazole), where the unusual value was attributed to the planar nature of the nitrate anion compared to the tetrahedral geometry of the other inserted anions, allowing the propagation of supramolecular interactions in a directional manner between chains[41]. Compared to **39-GlytrzE-NO_3**, the presence of water molecule has a negative effect in the term of cooperativity but not in term of hysteresis width; the hysteresis loop is larger for the non-hydrated compound (compound **40-GlytrzE-NO_3**) than for the hydrated one (with 40 K). It seems that the presence of water molecules will increase the network of

hydrogen bonds connections but in the same time the distance between the chains decreases and the cooperativity is weaker.

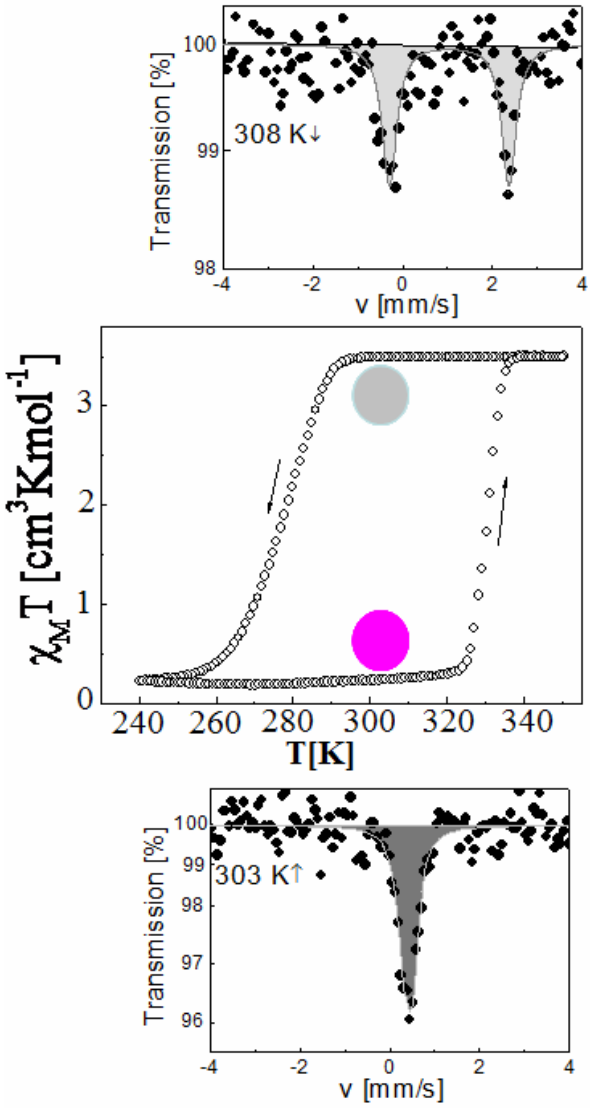

Figure 151 Center - Magnetic data for $[Fe(GlytrzE)_3](NO_3)_2$ (**40-GlytrzE-NO_3**); Top and bottom - ^{57}Fe Mössbauer spectra of **40-GlytrzE-NO_3** at 303 K and 308 K, in the warming and the cooling modes, respectively, showing the presence of LS and HS species in the same region of temperature.

This hypothesis is confirmed also by DSC results where a significant decrease of the entropy is observed for hydrated compound, from 88.4 J mol^{-1} K^{-1} (for **40-GlytrzE-NO_3**) to 77.7 J mol^{-1} K^{-1} (for **39-GlytrzE-NO_3**). The entropy variations for **40-GlytrzE-NO_3** and **39-GlytrzE-NO_3** are interestingly higher than the ones reported for other 1D Fe^{II} coordination polymers[26, 42, 43] and its high value cannot exclude the presence of a structural phase transformation.

For other set of samples, based on BF_4^- anion, **41-GlytrzE-BF_4** and **42-GlytrzE-BF_4**, the influence of the solvent is not so significant. The ST domain is shifted to lower temperature for the non-hydrated compound and the bistability domain is maintained to 15 K. The entropy gain, ΔS_{HL} (J mol^{-1} K^{-1}), is equal to 60 $Jmol^{-1}K^{-1}$, and suggest the presence of a first order phase transition associated to the SCO. Unfortunately a thermodynamic analysis could not be possible for **41-GlytrzE-BF_4** which presents a SCO below 100 K, and that cannot be tracked by our current calorimeter.

Compounds **42-GlytrzE-BF_4** and **43-Glytrz-TRF** present a mixture of LS and HS iron(II) states between 4 and 80 K (**42-GlytrzE-BF_4**) and between 250 K - 298 K, an admixture that gradually shift from predominantly LS to predominantly HS with increasing temperature. The origin of the incomplete ST at lower temperature can be assigned to crystal defects, for example a distribution of different chains lengths or to HS FeN_6 non active sites or water molecules in the coordination sphere[44]. Also, the presence of two non-coordinated water molecules for **43-Glytrz-TRF**, favor the presence of ends of chains, with two coordinated water molecules, which can explain the paramagnetic percentage at room temperature. The increase of number of water molecules in the formula, increase the number of terminal coordinated solvent molecules which decrease the ligand field strength and thus preventing a spin state change[45].

Let us discuss now the ^{57}*Fe Mössbauer results*. The evolution of the isomer

shift at 78 K in the LS state, γ_{LS}^{78K} *vs.* $T_{1/2}^{\uparrow}$ for [Fe(GlytrzE)$_3$](Anion)·nSolvent 1D complexes including monovalent anions is presented in Figure 152. For non-hydrated compounds, a linear decrease of γ_{LS}^{78K} when increasing $T_{1/2}^{\uparrow}$ is observed (Figure 152a). Exception can be seen in the hydrated series (Figure 152b) for which no variation of the isomer shift *vs.* $T_{1/2}$ is identified, only the BF_4^- compound (**41-GlytrzE-BF$_4$**) present a slightly lower value. This decrease of γ_{LS}^{78K} when increasing $T_{1/2}^{\uparrow}$ corresponds to an increase of the Fe-N bond covalency resulting in higher transition temperatures (Figure 152f). This increase in covalency originate from the chains bringing closer together as a consequence of the insertion of small guest anions[46]. Interestingly, this increase is not notice when water molecules are also included.

As deduced by comparison of the X-ray powder diffraction patterns recorded at 298 K for compounds **37-GlytrzE-ClO$_4$** to **42-GlytrzE-BF$_4$** (Figure 124a), the insertion of this series of monovalent anions affect less the structural organization of the chains, and allows validating comparisons of complementary spectroscopic techniques. Indeed, Mössbauer spectroscopy confirms that the inserted voluminous monovalent anion and solvent molecules modify the local symmetry of the Fe octahedra as deduced by the irregular value of the quadrupole splitting in the HS state (Figure 152d). For lower size anions a decrease of ΔE_Q^{HS} (298 K) is however noticed (Figure 152d) thus indicating an increase of the local distortion around the metallic ion. This increase of the local distortion indicates that chains are much closer in the case of lower size anion than for larger size anions. In the same time, the presence of non-coordinated solvent molecules, in the materials, affects the local distortion of the metallic centre. The presence of 0.5 H_2O affect the distortion, the solvent favor the formation of a intense H-bond networking, which probably imply a modification of the symmetry of the octahedron surrounding the metal centre. This effect translates in a smaller value of ΔE_Q^{HS} (298 K) identified for **41-GlytrzE-BF$_4$** (2.73(1) mm/s), compared to

42-GlytrzE-BF_4 (2.76(1) mm/s). In the case of **37-GlytrzE-ClO_4** and **38-GlytrzE-ClO_4**, it seems that the presence of a methanol molecule in the system does not affect the local distortion of the FeN_6 octahedron, as ΔE_Q^{HS} (298 K) = 2.78 mm/s, is identical for both compounds. This geometric feature is also seen on the evolution of the isomer shift for the LS state, δ^{LS} (78 K) versus $T_{1/2}$ (Figure 152a).

Indeed, when $T_{1/2}$ increases, that is when the anion volume decreases, δ^{LS} (78 K) decreases. For compounds **37-GlytrzE-ClO_4**, **40-GlytrzE-NO_3**, **41-GlytrzE-BF_4**, we note that in the LS state, ΔE_Q^{LS} at 78 K remains constant at 0.19(1) mm/s, because there is no valence contribution to consider, the lattice contribution to the quadrupole splitting indicates that the Fe^{II} sites are distorted, as expected for such metal centers connected within a chain by three *N1*,*N2*-1,2,4-triazole bridges.

For compounds **38-GlytrzE-ClO_4**, **42-GlytrzE-BF_4** and **43-Glytrz-TRF**, a linear decrease of ΔE_Q^{LS} at 78 K when decreasing size of counter-anion is observed, the lattice contribution to the quadrupole splitting indicates that the symmetry of Fe^{II} sites are influenced by the size of the counter-anion[42].

The lattice water molecules in compound **39-GlytrzE-NO_3** and **41-GlytrzE-BF_4** are reversibly removed (until 373 K) along with change in colour of the samples. The quick response of the dehydrated samples for water vapor (obtained in the sample holder) suggests that these compounds could be used to sense moisture/water. An irreversible dehydration/hydration effect accompanied by a progressive transformation into a phase of higher cooperativity occurs if the annealing process goes below 390 K occurs. This process is investigated also by SEM imaging which evidences the negative thermal treatment on framework integrity. In the case of **39-GlytrzE-NO_3** and **41-GlytrzE-BF_4**, the heating results in an amorphisation of the sample (Figure 137) and weak signals are observed after the annealing treatment.

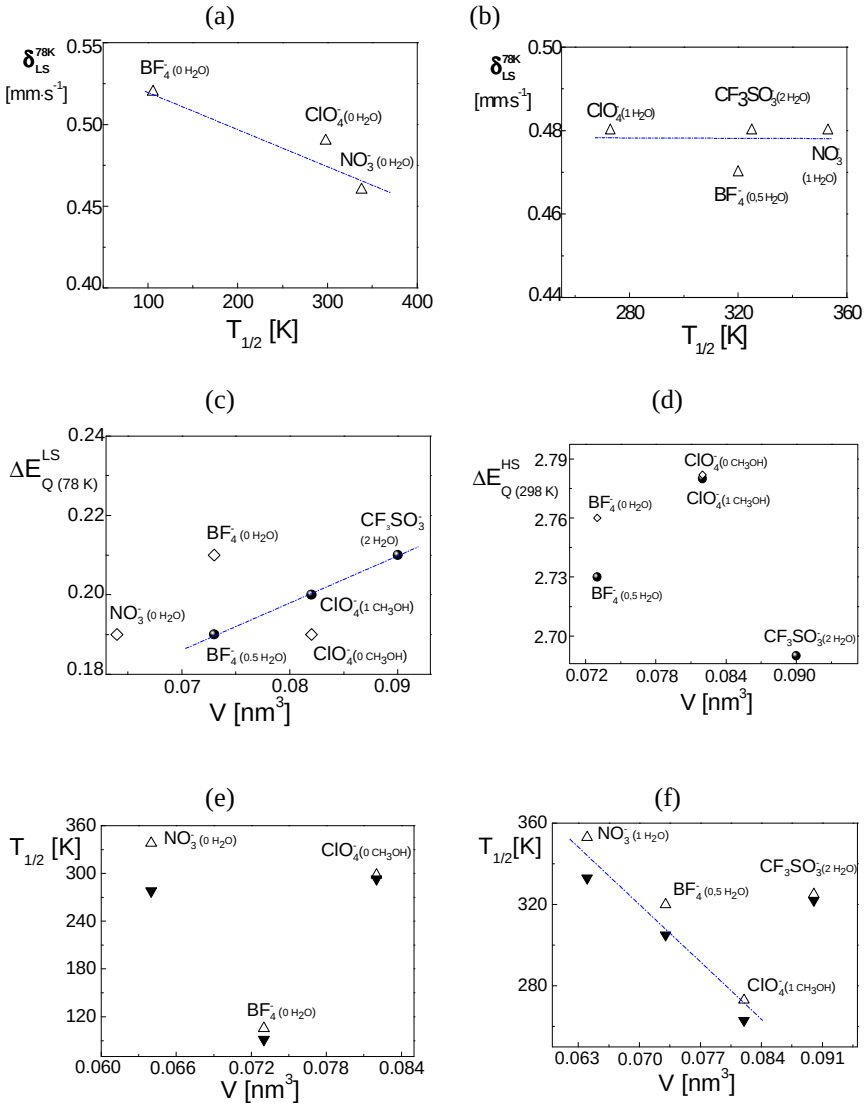

Figure 152 δ^{LS} (78 K) *vs* $T_{1/2}$ [K] for [Fe(GlytrzE)$_3$](Anion)·nSolvent (a) n = 0, (b) n = 0.5, 1 or 2; ΔE_Q^{LS} (78 K) *vs* V [nm^3][47] (c) and ΔE_Q^{HS} (298 K) *vs. V* [nm^3] (d); Variation of the transition temperatures, $T_{1/2}$, as deduced from ^{57}Fe Mössbauer spectroscopy, on cooling (▼) and warming modes (Δ) *vs* the anion volume for [Fe(GlytrzE)$_3$](Anion)·nSolvent (e) n = 0, (f) n = 0.5, 1 or 2. The volume of the $CF_3SO_3^-$ was fixed as 0.09 nm^3. The line is a guide to the eyes.

This change on the texture system of **39-GlytrzE-NO_3** affects less the magnetic properties compared with **41-GlytrzE-BF_4**, which allow us to

conclude that the framework of **39-GlytrzE-NO_3** is more stable than **41-GlytrzE-BF_4**. Compound **41-GlytrzE-BF_4**, is sensitive and on warming up to 390 K, the molecular system partially breaks down. A two step SCO system, operating below room temperature is obtained after the annealing process. These results support the fact that the crystallinity is affected with thermal pre-treatment destabilizing the framework. This effect was also identified in the $\{[Cu_3(\mu_3\text{-}O)(HGlytrz)_3\cdot(H_2O)_3]BF_4\cdot H_2O\}_n$ nano-ball system[1].

SCO reversibility can be affected by the rate of thermal treatment, its duration and atmosphere (helium) which eventually affect particles texture thus playing on SCO properties as it may induce phase transition or crystals defects, or probably to a removal of the non-coordinated water molecule. In case of a phase transition, the network might be unable to restore back itself to the original phase when external perturbation is brought back to normal due to network reshuffle.

In this context T-XRDP performed on **40-GlytrzE-NO_3** and **41-GlytrzE-BF_4** under helium atmosphere are remarkable and it was difficult to follow the SCO. It is also possible (either in **39-GlytrzE-NO_3**, **40-GlytrzE-NO_3** or **41-GlytrzE-BF_4**) that upon warming, in helium atmosphere, the 'soft' amino-acid network which is the integral part of this 1D polymers adopt different conformation tuned by the 'breathing' of iron centers during SCO originating the suggestion of phase transition and leads to the discrepancy in tracking the SCO. Retrospect of literature partially clear this possibility as the thermodynamic parameters for **39-GlytrzE-NO_3** and **40-GlytrzE-NO_3** (ΔS_{HL} = 77.7 and 88.4 $Jmol^{-1}K^{-1}$ for **39-GlytrzE-NO_3** and **40-GlytrzE-NO_3** respectively) observed by DSC are in the range of a phase transition. The remote possibility of compound still being in the bistability domain of thermal hysteresis (as observed by magnetic measurements) after the post-annealing treatment cannot be excluded. It has to be noted that although no

thermochromism was observed during the T-XRPD experiment under helium flux, after bringing back the sample to RT in air, the original pink colour was restored.

A relationship derived between the volume of the inserted monovalent counter-anion and the transition temperature, of Fe(II)- Ethyl-4H-1,2,4-triazol-4-yl-acetate systems is proposed. Indeed the insertion of planar counter-anions, such as NO_3^-, or tetrahedral counter-anions, such as BF_4^-, ClO_4^-, leads to higher transition temperature, $T_{1/2}$, as compared with bulkier anions such as $CF_3SO_3^-$. A new relationship between the entropy gap, evaluated from DSC measurements, and the volume of the inserted counter-anion is shown in Figure 153, shows a linear dependency, with decrease in entropy with increase in the size of the counter-anion;

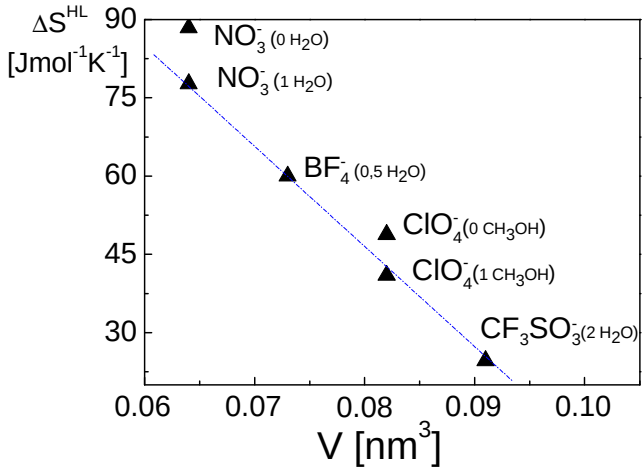

Figure 153 Variation of the entropy gap, $\Delta S^{HL}[Jmol^{-1}K^{-1}]$, as deduced from thermodynamic measurements, *vs* the anion volume for $[Fe(GlytrzE)_3](Anion)\cdot nSolvent$. The volume of the $CF_3SO_3^-$ was fixed as 0.09 nm^3.

This information provides a direct experimental evaluation of the cooperativity as function of the size of counter-anion, which is characteristic of 1D SCO compounds.

This is a rare family of 1D coordination polymers where simple change of anion and solvent leads to compounds that could operate as 'optical alerts' in a wide range of temperature, including the room temperature region.

The T-XRPD data for **39-GlytrzE-NO_3**, **40-GlytrzE-NO_3** and **41-GlytrzE-BF_4** is not only in harmony with data obtained by other complimentary technique but also revealed possible network perturbation under thermal treatment or atmosphere of the experiment, also evidenced in the study by imaging technique which until now was superficially probed.

We anticipate that the use of other amino-acids and amino-ester triazole systems to build new SCO framework, would provide us to build new types of frameworks which would unveil much more interesting properties, which will be discussed in the next chapter.

Notes and references

[1] A. D. Naik, M. M. Dîrtu, A. Leonard, B. Tinant, J. Marchand-Brynaert, B. L. Su, Y. Garcia. *Crystal Growth & Design* **2010**, *10*(4), 1798-1807.

[2] A. D. Naik, J. Beck, M. M. Dîrtu, C. Bebrone, B. Tinant, K. Robeyns, J. Marchand-Brynaert, Y. Garcia. *Inorg. Chim. Acta* **2011**, *368*(1), 21-28.

[3] M. M. Dîrtu, A. Rotaru, D. Gillard, J. Linares, E. Codjovi, B. Tinant, Y. Garcia. *Inorg. Chem.* **2009**, *48*(16), 7838-7852.

[4] M. M. Dîrtu, A. D. Naik, J. Marchand-Brynaert, Y. Garcia. *J. Phys. : Conf. Ser.* **2010**, *217*(1), 012085.

[5] M. M. Dîrtu, F. Schmit, A. D. Naik, A. Rotaru, J. Marchand-Brynaert, Y. Garcia. *Int. J. Mol. Sci.* **2011**, *12*(8), 5339-5351.

[6] A. D. Naik, L. Stappers, J. Snauwaert, J. Fransaer, Y. Garcia. *Small* **2010**, *6*(24), 2842-2846.

[7] A. D. Naik, J. Marchand-Brynaert, Y. Garcia. *Synthesis* **2008**, *1*, 149-154.

[8] L.G.Lavrenova, V. N. Ikorskii, V. A. Varnek, I. M. Oglezneva, S. V. Larionova. *Koord. Khim.* **1986**, *12*, 207.

[9] J. G. Haasnoot, G. Vos, W. L. Groeneveld. *Zeitschrift fur Naturforschung Section B-A Journal of Chemical Sciences* **1977**, *32*, 421.

[10] V. P. Sinditskii, V. I. Sokol, A. E. Fogelzang, M. D. Dutov, V. V. Serushkin, M. A. Poraikoshits, B. S. Svetlov. *Russ. J. Inorg. Chem.* **1987**, *32*(8), 1950-1955.

[11] G. Socrates. *Infrared and Raman Characteristic Group Frequencies: Tables and Charts, 3rd Edition*, **1994**.

[12] M. B. Bushuev, L. G. Lavrenova, V. N. Ikorskii, Y. G. Shvedenkov, V. A. Varnek, L. A. Sheludyakova, S. V. Larionov. *Russian Journal of Coordination Chemistry* **2004**, *30*(4), 284-290.

[13] P. J. van Koningsbruggen, Y. Garcia, E. Codjovi, R. Lapouyade, O. Kahn, L. Fournes, L. Rabardel. *J. Mater. Chem.* **1997**, *7*(10), 2069-2075.

[14] P. Gütlich, A. Hauser, H. Spiering. *Angew. Chem. Int. Ed.* **1994**, *33*(20), 2024-2054.

[15] P. Gütlich, J. Jung, H. A. Goodwin. In: (Eds.: E. Coronado, P. Delhaès, D. Gatteschi, and J. S. Miller), *Molecular Magnetism: From Molecular Assemblies to the Devices*, **1996**, p. 327.

[16] M. M. Dirtu, Y. Garcia, M. Nica, A. Rotarii, J. Linares, F. Varret. *Polyhedron* **2007**, *26*(9-11), 2259-2263.

[17] Y. Garcia, V. Ksenofontov, S. Mentior, M. M. Dîrtu, C. Gieck, A. Bhatthacharjee, P. Gutlich. *Chem. Eur. J.* **2008**, *14*(12), 3745-3758.
[18] Y. Garcia, P. J. van Koningsbruggen, R. Lapouyade, L. Rabardel, O. Kahn, M. Wieczorek, R. Bronisz, Z. Ciunik, M. F. Rudolf. *Comptes Rendus de l Academie des Sciences Serie Ii Fascicule C-Chimie* **1998**, *1*(8), 523-532.
[19] A. Rotaru, F. Varret, E. Codjovi, K. Boukheddaden, J. Linares, A. Stancu, P. Guionneau, J.-F. Létard. *J. Appl. Phys.* **2009**, *106*(5), 053515-053520.
[20] P. R. Wajnflasz J. *J. Phys. Colloq.* **1971**, *32*(C1-91).
[21] A. Bousseksou, J. Nasser, J. Linares, K. Boukheddaden, F. Varret. *J. Phys. I France* **1991**, *2*, 1381-1403.
[22] F. Varret, K. Boukheddaden, E. Codjovi, I. Maurin, H. Tokoro, S. Ohkoshi, K. Hashimoto. *Polyhedron* **2005**, *24*(16-17), 2857-2863.
[23] P. Gütlich, Y. Garcia, H. Spiering. *Magnetism: From Molecules to Materials*, Wiley-VCH, Verlag GmbH, **2003**, p. 271.
[24] P. Gütlich, Y. Garcia, H. A. Goodwin. *Chem. Soc. Rev.* **2000**, *29*(6), 419-427.
[25] M. M. Dirtu, C. Neuhausen, A. D. Naik, A. Rotaru, L. Spinu, Y. Garcia. *Inorg. Chem.* **2010**, *49*(12), 5723-5736.
[26] J. Krober, J. P. Audiere, R. Claude, E. Codjovi, O. Kahn, J. G. Haasnoot, F. Groliere, C. Jay, A. Bousseksou, J. Linares, F. Varret, A. Gonthiervassal. *Chem. Mater.* **1994**, *6*(8), 1404-1412.
[27] B. Weber, W. Bauer, T. Plaffeneder, M. M. Dîrtu, A. D. Naik, A. Rotaru, Y. Garcia. *Eur. J. Inorg. Chem.* **2011**, *in press.*
[28] O. Kahn, C. Jay-Martinez. *Science* **1998**, *279*(5347), 44-48.
[29] M. M. Dirtu, C. Neuhausen, A. D. Naik, A. Leonard, F. Robert, J. Marchand-Brynaert, B. L. Su, Y. Garcia. *Crystal Growth & Design* **2011**, *11*(4), 1375-1384.
[30] M. M. Dirtu, A. D. Naik, J. Marchand-Brynaert, Y. Garcia. *Journal of physics: conference series* **2010**, *217*(1), 012085.
[31] M. Casarin, C. Corvaja, C. Di Nicola, D. Falcomer, L. Franco, M. Monari, L. Pandolfo, C. Pettinari, F. Piccinelli. *Inorg. Chem.* **2005**, *44*(18), 6265-6276.
[32] O. Roubeau, J. M. A. Gomez, E. Balskus, J. J. A. Kolnaar, J. G. Haasnoot, J. Reedijk. *New J. Chem.* **2001**, *25*(1), 144-150.
[33] M. Seredyuk, A. B. Gaspar, V. Ksenofontov, S. Reiman, Y. Galyametdinov, W. Haase, E. Rentschler, P. Gütlich. *Chem. Mater.* **2006**, *18*(10), 2513-2519.
[34] Y. Garcia, S. J. Campbell, J. S. Lord, Y. Boland, V. Ksenofontov, P. Gutlich. *J. Phys. Chem. B* **2007**, *111*(38), 11111-11119.
[35] B. Weber, W. Bauer, J. Obel. *Angew. Chem. Int. Ed.* **2008**, *47*, 10098-10101.
[36] S. Cobo, G. Molnar, J. A. Real, A. Bousseksou. *Angewandte Chemie International Edition* **2006**, *45*(35), 5786-5789.

[37] I. Salitros, N. Madhu, R. Boca, J. Pavlik, M. Ruben. *Monatshefte fur Chemie* **2009**, *140*(7), 695-733.
[38] Y. Garcia, P. J. van Koningsbruggen, R. Lapouyade, L. Rabardel, O. Kahn, M. Wieczorek, R. Bronisz, Z. Ciunik, M. F. Rudolf. *Comptes Rendus de l Academie des Sciences Serie Ii Fascicule C-Chimie* **1998**, *1*(8), 523-532.
[39] O. Kahn, J. Krober, C. Jay. *Adv. Mater.* **1992**, *4*(11), 718-728.
[40] Y. Garcia, V. Niel, M. C. Munoz, J. A. Real. *Top. Curr. Chem.* **2004**, *233*, 229-257.
[41] M. M. Dirtu, C. Neuhausen, A. D. Naik, A. Rotaru, L. Spinu, Y. Garcia. *Inorg. Chem.* **2010**, *49*(12), 5723-5736.
[42] Y. Garcia, V. Ksenofontov, S. Mentior, M. M. Dîrtu, C. Gieck, A. Bhatthacharjee, P. Gutlich. *Chem. Eur. J.* **2008**, *14*(12), 3745-3758.
[43] M. M. Dirtu, C. Neuhausen, A. D. Naik, A. Rotaru, L. Spinu, Y. Garcia. *Inorg. Chem.* **2010**, *49*(12), 5723-5736.
[44] M. M. Dirtu, Y. Garcia, M. Nica, A. Rotarii, J. Linares, F. Varret. *Polyhedron* **2007**, *26*(9-11), 2259-2263.
[45] M. M. Dirtu, Y. Garcia, M. Nica, A. Rotarii, J. Linares, F. Varret. *Polyhedron* **2007**, *26*(9-11), 2259-2263.
[46] M. M. Dirtu, A. Rotaru, D. Gillard, J. Linares, E. Codjovi, B. Tinant, Y. Garcia. *Inorg. Chem.* **2009**, *48*(16), 7838-7852.
[47] H. D. Jenkins, H. K. Roobottom, J. Passmore, L. Glasser. *Inorg. Chem.* **1999**, *38*(16), 3609-3620.

Chapter VIII: One step versus two steps spin crossover molecular sensors, based on β-amino-esters[1]

VIII.1: Impact of counter-anion in selected 1D iron(II) spin crossover coordination polymers

Introducing remarks

In this chapter we describe a detailed study of new SCO compounds based on a new tailored 4-R-1,2,4-triazole from β-amino-acid, namely 4H-1,2-4-triazol-4-yl-propionate (**βAlatrz**) (Figure 154). The reason for introducing β-Alanine ethyl ester substituted on the 4 position of a 1,2,4-triazole core was to use an appropriate length of substituent (2 carbon spacer compared to a-aminoacid) which can keeps a certain distance between 1D chains in complexes which can introduce favorable supramolecular interactions due to H-acceptors on the substituent. Thus, the ST properties of five 1D Fe^{II} chains, $[Fe(\mathbf{\beta Alatrz})_3](CF_3SO_3)_2 \cdot 0.5H_2O$ (**44·0.5H$_2$O**) and its dehydrated form, $[Fe(\mathbf{\beta Alatrz})_3](CF_3SO_3)_2$ (**45**), $[Fe(\mathbf{\beta Alatrz})_3](ClO_4)_2 \cdot H_2O$ (**46·H$_2$O**) and $[Fe(\mathbf{\beta Alatrz})_3](BF_4)_2 \cdot H_2O$ (**47·H$_2$O**) and its dehydrated form $[Fe(\mathbf{\beta Alatrz})_3](BF_4)_2$ (**48**) were studied.

[1] Adapted from : M. M. Dîrtu, F. Schmit, A. D. Naik, A. Rotaru, J. Marchand-Brynaert, Y. Garcia *Int. J. Mol. Sci.*, **2011**, *12*, 5339-5351; M. M. Dîrtu, F. Schmit, A. D. Naik, A. Rotaru, J. Marchand-Brynaert, Y. Garcia *Hyperf. Inter.*, **2012**, 205, 69-73.

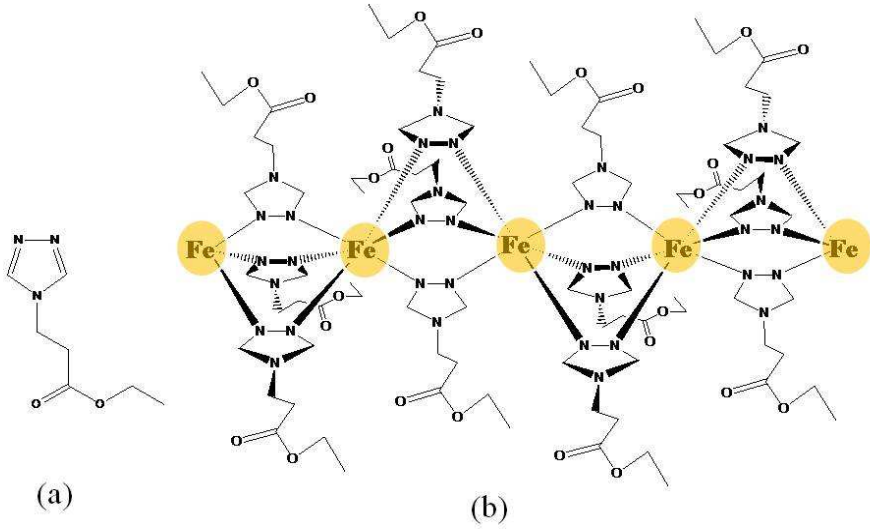

Figure 154 Molecular structure of (**a**) ethyl 4H-1,2,4-triazol-4-yl-propionate (**βAlatrz**); and (**b**) 1D chain complex $[Fe(\mathbf{\beta Alatrz})_3]^{2+}$.

Results

Synthesis and general characterization

The transamination reaction used in the synthesis of ethyl-4H-1,2,4-triazol-4-yl-acetate, **GlytrzE**, and 4H-1,2,4-triazol-4-yl acetic acid, **HGlytrz**,[1] proved to be a good synthetic strategy to build a β-amino-acid triazole. The synthetic route, starting with β-Alanine ethyl ester hydrochloride and *N*,*N*-Dimethylformamide-azine, helped us to obtain a new molecule, **βAlatrz**, with a good yield. The synthesis time is relatively longer than the synthesis of previous ligands and the final product had to be purified by "flash" column chromatography.

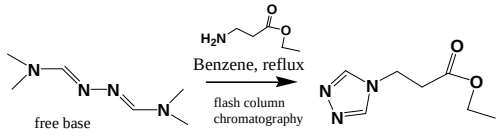

Figure 155 Synthetic protocol used for ethyl 4H-1,2-4-triazol-4-yl-propionate (**βAlatrz**).

1D coordination polymers were obtained as white powders by reaction of the corresponding Fe(II) inorganic precursor, $[Fe(H_2O)_6](CF_3SO_3)_2$[2], $[Fe(H_2O)_6](BF_4)_2$ and $[Fe(H_2O)_6](ClO_4)_2$ with a methanolic solution of **βAlatrz**. These complexes were successfully characterized by elemental analysis, TGA-DTA analyses, atomic absorption (AAS), X-Ray powder diffraction, IR, Raman, SEM, DSC, SQUID magnetometry and ^{57}Fe Mössbauer spectroscopy. The thermogravimetric and elemental analyses reveal the presence of guest water molecules, affording the following general formula $[Fe(\textbf{βAlatrz})_3](CF_3SO_3)_2 \cdot 0.5H_2O$ (**44·0.5H$_2$O**), $[Fe(\textbf{βAlatrz})_3](ClO_4)_2 \cdot H_2O$ (**46·H$_2$O**) and $[Fe(\textbf{βAlatrz})_3](BF_4)_2 \cdot H_2O$ (**47·H$_2$O**). Compounds **44·0.5H$_2$O** and **47·H$_2$O** were dehydrated by annealing that leads to new compounds, $[Fe(\textbf{βAlatrz})_3](CF_3SO_3)_2$ (**45**), $[Fe(\textbf{βAlatrz})_3](BF_4)_2$ (**48**) respectively which were also characterized to reveal the influence of solvent molecules on the spin state.

44·0.5H$_2$O present a rather crystalline character as revealed from X-ray powder diffraction (XRPD) patterns, compared with **45, 46·H$_2$O** and **47·H$_2$O** (Figure 156). Compound **44·0.5H$_2$O** and **47·H$_2$O** were dehydrated by annealing that leads to new compounds $[Fe(\textbf{βAlatrz})_3](CF_3SO_3)_2$ (**45**), $[Fe(\textbf{βAlatrz})_3](BF_4)_2$ (**48**) which were also characterized to reveal the influence of solvent molecules on the spin state. **44·0.5H$_2$O**, **45** and **47·H$_2$O** present a rather crystalline character as revealed from X-ray powder diffraction (XRPD) patterns (Figure 156). This result is also illustrated by the SEM analysis with blocks of hexagonal shape of about 2 μm width for **44·0.5H$_2$O** (Figure 157). Compound **46·H$_2$O** are distinguished by uniform aggregates, of ~ 2 μm diameter. Each aggregate appears to be regular. Contrary to these compounds, **47·H$_2$O** present a fibrous morphology (Figure 157).

Vibrational studies:

1. FT-IR and Raman analyses at room temperature

These analyses were performed: (i) to confirm the identity of the ligand framework before and upon complexation as the ester functionality is susceptible to hydrolysis; (ii) to ascertain the coordination mode of iron to the ligand and the presence of the counter-anions in the crystal lattice (Figure 158). Two sharp IR bands at 3118 (s) and 2983 (m) cm^{-1} of **βAlatrz**, are assigned to the νCH_2 modes.[3] The carboxylic group of ester shows two stretching vibrations corresponding to (C=O) and (C-O) at 1728(s) and 1205(s) cm^{-1}, respectively, which are almost unchanged (1732 and 1212 cm^{-1}) in **44·0.5H_2O** ruling out the possible ester hydrolysis and also confirming the non-involvement of carboxylic ester group in coordination. For **βAlatrz** the band assigned to ring torsion of triazole at ν = 634(m) cm^{-1}, the $\nu_{C=N}$ stretching vibration at 1535(m) cm^{-1} and the N-N stretching band at ν = 1022(s) cm^{-1}, are all shifted upon complexation in **44·0.5H_2O** to 632 cm^{-1}, $\nu_{C=N}$ = 1560 cm^{-1}, and ν_{N-N} = 1028 cm^{-1}, respectively. These values confirm the coordination of the iron to the 1,2,4-triazole ring[4, 5]. Indeed, the characteristic bands of the ligand are not only present in the spectra of the complexes but also are shifted towards larger wave numbers, from 3 to 15 cm^{-1} respectively. This energy increase is due to the deformation of the ligand upon coordination of the metal, the ligand molecule being indeed more constrained to perform vibration and twisting movements [6, 7].

For a better understanding of the molecular structure of these ligands, Raman spectra were collected too (Figure 158). The band present at 1728 cm^{-1} for **βAlatrz** is assigned to a C=O vibration. In complexes this band is retained and appears around 1732 cm^{-1}. The C-C stretching is also active in Raman as a medium band at 1098 cm^{-1} for **βAlatrz** and appears in the same wavenumber in all complexes. Presence of the monovalent counter-anion is also confirmed by IR and Raman: *IR* (cm^{-1}) $\upsilon_{(S-O)}$ ~ 1283(s), (**44·0.5H_2O** and **45**); $\upsilon_{(Cl-O)}$ ~ 1097 (s), (**46·H_2O**); $\upsilon_{(B-F)}$ ~ 1059 (s), (**47·H_2O** and **48**);

Raman (cm^{-1}) $\upsilon_{(S-O)}$ ~ 1034(s), 760(m) (**44·0.5H_2O** and **45**); $\upsilon_{(Cl-O)}$ ~ 1097(s), (**46·H_2O**); $\upsilon_{(B-F)}$ ~ 766 (s), (**47·H_2O** and **48**).[8]

2. FT-IR and RAMAN analyses at variable temperature for **47·H_2O**

The temperature dependent IR spectra have been measured in the MIR area (over 700 cm^{-1}) by means of reflections technique, by Dr. J. Wolny (Kaiserslautern). The most pronounced differences are observed in the 840-920 cm^{-1} area (Figure 158b). One could distinguish few temperature ranges as far as the spectral pattern is concerned. Between 300 and 255 K (blue lines, HS phase, cf. Figure 158b) no or minor changes occur. In the 255-205 K range (red lines, high-temperature ST) the gradual decrease of the intensity of the double band between 900 and 910 cm^{-1} is seen, with the concomitant developing of three new bands in the 870-880 cm^{-1} region. In the temperature range 200-155 K (pink-violet lines, the low-temperature transition) the three latter do not change significantly, however a new band develops clearly in the 900 cm^{-1} region. Further lowering of temperature brings only the (green and blue lines) lowering of the spectral resolution.

The DFT based (B3LYP/CEP-31G) normal analysis of the ligand reveals four IR strong bands in the 820-940 cm^{-1} region. The band at 823 cm^{-1} involves the C-H bending of the ester -CH_2 bands, coupled to some H_2C-O stretching. The band predicted at 843 cm^{-1} is the pure C-H out of plane bending of the triazole ring. The band at 935 and 940 cm^{-1} corresponds to a triazole ring stretching, with a pronounced *N1-N2* bond stretching, coupled to stretching and bending of the alanine ester fragment. In particular the triazole ring stretching in the coordinated ligand will produce some Fe-N stretching, the corresponding bands may shift on spin switching as observed in the studied sample. On the other hand, the change of the ligand

conformation (see further discussion) may result in change of the frequencies of the mode predicted at 823 cm^{-1}.

The temperature dependent Raman spectra, recorded by Dr. J. Wolny (Kaiserslautern) show more changes in the different spectral areas. They are shown in (Figure 159b). Firstly, one observes the number of peaks below 300 cm^{-1} at lower temperatures. They all begin to appear at ca. 210 K on cooling and disappear at the same temperature on heating. The spectra at 110 K show at least three peaks at ca. 195, 215 and 250 cm^{-1}, characteristic for oligomeric and polymeric LS Fe(II) triazole systems[9-13] and have been recently shown to be due iron-nitrogen bending vibrations.[13] The peaks at ca. 342 and 358 cm^{-1} assigned to E vibration of BF_4^- merge together to a asymmetric band at 300 K down to 210 K. Below this temperature one symmetric band develops centered at 349 cm^{-1}. This point towards some disorder in the packing of the phase containing HS centers. The next interesting area is that between 1015 and 1040 cm^{-1}. From 300 K down to 230 K the strongly asymmetric peaks at 1037-1039 cm^{-1} are present. At 210 K a new peak at 1015 cm^{-1} appears together with a shoulder at 1029 cm^{-1}. The latter turns to maximum at 110 K, with the full disappearance of 1040 cm^{-1} band. The normal coordinate analysis shows there are four modes in the 1026-1054 cm^{-1} range, that correspond to N4-C stretching in the triazole ring. Coupling of these modes to Fe-N stretching results in the dependence of the observed frequency on the spin state of the iron. Similarly, from 300 K down to 230 K two bands are observed at 1357 and 1372 cm^{-1}, that merge together down from 210 K and grows with decreasing temperature to give one peak at 1361 cm^{-1} at 190 K. Finally, formation of the LS phase is accompanied by shifting of the weak band at 1480 cm^{-1} seen at 300 K, towards 1490 cm^{-1} with a significant increase of intensity.

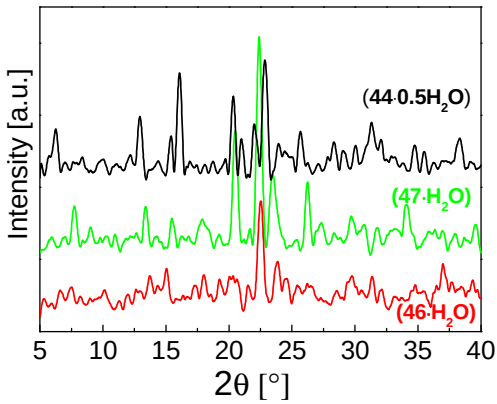

(a)

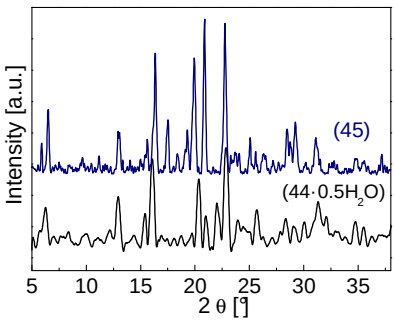

(b)

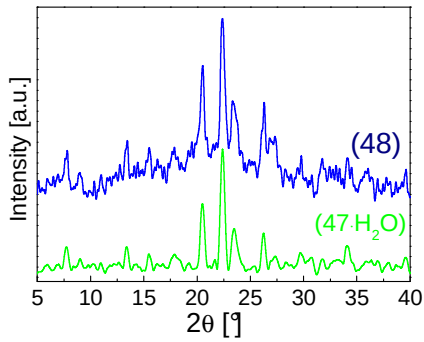

(c)

Figure 156 (a) X-Ray powder diffraction patterns at 293 K for **44·0.5H$_2$O, 46·H$_2$O** and **47·H$_2$O;** (b) X-ray powder diffraction patterns of **45**, (thermally treated compound in TGA); bottom: diffractogram of **44·0.5H$_2$O** (freshly prepared); (c) X-ray powder diffraction patterns of **48**, (thermally treated compound in TGA); bottom: diffractogram of **47·H$_2$O** (freshly prepared).

DFT calculations reveal two modes involving CH2(N) and CH2(O) "fan" movement (at 1357 and 1398 cm^{-1}). On the other hand at 1478 and 1493 cm^{-1} C-H in plane bending of the triazole ring, coupled with N3-C stretching is predicted.

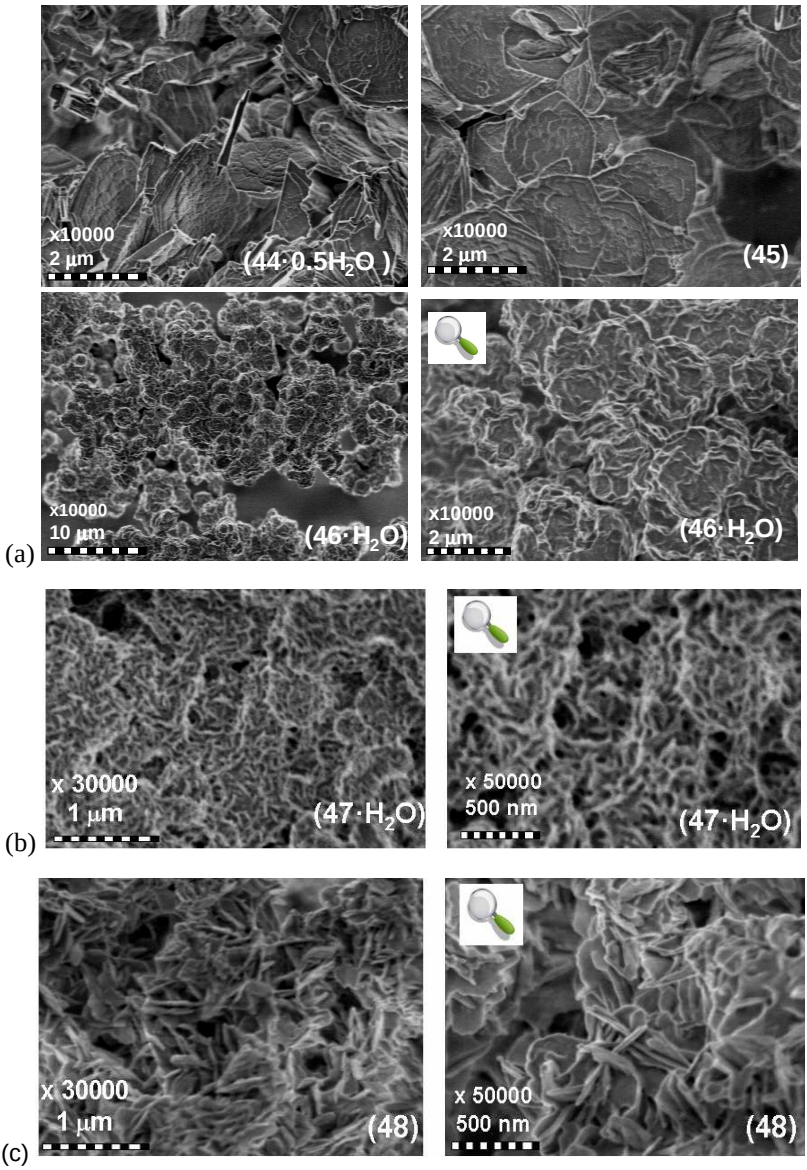

Figure 157 (a) SEM images of microcrystalline particles of **44·0.5H_2O, 45** and **46·H_2O** at 293 K; SEM analysis of **45** confirms the framework integrity preservation after thermal treatment; (b) SEM images of microcrystalline particles of **47·H_2O** at 293 K; (c) SEM analysis of **48**.

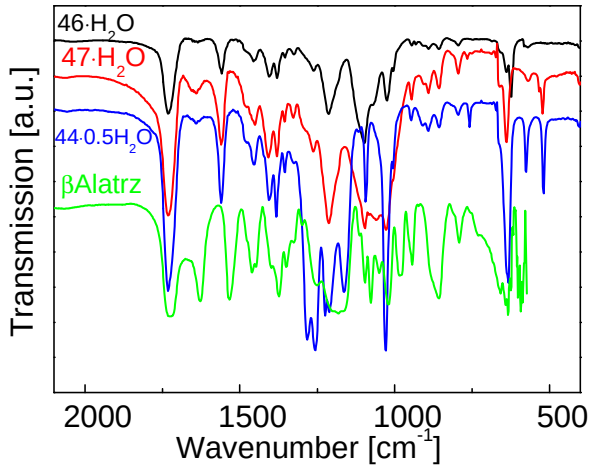

(a)

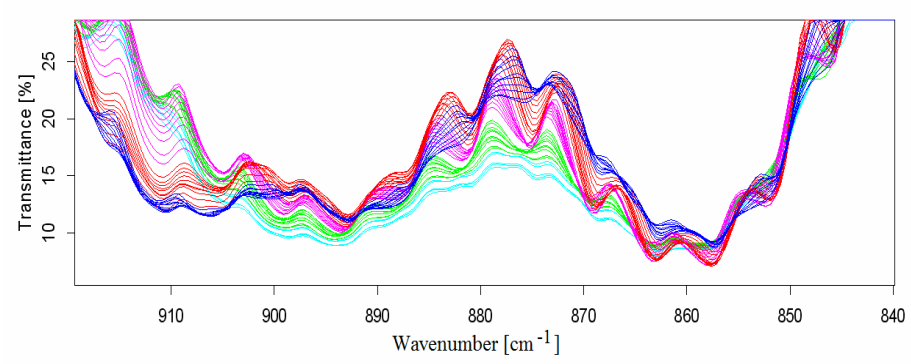

(b)

Figure 158 (a) IR spectra of the ligand **βAlatrz** and complexes **44·0.5H$_2$O**, **46·H$_2$O**, **47·H$_2$O**, over the range 400-2100 cm^{-1}; (b) Temperature dependence IR spectra, of **47·H$_2$O**, where the changes are the most pronounced between 840 and 1000 cm^{-1} (blue 300-255 K, red 250-205 K, pink-violet 200-155 K, green 150-105 K, light blue 100-80 K).

^{57}Fe Mössbauer spectroscopy confirm for **44·0.5H$_2$O** the presence of one $Fe^{II}N_6$ site, and exclude any oxidation product of iron. These spectroscopic data supports a linear chain structure with Fe^{II} ions linked by triple *N*1,*N*2-1,2,4-triazole bridges[14, 15].

(a)

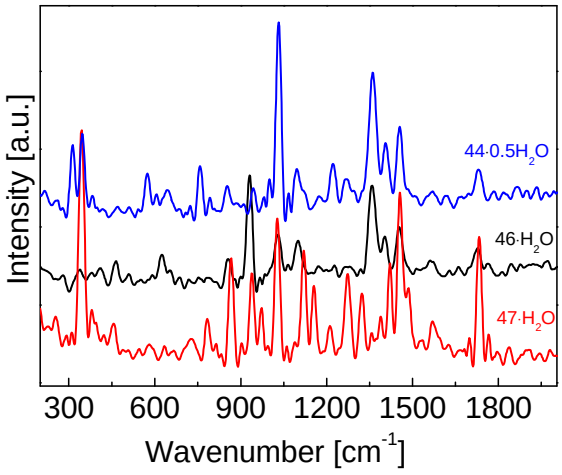
Intensity [a.u.]
44·0.5H2O
46·H2O
47·H2O
300
600
900
1200
1500
1800
Wavenumber [cm-1]

(b)

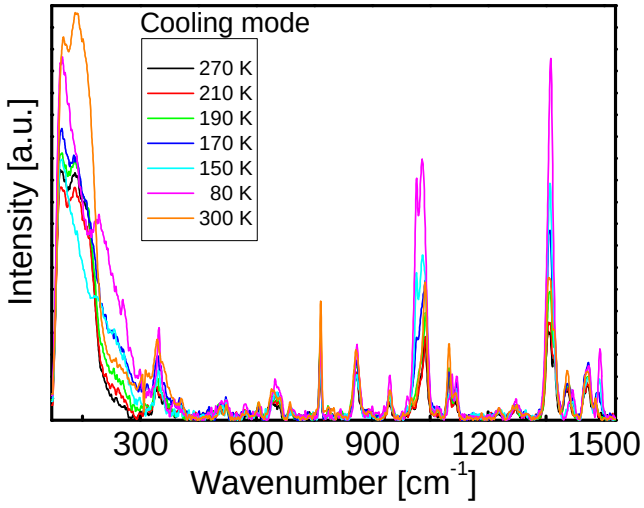
Cooling mode
270 K
210 K
190 K
170 K
150 K
80 K
300 K
Intensity [a.u.]
300
600
900
1200
1500
Wavenumber [cm-1]

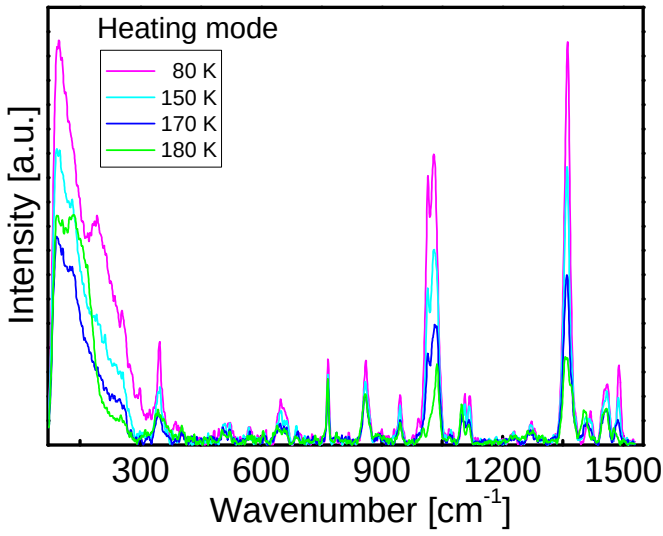

Figure 159 (a) Raman spectra of complexes **44·0.5H$_2$O**, **46·H$_2$O** and **47·H$_2$O**, over the range 180 – 2000 cm^{-1}; (b) Temperature dependence RAMAN spectra, of **47·H$_2$O**, where the changes are the most pronounced between 70 and 1530 cm^{-1}.

All compounds were prepared as white powders and present a reversible thermochromism on cooling to pink (Figure 160). These colors depend on the spin state of the Fe^{II} centers, as the ST involves a change in the electronic configuration which modifies the absorption spectrum of the complex.

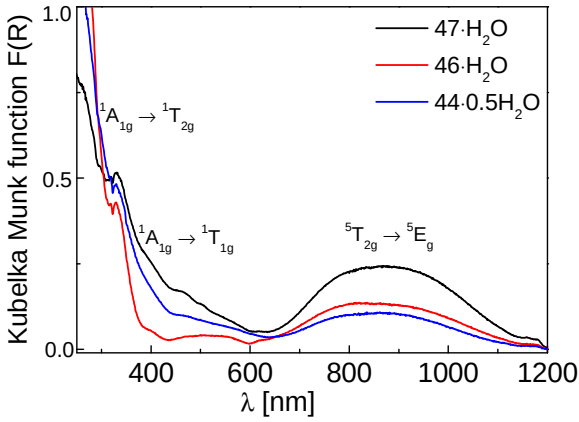

Figure 160 UV-Vis diffuse reflectance spectrum of **44·0.5H$_2$O**, **46·H$_2$O** and **47·H$_2$O** showing d–d transitions at 293 K.

The white color of all complexes, is due to the presence of the spin-allowed lowest energy d-d transition, $^5T_{2g} \rightarrow {}^5E_g$, for the HS sites in the near infrared region (~11500 cm^{-1})[16, 17]. Two supplementary bands, corresponding to the $^1A_{1g} \rightarrow {}^1T_{1g}$ and $^1A_{1g} \rightarrow {}^1T_{2g}$ d-d transitions of LS Fe^{II} sites are observed at ~ 18727 cm^{-1} and ~ 30300 cm^{-1}, respectively suggesting that some proportion of Fe^{II} may be in the LS state at room temperature. The ligand field strengths for the HS and the LS state, given by equations $10D_q^{HS} = E(^5E) - E(^5T_2)$ and $10D_q^{LS} = E(^1T) - E(^1A_1) + (E(^1T_2) – E(^1T_1))/4$,[16, 17] allowed us to estimate $10D_q^{HS}$ and $10D_q^{LS}$ to be approximately 11500 cm^{-1} and 26302 cm^{-1}, respectively. These values are characteristic for SCO complexes[16, 17]. Presence of LS state at room temperature has been confirmed by ^{57}Fe Mössbauer spectroscopy (*vide infra*).

The reversibility of the rehydration/dehydration process within a given framework structure with the change of crystallinity can play an important role on the SCO properties[18]. This process was investigated for **44·0.5H_2O** and **47·H_2O** by thermogravimetric analysis, XRD powder pattern and SEM imaging recorded after annealing treatment. The samples were first deposited in a crucible and heated at slower rate of 1K/min in air atmosphere (air flow 130 ml/min) to the temperature of complete dehydration (390 K) leading to **45** and **48** respectively. After a short standby period, the sample was cooled (1 K/min) to reach room temperature revealing no rehydration. Thus the dehydration-rehydration process is irreversible and **45** and **48** are air stable which will ease any further physical studies on this compound. Comparison of the powder XRD patterns (Figure 156) and SEM images (Figure 157) of **44·0.5H_2O** and **45** allow to exclude any framework rupture. Indeed, these two compounds are isostructural, **45** showing higher peak intensities indicating a better crystalline character. No deterioration is observed by SEM. It is not the case for **47·H_2O** and **48**. These two compounds seem to be isostructural, the 2θ[°] position of principal peaks are identical, but SEM analysis of **48** confirms that the framework integrity is

changed after thermal treatment, indicating a better crystalline character (Figure 157).

Thermal spin-crossover properties - One step Iron(II) 1D Chain Compounds

SQUID magnetometry

The temperature dependent magnetic properties of all compounds were determined by temperature dependent susceptibility measurements using a SQUID magnetometer operating at 1000 Oe.

For complex **44·0.5H$_2$O** (Figure 161) $\chi_M T$ is 3.10 cm^3 K mol^{-1} at 300 K, which is in the region expected for an Fe^{II} complex *essentially* in the HS state, with a small % of LS species. Upon cooling, $\chi_M T$ remains almost constant until 240 K where it drops sharply to $T_{1/2}^{\downarrow}$ = 228 K down to ~ 0.14 cm^3 K mol^{-1} at 77 K, which is typical for a diamagnetic Fe^{II} complex with possibly a few HS ions.

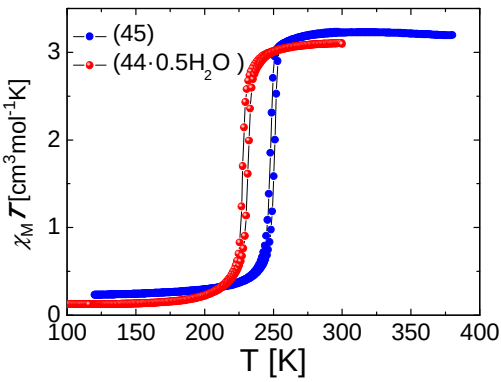

Figure 161 Thermal variation of $\chi_M T$ of **44·0.5H$_2$O** (depicted in red) and **45** (depicted in blue).

Upon warming, the $\chi_M T$ curve differs slightly revealing a small hysteresis width (4 K) at $T_{1/2}^{\uparrow}$ = 232 K for this very sharp spin transition. A hysteretic

behavior of width 4 K was observed too for **45** with a ST shifted upwards ($T_{1/2}^{\downarrow}$ = 248 K and $T_{1/2}^{\uparrow}$ = 252 K). The same curve shape is observed too which confirms the preservation of the 1D chain character[18] and does not support the appearance of a structural phase transition following the annealing process. The stabilization of the LS state upon water release is uncommon for this family of complexes[19] and was only observed for the 1D chain compounds [Fe(4-(2'-hydroxyethyl)-1,2,4-triazole)$_3$](anion)$_2$·nH_2O (anion = ClO_4^-, n = 2, 0; anion = I^-, n = 1, 0)[20], [Fe(4-amino-1,2,4-triazole)$_3$](anion)·nH_2O (anion = TiF_6^{2-}, n = 1, 0.5; anion = ZrF_6^{2-}, n = 0.5, 0)[14] as well as for [Fe(ethyl-4H-1,2,4-triazol-4-yl-acetate)$_3$]$(ClO_4)_2$·nCH_3OH (n = 1,0) but with methanol as solvent[1]. The effect of the release of non-coordinated solvent molecules on the spin state can be translated here as a positive pressure effect and the ST temperature is shifted forwards[21].

Compound **46·H_2O** present a gradual SCO (Figure 162). For **46·H_2O**, χ_MT increase slowly from 0.12 cm^3 K mol^{-1} at 4 K to 0.38 cm^3 K mol^{-1} at 64 K, indicative of HS iron(II) at low temperature (Figure 162).

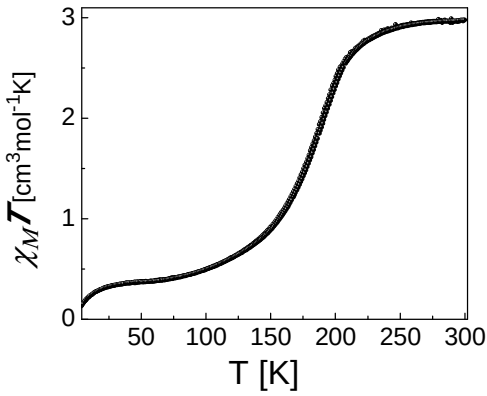

Figure 162 Thermal variation of $\chi_M T$ of **46·H_2O.**

Between 64 K and 175 K $\chi_M T$ increase slowly and then more abruptly to attain a maximum value of 2.98 cm^3 K mol^{-1} at 300 K, indicating an incomplete spin transition. In the cooling mode the gradual character of the

SCO is maintained with $T_{1/2}^{\downarrow}$ = 172 K. A ST with a 3 K wide thermal hysteresis loop is observed at $T_{1/2}^{\downarrow}$ = 172 K and $T_{1/2}^{\uparrow}$ = 175 K. The decrease of the magnetic moment at lower temperatures is most likely due to the zero-field splitting of the HS species, as often happens in SCO compounds.

^{57}Fe Mössbauer spectroscopy

An inspection of electronic and structural features for all compounds using ^{57}Fe Mössbauer spectroscopy was undertaken over the temperature range 77 K - 300 K.

An inspection of electronic and structural features for **44·0.5H$_2$O** and **45** using ^{57}Fe Mössbauer spectroscopy was undertaken over the temperature range 77 K–300 K (Figure 163). Selected Mössbauer parameters are summarized in Table 53 and 54. At 77 K, the spectrum of **44·0.5H$_2$O** consists of two quadrupole doublets of different resonance area fractions. The major quadrupole doublet with isomer shift δ^{LS} = 0.51(2) mm/s and quadrupole splitting, ΔE_Q^{LS} = 0.23(2) mm/s correspond to the LS state of Fe^{II}. The presence of an LS quadrupole splitting stems from a lattice contribution to the electric field gradient and therefore reveals a distorted character for the LS octahedron as expected within a chain, where constraints may not be negligible[22]. Another doublet, corresponding to HS Fe^{II} ions of weaker population (7%), with parameters (δ^{HS} = 1.14(1) mm/s and ΔE_Q^{HS} = 3.15(2) mm/s) confirms the incomplete nature of the ST at 77 K. Upon warming to 300 K, the intensity of the HS doublet slowly increases to 8% at 225 K, after which it increases dramatically to 87.5% at 300 K, confirming an incomplete thermally induced LS $\rightarrow$ HS conversion for a single Fe^{II} site. The presence of LS ions at room temperature could be related to crystal defects or end of chains. The hysteresis effect is clearly evidenced at 225 K (Figure 163).

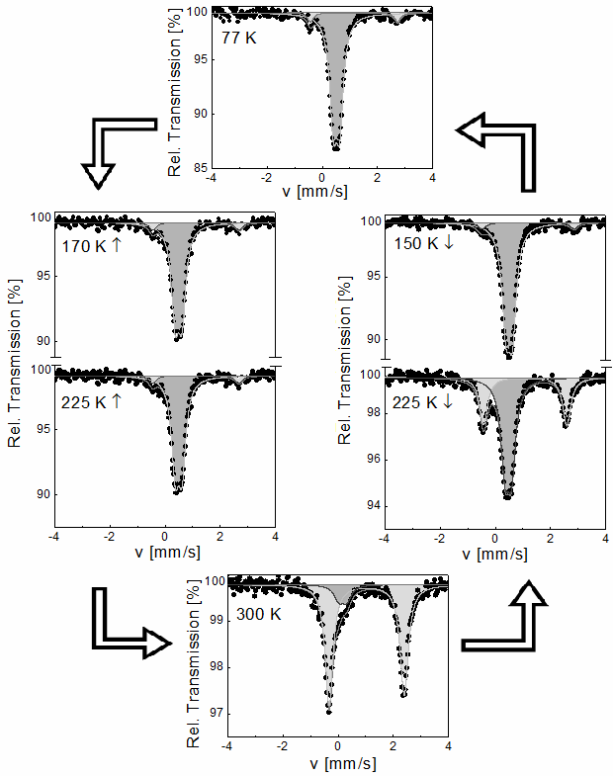

Figure 163 ^{57}Fe Mössbauer spectra cycles for **44·0.5H$_2$O** at selected temperatures. Grey and dark grey correspond to the HS and LS doublets, respectively.

As for as **45** is concerned, at 80 K, the spectrum (Figure 164) of **45** shows a single LS quadrupole doublet (δ^{LS} = 0.52(1) mm/s and $\Delta E_Q{}^{LS}$ = 0.25(2) mm/s) indicating a complete spin transition. The compound remains mostly in the LS state on warming up to 250 K, after which a second quadrupole doublet attributed to HS Fe^{II} ions grows in intensity (e.g., at 297 K, δ^{HS} = 1.03(1) mm/s and $\Delta E_Q{}^{HS}$ = 2.75(1) mm/s). The asymmetry of the lines observed in the HS state is attributed to a texture effect. Upon cooling to low temperature, the reverse situation is observed with a clear hysteresis effect at 250 K (Figure 164).

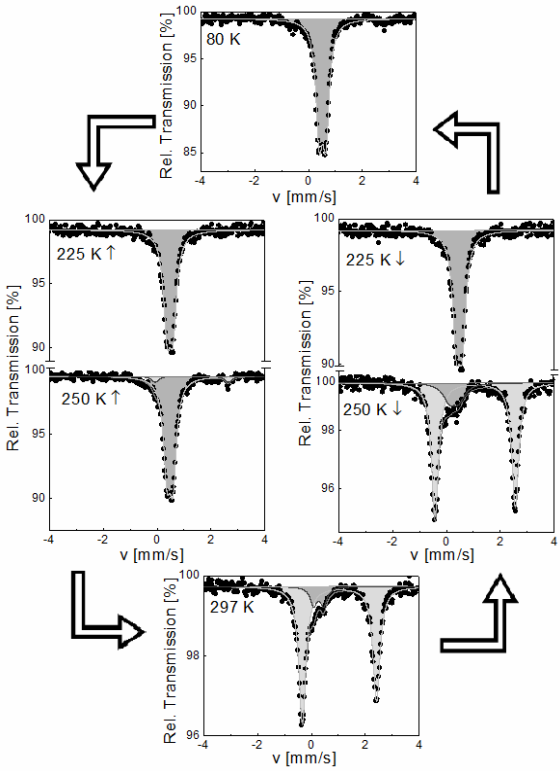

Figure 164 ^{57}Fe Mössbauer spectra cycles for **45** at selected temperatures; Grey and dark grey correspond to the HS and LS doublets, respectively.

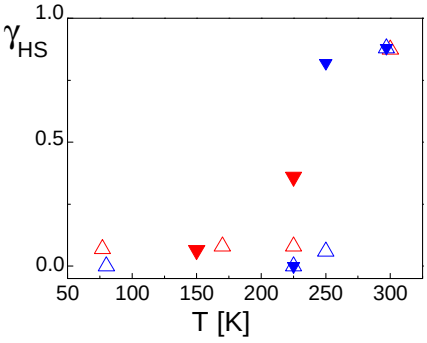

Figure 165 Temperature dependence of the molar fraction of HS molecules, γ_{HS}, for **44·0.5H$_2$O** (depicted in red) and **45 (**depicted in blue) deduced from ^{57}Fe Mössbauer spectroscopy, by slow warming (Δ) and cooling (▼) over the temperature range 80-300 K.

Selected Mössbauer spectra for **46·H$_2$O** are displayed in Figure 166 and parameters are summarized in Table 55. At 77 K, the spectrum of **46·H$_2$O** consists of two quadrupole doublets of different resonance area fractions.

The major quadrupole doublet (80 %) with isomer shift δ = 0.54(2) mm/s and quadrupole splitting, ΔE_Q = 0.29(2) mm/s corresponds to the LS state of Fe^{II}. The presence of a LS quadrupole splitting stems from a lattice contribution to the electric field gradient and therefore reveals a distorted character for the LS octahedron as expected for a constraint one within a 1D chain with a rigid linkage. Another doublet, corresponding to HS Fe^{II} ions (20 %), with δ = 1.14(1) mm/s and ΔE_Q = 3.15(2) mm/s confirms the incomplete nature of the ST at 77 K. Upon warming to 298 K, the area fraction of the HS doublet slowly increases until it reaches 93 %, confirming a thermally induced LS $\rightarrow$ HS conversion. This conversion is incomplete, which is due to a small amount of LS species. Upon cooling back to 77 K, the HS and LS population follows a reverse trend. Thus a spin conversion is observed at $T_{1/2}^{\uparrow}$ = 175 K (Figure 167). The temperature variation of δ^{HS}, of **46·H_2O**, reveals a slight linear increase on cooling which is attributed to the second order Doppler shift. δ and ΔE_Q of both LS and HS species are typical of an $Fe^{II}N_6$ chain compound in which iron centers are bonded by triple *N*1,*N*2-triazole bridges[14, 23].

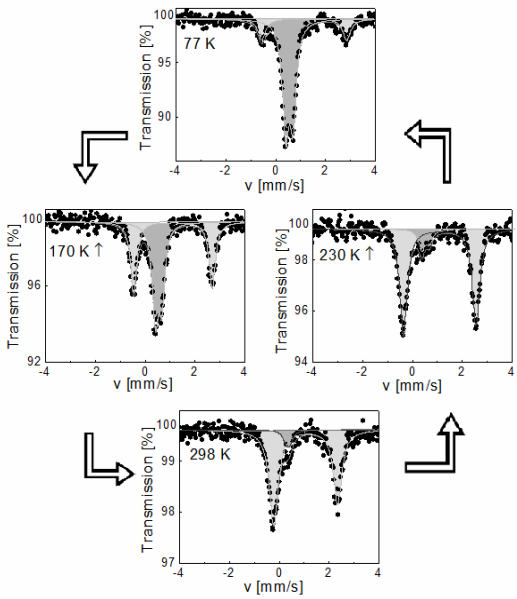

Figure 166 Selected Mössbauer spectra for **46·H_2O** showing LS and HS signals (in blue and red, respectively). The arrows indicate the followed thermal pathway.

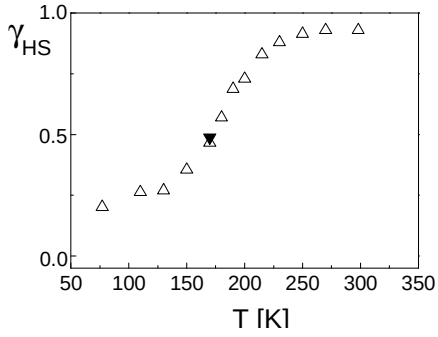

Figure 167 Temperature dependence of the molar fraction of HS molecules, γ_{HS}, for **46·H_2O** deduced from ^{57}Fe Mössbauer spectroscopy, by slow warming (Δ) and cooling (▼) over the temperature range 80-300 K.

Differential Scanning Calorimetry (DSC)

Compounds **44·0.5H_2O**, **45**, **46·H_2O** were investigated by DSC over the temperature range 100 – 300 K, at 10 K min^{-1} for both cooling and heating rates. Heating and cooling capacity profiles are depicted in Figure 168, and 169.

(a)

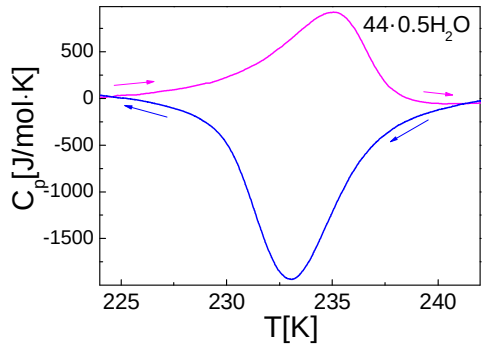

(b)

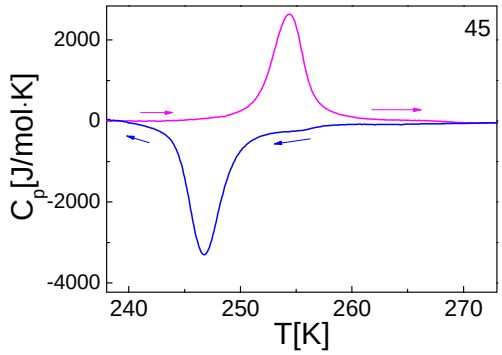

Figure 168 Heat capacity profiles for **44·0.5H$_2$O** and **45**. The arrows indicate the cooling (←) and warming (→) modes, respectively.

An endothermic peak is observed on warming for **44·0.5H$_2$O** at $T_{max}^{\uparrow}$ = 235(1) K and an exothermic peak is recorded at $T_{max}^{\downarrow}$ = 233(1) K, on cooling. These peaks correspond to a first-order phase transition in agreement with the transition temperatures determined by both SQUID and Mössbauer spectroscopy. The enthalpy and entropy variations associated to the active SCO centers are ΔH = 12(2) kJ/mol and ΔS = 51(2) J/mol/K. A similar profile, although with more abrupt peaks, was detected for **45** with phase transitions shifted upwards to $T_{max}^{\uparrow}$ = 254(1) K and $T_{max}^{\downarrow}$ = 247(1) K. The peaks are separated by a narrow temperature domain, which is indicative of the presence of a hysteresis loop. The enthalpy and entropy

associated to the ST, considering only the switching sites, were derived as follows: ΔH = 13(1) kJ/mol and ΔS = 59(2) J/mol/K.

Thermodynamic parameters for the SCO event in **46·H$_2$O** was evaluated also from DSC measurement. An endothermic peak was observed on warming at $T_{max}^{\uparrow}$ = 173 K and an exothermic peak is recorded at $T_{max}^{\downarrow}$ = 171 K, on cooling. The enthalpy ΔH^{HL} = 2.65 kJ.mol^{-1} and entropy ΔS^{HL} = 16 J.mol^{-1}K^{-1} associated to the ST were derived.

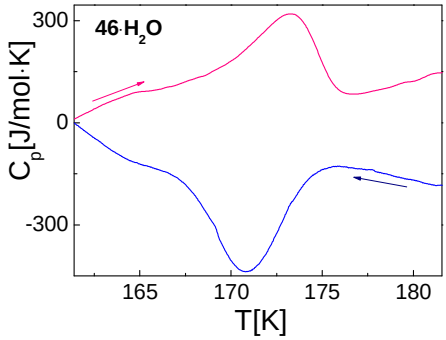

Figure 169 Heat capacity profiles for **46·H$_2$O**. The arrows indicate the cooling (←) and warming (→) modes, respectively.

Discussion

Different 1D spin-crossover Fe(II) complexes were obtained for a series of compounds, based on β-amino-acids, going from abrupt and complete ST and gradual and incomplete spin conversion.

A brief comparison of several aspects among **44·0.5H$_2$O** and **46·H$_2$O**, with [Fe(**αGlytrz**)$_3$](ClO$_4$)$_2$·CH$_3$OH[24] (Figure 170) is necessary to understand the possible effect of texture of particles, ligand spacer and anion geometry on the observed variation of $T_{1/2}$ values and different SCO behavior. **46·H$_2$O** with $T_{1/2}$ = 172 K is nearly 58 K lower than **44·0.5H$_2$O** ($T_{1/2}^{\downarrow}$ = 228 K and $T_{1/2}^{\uparrow}$ = 232 K) which shows an abrupt but incomplete SCO)[25] which is however lower than [Fe(**αGlytrz**)$_3$](ClO$_4$)$_2$·CH$_3$OH by 38 K[24]. The later

shows an abrupt, complete SCO with $T_{1/2}^{\downarrow}$ = 263 K and $T_{1/2}^{\uparrow}$ = 273 K[24]. Thus, with a similar anion but with one carbon less in the ligand spacer, the $T_{1/2}$ is considerably raised in [Fe(**αGlytrz**)$_3$](ClO$_4$)$_2$·CH$_3$OH (by 38 K) which could be due to the compactness of molecular packing with smaller ligand scaffold, thereby strengthening cooperative and supramolecular interactions within the closer chains. Nevertheless, the important role of non coordinated solvent in **46·H$_2$O** and [Fe(**αGlytrz**)$_3$](ClO$_4$)$_2$·CH$_3$OH cannot be ignored. At the microscopic level, it can be seen that **44·0.5H$_2$O**, which includes a linear type anion is highly crystalline with large hexagonal plates. In contrast, particles in **46·H$_2$O** are highly aggregated and amorphous. In [Fe(**αGlytrz**)$_3$](ClO$_4$)$_2$·CH$_3$OH, although XRPD is very different, SEM image shows undefined particles shape. These varied textures are expected to induce defects that ultimately could affect SCO behaviour. Thus **44·0.5H$_2$O** has shown more appealing SCO properties compared to **46·H$_2$O** despite sharing the same framework and lattice solvent. Indeed this is modulated further by different secondary interactions brought by different geometry and electro-negativity of anions. The Fe^{II} 1D ST chain compounds **44·0.5H$_2$O** and **45**, switches in the range 225-250 K. The isomer shift (δ^{LS}~0.51(1) mm/s at 77–80 K and ΔE_Q^{HS} = 1.03(1) mm/s at 297–300 K) is not affected by the dehydration process which indicates that non coordinated water molecules are not H-bonded to the triazole ligand [26], but should be located at a remote position to the complex in the crystal lattice, either isolated or hydrogen bonded to the sulfonate group of the non coordinated anions. Their releases have no influence on the structural organization as demonstrated by the similarity in X-ray powder diffraction data. However, a clear influence on the transition temperatures, i.e., on the respective energy levels of the HS and LS states[16], has been detected. Release of non coordinated water molecules has a paramount effect on the LS state stabilization of **45**. Its air stability and absence of solvent will ease further

physical measurements, particularly using hydrostatic pressure[21] so as to shift its hysteresis loop towards the room temperature region.

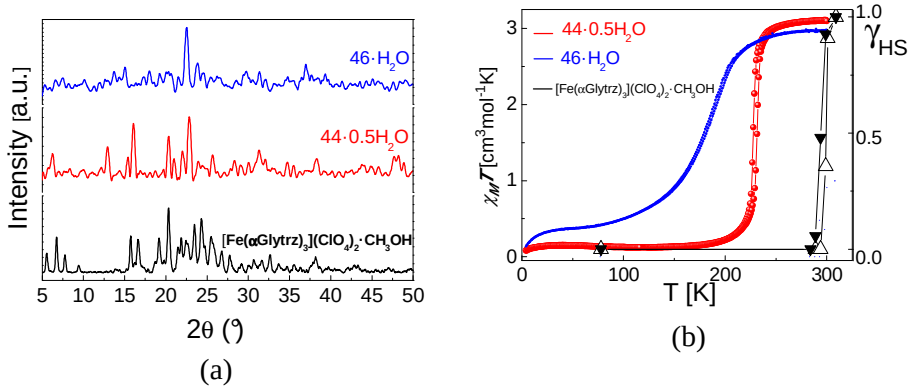

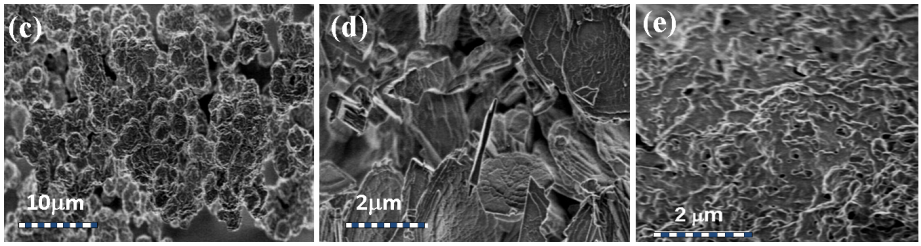

Figure 170 (a) Comparative XRPD pattern for **44·0.5H$_2$O** and **46·H$_2$O** and [Fe(**αGlytrz**)$_3$](ClO$_4$)$_2$·CH$_3$OH; (b) Thermal variation of $\chi_M T$ in **44·0.5H$_2$O** and **46·H$_2$O** and of γ_{HS} for [Fe(**αGlytrz**)$_3$](ClO$_4$)$_2$·CH$_3$OH (triangles); Comparison of texture of particles in bulk samples (c) **46·H$_2$O** (d) **44·0.5H$_2$O** (e) [Fe(**αGlytrz**)$_3$](ClO$_4$)$_2$·CH$_3$OH.

Since a simple modification on the nature of the non-coordinated species, as the counter-anions, give access to different SCO behaviors. In contrast with **44·0.5H$_2$O** and **45**, compound **46·H$_2$O**, containing ClO_4^- as ligand, displays a gradual SCO, with a very narrow hysteresis. Nevertheless, this behaviour is interesting since it is an atypical case of SCO, which characterize 1D chain based on 4-R-1, 2, 4-triazole. However, in some cases,[27, 28] such behavior is observed when the substituent R is voluminous. This type of spin conversion could probably achieve to a SCO behavior characteristic for isolated Fe(II)-triazole chain.

VIII. 2: Thermal spin-crossover properties - two step Iron (II) 1D Chain Compounds

SQUID magnetometry

The magnetic behaviour of [Fe(**βAlatrz**)$_3$](BF$_4$)$_2$·H$_2$O, **47·H$_2$O** is shown in Figure 171 ,using the product of χT versus temperature (χT *vs.* T), for cooling and heating measurements performed in the temperature range 4 - 300 K. The curves reveal a SCO occurring in two steps. At room temperature, this product is equal to 3.34 cm^3 K mol^{-1} in agreement with the expected values for a HS Fe(II) ion, with a very less diamagnetic contribution. As the temperature decreases, a constant value is maintained down to around 234 K followed by a decrease to 2.73 cm^3 K mol^{-1} at 220 K (step 1). Below 200 K the magnetic moment falls to 0.33 cm^3 K mol^{-1} at 97 K (step 2). The decrease of the magnetic moment at lower temperatures is most likely due to the zero-field splitting of the HS species, as it often encountered in SCO compounds[29]. In the warming mode, the two step character of the ST is maintained as in the cooling mode. Upon warming, the $\chi_M T$ curve differs slightly revealing two small hysteresis width, of 5 K (step 1) and 16 K (step 2) at $T_{1/2}^{\downarrow}$ = 230 K and $T_{1/2}^{\uparrow}$ = 235 K (step 1), and at $T_{1/2}^{\downarrow}$ = 172 K and $T_{1/2}^{\uparrow}$ = 188 K (step 2) respectively.

A hysteretic behavior of width 3 K was observed also for the desolvated material **48**, Figure 172, with a ST situated average of the two previous ST temperatures observed for compound **47·H$_2$O**, ~ 200 K. Compound **48** present a one step gradual SCO (Figure 172). Between 50 K and 150 K a smooth increase of $\chi_M T$ is identified. The transition goes on very gradual until 273 K, and leads 3.23 cm^3 K mol^{-1}, value expected for an iron (II) complex in the HS state, with a less diamagnetic contribution. The same magnetic behaviour was observed in both the cooling and the warming

modes, only the curves progression comes at different temperature, $T_{1/2}^{\downarrow}$ = 199 K, $T_{1/2}^{\uparrow}$ = 202 K. This is exactly in the middle of two step plateau, thereby demonstrating the usefulness of water molecules to observe two step SCO behaviour. The observed curve shape is changed; the loss of the intermediate plateau is identified. Thus a possible disruption of H-bonding established by water molecules, which could be a signature of appearance of a structural phase transition, as will be discussed below, or a change of the ligand conformation following the annealing process.

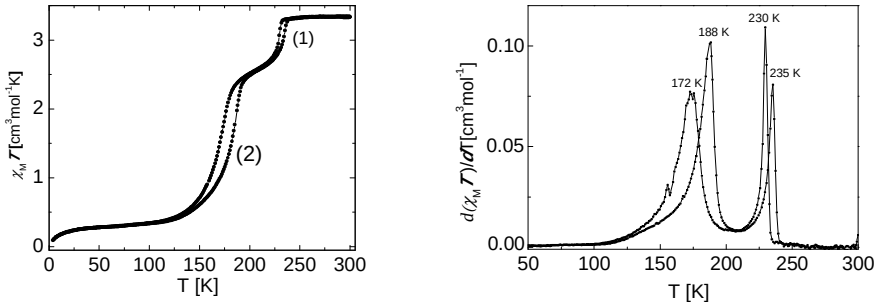

Figure 171 (left side) Magnetic behavior of **47·H$_2$O** (shown as χT *vs. T*. (right side) Temperature dependence of the derivative (d(χ_MT)/dT in both cooling and warming modes.

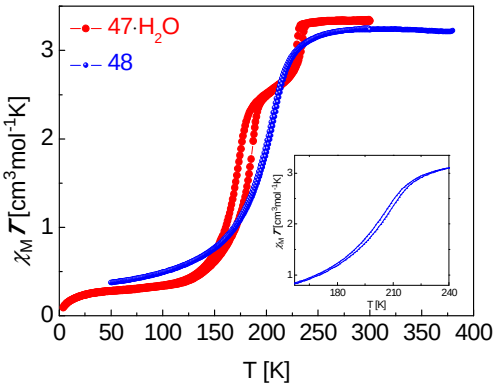

Figure 172 Thermal variation of $\chi_M T$ of compounds: **47·H$_2$O** (depicted in red) and **48** (depicted in blue).

^{57}Fe Mössbauer spectroscopy

An inspection of electronic and structural features for $[Fe(\beta\mathbf{Alatrz})_3](BF_4)_2 \cdot H_2O$, (**47·$\mathbf{H_2O}$**) using ^{57}Fe Mössbauer spectroscopy was undertaken over the temperature range 78 K–300 K (Figure 173). The obtained hyperfine parameters and the deduced HS fraction for **47·$\mathbf{H_2O}$** are gathered in Table 56. At 78 K, the spectrum of **47·$\mathbf{H_2O}$** consist of two doublets: one characteristic of HS Fe(II) ions (δ = *1.17(2)* mm.s^{-1}, ΔE_Q = *3.31(1)* mm.s^{-1}) and another doublet (88 %), characteristic of LS Fe(II) ions (δ = 0.53(1) mm.s^{-1}, ΔE_Q = *0.28(1)* mm.s^{-1}). The compound remains predominantly in the LS state on warming up to 160 K, after which the HS doublet grows in intensity reaching 61 % at 190 K. This behaviour is followed by a plateau with a slight slope, between 200 K and 230 K. Up to 230 K, the percentage of paramagnetic species increases and at room temperature raises to 83 %. At 300 K, spectra evidence the presence of residual LS fraction in proportion of 17%, characteristic of LS Fe(II) ions (δ = 0.15(1) mm.s^{-1}, ΔE_Q = *0.40(1)* mm.s^{-1}), which characterized an incomplete spin conversion at this temperature, in agreement with SQUID data. These values are typical of a $Fe^{II}N_6$ chain compound in which metal centers are bonded by triple *N1,N2*-triazole bridges and no evidence of iron (III) impurities is observed in the Mössbauer spectra[26]. The asymmetry of the peaks was attributed to a texture effect[30]. Upon cooling to low temperature, the reverse situation is observed, with a clear hysteresis effect at $T_{1/2}^{\downarrow}$ = 225 K, $T_{1/2}^{\uparrow}$ = 330 K (step 1) and $T_{1/2}^{\downarrow}$ = 173 K, $T_{1/2}^{\uparrow}$ = 184 K (step 2) (Figure 174). This curve confirms the results deduced from the magnetic data. The high-temperature step, centered at 227 K, is rather gradual while the low-temperature step, centered at 180 K, is more abrupt (Figure 174). Worthwhile to note that the data of the HS fraction were obtained assuming equal Mössbauer Lamb factors for HS and LS states.

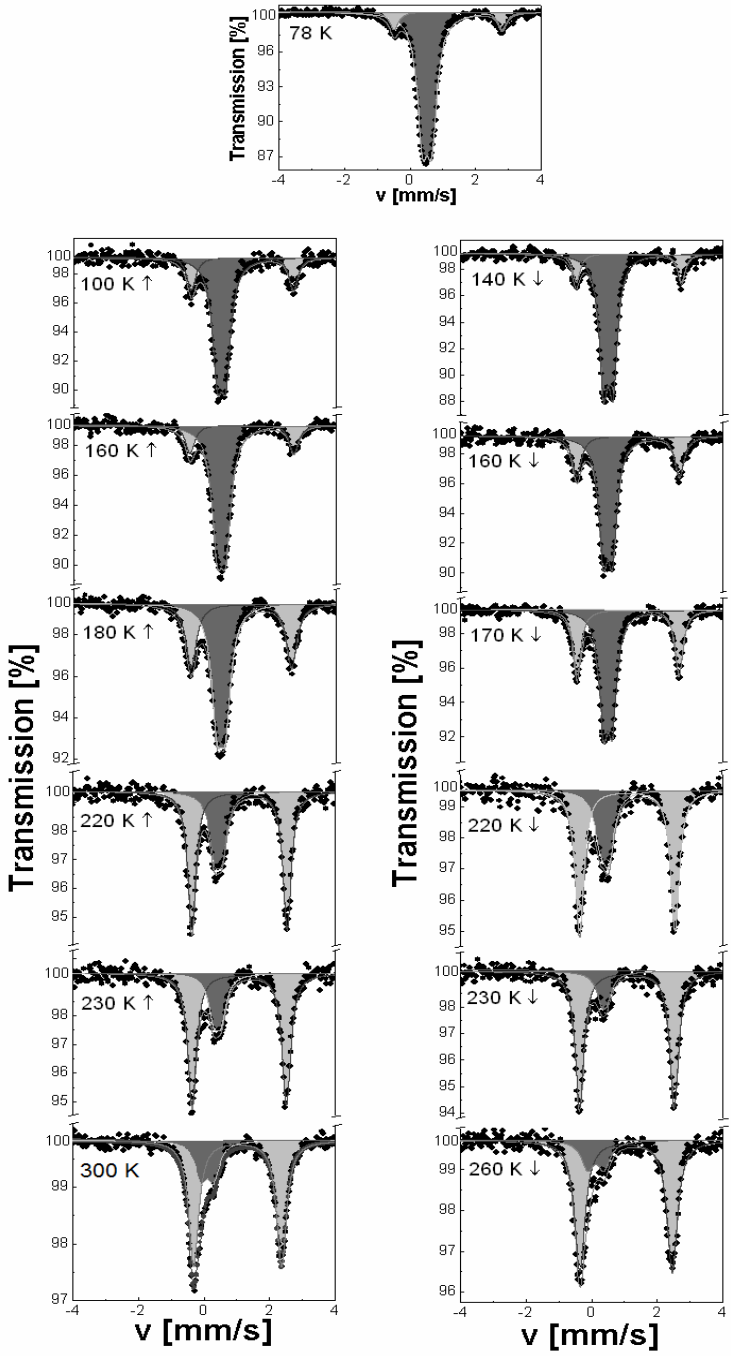

Figure 173 Selected ^{57}Fe Mössbauer spectra of **47·H_2O** on warming and cooling modes. Grey and dark grey correspond to the HS and LS doublets, respectively.

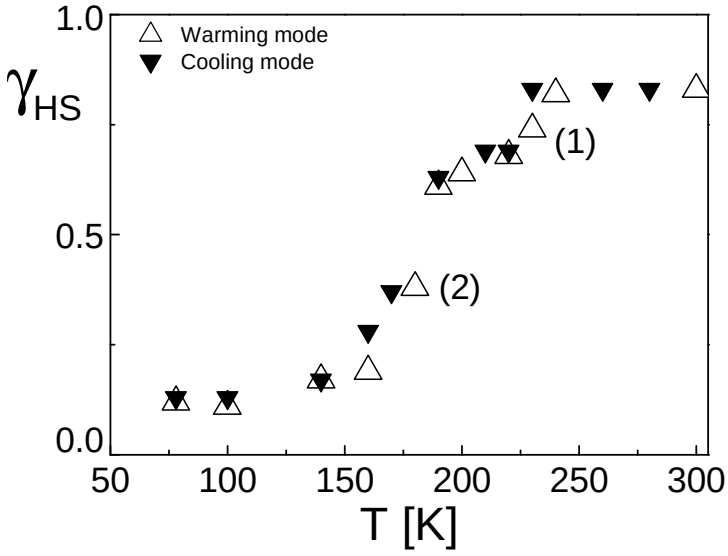

Figure 174 Temperature dependence of the HS molar fraction, γ_{HS}, for **47·H$_2$O** deduced from ^{57}Fe Mössbauer spectroscopy, by slow warming (Δ) and cooling (▼) over the temperature range 78-300 K.

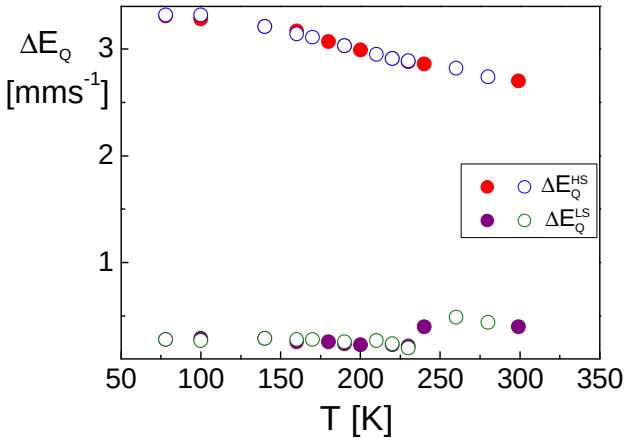

Figure 175 Temperature dependence of the quadrupole splitting ΔE_Q (mm/s) over the temperature range (300 - 78 K) on cooling and warming, of **47·H$_2$O,** as deduced from ^{57}Fe Mössbauer spectroscopy.

The evolution of the HS quadrupole splitting follows a decrease behavior with temperature (Figure 175). The slope (ΔE^{HS}_Q/dT) was evaluated and gives a value equal to -3.1 x 10^{-3} mm s^{-1} K^{-1}, characteristic of 1D Fe(II)

chains.[31, 32] This value indicates a local symmetry lower than an octahedral one[31], which translates a distorted $Fe^{II}N_6$ octahedra. This parameter is consistent with the values found in the literature for such compounds, based on 1,2,4-triazole core[26].

The evolution of the LS quadrupole splitting as a function of temperature clearly evidences two temperature domains of different slopes (Figure 176). Interestingly, a jump is found on cooling and warming around 235 K, a feature that could be a signature of a phase transition.

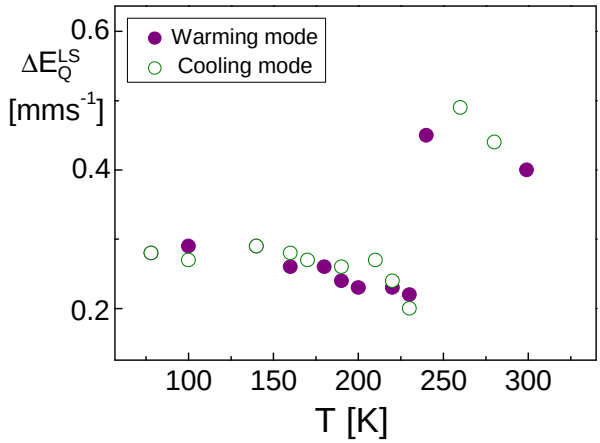

Figure 176 Temperature dependence of the quadrupole splitting $\Delta E_Q{}^{LS}$ (mms^{-1}) over the temperature range (78-300 K) on cooling and warming, of **47·H_2O**, for as deduced from ^{57}Fe Mössbauer spectroscopy.

At the same times, such a discontinuity could be associated with a two step ST.[31-34] Indeed, a similar behavior is reported for the binuclear compound: $[Fe(bt)(NCS)_2]_2$bpym, with bt = 2,2'-bi-2-thiazoline and bpym = 2,2'-bipyrimidine, $\Delta E_Q{}^{LS}$ being much more sensitive to short-range intramolecular interactions over intermolecular interactions[31]. This can be explained by the fact that the propagation of the local distortion between adjacent $Fe^{II}N_6$ cores is more important in the case of the presence of intramolecular interactions, in this system[31, 34].

Such discontinuities of ΔE_Q^{LS}, due to the presence of intra- and inter-molecular interactions are also present in the [Fe(2,2'-bi-2-thiazoline)$(NCS)_2]_2$(2,2'-bipy), (bipy = 2,2'-bipyridyl) system[31]. The amplitude of the jump, characteristic of this compound, is around ΔE_Q^{LS} = 0.1 $mm.s^{-1}$ and characterizes intramolecular interactions. Amplitude of jump equal to 0.02 - 0.03 $mm.s^{-1}$ is typical of a sample which presents intermolecular interactions, as for [Fe^{II}(5-NO_2-sal-N(1,4,7,10))] (5-NO_2-sal-N(1,4,7,10) = bis(5-nitrosalicylidene) triethylenetetramine-1,4,7,10- tetra-azadecane)[34].

In the case of **47·H_2O**, the amplitude of the jump (around 235 K) is around 0.2 mm s^{-1}, (which is well above the measurement error) and translates the presence of dense intra-molecular interactions. As we can expect, only one jump was identified in the region of the second step of the ST. Thus the hypothesis is that the second ST step is not associated to the intramolecular interactions, but perhaps to the intermolecular connectors.

In the temperature dependence of the quadrupole splitting ΔE_Q^{HS} (mm/s) no discontinuity is identified, probably because the HS $Fe^{II}N_6$ octahedra are less affected by intramolecular interactions.

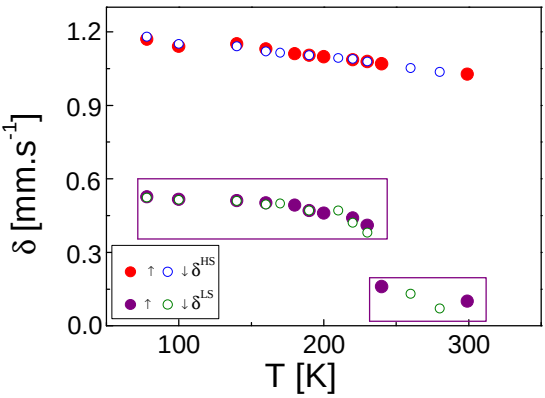

Figure 177 Temperature dependence of the isomer shift δ^{HS}/δ^{LS} (mms^{-1}) (depicted in red/mauve – warming mode and in blue/green –cooling mode) over the temperature range (300 - 78 K), of **47·H_2O**, as deduced from ^{57}Fe Mössbauer spectroscopy.

The temperature variation of δ^{HS} shown in Figure 177 reveals a linear increase on cooling which is attributed to the second order Doppler shift[35] temperature variation of δ^{LS} shown in the same figure clearly evidences two linear temperature domains of different slopes, this is present in the same region as the jump of the quadrupole splitting function of temperature.

Differential scanning calorimetry (DSC)

The heat capacity curve of compound $[Fe(\beta\textbf{Alatrz})_3](BF_4)_2 \cdot H_2O$, **47·$H_2O$** obtained by DSC, shows two asymmetrical and well-separated peaks associated with the two steps of the transition (Figure 178). The peaks corresponding to step (1) are centered at $T_{max}^{\uparrow}$ = 241 K and $T_{max}^{\downarrow}$ = 233 K, respectively in the warming and in the cooling mode. For step (2), in the warming and cooling mode, two peaks with maximum at $T_{max}^{\uparrow}$ = 189 K and $T_{max}^{\downarrow}$ = 175 K are observed. Considering that the total value of enthalpy and entropy stand for about 83 % of SCO centers that undergo the spin transition (at 300 K 83 % of HS fraction was identified by Mössbauer spectroscopy), the complete transition would give $\Delta H_{HL}(1)$ = 3.7 kJ.mol^{-1} and $\Delta S_{HL}(1)$ = 15.6 J.mol^{-1}K^{-1} and $\Delta H_{HL}(2)$ = 3.1 kJ.mol^{-1} and $\Delta S_{HL}(2)$ = 17.2 J.mol^{-1}K^{-1} respectively.

To the first view, if we take the independent values of the entropy, for each step, we can believe that the entropy values are not typical for SCO compounds. But the total value of the ΔS_{HL} is equal to 34 J.mol^{-1}K^{-1}. Solely the electronic contribution to LS-HS change, R·ln5, amount to ca. 13.4 J/molK. On the top of that comes the vibrational contribution. The classic $Fe(phen)_2(NCS)_2$ change spin at 176 K (the entropic contribution is temperature dependent)[36]. The ΔS corresponding to this compound is equals to 48.8 J.mol^{-1}K^{-1}[36], thus towards a vibrational contribution of

appreciatively 35 J.mol^{-1}K^{-1}. The data for triazole Fe(II) polymers show ΔS of 34 kJ.mol^{-1}[14]. Thus the value obtains for **47·H$_2$O** can translate an effect on LS → HS transition that brings the negative contribution to entropy, which largely compensates the vibrational contribution due Fe-N bond elongation.

The different change in the entropy is observed between step (1) and step (2) in compound **47·H$_2$O**, could be due to a variation of unit cell volume between two steps[37] or to the % of the active Fe(II) site which switch in different times. The entropy contents are typical values for SCO compounds.[38]

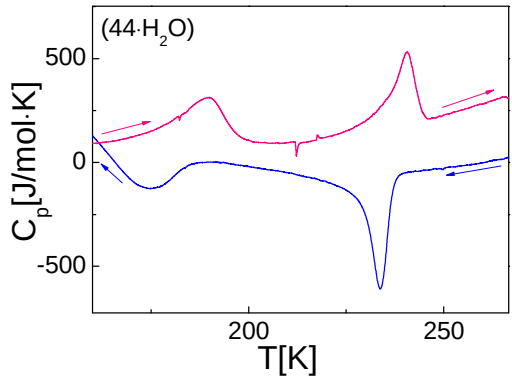

Figure 178 DSC profiles for **47·H$_2$O** in the cooling and warming mode.

The heat capacity curves shown in Figure 179, for compound **48**, shows a small and broad peak with maximum around 201 K. The thermodynamic quantities associated with the transition, ΔH_{HL} = 3.0(1) kJ.mol^{-1} and ΔS_{HL} = 14.9(2) J.mol^{-1}K^{-1}, are in the same range as those observed for the other compounds of the family. However, in this case the ST is incomplete, as is shown in the magnetic description curve; only 75 % of the spin conversion undergoes the SCO phenomenon.

In order to evaluate the magnitude of intermolecular interactions, we have first considered the widely used regular solution model, proposed by Slichter and Drickamer[39]. This model gives information about the cooperativity of

the compound. The model considers two independent groups of the SCO centers that undergo the ST at different temperatures.

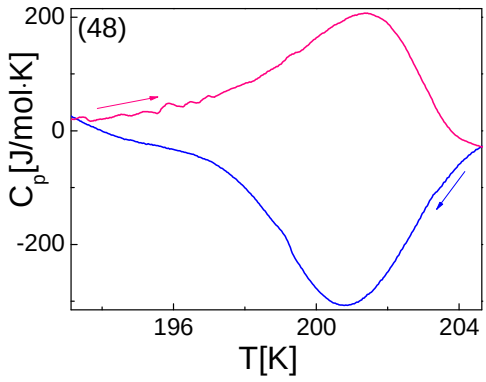

Figure 179 DSC profiles for **48** in the cooling and warming mode.

The cooperativity factor, Γ translate the strength of cooperative intermolecular interactions and is given using the Gibbs free energy expression (eq. r). The system is thus described by two equations (eq. r and s), where ΔH and ΔS are the experimental enthalpy and the entropy variation corresponding to two steps transition, respectively.

$$G = \gamma_{HS}(\Delta H - T\Delta S) + RT\left[\ln(1-\gamma_{HS}) + (1-\gamma_{HS})\ln(1-\gamma_{HS})\right] + \Gamma\gamma_{HS}(1-\gamma_{HS}) \qquad \textbf{(eq. r)}$$

$$\ln\left[(1-\gamma_{HS})/\gamma_{HS}\right] = \left[\Delta H + \Gamma(1-2\gamma_{HS}) - T\Delta S\right]/RT \qquad \textbf{(eq. s)}$$

The result for compound **47·H_2O** is presented in Figure 180 and Table 57, and compared with the experimental HS fraction obtained from magnetic measurements.[35] Thus the interaction constants corresponding to the best accordance with the magnetic data are Γ_1 = 3.9 kJ/mol, Γ_2 = 3.5 kJ/mol and then $\Gamma_1/2RT = 1.01 > 1$, $\Gamma_2/2RT = 1.17 > 1$ as expected for a continuous process, with hysteresis.[39]

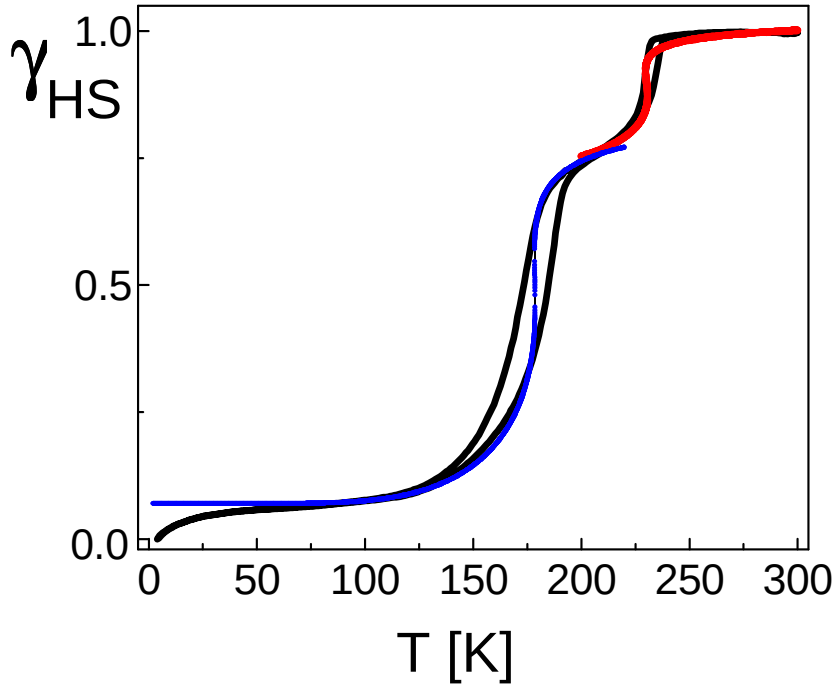

Figure 180 Experimental and simulated (red and blue line) HS molar fraction vs. *T* curves for compound **47·H$_2$O**.

Table 57 Macroscopic Quantities $\Delta H(1)$, $\Delta H(2)$ (kJ/mol) and $\Delta S_{HL}(1)$, $\Delta S_{HL}(2)$ (kJ/mol·K), resulting from DSC measurements and the Spin-Independent Model.

	ΔH(1) [kJ/mol]	**ΔH(2) [kJ/mol]**	**$\Delta S_{HL}(1)$ [J/mol·K]**	**$\Delta S_{HL}(2)$ [J/mol·K]**	**Γ_1 [kJ/mol]**	**Γ_2 [kJ/mol]**
Experiment	3.7(1)	3.1(1)	15.6(1)	17.1(1)		
"Spin-Independent" fit	3.5(1)	3.0(1)	15.2(2)	16.8(2)	**3.9**	**3.5**

FORC diagram investigation

The recording of magnetic measurements in DC mode reported above only provides a primary analysis of the hysteresis loop of **47·H_2O**. As described in Chapter III, we have extended this study by recording First-Order Reversal Curves (FORCs) to determine the distribution of switching temperatures and interactions fields for all of the 'particles' that contribute to the hysteresis loop.[40] Thus an interaction parameter, *J*, which is derived from a two-level Ising like description of interacting SCO units, was determined.

Figure 181 shows the experimental FORCs for **47·H_2O** obtained on a SQUID magnetometer. The sample was slowly warmed up to a reversal temperature located on the upper branch of the hysteresis loop and the sample was subsequently cooled. The temperature step was fixed at 0.5 K, with a sweeping rate of 0.8 K/min. It was essential to use such a small temperature step to obtain the best accurate data.[41] Kinetic effects were also avoided by working in cooling mode only.

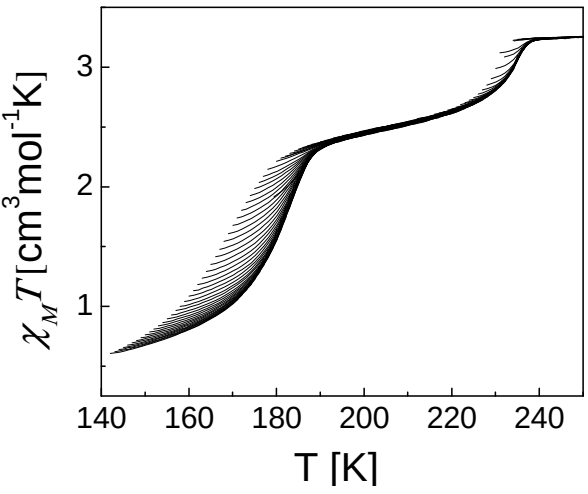

Figure 181 FORCs of the thermal hysteresis loop of **47·H_2O** recorded in the cooling mode, with T_a, T_b increments of 0.5 K.

Indeed, preliminary measurements attempted in the warming mode revealed that it was not possible to fix the reversal temperature on the lower branch of the hysteresis loop due to the thermal inertia of the SQUID magnetometer.

As it has been shown in ref. [41] by using the Jacobian transformation, a correspondence can be performed between FORC distributions in *c-b* and *J-Δ* coordinates. The FORC diagram is actually a 3D image represented by the 2D contour plot of the FORC distribution. Colors provide information about the probability that a single domain could be characterized by a given value *c-b* or *J-Δ* (Figure 182, 183). The probability is very low in the blue region and becomes very high in the red region. Assuming the presence of two independent ST, two interaction parameters *J1* characteristic for the first step (between $T_{max}^{\uparrow}$ = 241 K and $T_{max}^{\downarrow}$ = 233 K) and *J2* characteristic for the second step (between $T_{max}^{\uparrow}$ = 189 K and $T_{max}^{\downarrow}$ = 175 K) equal to 180.5 K and 234.6 K respectively, were obtained. The total value corresponding to the system is equal to 415 K, which is in the same range as the one obtained for $[Fe(NH_2trz)_3](NO_3)_2$ system (*J* = 496 K, Chapter III). This value is much higher than the one found for the 2D ST compound $[Fe(btr)_2(NCS)_2]\cdot H_2O$ (J = 235 K)[41] which presents an hysteresis width of 25 K,[42] free of any structural phase transition[19, 43].

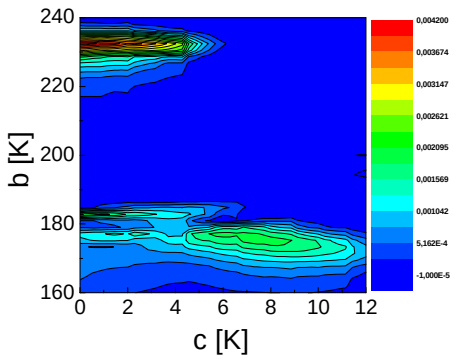

Figure 182 Experimental FORC diagram derived from Figure 181, in coercivity-bias coordinates: 2D contour plot representation.

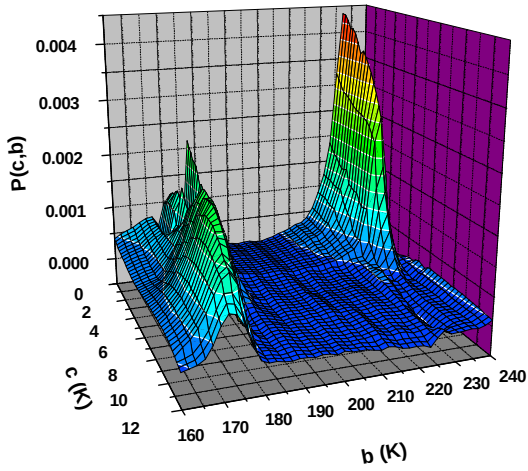

Figure 183 Experimental joint FORC diagram in *b-c* coordinates - 3D representation.

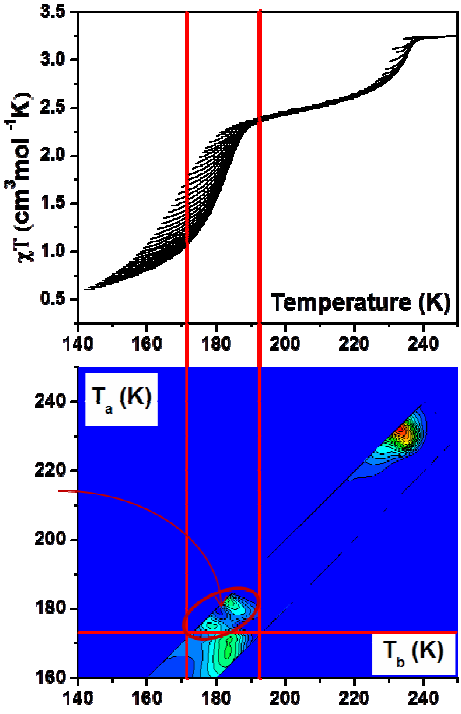

Figure 184 Experimental FORC diagram derived from Figure 182.

Discussion

Compound [Fe(**βAlatrz**)$_3$](BF$_4$)$_2$·H$_2$O, **47·H$_2$O** undergoes a complete two-step spin transition. Such two-step ST has already been reported for 1D chains, but never on the systems based on 1,2,4-triazole. The two steps ST behaviour is particularly interesting for the investigation of their influence through cooperativity/anti-cooperativity, intramolecular and intermolecular interactions on the metal centers lying in the neighborhood[31]. Most of the compounds, which present two steps ST behaviour, are found in the cases of mono-, bi- and tri-nuclear compounds[44]. Only a few of the 1D, 2D and 3D systems present such characteristics. In the mononuclear system, [Fe(2-pic)$_3$]Cl$_2$·EtOH (2-pic = 2-picolylamine) there is a unique iron crystallographic site and the step arises from short range interactions, whereby –HS–LS–HS–LS– formation appears to be energetically favored[45]. A different mononuclear system presenting a two steps ST is Fe[(5NO$_2$-sal-N(1,4,7,10))] (5-NO$_2$-sal-N(1,4,7,10) = 2,2' -(2,5,8,11-tetraazadodeca-1,11-diene-1,12-diyl) 4-nitrophenolato[45]. This compound has one transition, associated with a structural phase transition evidenced by X-ray diffraction studies at three temperatures, with a pronounced step and a plateau of ca. 40 K between the two steps. The two-step transition curve of a binuclear iron(II) complex [Fe(bt)(NCS)$_2$]$_2$(bpym), (bt = 2,2-bi-2-thiazoline; bpym = 2,2'-bipyrimidine), was attributed to a synergistic effect between intramolecular interactions favoring the mixed-spin state and intermolecular interactions favoring like-spin species domains[31]. It is noted that the low-temperature step is more abrupt than the high-temperature one. For [Fe(mtz)$_6$]X$_2$, (mtz = 1-methyltetrazole, X$^-$ = ClO$_4^-$ or BF$_4^-$), the two steps ST are due to the presence of two different Fe(II) crystallographic sites; one of the sites undergoes a spin transition around 100 K, while the other remains HS in the whole temperature range[46]. In the case of the 3D system [Fe(btr)$_3$](ClO$_4$)$_2$ (btr = 4,4'-bis-1,2,4-triazole)[47] the two-step spin

conversion is associated with the presence of two slightly different Fe(II) sites.

In the 2D ST network, $Fe(py)_2[Ag(CN)_2]_2$ (py = pyridine), which present only one Fe(II) site, the two steps ST is due to a disorder effect between the two steps, considering of a mixing of HS and LS species without long-range order[48].

The first 1D coordination polymers, presenting two steps ST are $[Fe(NCS)_2(bdpp)]$, (bdpp = 4,6-bis(2',2''-pyridyl)pyrazine) and its selenium analogue $[Fe(NCSe)_2(bdpp)]$[49]. For $[Fe(NCS)_2(bdpp)]$, the two-steps ST is due to the presence of two different Fe(II) crystallographic sites, while for the selenium analogue to the order disorder phenomenon of the $NCSe^-$ anion[50]. A recent study reveals interesting two step switches, compounds based on 4,4'-bipyridine, 1,2-bis(4-pyridyl)ethane and 1,3- bis(4-pyridyl)propane[51]. The stepwise ST is due to a pronounced zigzag structure of the 1D chain in combination with several interchain contacts, even if all iron centers are equivalent in the HS state.[51]

Contrary to **47·H_2O**, these compounds present two steps ST below 214 K. The two main findings of compound **47·H_2O** are the 1D character of the chain structure with Fe^{II} ions linked by triple *N*1,*N*2-1,2,4-triazole bridges and the occurrence of a two-step spin conversion with a plateau of ca. 50 K between these two steps. These two aspects will be discussed below. Compound **47·H_2O** was analyzed essentially by IR and Raman spectroscopy. The band assigned to ring torsion of **βAlatrz** at ν = 634 cm^{-1} and the N-N stretching band at ν = 1022 cm^{-1} are shifted[9] upon complexation to 637 cm^{-1} and 1024 cm^{-1}, respectively e.g. for **47·H_2O.** These values confirm a coordination of the iron to the 1,2,4-triazole ring.[52] ^{57}Fe Mössbauer spectroscopy confirms the presence of only one $Fe^{II}N_6$ site, undergoing SCO behaviour on cooling and the absence of oxidation product of Iron. Mössbauer parameters of this compound (see ^{57}Fe Mössbauer

section) are typical for 1D polymeric chain, with triazole as ligand.[53] [Fe(**βAlatrz**)$_3$](BF$_4$)$_2$·2H$_2$O is a 1D SCO compound exhibiting a marked thermal hysteresis loop with transition temperatures $T_{1/2}^{\downarrow}$ = 230 K and $T_{1/2}^{\uparrow}$ = 235 K (step 1), and at $T_{1/2}^{\downarrow}$ = 172 K and $T_{1/2}^{\uparrow}$ = 188 K (step 2). Interestingly, when the two non coordinated water molecules are released, the spin conversion is transformed; the dehydrated compound, appealed **48**, presents only an one step spin conversion, with $T_{1/2}^{\downarrow}$ = 199 K, $T_{1/2}^{\uparrow}$ = 202 K, as transition temperatures.

To explain the two step spin behavior of **47·H$_2$O**, different empirical hypothesis and models can be proposed.

With regard to the plateau in the ST curve, a quasi-chemical model, using specific molecular interactions for the description of stepwise or incomplete spin transitions for mononuclear complexes, can be applied to the system **47·H$_2$O**.[54] This model is based on the dimensionality of the chain compounds and on the interchain interactions, which play an important role on the cooperative effects of the samples. During a HS→LS transition, from HS molecules into smaller LS molecules, a rearrangement of the ligands can be involved. If the Fe···Fe distances do not followthe changes in the Fe-N bonds distance in the LS species, then the corresponding bond in the HS molecules is elongated and stabilized.[54] Thus, taking into account this model and the structural and magnetic properties identified for complementary 1D systems, recently published[51], the factors which determine a two steps ST of **47·H$_2$O** can be explained as follows.

- The first hypothesis is that a zigzag structure of the 1D chain in combination with several interchain interactions results in a two step ST, even if all Fe^{II}N$_6$ centers are equivalent in the HS state, as identified by Mössbauer spectroscopy. At the same time a two step ST was identified also for a “nearly” linear chain with the presence of interchain interactions.[51] Considering the possible potential ligand conformations (Figure 186) and subsequent constraints linked

to Fe^{II} ions, by triple *N*1,*N*2-1,2,4-triazole bridges, the system **47·H_2O** can be formed by "nearly" linear chains. These can cause a two step ST, due to the constraints of the ligands, the Fe···Fe distances does not follow the changes in the Fe-N bonds in the LS species, then the corresponding bonds are elongated and stabilized.

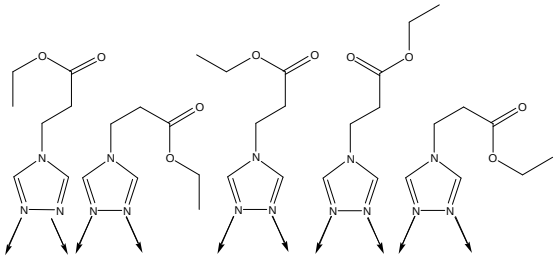

Figure 186 Possible conformations of **βAlatrz** in the chains of **47·H_2O.**

- In contrast to ST systems where uniform configurations are maintained during the switching process, same transition domains can appear with open frontier.[55, 56] This may be due to the presence of intrinsic effects on the border of the domains during the switching processes. At high temperature the system is in HS state. Thus in cooling mode, the expansion of the LS state can be observed in different orientations and sizes of particles. If we consider that, the ST process starts from the bottom of one domain of particles (Figure 187). The LS phase propagation is inhomogeneous, and the spontaneous occurrence of inhomogeneous stresses lead 30 % of the HS species switches to LS (until time t2 – Figure 187) and the remaining in the second part.

Figure 187 Empirical description of the ST domains, during the cooling process (t1<t2<t3<t4<t5) .

Besides these two hypothesis, three other models are proposed to explain the two steps ST which characterize compound **47·H_2O.**

- 1st Model: The characteristic behaviour of **47·H_2O** can be explained by the fact that, at 300 K (stage 1, Figure 188) all Fe(II) ions are in HS state. The ends of the chains are in LS at room temperature (17 %, Fe(II) LS) and in the HS state at 80 K (12%, representing the residual HS ratio) as found by both SQUID and Mössbauer. These ends of chain do not switch and the chain can be schematized as follows:

Ends of Chain – (HS-HS- HS-HS-HS-HS- HS-HS-HS-HS)$_n$ -Ends of Chain

When the temperature reaches 220 K, a part of the HS Fe(II) ions switch to the LS state. The ST of these Fe(II) (noted as *A* in Figure 188) involves a change in the ligand conformation (Figure 186) which influences the local environment of the LS ions (Figure 188). For sterical reasons only one third of the ligands changes its conformation. This form is stabilized on all the range of temperatures of the intermediate plateau (IInd stage, Figure 188). When temperature decreases below 200 K, the remaining HS metal centers undergo a ST to the LS state, without losing the initial conformation of their ligands. At 80 K, the chains are formed by LS Fe(II) ions in which one ion to three (noted as A, Figure 188), have a different conformation of the ligand, from the one observed at room temperature. The other Fe(II) ions (noted as B, Figure 188) maintain the initial conformation of the ligand.

To schematize:

At 300 K (Ist stage) - all the Fe(II) ions, noted as A and B (Figure 188) are in the HS state and their ligands have the same conformation. The chain can be schematized as follow:

Ends of Chain - (B^{HS}-B^{HS}-A^{HS}- B^{HS}-B^{HS} –A^{HS} - B^{HS}-B^{HS}-A^{HS}-B^{HS}-B^{HS}-A^{HS}-B^{HS}-B^{HS}-A^{HS}-B^{HS}-B^{HS})$_n$ - Ends of Chain

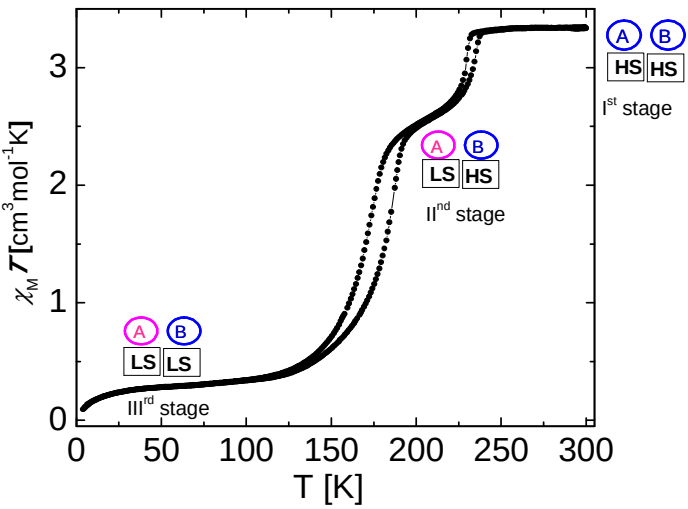

Figure 188 Magnetic behavior of **47·H_2O** shown as χT vs *T*. The letters A and B represent two types of Fe(II) ions in respective ratios of 1/3 and 2/3 of the total number of ions which present a ST.

At 220 K (IInd stage) - the Fe(II) ions, noted as B, remain in the HS state, while the Fe(II) ions, noted as A, are now in the LS state. The configuration of the ligands around the B ions is unchanged while the configuration of the ligands around the A ions changes. Thus the chain can be schematized as follow:

Ends of Chain – $(B^{HS}\text{-}B^{HS}\text{-}A^{LS}\text{-}\ B^{HS}\text{-}B^{HS}\ \text{–}A^{LS}\ \text{-}\ B^{HS}\text{-}B^{HS}\text{-}A^{LS}\text{-}B^{HS}\text{-}B^{HS}\text{-}A^{LS}\text{-}B^{HS}\text{-}B^{HS}\text{-}A^{LS}\text{-}B^{HS}\text{-}B^{HS})_n$ - Ends of Chain

At 80 K (IIIrd stage) - All the Fe(II) ions, A and B, are in LS state, with different ligand conformation. In the Fe(II) ions, noted as B, the ligands preserved their initial conformation while the conformation of the metal centers of Fe(II), noted as A, remains the same as at 200 K, on the plateau. Thus the chain can be schematized as follow:

Ends of Chain – $(B^{LS}\text{-}B^{LS}\text{-}A^{LS}\text{-}\ B^{LS}\text{-}B^{LS}\text{-}A^{LS}\ \text{-}\ B^{LS}\text{-}B^{LS}\text{-}A^{LS}\ \text{-}\ B^{LS}\text{-}B^{LS}\text{-}A^{LS}\ \text{-}\ B^{LS}\text{-}B^{LS}\text{-}A^{LS}\ \text{-}\ B^{LS}\text{-}B^{LS})_n$ - Ends of Chain

This hypothesis is supported by different observations. When the compound **47·H_2O** is dehydrated, the ST is realized in a single step. The solvent allows the stability of the intermediary stage at level of the plateau (II^{nd} stage). This behaviour could be explained by a stabilization of the molecular system due to the involvement of the water molecules in the intra- or/and inter-molecular interactions, although the discontinuity of the ΔE_Q^{LS} describes the presence of intramolecular interactions (see ^{57}Fe Mössbauer part). However, the origin of the cooperativity giving an abrupt ST behavior with hysteresis loop is not explained by the presence of intramolecular interactions, as in a first stage, only one in three ions switch to a LS state (2^{nd} stage, Figure 188). In order to explain the cooperativity of the system, one model is exposed in Figure 189.

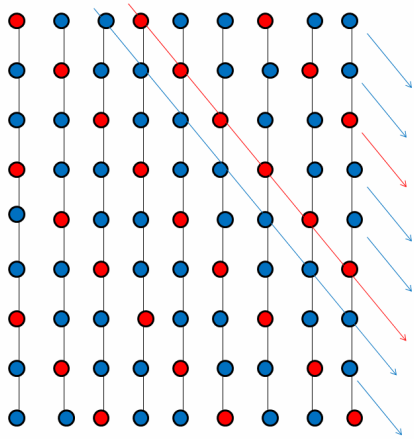

Figure 189 Illustration of the crystal network at the level of the plateau between the two ST phenomenon; in red dots: Fe(II) ions, noted as A, have a different ligand conformation (compared to the r.t. conformation); in blue dots: Fe(II) ions, noted as B have a similar ligand conformation to the one observed at r.t.; the diagonal lines are representatives of the propagation of the intermolecular cooperativity by the intermediate of the phonons network.

Along this model, an inter-chain cooperativity with diagonal propagation (following the directions of the blue and red arrows) is proposed. In this purpose the distance between chains is supposed to be small. Another aspect

supporting this model is that the Mössbauer parameters of the LS sites, ΔE_Q^{LS} and δ^{LS} (Figure 176, 177) show a discontinuity as a function of temperature, of 0.2 mm/s, between 230 K and 240 K. This discontinuity implies that a variation in the Fe(II) ions environment appears, in this range of temperature. In the absence of different type of sites than $Fe(II)N_6$, around the Fe(II) ions, this discontinuity, in the linear trend of ΔE_Q^{LS} function of temperature, can indicate a ligand change conformation.

Considering that the jump in the quadrupole splitting appears in the same temperature range as the ST phenomenon (230 K - 235 K), we may conclude that the conformation variation is induced by the ST. The magnitude of ΔE_Q^{LS} discontinuity (0.2 mm/s) indicates the presence of intramolecular interactions during the ST, near to r.t.[31]. The presence of intermolecular interactions is not excluded, because compound **47·H_2O** presents a cooperative ST behaviour (Figure 171). The presence of intra- and intermolecular interactions may generate hardly perceptible discontinuities as they can be "hidden" by the intramolecular interactions. In this case, the intermolecular interactions may stabilize the intermediate conformation (II^{nd} stage). Indeed, when the compound is dehydrated, it does not present any intermediary state, the ST occurs in one-step. However, a reorganization of the structure, following the annealing process on **47·H_2O** could not be excluded. As, there is no discontinuity in the Mössbauer parameters ΔE_Q^{LS} and δ^{LS}, at the transition temperature of the second hysteresis, we conclude that this hysteresis is due to intermolecular interactions.

This discontinuity can be explained also by the presence of Fe(II) LS ions at 300 K (residual Fe(II) LS ions placed at the ends of chains) which do not switch but remain sensitive to the variation of their local environment, when the Fe(II) HS ions, situated in their proximity, present a ST to the LS state.

Concerning the Fe(II) HS sites, the Mössbauer parameters, ΔE_Q^{HS} and δ^{HS} does not present any discontinuity function of temperature. Therefore it can be considered there is no variation of the HS environment of $Fe(II)^{HS}$ ions.

Below 250 K, as the Fe(II) HS ions become LS, an increase of the symmetry can be observed and therefore a decrease of the quadrupole splitting values is identified. The evolution of this parameter is linear and constant, different from zero, as in the case of most of the chains, because of the presence of local torsions on the $Fe^{II}N_6$ site. The change of the local environment of the $Fe(II)^{LS}$ ions, A, can leads to a crystallographic phase transition. In this case the thermodynamic parameters, characteristic of the ST, should be brought up compared to the typical values attributed to a first order phase transition [31, 57]. Seeing the entropy values obtained for **47·H$_2$O** ($\Delta S_{HL}(1)$ = 15.6 J.mol^{-1}K^{-1} and $\Delta S_{HL}(2)$ = 17.6 J.mol^{-1}K^{-1}) a crystallographic phase transition would occur on the same temperature interval as the ST can be excluded, these values are in the limit of first order phase transition, translated by the Fe(II) spin transition.

This model remains however problematic. If at 80 K all the Fe(II) ions are in the LS state and *one of three* Fe(II) ions (A) in the chain have a different ligand conformation from Fe(II) ions (B), they must have been visible by Mössbauer spectroscopy; the spectra should present two types of sites at this temperature or line broadening should have been observed, but it is not the case. For compound **47·H$_2$O** only one site (LS) is identified at 80 K. The explanation can be that the different conformation of the ligand around the Fe(II) ions will not introduce a strong variation of the Mössbauer parameters.

Lets us now consider a second model which takes in account the intramolecular interactions between the Fe(II) ions, for the first step of the

ST, oppositely to the previous one which propose an intermolecular propagation.

- 2nd Model: Two types of chains (A and B) are considered for the second model, to explain the unusual magnetic characteristics of **47·H_2O**. At room temperature (1st stage), the compound is formed by HS ions with the end of chains in the LS and HS states (representing the LS and the HS residual ratio at room temperature and at 80 K, respectively). In the cooling process, from r.t. to 220 K (2nd stage), one third (1/3) of the Fe(II) ions switch to LS state, involving a change of the conformations of the ligands. Thus the system is stabilized on the plateau, (1/3) of Fe(II) ions are in LS (A) and two thirds (2/3) of Fe(II) ions maintain their HS (B) state. Below 220 K the two thirds of HS Fe(II) ions(B) switch to LS state. This does not involve any environment change of the A and B chains ions.

To schematize:

At 300 K (Ist stage) - all the Fe(II) ions, noted as A and B, are in the HS state and the ligand has identical conformation.

Ends of Chain - $(B^{HS}\text{-}B^{HS}\text{-}B^{HS}\text{-}B^{HS}\text{-}\ B^{HS}\text{-}B^{HS}\text{-}B^{HS}\text{-}B^{HS}\text{-}B^{HS})_n$ - Ends of Chain

Ends of Chain - $(B^{HS}\text{-}B^{HS}\text{-}B^{HS}\text{-}B^{HS}\text{-}\ B^{HS}\text{-}B^{HS}\text{-}B^{HS}\text{-}B^{HS}\text{-}B^{HS})_n$ - Ends of Chain

Ends of Chain - $(A^{HS}\text{-}A^{HS}\text{-}\ A^{HS}\text{-}A^{HS}\ \text{-}\ A^{HS}\text{-}A^{HS}\ \text{-}\ A^{HS}\text{-}A^{HS})_n$ - Ends of Chain

At 220 K (IInd stage) - the Fe(II) ions, noted as B, remain in the HS state, while the Fe(II) ions, noted as A, undergo to the LS state. The configuration of the ligands around the B ions is unchanged while the configuration of the ligands around the A ions changes.

Ends of Chain - $(B^{HS}\text{-}B^{HS}\text{-}\ B^{HS}\text{-}B^{HS}\ \text{-}\ B^{HS}\text{-}B^{HS}\ \text{-}\ B^{HS}\text{-}B^{HS})_n$ - Ends of Chain

Ends of Chain - $(B^{HS}\text{-}B^{HS}\text{-}\ B^{HS}\text{-}B^{HS}\ \text{-}\ B^{HS}\text{-}B^{HS}\ \text{-}\ B^{HS}\text{-}B^{HS})_n$ - Ends of Chain

Ends of Chain - $(A^{HS}\text{-}A^{HS}\text{-}\ A^{HS}\text{-}A^{HS}\ \text{-}\ A^{HS}\text{-}A^{HS}\ \text{-}\ A^{HS}\text{-}A^{HS})_n$ - Ends of Chain

At 80 K (IIIrd stage) - All the Fe(II) ions, A and B, are in LS state, with different ligand conformation. The Fe^{II} B ligands conserved their initial conformation while the conformation of the A Fe(II) metal centers remains the same as at 200 K, on the plateau.

Ends of Chain - $(B^{LS}\text{-}B^{LS}\text{-}B^{LS}\text{-}B^{LS}\text{-}B^{LS}\text{-}B^{LS}\text{-}B^{LS}\text{-}B^{LS})_n$ - Ends of Chain

Ends of Chain - $(B^{LS}\text{-}B^{LS}\text{-}B^{LS}\text{-}B^{LS}\text{-}B^{LS}\text{-}B^{LS}\text{-}B^{LS}\text{-}B^{LS})_n$ - Ends of Chain

Ends of Chain - $(A^{LS}\text{-}A^{LS}\text{-}A^{LS}\text{-}A^{LS}\text{-}A^{LS}\text{-}A^{LS}\text{-}A^{LS}\text{-}A^{LS})_n$ - Ends of Chain

This model relies mainly on the same basis as the previous one. However, it differs from the previous one by the fact that it takes into account a intramolecular cooperativity (and may be intermolecular) between the Fe(II ions, for the first step of the ST, oppositely to the previous model which proposed an intermolecular propagation. Thus, intra- and intermolecular hydrogen bonds may stabilize the intermediary state, observed on the plateau.

The modeling considers that different arrangements of the chains in the solid are possible. They can be distributed in a random way or they can form domains. The problematic of the distinguishing between two LS sites in Mössbauer is related to this last model.

In these two attempted models, a change in the environment of Fe(II) ions, A^{LS}, by modification of the ligand conformation has been assumed. This modification may be due to an order-disorder phenomenon of the counter anion, BF_4^- (which is not confirmed by variable temperature IR studies) or to a modification of the hydrogen bonds caused by the solvent molecules, H_2O. This phenomenon is present in the case of a SCO hexa-coordinate complexes of iron(II) with monodentate 1-alkyltetrazole ligands[58]. Thus, the

environment change of Fe(II) ions, A^{LS} can provoke a crystallographic phase change.

In the third model we take in account the presence of different chain lengths, which is not the case in two previous models.

- 3rd Model: The reason for the two steps magnetic behaviour of **47·H_2O** may be also, the presence of different chain lengths. Two types of chains (A and B) of different chain lengths are considered, the B chains (one third (1/3) of the Fe(II) ions) are longer compared to A chains (two third (2/3) of the Fe(II) ions). At room temperature (1st stage), the compound is formed only by HS 1D chains. In the cooling process, from r.t. to 220 K (2nd stage), the Fe(II) ions which form the long chain (B) will switch to LS state, while the Fe(II) ions which form the short chain (A) remain in the HS state. The system is stabilized on the plateau and decreasing the temperature below 220 K, the two thirds of HS Fe(II) ions (A) switch to LS state, follows. The Fe(II) ions forming the short chain (A) switch after the Fe(II) ions forming the long chain (B) because in the case of the A chains, the cooperativity is reduced and the HS state is stabilized[18].

To schematize:

At 300 K (Ist stage) - At room temperature (1st stage), the compound is formed only by HS one-dimensional chains, one third (1/3) of the Fe(II) ions chains (noted as B) are longer compared to A, which represent two third (2/3) of the Fe(II) ions.

Ends of Chain - (B^{HS}-B^{HS}-B^{HS}-B^{HS}- B^{HS}-B^{HS}-B^{HS}-B^{HS}-B^{HS}) - Ends of Chain

Ends of Chain - (A^{HS}-A^{HS}-A^{HS}-A^{HS} - A^{HS}) - Ends of Chain

Ends of Chain - (A^{HS}-A^{HS}- A^{HS}-A^{HS} - A^{HS}) - Ends of Chain

At 220 K (IInd stage) - the Fe(II) ions, noted as A, remain in the HS state, while the Fe(II) ions, noted as B, undergo to the LS state.

Ends of Chain - (B^{LS}-B^{LS}-B^{LS}-B^{LS}- B^{LS}-B^{LS}-B^{LS}-B^{LS}-B^{LS}) - Ends of Chain

Ends of Chain - (A^{HS}-A^{HS}-A^{HS}-A^{HS} - A^{HS}) - Ends of Chain

Ends of Chain - (A^{HS}-A^{HS}- A^{HS}-A^{HS} - A^{HS}) - Ends of Chain

At 80 K (IIIrd stage) - All the Fe(II) ions, A and B, are in LS state.

Ends of Chain - (B^{LS}-B^{LS}-B^{LS}-B^{LS}- B^{LS}-B^{LS}-B^{LS}-B^{LS}-B^{LS}) - Ends of Chain

Ends of Chain - (A^{LS}-A^{LS}-A^{LS}-A^{LS}-A^{LS}) - Ends of Chain

Ends of Chain - (A^{LS}-A^{LS}-A^{LS}-A^{LS}-A^{LS}) - Ends of Chain

This discontinuity of the Mössbauer parameters, $\Delta E_Q{}^{LS}$and δ^{LS} (Figure 176, 177) can be explained in this case, as in the case of the first model. The presence of Fe(II) LS ions at 300 K (residual Fe(II) LS ions placed at the ends of chains) which do not switch, remains sensitive to the variation of their local environment, when the Fe(II) HS ions, situated in their proximity, present a ST to the LS state.

The unusual ST behaviour, which characterize **47·H_2O** was never observed before for the 1D chains, based on a triazole core. It would therefore be interesting to understand the connection between the magnetic properties and the structure of the compound. In order to accomplish this goal, analyses that are more exhaustive are necessary, to conclude on the arrangement of the coordination complexes, their environment and the length of chains, that they form as function of temperature. In this case, X-ray diffraction on single crystals and EXAFS and NIS measurement would be a real help.

Notes and references

[1] A. D. Naik, J. Marchand-Brynaert, Y. Garcia. *Synthesis* **2008**, *1*, 149-154.

[2] K. S. Hagen. *Inorg. Chem.* **2000**, *39*(25), 5867-5869.

[3] D. Chwaleba, M. M. Ilczyszyn, M. Ilczyszyn, Z. Ciunik. *J. Mol. Struct.* **2007**, *831*(1-3), 119-134.

[4] J. G. Haasnoot, G. Vos, W. L. Groeneveld. *Zeitschrift fur Naturforschung Section B-A Journal of Chemical Sciences* **1977**, *32*, 421.

[5] J. H. Adriaanse, S. H. C. Askes, Y. van Bree, S. van Oudheusden, E. D. van den Bos, E. Gunay, I. Mutikainen, U. Turpeinen, G. A. van Albada, J. G. Haasnoot, J. Reedijk. *Polyhedron* **2009**, *28*(14), 3143-3149.

[6] J. G. Haasnoot, G. Vos, W. L. Groeneveld. *Zeitschrift fur Naturforschung Section B-A Journal of Chemical Sciences* **1977**, *32*, 421.

[7] V. P. Sinditskii, A. E. Fogelzang, M. D. Dutov, V. I. Sokol, V. V. Serushkin, B. S. Svetlov, M. A. Poraikoshits. *Russ. J. Inorg. Chem.* **1987**, *32*(8), 1944-1949.

[8] K. Nakamoto. *Infrared and Raman Spectra of Inorganic and Coordination Compounds : Applications in Coordination, Organometallic, and Bioinorganic Chemistry*, **1997**.

[9] J. G. Haasnoot, G. Vos, W. L. Groeneveld. *Zeitschrift fur Naturforschung Section B-A Journal of Chemical Sciences* **1977**, *32*(12), 1421-1430.

[10] E. Smit, B. Manoun, D. de Waal. *J. Raman Spectrosc.* **2001**, *32*(5), 339-344.

[11] J. A. Wolny, S. Rackwitz, K. Achterhold, Y. Garcia, K. Muffler, A. D. Naik, V. Schunemann. *Phys. Chem. Chem. Phys.* **2010**, *12*(44), 14782-14788.

[12] A. Tokarev, L. Salmon, Y. Guari, G. Molnar, A. Bousseksou. *New J. Chem.* **2011**, *35*(10), 2081-2088.

[13] S. Rackwitz, K. Muffler, K. Achterhold, R. Rüffer, Y. Garcia, R. Diller, V. Schünemann, J. A. Wolny. *Phys. Chem. Chem. Phys.* **2012**, *submitted*.

[14] M. M. Dîrtu, A. Rotaru, D. Gillard, J. Linares, E. Codjovi, B. Tinant, Y. Garcia. *Inorg. Chem.* **2009**, *48*(16), 7838-7852.

[15] M. M. Dîrtu, C. Neuhausen, A. D. Naik, A. Rotaru, L. Spinu, Y. Garcia. *Inorg. Chem.* **2010**, *49*(12), 5723-5736.

[16] P. Gütlich, A. Hauser, H. Spiering. *Angew. Chem. Int. Ed.* **1994**, *33*(20), 2024-2054.

[17] P. Gütlich, J. Jung, H. A. Goodwin. In: (Eds.: E. Coronado, P. Delhaès, D. Gatteschi, and J. S. Miller), *Molecular Magnetism: From Molecular Assemblies to the Devices*, **1996**, p. 327.
[18] Y. Garcia, P. J. van Koningsbruggen, R. Lapouyade, L. Fournes, L. Rabardel, O. Kahn, V. Ksenofontov, G. Levchenko, P. Gutlich. *Chem. Mater.* **1998**, *10*(9), 2426-2433.
[19] Y. Garcia, V. Niel, M. C. Muñoz, J. A. Real. *Top. Curr. Chem.* **2004**, *233*, 229-257.
[20] Y. Garcia, P. J. van Koningsbruggen, R. Lapouyade, L. Rabardel, O. Kahn, M. Wieczorek, R. Bronisz, Z. Ciunik, M. F. Rudolf. *C. R. Acad. Sci. Paris, IIc* **1998**, *1*(8), 523-532.
[21] Y. Garcia, V. Ksenofontov, P. Gutlich. *Hyp. Int.* **2002**, *139*(1-4), 543-551.
[22] M. M. Dîrtu, Y. Garcia, M. Nica, A. Rotarii, J. Linares, F. Varret. *Polyhedron* **2007**, *26*(9-11), 2259-2263.
[23] M. M. Dîrtu, C. Neuhausen, A. D. Naik, A. Rotaru, L. Spinu, Y. Garcia. *Inorg. Chem.* **2010**, *49*(12), 5723-5736.
[24] M. M. Dîrtu, A. D. Naik, J. Marchand-Brynaert, Y. Garcia. *J. Phys. : Conf. Ser.* **2010**, *217*(1), 012085.
[25] M. M. Dîrtu, F. Schmit, A. D. Naik, A. Rotaru, J. Marchand-Brynaert, Y. Garcia. *Int. J. Mol. Sci.* **2011**, *12*(8), 5339-5351.
[26] Y. Garcia, V. Ksenofontov, S. Mentior, M. M. Dîrtu, C. Gieck, A. Bhatthacharjee, P. Gutlich. *Chem. Eur. J.* **2008**, *14*(12), 3745-3758.
[27] M. Seredyuk, A. B. Gaspar, V. Ksenofontov, Y. Galyametdinov, M. Verdaguer, F. Villain, P. Gutlich. *Inorg. Chem.* **2008**, *47*(22), 10232-10245.
[28] M. Seredyuk, A. B. Gaspar, V. Ksenofontov, Y. Galyametdinov, J. Kusz, P. Gutlich. *J. Am. Chem. Soc.* **2008**, *130*(4), 1431-1439.
[29] Y. Garcia, C. M. Grunert, S. Reiman, O. van Campenhoudt, P. Gutlich. *Eur. J. Inorg. Chem.* **2006**, -(17), 3333-3339.
[30] N. N. Greenwood. *Mossbauer spectroscopy [by] N. N. Greenwood, T. C. Gibb,* (Ed.: T. C. Gibb), London, Chapman and Hall, **1971**.
[31] J. A. Real, H. Bolvin, A. Bousseksou, A. Dworkin, O. Kahn, F. Varret, J. Zarembowitch. *J. Am. Chem. Soc.* **1992**, *114*(12), 4650-4658.
[32] F. Varret, A. Ducouret-Cereze. *J. Phys. Colloques* **1988**, *49*(C8), C8-847.
[33] Y. Garcia, C. M. Grunert, S. Reiman, O. van Campenhoudt, P. Gutlich. *Eur. J. Inorg. Chem.* **2006**, (17), 3333-3339.
[34] D. Boinnard, A. Bousseksou, A. Dworkin, J. M. Savariault, F. Varret, J. P. Tuchagues. *Inorg. Chem.* **1994**, *33*(2), 271-281.
[35] P. Gütlich, H. A. Goodwin. Spin Crossover in Transition Metal Compounds III, In: *Top. Curr. Chem.*, Springer, Berlin-Heidelberg, **2004**, pp. 233-235.
[36] E. Konig, K. Madeja. *Chem. Commun. (London)* **1966**, (3), 61-62.

[37] V. Niel, A. L. Thompson, A. E. Goeta, C. Enachescu, A. Hauser, A. Galet, M. C. Munoz, J. A. Real. *Chemistry* **2005**, *11*(7), 2047-2060.
[38] P. Gütlich, H. A. Goodwin, M. Sorai. Heat Capacity Studies of Spin Crossover Systems, In: *Spin Crossover in Transition Metal Compounds III*, Springer Berlin / Heidelberg, **2004**, pp. 137-171.
[39] C. P. Slichter, H. G. Drickamer. *J. Chem. Phys.* **1972**, *56*(5), 2142.
[40] C. R. Pike, A. P. Roberts, K. L. Verosub. *J. Appl. Phys.* **1999**, *85*, 6660.
[41] R. Tanasa, C. Enachescu, A. Stancu, E. Codjovi, J. Linares, F. Varret, J. G. Haasnoot. *Phys. Rev. B* **2005**, *71*, 014431.
[42] W. Vreugdenhil, J. H. Vandiemen, R. A. G. Degraaff, J. G. Haasnoot, J. Reedijk, A. M. vanderKraan, O. Kahn, J. Zarembowitch. *Polyhedron* **1990**, *9*(24), 2971-2979.
[43] S. Pillet, J. Hubsch, C. Lecomte. *Eur. Phys. J. B* **2004**, *38*(4), 541-552.
[44] P. Gütlich, Y. Garcia, H. Spiering. *Magnetism: From Molecules to Materials*, Wiley-VCH, Verlag GmbH, **2003**, p. 271.
[45] H. Köppen, E. W. Müller, C. P. Köhler, H. Spiering, G. P. E.Meissner. *Chem. Phys. Lett.* **1982**, *91*, 348.
[46] L. Wiehl. *Acta Crystallogr. , Sect. B* **1993**, *49*(2), 289-303.
[47] Y. Garcia, O. Kahn, L. Rabardel, B. Chansou, L. Salmon, J. P. Tuchagues. *Inorg. Chem.* **1999**, *38*(21), 4663-4670.
[48] J. A. Rodriguez-Velamazan, M. Castro, E. Palacios, R. Burriel, T. Kitazawa, T. Kawasaki. *J. Phys. Chem. B* **2007**, *111*(6), 1256-1261.
[49] S. M. Neville, B. A. Leita, G. J. Halder, C. J. Kepert, B. Moubaraki, J. F. Letard, K. S. Murray. *Chemistry* **2008**, *14*(32), 10123-10133.
[50] S. M. Neville, G. J. Halder, K. W. Chapman, M. B. Duriska, P. D. Southon, J. D. Cashion, J. F. Letard, B. Moubaraki, K. S. Murray, C. J. Kepert. *J. Am. Chem. Soc.* **2008**, *130*(9), 2869-2876.
[51] W. Bauer, W. Scherer, S. Altmannshofer, B. Weber. *Eur. J. Inorg. Chem.* **2011**, *2011*(18), 2803-2818.
[52] V. P. Sinditskii, V. I. Sokol, A. E. Fogelzang, M. D. Dutov, V. V. Serushkin, M. A. Poraikoshits, B. S. Svetlov. *Russ. J. Inorg. Chem.* **1987**, *32*(8), 1950-1955.
[53] P. J. van Koningsbruggen, Y. Garcia, E. Codjovi, R. Lapouyade, O. Kahn, L. Fournes, L. Rabardel. *J. Mater. Chem.* **1997**, *7*(10), 2069-2075.
[54] A. B. Koudriavtsev, A. F. Stassen, J. G. Haasnoot, M. Grunert, P. Weinberger, W. Linert. *Phys. Chem. Chem. Phys.* **2003**, *5*(17), 3676-3683.
[55] C. chong, A. Slimani, F. Varret, K. Boukheddaden, E. Collet, J. C. ameline, R. Bronisz, A. Hauser. *Chem. Phys. Lett.* **2011**, *504*(1-3), 29-33.
[56] M. Nishino, C. Enachescu, S. Miyashita, K. Boukheddaden, F. Varret. *Phys. Rev. B* **2010**, *82*(2), 020409.

[57] Y. Miyazaki, T. Nakamoto, S. Ikeuchi, K. Saito, A. Inaba, M. Sorai, T. Tojo, T. Atake, G. S. Matouzenko, S. Zein, S. A. Borshch. *J. Phys. Chem. B* **2007**, *111*, 12508-12517.

[58] E. W. Mueller, J. Ensling, H. Spiering, P. Gütlich. *Inorg. Chem.* **1983**, *22*(14), 2074-2078.

General discussion and concluding remarks

Our present work is devoted to the fundamental aspects of new iron(II) based molecular sensors. In a bird view, the approach, direction and protocol are an ecliptic blend of synthetic organic-inorganic chemistry, up to date high-tech characterization tools, supporting theories, postulations, and lots of positive results and finally number of perspectives for future research to expand its horizon. We begin this work with loads of ideas and eventually achieved that are inevitably found their way in this thesis. We are of the opinion that this database would undoubtedly enrich the existing knowledge in this field and resourceful to the scientific society. Following sections will give a quick overview of the whole work.

1,2,4-triazole moiety was documented to be one of the best suited molecular fragments for SCO purpose with its inherent binding and bridging modes of coordinating to metal ions and which has ample of opportunities for tailoring to desired scaffold. Intensive focus in this direction was to alteration of substitution on *N4* position and depending upon the nature of substituent a favorable or deleterious influence can be expected. Our investigation is preponderantly dedicated over iron complexes of 1,2,4-triazole and its novel derivatives. We focus mainly on molecules that have transparency in the visible region of UV-visible spectrum so as to minimize the interferences from their absorption with d-d transition. Thus most of the precursor molecules are colorless to off-white and resulting iron complexes display distinct thermochromism to either pink or white.

Investigation begins with simplest member of 1,2,4-triazole series – 4-amino-1,2,4-triazole, a series of new materials were prepared, characterized (Chapter 1). We have carefully investigated the ST of a series of Fe^{II} 1D NH_2trz coordination polymers $[Fe(NH_2trz)_3](Anion)_2 \cdot nH_2O$ introducing for

the first time divalent inorganic anions of different sizes (TiF_6^{2-}, ZrF_6^{2-}, TaF_7^{2-}, SnF_6^{2-}, GeF_6^{2-}) to understand the variation of $T_{1/2}$ *vs.* the volume of the inserted anion. Surplus effect by supramolecular organization and interactions of the network was shown with a crystal structure of analogous $[Cu(NH_2trz)_3]ZrF_6 \cdot H_2O$ which gave insight into the role of supramolecular interaction in the propagation of elastic cooperative interactions and reasons for wide hysteresis loop. Hydrostatic pressure measurements were carried out on selected SCO compounds to see its influence $T_{1/2}$. This external pressure is different from the electrostatic pressure set up by anion-cation interactions, that we have here estimated numerically, for the first time. With available data on Fe···Fe distance of the cationic chain $[Fe(NH_2trz)_3]^{2+}$ that was determined by EXAFS spectroscopy, it was also possible to estimate for the first time, the chain length distribution τ that range between 1 and 4 nm, for these 1D coordination polymers.

As a continuation of the work, an internal anionic nuclear probe was successfully implanted into the crystal lattice of $[Fe(NH_2trz)_3]^{2+}$ 1D chain compound for the first time in view of sensing elastic cooperative interactions associated to their propagation in the crystal lattice and to study the role of lattice dynamics and supramolecular interactions in 1D chain compounds (Chapter 2). These new materials, including SnF_6^{2-} as counter-anions, offer a unique opportunity to probe locally the thermally induced ST by means of two Mössbauer isotopes located within the chain (^{57}Fe) and in the anionic sublattice (^{119}Sn). We have also found that the non-coordinated anion, which is found between the chains, is able to feel the ST of individual chains. This behaviour was suggested primarily on the basis of the evolution of its local distortion registered by ^{119}Sn Mössbauer spectroscopy. This result constitutes the second example of ST sensing through the non-coordinated anion and the very first example obtained from Mössbauer spectroscopy.

Advancing through probing protocols, we investigated First-Order Reversal Curves (FORCs) to determine the distribution of switching temperatures and interactions fields for all of the 'particles' that contribute to the hysteresis loop which is limited in the routine magnetic measurements in DC mode that only provide a primary analysis of the hysteresis loop.

The inadequate data in the literature on SCO properties of an interesting system $[Fe(NH_2trz)_3](NO_3)_2$ that has to be filled in order to realize unambiguously the reasons for its interesting SCO properties prompted us to work on it. This system is found to exhibit an abrupt, reversible, thermochromic associated to a wide hysteretic SCO. As most of Fe^{II}–1,2,4-triazole systems hardly crystallize, due to insolubility of the coordination polymers we have to rely on the crystal structure of other analogous metal complexes. This gives rise to the crystal structure of a copper-triazole 1D chain $[Cu(NH_2trz)_3](NO_3)_2$ that was obtained thanks to the solvothermal crystallization technique. It also represents one of the rare example of crystallized 1D chain complexes with triple *N*1,*N*2-1,2,4-triazole bridges. It is understood from such systems that extensive network of both intra and inter molecular interactions which strengthen the elastic interactions between switching centers are responsible for wide hysteresis loops. Planar geometry of the nitrate anion with its 'tripod' character establish fourth supramolecular bridge in addition to the triple 1,2,4-triazole bridge between metallic centers is pointed out. This extra-bridge is believed to further strengthen elastic interactions within the chain.

Synthetic organic chemistry played significant role in our research. The design of novel ligands based on introducing several factors in the framework - ligand field strength, electronic polarity of the molecule, supramolecular organizational tendency of the molecule, conformational flexibility, various modes of binding and bridging to metal centers, shock absorbing cushion effect, robust in terms of stability/shelf-life are some of

the factors that were kept in mind while designing a precursor for spin crossover materials. One of the simplest analogues of 4-amino-1,2,4-triazole which we planned to design is 4-hydroxy-1,2,4-triazole for which there was not synthetic protocol available in the literature. Recently our group reported a simplified 'transamination' reaction wherein any primary amine can be exchanged so as to form substituted triazole. With this, a new protocol was successfully achieved to prepare this ligand molecule in a shortest possible time, in 4-5 hr in a non-toxic solvent toluene. Preliminary results indicate usefulness of this ligand not only in SCO materials $[Fe(OH\text{-}trz)_3](Anion)_2 \cdot H_2O$ system but also for other transition meal complexes as seen in the 1D copper chains $[Cu(OH\text{-}trz)(ReO_4)OH]$, $[Zn(OHtrz)_2Cl](NO_3)$ (Chapter IV). This ligand yet to be explored for its full potential and could be topic of future research.

It was of the vision that bulky substitution on triazole often leads to undesirable products. But we have shown how this can be compensated to some extent by incorporation of certain other elements which influence cooperativity in the network. In this direction (Chapter V), we propose a designing of a new precursor for SCO, a new module for 1D CP, 4-(3'-N-phtalimido-propyl)-1,2,4-triazole (phtptrz), where a bulky substituent is attached to *N4* of 1,2,4-triazole via a multiple carbon spacer. This aromatic group, although bulkier, is a potential promoter of supramolecular interactions due to π–π stacking and H-bonding interactions involving carbonyl groups. Although bulky substituent on the triazole ring with multiple carbon spacer of the ligand scaffold is not favorable for cooperative SCO, as trinuclear species formation can be expected. However the gradual pace of the ST for these compounds could therefore be explained by the presence of the propyl spacer, capable to play a role of shock absorber blocking the elastic propagation from one iron(II) ion to another. Nevertheless, kinetics and dynamics of such gradual SCO are now being

explored for additional understanding of the weak cooperativity in SCO process[3].

Our next endeavor is to manipulate electronic distribution in the ligand framework, at the same time keeping triazole moiety intact at one end. What could be exciting is to introduce a multifunctional group like carboxylic group on the aliphatic framework bearing triazole with variable spacer in between. Among database of suitable and potential organic fragments what inspired us is the natural biomolecule – amino-acids. The amine terminal could be converted to triazole without affecting the carboxylic terminal which could lead ligand with polarity of electron distribution. This aspiration was for the first time achieved through the simplest α-aminoacid-glycine. This leads to (4H-1,2,4-triazol-4-yl acetic acid) wherein triazole and carboxylic group are separated by just one carbon spacer which would have overall effect of bringing the adjacent chains closer in the iron 1D CPs. This would have dramatic effect on intrachain cooperativity. The first series of iron 1D chain compound with this ligand was hard to analyze, interpret and moreover display poor SCO properties. Our vision was primarily the structural factors. This prompted us to investigate several crystal structural analyses of similar transition metal complexes. One among them is the crystal structure determination of [Cd(HGlytrz)(Glytrz)Cl]·$2H_2O$ that display self-assembly process. This structure is crucial in the sense that it not only promptly forms 1D chain but also reveals that alternative ligand in the 1D chain is deprotonated. This inequality not only altered the overall inductive effect but also significantly affect the supramolecular organization. Possibly this is one of the reason for non-SCO behavior of the above series. The other reason could be the susceptibility of the deprotonated ligand towards to pH or moisture that could even slowly degrade the complexes.

Now the challenge to use this ligand in a beneficial way is to block the carboxylic group by non-coordinating group. The best way of functional group transformation was to make esterification of this terminal. The easiest,

of course theoretically, is to begin transamination with ester of glycine. After a series of attempt we standardize a protocol which not only gave the desired ligand but also laid foundation of a new era in aminoacid ester functionalization. Our aspiration was fulfilled with magnificent results with this tiny synthon. Abrupt, hysteretic, reversible, thermochromic SCO with wide thermal regime were observed in different members of the ligand with different anion. This ligand credited us with hysteretic SCO system $[Fe(GlytrzE)_3](ClO_4)_2$ that operates around room temperature, a system many SCO experts' dreams for.

Further continuing this work, we also planned to investigate the influence of spacer length in this ligand system. Thus β-amino acids that has two-carbon spacer is introduced for this process and through transamination we prepared 4H-1,2-4-triazol-4-yl-propionate (βAlatrz). The idea behind this was to see the influence of spacer length as this could slightly widen the intermolecular chain spacing. At the same time there is a possibility of introducing the shock absorbing effect of this spacer on the cooperativity. Of course these are not only the factors that determine the SCO, but factors like, anion geometry, size, solvent occupancy of lattice would modulate the final outcome. The results are detailed in chapter VIII. Among several interesting molecules that exhibit reversible, abrupt SCO, the two-step SCO observed in this series in $[Fe(\beta Alatrz)_3](BF_4)_2 \cdot H_2O$ is outstanding. This two-step SCO is going to be the first one to be reported for the triazole based 1D chains. To explain this unusual behavior several models were also described in this chapter. Temperature dependent IR and Raman experiments with DFT calculation momentously enriched our knowledge about the relationship between vibrational degree of freedom of ligand framework and two-step SCO properties. Finally all these careful interpretation of magnetic results with lot of spectroscopic, analytical and microscopic results were immensely supported by several crystal structure analyses of several transition metal complexes. Needless to mention that ^{57}Fe Mössbauer spectroscopy is the

core characterization tool in our research which is the only tool that reveals the fate of iron in any environment.

Following section briefly describe the diverse architecture observed in several crystals structures that augmented our knowledge on self-assembly behavior of the novel ligands with different metal ions.

The normal tendency of triazole derivatives is formation of 1D chains involving *N1*, *N2* in bridging metal centers. Depending upon the substitution on *N4* position, or anion the number of such bridging between metal canters vary between 2 and 3. Chain length of such 1D systems are often restricted by the bulkiness of the *N4* substitution. Heavy substitution normally restricts the chain length to trinuclearity. In cases of $[Cu(NH_2trz)_3](NO_3)_2$, $[Cu(NH_2trz)_3]ZrF_6 \cdot H_2O$, [Cu(OH-trz)($ReO_4$)OH], $[Zn(OHtrz)_2Cl](NO_3)$ and $[Cd(HGlytrz)(Glytrz)Cl] \cdot 2H_2O$ the chains where *N4* position is occupied by smaller groups like $–NH_2$ or –OH which offer no steric clashes forms exclusively infinite 1D chains. When *N4* positions are substituted by bulky propyl phthalamido group, chain propagation is restricted and trinuclear complexes such as $[Cu_3(phtptrz)_{10}(H_2O)_2](SiF_6)_3 \cdot 44H_2O$ and $[Cu_3(phtptrz)_8(H_2O)_4](ZrF_6)_3 \cdot 19H_2O$ are obtained. The magnetic properties considerably affected between 1D chains and trinuclear complexes. For example in both above cases of trinuclear complexes the dominant exchange interaction is found to be ferromagnetic.

Interestingly when $[Cd(HGlytrz)(Glytrz)Cl] \cdot 2H_2O$ was prepared by solvothermal synthesis, unexpectedly a 2D $[Cd_2(Glytrz)_2Cl_2]$ chiral helicate that crystallized in non-centrosymmetric space group is observed. Such unexpected results have an enormous significance because of technological properties like single harmonic generator, piezo-pyro-ferro electricity, and triboluminescence.

The tailored tiny synthon 4H-1,2,4-triazol-4-yl acetic acid undergoes stunning self assembly to form a 3D array of porous nanoball architecture $[Cu_3(\mu_3\text{-}O)(HGlytrz)_6(H_2O)_3]BF_4 \cdot H_2O$. This decoding of inherent self

assembly in this copper metal-organic framework is intriguing. Such cavernous solids not only find application in gas storage, nano-reactors for catalysis, anion-cation recognition sites, but also in molecular magnetism due to spin frustration among the strained metal sites.

Notes and references

[1] L. Cambi, L. Szego. *Ber. Deutsch. Chem. Ges.* **1931**, *64*, 2591.
[2] Orgel, L. Tenth Solvay Conference. 1956.
Ref Type: Conference Proceeding
[3] J. Linares, E. Codjovi, Y. Garcia. *Sensor* **2012**, *12*(4), 4479-4492.

Perspectives

As early as 1931, L. Cambi, and L. Szego noticed anomalous magnetic properties while working on tris(N,N-dialkyldithiocarbamato)iron(III) complexes and their investigation credited them with the phenomenal discovery of SCO[1]. Nearly after 20 years, L.Orgel's[2] viewpoint based on spin-equilibrium promised future prospects on SCO materials, which are now considered as one of the most prospective class of molecular switches.

In recent years molecular electronics made a quantum jump with the inflow of large number of switchable materials of both organic and inorganic origin and foresee to reap them as prospective components in fabricating accessories for information processing, data storage, sensors, bio-markers, drug delivery, biological imaging etc. Single molecule magnets, quantum dots, thermo-photo-electrochromic materials, and iron(II) SCO materials are at the forefront of this race.

Today synthetic/materials/nano/computational chemists and physicists made substantial contribution to this flourishing area, and inventively provided wealth of information that helped in probing and understanding the process and dynamics of SCO not only in solids, but also in nanoparticles, liquids, liquid crystals and thin-films of SCO materials. Continued documentation in peer reviewed journals, frequent exclusive international conferences, increasing investment in the industrial sectors justified the prospects of this domain.

Perspectives of our work are numerous because the analytical procedure developed here could be applied in future to a large number of solid-state

molecular switches, particularly 1D chains based on 4-R-1,2,4-triazole. For instance, by using the anion database a linear relationship between anion volume and transition temperatures was determined and that could lead to many new SCO complexes (see Chapter I). Another interesting prospect stems from the introduction of our novel inorganic fluoride anions in SCO cations of various dimensionalities to go beyond the classical inorganic anions routinely used in SCO research. Another exciting perspective, from the synthetic chemistry point of view, has already started with the introduction of the novel 4-hydroxy-1,2,4-triazole ligand (see Chapter IV). This molecule was expected from long time in the field, and that open the door to a new SCO systems and a wide range of new materials.

It should be particularly interesting to synthesise a new class of 1D chains (without solvent molecule) based on Fe(II) - OH-trz, which could become thermo-sensitive above room temperature, thanks to the small volume of the substituent. Moreover, it should also lead to modification of the SCO properties and leads to good candidates for applications. Already DFT calculations have started to explain the gradual nature of the SCO behaviour.

Since our work can be considered as pionnering in the SCO and MOF fields with the introduction of α– and β–amino acids and amino esters derivatives, the inorganic complexes series presented in this thesis should also be enlarged in order to grow the number of potentially thermo-sensitive materials. It is especially due to the fact that these ligands give access to a very large variety of accessible molecular dimensionalities (see chapter 6, 7 and 8). These ligands are known to be bio-compatible, easily grafted on coordinating moieties and to metal ions, and could crystallise in non centro-symmetric packings.[3-6] It would open the way to future research on SCO

compounds. Finally, these hybrid SCO materials could be prepared in order to drive to other specific molecular arrangement (e.g. liquid crystals or nanoparticles) which could lead to novel interesting properties linked to the large presence of particles interfaces. Last but not least, our ligands could be derived so as to present a noticeable dipole moment that would make the resulting SCO compounds activated by an electric field.

Notes and references

[1] L. Cambi, L. Szego. *Ber. Deutsch. Chem. Ges.* **1931**, *64*, 2591.
[2] Orgel, L. Tenth Solvay Conference. 1956.
[3] A. D. Naik, J. Marchand-Brynaert, Y. Garcia. *Synthesis* **2008**, *1*, 149-154.
[4] H. Imai, K. Inoue, K. Kikuchi, Y. Yoshida, M. Ito, T. Sunahara, S. Onaka. *Angew. Chem. Int. Ed Engl.* **2004**, *43*(42), 5618-5621.
[5] A. D. Cutland-Van Noord, J. W. Kampf, V. L. Pecoraro. *Angew. Chem. Int. Ed.* **2002**, *41*(24), 4667-4670.
[6] J. D. Ranford, J. J. Vittal, D. Wu, X. Yang. *Angew. Chem. Int. Ed.* **1999**, *38*(23), 3498-3501.

List of publications and communications

Written communications

'Structures of new Cu(II) and Co(II) 4-amino-1,2,4-triazole coordination compounds'
M. M. Dîrtu, Y. Garcia, B. Tinant, Acta Cryst. 2006, A62, s275

DOI: 10.1107/S0108767306094517

Iron(II) spin transition 1,2,4-triazole chain compounds with novel inorganic fluorinated counteranions

M. M. Dîrtu, Y. Garcia, M. Nica, A. Rotaru, J. Linares, F. Varret, Polyhedron 2007, 26, 2259-2263.

DOI: org/10.1016/j.poly.2006.11.00

Cited by:

1. Ramos S. M., Silva, J.A., Martins, N.D., Matos B., A., Sobral, A.J.F.N. *Acta Crystall. E: Structure Reports Online* **2008**, 64(9), o1762
2. D. Savard , C. Cook , G. D. Enright , I. Korobkov , T. J. Burchell, M. Murugesu ***CrystEngComm***, 2011,**13**, 5190-5197

Rapid Cooling Experiments and Use of an Anionic Nuclear Probe to Sense the Spin Transition of the 1D Coordination Polymers $[Fe(NH_2trz)_3]SnF_6 \bullet nH_2O$ (NH_2trz = 4-amino-1,2,4-triazole)

Y. Garcia, V. Ksenofontov, S. Mentior, M. M. Dîrtu, C. Gieck, A. Bhatthacharjee, P. Gütlich. Chem. Eur. J. 2008, 14, 3745.

DOI: 10.1002/chem.200701305

Cited by:

1. L. Xu, X. -Ch. Zhang, W. -G. Liu, B. Liu, *J. Struct. Chem*. **2012**, 53, 1, 179.
2. Debajit S., Vishwas S., Srinivasan N., Dalton Trans. **2012**, 41, 14, 4135.
3. S. Schlamp, P. Thoma, B. Weber *Eur. J. Inorg. Chem.* **2012,** 2012, 16.
4. C. Lochenie, W. Bauer, S. Schlamp, P. Thoma, B. Weber *Z. Anorg. All. Chem*. **2012**, 638, 1.
5. T. M. Pfaffeneder, S. Thallmair, W. Bauer, B. Weber, *New J. Chem*. **2011**, 35, 3, 691.
6. S Schlamp, B. Weber, A. D. Naik, Y. Garcia *Chem. Commun*. **2011**, 47, 25, 7152.

7. S.-W. Wang, L. Yang, J.-L. Feng, B.-D. Wu, J.-G. Zhang, T.-L. Zhang, Z.-N. Zhou *Z. Anorg. All. Chem*. **2011**, 637, 14-15.
8. X.-C. Zhang, L. Xu, W.-G. Liu, B. Liu *Bull. Kor. Chem. Soc.* **2011**, 32, 5, 1692.
9. N. V. Fischer, A. Inayat, W. Schwieger, N.Burzlaff *J. Coord. Chem*. **2010**, *63*, 2831.
10. X.-C. Zhang, B. Liu *Inorg. Chem. Commun*., **2009**, 12, 8, 808.
11. A Bhattacharjee, V. Ksenofontov, H. A. Goodwin, P Gütlich *J. Phys. Condens. Matter* **2009**, 21, 2, 026011.
12. J. Tang, J. Sanchez Costa, S. Smulders, G. Molnar, A. Bousseksou, S. J. Teat, Y. Li, G. A. van Albada, P. Gamez, J. Reedijk, *Inorg. Chem*. **2009**, *48*, 2128.

Calorimetric measurements of diluted spin crossover complexes $[Fe_xM_{1-x}(btr)_2(NCS)_2]\cdot H_2O$ with M^{II} = Zn and Ni

A. Rotaru, M. M. Dîrtu, C. Enachescu, R. Tanasa, J. Linares, A. Stancu, Y. Garcia Polyhedron 2009, 28, 2531-2536.

DOI:10.1016/j.poly.2009.04.046

Cited by:

1. Kitchen J. A., Brooker S., *Dalton Trans*. **2010**, *39*, 3358.
2. Kusz J., Bronisz R., Zubko M., Bednarek G., *Chem. Eur. J*. **2011**, *17*, 6807.

Prediction of the spin transition temperature in Fe^{II} 1D coordination polymers: an anion based database

M. M. Dîrtu, A. Rotaru, D. Gillard, J. Linares, E. Codjovi, B. Tinant, Y. Garcia Inorg. Chem. 2009, 48, 7838-7852.

DOI: 10.1021/ic900814b

Cited by:

1. Y.-C. Chuang, C.-T. Liu, C.-F. Sheu, W.-L. Ho, G.-H. Lee, C.-C. Wang, Y. Wang *Inorg. Chem.* **2012**, *51* (8), 4663-4671.
2. Aromi, G.; Barrios, Leoni A.; Roubeau, O.; Gamez, P. *Coord. Chem. Rev.* **2011**, *255*(5-6), 485.
3. Roubeau, O; Castro, M; Burriel, R; Haasnoot, J G.; Reedijk, J. J. Phys. Chem. B **2011**, *115*(12), 3003.
4. Kusz J., Bronisz R., Zubko M., Bednarek G., *Chem. Eur. J*. **2011**, *17*, 6807.
5. Romanenko, G V.; Maryunina, K Y.; Bogomyakov, A S.; Sagdeev, R Z.; Ovcharenko, V I. *Inorg. Chem.* **2011**, *50*(14), 6597.
6. Halcrow, M. A. *Chem. Soc. Rev.* **2011**, *40*(7), 4119.

7. Savard, D.; Cook, C.; Enright, G. D.; Korobkov, I.; Burchell, T. J.; Murugesu, M. .*Cryst. Eng. Comm* **2011**, *13*(16), 5190.
8. Mader, D.; Pillet, S.; Carteret, C.; Stebe, M.-J.; Blin, J.-L. J. of Disp. Sc. Tech. **2011**, *32*(12), 1771.
9. J.A. Kitchen, N.G. White, G., N. L. Jameson, J. L. Tallon, S. Brooker *Inorg. Chem.* **2011**, *50* (10), 4586.
10. Bialonska A., Ciunik Z., Drabent K., *J. Mol. Struct*. **2010**, *970*, 111.
11. Bialonska A., Bronisz R. *Inorg. Chem*. **2010**, *49*, 4534.

Engineering three-dimensional chains of porous nanoballs from a 1,2,4-triazole carboxylate supramolecular synthon

A. D. Naik, M. M. Dîrtu, A. Léonard, B. Tinant, J. Marchand-Brynaert, B. L. Su, Y. Garcia Cryst. Growth Des., 2010, 10, 1798-1807.

DOI: 10.1021/cg901473d

Cited by:
1. Sam C.K. Hau, Ping-Shing Cheng, Thomas C.W. Mak*Polyhedron* **2012, in press**
2. K. Zhao, Y. Jiang, X. Qiu, J. Tian, X. Li J. Coord. Chem. **2011**, *64* (8), 1375.
3. J. Thomas-Gipson, G. Beobide, O. Castillo, J. Cepeda, A. Luque, S. Pérez-Yáñez, A. T. Aguayo, P. Román *Cryst. Eng. Comm*. **2011**, *13*, 3301.

Effect of texture alteration by thin film fabrication on the spin crossover of [Fe(3-Br-phen)$_2$(NCS)$_2$]·0.5CH$_3$OH

A. D. Naik, M. M. Dîrtu, Y. Garcia J. Phys. Conf. Ser., 2010, 217, 012032.

DOI:10.1088/1742-6596/217/1/012032

Cited by: H. Naggert, Al. Bannwarth , S. Chemnitz , T. von Hofe , E. Quandt, F. Tuczek *Dalton Trans.*, **2011**,40, 6364.

Room temperature hysteretic spin transition in 1D iron(II) coordination polymers

M. M. Dîrtu, A. D. Naik, J. Marchand-Brynaert, Y. Garcia J. Phys. Conf. Ser, 2010, 217, 012085.

DOI:10.1088/1742-6596/217/1/012085

Insights into the origin of cooperative effects in the spin transition of $[Fe(NH_2trz)_3](NO_3)_2$: the role of supramolecular interactions evidenced in the crystal Structure of $[Cu(NH_2trz)_3](NO_3)_2 \cdot H_2O$

M. M. Dîrtu, C. Neuhausen, A. D. Naik, A. Rotaru, L. Spinu, Y. Garcia Inorg. Chem., 2010, 49, 5723-5736.

DOI: 10.1021/ic100667f

Cited by:

1. Y. Komatsu, K. Kato, Y.Yamamoto, H. Kamihata, Y. H. Lee, A. Fuyuhiro, S. Kawata, S. Hayami Eur. J. Inorg. Chem. **2012**, *2012* (16), 2769.
2. W.-T. Liu, J.-Y. Li, Z.-P. Ni, X. Bao, Y.-C. Ou, J.-D. Leng, J.-L. Liu, M.-L. Tong *Cryst. Growth. Deseign* **2012**, *12* (3), 1482.
3. L. Xu, X. -Ch. Zhang, W. -G. Liu, B. Liu J. Struct. Chem. **2012**, *53* (1), 179.
4. T. M. Ross, B. Moubaraki, S. R. Batten, K. S. Murray *Dalton Trans.* **2012**, *41* (9), 2571.
5. J. A. Wolny, S. Rackwitz, K. Achterhold, K. Muffler, V. Schünemann *Hyper. Interac.* **2012**, *204* (1-3), 129.
6. A. Rotaru, J.-H.Lim, D. Lenormand, A. Diaconu, J. Wiley, P. Postolache, A. Stancu, L. Spinu *Phys. Rev. B* **2011**, *84* (13), 134431.
7. J. Kusz, R. Bronisz, M. Zubko, G. Bednarek *Chem. Eur. J.* **2011**, 17(24), 6807.
8. A. Urakawa, W. Van Beek, M. Monrabal-Capilla, J. R. Galán-Mascarós, L. Palin, M. Milanesio *J. Phys. Chem. C 115* (4), 1323.
9. T. M. Pfaffeneder, S. Thallmair, W. Bauer, B. Weber *New J. Chem.* **2011**, *35* (3), 691
10. Halcrow, M. A. *Chem. Soc. Rev.* **2011**, *40*(7), 4119.
11. H. Hagiwara, N. Matsumoto, S. Iijima, M. Kojima *Inorg. Chim. Acta* **2011**, *366* (1), 283.
12. H. Hagiwara, O. Sakaguchi, K. Nishi, S. Hashimoto, N. Matsumoto *Bull. Chem. Soc. Jap.* **2011**, *84* (9), 936.
13. A. Grosjean, N. Daro, B. Kauffmann, A. Kaiba, J.-F. Létard, P. Guionneau *Chem. Commun.* **2011**, *47* (45), 12382.

Zinc complexes with 1,2,4-triazole functionalized amino acid derivatives: synthesis, structure and β–lactamase assay

A. D. Naik, J. Beck, M. M. Dîrtu, C. Bebrone, B. Tinant, K. Robeyns, J. Marchand-Brynaert, Y. Garcia Inorg. Chim. Acta, 2011, 368, 21-28.

DOI: 10.1016/j.ica.2010.12.017

Superlative scaffold of 1,2,4-triazole derivative of glycine steering linear chain to a chiral helicate

M. M. Dîrtu, C. Neuhausen, A. D. Naik, A. Léonard, F. Robert, J. Marchand-Brynaert, B. L. Su, Y. Garcia Cryst. Growth Des., 2011, 11, 1375-1384.

DOI: 10.1021/cg101634w

Influence of hydrogen bonding on the hysteresis width in iron(II) spin crossover complexes

B. Weber, W. Bauer, T. Pfaffeneder, M. M. Dîrtu, A. D. Naik, A. Rotaru, Y. Garcia Eur. J. Inorg. Chem., 2011, 3193–3206.

DOI: 10.1002/ejic.201100394

Cited by:

1. T. D. Roberts, F. Tuna, T. L. Malkin, C. A. Kilner, M. A. Halcrow *Chem. Sci.* **2012**, *3*, 2, 349.
2. Y.-C. Chuang, C.-T. Liu, C.-F. Sheu, W.-L. Ho, G.-H. Lee, C.-C. Wang, Y. Wang *Inorg. Chem.* **2012,** *51*, 8, 4663

Spin transition sensors based on a β-aminoacid 1,2,4-triazole derivative

M. M. Dîrtu, F. Schmit, A. D. Naik, A. Rotaru, J. Marchand-Brynaert, Y. GarciaInt. J. Mol. Sci., 2011, 12(8), 5339-5351.
Special issue 'Molecular electronics' (Guest editor: A. Bousseksou)

doi:10.3390/ijms12085339

Coordination polymers and metal organic frameworks derived from 1,2,4-triazole amino acid linkers

A. D. Naik, M. M. Dîrtu, A. Railliet, J. Marchand-Brynaert, Y. Garcia Polymers, 2011, 3, 1750-1775.
Special issue 'Molecular electronics' (Guest editor: K. Fromm)

DOI:10.3390/polym3041750

Impact of ligand spacer and counter-anion in selected 1D iron(II) spin crossover coordination polymers

M. M. Dîrtu, F. Schmit, A. D. Naik, A. Rotaru, J. Marchand-Brynaert, Y. Garcia Hyperfine Interact., 2012, q224505016q83077.

DOI: 10.1007/s10751-011-0402-9

Neutral and anionic duality of 1,2,4-triazole α-amino acid scaffold in 1D coordination polymers

A. D. Naik, M. M. Dîrtu, Y. Garcia Hyperfine Interact., 2012, 1-3, 57.

DOI: 10.1007/s10751-011-0414-5

Coordination preference and magnetic properties of iron(II) assemblies with a bis-azole bearing 1,2,4-triazole and tetrazole

A. D. Naik, A. P. Railliet, M. M. Dîrtu, Y. Garcia Hyperfine Interact., 2012, 1-3, 119.

DOI: 10.1007/s10751-011-0422-5

Weak cooperativity in selected iron(II) 1D coordination polymers

M. M. Dîrtu, D. Gillard, A. D. Naik, A. Rotaru, Y. Garcia Hyperfine Interact., 2012, 205(1-3), 75.

DOI: 10.1007/s10751-011-0412-7

Iron(II) spin transition coordination polymers with a zigzag structure

W. Bauer, M. M. Dîrtu, Y. Garcia, B. Weber Cryst. Eng. Comm. 2012, 14, 1223 (cover page)

DOI: 10.1039/C2CE06253D

Oral communications

1. ***'Insight to the origin of the bistability domain of iron(II) polymeric chain compounds'***

2005 - International Chemical Congress of Pacific Basin Societies - Spin-crossover in Coordination Chemistry: Recent Advances and the Future Outlook(PACIFICHEM 2005, Honolulu, Hawaii (USA)

2007 - GFSM'2007 - Materials and thin films - Conference of the French Speaking Group of Mössbauer Spectroscopy - Caen (France)

2007- Ph.D. Students 'Day of the Faculty of Sciences of the Université Catholique de Louvain

2008 - IAP meeting - Powder synthesis at the nano- and microscale Faculty of Sciences of the Université Catholique de Louvain

2. ***'Hydrothermal synthesis and structural characterisation of new coordination polymers'***

2009 - IAP meeting - Powder synthesis at the nano- and microscale Faculty of Sciences of the Université Catholique de Louvain (*flash communication)*

3. ***'Optical properties of iron(III) spin crossover complexes'***

2010 - Royal Society of Chemistry Workshop on Multifunctional Materials - Dublin (Ireland)

Poster communications

1. ***'Spin crossover and structural characterization of 4-amino-1,2,4-triazole chain complexes'***

2005 - Ph.D. Students'Day of the Faculty of Sciences of the Université Catholique de Louvain

2006 - Conference of the French Speaking Group of Mössbauer Spectroscopy – Nanoparticles (and flash communication)

2006 - 23rd European Crystallographic Meeting – KUL Leuven

2. ***'Study of the insertion of fluorinated inorganic anions in 1D Fe(II) 1,2,4-triazole spin transition chain compounds'***

2006 - ICMM 2006- 10th International Conference on Molecule-Based Magnets August 13-17 2006, Victoria, B. C. (Canada)

2006 - Training school on NMR, MRI, μSR and Mössbauer techniques September 17-30 2006, Pavia (Italy)

2006 - Joint RSC UK Macrocycles and Supramolecular Chemistry and the Coordination Chemistry Group Meeting , Belfast, Northen Ireland (UK)

3. ***'Synthesis, crystal structure and Mössbauer study of new mononuclear spin crossover complexes'***

2007 - GFSM - Conference of the French Speaking Group of Mössbauer Spectroscopy Materials and thin films (*oral flash presentation)*, Caen, France

3. ***'Antiferromagnetism and spin conversion in Fe(II) 1,2,4-triazole chains'***

2007 - GFSM - Conference of the French Speaking Group of Mössbauer Spectroscopy Materials and thin films (*oral flash presentation)*, Caen, France

2007- Ph.D. Students 'Day of the Faculty of Sciences of the Université Catholique de Louvain

2007 - Meeting of the Société Royale de Chimie - Chemistry, light and renewable energies, Mons (Belgium)

2007 - ICAME- International Conference on Applications of the Mössbauer Effect , Indian Institute of Technology, Kanpur (India)

4. ***'Spin crossover in a tailored 2D supramolecular network belonging to the 'phen' family'***

2007 - Meeting of the Société Royale de Chimie - Chemistry, light and renewable energies, Mons (Belgium)

5. ***'The two-step spin crossover in a novel mononuclear iron(III) complex studied by Mössbauer spectroscopy'***

2007 - ICAME- International Conference on Applications of the Mössbauer Effect , Indian Institute of Technology, Kanpur (India)

2008 GFSM - Conference of the French Speaking Group of Mössbauer Spectroscopy Chemistry and functional materials - Louvain-la-Neuve

2010 - GFSM - Conference of the French Speaking Group of Mössbauer Spectroscopy - Mössbauer spectroscopy at the heart of applications - Lisbon (Portugal)

6. ***'Internal pressure sensed by novel divalent anions in Fe(II) 1D spin transition compounds – A Mössbauer study'***

2007 - ICAME- International Conference on Applications of the Mössbauer Effect , Indian Institute of Technology, Kanpur (India)

2008 - Thematic doctoral school chimie moléculaire, supramoléculaire et fonctionnelle, Liege (Belgium)

7. ***'New transamination products as prospective precursors for a novel generation of spin crossover materials'***

2008 GFSM - Conference of the French Speaking Group of Mössbauer Spectroscopy Chemistry and functional materials - Louvain-la-Neuve (*flash presentation)*

8. ***'Uncovering the nature of the two-step spin crossover in $[Fe(salampy)]^+$ by XRD and Mössbauer spectroscopy'***

2009 – GFSM - Conference of the French Speaking Group of Mössbauer Spectroscopy - Recent applications of Mössbauer spectroscopy: from biology to materials (Grenoble (France)

9. ***'Using ^{119}Sn and ^{57}Fe as nuclear probes to the study of anionic sublattice dynamics in Fe^{II} spin transition coordination polymers'***

2009 – ICAME - International Conference on Applications of the Mössbauer Effect, *Vienna (Austria)*

10. ***'Triazole functionalised glycine as promising precursor to fabricate novel spin crossover materials'***

2009 – ICAME - International Conference on Applications of the Mössbauer Effect, Vienna (Austria)

11. ***Engineering 3D chains of porous nanoballs from an 1,2,4-triazole derivatised aminoacid' supramolecular synthon'***

2009 - Meeting of the Royal Society of Chemistry - Les matériaux du future, Liège (Belgium)

2010 - Thematic doctoral school chimie moléculaire, supramoléculaire et fonctionnelle, Mons (Belgium)

12. ***'Effet of texture alteration by thin film fabrication on the spin crossover of*** $[Fe(3\text{-}Br\text{-}phen)_2(NCS)_2]\cdot 0.5CH_3O$***'***

2009 - GDR magnetism and molecular switches, Dourdan (France)

13. ***'Hysteretic spin transition near, above and below room temperature in new 1D coordination polymers'***

2009 - GDR magnetism and molecular switches, Dourdan (France)
2010 - International Chemical Congress of Pacific Basin Societies (PACIFICHEM
2010 - Functional Molecule-Based Magnets, Honolulu, Hawaii (USA)

14. ***'Thin film processing of a mononuclear iron(II) spin crossover complex'***

2010 - Thematic doctoral school chimie moléculaire, supramoléculaire et fonctionnelle, Mons (Belgium)

15. ***'Superlative scalfold of 1,2,4-triazole derivative of glycine steering linear chain to 2D chiral helicate'***

2010 - 6th Belgian Crystallography Symposium BCS-4, *Academy House, Brussels*

16. ***'Zinc complexes with 1,2,4-triazole functionalized amino acid derivatives: synthesis, structure and beta-lactamase assay'***

2011 - Thematic doctoral school chimie moléculaire, supramoléculaire et fonctionnelle, Liège (Belgium)

17. ***'Iron(II) spin crossover coordination polymers with a 1,2,4-triazol-4-yl-propanoic acid'***

2011 - Thematic doctoral school chimie moléculaire, supramoléculaire et fonctionnelle, Liège (Belgium)

18. ***'Mössbauer study of new spin transition complexes based on functionalized amino acids'***

2011 - Thematic doctoral school chimie moléculaire, supramoléculaire et fonctionnelle, Liège (Belgium)

2011 - GFSM'2011- French Speaking Group of Mössbauer Spectroscopy International Meeting Mössbauer spectroscopy and magnetic materials, Strasbourg (France)

2011 - Ph.D. Students'Day of the Faculty of Sciences of the Université Catholique de Louvain

2011 -7th Seeheim Wokshop on Mössbauer Spectroscopy), Frankfurt (Germany).

2011 - ACIN 2011- First international symposium on advanced complex inorganic nanomaterials; Namur (Belgium)

19. ***'1,2,4-triazole functionalized β-analine as a prospective scaffold for iron(II) spin crossover coordination polymers'***

2011 - ACIN 2011- First international symposium on advanced complex inorganic nanomaterials; Namur (Belgium)

20. ***'Thin film fabrication and texture effect of a model spin crossover system'***

2011 - ACIN 2011- First international symposium on advanced complex inorganic nanomaterials; Namur (Belgium)

21. ***'Superlative scaffold of 1,2,4-triazole -amino-acid steering molecular architecture of new coordination polymers'***

2011 - ACIN 2011- First international symposium on advanced complex inorganic nanomaterials; Namur (Belgium)

22. ***'Hysteretic spin transition materials with tuneable transition temperatures'***

2011 - ACIN 2011- First international symposium on advanced complex inorganic nanomaterials; Namur (Belgium)

23. ***'Low-spin state stabilization by water release on a 1D Iron(II) coordination polymer'***

2011 - ICAME 2011- International Conference on Applications of the Mössbauer Effect, Kobe (Japan)

24. ***'Weak cooperativity in iron(II) 1D coordination polymers'***

2011 - ICAME 2011- International Conference on Applications of the Mössbauer Effect, Kobe (Japan)

Appendix

Crystal structure data

Table 1 Crystallographic data and structure refinement for $[Cu(NH_2trz)_3]ZrF_6 \cdot H_2O$ (**11**) and $[Cu(NH_2trz)_3](NO_3)_2 \cdot H_2O$ (**18**).

	11	**18**
Empirical formula	$C_6H_{14}OCuN_{12}ZrF_6$	$C_6\ H_{13}\ Cu\ N_{14}\ O_7$
T [K]	100(1)	293(2)
M [g/mol]	539.05	456.84
Crystal system	monoclinic	monoclinic
Space group	$P2_1/n$ (n° 14)	C 2/c (n°15)
a [Å]	10.997(4)	16.635(6)
b [Å]	7.771(3)	13.223(4)
c [Å]	19.421(8)	7.805(3)
β [°]	91.39(2)	102.56(3)
V [$Å^3$]	1659.2(1)	1675.7(1)
Z, D [$g.cm^{-3}$]	4, 2.158	4, 1.811
Crystal size [mm]	0.40 x 0.10 x 0.06	0.1 x 0.1 x 0.9
F(000), Reflections collected	1060, 15701	928, 873
Independent reflections	3352	873
No. parameters, Goodness of fit on F^2	291, 1.172	149, 1.076
R1, *w*R2 [I>2σ(I)]	0.0382, 0.1061	0.0534, 0.1423
Largest peak and hole [$e.Å^{-3}$]	0.86, -0.88	0.986, -0.631

Table 2 (a) Selected bond distances (Å) and (b) inter-atomic distances (up to 3.2 Å) and angles (°) for hydrogen bonds interactions in $[Cu(NH_2trz)_3]ZrF_6 \cdot H_2O$ (**11**).

(a)

		N11-N12	1.388(4)
Cu1••• Cu2	3.8850(3)	N11-C15	1.310(4)
		N12-C13	1.311(4)
Bond lengths		N14-C13	1.345(4)
Cu1-N1	2.299(3)	N14-N16	1.417(4)
Cu1-N21	2.080(3)	N14-C15	1.351(4)
Cu2-N2	2.023(3)	N21-N22	1.374(4)
Cu2-N12	2.385(3)	N21-C25	1.317(4)
Cu2-N22	2.029(3)	N22-C23	1.322(4)
Cu1-N11	2.014(3)	N24-N26	1.415(4)
		N24-C25	1.352(4)
		C23-N24	1.346(4)

(b)

D – H	D – H	H ••• A	<D H A	D•••A	A
N6-H6A	0.87	2.00	163	2.845	F4
N6-H6B	0.77	2.21	154	2.924	F2 [x, y-1, z]
N16-H16A	0.84	2.06	166	2.882	F5 [x, y-1, z]
N16-H16B	0.87	2.08	166	2.924	F4 [-x+3/2, y-1/2, -z+1/2]
N26-H26A	0.84	2.10	156	2.888	F3 [x+1, y, z]
N26-H26A	0.84	2.58	122	3.109	
N26-H26B	0.95	1.89	171	2.835	F1 [-x+3/2, y-1/2, -z+1/2]
O1-H100	0.90	1.94	169	2.836	F1 [x+1, y-1, z]
O1-H101	0.93	2.00	146	2.824	N6 [-x+1, -y-1, -z]
O1-H101	0.93	2.34	130	3.029	F2 [x, y-1, z]
C3-H3	0.95	2.19	152	3.066	F4 [x, y-1, z]
C5-H5	0.95	2.12	176	3.067	O1 [x, 1+y, z]
					O1 [x, y, z]

Table 20 (a) Selected bond distances (Å) and angles (°); (b) Inter-atomic distances (Å) and angles (°) for hydrogen bonds interactions in $[Cu(NH_2trz)_3]NO_3 \cdot H_2O$ (**18**).

(a)

Bond lengths		**Bond Angles**			
Cu1-N3	2.372(4)	N4-Cu1-N4	180.0(4)	C3-N7-N7	106.7(3)
Cu1-N4	1.991(4)	N4-Cu1-N7	90.53(17)	C3-N7-Cu1	126.0(4)
Cu1-N7	2.081(4)	N4-Cu1-N7	89.47(17)	N7-N7-Cu1	126.81(13)
N3-N4	1.391(5)	N7-Cu1-N7	180.0(3)	N7-C3-N6	110.6(6)
N4-C2	1.300(8)	N4-Cu1-N3	89.88(17)	O2-N8-O1	118.4(10)
N5-N6	1.402(10)	N4-Cu1-N3	90.12(17)	O2-N8-O3	122.3(11)
N6-C3	1.344(7)	N7-Cu1-N3	87.10(16)	O1-N8-O3	119.2(11)
N7-C3	1.305(7)	N7-Cu1-N3	92.60(16)	C3-N6-N5	127.4(4)
N7-N7	1.385(8)	N3-Cu1-N3	180.0(3)	C3-N6-N5	127.4(4)
N8-O1	1.204(9)	C2-N2-C1	105.5(5)	C3-N6-C3	105.3(7)
N8-O2	1.195(12)	C2-N2-N1	128.1(5)	N4-C2-N2	110.2(5)
N8-O3	1.225(10)	C1-N3-N4	126.2(5)	C2-N4-N3	107.0(5)
		C1-N3-N4	106.0(4)	C2-N4-Cu1	128.3(4)
		C1-N3-Cu1	128.1(4)	N3-N4-Cu1	124.4(3)
		N4-N3-Cu1	125.4(3)	N3-C1-N2	111.2(5)

(b)

D – H	D – H	H ••• A	<D H A	D•••A	A
N5-H5A	0.86	3.023	89	3.126	O1 [-0.5+x, 0.5-y, -0.5+z]
N5-H5A	0.86	3.023	89	3.126	O1 [0.5-x, 0.5-y, 1-z]
N1-H1A	0.86	3.102	90	3.224	O3 [0.5-x, 0.5-y, -z]
N5-H5A	0.86	2.720	125	3.229	O2 [0.5-x, 0.5+y, 0.5-z]
N5-H5A	0.86	2.720	119	3.229	O2 [-0.5+x, 0.5+y, z]
C2-H2	1.01	2.974	87	3.087	O1 [0.5-x, 0.5-y, -z]
C3-H3	0.90	2.963	87	3.048	O1 [-0.5+x, 0.5-y, -0.5+z]
N1-H1A	0.86	2.312	165	3.151	O1 [x, y, -1+z]
N1-H1A	0.86	3.129	84	3.159	O2 [x, -y, -0.5+z]
C1-H1	1.01	2.248	157	3.125	O3 [x, y, z]
C2-H2	1.01	2.151	163	3.129	O3[x, y, -1+z]
C3-H3	0.90	2.350	162	3.215	O4 [0.5-x, 0.5-y, -z]
O4-H4	0.78	2.648	149	3.339	O1 [1-x, y, 0.5-z]
O4-H4	0.78	2.312	137	2.931	O2 [1-x, y, 0.5-z]

Table 24 Crystallographic data and structure refinement for [Cu(OH-trz)(ReO_4)OH]· $2H_2O$ (**19**) and [$Zn(OHtrz)_2Cl$](NO_3) (**20**).

	19	**20**
Empirical formula	$CuC_2H_2N_3O_8Re$	$ZnC_4H_4ClN_7O_5$
T [K]	293(2)	293(2)
Crystal system	Pnma	P2(1)/m
Space group	Orthorhombic	Monoclinic
a [Å]	12.170(3)	7.3360(15)
b [Å]	6.7591(12)	7.1498(14)
C [Å]	14.587(3)	11.312(2)
α, γ [°]	90.00	90
β [°]	90.00	107.90(3)
V [$Å^3$]	1199.9(4)	564.60(19)
Z, D [g/cm^3]	4, 2.468	2, 1.947
F(000), Reflections collected	812, 1105	328, 620
Independent reflections	1105	620
$2\theta_{max}$ [°]	25.250	4.08 to 20.81
Goodness of fit on F^2	1.141	0.978
R1, *w*R2 [I>2σ(I)]	0.0508, 0.1415	R1 = 0.0452, wR2 = 0.0964
R1, *w*R2 [all data]	0.0740, 0.1592	R1 = 0.0600, wR2 = 0.1007
Largest peak and hole [$e.Å^{-3}$]	1.866 and -1.645	0.520 and -0.641

Table 25 Selected Bond Distances (Å) and Bond Angles (°) in [Cu(OH-trz)(ReO_4)OH]·$2H_2O$, **19**.

Bond lengths		**Bond angles**	
Re1-O2	1.714(15)	O2- Re1- O3	110.2(8)
Re1-O3	1.730(13)	O2- Re1- O4	109.6(4)
Re1-O4	1.736(8)	O3- Re1- O4	108.9(4)
O5-N2	1.550(18)	O4- Re1- O4	109.7(7)
Cu1-O1	1.929(4)	Cu1- O1- Cu1	122.3(4)
Cu1-N1	1.996(8)	O1- Cu1- O1	180.0(4)
C1-N1	1.317(12)	O1- Cu1- N1	92.2(3)
C1-N2	1.322(11)	O1- Cu1- N1	87.8(3)
N1-N1	1.361(15)	N1- C1- N2	110.6(9)
N2-C1	1.322(11)	C1- N1- N1	106.5(5)
		C1- N1- Cu1	132.5(6)
		N1- N1- Cu1	120.4(2)
		C1- N2- C1	105.9(11)
		C1- N2- O5	126.7(6)

Table 26 Inter-atomic distances (Å) and angles (°) for hydrogen bonds interactions in [Cu(OH-trz)(ReO_4)OH]·$2H_2O$, **19.**

D – H	**D – H**	**H ••• A**	**<D H A**	**D•••A**	**A**
C1-H1	0.93	2.794	103	3.135	O1 [1-x, 0.5+y, -z]
C1-H1	0.93	2.713	120	3.274	O2 [1-x, 0.5+y, 1-z]
C1-H1	0.93	2.369	143	3.162	O3 [1.5-x, 2-y, -0.5+z]
C1-H1	0.93	2.822	65	2.569	O5 [x, y, z]

Table 27 Bond lengths (Å) and angles (°) for $[Zn(OHtrz)_2Cl](NO_3)$, **20**.

Bond lengths		Bond angles	
Zn(1)-N(1)#1	2.127(6)	N(3)-Zn(1)-N(3)#1	180.0
Zn(1)-N(1)	2.127(6)	N(1)#1-Zn(1)-Cl(1)#1	88.78(16)
Zn(1)-N(3)	2.150(6)	N(1)-Zn(1)-Cl(1)#1	91.22(16)
Zn(1)-N(3)#1	2.150(6)	N(3)-Zn(1)-Cl(1)#1	91.96(16)
Zn(1)-Cl(1)#1	2.4773(18)	N(3)#1-Zn(1)-Cl(1)#1	88.04(16)
Zn(1)-Cl(1)	2.4773(18)	N(1)#1-Zn(1)-Cl(1)	91.22(16)
Cl(1)-Zn(1)#2	2.4773(18)	N(1)-Zn(1)-Cl(1)	88.78(16)
N(1)-C(1)	1.307(9)	N(3)-Zn(1)-Cl(1)	88.04(16)
N(1)-N(1)#3	1.378(11)	N(3)#1-Zn(1)-Cl(1)	91.96(16)
N(2)-C(1)#3	1.335(9)	Cl(1)#1-Zn(1)-Cl(1)	180.00(15)
N(2)-C(1)	1.335(9)	Zn(1)#2-Cl(1)-Zn(1)	92.36(9)
N(2)-O(1)	1.381(11)	C(1)-N(1)-N(1)#3	107.3(4)
N(3)-C(2)	1.295(10)	C(1)-N(1)-Zn(1)	131.5(5)
N(3)-N(3)#3	1.380(11)	N(1)#3-N(1)-Zn(1)	121.09(15)
N(4)-C(2)	1.349(10)	C(1)#3-N(2)-C(1)	107.8(8)
N(4)-C(2)#3	1.349(10)	C(1)#3-N(2)-O(1)	126.1(4)
N(4)-O(2)	1.371(12)	C(1)-N(2)-O(1)	126.1(4)
N(5)-O(3)	1.187(12)	C(2)-N(3)-N(3)#3	107.4(4)
N(5)-O(5)	1.235(14)	C(2)-N(3)-Zn(1)	131.9(5)
N(5)-O(4)	1.270(13)	N(3)#3-N(3)-Zn(1)	120.69(16)
Bond angles		C(2)-N(4)-C(2)#3	106.0(10)
N(1)#1-Zn(1)-N(1)	180.0(1)	C(2)-N(4)-O(2)	127.0(5)
N(1)#1-Zn(1)-N(3)	91.0(2)	C(2)#3-N(4)-O(2)	127.0(5)
N(1)-Zn(1)-N(3)	89.0(2)	N(1)-C(1)-N(2)	108.7(7)
N(1)#1-Zn(1)-N(3)#1	89.0(2)	N(3)-C(2)-N(4)	109.6(7)
N(1)-Zn(1)-N(3)#1	91.0(2)	O(3)-N(5)-O(5)	122.4(12)

Table 31 Crystallographic data and structure refinement for 4-(3'-N-phtalimido-propyl)-1,2,4-triazole (**phtptrz**), $[Cu_3(phtptrz)_{10}(H_2O)_2](SiF_6)_3 \cdot 44H_2O$ (**28**) and $[Cu_3(phtptrz)_{10}(H_2O)_2](SiF_6)_3 \cdot 44H_2O$ (**29**).

	phtptrz	**28**	**29**
Empirical formula	$C_{13}H_{12}N_4O_2$	$C_{65}H_{106}Cu_{1.5}F_9N_{20}O_{33}Si_{1.5}$	$C_{52}H_{67}Cu_{1.5}F_9N_{16}O_{19.5}Zr_{1.5}$
T[K]	293(2)	120(2)	293(2)
Crystal system	$P2_1/a$	P-1	P-1
Space group	monoclinic	triclinic	Triclinic
a [Å]	12.159(5)	14.164(4)	12.596(5)
b [Å]	7.255(3)	17.830(5)	14.637(5)
c [Å]	14.121(6)	19.554(7)	18.010(7)
α [°]	90.00	104.7	93.419
γ [°]	90.00	109.78	97.07
β [°]	110.27	92.75	91.72
V [$Å^3$]	1168.5(8)	4446	3287
Z, D [g/cm^3]	4, 1.457	4, 1.497	2, 1.648
Reflections collected/unique	2235/2066	2235/15244	12931/93323
$2\theta_{max}$ [°]	26.39	25.35	26.38
Goodness of fit on F^2	1.064	1.083	1.034
R1, *w*R2 [I>2σ(I)]	0.0359, 0.0906	0.0416, 0.1722	R1 = 0.0208, wR2 = 0.0339
R1, *w*R2 [all data]	0.0382, 0.0921	0.0382, 0.1678	R1 = 0.0676, wR2 = 0.1630
Largest peak and hole [$e.Å^{-3}$]	0.227 and -0.174	0.876 and -1.905	0.960 and -1.356

Table 32 Lengths of the bonds (a) and the angles (b) around the Cu_1^{II} and Cu_2^{II} for the compound $[Cu_3(phtptrz)_{10}(H_2O)_2](SiF_6)_3 \cdot 44H_2O$ (**28**).

Bond lengths		**Bond angles**	
Cu1-N42	1.933(3)	N12-Cu1-N22	93.29(14)
Cu1-N32	2.021(3)	N12-Cu1-N32	87.72(14)
Cu1-N22	1.933(4)	N12-Cu1-N42	94.99(14)
Cu1-N12	2.258(4)	N12-Cu1-O1	94.77(14)
Cu1-O1	1.998(3)	N22-Cu1-N32	91.69(15)
Cu1-O2	2.558(3)	N32-Cu1-N42	90.73(14)
		N42-Cu1-O1	90.63(14)
		O1-Cu1-N22	86.60(15)
		N12-Cu1-O2	175.10(13)
Cu1···Cu2	2.035		
Cu2-N42	1.998(3)	N52-Cu2-N42	91.7
Cu2-N32	2.100(4)	N52-Cu2-N32	85.5
Cu2-N52	2.378(4)	N32-Cu2-N42	90.8

Table 33 Inter-atomic distances (Å) and angles (°) for the interactions through hydrogen bonds for $[Cu_3(phtptrz)_{10}(H_2O)_2](SiF_6)_3.44H_2O$ (**28**).

D-H	d(D-H)	d(H•••A)	<DHA	d(D•••A)	A
O1-H1A	0.81	2.006	160.91	2.784	O64 [x, y-1, z]
O60-H60A	0.917	2.092	139.59	2.853	O319 [-x, -y, -z]
O61-H61A	0.922	1.988	155.87	2.855	F1 [-x+1, -y, -z+1]
O61-H61A	0.922	2.414	134.03	3.126	F2 [-x+1, -y, -z+1]
O61-H61B	0.986	1.845	148.15	2.732	O81 [-x, -y, -z+1]
O62-H62A	0.916	1.893	176.65	2.808	F7[-x+1, -y, -z+1]
O62-H62B	0.921	1.912	167.69	2.818	O70 [-x+1, -y+1, -z+1]
O63-H63A	0.922	2.118	156.11	2.985	[x+1, y, z]
O65-H65B	0.909	1.892	158.69	2.759	F3 [x, y+1, z]
O69-H69B	0.924	1.88	161.25	2.77	O61 [-x+1, -y+1, -z+1]
O71-H71B	0.93	1.865	166.81	2.779	F4 [-x+1, -y, -z]
O73-H73A	1	2.258	151.5	3.194	O519 [-x+1, -y+1, -z]
O73-H73B	1	1.836	164.07	2.822	O419 [-x, -y+1, -z]
O74-H74A	1	2.468	163.49	3.462	O75 [-x+2, -y+2, -z+1]
O74-H74A	1	2.618	110.62	3.129	O74 [-x+2, -y+2, -z+1]
O76-H76A	0.932	2.514	153.78	3.376	O80 [x, y+1, z]
O76-H76B	0.941	1.747	173.14	2.684	F10 [-x+1, -y+1, -z+1]
O77-H77A	0.924	2.012	146.13	2.827	N12 [x+1, y+1, z]
O77-H77B	0.95	1.905	156.55	2.802	O61 [-x+1, -y+1, -z+1]
O81-H81A	0.987	2.38	133.85	3.146	O74 [x-1, y-1, z]
O81-H81A	0.987	2.619	154.26	3.534	O80 [x-1, y, z]
O81-H81B	0.979	2.007	141.13	2.836	O74 [-x+1, -y+1, -z+1]

Table 34 Lengths of the bonds (Å) (a) and the angles (°) (b) around the Cu_1^{II} and Cu_2^{II} for the compound $[Cu_3(phtptrz)_8(H_2O)_4](ZrF_6)_3 \bullet 19H_2O$ (**29**).

Bond lengths		**Bond angles**	
Cu1-N11	2.019(3)	N41-Cu1-N11	90.11(13)
Cu1-N21	2.028(4)	N41-Cu1-N21	96.31(13)
Cu1-N31	2.026(4)	N41-Cu1-N31	89.07(13)
Cu1-N41	2.266(4)	N41-Cu1-N51	91.07(13)
Cu1-N51	2.005(4)	N41-Cu1-O1	175.30(11)
Cu1-O1	2.468(4)	N11-Cu1-N21	92.88(13)
		N21-Cu1-N51	88.32(14)
		N51-Cu1-N31	88.82(14)
		N31-Cu1-N11	88.86(13)
Cu···Cu	3.852	N31-Cu2-N11	91.60(13)
Cu2-N11	2.035(3)	N31-Cu2-N21	93.44(14)
Cu2-N31	2.021(3)	N31-Cu2-N'11	88.40(13)
Cu2-N21	2.429(4)	N31-Cu2-N'21	86.56(14)
		N11-Cu2-N21	89.26(14)
		N21-Cu2-N'11	90.74(14)
		N'11-Cu2-N'21	89.26(14)
N31-Cu2-N'31	180.0(3)	N'21-Cu2-N11	90.74(14)

Table 36 Crystallographic data and structure refinements for ethyl-4H-1,2,4-triazol-4-yl acetic acid (**HGlytrz)** and ethyl-4H-1,2,4-triazol-4-yl-acetate (**GlytrzE)**.

	HGlytrz	**GlytrzE**
Empirical formula	$C_4H_5N_3O_2$	$C_6 H_9 N_3 O_2$
T [K]	120(2)	293(2)
M [g/mol]	127.11	155.16
Crystal system	orthorhombic	tetragonal
Space group	Fdd2 (n° 43)	P 41 (n° 76)
a [Å]	22.360(8)	9.025(4)
b [Å]	19.782(8)	9.025(4)
c [Å]	4.691(2)	10.200(4)
α, γ, β [°]	90	90
V [$Å^3$]	2075(1)	830.8(6)
Z, D [g/cm^3]	16, 1.628	4, 1.241
Reflections collected/unique	3210, 1056	9692
Goodness of fit on F^2	1.267	1.060
R1, *w*R2 [I>2σ(I)]	0.0341, [1.008]	0.0522, 0.1450
R1, *w*R2 [all data]	0.0342, 0.0909	0.0565, 0.1509
Largest peak and hole [$e.Å^{-3}$]		0.132 and -0.150

Table 37 Selected bond distances (Å) and bond angles (°) in ethyl-4H-1,2,4-triazol 4-yl acetic acid (**HGlytrz**) and ethyl-4H-1,2,4-triazol-4-yl-acetate (**GlytrzE**).

HGlytrz	
N1-C5	1.311(3)
N1-N2	1.388(2)
N2-C3	1.312(3)
N4-C5	1.348(3)
N4-C3	1.360(2)
N4-C6	1.457(3)
C6-C7	1.527(3)
C7-O9	1.215(3)
C7-O8	1.307(2)

C5-N1-N2	108.74(17)
C3-N2-N1	105.37(17)
C5-N4-C3	105.63(17)
C5-N4-C6	126.18(17)
C3-N4-C6	127.58(17)
N2 -C3-N4	110.98(18)
N1-C5-N4	109.27(17)
N4-C6-C7	110.61(17)
O9-C7-O8	122.63(18)
O9-C7-C6	121.88(17)
O8-C7-C6	115.47(17)

GlytrzE			
N1-C5	1.296(5)	C6-H6B	1.02(6)
N1-N2	1.383(5)	C7-O8	1.202(4)
N2-C3	1.306(5)	C7-O9	1.312(4)
C3-N4	1.348(5)	O9-C10	1.467(7)
C3-H3	1.06(7)	C10-C11	1.263(10)
N4-C5	1.351(5)	C10-H10A	0.970(0)
N4-C6	1.452(4)	C10-H10B	0.970(0)
C5-H5	1.06(6)	C11-H11A	0.960(0)
C6-C7	1.485(5)	C11-H11B	0.960(0)
C6-H6A	0.88(7)	C11-H11C	0.960(0)

C5-N1-N2	106.5(3)	N4-C6-C7	111.7(3)
C3-N2-N1	106.9(3)	N4-C6-H6A	105(4)
N2-C3-N4	110.7(3)	C7-C6-H6A	116(4)
N2-C3-H3	130(3)	N4-C6-H6B	115(3)
N4-C3-H3	120(3)	C7-C6-H6B	101(4)
C3-N4-C5	104.4(3)	H6A-C6-H6B	108(5)
C3-N4-C6	127.6(3)	O8-C7-O9	124.6(3)
C5-N4-C6	127.9(3)	O8-C7-C6	125.9(3)
N1-C5-N4	111.4(3)	O9-C7-C6	109.5(3)
N4-C5-H5	116(3)	C7-O9-C10	117.6(4)
		C11-C10-O9	115.2(6)

Table 38 Inter-atomic distances (Å) and angles (°) for the interactions through hydrogen bonds for **HGlytrz** and **GlytrzE**.

HGlytrz					
D–H	**d(D – H)**	**d(H•••A)**	**< DHA**	**d(D•••A)**	**Symmetry to apply to A**
O8-H8	1.02(2)	1.56(2)	171(2)	2.570(3)	N1 [x+1/y, 1/y-y, z-3/4]
C3-H3	1.01(2)	2.27(3)	129(2)	3.007(3)	O9 [-x, 0.5-y, z-0.5]
C5-H5	1.04(3)	2.45(3)	130(2)	3.213(3)	O8 [¼-x, y-1/4, 3/4+z]
GlytrzE					
C10 - H10A	0.97(2)	2.310(2)	102(2)	2.691(9)	O8 [x, y, z]
C3 - H3	1.06(1)	2.390(2)	156(2)	3.378(6)	N2 [y, 1-x, -1/4+z]
C6 – H6B	1.02(2)	2.446(3)	162(1)	3.426(5)	N1 [y, 1-x, -1/4+z]
C5 – H5	1.05(1)	2.496(2)	136(2)	3.326(5)	O8 [1-y, -1+x, 1/4+z]

Table 39 Crystallographic data and structure refinements for [Cd(HGlytrz)(Glytrz)Cl]·2H_2O, (**30**) and $[Cd_2(Glytrz)_2Cl_2]$, (**31**) and [$Cu_3(\mu_3$-O)(HGlytrz)$_6$·(H_2O)$_3$]BF_4·H_2O, (**32).**

	30	**31**	**32**
Empirical formula	$C_8H_8ClN_6O_6Cd$	$C_4H_4N_3O_2ClCd$	$C_2H_2B_{0.25}Cu_{0.5}FN_{1.5}O_{2.17}$
T [K]	293(2)	293(2)	120(2)
M (g/mol)	432.05	273.95	135.19
Crystal system	Monoclinic	Orthorhombic	Cubic
Space group	*P*2(1)/c, (n°14)	$P2_12_12_1$, (n°19)	$I\bar{4}3m$, (n°217)
a, b, c [Å]	12.164(2), 7.67(2), 15.945(3)	7.590(4), 6.432 (2), 31.963(6)	21.037(6) Å
α, γ [°]	90	90	90
β [°]	101.51(3)	90	90
V/Å^3	1457.4(5)	1560.3(1)	9310(5)
Z	4	8	1.427
D (g/cm^3)	1.969	2.332	1.16
F(000)	844	1040	3196
Reflections collected/unique	16333/5006	3618/1493	23138/967
Goodness of fit on F^2	1.037	1.256	1.065
R1, *w*R2 [I>2σ(I)]	0.0436, 0.1134	0.0325, 0.0850	0.0626,[922]
R1, *w*R2 [all data]	0.0548, 0.1187	0.0461, 0.1049	0.0647, 0.1717
Largest peak and hole [e.Å^{-3}]	1.174, -1.681	0.623, -0.583	0.62, -0.59

Table 40 Selected bond distances (Å) and bond angles (°) in [Cd(HGlytrz)(Glytrz)Cl]·2H_2O (**30**).

Bond lengths		**Bond angles**	
Cd1- N2	2.312(3)	N5- Cd1- Cl1	100.58(8)
Cd1- N5	2.339(3)	N1- Cd1- Cl1	91.90(8)
Cd1- N1	2.343(3)	N4- Cd1- Cl1	85.10(8)
Cd1-N4	2.371(3)	N2 -Cd1 -Cl1	93.73(8)
Cd1- Cl1	2.6159(10)	N5- Cd1- Cl1	85.48(8)
Cd1- Cl1	2.6555(10)	N1- Cd1- Cl1	85.92(8)
N1- N2	1.387(4)	N4- Cd1- Cl1	88.80(8)
N2- Cd1	2.312(3)	Cl1- Cd1- Cl1	173.657(15)
N4- N5	1.375(4)	C1- N1- Cd1	129.3(2)
N5- Cd1	2.339(3)	N2- N1- Cd1	123.5(2)
O1- C4	1.255(5)	C2- N2- Cd1	132.4(2)
O2- C4	1.251(4)	N1- N2- Cd1	120.24(19)
O3- C8	1.306(4)	C5- N4- Cd1	125.0(2)
O4- C8	1.206(4)	N5- N4- Cd1	124.7(2)
Cl1- Cd1	2.6159(10)	C6- N5- Cd1	133.7(2)
Bond angles		N4- N5- Cd1	118.3(2)
N2- Cd1- N5	92.10(11)	Cd1- Cl1- Cd1	93.67(4)
N2- Cd1- N1	175.61(10)	O2 -C4- O1	127.0(4)
N5- Cd1- N1	92.24(11)	O2- C4- C3	114.7(3)
N2- Cd1- N4	89.59(10)	O1- C4- C3	118.3(3)
N5 -Cd1- N4	174.13(10)	O4- C8- O3	127.0(4)
N1- Cd1- N4	86.03(10)	O4- C8- C7	123.0(3)
N2 -Cd1- Cl1	87.99(8)	O3- C8- C7	110.0(3)

Table 41 Selected bond distances (Å) and bond angles (°) in $[Cd_2(Glytrz)_2Cl_2]$, (**31**).

Bond lengths		Bond angles	
Cd(1)-N(1)	2.294(12)	N(5)-N(4)-Cd(2)	125(1)
Cd(1)-N(5)#1	2.367(14)	N(4)-N(5)-Cd(1)#4	124 (1)
Cd(1)-O(4)#2	2.385(11)	O(1)-C(4)-O(2)	124(1)
Cd(1)-O(3)#2	2.405(10)	N(1)-Cd(1)-N(5)#1	88.9(5)
Cd(1)-Cl(2)#1	2.519(4)	N(1)-Cd(1)-O(4)#2	97.0(4)
Cd(1)-Cl(1)	2.571(5)	N(5)#1-Cd(1)-O(4)#2	80.6(4)
Cd(1)-C(8)#2	2.698(18)	N(1)-Cd(1)-O(3)#2	152.3(4)
Cd(2)-O(2)#3	2.269(10)	N(5)#1-Cd(1)-O(3)#2	85.8(4)
Cd(2)-N(4)	2.284(12)	O(4)#2-Cd(1)-O(3)#2	55.4(4)
Cd(2)-N(2)	2.372(13)	N(1)-Cd(1)-Cl(2)#1	105.7(3)
Cd(2)-O(1)#3	2.519(9)	N(5)#1-Cd(1)-Cl(2)#1	89.0(3)
Cd(2)-Cl(1)	2.549(4)	O(4)#2-Cd(1)-Cl(2)#1	154.8(3)
Cd(2)-Cl(2)	2.610(4)	O(3)#2-Cd(1)-Cl(2)#1	101.3(3)
Cl(2)-Cd(1)#4	2.519(4)	N(1)-Cd(1)-Cl(1)	90.6(3)
O(1)-C(4)	1.212(18)	N(5)#1-Cd(1)-Cl(1)	173.3(3)
O(1)-Cd(2)#5	2.519(9)	O(4)#2-Cd(1)-Cl(1)	92.9(3)
O(2)-Cd(2)#5	2.269(10)	O(3)#2-Cd(1)-Cl(1)	91.6(3)
O(3)-Cd(1)#6	2.405(10)	Cl(2)#1-Cd(1)-Cl(1)	97.6(2)
O(4)-Cd(1)#6	2.385(11)	O(2)#3-Cd(2)-N(4)	156.4(4)
N(1)-N(2)	1.406(16)	O(2)#3-Cd(2)-N(2)	91.0(4)
N(4)-N(5)	1.414(16)	N(4)-Cd(2)-N(2)	89.2(5)
N(5)-Cd(1)#4	2.367(13)	O(2)#3-Cd(2)-O(1)#3	54.4(3)
		N(4)-Cd(2)-O(1)#3	102.7(4)
Bond angles		N(2)-Cd(2)-O(1)#3	79.0(4)
Cd(2)-Cl(1)-Cd(1)	104.8(2)	O(2)#3-Cd(2)-Cl(1)	98.3(3)
Cd(1)#4-Cl(2)-Cd(2)	106.4(2)	N(4)-Cd(2)-Cl(1)	105.3(3)
N(2)-N(1)-Cd(1)	122.5(9)	N(2)-Cd(2)-Cl(1)	89.8(3)
N(1)-N(2)-Cd(2)	125(10)	O(1)#3-Cd(2)-Cl(1)	149.7(3)

Table 43 Selected bond distances (Å) and bond angles (°) in $[Cu_3(\mu_3\text{-}O)(HGlytrz)_6 \cdot (H_2O)_3]BF_4 \cdot H_2O$ (**32**).

Bond lengths	
Cu1-O9	1.944(11)
Cu1-O10	1.946(2)
Cu1-N2	1.950(9)
Cu1-O100	2.32(2)
N2-C3	1.315(15)
N2-N2	1.368(18)
C3-N4	1.310(14)
N4-C3	1.310(14)
N4-C6	1.482(19)
C7-O8	1.19(2)
C7-O9	1.274(19)
B1-F2	1.308(13)

Bond angles	
O9-Cu1-O10	176.7(14)
O9-Cu1-N2	90.7(3)
O10-Cu1-N2	89.2(3)
N2-Cu1-N2	175.8(6)
O9-Cu1-O100	94.7(7)
O10-Cu1-O100	88.7(14)
N2-Cu1-O100	91.9(3)
Cu1-O10-Cu1	119.85(18)
C3-N2-Cu1	133.0(8)
N2-N2-Cu1	120.9(3)
C7-O9-Cu1	116.2(11)
O8-C7-O9	124.7(15)
O8-C7-C6	121.5(15)
O9-C7-C6	113.8(13)

Appendix

Mösbauer Data

Table 4 Overview of the ^{57}Fe Mössbauer parameters for **4** on warming and cooling modes over the temperature range 78-300 K.

T **[K]**	***δ*** **[mm/s]**	***ΔE$_Q$*** **[mm/s]**	***Γ/2*** **[mm/s]**	**Relative Area [%]**	**Sites**
78(1) ↑	1.15(1)	3.41(2)	0.17(1)	7	HS
	0.53(1)	0.29(1)	0.15(1)	93	LS
100(1) ↑	1.16(1)	3.40(1)	0.18(3)	7.7	HS
	0.52(2)	0.29(1)	0.14(2)	92.3	LS
110(1) ↑	1.14(1)	3.40(1)	0.16(2)	7.0	HS
	0.52(1)	0.29(2)	0.15(1)	93.0	LS
120(1) ↑	1.13(2)	3.42(3)	0.17(2)	7.0	HS
	0.52(1)	0.28(2)	0.15(1)	93.0	LS
160(1) ↑	1.13(3)	3.33(3)	0.18(1)	12.0	HS
	0.51(1)	0.28(3)	0.14(1)	88.0	LS
183(1) ↑	1.11(1)	3.25(1)	0.16(1)	15.3	HS
	0.50(2)	0.27(1)	0.15(3)	84.7	LS
220(1) ↑	1.09(1)	3.08(1)	0.15(1)	43.0	HS
	0.48(1)	0.27(1)	0.13(1)	57.0	LS
240(1) ↑	1.08(1)	3.01(1)	0.14(1)	82.0	HS

	0.47(1)	0.26(1)	0.14(1)	18.0	LS
260(1) ↑	1.07(1)	2.91(1)	0.13(1)	96.0	HS
	0.40(2)	0	0.14(2)	4.0	LS
263(1) ↑	1.18(1)	3.03(1)	0.18(1)	96.3	HS
	0.7*	0.2*	0.51(5)	3.7	LS
280(1) ↑	1.05(1)	2.83(1)	0.14(5)	100.0	HS
300(1)	1.05(1)	2.77(1)	0.13(1)	100.0	HS
263(1) ↓	1.16(1)	3.03(1)	0.21(1)	98.8	HS
	0.52(6)	0	0.10(1)	1.2	LS
243(1) ↓	1.21(3)	3.11(1)	0.21(1)	98.1	HS
	0.54(7)	0.24(1)	0.10(1)	1.9	LS
223(1) ↓	1.22(1)	3.19(1)	0.22(1)	95.0	HS
	0.57(3)	0.29(2)	0.13(2)	5.0	LS
203(1) ↓	1.24(8)	3.28(2)	0.23(5)	70.3	HS
	0.51(2)	0.25(1)	0.15(9)	29.7	LS
183(1) ↓	1.21(2)	3.14(2)	0.23(1)	65.0	HS
	0.51(3)	0.24(3)	0.2*	35.0	LS
163(1) ↓	1.27(2)	3.44(2)	0.24(1)	31.0	HS
	0.52(1)	0.26(1)	0.22*	69.0	LS
120(1) ↓	1.12 (2)	3.42(2)	0.20(1)	9.1	HS
	0.55(2)	0.27(1)	0.15(1)	90.9	LS

Table 5 Overview of the ^{57}Fe Mössbauer parameters for **1**.

T [K]	δ [mm/s]	ΔE_Q [mm/s]	$\Gamma/2$ [mm/s]	Relative Area [%]	Sites
78(1) ↑	1.15(1)	3.55(2)	0.16(1)	16	HS
	0.53(4)	0.29(1)	0.14(2)	84	LS
150(1) ↑	1.13(1)	3.45(4)	0.18(1)	22.6	HS
	0.51(2)	0.28(1)	0.15(1)	77.4	LS
163(1) ↑	1.55(6)	3.67(1)	0.21(2)	32.3	HS
	0.77(1)	0.26(4)	0.16(1)	66.8	LS
183(1) ↑	1.52(2)	3.60(3)	0.25(2)	34.3	HS
	0.76(8)	0.22(1)	0.22*	65.7	LS
198(1) ↑	1.52(3)	3.51(6)	0.22(5)	49	HS
	0.76(4)	0.24(5)	0.18*	51	LS
240(1) ↑	1.08(2)	3.01(1)	0.14(6)	82.1	HS
	0.34(2)	0.1*	0.59(3)	17.9	LS
243(1) ↑	1.47(2)	3.24(4)	0.21(5)	94	HS
	0.72(3)	0.07(1)	0.20(1)	6	LS
250(1) ↑	1.07(1)	2.95(1)	0.15(1)	94.5	HS

	0.51*	0.26(2)	0.2*	5.5	LS
260(1) ↑	1.00(5) 0.46(1)	2.92(1) 0.49(3)	0.13(4) 0.16(2)	95 5	HS LS
280(1) ↑	1.05(6) 0.36(1)	2.83(3) 0.44(2)	0.13(5) 0.16(2)	96.6 3.4	HS LS
300(1)	1.04(1)	2.76(1)	0.13(2)	100	HS
273(1) ↓	1.44(1) 0.64 (5)	3.09(1) 0	0.18(1) 0.09(1)	98.8 1.2	HS LS
243(1) ↓	1.47(3) 0.76(4)	3.23(3) 0.22(2)	0.19(1) 0.11(9)	95.9 4.1	HS LS
223(1) ↓	1.49(1) 0.74(6)	3.32(1) 0.20(2)	0.22(1) 0.17(2)	90 10	HS LS
220(1) ↓	1.09(8) 0.48(2)	3.06(2) 0.20(9)	0.15(5) 0.15(9)	87.7 12.3	HS LS
200(1) ↓	1.05(2) 0.51(1)	3.18(2) 0.22(1)	0.15(1) 0.14(2)	71.3 28.7	HS LS
198(1) ↓	1.15(2) 0.77(1)	3.48(1) 0.22(1)	0.23(1) 0.18*	65.6 34.4	HS LS
183(1) ↓	1.53(2) 0.76(2)	3.59(2) 0.25(1)	0.23(2) 0.17*	42.8 57.2	HS LS

Table 6 Overview of the ^{57}Fe Mössbauer parameters for **2**.

T [K]	δ [mm/s]	ΔE_Q [mm/s]	$\Gamma/2$ [mm/s]	Relative Area [%]	Sites
78(1) ↑	1.16(1)	3.52(1)	0.17(1)	27	HS
	0.53(1)	0.30(1)	0.14(2)	73	LS
100(1) ↑	1.03(2)	3.50(1)	0.18(1)	26	HS
	0.40(1)	0.30(1)	0.14(1)	74	LS
120(1) ↑	1.15(2)	3.49(1)	0.18(2)	28	HS
	0.52(1)	0.30(1)	0.14(1)	72	LS
140(1) ↑	1.14(2)	3.44(1)	0.18(1)	31	HS
	0.52(1)	0.29(2)	0.14(1)	69	LS
160(1) ↑	1.12(1)	3.38(1)	0.17(1)	37	HS
	0.52(1)	0.28(1)	0.15(1)	63	LS
200(1) ↑	1.10(1)	3.19(1)	0.15(1)	73	HS
	0.51(1)	0.24(1)	0.13(2)	27	LS
220(1) ↑	1.09(2)	3.08(42)	0.14(2)	90	HS
	0.48(1)	-	0.21(1)	10	LS
240(1) ↑	1.08(1)	3.00(1)	0.14(1)	94	HS
	0.33(1)	0.38(1)	0.19(1)	6	LS
280(1) ↑	1.05(1)	2.83(1)	0.15(1)	100	HS

300(1)	1.04(1)	2.76(1)	0.14(1)	100	HS
273(1) ↓	1.18(1) 0.48(2)	3.08(1) 0.2*	0.19(1) 0.15(1)	98.1 1.9	HS LS
243(1) ↓	1.21(1) 0.43(1)	3.22(1) 0.13(1)	0.17(1) 0.15(2)	94.3 5.7	HS LS
223(1) ↓	1.24(1) 0.48(1)	3.32(1) 0.18(1)	0.17(1) 0.13(2)	90 10	HS LS
198(1) ↓	1.26(1) 0.51(1)	3.48(1) 0.24(1)	0.18(1) 0.13(1)	64 36	HS LS
178(1) ↓	1.28(1) 0.51(2)	3.62(1) 0.27(1)	0.19(1) 0.14(2)	60 40	HS LS
158(1) ↓	1.30(1) 0.51(1)	3.71(1) 0.28(1)	0.19(1) 0.15(1)	31 69	HS LS

Table 7 Overview of the ^{57}Fe Mössbauer parameters for **3**.

T [K]	δ [mm/s]	ΔE_Q [mm/s]	$\Gamma/2$ [mm/s]	Relative Area [%]	Sites
78(1) ↑	1.16(1)	3.42(1)	0.16(1)	7	HS
	0.53(1)	0.29(1)	0.14(1)	93	LS
90(1) ↑	1.13(2)	3.46(2)	0.21(4)	8.8	HS
	0.52(1)	0.29(1)	0.14(1)	91.2	LS
110(1) ↑	1.14(1)	3.41(1)	0.17(1)	7.4	HS
	0.52(1)	0.28(1)	0.14(1)	93.6	LS
130(1) ↑	1.13(1)	3.40(2)	0.17(1)	7.8	HS
	0.52(1)	0.28(2)	0.14(1)	92.2	LS
150(1) ↑	1.11(1)	3.32(1)	0.17(1)	9	HS
	0.51(1)	0.28(1)	0.14(1)	91	LS
200(1) ↑	1.11(1)	3.14(1)	0.16(1)	22.7	HS
	0.49(1)	0.26(1)	0.13(2)	77.3	LS
220(1) ↑	1.09(1)	3.07(1)	0.15(1)	38	HS
	0.47(1)	0.25(1)	0.13(2)	61	LS
240(1) ↑	1.08(1)	3.00(1)	0.14(2)	57	HS
	0.47(1)	0.25(1)	0.13(1)	43	LS
250(1) ↑	1.07(2)	2.96(2)	0.14(1)	83.4	HS

	0.46(1)	0.25(2)	0.13(2)	16.6	LS
260(1) ↑	1.07(1)	2.92(1)	0.14(1)	90	HS
	0.43(3)	0.35*	0.15*	10	LS
273(1) ↑	1.17(1)	2.99(1)	0.10(1)	97.6	HS
	0.44(2)	-	0.17(2)	2.4	LS
293(1) ↑	1.16(1)	2.91(1)	0.17(1)	98	HS
	0.34(2)	0.18(4)	0.10(4)	2	LS
300(1)	1.04(1)	2.77(1)	0.13(1)	100	HS
280(1) ↓	1.05(1)	2.85(1)	0.13(2)	97	HS
	0.34*	-	0.2*	3	LS
253(1) ↓	1.19(1)	3.08(1)	0.18*	96	HS
	0.41(1)	-	0.12*	4	LS
233(1) ↓	1.21(1)	3.16(2)	0.21(1)	95.4	HS
	0.48(3)	-	0.15(3)	4.6	LS
213(1) ↓	1.23(1)	3.24 (2)	0.20(2)	79	HS
	0.50(1)	0.24(2)	0.15(2)	21	LS
193(1) ↓	1.23(1)	3.27(1)	0.20(1)	47	HS
	0.51(1)	0.25(1)	0.18*	53	LS
153(1) ↓	0.11(1)	3.47(2)	0.20(1)	20	HS
	0.52(1)	0.27(1)	0.16(1)	80	LS

Table 8 Overview of the ^{57}Fe Mössbauer parameters for **5**.

T [K]	δ [mm/s]	ΔE_Q [mm/s]	$\Gamma/2$ [mm/s]	Relative Area [%]	Sites
78(1) ↑	1.16(1)	3.39(3)	0.16(2)	20.4	HS
	0.52(1)	0.31(1)	0.13(1)	79.6	LS
120(1) ↑	1.17(2)	3.32(4)	0.17(3)	23	HS
	0.52(1)	0.32(1)	0.15(1)	77	LS
140(1) ↑	1.13(2)	3.30(4)	0.18(3)	21	HS
	0.52(1)	0.30(1)	0.17(1)	79	LS
173(1) ↑	1.27(1)	3.38(2)	0.21(2)	31	HS
	0.51(1)	0.28(1)	0.16(1)	69	LS
193(1) ↑	1.26(1)	3.33(2)	0.23(2)	35	HS
	0.50(1)	0.26(1)	0.19*	65	LS
200(1) ↑	1.12(1)	3.14(3)	0.17(2)	39.3	HS
	0.49(1)	0.28(1)	0.15(1)	60.7	LS
220(1) ↑	1.10(2)	3.07(4)	0.17(3)	44.6	HS
	0.47(1)	0.28(2)	0.14(2)	55.4	LS
240(1) ↑	1.08(1)	3.00(2)	0.16(1)	80.1	HS
	0.47(4)	0.30(3)	0.17*	19.9	LS

253(1) ↑	1.20(1) 0.44(1)	3.11(1) -	0.24* 0.20(3)	95.3 4.7	HS LS
273(1) ↑	1.19(1) 0.43(1)	3.04(1) -	0.24(1) 0.2*	95.5 4.5	HS LS
300(1)	1.04(1)	2.77(2)	0.14(1)	100	HS
293(1) ↓	1.16(1) 0.44(1)	2.94(1) -	0.23(1) 0.17(2)	96 4	HS LS
273(1) ↓	1.18(1) 0.44(1)	3.01(1) -	0.23(1) 0.21(2)	96.3 3.7	HS LS
253(1) ↓	1.20(1) 0.44(1)	3.10(1) -	0.24* 0.20*	95 5	HS LS
233(1) ↓	1.22(1) 0.44(1)	3.20(1) -	0.24* 0.24(2)	92 8	HS LS
213(1) ↓	1.14(1) 0.50(1)	3.29(2) 0.26(1)	0.24(1) 0.19(1)	54.5 45.5	HS LS
193(1) ↓	1.17(1) 0.51(1)	3.32(3) 0.26(1)	0.24* 0.20(1)	41 59	HS LS
173(1) ↓	1.17(1) 0.50(1)	3.43(2) 0.24(1)	0.22(2) 0.19*	32 68	HS LS

Table 9 Overview of the ^{57}Fe Mössbauer parameters for **6**.

T [K]	δ [mm/s]	ΔE_Q [mm/s]	$\Gamma/2$ [mm/s]	Relative Area [%]	Sites
78(1) ↑	1.17(1)	3.37(1)	0.16(2)	18.5	HS
	0.52(1)	0.31(1)	0.14(1)	81.5	LS
120(1) ↑	1.15(1)	3.34(1)	0.17(1)	19.2	HS
	0.52(1)	0.31(1)	0.13(1)	80.8	LS
143(1) ↑	1.28(1)	3.55(2)	0.18*	20	HS
	0.52(1)	0.26(1)	0.22*	80	LS
150(1) ↑	1.13(1)	3.29(1)	0.16(1)	22	HS
	0.51(1)	0.31(1)	0.13(1)	78	LS
163(1) ↑	1.28(1)	3.46(2)	0.19*	21	HS
	0.51(1)	0.28(1)	0.18(1)	79	LS
183(1) ↑	1.26(1)	3.37(1)	0.19*	22	HS
	0.50(1)	0.28(1)	0.16(1)	78	LS
203(1) ↑	1.24(1)	3.31(2)	0.17*	28.6	HS
	0.50(1)	0.28(1)	0.15(1)	71.4	LS
220(1) ↑	1.09(1)	3.07(1)	0.14(1)	40.2	HS
	0.48(1)	0.27(1)	0.12(1)	59.8	LS
240(1) ↑	1.08(1)	3.01(1)	0.14(1)	77.5	HS

	0.46(1)	0.25(3)	0.15*	22.5	LS
260(1) ↑	1.07(1) 0.47(1)	2.92(1) 0.48(1)	0.13(1) 0.15*	93.7 6.3	HS LS
273(1) ↑	1.18(1) 0.49(1)	3.01(1) 0.30(2)	0.21(1) 0.2*	96 4	HS LS
300(1)	1.04(1) 0.41(4)	2.78(1) 0.30(1)	0.13(1) 0.15*	98 2	HS LS
293(1) ↓	1.16(1) 0.53(1)	2.91(1) -	0.21(1) 0.18*	96 4	HS LS
273(1) ↓	1.18(1) 0.49(1)	3.01(1) -	0.24* 0.2*	96 4	HS LS
253(1) ↓	1.19(1) 0.53(1)	3.08(1) -	0.2* 0.21(1)	96 4	HS LS
223(1) ↓	1.22(1) 0.47(1)	3.18(1) -	0.29(1) 0.2*	96 4	HS LS
203(1) ↓	1.24(1) 0.50(1)	3.27(1) 0.27(1)	0.23(1) 0.16(1)	68.3 31.7	HS LS
183(1) ↓	1.26(1) 0.51(1)	3.32(2) 0.25(1)	0.28(1) 0.21(1)	49 51	HS LS
163(1) ↓	1.26(1) 0.511)	3.45(1) 0.24(1)	0.24(2) 0.25*	29 71	HS LS

Table 10 Overview of the ^{57}Fe Mössbauer parameters for **7**.

T [K]	δ [mm/s]	ΔE_Q [mm/s]	$\Gamma/2$ [mm/s]	Relative Area [%]	Sites
78(1) ↑	1.16(1)	3.41(1)	0.21(1)	38.3	HS
	0.54(1)	0.29(1)	0.14(1)	61.7	LS
110(1) ↑	1.15(1)	3.39(1)	0.20(1)	40	HS
	0.54(1)	0.28(1)	0.15(1)	60	LS
130(1) ↑	1.15(1)	3.38(1)	0.20(1)	40.3	HS
	0.54(1)	0.28(1)	0.15(1)	59.7	LS
150(1) ↑	1.13(1)	3.34(1)	0.19(1)	45	HS
	0.52(1)	0.27(1)	0.15(1)	54	LS
170(1) ↑	1.12(1)	3.28(1)	0.19(1)	52	HS
	0.52(1)	0.26(1)	0.15(1)	48	LS
190(1) ↑	1.12(1)	3.25(1)	0.18(1)	57.5	HS
	0.52(1)	0.26(1)	0.15(1)	42.5	LS
210(1) ↑	1.10(1)	3.16(1)	0.17(1)	77	HS
	0.51(1)	0.23(1)	0.18(1)	23	LS
230(1) ↑	1.09(1)	3.08(1)	0.17(1)	86	HS
	0.48(1)	0.26(1)	0.21(1)	14	LS
250(1) ↑	1.08(1)	3.01(1)	0.18(1)	92	HS
	0.43(1)	0.41(3)	0.18*	8	LS
275(1) ↑	1.06(1)	2.91(1)	0.18(1)	94.4	HS
	0.38(3)	0.36*	0.16*	5.6	LS
300(1) ↑	1.04(1)	2.80(1)	0.18(1)	94.5	HS
	0.28(5)	0.29(1)	0.18*	5.5	LS

Table 11 Overview of the ^{57}Fe Mössbauer parameters for **8**.

T [K]	δ [mm/s]	ΔE_Q [mm/s]	$\Gamma/2$ [mm/s]	Relative Area [%]	Sites
78(1) ↑	1.16(1)	3.43(1)	0.17(1)	28.2	HS
	0.53(1)	0.29(1)	0.13(1)	71.8	LS
137(1) ↑	1.23(1)	3.59(1)	0.26(1)	47.9	HS
	0.45(1)	0.26(1)	0.20(1)	52.1	LS
163(1) ↑	1.21(1)	3.54(4)	0.28(1)	56.4	HS
	0.45(1)	0.26(1)	0.20(1)	43.6	LS
183(1) ↑	1.18(1)	3.45(1)	0.21(1)	76.2	HS
	0.44(1)	0.24(1)	0.15(1)	23.8	LS
203(1) ↑	1.16(1)	3.35(1)	0.23(1)	97.5	HS
	0.44(1)	0.15(1)	0.14(1)	2.5	LS
223(1) ↑	1.15(1)	3.27(1)	0.23(1)	98.5	HS
	0.39(1)	0.15(1)	0.12(1)	1.5	LS
253(1) ↑	1.12(1)	3.16(1)	0.26(1)	100	HS
295(1) ↑	1.03(1)	2.78(1)	0.15(1)	100	HS
203(1) ↓	1.17(1)	3.37(1)	0.21(1)	97.7	HS
	0.36(1)	0.15(1)	0.10(1)	2.3	LS
183(1) ↓	1.18(1)	3.42(1)	0.20(1)	90.5	HS
	0.45(1)	0.26(1)	0.14(1)	9.5	LS
163(1) ↓	1.20(1)	3.52(4)	0.22(1)	61.1	HS
	0.44(1)	0.27(3)	0.15(1)	38.9	LS
147(1) ↓	1.22(1)	3.57(1)	0.25(1)	50.4	HS
	0.45(2)	0.26(2)	0.18(1)	49.6	LS

Table 12 Overview of the ^{57}Fe Mössbauer parameters for **9**.

T [K]	δ [mm/s]	ΔE_Q [mm/s]	$\Gamma/2$ [mm/s]	Relative Area [%]	Sites
80(1) ↑	1.16(1)	3.53(1)	0.17(1)	31.8	HS
	0.53(1)	0.28(1)	0.14(1)	68.2	LS
120(1) ↑	1.14(1)	3.50(1)	0.18(1)	33	HS
	0.52(1)	0.27(1)	0.14(1)	67	LS
160(1) ↑	1.13(1)	3.42(1)	0.18(1)	36	HS
	0.51(1)	0.26(1)	0.15(1)	64	LS
180(1) ↑	1.12(1)	3.38(1)	0.18(1)	38.3	HS
	0.51(1)	0.25(1)	0.14(1)	61.7	LS
200(1) ↑	1.11(1)	3.30(1)	0.18(1)	42.7	HS
	0.50(1)	0.25(1)	0.14(1)	57.3	LS
220(1) ↑	1.10(1)	3.21(1)	0.17(1)	51	HS
	0.50(1)	0.24(1)	0.15(1)	49	LS
240(1) ↑	1.09(1)	3.09(1)	0.16(1)	68.3	HS
	0.50(1)	0.23(1)	0.15(1)	31.7	LS
260(1) ↑	1.08(1)	3.02(1)	0.16(1)	79	HS
	0.47(1)	0.19(1)	0.22(1)	21	LS
280(1) ↑	1.07(1)	2.95(1)	0.15(1)	86.7	HS
	0.42(1)	0.26(1)	0.26(1)	13.3	LS
300(1) ↑	1.06(1)	2.88(1)	0.15(1)	91.3	HS
	0.38(2)	0.35(1)	0.22(1)	8.7	LS

Table 13 Overview of the ^{57}Fe Mössbauer parameters for **10**.

T [K]	δ [mm/s]	ΔE_Q [mm/s]	$\Gamma/2$ [mm/s]	Relative Area [%]	Sites
80(1) ↑	1.16(1)	3.49(1)	0.19(1)	39.2	HS
	0.54(1)	0.28(1)	0.14(1)	60.8	LS
120(1) ↑	1.14(1)	3.47(1)	0.19(1)	40	HS
	0.53(1)	0.27(1)	0.14(1)	60	LS
160(1) ↑	1.13(1)	3.39(1)	0.19(1)	44.2	HS
	0.52(1)	0.26(1)	0.14(1)	55.8	LS
180(1) ↑	1.12(1)	3.33(1)	0.18(1)	47.7	HS
	0.52(1)	0.25(1)	0.14(1)	52.3	LS
200(1) ↑	1.10(1)	3.27(1)	0.18(1)	52.8	HS
	0.51(1)	0.24(1)	0.15(1)	47.2	LS
220(1) ↑	1.10(1)	3.27(1)	0.18(1)	53	HS
	0.51(1)	0.24(1)	0.15(1)	47	LS
240(1) ↑	1.09(1)	3.07(1)	0.16(1)	79.6	HS
	0.50(1)	0.22(1)	0.16(1)	20.4	LS
260(1) ↑	1.08(1)	3.00(1)	0.16(1)	83.2	HS
	0.44(2)	-	0.37(1)	16.8	LS
300(1) ↑	1.06(1)	2.89(1)	0.17(1)	94.2	HS
	0.5*	0.26(4)	0.18*	5.8	LS

Table 22 Overview of the ^{57}Fe Mössbauer parameters for **17** on warming and cooling modes over the temperature range 293 - 380 K.

T [K]	δ [mm/s]	ΔE_Q [mm/s]	$\Gamma/2$ [mm/s]	Relative Area [%]	Sites
293(1)	0.44(1)	0.19(1)	0.16(2)	100	LS
330(1) ↑	0.45(1)	0.18(1)	0.19(1)	100	LS
342(1) ↑	0.98(3)	2.59(1)	0.17(1)	25.7	HS
	0.41(1)	0.16(1)	0.16(1)	74.3	LS
346(1) ↑	1.03(3)	2.59(1)	0.18(2)	38.5	HS
	0.42(1)	0.16(3)	0.15(1)	61.5	LS
351(1) ↑	0.99(1)	2.57(2)	0.16(2)	74.0	HS
	0.41(1)	0.13(2)	0.16(1)	26.0	LS
358(1) ↑	0.99(1)	2.55(1)	0.17(1)	80.0	HS
	0.35(1)	0.19(1)	0.2*	20.0	LS
363(1) ↑	0.99(1)	2.54(1)	0.17(1)	85.3	HS
	0.38(2)	0.19(1)	0.15*	14.7	LS
380(1)	0.97(1)	2.49(1)	0.17(1)	92.0	HS
	0.34(1)	-	0.15*	8.0	LS
361(1) ↓	0.99(1)	2.54(2)	0.17(1)	87.0	HS
	0.37(1)	0.0(1)	0.18(1)	13.0	LS
346(1) ↓	0.99(1)	2.59(2)	0.17(1)	83.6	HS
	0.35(1)	0.16*	0.27(1)	16.4	LS
330(1) ↓	1.00(1)	2.63(2)	0.17(2)	80.8	HS
	0.45(1)	0.29(1)	0.20(1)	19.2	LS
315(1) ↓	1.01(1)	2.69(1)	0.16(1)	28.6	HS
	0.42(1)	0.17(1)	0.16(1)	71.4	LS
305(1) ↓	0.44(1)	0.17(1)	0.20(1)	100	LS
293(1) ↓	0.44(1)	0.19(1)	0.17(2)	100	LS

Table 45 Overview of the ^{57}Fe Mössbauer parameters for $[Fe(GlytrzE)_3](ClO_4)_2$ (**37**) on warming and cooling modes over the temperature range 78-308 K.

T [K]	*δ* [mm/s]	*ΔE*$_Q$ [mm/s]	*Γ*/2 [mm/s]	Relative Area [%]	Sites
78(1) ↑	0.49(1)	0.19(1)	0.15(1)	100	LS
288(1) ↑	0.43(1)	0.19(2)	0.15(1)	100	LS
293(1) ↑	0.46(2)	0.20(1)	0.12(2)	100	LS
298(1) ↑	1.04(1)	2.78(2)	0.16(1)	35.8	HS
	0.42(2)	0.19(1)	0.15(1)	64.2	LS
300(1) ↑	1.03(1)	2.78(1)	0.15(1)	91	HS
	0.34(5)	-	0.18(2)	9	LS
308(1)	1.03(1)	2.74(4)	0.16(1)	100	HS
298(1) ↓	1.03(1)	2.77(1)	0.16(1)	92.6	HS
	0.31(3)	0.21(2)	0.17*	7.4	LS
293(1) ↓	1.04(1)	2.80(1)	0.16(1)	48	HS
	0.43(1)	0.20(1)	0.13(1)	52	LS
288(1) ↓	1.00(1)	2.73(2)	0.15(1)	5.7	HS
	0.43(2)	0.19(2)	0.14(1)	94.3	LS
283(1) ↓	0.43(1)	0.19(1)	0.15(1)	100	LS

Table 46 Overview of the ^{57}Fe Mössbauer parameters for $[Fe(GlytrzE)_3](ClO_4)_2 \cdot CH_3OH$ (**38-GlytrzE-ClO$_4$**) on warming and cooling modes over the temperature range 78-308 K.

T **[K]**	***δ*** **[mm/s]**	***ΔE$_Q$*** **[mm/s]**	***Γ/2*** **[mm/s]**	**Relative Area [%]**	**Sites**
78(1) ↑	0.48(1)	0.20(1)	0.16(1)	100	LS
240(1) ↑	0.47(1)	0.20(1)	0.15(1)	100	LS
260(1) ↑	1.06(1)	2.93(2)	0.17(1)	22.4	HS
	0.49(3)	0.20(1)	0.14(1)	77.6	LS
270(1) ↑	1.04(1)	2.92(2)	0.15(1)	38.0	HS
	0.45(3)	0.20(1)	0.15(1)	62.0	LS
280(1) ↑	1.04(1)	2.88(2)	0.15(1)	70.2	HS
	0.44(3)	0.21(1)	0.12(1)	29.8	LS
300(1)	1.03(1)	2.78(1)	0.15(1)	100	HS
280(1) ↓	1.05(1)	2.87(1)	0.15(1)	100	HS
					LS
270(1) ↓	1.06(1)	2.91(1)	0.15(1)	87.4	HS
	0.47(1)	0.22(1)	0.12(1)	12.6	LS
250(1) ↓	1.05(1)	2.91(1)	0.20(1)	83.2	HS
	0.46(1)	0.21(1)	0.14(1)	16.8	LS
240(1) ↓	0.46(1)	0.20(1)	0.15(1)	100	LS

Table 47 Overview of the ^{57}Fe Mössbauer parameters for $[Fe(GlytrzE)_3](NO_3)_2$ (**40**) on warming and cooling modes over the temperature range 78-308 K.

T [K]	δ [mm/s]	ΔE_Q [mm/s]	$\Gamma/2$ [mm/s]	Relative Area [%]	Sites
78(1) ↑	0.46(3)	0.19(1)	0.17(1)	100	LS
298(1) ↑	0.39(1)	0.19(1)	0.17(1)	100	LS
303(5) ↑	0.39(1)	0.20(1)	0.16(1)	100	LS
323(5) ↑	0.40 (1)	0.17(1)	0.13(1)	100	LS
344(5) ↑	1.01(1)	2.43(1)	0.17(1)	90	HS
	0.67(1)	0.24(1)	0.10(1)	10	LS
368(5) ↑	0.98(1)	2.47(1)	0.17(1)	100	HS
353(5) ↓	1.00(1)	2.54(1)	0.17(1)	100	HS
328(5) ↓	1.02(1)	2.64(1)	0.18(1)	100	HS
308(5) ↓	1.03(1)	2.66(1)	0.18(1)	100	HS
293(5) ↓	0.97(1)	2.81(1)	0.16(1)	56	HS
	0.40(1)	0.0(1)	0.27(1)	44	LS
285(1) ↓	1.06(1)	2.74(1)	0.20 (1)	45.4	HS
	0.33(1)	0.20(1)	0.22(1)	54.6	LS
270(1) ↓	1.07(1)	2.88(1)	0.20(1)	35.5	HS
	0.36(1)	0.0(1)	0.26(1)	64.5	LS
240(1) ↓	1.13(1)	3.08(1)	0.19(1)	22	HS
	0.41(1)	0.14(1)	0.25(1)	78	LS
200(1) ↓	1.16(1)	3.11(1)	0.10(1)	17	HS
	0.44(1)	0.22(1)	0.18(1)	83	LS
150(1) ↓	1.16(1)	3.38(1)	0.17(1)	10	HS
	0.47(1)	0.23(1)	0.19(1)	90	LS
150(1) ↓	1.16(1)	3.38(1)	0.17(1)	10	HS
	0.47(1)	0.23(1)	0.19(1)	90	LS

Table 48 Overview of the ^{57}Fe Mössbauer parameters for $[Fe(GlytrzE)_3](BF_4)_2 \cdot 0.5H_2O$ (**41**) on warming and cooling modes over the temperature range 78-308 K.

T **[K]**	***δ*** **[mm/s]**	***ΔE$_Q$*** **[mm/s]**	***Γ/2*** **[mm/s]**	**Relative Area [%]**	**Sites**
78(1) ↑	0.47(1)	0.19(1)	0.15(1)	100	LS
298(1) ↑	0.42(1)	0.19(1)	0.15(1)	100	LS
318(1) ↑	0.40(1)	0.09(1)	0.10(2)	2	LS
	1.04(1)	2.73(1)	0.17(1)	98	HS
298(1) ↓	1.03(1)	2.73(1)	0.13(1)	79	HS
	0.21(1)	0.27(1)	0.10(1)	21	LS
110(1) ↓	1.14(1)	3.38(1)	0.15(1)	79	HS
	0.44(1)	0.22(1)	0.21(1)	21	LS
77(1) ↑	1.15(1)	3.39(1)	0.14(1)	72	HS
	0.46(1)	0.21(1)	0.25(2)	28	LS

Table 49 Overview of the ^{57}Fe Mössbauer parameters for $[Fe(GlytrzE)_3](BF_4)_2$ (**42**) on warming and cooling modes over the temperature range 78-308 K.

T [K]	δ [mm/s]	ΔE_Q [mm/s]	$\Gamma/2$ [mm/s]	Relative Area [%]	Sites
78(1) ↑	1.16(1)	3.39(1)	0.13(1)	51	HS
	0.55(3)	0.21(3)	0.15(1)	49	LS
90(1) ↑	1.16(1)	3.39(1)	0.14(1)	67	HS
	0.53(1)	0.29(1)	0.15(1)	33	LS
95(1) ↑	1.15(1)	3.38(1)	0.13(1)	71	HS
	0.50(1)	0.30(1)	0.19(1)	29	LS
100(1) ↑	1.15(1)	3.38(1)	0.13(1)	76	HS
	0.49(1)	0.26(1)	0.23(1)	24	LS
105(1) ↑	1.15(1)	3.37(1)	0.13(1)	77	HS
	0.46(1)	0.24(1)	0.23(1)	23	LS
110(1) ↑	1.15(1)	3.36(1)	0.13(1)	79	HS
	0.49(1)	0.25(1)	0.22(1)	21	LS
120(1) ↑	1.14(1)	3.36(1)	0.13(1)	80	HS
	0.47(2)	0.26(1)	0.24(1)	20	LS
150(1) ↑	1.14(1)	3.30(1)	0.13(1)	82	HS
	0.39(2)	0.28(1)	0.23(1)	18	LS
250(1) ↑	1.07(1)	2.95(1)	0.13(1)	80	HS
	0.31(1)	0.27(1)	0.20(1)	20	LS
298(1) ↑	1.05(1)	2.76(1)	0.13(1)	80	HS
	0.14(1)	0.43(1)	0.21(1)	20	LS
100(1) ↓	1.15(1)	3.38(1)	0.13(1)	79	HS
	0.45(1)	0.27(1)	0.23(1)	21	LS
95(1) ↓	1.15(1)	3.38(1)	0.14(1)	76	HS
	0.49 (1)	0.26(1)	0.23(1)	24	LS
90(1) ↓	1.16(1)	3.38(1)	0.13(1)	73	HS
	0.54(1)	0.24(1)	0.18(1)	27	LS
85(1) ↓	1.16(1)	3.39(1)	0.14(1)	58	HS
	0.54(1)	0.31(1)	0.17(1)	42	LS
77(1) ↓	1.16(1)	3.41(1)	0.13(1)	41	HS
	0.53(1)	0.30(1)	0.15(1)	59	LS

Table 50 Overview of the ^{57}Fe Mössbauer parameters for [Fe(GlytrzE)$_3$] $(CF_3SO_3)_2 \cdot 2H_2O$ (**43**) on warming and cooling modes over the temperature range 78-308 K.

T [K]	*δ* [mm/s]	*ΔE$_Q$* [mm/s]	*Γ/2* [mm/s]	Relative Area [%]	Sites
78(1) ↑	1.15(1)	3.36(1)	0.19(1)	19.5	HS
	0.49(1)	0.21(1)	0.17(1)	80.5	LS
298(1) ↑	1.04(1)	2.69(1)	0.17(1)	30.8	HS
	0.43(1)	0.22(1)	0.15(1)	69.2	LS
310(1) ↑	1.04(1)	2.68(1)	0.27(1)	39	HS
	0.43(1)	0.22(1)	0.15(1)	61	LS
323(1) ↑	1.04(1)	2.72(1)	0.28(1)	53	HS
	0.44(1)	0.22(1)	0.17(1)	47	LS
335(1) ↑	1.01(1)	2.62(1)	0.18(1)	94	HS
	0.43(1)	0.0(1)	0.30(1)	6	LS
345(1) ↑	1.02(1)	2.63(1)	0.16(1)	96	HS
	0.44(1)	0.26(1)	0.10(2)	4	LS
323(1) ↓	1.03(1)	2.70(1)	0.22(1)	96	HS
	0.34(1)	0.32(1)	0.10(3)	4	LS

Table 53 Overview of the ^{57}Fe Mössbauer parameters for **44·0.5H$_2$O** on warming and cooling modes over the temperature range 78-300 K.

T [K]	*δ* [mm/s]	*ΔE$_Q$* [mm/s]	*Γ/2* [mm/s]	Relative Area [%]	Sites
77(1) ↑	1.14(1)	3.15(2)	0.12(1)	7	HS
	0.51(2)	0.23(2)	0.16(1)	93	LS
170(1) ↑	1.11(1)	3.12(1)	0.15(2)	8	HS
	0.48(2)	0.24(1)	0.15(1)	92	LS
225(1) ↑	1.11(1)	3.12(1)	0.16(1)	8	HS
	0.49(1)	0.25(1)	0.16(1)	92	LS
300(1)	1.03(1)	2.71(1)	0.18(1)	87.5	HS
	0.17(1)	0.28(1)	0.2*	12.5	LS
225(1) ↓	1.07(1)	3.01(1)	0.17(1)	36	HS
	0.47(1)	0.23(1)	0.17(1)	64	LS
150(1) ↓	1.18(1)	3.34(1)	0.17(1)	6.4	HS
	0.50(1)	0.23(1)	0.17(1)	93.6	LS

Table 54 Overview of the ^{57}Fe Mössbauer parameters for **45** on warming and cooling modes over the temperature range 78-300 K.

T [K]	*δ* [mm/s]	*ΔE$_Q$* [mm/s]	*Γ/2* [mm/s]	Relative Area [%]	Sites
80(1) ↑	0.52(1)	0.25(2)	0.13(1)	100	LS
225(1) ↑	0.47(2)	0.22(1)	0.15(1)	100	LS
250(1) ↑	1.28(1)	2.71(1)	0.15*	6	HS
	0.47(1)	0.23(1)	0.15(1)	94	LS
297(1)	1.03(1)	2.75(1)	0.16(1)	88	HS
	0.26(1)	0.37(1)	0.15*	12	LS
250(1) ↓	1.07(1)	2.98(1)	0.16(1)	82	HS
	0.27(1)	0.36(1)	0.27(1)	18	LS
225(1) ↓	0.47(1)	0.22(1)	0.16(1)	100	LS

Table 55 Overview of the ^{57}Fe Mössbauer parameters for **46·H_2O** on warming and cooling modes over the temperature range 78-300 K.

T [K]	*δ* [mm/s]	*ΔE*$_Q$ [mm/s]	*Γ*/2 [mm/s]	Relative Area [%]	Sites
77(1) ↑	1.15(2)	3.40(1)	0.19(1)	20	HS
	0.54(1)	0.29(1)	0.15(1)	80	LS
110(1) ↑	1.14(2)	3.28(2)	0.16(4)	26	HS
	0.55(1)	0.28(1)	0.15(1)	74	LS
130(1) ↑	1.14(1)	3.21(1)	0.16(1)	27	HS
	0.54(7)	0.29(1)	0.16(1)	73	LS
150(1) ↑	1.23(1)	3.22(1)	0.17(2)	36	HS
	0.53(1)	0.29(1)	0.15(1)	64	LS
170(1) ↑	1.11(1)	3.14(2)	0.15(1)	47	HS
	0.54(1)	0.26(1)	0.13(1)	53	LS
180(1) ↑	1.12(1)	3.12(1)	0.16(1)	57	HS
	0.51(1)	0.26(1)	0.15(1)	43	LS
190 (1) ↑	1.11(1)	3.06(1)	0.18(1)	69	HS
	0.54(1)	0.23(2)	0.14(1)	31	LS
200(1) ↑	1.11(1)	3.04(1)	0.18(1)	73	HS
	0.49(1)	0.25(1)	0.19(1)	27	LS
215(1) ↑	1.10(1)	2.97(1)	0.19(1)	83	HS
	0.43(1)	0.25(1)	0.18(1)	17	LS
230(1) ↑	1.10(1)	2.90(1)	0.18(1)	88	HS
	0.53(1)	0.31(1)	0.15*	12	LS
250(1) ↑	1.07(1)	2.81(1)	0.18(1)	92	HS
	0.25(2)	0.2*	0.15*	8	LS
270(1) ↑	1.07(1)	2.71(1)	0.19(1)	93	HS
	0.28(1)	0.23(2)	0.13(1)	7	LS
298(1)	1.06(1)	2.56(1)	0.20(1)	93	HS
	0.35(2)	0.15*	0.15*	7	LS
170(1) ↓	1.11(1)	3.15(1)	0.18(1)	48	HS
	0.51(1)	0.24(2)	0.18(1)	52	LS

Table 56 Overview of the ^{57}Fe Mössbauer parameters of **47·H_2O** on warming and cooling modes over the temperature range 78-300 K.

T [K]	*δ* [mm/s]	*ΔE*$_Q$ [mm/s]	*Γ*/2 [mm/s]	Relative Area [%]	Sites
78(1) ↑	1.17(2)	3.31(1)	0.16(1)	12	HS
	0.53(1)	0.28(1)	0.19(1)	88	LS
100(1) ↑	1.14(2)	3.28(1)	0.15(1)	11	HS
	0.52(1)	0.29(1)	0.18(1)	89	LS
140(1) ↑	1.15(1)	3.21(1)	0.18(1)	17	HS
	0.51(1)	0.29(1)	0.18(1)	83	LS
160(1) ↑	1.13(2)	3.17(1)	0.17(1)	19	HS
	0.50(1)	0.26(1)	0.19(1)	81	LS
180(1) ↑	1.11(1)	3.07(2)	0.19(2)	38	HS
	0.49(1)	0.26(1)	0.20(1)	62	LS
190(1) ↑	1.10(1)	3.03(1)	0.18(1)	61	HS
	0.47(1)	0.24(2)	0.18(2)	39	LS
200(1) ↑	1.10(1)	2.99(1)	0.15(1)	64	HS
	0.46(1)	0.23(3)	0.18(2)	36	LS
220(1) ↑	1.09(1)	2.91(1)	0.15(1)	68	HS
	0.44(2)	0.23(2)	0.19(1)	32	LS
230(1) ↑	1.08(1)	2.88(1)	0.16(1)	74	HS
	0.41(1)	0.22(1)	0.19(1)	26	LS
240(1) ↑	1.07(1)	2.86(1)	0.15(1)	83	HS
	0.18(1)	0.45(1)	0.3(1)	17	LS
300(1)	1.03(1)	2.69(1)	0.18(1)	83	HS
	0.15(2)	0.40(1)	0.21(1)	17	LS
280(1) ↓	1.04(1)	2.74(2)	0.20(1)	80	HS
	0.12(1)	0.44(1)	0.19(1)	20	LS
260(1) ↓	1.06(1)	2.82(1)	0.19(1)	81	HS
	0.13(2)	0.49(1)	0.22(2)	19	LS
230(1) ↓	1.08(1)	2.89(1)	0.16(1)	83	HS
	0.38(2)	0.20(2)	0.20(1)	17	LS
220 (1) ↓	1.09(1)	2.91(1)	0.16(1)	69	HS
	0.42(2)	0.24(1)	0.19(1)	31	LS

210(1) ↓	1.10(1)	2.95(1)	0.17(1)	69	HS
	0.47(1)	0.27(2)	0.15(2)	31	LS
190(1) ↓	1.10(1)	3.03(1)	0.16(1)	63	HS
	0.47(1)	0.26(2)	0.18(2)	37	LS
170(1) ↓	1.11(1)	3.11(1)	0.15(1)	37	HS
	0.50(1)	0.27(1)	0.16(1)	63	LS
160(1) ↓	1.12(2)	3.14(3)	0.17(2)	28	HS
	0.495(7)	0.28(1)	0.17(1)	72	LS
140(1) ↓	1.14(2)	3.21(2)	0.14(1)	17	HS
	0.51(1)	0.29(1)	0.16(1)	83	LS
100(1) ↓	1.15(1)	3.32(1)	0.20(1)	73	HS
	0.50(1)	0.27(10)	0.19(2)	87	LS

Symbols:

↑ indicates warming and ↓ indicates cooling; δ = isomer shift relative to α-iron, ΔE_Q = quadrupole splitting, $\Gamma/2$ = half width at half maximum, *Fixed parameter.

Appendix

Thermodynamic data

Table 51 Transition temperatures as deduced from DSC measurements, thermodynamic parameters and transition temperatures for **37-GlytrzE-ClO_4** to **43-GlytrzE-CF_3SO_3**; * The volume of the $CF_3SO_3^-$ was fixed as 0.09 nm^3.

Code	Solvent n H_2O	Volume[1] (nm^3)	$T_{max}^{\uparrow}$ (K)	$T_{max}^{\downarrow}$ (K)	ΔT (K)	ΔH_{HL} (kJ mol^{-1})	ΔS_{HL} (J mol^{-1} K^{-1})	ΔS_{vib} (J mol^{-1} K^{-1})
37-GlytrzE-ClO_4	0	0.082	297	292	5	14	41	27.6
38-GlytrzE-ClO_4	1	0.082	272	261	11	13	48.8	35.4
39-GlytrzE-NO_3	1	0.064	358	338	20	27	77.7	64.3
40-GlytrzE-NO_3	0	0.064	340	280	60	27.4	88.4	75
41-GlytrzE-BF_4	0.5	0.073	320	299	21	17.3	60	46.6
43-GlytrzE-CF_3SO_3	2	0.09*	330	320	10	8	24.6	11.2

Table 52 Transition temperatures as deduced from DSC measurements, thermodynamic parameters and transition temperatures For **39-GlytrzE-NO_3** to **40-GlytrzE-NO_3.**

Code	No. of runs after 15 min at 390 K	$T_{max}^{\uparrow}$ (K)	$T_{max}^{\downarrow}$ (K)	ΔH_{HL} (kJ mol^{-1})	ΔS_{HL} (J mol^{-1} K^{-1})	ΔS_{vib} (J mol^{-1} K^{-1})	ΔS_{HL} *(avg.)* (J mol^{-1} K^{-1})
39-GlytrzE-NO_3	1	-	178	14	78.6	65.3	73
		253	-	17	67.2	53.8	
	2	-	195	12	61.5	48.1	63
		253	-	15	59.3	45.9	
	3	-	196	12	61.2	47.8	
40-GlytrzE-NO_3	1	-	197	18	91.4	78	90.8
		255	-	23	90.2	76.8	
	2	-	197	18.3	92.9	79.5	91.6
		255	-	23	90.2	76.8	

Materials

All reagents and solvents were used as received from commercial sources: hexafluorotitanic acid, 99.9 %, 60 wt.% solution in water, hexafluorozirconic acid, 45 wt.%, solution in water, ammonium hexafluorostanate(IV), 99.99 %, ammonium heptaflurotantalate(V), 99.99 %, Benzene, *N*,*N*-Dimethylformamide, aq. hydrazine hydrate, thionyl chloride, $Fe(BF_4)_2 \cdot 6H_2O$ from Sigma-Aldrich; ammonium hexafluorogermanate (IV), 99.99 %, iron(II) chloride tetrahydrate 99 %, 4-amino-1,2,4-triazole, 99 %, copper(II) nitrate trihydrate, extra pure, iron(II) sulfate heptahydrate, , glycine ethyl ester hydrochloride, CF_3SO_3H, alanine ester hydrochloride from Acros; iron powder 99.99 % from Janssen Chemica; Cu powder, 99.5 % from Merck; barium nitrate and Methanol from VWR; cadmium chloride from UCB; $Fe(ClO_4)_2 \cdot 6H_2O$ from Alfa Aesar.

^{1}H and ^{13}C NMR spectra were recorded on a Brüker AC 300 MHz on a Bruker AC 300 instrument. Mass spectral data were obtained on Thermofinnigan LCQ Ion trap spectrometer (APCI mode). HRMS were carried out on a Micromass Q TOF 2 spectrometer in ESI mode, detecting positive mode.

Infrared spectra were recorded on a BioRad FTS-135 spectrometer using KBr pellets (chapter I, II and III) and on a Shimadzu FTIR-84005. Shimadzu FTIR-8400S spectrometer with KBr discs (chapter IV-VII), at r.t. between 4000 and 400 cm^{-1}. Raman spectra with 1064 nm excitation were recorded between 2300 to 400 cm^{-1} with a Bruker RFS 100/s FT-Raman spectrometer (I = 200 mW) at r.t using a diode-pumped, air-cooled Nd:YAG laser as the excitation source. Elementary analyses were performed at the University College London (UK). Atomic absorptions were carried out with Varian Spectra A-300. Sampling was done in aqueous nitric acid solutions

and standard solutions were prepared with Möhr salt. Melting point were determined with an oil bath 3937-S Buchi device.

Thermogravimetric analyses (TGA-DTA) analyses were performed in air (100 mL/min) either at a heating rate of 10 K/min (298 to 1173 K) or 1K/min (298 to 400 - 423 K) using a Universal V2.5H TA instrument and Mettler Toledo TGA/SDTA 851e analyzer, with alumina crucibles filled with approximately 10 mg of sample. Differential scanning calorimetry (DSC) measurements were carried out in a $He_{(g)}$ atmosphere using a Perkin-Elmer DSC Pyris 1 instrument equipped with a cryostat and operating down to 98 K. Aluminum capsules were loaded with 20-50 mg of sample and sealed. The heating and cooling rates were fixed at 5 and 10 K min^{-1}. Temperatures and enthalpies were calibrated over the temperature range of interest using the crystal-crystal transitions of pure cyclopentane (≥ 99%) and the solid-liquid transitions of pure Indium (99.99%).[1, 2] For high temperatures the samples were maintained at room temperature for 5 min in order to allow the system to equilibrate, and was further warmed from 293 K to 400 K. The samples were maintained at the highest temperature for 5-10 min to reach equilibrium, followed by a similar scanning mode as on warming, between 400 K and room temperature. The experiment was carried out 4 times to check the reproducibility.

A Heraeus VTR 5036 oven was used for the annealing experiments (Chapter II).

X-ray powder diffraction patterns were recorded on a Siemens D5000 counter diffractometer, with a Cu anticathode ($\lambda K\alpha$ = 1.5418 Å) in Bragg-Brentano geometry, operating at room temperature. Samples were deposited on silicon after calibration with a quartz standard.

In chapter II, X-ray powder patterns were recorded at room temperature from 2θ = 5 to 70° using interval of 0.02° using a SIEMENS D-5000 counter

diffractometer working with Cu K_α radiation (λ = 1.5418 Å). Temperature dependent XRPD measurements were performed on an Oxford Diffraction Xcalibur 2 single-crystal diffractometer equipped with a Cryojet XL cryostat liquid nitrogen blower using Mo K_α radiation (λ = 0.71073 Å). The sample was filled into a borosilicate glass capillary of diameter 0.3 mm. The sample to detector distance was 130 mm. In order to cover a wider range of 2θ, the diffractogrammes were recorded for two detector positions with an offset of 0 and 12°, respectively. The detector position at θ = 12° resulted in a systematic distortion of the diffractogramme. Correct *d* values were calculated by using a reference mineral (Kyanite) with known peak positions. The acquisition time per sample was 180 s and the sample rotation was 3°/s. The sample was mounted at room temperature and slowly cooled to 100 K. In a second run, the sample was slowly warmed from 100 K to room temperature. 10 minutes per cooling step were necessary between two measurements. The reading error on the temperature was ~ 1 K. The relative intensity of the HS phase I_{HS}/I_{tot} was obtained by a least square refinement to Gaussian line shape.[3] In chapter III, powder X-ray diffraction patterns were recorded on a Philips X'Pert counter diffractometer working with Cu K_α radiation and operating over the temperature range (293-380 K). The heating/cooling rate was 10 K/minutes between two steps of analysis. Indexation of unit cell parameters was carried out using the DICVOL04 software.[4]

Scanning electron microscopy (SEM) coupled with EDX imagings were performed with a Gemini Digital Scanning Microscope 982 with 1 kV accelerating voltage using an aluminium sample holder. For EDX measurements samples were coated with a thickness of 25 nm of gold to make it conductive using 208 HR Cressington Sputter coater.

The gas adsorption study for **30-32** was carried out on a Micromeritics ASAP 2010 porosimeter. Prior to analyses and in order to remove eventual

surface adsorbed/coated DMF after synthesis; fresh crystals of **30-32** were soaked in water and filtered under vacuum. Samples of 60-100 mg were then outgassed under vacuum at 150 °C or at room temperature. Both $N_{2(g)}$ and $H_{2(g)}$ adsorption-desorption isotherms were recorded at 77 K in a relative pressure range from 0.0010 to 0.995 (with respect to $N_{2(g)}$). The same samples were subjected to Hg porosimetry measurements using a Micromeritics Autopore IV. A penetrometer with appropriate stem volume was chosen in order to record significant Hg intrusion. Prior to analysis, the sample was evacuated at r.t. and Hg was then forced into the sample under pressure up to 30000 psi (corresponding to a minimum pore size of 6 nm according to the Washburn equation[5]).

Diffuse Reflectance spectra were recorded with a Varian CARY 5E spectrometer using polytetrafluoroethylene (PTFE) as a reference. Spectra were measured on pure solids to avoid matrix effects. Diffuse Reflectance spectra were sometimes normalized to allow meaningful comparisons.

Diffuse reflectivity measurements were performed using a hydrostatic pressure device (operating with He gas) and an optical detection system which has been described in[6, 7]. The powder samples have been thermally cycled at least ten times over the temperature range 78-300 K, before starting the measurements. This thermal treatment lead to the auto-milling of the crystallites, because of the internal stress induced by the volume variation during the spin transition, and ensures a full reproducibility of the hysteresis loop[6, 7]. The light source used is a Quartz Tungsten Halogen lamp from LOT-ORIEL of 100 W maximal powers, combined with an interferential filter operating at 550 nm. Scanning electron microscopy (SEM) was performed using a Gemini Digital Scanning Microscope 982 with 1 kV accelerating voltage with an aluminum sample holder.

^{57}Fe Mössbauer spectra were recorded in transmission geometry over the temperature range (78-300 K) with conventional Mössbauer spectrometers equipped with a ^{57}Co(Rh) radioactive source operating at room temperature. The samples were sealed in aluminum foil and mounted on a nitrogen Oxford bath cryostat. The spectra were fitted to the sum of Lorentzians by a least-squares refinement using Mossfit[8] (Chapter I) or Recoil 1.05 Mössbauer Analysis Software[9]. All isomer shifts refer to α-Fe at room temperature. ^{119}Sn Mössbauer measurements were measured in transmission geometry using an ^{119}Sn ($CaSnO_3$) source operating at room temperature. Spectra were recorded on cooling using a cryostat operating over the range (300-4.2 K). All isomer shifts refer to $CaSnO_3$.

Magnetic susceptibilities were measured over the temperature range 1.8 - 300 K or 350 K using a Quantum Design MPMS2 or MPMS5 SQUID magnetometer equipped with a 5.5 T magnet operating at 1 T. The samples were inserted into gelatin capsules and mounted on a plastic straw. The magnetic data were corrected for diamagnetic contributions, which were estimated from Pascal's constants. The FORC distribution is determined at each point by fitting a mixed second-order polynomial of the form $[a_1+a_2T_a+a_3T_b+a_4T_a^2+a_5T_b^2+a_6T_aT_b]$ to a local moving grid. Then interpolation is done to obtain the distribution value we take into consideration also the neighboring interpolated point. In this case the value of $-a_6$ provides the mixed second derivative of the fitted surface and it can be assigned to the centre of grid as a representation of the density of the FORC distribution $\rho(T_a,T_b)$ at that point. The value of the magnetization is interpolated in every measured point with that polynomial of order 2. The distribution is given by the negative value of the derivative of the second order of the magnetization oppose to the transition temperatures (a_6).

X-ray structure Data Collection and Refinement: In Chapter I, X-ray intensity data were collected at different temperatures with a MAR345 image plate using Mo-Kα (λ = 0.71069Å) radiation. The crystal was mounted in inert oil and transferred to the cold gas stream for flash cooling. The data were not corrected for absorption, but the data collection mode partially takes the absorption phenomena into account. The unit cell parameters were refined using all the collected spots after the integration process. The structure was solved by direct methods and refined by full-matrix least-squares on F^2 using SHELX97[10]. When it was possible, all the hydrogen atoms were localized by Fourier-difference synthesis. They were included in the refinement with a common isotropic temperature factor.

In chapter III, the measurement was carried out at 293 K using an Oxford Diffraction Xcalibur 2 diffractometer with Mo K_α radiation. The exposure time was 10 s per frame and the crystal-detector distance was 60 mm. Data reduction and analytical absorption corrections were performed using the CRYSALIS RED software suite.[11] The final lattice parameters were calculated from all reflections observed in the actual data collection. The structure was solved by direct methods using SIR 2004,[12] which revealed the atomic positions, and refined by using the SHELX-97 program package.[10] The final refinements were carried out on F_o^2. Atomic scattering factors for spherical neutral free atoms were taken from standard sources, and anomalous dispersion corrections were applied.[13]

Experimental section

Organic molecules

Chapter IV

4-hydroxy-1,2,4-triazole **(OH-TRZ):** *N*,*N*-Dimethylformamide azine dihydrochloride (**I**) was obtained following the reported method[14, 15].

N,*N*-Dimethylformamide Azine Dihydrochloride **(I):** $SOCl_2$ (28.6 mL, 0.4 mol) or oxalyl chloride (34.5 mL, 0.4 mol) was added with stirring to freshly distilled DMF (150 mL) at 5 °C. To the aged (24 h) solution of this mixture, was added slowly aqueous hydrazine hydrate (5 mL, 0.1 mol) in DMF (20 mL). The mixture was stirred at r.t. for 2 d and the white recipitate of dimethylformamide azine dihydrochloride was collected by filtration and washed with DMF and CH_3OH; Yield: 19.4 g (91%); mp. 251 °C (Lit.13 mp. 250 °C). (***Caution***: Benzene is potentially *carcinogenic*; all operations involving this solvent should be conducted in a fume hood.)

To a suspension of Hydroxylamine hydrochloride (2.44 g, 35.16 mmol, 1 equiv.) in toluene (20 mL) at approx. 110 ˚C was added solid **I** (5 g, 35.16 mmol, 1 equiv.) with stirring. The mixture was refluxed then for ~ 3 - 4 h with vigorous stirring. The reaction can be monitored by checking the pH of the gaseous side products escaping from the outlet of the condenser. When the pH arrives from 6 to 3 and the reaction mixture gains pale rose color the reaction is halted and the experimental set-up was adjusted for distillation. Rosy distillate is discarded and the white viscous residue was solvent extracted with warm chloroform ($CHCl_3$). The off white insoluble compound thus obtained (3.63 g) was packed in Whatman filter paper and extracted by Soxhalet method for 10 h, with $CHCl_3$. Finally, the remaining solvent was removed under vacuum and a white solid was obtained. Yield 2.35 g (65 %).

To free from hydrochloride, the product was reacted with equivalent quantity of sodium ethoxide at 0°C in ethanol. The final product (soluble in ethanol) was separated by filtration from NaCl. 4-hydroxy-1,2,4-triazole was obtained by vacuum evaporation as white powder. ^{1}H NMR (300 MHz, DMSO, 298 K): δ = 9.75 (s, 2 H). ^{13}C NMR (300 MHz, DMSO, 298 K): δ = 141. MS: *m*/*z* = 86.09 ($M + H^+$). FTIR (KBr disc, in cm^{-1}): 3112(s), 1151(vs), 1062(s), 865(s), 605(s). Anal. Calcd. for $C_2H_3N_3O$ (85.07 g/mol): C, 28.24, H, 3.55, N, 49.40; Found C, 28.19, H, 3.40, N, 49.30.

Chapter V

4-(3'-N-phtalimido-propyl)-1,2,4-triazole **(Phtptrz):** 3.120 g of triphenylphosphine (11.88 mmol, 1.5 eq.) dissolved in 20 mL of 1:1 mixture of dry acetonitrile and tetrahydrofuran were cooled down to 0°C. 2.340 mL of DIAD (Diisopropyl azodicarboxylate) (11.88 mmol, 1.5 eq.) were added under stirring and the mixture was stirred for 10 min. Then a mixture of 1.158 g phthalimide (7.87 mmol, 1 eq.) and 1 g of (4-(3'-hydroxypropyl)-1,2,4-triazole (7.87 mmol, 1 eq.) in 20 mL of 1:2 mixture of acetonitrile and tetrahydrofuran was added and the mixture allowed to warm to r.t.. The reaction mixture was stirred 12 h. A white product was filtered from the reaction mixture and recrystallised in 10 mL of water to afford pale yellow sharp plates. Yield 1.29 g (64 %); M.p 178 ^{o}C. ^{1}H NMR (200 MHz, $CDCl_3$, 298 K): δ = 2.15-2.28 (m, 2 H), 3.76 (t, 2 H, *J* = 6.3 Hz), 4.10 (t, 2H, *J* = 7.0 Hz), 7.77-7.81 (m, 2H), 7.85-7.89 (m, 2H), 8.34 (s, 2H) ppm. ^{13}C NMR (50 MHz, $CDCl_3$ 298 K): δ = 168.5, 143, 134.5, 132, 123.6, 42.9, 34.8, 30.4. MS: *m*/*z* = 257.1 ($M + H^+$). FTIR (KBr disc, in cm^{-1}): 3444 (ws), 3138 (m), 3107 (m), 3041 (w), 2965 (w), 1760 (s), 1703 (s), 1521 (m), 1441 (m), 1399 (s), 1365 (m), 1346 (s), 1186 (s), 1118 (m), 1075 (m), 1030 (m), 969, (m),

810 (w), 726 (m), 531 (m), 631 (m). Anal. Calcd. for $C_{13}H_{12}N_4O_2$ (256.26 g/mol): C, 60.93, H, 4.72, N, 21.86; Found C, 60.99, H, 4.92, N, 21.74.

Chapter VI and VII

Ethyl 4H-1,2,4-triazol-4-yl-acetate **(GlytrzE):** *N*,*N*-Dimethylformamide azine dihydrochloride (**I**) and its free base (**II**) were obtained following the reported method.[15] Compound **II** was recrystallised twice from benzene with charcoal and used in transamination reactions. The reaction was carried out in a dry round-bottomed flask fitted with a reflux condenser. To a suspension of glycine ethyl ester hydrochloride (1.17 g, 8 mmol, 1.2 equiv.) in benzene (30 mL) at approx. 60 ˚C was added solid **II** (1 g, 7 mmol, 1 equiv.) with stirring. The mixture was refluxed then for 24 h with vigorous stirring. The reaction can be monitored by running thin layer chromatography at interval of time. Finally, solvent was removed under vacuum and chromatographic purification (SiO_2, $CH_2Cl_2 \rightarrow$ 5 % isopropanol in CH_2Cl_2) of the yellow oil gave a cream solid. Yield 700 mg (65 %), m.p 93 ^oC. R_f 0.25 (5 % isopropanol in CH_2Cl_2). ^1H NMR (300 MHz, $CDCl_3$, 298 K): δ = 8.50 (s, 2 H), 5.08 (s, 2 H), 4.20 (*q*, 2H, *J* = 7.11 Hz), 1.25 (*t*, 3H, *J* = 7.11). ^{13}C NMR (300 MHz, $CDCl_3$ 298 K): δ = 169.4, 146.2, 63.9, 47.6, 15.0. MS: *m*/*z* = 156.12 ($M + H^+$). FTIR (KBr disc, in cm^{-1}): 3112(s), 1743(vs), 1539(s), 1236(s), 1215(s), 1018(s), 636(s). Anal. Calcd. for $C_6H_9N_3O_2$ (155.16): C, 46.45, H, 5.85, N, 27.08; Found C, 46.34, H, 5.91, N, 26.88.

4H-1,2,4-triazol-4-yl acetic acid **(HGlytrz):** Acid hydrolysis of ethyl 4H-1,2,4-triazol-4-yl-acetate (**GlytrzE**), refluxing with 6N HCl for 6-8 h, and drying under reduced pressure gave a colorless oil. This residue was co-evaporated with water to give **HGlytrz** as a white precipitate. M.p 161°C.

The compound was dried under vacuum. Yield 90 %. It was recrystallized from MeOH to obtain single crystals suitable for X-ray diffraction. This approach has substantially improved the yield of **HGlytrz** compared to our earlier method where compound analysis was fully described[15]. IR (KBr): 3442 (br), 3110 (s), 1900 (s), 1548 (m), 1496 (m), 1257(s), 1191 (m), 1087 (m), 1020 (s), 970 (s), 883 (s), 790 (s), 655 (s), 622 cm–1 (s). 1H NMR (300 MHz, DMSO-*d*6, 298 K): d = 8.49 (s, 2 H), 4.98 (s, 2 H). 13C NMR (75 MHz, DMSO-*d*6, 298 K): d = 170.1, 144.8, 46.3. MS: *m*/*z* = 128.04 (M + H+). Anal. Calcd for $C_4H_5N_3O_2$ (127.10): C, 37.80; H, 3.97; N, 33.06. Found: C, 37.57, H, 4.10, N, 32.59.

Chapter VIII

Ethyl 4H-1,2-4-triazol-4-yl-propionate **(βAlatrz):** *N*,*N*-Dimethylformamide azine dihydrochloride (**I**) and its free base (**II**) were obtained following the reported method[15]. The free base was recrystallised twice from benzene with charcoal and used in transamination reactions[15]. To a suspension of *β-alanine ethyl ester hydrochloride* (3 g, 19.53 mmol) in benzene (100 mL) at approx. 60 °C was added solid **II** (2.14 g, 15.04 mmol) with stirring, obtaining a transparent yellow solution. The mixture was refluxed then (at 130 °C) for 93 h with vigorous stirring. The reaction was monitored by NMR analysis at interval of time. Finally, the solvent was removed under vacuum and a chromatographic purification (SiO_2, CH_2Cl_2 → 5 % isopropanol in CH_2Cl_2) of the yellow oil gave pale yellow oil. Yield 2 g (60 %). ^{1}H NMR (300 MHz, $CDCl_3$, 298 K): δ = 8.25 (s, 2H), 4.34 (*t*, 3H, *J* = 6.17 Hz), 4.14 (*dd*, 2H, *J* = 7.10 Hz & 7.15 Hz), 2.78 (*t*, 2H, *J* = 6.17 Hz), 1.23 (*t*, 3H, *J* = 7.16 Hz). ^{13}C NMR (300 MHz, $CDCl_3$ 298 K): δ = 170.1, 143, 61.6, 40.6, 35.5, 14.1. MS: *m*/*z* = 170.03 (M + H^+). FTIR (thin film from CH_2Cl_2 on ZnSe HATR through plate, cm^{-1}): 3118(s), 1728(vs),

1535(s), 1236(s), 1205(s), 1186(s), 1022(m), 637(s). Anal. Calcd. for $C_7H_{11}N_3O_2$ (169.18 g/mol): C, 49.70, H, 6.55, N, 24.84; Found C, 49.7, H, 6.81, N, 24.61.

Inorganic molecules

Chapter I

$[Fe(NH_2trz)_3]TiF_6 \cdot 0.5H_2O$ **(1)**: Iron powder (0.0857 g, 1.534 mmol) was mixed with 0.1 mL H_2TiF_6 (1.534 mmol) and stirred at room temperature and in air for 30 minutes, the solution of which was filtered leading to a green solution of $[Fe(H_2O)_6]TiF_6$. This aqueous precursor solution was added to a hot methanolic solution (5 mL) containing NH_2trz (0.3871 g, 4.6 mmol). A white precipitate was formed immediately and stirred for ~ 1 h at room temperature. It was filtered, washed with 5-10 mL methanol and dried in a desiccator. Yield: 0.61 g, 83%. *Anal*. for $FeC_6H_{13}N_{12}O_{0.5}TiF_6$ (479 g/mol): calcd. C, 15.05; H, 2.74; N, 35.09; Fe, 11.66. Found: C, 15.51; H, 2.80; N, 35.54; Fe, 10.14 %. IR (cm^{-1}): ν(NH_2) ~ 3305 (s), ν(N-N) ~ 1217 (s), ν(C-H out of plane) ~ 1027 (m), ν(C-H ring torsion) = 621 (vs), ν(Ti-F) ~ 569 (m).

$[Fe(NH_2trz)_3]TiF_6 \cdot H_2O$ **(2)**: It was synthesized following the same procedure as for **1** except that warm ethanol was used to dissolve NH_2trz. A white precipitated was obtained. Yield: 0.43 g, 86.5 %. *Anal*. for $FeC_6H_{14}N_{12}OTiF_6$ (488.01 g/mol): calcd. C, 14.77; H, 2.89; N, 34.44; Fe, 11.44. Found: C, 15.26; H, 2.59; N, 34.87; Fe, 12,57 %. IR (cm^{-1}): ν(NH_2) ~ 3318 (s), ν(N-N) ~ 1218 (s), ν(C-H out of plane) ~ 1031 (m), ν(C-H ring torsion) = 624 (vs), ν(Ti-F)~567 (m).

$[Fe(NH_2trz)_3]ZrF_6 \cdot 0.5H_2O$ **(3)**: Iron powder (0.0857 g, 1.534 mmol) was mixed with 0.1 mL H_2ZrF_6 (1.5 mmol) and stirred at room temperature and in air for 30 minutes, the solution of which was filtered leading to a pale green solution of $[Fe(H_2O)_6]ZrF_6$. The same procedure was used as for **1** working with NH_2trz dissolved in MeOH, affording a white precipitate. Yield: 0.94 g, 66.4 %. *Anal*. for $FeC_6H_{13}N_{12}O_{0,5}ZrF_6$ (520.97 g/mol): calcd. C, 13.80; H, 2.51; N, 32.18; Fe, 10.69. Found: C, 14.36; H, 2.47; N, 32.81; Fe, 9.96 %. IR *(cm^{-1})*: ν(NH_2)~3308 (s), ν(N-N) ~ 1218 (s), ν(C-H out of plane) ~ 997 (m), ν(C-H ring torsion) = 625 (vs), ν_1(Zr-F)~590 (m).

$[Fe(NH_2trz)_3]ZrF_6$ **(4)**: It was synthesized following the same procedure as for **3** except that warm ethanol was used to dissolve NH_2trz. A white precipitated was obtained. Yield: 0.64 g, 50 %. *Anal*. for $FeC_6H_{12}N_{12}ZrF_6$ (511.96 g/mol): calcd. C, 14.04; H, 2.36; N, 32.75; Fe, 10.88. Found: C, 14.80; H, 2.49; N, 33.03; Fe, 9.65 %. IR (cm^{-1}): ν(NH_2)~3226 (m), ν(N-N) ~ 1218 (s), ν(C-H out of plane) ~ 997 (m), ν(C-H ring torsion) = 624 (vs), ν_1(Zr-F)~590 (m).

$[Fe(NH_2trz)_3]SnF_6 \cdot 0.5H_2O$ **(5)**: $(NH_4)_2SnF_6$ (0.3388 g, 1.26 mmol) dissolved in 10 mL water was added to a 5 mL aqueous solution of $FeCl_2 \bullet 4H_2O$ (0.2506 g, 1.26 mmol). A pale green solution of $[Fe(H_2O)_6]SnF_6$ was obtained. The same procedure was used as for **1** working with NH_2trz dissolved in MeOH, affording a white precipitate. Yield: 0.38 g, 76%. *Anal.* for $FeC_6H_{13}N_{12}O_{0,5}SnF_6$ (550.96 g/mol): calcd. C, 13.11; H, 2.38; N, 30.57; Fe, 10.16. Found: C, 13.31; H, 2.31; N, 29.84; Fe, 9.80 %. IR (cm^{-1}): ν(NH_2)~ 3215 (s), ν(N-N) ~ 1217 (s), ν(C-H out of plane)~1000 (m), ν(C-H ring torsion) = 612 (s), ν(Sn-F)~ 601 (m).

$[Fe(NH_2trz)_3]SnF_6 \cdot H_2O$ **(6)**: It was synthesized following the same procedure as for **5** except that a warm ethanol was used to dissolve NH_2trz. A white precipitated was obtained. Yield: 0.4 g, 80%. *Anal.* for $FeC_6H_{14}N_{12}OSnF_6$

(559.96 g/mol): calcd. C, 12.90; H, 2.53; N, 30.08; Fe, 9.99. Found: C, 13.04; H, 2.27; N, 29.80; Fe, 9.17 %. IR (cm^{-1}): ν(NH_2) ~3225 (s), ν(N-N) ~1217 (s), ν(C-H out of plane) ~ 998 (m), ν(C-H ring torsion) = 610 (s), ν(Sn-F)~ 600 (m).

$[Fe(NH_2trz)_3]TaF_7 \cdot 3H_2O$ **(7)**: An aqueous solution (10 mL) containing 0.3176 g of $FeCl_2 \bullet 4H_2O$ (1.59 mmol) was added to an aqueous solution (5 mL) containing 0.5591 g of $(NH_4)_2TaF_7$ (1.59 mmol) and ~ 0.01 g of ascorbic acid. A pale green solution of $[Fe(H_2O)_6]TaF_7$ was obtained. The same procedure was used as for **2** working with NH_2trz dissolved in methanol, affording a white precipitate. Yield: 0.8 g, 74%. *Anal.* for $FeC_6H_{18}N_{12}O_3TaF_7$ (676.03 g/mol): calcd. C, 10.66; H, 2.68; N, 24.86; Fe, 8.26. Found: C, 10.66; H, 1.79; N, 24.44; Fe, 8.84 %. IR (cm^{-1}): ν(NH_2) ~3220 (s), ν(N-N) ~1220 (s), ν(C-H out of plane) ~ 1000 (m), ν(C-H ring torsion) = 613 (s), ν(Ta-F)~ 1394, 536 (m).

$[Fe(NH_2trz)_3]TaF_7 \cdot 2.5H_2O$ **(8)**: It was synthesized following the same procedure as for **7** except that warm ethanol was used to dissolve NH_2trz. A white precipitated was obtained. Yield: 0.8 g, 81%. *Anal.* for $FeC_6H_{16.5}N_{12}O_{2.5}TaF_7$ (667.03 g/mol): calcd. C, 10.75; H, 2.56; N, 25.08; Fe, 8.37. Found: C, 10.80; H, 2.57; N, 2520; Fe, 9.50 %. IR (cm^{-1}): ν(NH_2) ~3223 (s), ν(N-N) ~1221 (s), ν(C-H out of plane) ~ 1000 (m), ν(C-H ring torsion) = 612 (s), ν(Ta-F)~ 1396, 534 (m).

$[Fe(NH_2trz)_3]GeF_6 \cdot H_2O$ **(9)**: $FeCl_2 \cdot 4H_2O$ (0.2232 g, 1.12 mmol) dissolved in 3 mL distilled water was added to an aqueous solution (5 mL) of $(NH_4)_2GeF_6$ (0.25 g, 1.12 mmol) with a pinch of ascorbic acid. A pale green solution of $[Fe(H_2O)_6]GeF_6$ was obtained after stirring for a few minutes. The same procedure was used as for **1** working with NH_2trz dissolved in MeOH, affording a white precipitate. Yield: 0.5 g, 70%. *Anal.* for $FeC_6H_{14}N_{12}OGeF_6$ (513.98 g/mol): calcd. C, 14.06; H, 2.75; N, 32.78; Fe,

10.89. Found: C, 14.01; H, 2.52; N, 32.19; Fe, 9.92 %. IR (cm^{-1}): ν(NH_2) ~ 3230 (s), ν(N-N) ~ 1217 (s), ν(C-H out of plane) ~ 997 (m), ν(C-H ring torsion) = 624 (s), ν(Ge-F) ~ 600 (s).

$[Fe(NH_2trz)_3]GeF_6 \cdot 0.5H_2O$ **(10)**: It was synthesized following the same procedure as for **9** except that warm ethanol was used to dissolve NH_2trz. A white precipitated was obtained. Yield: 0.45 g, 80%. *Anal.* for $FeC_6H_{13}N_{12}O_{0.5}GeF_6$ (504.96 g/mol): calcd. C, 14.31; H, 2.60; N, 33.37; Fe, 11.09. Found: C, 14.31; H, 2.57; N, 32.38; Fe, 9.94 %. IR (cm^{-1}): ν(NH_2) ~ 3300 (s), ν(N-N) ~ 1217 (s), ν(C-H out of plane) ~ 997 (m), ν(C-H ring torsion) = 621 (s), ν(Ge-F) ~ 603 (s).

$[Cu(NH_2trz)_3]ZrF_6 \bullet H_2O$ **(11)**: A 5 ml aqueous solution of $[Cu(H_2O)_6]ZrF_6$ was obtained by stirring copper powder 0.0455 g (0.7 mmol) with 0.22 mL (0.72 mmol) of H_2ZrF_6 at room temperature for 30 minutes; the solution of which was filtered leading to a pale blue-green solution. This precursor solution was added to 10 mL aqueous solution of NH_2trz (0.1808 g, 2.15 mmol). A blue precipitate appeared after adding the first drops of the copper solution. The volume of distilled water was increased to 65 mL and the solution was warmed at 80 °C for 3 h to dissolve the precipitate. A blue solution was obtained and kept for crystallization at room temperature. After 8 months, blue needle crystals were obtained. Yield: 0.1g, 30%. IR (cm^{-1}): ν(NH_2) ~ 3230 (m), ν(N-N) ~ 1220 (m), ν(C-H out of plane) ~ 988 (m), ν(C-H ring torsion) = 625 (s), ν_1(Zr-F) ~ 590 (m).

$[Fe_3(NH_2trz)_{10}(H_2O)_2](SbF_6)_6 \cdot 1.5CH_3OH$ **(12)**: $FeCl_2 \cdot 4H_2O$ (0.3 g, 1.51 mmol) and ~ 0.01 g of ascorbic acid dissolved in 5 mL water were added to $KSbF_6$ (0.8294 g, 3.02 mmol) that was sparingly soluble in 10 mL of water. The resulting pale green solution of $[Fe(H_2O)_6](SbF_6)_2$ was added to a methanolic solution (5 mL) containing NH_2trz (0.3806 g, 4.5 mmol). An off white precipitate was formed after 10 mn of continuous stirring at r.t. It was

filtered, washed with 5-10 mL methanol and dried in a desiccator. Yield: 0.8 g, 21%. Anal. for $Fe_3C_{21.5}H_{48}N_{40}O_{3.5}Sb_6F_{12}$ (2506.88 g/mol): calcd. C, 10.30; H, 2.01; N, 22.35; Fe, 6.68. Found: C, 9.36; H, 2.64; N, 21.48; Fe, 6.5 %. IR (cm^{-1}): ν(NH_2) ~3330 (s), ν(N-N) ~ 1221 (s), ν(C-H out of plane) ~ 997 (m), ν(C-H ring torsion) = 622 (s), ν(Sb-F)~ 642, 732 (m).

$[Fe_3(NH_2trz)_{10}(H_2O)_2](SbF_6)_6 \cdot 0.5C_2H_5OH$ **(13)**: It was synthesized following the same procedure as for **12** except that ethanol was used to dissolve NH_2trz. An off white precipitated was obtained. Yield: 1 g, 27 %. *Anal.* for $Fe_3C_{21}H_{47}N_{40}O_{2.5}Sb_6F_{36}$ (2481.85 g/mol) calcd. C, 10.18; H, 1.91; N, 22.62; Fe, 6.78. Found: C, 9,82; H, 2.60; N, 21.39; Fe, 6.58. IR (cm^{-1}) : ν(NH_2) ~ 3300 (s), ν(N-N) ~ 1219, ν(C-H out of plane) ~ 1000, ν(C-H ring torsion) ~ 621(s), ν(Sb-F) ~ 745, 640 (m).

Chapter II

$[Fe(H_2O)_6]SnF_6$ which was kindly supplied by Prof. G. Levchenko, Donetsk Physical Technical Institute (Ukraine). Its hydration degree was checked by thermogravimetric measurements.

$[Fe(NH_2trz)_3]SnF_6 \cdot H_2O$ **(14):** The synthesis was carried out under nitrogen atmosphere as follows: $[Fe(H_2O)_6](SnF_6)$ (1.59 g, 4 mmol) and a few mg of ascorbic acid were heated to 65 °C in methanol (10 mL) leading to a pink solution. It was filtered and added to a warm solution of NH_2trz (1.4 g, 16.6 mmol) dissolved in methanol (10 mL). A white precipitate was instantaneously observed. The mixture was stirred at room temperature for a few hours under nitrogen atmosphere. The precipitate was filtered, washed with few mL of methanol, and dried in air leading to a white powder with slightly pinkish glints (1.43 g, 64%). Elemental analysis calcd. (%) for $FeC_6H_{14}N_{12}OSnF_6$ (558.78 g/mol): calcd. C 12.90, H 2.53, N 30.08; found: C

13.52, H 2.52, N 30.15. IR (KBr): $\nu(H_2O)$ = 3313 (s); $\nu(NH_2)$ = 3228 (s), 3114 (s); ν(CH) = 3002 (m); $\delta(NH_2)$ = 1634 (s); ν(N-NH_2) = 1218 (s); δ(C-H) = 1091 (s); ν_{ring} = 997 (s); γ(CH) = 883 (w); ν(C-H ring torsion) = 624 (vs); ν(Sn-F) = 555 (vs) cm^{-1}. UV/Vis (PTFE): λ_{max} = 838 nm ($^5E \leftarrow {}^5T_2$).

$[Fe(NH_2trz)_3]SnF_6 \cdot 0.5H_2O$ **(15):** A similar synthesis was carried out as for (**14**) leading to a slightly pink powder that was dried under vacuum in an oven at 50 °C for 30 min. After 15 min, the powder was gently ground. This process led to a white powder whose hydration degree was confirmed by TGA analyses. IR (KBr): $\nu(H_2O)$ = 3321 (s); $\nu(NH_2)$ = 3230 (s), 3114 (s); ν(CH) = 3000 (w); $\delta(NH_2)$ = 1634 (s); ν(N-NH_2) = 1218 (s); δ(C-H) = 1091 (s); ν_{ring} = 997 (s); γ(CH) = 883 (w); ν(C-H ring torsion) = 624 (vs); ν (Sn-F) = 555 (vs) cm^{-1}. UV/Vis (PTFE): λ_{max} = 838 nm ($^5E \leftarrow {}^5T_2$).

$[Fe(NH_2trz)_3]SnF_6 \cdot 1.5H_2O$ **(16):** The synthesis was carried out under nitrogen atmosphere as follows: $[Fe(H_2O)_6](SnF_6)$ (1.6 g, 4 mmol) and a few mg of ascorbic acid were heated to 65 °C in DMF (10 mL) leading to a red solution. Some drops of water were added to the solution and it turned yellow. It was filtered and a warm yellow solution of NH_2trz (1.4 g, 16.6 mmol) dissolved in DMF (10 mL) were added to this solution. A white precipitate was observed and the mixture was stirred at room temperature for one day under nitrogen atmosphere. The white precipitate was filtered, and dried in air (1.62 g, 71%). Elemental analysis calcd. (%) for $FeC_6H_{15}N_{12}O_{1.5}SnF_6$ (567.79 g/mol): calcd. C 12.87, H 2.7, N 30.03; found: C 13.27, H 2.29, N 29.82. IR (KBr): $\nu(H_2O)$ = 3317 (s); $\nu(NH_2)$ = 3329 (s), 3115 (s); ν(CH) = 2998 (m); $\delta(NH_2)$ = 1654 (s); ν(N-NH_2) = 1218 (s); δ(C-H) = 1090 (s); ν_{ring} = 996 (s); γ(CH) = 912 (w); ν(C-H ring torsion) = 624 (vs); ν(Sn-F) = 555 (vs) cm^{-1}. UV/Vis (PTFE): λ_{max} = 855 nm ($^5E \leftarrow {}^5T_2$).

Chapter III

$[Fe(NH_2trz)_3](NO_3)_2$ **(17):** $[Fe(NH_2trz)_3](NO_3)_2$ was synthesized as a pink powder using a procedure described elsewhere.[16] Before all analysis the compound was maintained in vacuum condition to remove eventual presence of surface water in $[Fe(NH_2trz)_3]NO_3)_2$. Fractional degree of hydration, when exposed to air (0.13 mol H_2O) was confirmed by TGA measurements.

$[Cu(NH_2trz)_3](NO_3)_2 \cdot H_2O$ **(18):** An aqueous solution (3 mL) of $Cu(NO_3)_2 \cdot 3H_2O$ (0.0957 g, 0.396 mmol) was added drop wise to a 2 mL aqueous solution of NH_2trz (0.1 g, 1.189 mmol) leading to a blue precipitate. After 30 min of vigorous stirring at room temperature, a blue solid was filtered off in air, washed with distilled water (2 mL) and dried in a desiccator. Yield: 0.1 g, 55%. Anal. for $CuC_6H_{14}N_{14}O_7$ (457.81g/mol): calcd. C, 15.74; H, 3.08; N, 42.83, Cu, 13.88 %. Found: C, 15.88; H, 2.98; N, 42.64, Cu, 13.2 %. IR (KBr, cm^{-1}): $\nu(NH_2)$ ~ 3305 (w), ν_3(N-O) ~ 1384 (vs), ν(N-N) ~ 1218(w), ν(C-H out of plane) ~ 985(m), ν_2(N-O) ~ 827 (w); ν (C-H ring torsion) ~ 621 (s). Single crystals of $[Cu(NH_2trz)_3](NO_3)_2 \cdot H_2O$ were obtained as follows: 10 mg of **18** was dissolved in distilled water (2 mL) and transferred in a poly(tetrafluoroethylene) container of an acid digestion bomb. The mixture was heated in an oven at 155 ˚C for 36 h. A small amount of black precipitate formed after reaction was eliminated by filtration at room temperature. The blue filtrate was allowed to stand at room temperature, and blue single crystals in form of needles were obtained by evaporation of the solvent within one week.

Chapter IV

$[Cu(OH\text{-}trz)(ReO_4)OH] \cdot 2H_2O$ (**19**): A 5 ml aqueous solution of $[Cu(H_2O)_6](ReO_4)_2$ was obtained by stirring $CuCl_2.2H_2O$ (37.5 mg, 0.219 mmol) with 4 mL aqueous solution of NH_4ReO_4 (118.0 mg, 0.439 mmol) at

room temperature for 30 minutes; the solution of which was filtered leading to a pale blue-green solution. This precursor solution was added to 4mL aqueous solution of **OH-trz** (56.1 mg, 0.659 mmol). A clear blue solution was obtained after adding the first drops of the copper precursor. The final solution was kept for crystallization at room temperature. After 12 months, blue needle crystals were obtained. Yield: 0.035 g, 35 %. (Due to limited quantity of crystals only XRD analysis was carried out).

$[Zn(OH\text{-}trz)_2Cl](NO_3)$ **(20):** A 5 ml aqueous solution of $[Zn(H_2O)_6](NO_3)_2$ (58.3 mg, 0.196 mmol) was added to 4 mL aqueous solution of OH-trz (50.0 mg, 0.588 mmol). A colorless solution was obtained after adding the precursor. The final solution was kept for crystallization at room temperature. After 2 weeks, colorless needle crystals were obtained. Yield: 0.025 g, 20 %.

$[Fe(OH\text{-}trz)_3](NO_3)_2 \cdot H_2O$ (**LOH-NO_3**): 4 mL aqueous solution of $FeSO_4 \cdot 7H_2O$ (108.9 mg, 0.39 mmol) was mixed with 4 mL aqueous solution of $Ba(NO_3)_2$ (102.4 mg, 0.39 mmol) and stirred at room temperature and in air for 5 minutes. An off white precipitate was formed instantaneously. A pale green solution of $[Fe(H_2O)_6(NO_3)_2$ was obtained after filtration in air. **OH-trz** (100.0 mg, 1.175 mmol) was dissolved in 2 mL methanolic solution. $[Fe(H_2O)_6(NO_3)_2$ solution, acidified with HNO_3 (0.1 mol/L, 1 mL), with a pinch of ascorbic acid was added with stirring to the above solution of *OH-trz*. A pink precipitate was obtained after stirred for 15 minutes room temperature and filtered, washed with 2 mL of CH_3OH/H_2O and dried under vacuum. Yield: 120 mg, 67 %. Anal. for $FeC_6H_{11}N_{11}O_{10}$ (453.07 g/mol): calcd. C, 15.91, H, 2.45, N, 34.01, Fe, 12.33 %. Found C, 15.85; H, 2.32; N, 34.00; Fe, 12.00 %. IR (KBr, cm^{-1}): υ(C=N) ~ 1540 (w), υ(N-N) ~ 1080 cm^{-1} (vs), υ(C-H ring torsion) ~ 606, 620 (m), $\upsilon_{(N\text{-}O)}$ ~ 1384(s).

$[Fe(OH\text{-}trz)_3](BF_4)_2 \cdot H_2O$ **(LOH-BF_4):** 4 mL of a pale green methanolic solution of $Fe(BF_4)_2.6H_2O$ (132.2 mg, 0.39 mmol), acidified with HBF_4 (48

%, 1 mL), with a pinch of ascorbic acid was added to 2 mL methanolic solution of *OH-trz* (100.0 mg, 1.175 mmol). A white precipitate was obtained after stirred for 5 minutes at room temperature and filtered, washed with 2 mL of CH_3OH/H_2O and dried under vacuum. Yield: 128 mg, 65 %. Anal. for $FeC_6H_{11}N_9O_4B_2F_8$ (502.67 g/mol) calcd. C, 14.34, H, 2.21, N, 25.08, Fe, 11.11 %. Found C, 14.35; H, 2.10; N, 25.01; Fe, 10.96 %. IR (KBr, cm^{-1}): υ(C=N) ~ 1566 (m), υ(N-N) ~ 1077 cm^{-1} (b), υ(C-H ring torsion) ~ 610 (m), $\upsilon_{(B-F)}$ ~ 1070 (vs, with shoulders)

$[Fe(OH\text{-}trz)_3](ClO_4)_2 \cdot H_2O$ **(LOH-ClO_4):** 4 mL of a pale green aqueous solution of $Fe(ClO_4)_2.6H_2O$ (142.1 mg, 0.39 mmol), acidified with $HClO_4$ (0.1 mol/L, 1 mL), with a pinch of ascorbic acid was added to 2 mL methanolic solution of *OH-trz* (100.0 mg, 1.175 mmol). A white precipitate was obtained after stirred for 5 minutes at room temperature and filtered, washed with 2 mL of CH_3OH/H_2O and dried under vacuum. Yield: 135 mg, 66 %. Anal. for $FeC_6H_{11}N_9O_{12}Cl_2$ (527.96 g/mol): calcd. C, 13.65, H, 2.10, N, 23.88, Fe, 10.58. Found C, 13.59; H, 2.00; N, 23.89; Fe, 10.30 %. IR (KBr, cm^{-1}): υ(C=N) ~ 1570 (w), υ(N-N) ~ 1072 cm^{-1} (b), υ(C-H ring torsion) ~ 609, 627 (m), $\upsilon_{(Cl-O)}$ ~ 1111 (vs, with shoulders).

$[Fe(OH\text{-}trz)_3](CF_3SO_3)_2 \cdot H_2O$ **(LOH-TRF):** $[Fe(H_2O)_6](CF_3SO_3)_2$ was first synthesized as a very pale green powder using a described procedure[17], starting with an aqueous solution (1 mL) containing an iron powder in excess (2 g) carefully mixed to triflic acid (5 mL, 56.5 mmol). Yield: 9.8 g, 74 %. $[Fe(H_2O)_6](CF_3SO_3)_2$ (181.1 mg, 0.39 mmol) was dissolved in CH_3OH (5 mL), acidified with CF_3SO_3H (0.1 mol/L, 1 mL) with a pinch of ascorbic acid and added to the above solution of OH-trz (100 mg, 1.175 mmol) dissolved in warmed CH_3OH (2 mL). A white precipitate was obtained after stirred for 10 minutes room temperature and filtered, washed with 2 mL of CH_3OH/H_2O and dried under vacuum. Yield: 133.5 mg, 60 %. Anal. for $FeC_8H_{11}N_9O_{10}F_6S_2$ (627.19 g/mol): calcd. C, 15.32; H, 1.77; N, 20.10; S,

10.22; Fe, 8.90 %. Found C, 15.30; H, 1.80; N, 20.12; S, 10.17; Fe, 8.75 %. IR (KBr, cm^{-1}): υ(C=N) ~ 1558 (w), υ(N-N) ~ 1073 cm^{-1} (b), υ(C-H ring torsion) ~ 609, 640 (m), $\upsilon_{(S-O)}$ ~ 1251 (vs, with shoulders).

Chapter V

$[Fe(phtptrz)_3]I_2$ (**21-phtptrz-I**): 2 mL aqueous solution of $FeCl_2.4H_2O$ (92.1 mg, 0.05 mmol) with a pinch of ascorbic acid was mixed with 2 mL aqueous solution of KI (153.9 mg, 0.10 mmol). A pale green solution was obtained after stirring at room temperature, for 5 minutes. This solution was added to 5 mL warmed methanolic solution of **phtptrz** (356.4 mg, 0.14 mmol). An off white precipitate was obtained after stirred for 15 minutes room temperature and filtered, washed with 2 mL of CH_3OH/H_2O and dried under vacuum. Yield: 290 mg, 67 %. Anal. for $FeC_{39}H_{36}N_{12}O_6I_2$ (1078.45 g/mol): calcd. C, 43.43, H, 3.36, N, 15.59, Fe, 5.18 %. Found C, 43.38; H, 3.57; N, 15.57; Fe, 4.62 %. IR (KBr, cm^{-1}): υ(C=O) ~ 1769 (m); 1711 (s), υ(C=N) ~ 1553 (m), υ(N-N) ~ 974 cm^{-1} (w), υ(C-H ring torsion) ~ 632 (m).

$[Fe(phtptrz)_3](ReO_4)_2 \cdot CH_3OH$ **(22- phtptrz-ReO_4)**: 4 mL aqueous solution of $FeCl_2.4H_2O$ (75 mg, 0.038 mmol) with a pinch of ascorbic acid was mixed with 4 mL aqueous solution of NH_4ReO_4 (202.0 mg, 0.075 mmol). A pale green solution was obtained after stirring at room temperature, for 5 minutes. This solution was added to 4 mL warmed methanolic solution of **phtptrz** (290.1 mg, 0.113 mmol). An off white precipitate was obtained after stirred for 15 minutes room temperature and filtered, washed with 2 mL of CH_3OH/H_2O and dried under vacuum. Yield: 310 mg, 59 %. Anal. for $FeC_{40}H_{40}N_{12}O_{15}Re_2$ (1357.09 g/mol): calcd. C, 35.40, H, 2.97, N, 12.39, Fe, 4.12 %. Found C, 34.21; H, 3.08; N, 11.99; Fe, 3.77 %. IR (KBr, cm^{-1}): υ(C=O) ~ 1769 (m), 1711 (s), υ(C=N) ~ 1556 (m), υ(N-N) ~ 987 cm^{-1} (w), υ(C-H ring torsion) ~ 632 (m), $\upsilon_{(Re-O)}$ ~ 1398; 910 (s).

$[Fe(phtptrz)_3](TaF_7)_2 \cdot 6H_2O$ **(23- phtptrz-TaF_7)**: 3 mL aqueous solution of $FeCl_2.4H_2O$ (87.3 mg, 0.044 mmol) with a pinch of ascorbic acid was mixed with 3 mL aqueous solution of $(NH_4)_2TaF_7$ (153.7 mg, 0.044 mmol). A pale green solution was obtained after stirring at room temperature, for 5 minutes. This solution was added to 6 mL warmed methanolic solution of **phtptrz** (337.6 mg, 0.132 mmol). An off white precipitate was obtained after stirred for 15 minutes room temperature and filtered, washed with 2 mL of CH_3OH/H_2O and dried under vacuum. Yield: 328 mg, 60 %. Anal. for $FeC_{39}H_{48}N_{12}O_{12}TaF_7$ (1246.67 g/mol): calcd. C, 37.57, H, 3.88, N, 13.48, Fe, 4.48 %. Found C, 36.71; H, 2.89; N, 12.85; Fe, 4.63 %. IR (KBr, cm^{-1}): υ(C=O) ~ 1769 (m), 1711 (s), υ(C=N) ~ 1556 (m), υ(N-N) ~ 987 cm^{-1} (w), υ(C-H ring torsion) ~ 635 (m), $\upsilon_{(Ta-F)}$ ~ 1400; 530 (s).

$[Fe(Phtptrz)_3](NO_3)_2 \cdot H_2O$ **(24-Pht-ptrz-NO_3):** 2 mL aqueous solution of $FeSO_4 \cdot 7H_2O$ (54.2 mg, 0.195 mmol) was mixed with 1 mL aqueous solution of $Ba(NO_3)_2$ (50.9 mg, 0.195 mmol) and stirred at room temperature and in air for 5 minutes. An off white precipitate was formed instantaneously. A pale green solution of $[Fe(H_2O)_6(NO_3)_2$ was obtained after filtration in air. **phtptrz** (150.0 mg, 0.585 mmol) was dissolved in 6 mL warmed methanolic solution. $[Fe(H_2O)_6(NO_3)_2$ solution with a pinch of ascorbic acid was added with stirring to the above solution of **phtptrz.** A white precipitate was obtained after stirred for 15 minutes room temperature and filtered, washed with 2 mL of CH_3OH/H_2O and dried under vacuum. Yield: 47.7 mg, 70 %. Anal. for $FeC_{39}H_{38}N_{14}O_{13}$ (966.66 g/mol): calcd. C, 48.46, H, 3.96, N, 20.29, Fe, 5.78 %. Found C, 49.35; H, 4.21; N, 20.50; Fe, 5.70 %. IR (KBr, cm^{-1}): υ(C=O) ~ 1773 (m), 1710 (s), υ(C=N) ~ 1556 (m), υ(N-N) ~ 984 cm^{-1} (w), υ(C-H ring torsion) ~ 627 (m), $\upsilon_{(N-O)}$ ~ 1383(s).

$[Fe(Phtptrz)_3](BF_4)_2 \cdot H_2O$ **(25-Pht-ptrz-BF_4):** 1 mL of a pale green aqueous solution of $Fe(BF_4)_2.6H_2O$ (65.9 mg, 0.195 mmol) with a pinch of ascorbic acid was added to 6 mL warmed methanolic solution of **phtptrz** (150.0 mg,

0.585 mmol). An off white precipitate was obtained after stirred for 15 minutes room temperature and filtered, washed with 2 mL of CH_3OH/H_2O and dried under vacuum. Yield: 158.6 mg, 80 %. Anal. for $FeC_{39}H_{38}N_{12}O_7B_2F_8$ (1016.26 g/mol): calcd. C, 46.09, H, 3.77, N, 16.54, Fe, 5.50 %. Found C, 46.35; H, 3.66; N, 16.45; Fe, 5.30 %. IR (KBr, cm^{-1}): υ(C=O) ~ 1769 (m), 1711 (s), υ(C=N) ~ 1555 (m), υ(N-N) ~ 986 cm^{-1} (b), υ(C-H ring torsion) ~ 634 (m), $\upsilon_{(B-F)}$ ~ 1087 (vs, with shoulders)

$[Fe(Phtptrz)_3](ClO_4)_2 \cdot H_2O$ **(26-Pht-ptrz-ClO_4):** 1 mL of a pale green aqueous solution of $Fe(ClO_4)_2.6H_2O$ (70.8 mg, 0.195 mmol) with a pinch of ascorbic acid was added to 6 mL warmed methanolic solution of **phtptrz** (150.0 mg, 0.585 mmol). An off white precipitate was obtained after stirred for 15 minutes room temperature and filtered, washed with 2 mL of CH_3OH/H_2O and dried under vacuum. Yield: 152.4 mg, 75 %. Anal. for $FeC_{39}H_{28}N_{12}O_{15}Cl_2$ (1041.56 g/mol): calcd. C, 44.97, H, 3.68, N, 16.14, Fe, 5.36, Cl, 6.81 %. Found C, 44.73; H, 3.59; N, 15.95; Fe, 5.4 %; Cl, 6.19. IR (KBr, cm^{-1}): υ(C=O) ~ 1769 (m), 1711 (s), υ(C=N) ~ 1548 (m), υ(N-N) ~ 988 cm^{-1} (w), υ(C-H ring torsion) ~ 622 (m), $\upsilon_{(Cl-O)}$ ~ 1104 (vs, with shoulders).

$[Fe(Phtptrz)_3](CF_3SO_3)_2 \cdot H_2O$ **(27-Pht-ptrz-TRF):** $[Fe(H_2O)_6](CF_3SO_3)_2$ was first synthesized as a very pale green powder using a described procedure[17], starting with an aqueous solution (1 mL) containing an iron powder in excess (2 g) carefully mixed to triflic acid (5 mL, 56.5 mmol). Yield: 9.8 g, 74 %. $[Fe(H_2O)_6](CF_3SO_3)_2$ (90.2 mg, 0.195 mmol) was dissolved in CH_3OH (1.5 mL) with a pinch of ascorbic acid and added to the above solution of phtptrz (150 mg, 0.585 mmol) dissolved in warmed CH_3OH (5 mL). An off white precipitate was obtained after stirred for 15 minutes room temperature and filtered, washed with 2 mL of CH_3OH/H_2O and dried under vacuum. Yield: 133.5 mg, 60 %. Anal. for $FeC_{41}H_{28}N_{12}O_{13}F_6S_2$ (1140.78 g/mol): calcd. C, 43.17; H, 3.36; N, 14.73; S, 5.62; Fe, 4.90 %. Found C, 43.14; H,

3.51; N, 14.98; S, 5.30; Fe, 4.45 %. IR (KBr, cm^{-1}): υ(C=O) ~ 1769 (m), 1711 (s), υ(C=N) ~ 1553 (m), υ(N-N) ~ 988 cm^{-1} (w), υ(C-H ring torsion) ~ 637 (m), $\upsilon_{(S-O)}$ ~ 1280, 1254 (vs, with shoulders).

$[Cu_3(phtptrz)_{10}(H_2O)_2](SiF_6)_3 \cdot 44H_2O$ (**28):** A 7 ml aqueous solution of $[Cu(H_2O)_6]SiF_6$ was obtained by stirring $Cu(CH_3COO)_2 \bullet H_2O$, 0.0348 g (0.017 mmol) with 0.0610 g (0.017 mmol) of $(NH_4)_2TaF_7$ has at room temperature for 30 minutes; the solution of which was filtered leading to a blue pale solution. To this precursor solution it was added 1 mL warmed methanolic solution of phtptrz (0.1341 g, 0.052 mmol). A blue precipitate appeared after adding the first drops of the copper solution. The volume of distilled water was increased to 20 mL, the blue colored precipitate is filtered and the filtrate is left to crystallize by slow evaporation at r.t.. After one night, blue crystals of square shape have been obtained. These crystals contain SiF_6^{2-}. This ion comes probably from the reaction between the silicium oxides of the glass by the solution containing TaF_7^{2-}. This is common type of reaction when fluorinated ions are involved.[18] Yield: 0.05 g, 20%. IR (cm^{-1}): υ(C=O) ~ 1769 (m), 1711 (s), υ(C=N) ~ 1556 (m), υ(N-N) ~ 987 cm^{-1} (w), υ(C-H ring torsion) ~ 635 (m), ν_1(Si-F) ~ 740 (s).

$[Cu_3(phtptrz)_8(H_2O)_4](ZrF_6)_3 \cdot 19H_2O$ **(29)**: An aqueous solution of $[Cu(H_2O)_6]ZrF_6$ was obtained by stirring $Cu(CH_3COO)_2 \bullet H_2O$, 0.0519 g (0.026 mmol) with 0.1 mL (0.026 mmol) of H_2ZrF_6 (50%), has at room temperature for 30 minutes; the solution of which was filtered leading to a blue pale solution. This precursor solution was added to 5 mL of warmed methanolic solution of phtptrz (0.2000 g, 0.078 mmol). A blue precipitate appeared after adding the first drops of the copper solution. The volume of distilled water was increased to 20 mL, the blue colored precipitate is filtered and the filtrate is left to crystallize by slow evaporation at r.t.. After 2 weeks blue crystals have been obtained. Yield: 0.05 g, 22%. IR (cm^{-1}): υ(C=O) ~

1767 (m), 1709 (s), υ(C=N) ~ 1550 (m), υ(N-N) ~ 987 cm^{-1} (w), υ(C-H ring torsion) ~ 630 (m), ν_1(Zr-F) ~ 590 (m).

Chapter VI

$[Cd(HGlytrz)(Glytrz)Cl]\cdot 2H_2O$ **(30)** and $[Cd_2(Glytrz)_2Cl_2]$ **(31):** An aqueous solution (3 mL) of $CdCl_2$ (0.036 g, 0.196 mmol) was added dropwise to an aqueous solution (2 mL) of **HGlytrz** (0.05 g, 0.393 mmol) affording a white precipitate. After 30 min. of efficient stirring at room temperature, the white precipitate was transferred with dried methanol (2 mL) into Teflon container that was placed in cylinder of capacity 25 mL. The closed chamber was then placed inside a preheated box furnace at 150 ˚C for 48 h. After cooling to room temperature, a colorless solution was obtained which after evaporation of the solvent afforded colorless hexagonal plates single crystals within a day (**31**). Yield: 34 mg. 35%. Anal. Calcd. for $C_4H_4N_3O_2ClCd$ (**31**) C, 17.54; H, 1.47; N, 15.34 %. Found: C, 17.18; H, 2.14; N 14.92 %. FTIR (KBr disc, cm^{-1}): 3468 (br), 3120 (s), 1698 (w), 1649 (sh), 1592 (s), 1412 (m), 1315 (m), 1033 (s), 628 (m). Diffuse reflectance spectrum (λ_{max}, nm, *vs* PTFE): 260, 290. In the absence of solvothermal treatment, the white precipitate obtained upon recrystallization from hot aq. MeOH afforded few rectangular colorless blocks (**30**). FTIR (KBr disc, cm^{-1}): 3360 (br), 1739 (s), 1618 (m), 1573 (m), 1385 (m), 1234 (s), 1042 (m), 625 (m). Because of their low yield, no further analysis was carried out except single crystal structure determination.

$[Cu_3(\mu_3\text{-}O)(HGlytrz)_6\cdot(H_2O)_3]BF_4\cdot H_2O$ (**32**)**: HGlytrz** (0.1 g) was dissolved in 8 mL of water, heated to 60°C and to this was added aq. $Cu(BF_4)_2$ (0.5 mL, excess) with stirring. The small quantity of blue precipitate that appeared was re-dissolved by the addition of 2 mL of DMF. To this blue solution, NaOH (1 eq.) in water (5 mL) was added with vigorous stirring, the

dark blue mixture thus obtained was nearly boiled for 5 min and allowed to cool to room temperature. After 4-5 days, 35 mg dark blue cubes were obtained (**32**). They were filtered, washed with water and dried in air. A crystal from the mother solution was used for X-ray crystallographic analysis. Yield: 35%. Anal. Calcd for $C_2H_2N_{1.5}O_{2.17}B_{0.25}FCu_{0.5}\cdot H_2O$ (**32**) C, 15.66; H, 1.3; N, 13.70; Cu, 20.20 %. Found: C, 15.18; H, 3.54; N 12.92; Cu, 20.72 %. FTIR (KBr disc): 3465 (br), 1650 (br,s), 1384 (s), 1306 (m), 1091 (m), 698 (w), 636 (w), 406 (w) cm^{-1}. Diffuse reflectance spectrum (λ_{max}, vs PTFE): 667, 321, 249 nm. When the same reaction was carried out with **GlytrzE**, a dark green solution with sky blue precipitate was obtained which was insoluble in common solvents and no further analysis on this precipitate was carried out as we decided to focus only on crystal samples. The slow evaporation of the filtrate led to isolation of a small quantity (10 mg) of dark blue crystals (**32**) in 2 weeks that were filtered and air dried. For unambiguous adsorption measurements it was essential to work with a pure compound, preferably a crystal sample in large amount. Multiple small scale synthesis led us to isolate 300 mg of crystal sample, which was a tedious task. SEM analysis from various batches shows the presence of microcrystals of cubic shape but of various sizes. Majority of the crystals are of roughly 50 μm^3, while crystals of 15 μm^3 were also found. It was necessary to confirm the identity of these sub-microcrystals to properly study the large batch. IR of both types of crystals is exactly similar. An energy dispersive X-ray (EDX) coupled to a SEM performed on gold coated 15 μm^3 crystals shows similar constituent pattern to that of large crystals.

Chapter VII

$[Fe_2(HGlytrz)(Glytrz)_2](ClO_4)_2\cdot 2CH_3OH$ **(33-HGlytrz-ClO_4): HGlytrz** (100 mg, 0.78 mmol) was dissolved in CH_3OH (1 mL). $Fe(ClO_4)_2.6H_2O$ (95.0 mg, 0.262 mmol) was dissolved in CH_3OH (1 mL), with a pinch of ascorbic acid and added with stirring to the above solution of **HGlytrz**. An off-white

precipitate was formed after 20 minutes of continuous stirring at room temperature, under slow stream of N_2 gas. The precipitate was filtered in air, washed with CH_3OH/Ethyl Ether (2 mL) and dried either under vacuum. Yield : 100 mg, 77 %. *Anal. Calcd*. for ($Fe_2C_{14}H_{21}N_9O_{16}Cl_2$; 493.59 g/mol); C, 22.73, H, 2.81, N, 16.72, Fe, 14.81 %; *Found* C, 22.87, H, 2.77, N, 16.89, Fe, 14.75 %. IR (KBr, cm^{-1}): υ(C=O) ~ 1751 (m), *ν*(COO^-)as. ~ 1674 (s), *ν*(COO^-)sym. ~1280 (m), υ(C=N) ~ 1563 (m), υ(C-H out of plane) ~ 1021 (m), υ(C-H ring torsion) ~ 626 (m), υ(Cl-O) ~ 1050 (s, with shoulder).

$[Fe(HGlytrz)_3](NO_3)_2 \cdot CH_3OH$ **(34-HGlytrz-NO_3):** 1 mL aqueous solution of $FeSO_4 \cdot 7H_2O$ (109.3 mg, 0.39 mmol) was mixed with 1 mL aqueous solution of $Ba(NO_3)_2$ (102.8 mg, 0.39 mmol) and stirred at room temperature and in air for 5 minutes. A white precipitate was formed instantaneously. A pale green solution of $[Fe(H_2O)_6(NO_3)_2$ was obtained after filtration in air. **HGlytrz** (150.0 mg, 1.18 mmol) was dissolved in CH_3OH (1 mL). $[Fe(H_2O)_6(NO_3)_2$ solution with a pinch of ascorbic acid was added with stirring to the above solution of **HGlytrz**. An off-white precipitate was obtained after stirred for 12 hours under slow stream of N_2 gas and filtered, washed with 2 mL of fresh CH_3OH and dried under vacuum. Yield : 100 mg, 42.8 %. Anal. Calcd. for ($FeC_{13}H_{19}N_{11}O_{13}$; 593.21 g/mol); C, 26.32, H, 3.23, N, 25.97, Fe, 9.41%; Found C, 25.34, H, 3.42, N, 26.0, Fe, 8.9 %. IR (KBr, cm^{-1}): υ(C=O) ~ 1746 (s), υ(C=N) ~ 1560 (m), υ(C-H out of plane) ~ 1025 (m), υ(C-H ring torsion) ~ 627 (m), υ(N-O) ~ 1382 (s, with shoulder).

$[Fe_2(HGlytrz)(Glytrz)_2](BF_4)_2 \cdot CH_3OH$ **(35-HGlytrz-BF_4): HGlytrz** (150 mg, 1.18 mmol) was dissolved in 1 mL of CH_3OH. $Fe(BF_4)_2.6H_2O$ (132.8 mg, 0.39 mmol) was dissolved in CH_3OH (1 mL) with a pinch of ascorbic acid and added with stirring to the above solution of **HGlytrz**. An off-white precipitate was formed after 20 minutes of continuous stirring at room temperature, under slow stream of N_2 gas. The precipitate was filtered in air, washed with CH_3OH/Ethyl Ether (2 mL) and dried either under vacuum.

Yield: 130 mg, 74.8 %. *Anal. Calcd*. for $Fe_2C_{13}H_{17}N_9O_7B_2F_8$; 696.64 g/mol); C, 22.41, H, 2.46, N, 18.10, Fe, 16.03 %; *Found* C, 21.97, H, 2.62, N, 17.38, Fe, 15.8 %. IR (KBr, cm^{-1}): υ(C=O) ~ 1746 (s), *v*(COO^-)as. ~ 1623 (s), *v*(COO^-)sym. ~1265 (m), υ(C=N) ~ 1558 (m), υ(C-H out of plane) ~ 1026 (m), υ(C-H ring torsion) ~ 623 (m), υ(B-F) ~ 1060 (s, with shoulder).

$[Fe_2(HGlytrz)(Glytrz)_2](CF_3SO_3)_2 \cdot CH_3OH$ **(36-**HGlytrz-**TRF): HGlytrz** (100 mg, 78.6 mmol) was dissolved in CH_3OH (1 mL). $[Fe(H_2O)_6](CF_3SO_3)_2$ (121.2 mg, 0.26 mmol) was dissolved in CH_3OH (1 mL), with a pinch of ascorbic acid and added with stirring to the above solution of **HGlytrz**. An off-white precipitate was formed after 30 minutes of continuous stirring at room temperature, under slow stream of N_2 gas. The precipitate was filtered in air, washed with CH_3OH/Ethyl Ether (2 mL) and dried either under vacuum. Yield: 100 mg, 74.8 %. *Anal. Calcd*. for $(C_8H_{14}N_6O_6Fe(CF_3SO_3)$; 821.16 g/mol); C, 21.94, H, 2.09, N, 15.35, Fe, 13.6 %; *Found* C, 21.45, H, 2.76, N, 15.72, Fe, 13.1 %. IR (KBr, cm^{-1}): υ(C=O) ~ 1744 (s), *v*(COO^-)as. ~ 1626 (s), *v*(COO^-)sym. ~1282 (m), υ(C=N) ~ 1558 (m), υ(C-H out of plane) ~ 1026 (m), υ(C-H ring torsion) ~ 635 (m), υ(SO_3^-) ~ 1259 (s, with shoulder).

$[Fe(GlytrzE)_3](ClO_4)_2$ **(37- GlytrzE-ClO_4)**: $Fe(ClO_4)_2.6H_2O$ (78 mg, 0.21 mmol) was dissolved in CH_3OH (2 mL) with a pinch of ascorbic acid and added with stirring to a solution of **GlytrzE** (100 mg, 0.64 mmol) dissolved in CH_3OH (5 mL). The immediate white precipitate which was obtained was stirred for 10 min and filtered, washed with CH_3OH (2 mL) and dried *under vacuum*. Yield: 100 mg, 83 %. Anal. for $FeC_{18}H_{27}N_9O_{14}FeCl_2$ (720.22 g/mol): calcd. C, 30.02; H, 3.78; N, 17.5; Fe, 7.9%. Found C, 29.06; H, 3.74; N, 16.90; Fe, 7.5%. IR (KBr, cm^{-1}): υ(C=O) ~ 1747 (vs), υ(C-O) ~ 1240 (vs), υ(C=N) ~ 1560 (m), υ(C-H out of plane) ~ 1026 (m), υ(C-H ring torsion) ~ 625 (m), υ(Cl-O) ~ 1105 (s, with shoulder).

$[Fe(GlytrzE)_3](ClO_4)_2 \cdot CH_3OH$ **(38- GlytrzE-ClO_4):** The same procedure as for **37** was applied except that the precipitate was dried under a slow stream of $N_{2(g)}$. Yield: 100 mg, 83 %. Anal. for $FeC_{19}H_{31}N_9O_{15}Cl_2$ (752.26 g/mol): calcd. C, 30.34; H, 4.15; N, 16.76; Fe, 7.4%. Found C, 30.01; H, 3.92; N, 16.60; Fe, 7.30%. IR (KBr, cm^{-1}): υ(C=O) ~ 1747 (vs), υ(C-O) ~ 1240 (vs), υ(C=N) ~ 1560 (m), υ(C-H out of plane) ~ 1026 (m), υ(C-H ring torsion) ~ 625 (m), υ(Cl-O) ~ 1105 (s, with shoulder).

$[Fe(GlytrzE)_3](NO_3)_2 \cdot H_2O$ **(39-GlytrzE-NO_3):** An aqueous solution (1 mL) of $FeSO_4 \cdot 7H_2O$ (59.5 mg, 0.21 mmol) was mixed with an aqueous solution (1mL) of $Ba(NO_3)_2$ (56.0 mg, 0.21 mmol) and stirred at room temperature and in air for 5 min. A white precipitate was formed instantaneously, which was filtered in air and digested to afford a pale green solution of $[Fe(H_2O)_6(NO_3)_2$. This solution with a pinch of ascorbic acid was added with stirring to a solution of **GlytrzE** (100.0 mg, 0.64 mmol) dissolved in CH_3OH (1 mL). A pink precipitate was obtained after stirring for 2 h under a slow stream of $N_{2(g)}$ and filtered, washed with CH_3OH (2 mL) and dried under vacuum at room temperature. Yield: 95 mg, 68.7 %. Anal. for $FeC_{18}H_{27}N_{13}O_{13}$ (663.34 g/mol): calcd. C, 32.57; H, 4.41; N, 23.23; Fe, 8.43 %. Found C, 32.68; H, 4.36; N, 22.80; Fe, 8.35. IR (KBr, cm^{-1}): υ(C=O) ~ 1747 (vs), υ(C-O) ~ 1226 (vs), υ(C=N) ~ 1560 (m), υ(C-H out of plane) ~ 1028 (m), υ(C-H ring torsion) ~ 636 (m), υ(N-O) ~ 1384 (s, with shoulder).

$[Fe(GlytrzE)_3](NO_3)_2$ **(40-GlytrzE-NO_3):** The synthesis of this compound was identical as for **39-GlytrzE-NO_3** except that the precipitate was dried under vacuum at 40°C. Yield: 105 mg, 76 %. Anal. for $FeC_{18}H_{27}N_{13}O_{13}$ (663.34 g/mol): calcd. C, 32.57; H, 4.41; N, 23.23; Fe, 8.43 %. Found C, 32.68; H, 4.36; N, 22.80; Fe, 8.35. IR (KBr, cm^{-1}): υ(C=O) ~ 1747 (vs), υ(C-O) ~ 1226 (vs), υ(C=N) ~ 1560 (m), υ(C-H out of plane) ~ 1028 (m), υ(C-H ring torsion) ~ 636 (m), υ(N-O) ~ 1384 (s, with shoulder).

$[Fe(GlytrzE)_3](BF_4)_2 0.5H_2O$ **(41-GlytrzE-BF_4):** $Fe(BF_4)_2.6H_2O$ (72.5 mg, 0.21 mmol) was dissolved in CH_3OH (2 mL) with a pinch of ascorbic acid and added to a solution of **GlytrzE** (100 mg, 0.64 mmol) dissolved in CH_3OH (5 mL). The mixture was stirred for 20 min at room temperature after which a pale pink precipitate was obtained. It was filtered, washed with CH_3OH (2 mL) and dried under *vacuum* for 2 h. Yield: 90 mg, 60 %. Anal. for $FeC_{18}H_{28}N_9O_{6.5}B_2F_8$ (703.93 g/mol): calcd. C, 30.71, H, 4.01, N, 17.91, Fe, 7.93 %. Found C, 30.72; H, 3.83; N, 17.89; Fe, 7.9 %. IR (KBr, cm^{-1}): υ(C=O) ~ 1747 (vs), υ(C-O) ~ 1226 (vs), υ(C=N) ~ 1562 (m), υ(C-H out of plane) ~ 1031 (m), υ(C-H ring torsion) ~ 634 (m), $\upsilon_{(B-F)}$ ~ 522 (w), 1083 (vs, with shoulders).

$[Fe(GlytrzE)_3](BF_4)_2$ **(42-GlytrzE-BF_4)**: The same procedure as for **41-GlytrzE-BF_4** was followed except that the precipitate was dried under *vacuum* for 2 days. Yield: 25 mg, 17 %. Anal. Calcd. for $(C_{18}H_{27}N_9O_6Fe(BF_4)_2$; 694.92 g/mol); C, 31.11, H, 3.92, N, 18.14, Fe, 8.04 %; Found C, 31.05, H, 3.80, N, 18.01, Fe, 8.1 %. IR (KBr, cm^{-1}): υ(C=O) ~ 1747 (vs), υ(C-O) ~ 1226 (vs), υ(C=N) ~ 1562 (m), υ(C-H out of plane) ~ 1031 (m), υ(C-H ring torsion) ~ 634 (m), $\upsilon_{(B-F)}$ ~ 522 (w), 1083 (vs, with shoulders).

$[Fe(GlytrzE)_3](CF_3SO_3)_2 \cdot 2H_2O$ **(43-Glytrz-TRF):** $[Fe(H_2O)_6](CF_3SO_3)_2$ was first synthesized as a very pale green powder using a described procedure[17], starting with an aqueous solution (1mL) containing an iron powder in excess (2 g) carefully mixed to triflic acid (5 mL, 56.5 mmol). Yield: 9.8 g, 74 %. $[Fe(H_2O)_6](CF_3SO_3)_2$ (99.2 mg, 0.21 mmol) was dissolved in CH_3OH (2 mL) with a pinch of ascorbic acid and added to the above solution of **GlytrzE** (100 mg, 0.64 mmol) dissolved in CH_3OH (5 mL). The mixture was stirred for 20 min at room temperature, after which a pale-pink precipitate was obtained. It was filtered, washed with CH_3OH (2 mL) and dried under *vacuum*. Yield: 150 mg, 69 %. Anal. for $FeC_{20}H_{31}N_9O_{14}F_6S_2$ (855.48 g/mol):

calcd. C, 28.08; H, 3.65; N, 14.74; Fe, 6.53%. Found C, 27.99; H, 3.32; N, 14.26; Fe, 6.2%. IR (KBr, cm^{-1}): υ(C=O) ~ 1749 (vs), υ(C-O) ~ 1226 (vs), υ(C=N) ~ 1564 (m), υ(C-H out of plane) ~ 1030 (m), υ(C-H ring torsion) ~ 632 (m), $\upsilon_{(S-O)}$ ~ 1251 (vs, with shoulders).

Chapter VIII

$[Fe(\beta Alatrz)_3](CF_3SO_3)_2 \cdot 0.5H_2O$ **(44·0.5H_2O):** $[Fe(H_2O)_6]$ $(CF_3SO_3)_2$ was first synthesized as a very pale green powder using a described procedure[17], $[Fe(H_2O)_6](CF_3SO_3)_2$ (183.2 mg, 0.396 mmol) was dissolved in CH_3OH (5 mL) with a pinch of ascorbic acid and added to the above solution of **βAlatrz** (205.7 mg, 1.216 mmol) dissolved in CH_3OH (5 mL). The mixture was stirred for 15 min at room temperature, after which a white precipitate was obtained. It was filtered, washed with CH_3OH (2 mL) and dried in air. Yield: 265.9 mg, 75.4 %. Anal. for $FeC_{23}H_{34}N_9O_{12.5}F_6S_2$ (870.54 g/mol): calcd. C, 31.73; H, 3.94; N, 14.48; F, 13.09; S, 7.37; Fe, 6.42 %. Found C, 31.64; H, 3.76; N, 14.41; F, 12.12; S, 6.37; Fe, 6.59 %. IR (KBr, cm^{-1}): υ(C=O) ~ 1732 (vs), υ(C-O) ~ 1211, 1093 (s), υ(C=N) ~ 1560 (m), υ(C-H out of plane) ~ 1028 (m), υ(C-H ring torsion) ~ 632 (m), $\upsilon_{(S-O)}$ ~ 1282, 1255 (vs, with shoulders).

$[Fe(\beta Alatrz)_3](CF_3SO_3)_2$ **(45):** Anal. for $FeC_{23}H_{33}N_9O_{12}F_6S_2$ (861.53 g/mol): calcd. C, 32.07; H, 3.86; N, 14.63; F, 13.23; Fe, 6.48 %. Found C, 31.87; H, 3.82; N, 14.49; F, 13.13; Fe, 6.44 %. IR (KBr, cm^{-1}): υ(C=O) ~ 1732 (vs), υ(C-O) ~ 1211, 1093 (s), υ(C=N) ~ 1560 (m), υ(C-H out of plane) ~ 1028 (m), υ(C-H ring torsion) ~ 632 (m), $\upsilon_{(S-O)}$ ~ 1282, 1255 (vs, with shoulders).

$[Fe(\beta Alatrz)_3](ClO_4)_2 \cdot H_2O$ **(46·H_2O):** $Fe(ClO_4)_2.6H_2O$ (147.2 mg, 0.406 mmol) was dissolved in CH_3OH (2 mL) with a pinch of ascorbic acid and

added with stirring to a solution of **βAlatrz** (201.8 mg, 1.19 mmol) dissolved in CH_3OH (2 mL). The immediate white precipitate which was obtained was stirred for 15 min and filtered, washed with CH_3OH (2 mL) and dried in air. Yield: 295.7 mg, 95.3 %. Anal. for $FeC_{21}H_{35}N_9O_{15}Cl_2$ (780.31 g/mol): calcd. C, 32.32; H, 4.52; N, 16.16; Fe, 7.16 %. Found C, 32.83; H, 4.35; N, 16.31; Fe, 7.0 %. IR (KBr, cm^{-1}): υ(C=O) ~ 1732 (vs), υ(C-O) ~ 1213(vs), υ(C=N) ~ 1558 (m), υ(C-H out of plane) ~ 1024 (m), υ(C-H ring torsion) ~ 637 (m), υ(B-F) ~ 1024 (s, with shoulder).

$[Fe(\beta Alatrz)_3](BF_4)_2 \cdot 2H_2O$ **(47·H_2O):** $Fe(BF_4)_2.6H_2O$ (115.6 mg, 0.34 mmol) was dissolved in CH_3OH (2 mL) with a pinch of ascorbic acid and added to a solution of **βAlatrz** (171.5 mg, 1.013 mmol) dissolved in CH_3OH (2 mL). The mixture was stirred for 15 min at room temperature after which a white precipitate was obtained. It was filtered, washed with CH_3OH (2 mL) and dried in air. Yield: 233.2 mg, 89.3 %. Anal. for $FeC_{21}H_{37}N_9O_8B_2F_8$ (773.03 g/mol): calcd. C, 32.63, H, 4.82, N, 16.31, Fe, 7.22 %. Found C, 32.60; H, 4.35; N, 16.13; Fe, 7.10 %. IR (KBr, cm^{-1}): υ(C=O) ~ 1731 (vs), υ(C-O) ~ 1213, 1095 (vs), υ(C=N) ~ 1560 (m), υ(C-H out of plane) ~ 1027 (m), υ(C-H ring torsion) ~ 638 (m), $\upsilon_{(B-F)}$ ~ 1059 (vs, with shoulders).

$[Fe(\beta Alatrz)_3](BF_4)_2$ **(48):** Anal. for $FeC_{21}H_{33}N_9O_6B_2F_8$ (737.00 g/mol): calcd. C, 34.18, H, 4.51, N, 17.10, Fe, 7.59 %. Found C, 33.36; H, 4.50; N, 16.56; Fe, 7.35 %. IR (KBr, cm^{-1}): υ(C=O) ~ 1731 (vs), υ(C-O) ~ 1213, 1095 (vs), υ(C=N) ~ 1560 (m), υ(C-H out of plane) ~ 1027 (m), υ(C-H ring torsion) ~ 638 (m), $\upsilon_{(B-F)}$ ~ 1059 (vs, with shoulders).

Notes and references

[1] A. Rotaru, M. M. Dîrtu, C. Enachescu, R. Tanasa, J. Linares, A. Stancu, Garcia Y. *Polyhedron* **2009**, *28*, 2531.
[2] K. H. Breuer, W. Eysel. *Thermochim. Acta* **1982**, *57*(3), 317-329.
[3] E. Koenig, G. Ritter, W. Irler, H. A. Goodwin. *J. Am. Chem. Soc.* **1980**, *102*(14), 4681-4687.
[4] A. Boultif, D. Louer. *J. Appl. Cryst.* **2004**, *37*(5), 724-731.
[5] E. W. Washburn. *Phys. Rev.* **1921**, *17*, 273-283.
[6] J. Jeftic, N. Menendez, A. Wack, E. Codjovi, J. Linares, A. Goujon, G. Hamel, S. Klotz, G. Syfosse, F. Varret. *Measurement Science and Technology* **1999**, *10*(11), 1059.
[7] R. Tanasa, A. Stancu, J. F. Letard, E. Codjovi, J. Linares, F. Varret. *Chem. Phys. Lett.* **2007**, *443*, 435.
[8] Teillet, J. and Varret, F. Mossfit. 2004.
[9] Lagarec, K. and Rancourt, D. G. *Recoil, Mössbauer Spectral Analysis Software for Windows*. [1.0]. 1998. Department of Physics, University of Ottawa, Canada.
[10] Sheldrick, G. M. Program for crystal structure refinement. 1997. University of Göttingen: Göttingen, Germany.
[11] Oxford Diffraction. *CRYSALIS RED* v.1.71. 2004. Oxford, UK, Oxford Diffraction Ltd.
[12] M. C. Burla, R. Caliandro, M. Camalli, B. Carrozzini, G. L. Cascarano, L. De Caro, C. Giacovazzo, G. Polidori, R. J. Spagna. *J. Appl. Crystallogr.* **2005**, (38), 381.
[13] Cromer, D. T. and Waber, J. T. International Tables for X-ray Crystallography, IV; Table 2.2 A and Table 2.3.1 . 1974. England, Kynoch Press Birmingham.
[14] R. K. Bartlett, I. R. Humphrey. *J. Chem. Soc. C* **1967**, 1664-1666.
[15] A. D. Naik, J. Marchand-Brynaert, Y. Garcia. *Synthesis* **2008**, *1*, 149-154.
[16] L.G.Lavrenova, V. N. Ikorskii, V. A. Varnek, I. M. Oglezneva, S. V. Larionova. *Koord. Khim.* **1986**, *12*, 207.
[17] K. S. Hagen. *Inorg. Chem.* **2000**, *39*(25), 5867-5869.
[18] K. Drabent, Z. Ciunik. *Chem. Commun.* **2001**, (14), 1254-1255.